



Acta Chimica Slo Acta Chimica Slo Slovenica Acta C

2

65/2018



EDITOR-IN-CHIEF

KSENIJA KOGEJ

Slovenian Chemical Society, Hajdrihova 19, SI-1000 Ljubljana, Slovenija,

E-mail: ACSi@fkt.uni-lj.si, Telephone: (+386)-1-479-8538

ASSOCIATE EDITORS

Janez Cerkovnik, University of Ljubljana, Slovenia

Krištof Kranjc, University of Ljubljana, Slovenia

Ksenija Kogej, University of Ljubljana, Slovenia

Franc Perdih, University of Ljubljana, Slovenia

Aleš Podgornik, University of Ljubljana, Slovenia

Helena Prosen, University of Ljubljana, Slovenia

Damjana Rozman, University of Ljubljana, Slovenia

Melita Tramšek, Jožef Stefan Institute, Slovenia

Irena Vovk, National Institute of Chemistry, Slovenia

ADMINISTRATIVE ASSISTANT

Marjana Gantar Albreht, National Institute of Chemistry, Slovenia

EDITORIAL BOARD

Wolfgang Buchberger, Johannes Kepler University, Austria

Alojz Demšar, University of Ljubljana, Slovenia

Stanislav Gobec, University of Ljubljana, Slovenia

Marko Goličnik, University of Ljubljana, Slovenia

Günter Grampp, Graz University of Technology, Austria

Wojciech Grochala, University of Warsaw, Poland

Danijel Kikelj, Faculty of Pharmacy, Slovenia

Janez Košmrlj, University of Ljubljana, Slovenia

Blaž Likozar, National Institute of Chemistry, Slovenia

Mahesh K. Lakshman, The City College and

The City University of New York, USA

Janez Mavri, National Institute of Chemistry, Slovenia

Friedrich Sreinc, University of Minnesota, USA

Walter Steiner, Graz University of Technology, Austria

Jurij Svete, University of Ljubljana, Slovenia

Ivan Švancara, University of Pardubice, Czech Republic

Jiri Pinkas, Masaryk University Brno, Czech Republic

Gašper Tavčar, Jožef Stefan Institute, Slovenia

Christine Wandrey, EPFL Lausanne, Switzerland

Ennio Zangrando, University of Trieste, Italy

ADVISORY EDITORIAL BOARD

Chairman

Branko Stanovnik, Slovenia

Members

Josef Barthel, Germany

Udo A. Th. Brinkman, The Netherlands

Attilio Cesaro, Italy

Dušan Hadži, Slovenia

Vida Hudnik, Slovenia

Venčeslav Kaučič, Slovenia

Željko Knez, Slovenia

Radovan Komel, Slovenia

Janez Levec, Slovenia

Stane Pejovnik, Slovenia

Anton Perdih, Slovenia

Slavko Pečar, Slovenia

Andrej Petrič, Slovenia

Boris Pihlar, Slovenia

Milan Randić, Des Moines, USA

Jože Škerjanc, Slovenia

Miha Tišler, Slovenia

Durđa Vasić-Rački, Croatia

Marjan Veber, Slovenia

Gorazd Vesnaver, Slovenia

Jure Zupan, Slovenia

Boris Žemva, Slovenia

Majda Žigon, Slovenia

Acta Chimica Slovenica is indexed in: *Chemical Abstracts Plus*, *Current Contents (Physical, Chemical and Earth Sciences)*, *PubMed*, *Science Citation Index Expanded* and *Scopus*. Impact factor for 2016 is IF = 0.983.



Articles in this journal are published under Creative Commons Attribution 3.0 License

<http://creativecommons.org/licenses/by/3.0/>

Izdaja – Published by:

SLOVENSKO KEMIJSKO DRUŠTVO – SLOVENIAN CHEMICAL SOCIETY

Naslov redakcije in uprave – Address of the Editorial Board and Administration

Hajdrihova 19, SI-1000 Ljubljana, Slovenija

Tel.: (+386)-1-476-0252; Fax: (+386)-1-476-0300; E-mail: chem.soc@ki.si

Izdajanje sofinancirajo – Financially supported by:

Slovenian Research Agency, Ljubljana, Slovenia

National Institute of Chemistry, Ljubljana, Slovenia

Jožef Stefan Institute, Ljubljana, Slovenia

Faculty of Chemistry and Chemical Technology at University of Ljubljana, Slovenia

Faculty of Chemistry and Chemical Engineering at University of Maribor, Slovenia

Faculty of Pharmacy at University of Ljubljana, Slovenia

University of Nova Gorica, Nova Gorica, Slovenia



Acta Chimica Slovenica izhaja štirikrat letno v elektronski obliki na spletni strani <http://acta.chem-soc.si>. V primeru posvečenih števil izhaja revija tudi v tiskani obliki v omejenem številu izvodov.

Acta Chimica Slovenica appears quarterly in electronic form on the web site <http://acta.chem-soc.si>. In case of dedicated issues, a limited number of printed copies are issued as well.

Transakcijski račun: 02053-0013322846 Bank Account No.: SI56020530013322846-Nova Ljubljanska banka d. d., Trg republike 2, SI-1520 Ljubljana, Slovenia, SWIFT Code: LJBA SI 2X

Oblikovanje ovitka – Design cover: KULT, oblikovalski studio, Simon KAJTNA, s. p. Grafična priprava za tisk: Majanafin, d. o. o.

Tisk-Printed by: Tiskarna Stušek, Ljubljana

© Copyright by Slovenian Chemical Society

Dear authors, readers and reviewers of *Acta Chimica Slovenica*



Thanks to previous editorial teams, Editors-in-Chief, Advisory Board members and to devoted Slovenian chemists, *Acta Chimica Slovenica* (ACSi) is today a leading Slovenian journal in the broad field of chemistry. A lot of effort has been invested over the years to increase the quality of the journal and to make it internationally recognized. Previous Editorials summarize all the important achievements, milestones and people in the history of ACSi, who deserve thanks for this. It is not my intention to repeat all that in order not to miss even the smallest merit. In the extremely competitive field of scientific publishing, *Acta Chimica Slovenica* has an impact factor fluctuating around 1 and attracts contributions of scientists from Slovenia and abroad. From its inception, ACSi was a venue publishing mostly research works of Slovenian chemists, but it later developed into an international journal that nowadays publishes more articles contributed by foreign scientists. The interest of the latter to publish in ACSi has increased tremendously and along with that also the working load of the Associate Editors. In the first half of 2018, we have received almost 400 manuscripts, out of which around 80% are sent back to the authors already at the first stage of the reviewing process because they do not fulfill technical requirements of the journal or, which is more seldom, do not fit in the scope of the journal. This tells clearly that in order to keep the high level and regular appearance of the journal, the team of Associate Editors, together with reviewers and authors, has to work devotedly.

I would like to share some news about activities and changes in ACSi that happened since I took over as the Editor-in-Chief (EiC) in January 2018. Due to high costs of printing and limited financial funds, we had to stop with the production of hard copy issues of the journal. Now the journal is available only as an on-line version, except for issues dedicated to prominent Slovenian and other scientists; these will still be delivered also in a limited number of printed copies. At the same time we have introduced e-mail alerts of new issues that are distributed to members of the Slovenian Chemical Society and to all authors of manuscripts in that issue. Hopefully, such alerts will have a positive effect on the popularity and reading of the journal and will fill the gap that appeared after omitting hard copies.

In an effort to help authors to prepare better manuscripts we have updated Author Guidelines and we invite all to read them carefully before submitting your papers to ACSi. In strive for high quality of our journal, the most important concern of the Associate Editors and also of the authors themselves should be publishing original, innovative and high impact research. This requires competent and diligent reviewers, who freely devote their time to review the manuscripts and thus help authors and editors to produce better papers. We are truly indebted to the reviewers, as we know that reviewing is the critical and most time consuming step in this process. I take this opportunity to invite members of the Editorial and Advisory Boards of ACSi to help the Associate Editors in this task, if they are asked for advice or appraisal of contributions to the journal. With their comprehensive scientific experiences they can only enrich the magazine.

In addition to publishing Reviews, Scientific and Technical Articles and Short Communications, we have introduced a new type of contributions, Feature Articles (FAs), which are written on invitation of the editorial team. They should report on the latest activity of the author and his/her research group bearing the broad scope of ACSi in mind. The present issue of *Acta Chimica Slovenica* features a cover picture and the first Feature Article in this category written by our colleague Damjana Rozman and co-authors and offers an opportunity to promote this type of articles

to the readers of *ACSi*. The group of Damjana Rozman has received the award for one of the most excellent research achievements at the University of Ljubljana in 2017 for their work in the field of computational modelling of liver metabolism. We believe that such achievements should be honored and we are pleased that the authors were willing to make this contribution to *ACSi*. The ambition of the Associate Editors team is to have one (or possibly more) Feature Article in each issue. We therefore motivate all authors, readers, reviewers and other members of the scientific community to send short proposals for Feature Articles to the editorial board of *ACSi* for their consideration. At this point, I invite our colleagues from industry to participate as well by reporting on technologically important findings and innovations.

Some of the changes in *ACSi* are yet to happen, hopefully still in 2018. We would like to upgrade the web-page of *ACSi* and make it more contemporary, attractive and user friendly. This part depends on financial funds that have decreased substantially in the last years. *ACSi* is issued by the Slovenian Chemical Society (SCS), through which also the costs of journal production are covered with financial contributions from Slovenian Research Agency, National Institute of Chemistry, Jožef Stefan Institute, Slovenian Faculties, and other beneficiaries. The new president of SCS Albin Pintar is very cooperative in this

respect and understands that fast dissemination of scientific papers using new tools is nowadays the key to success. I hope that with our joint efforts *Acta Chimica Slovenica* will grow in its value and presence in the scientific community.

Finally, I have to say that the activities with which the editorial team of *ACSi* has started in 2018 would not be possible without inputs and hard work of the previous Editors of *ACSi*. Their dedicated work has put *ACSi* on the map of scientific publishing in pure and applied chemistry. Only on such solid foundations can we build on. I would sincerely like to thank the previous EiC Aleksander Pavko, for helping me do the first steps as the EiC and mediating to me his rich experience in editorship. Without his continuous help and encouragement my beginning would definitely be more difficult, so as without the always timely support of our administrative assistant Marjana Albreht Gantar and technical editor Stanislav Oražem. At the same time the group of Associate Editors of *ACSi* is really excellent and teaches me all what I do not know yet in the field of scientific publishing. Our common goal is to further improve *Acta Chimica Slovenica* through your help as well.

Ksenija Kogej
Editor-in-Chief
June 20, 2018

Graphical Contents



Acta Chimica Slo
Acta Chimica Slo
Slovenica Acta C

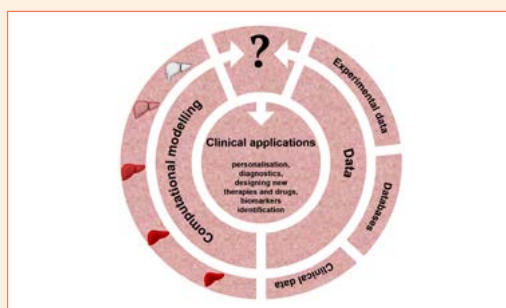
Year 2018, Vol. 65, No. 2

FEATURE ARTICLE

253–265 Biochemistry and molecular biology

Computational Modelling of Liver Metabolism and its Applications in Research and the Clinics

Tanja Cvitanović Tomaš, Miha Moškon, Miha Mraz and Damjana Rozman



SCIENTIFIC PAPER

266–270 General chemistry

The Antioxidant Response System in Wheat Exposed to Pesticides and its Combined-induced Oxidative Damage

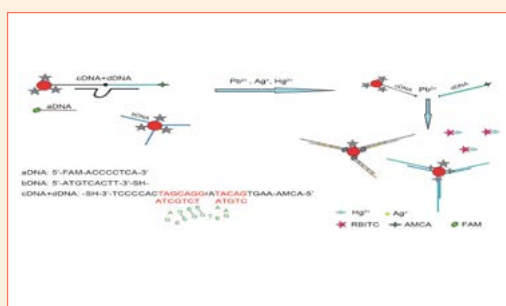
Nilgün Candan Yücel, Elif Hakli Heybet and Ozay Ozgür Gokmen

Antioxidant Enzyme Activities			
Groups	SOD (IU/mg)	CAT (IU/mg)	GSH-Px 10^3 (IU/mg)
control	61.43	132.23	51.31
1 mg kg ⁻¹ CP	96.87 **	211.36**	59.30
15 mg kg ⁻¹ CP	82.18	150.62	29.03**
5 mg kg ⁻¹ DM	76.14	147.79	78.68**
35 mg kg ⁻¹ DM	116.51**	306.41**	71.27
1 mg kg ⁻¹ CP+ 5 mg kg ⁻¹ DM	118.09**	160.00	64.53

271–277 Analytical chemistry

Simultaneous Sensitive Detection of Lead(II), Mercury(II) and Silver Ions Using a New Nucleic Acid-Based Fluorescence Sensor

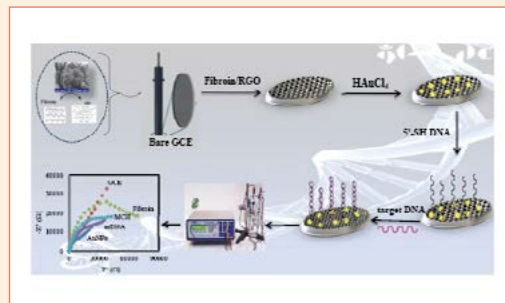
Yuan Deng, Yinran Chen and Xiaodong Zhou



278–288 Analytical chemistry

A Highly Selective DNA Sensor Based on Graphene Oxide-Silk Fibroin Composite and AuNPs as a Probe Oligonucleotide Immobilization Platform

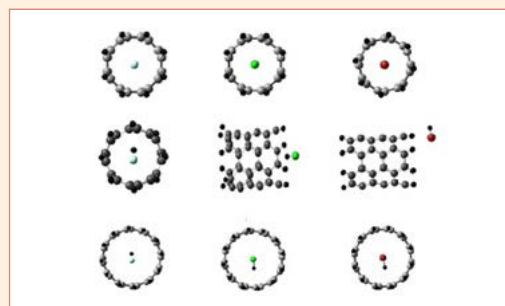
Ali Benvidi, Zohreh Abbasi, Marzieh Dehghan Tezerjani, Maryam Banaei, Hamid Reza Zare, Hossein Molahosseini and Shahriar Jahanbani



289–295 Physical chemistry

Interaction of HF, HBr, HCl and HI Molecules with Carbon Nanotubes

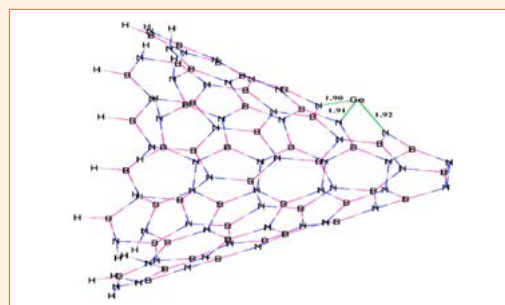
Wiem Felah Gtari and Bahoueddine Tangour



296–302 Physical chemistry

Theoretical Study of Ability of Boron Nitride Nanocone to Oxidation of Sulfur Monoxide

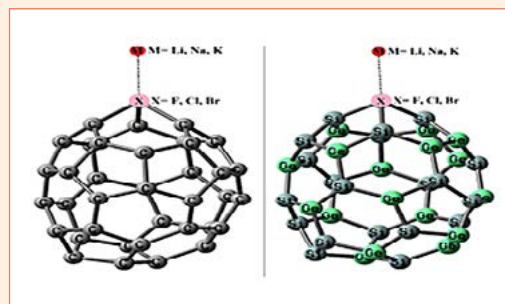
Xuewu Zuo, Kouros Behradfar, Jia-Bao Liu, Milad Janghorban Lariche and Meysam Najafi



303–311 Physical chemistry

Possibility of C_{38} and $Si_{19}Ge_{19}$ Nanocages in Anode of Metal Ion Batteries: Computational Examination

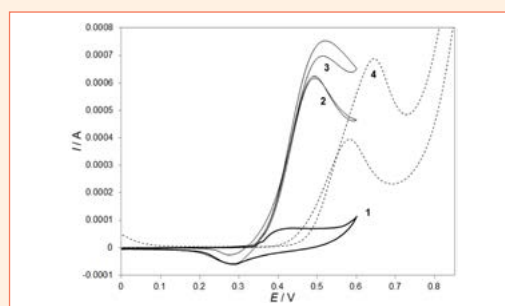
Rong-Jun Bie, Muhammad Kamran Siddiqui, Razieh Razavi, Milad Taherkhani and Meysam Najafi



312–318 Applied chemistry

Effect of Copper Alloying on Electro-Catalytic Activity of Nickel for Ethanol Oxidation in Alkaline Media

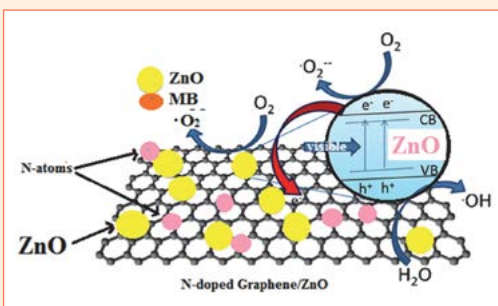
Niloufar Bahrami Panah, Iman Danaee, Mahmood Payehghadr and Afroz Madahi



319–327 Materials science

Solvothermal Synthesis of ZnO-Nitrogen Doped Graphene Composite and its Application as Catalyst for Photodegradation of Organic Dye Methylene Blue

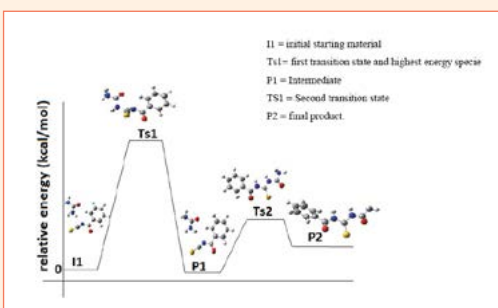
Rajinder Singh, Manesh Kumar, Heena Khajuria, Jigmet Ladol, and Haq Nawaz Sheikh



328–332 Physical chemistry

DFT Study of the Reaction Mechanism of N-(Carbonylcarbamothioyl) Benzamide

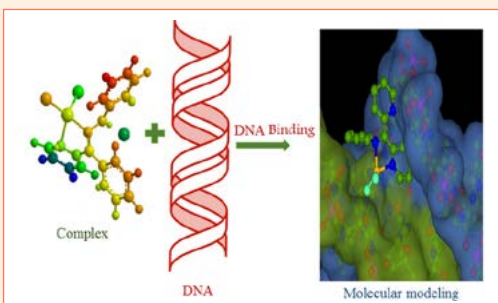
Felix Odame



333–343 Inorganic chemistry

Biological Significance of Hetero-Scaffolds Based Gold(III) Complexes

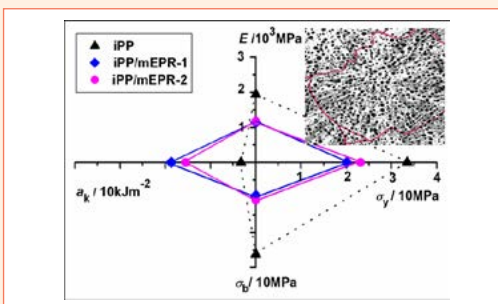
Darshana N. Kanthecha, Dilip B. Raval, Vasudev R. Thakkar and Mohan N. Patel



344–353 Materials science

Polypropylene Blends with m-EPR Copolymers: Mechanical and Rheological Properties

Iztok Švab, Anđela Pustak, Matjaž Denac, Andrijana Sever Škapin, Mirela Leskovic, Vojko Musil and Ivan Šmit



354–364 General chemistry

Capsicum annuum Fruit Extract: A Novel Reducing Agent for the Green Synthesis of ZnO Nanoparticles and Their Multifunctional Applications

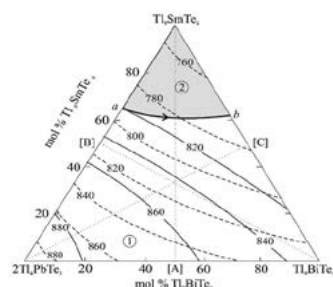
Haraluru Shankraiah Lalithamba, Mahadevaiah Raghavendra, Kogali Uma, Kalanakoppal Venkatesh Yatish, Das Mousumi, and Govindappa Nagendra



365–371 Inorganic chemistry

Phase Equilibria in the Tl_4PbTe_3 - Tl_9SmTe_6 - Tl_9BiTe_6 Section of the Tl-Pb-Bi-Sm-Te System

Samira Zakir Imamaliyeva, Alakbarzade Ganira Ilgar, Mahmudova Matanat Aydin, Amiraslanov Imameddin Rajabali and Mahammad Baba Babanly



372–379 Inorganic chemistry

Synthesis, X-ray Structural Characterization, and DFT Calculations of Mononuclear Nickel(II) Complexes Containing Diamine and Methacrylate Ligands

Rasoul Vafazadeh, Mansoor Namazian, Behnoosh Shahpoori-Arani, Anthony C. Willis and Paul D. Carr



380–387 Analytical chemistry

Determination of Titanium Dioxide Content in Bauxites Using X-ray Fluorescence Spectrometry by Fusion and by Pressing

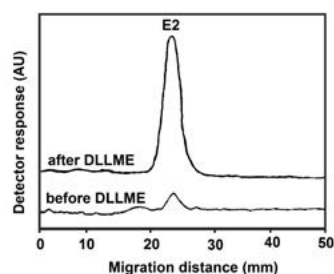
Dragana Blagojević, Dragica Lazić, Dragana Kešelj, Gordana Ostojić and Mugdin Imamović



388–393 Analytical chemistry

Thin-Layer Chromatography: an Efficient Technique for the Optimization of Dispersive Liquid-Liquid Microextraction

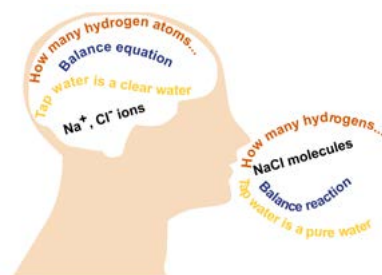
Elena Kupcová, Katarína Reiffová and Yaroslav Bazel



394–400 General chemistry

The Accuracy of Macro–Submicro–Symbolic Language of Future Chemistry Teachers

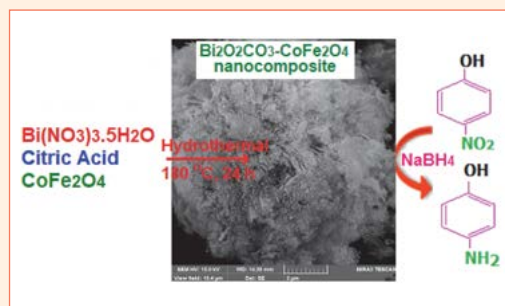
Dušica D. Rodić, Tamara N. Rončević and Mirjana D. Segedinac



448–461 Materials science

Hydrothermal Synthesis of Novel Magnetic Plate-Like $\text{Bi}_2\text{O}_2\text{CO}_3/\text{CoFe}_2\text{O}_4$ Hybrid Nanostructures and Their Catalytic Performance for the Reduction of Some Aromatic Nitrocompounds

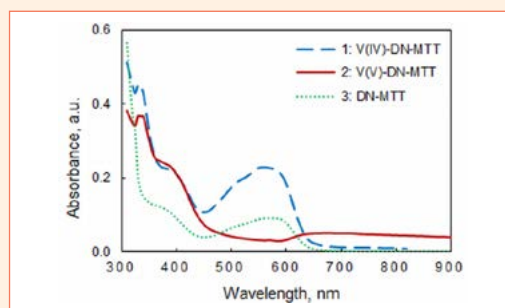
Parisa Zarringhadam and Saeed Farhadi



462–469 Inorganic chemistry

Complex Formation in a Liquid-Liquid Extraction System Containing Vanadium(IV/V), 2,3-Dihydroxynaphthalene and Thiazolyl Blue

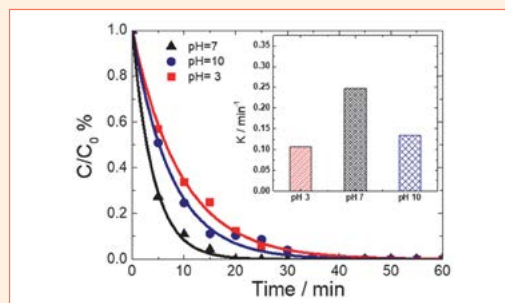
Galya K. Toncheva, Zlatimir T. Zhelev, Vassil B. Delchev and Kiril B. Gavazov



470–474 Chemical, biochemical and environmental engineering

Factors Influencing Imazapyr Herbicide Removal from Wastewater Using Photocatalytic Ozonation

Salma Bougarrani, Laila El Azzouzi, Soukaina Akel, Lahbib Latrach, Asmae Bouziani and Mohammed El Azzouzi

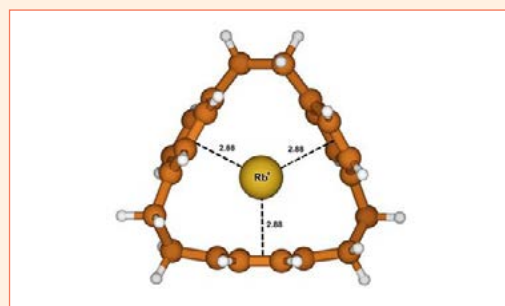


SHORT COMMUNICATION

475–480 Physical chemistry

Interaction Between the Rubidium Cation and [2.2.2]Paracyclophane: Experimental and Theoretical Study

Emanuel Makrlík, Stanislav Böhm, David Sýkora, Magdalena Kvíčalová and Petr Vaňura



Feature Article

Computational Modelling of Liver Metabolism and its Applications in Research and the Clinics

Tanja Cvitanović Tomaš,^{1,†} Miha Moškon,^{2,†} Miha Mraz²
and Damjana Rozman^{1,*}

¹ Centre for Functional Genomics and Bio-chips, Institute of Biochemistry, Faculty of Medicine, University of Ljubljana, Slovenia

² Faculty of Computer and Information Science, University of Ljubljana, Slovenia

[†] These authors contributed equally to this work.

* Corresponding author: E-mail: damjana.rozman@mf.uni-lj.si

Received: 15-05-2018

Abstract

Computational models of liver metabolism are gaining an increasing importance within the research community. Moreover, their first clinical applications have been reported in recent years in the context of personalised and systems medicine. Herein, we survey selected experimental models together with the computational modelling approaches that are used to describe the metabolic processes of the liver *in silico*. We also review the recent developments in the large-scale hepatic computational models where we focus on object-oriented models as a part of our research. The object-oriented modelling approach is beneficial in efforts to describe the interactions between the tissues, such as how metabolism of the liver interacts with metabolism of other tissues *via* blood. Importantly, this modelling approach can account as well for transcriptional and post-translational regulation of metabolic reactions which is a difficult task to achieve. The current and potential clinical applications of large-scale hepatic models are also discussed. We conclude with the future perspectives within the systems and translational medicine research community.

Keywords: Hepatic metabolism; systems medicine; modelling and simulation; large-scale metabolic models; NAFLD; liver

1. Introduction

Novel high throughput technologies and advanced computation impact the medicine quickly and influentially. Despite this, we still face a number of multifactorial diseases where the diagnosis and treatment remain a hurdle. This is the case as well for the multifactorial liver pathologies where the combinations of poorly defined genetic factors, together with environmental factors, interplay with each other and result in distinct disease phenotypes.

Non-alcoholic fatty liver disease (NAFLD) is the most prevalent form of chronic liver disease in the world. It affects 25% of the global adult population and as many as 1/3 of people in the developed world.¹ The disease is manifested by a spectrum of liver pathologies ranging from simple steatosis (fatty liver) to liver cell injury with fibrosis and can end in cirrhosis or liver cancer (hepatocellular

carcinoma, HCC). The rising incidence of NAFLD has led to dramatic rise of liver cancer, a disease with poor outcomes and limited therapeutic options. Without treatment, HCC is fatal, with a 5-year survival of only five percent.

Due to individuality of humans and the combinatorial effects, it is virtually impossible to predict all combinations that can lead to a liver disease phenotype. It appears that in each individual a different combination of genetic and environmental factors might be responsible for the multifactorial disease appearance and progression. In addition, such multifactorial conditions combine during the aging. This limits the ability to predict the individuals' disease progression and to discover and/or apply efficient individualized treatments.

We are thus faced with a challenging situation where on one hand there is a large progress in understanding the

molecular players of the liver disease stages and the overlap with other diseases while the inconsistencies from different studies and different populations leave the impression that we are close to the starting point. A major challenge of today's medicine is thus to incorporate the technological revolution accompanied with expansion of various data into the everyday clinical practice. One example is the knowledge regarding the genetic bases of liver diseases. Despite multiple studies and numerous potentially involved genes, the polymorphisms of a single gene *PNPLA3* named also adiponutrin, correlate with the non-alcoholic fatty liver disease progression to later disease stages, including the hepatocellular carcinoma (reviewed in^{2,3}).

At present we do not understand the mechanisms and pathways that define a particular liver disease stage, we cannot predict the fate of disease progression nor can we treat NAFLD. To solve such complex questions we must apply innovative systems solutions that in addition to experimentation include also modelling and validation in clinical samples. These will be described in more details in the following chapters of the paper.

2. Selected Liver Disease Models that Produce Data for Computation

Cholesterol presents one of the most important metabolites synthesized within liver. Starting point of cholesterol biosynthesis is an acetyl-CoA molecule. The pathway consists of more than 20 enzyme catalysed reactions.⁴ Unlike the pre-squalene part of the cholesterol biosynthesis the exact order of reactions in the post-squalene part has not yet been clarified. Enzyme lanosterol 14 α -demethylase i.e. CYP51, the evolutionary most conserved member of the cytochrome P450 family, catalyses the conversion of lanosterol to FF-MAS in the post-squalene part of cholesterol biosynthesis.⁵ *Cyp51* is regulated by transcription factor SREBP, via cyclic adenosine monophosphate (cAMP)⁶ and by the circadian regulation.⁷ Liver disease mouse model in which CYP51 was blocked as the rate limiting enzyme of the post-lanosterol part of cholesterol biosynthesis, exposed the progression of NAFLD in mice, and resulted in a phenotype similar to the metabolic progression of NAFLD towards HCC in humans.⁸ It is impossible to monitor the long-term metabolic progression of NAFLD in human individuals since repetitive liver biopsies are strictly avoided in practice. The complete removal of both *Cyp51* gene alleles in mice causes death of the embryo in the 15th day of development, which indicates the importance of cholesterol in embryogenesis.⁹ Cholesterol synthesis mutations may cause severe defects such as *Antley-Bixler syndrome*, *Smith-Lemli-Opitz syndrome* and several other genetic diseases.¹⁰

There are still no approved therapies for NAFLD, which is becoming a major health concern due to increas-

ing incidence of obesity in Europe. The problem of NAFLD is its multifactorial nature, with a largely uncharacterized genetic basis and only a few known associated genes.¹¹ For several patients, NAFLD presents an initial step of a serious condition called non-alcoholic steatohepatitis (NASH), which includes fibrosis and is the fastest growing cause of HCC.³ While HCC prevails in males and is increased in postmenopausal females, the sex-based metabolic cues have not been investigated.¹² Clinical research and more individualized disease progression monitoring is thus hampered by a lack of reliable non-invasive biomarkers. It currently seems impossible to predict all genetic and environmental factors and their combinations that leads to NAFLD phenotypes. To bridge this gap it is timely to apply a multidisciplinary systems medicine approach to combine experimentation and clinical work with the state-of-the-art multiscale and spatio-temporal liver models.¹³ Only in this way we will be able to fully understand NAFLD as a multifactorial condition and deduce metabolic causes and risk factors in females and males. This article will survey the combination of experimental, clinical, bioinformatics and modelling approaches that present the state-of-the art in identifying potential targets of complex multifactorial NAFLD and other complex liver diseases.

3. From Dynamical Models of Biochemical Reactions to Virtual Organisms

Computational modelling approaches that are currently used in the systems biology and systems medicine research communities can be differentiated into two main groups. First are the *bioinformatic approaches*, which allow us to analyse the experimental data, perform statistical analyses and conduct statistical modelling. The second are *computational biology* also known as *mechanistic* or *dynamical modelling* approaches, which allow us to perform dynamical modelling and execute computational simulations of the systems under the study.¹⁴ Even though bioinformatic approaches serve to be complementary to the dynamical modelling approaches, the focus of this paper will be made solely on the later.

Dynamical modelling approaches differ in dependence on the data that are available either from experimentalists or already in published literature. They differ as well based on the type and scale of the system we are investigating and also on the level of details we are aiming to describe *in silico*¹⁵ (see Table 1 and Figure 1).

Isolated segments of gene regulatory, signalling or metabolic networks are usually described with *ordinary differential equations* (ODEs). ODEs are composed of the classical Michaelis-Menten equations for modelling the enzymatic reactions. They contain as well Hill equations for modelling the gene regulation and expression, and also

Table 1: Dynamical modelling approaches depend on the focus, the data and the size of the observed (sub)system. Abbreviations: NF- κ B – nuclear factor kappa beta, ODEs – ordinary differential equations, PDEs – partial differential equations, SSA – stochastic simulation algorithm, GEMs – genome scale metabolic models, WCM – whole-cell model, *M. genitalium* – *Mycoplasma genitalium*, 3D – three dimensional, ABM – agent-based model, OOM – object-oriented modelling.

Focus	Parameters	Multi-scale	Size	Examples (applications)	Examples (approaches)
molecular modelling, isolated segments, only vital reactions	needed	No	small	oscillatory network of transcription factor NF- κ B ¹⁶	ODEs, PDEs, SSA
subcellular processes / reaction networks	not needed	no	large	Comprehensive model of human metabolism ¹⁷	Boolean networks, GEMs
integration of subcellular processes, whole-cells	needed	yes	large	WCM of <i>M. genitalium</i> ¹⁸	integrated models, WCMs
tissues, organs, cell populations	needed	yes	from small to large	3D liver tissue models ¹⁹	ABM, coupled ODEs and/or PDEs
all of the above	partially needed	yes	large	<i>LiverSex</i> model ²⁰	OOM

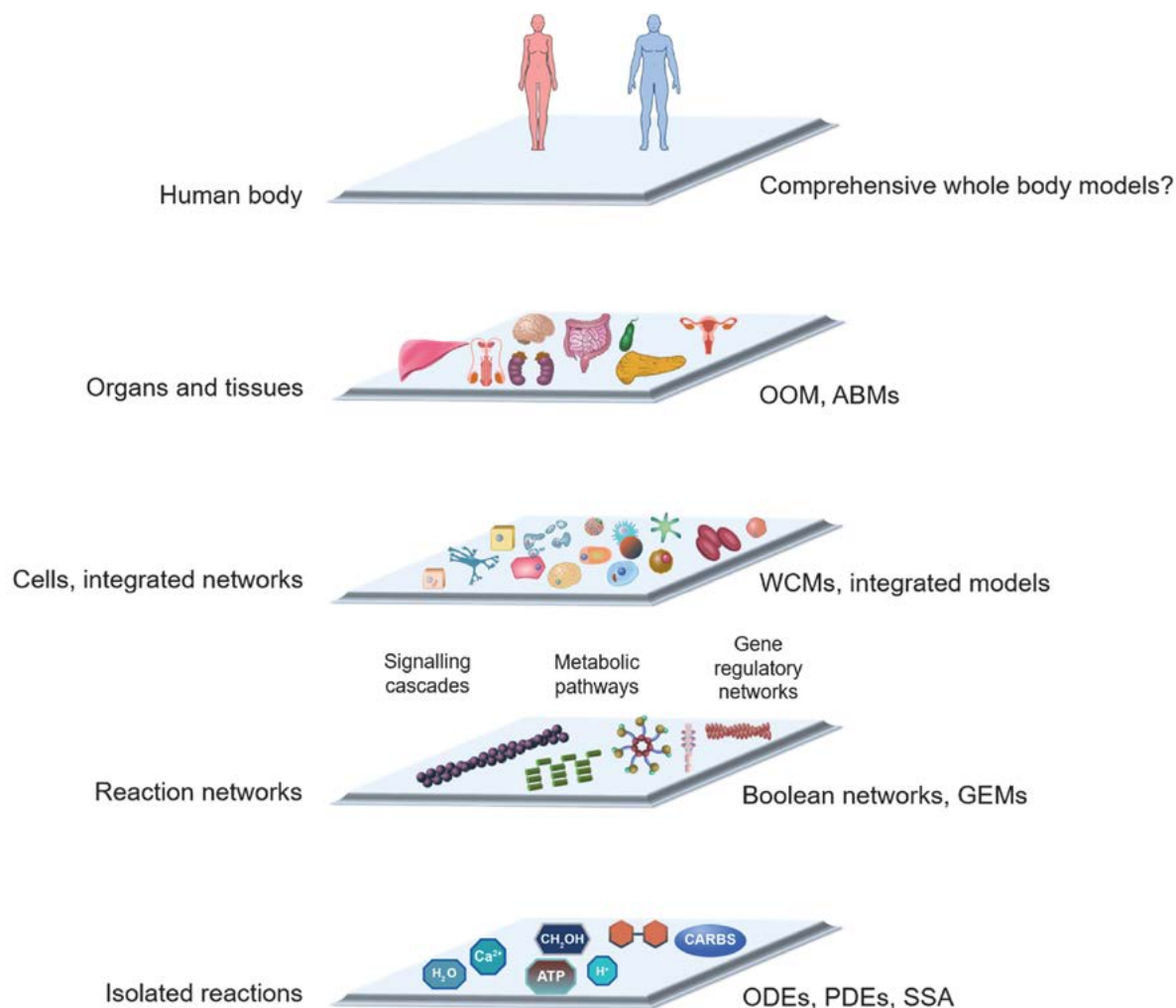


Figure 1: The focus of computational models scales from simple models describing selected chemical reactions to complex models describing reaction networks and finally organs and tissues. Abbreviations: ODEs – ordinary differential equations, PDEs – partial differential equations, SSA – stochastic simulation algorithm, GEMs – genome scale metabolic models, WCMs – whole-cell models, ABMs – agent-based models, OOM – object-oriented model

first order differential equations for modelling the protein degradation and similar processes.²¹ Models based on ODEs usually present the basis for the so called *deterministic modelling*, which describes the average of the system's response. Deterministic modelling also presumes a homogeneous distribution of the observed entities through the constant volume of the observed molecular space.²² An entity can be anything, from small molecules to proteins and genes. When concentrations of the observed chemical species become small, the noise influences become too large to be simply omitted from the models.^{23,24} In such cases a single-molecule level which is named also the *stochastic modelling* approach, need to be applied.^{23,25,26} The stochastic modelling bases on the *Stochastic Simulation Algorithm* (SSA)²⁷ and on its variations (e.g., see²⁸). It can account for the stochasticity of the observed biochemical reactions on the account of a larger computational complexity.

Stochastic as well as deterministic modelling approaches described above require the estimation of biologically relevant parameter values. Parameters are values (numbers) that are mostly based on the rate constants k for the observed biochemical reactions. It is the fact that these models (stochastic and deterministic) are useful only with realistic parameter values.²⁹ This means that the simulations that would produce biologically relevant results cannot be performed without the evaluation of kinetic parameter values. Specific parameter values, such as protein binding affinities or their degradation rates, can be experimentally measured. However, several pitfalls exist here. For example, (1) mathematical models usually describe complex processes in a simplified manner, which do not necessarily correspond to the measured biochemical constants (for example, multiple reactions can be lumped into a single *virtual* reaction) (2) reaction rates may strongly depend on environmental conditions (for example, reaction rates increase at higher temperatures) (3) variations of evaluated parameters may be extremely large (for example, reaction rates may differ significantly within the colony of genetically identical cells) and finally (4) not all parameters can be evaluated neither *in vivo* nor *in vitro*.²⁹ It can thus happen that the majority of the parameter values that are needed in the model, have to be deduced or inferred. Deduction of the missing parameter values is possible with the so called *parameter estimation techniques*. These techniques compare the available experimental results with the simulation results from the model, and upon that globally minimize the error function^{30,31}. Different parameter estimation techniques that aim to integrate the experimental results within the computational models have already been described (see e.g.^{32–34}). Even though specific techniques that might be able to cope with the large-scale models have also been proposed recently (see e.g.³⁵), they are in general still far from being scalable.²⁹ Moreover, comprehensive *in vivo* measurements in animals are still not available even for the most studied organisms.²⁹ We must underline at

this point that there are few *in vivo* studies in humans that are ethically feasible. It is, for example, impossible to count on kinetic data from human organs *in vivo*. Even *ex vivo* studies relying on data from human liver, are frequently small and difficult to compare with one another.³⁶ Consequently, majority of experiments that require e.g. a time-series of data, or data from the inner body organs, rely on experiments on laboratory animals, in line with ethical considerations for work on laboratory animals, including the 3R (reduce, replace, refine) principles.

Computational approaches that are able to deal with large-scale models have thus evolved into different forms that allow us to fully or partially omit the parameter estimation problem. These approaches are mainly focused to specific segments of observed biological system. For example, gene regulatory or signalling networks can be described with *Boolean networks* (see e.g.³⁷), while metabolic networks use the stoichiometric description in the form of *genome-scale metabolic models*.³⁸

Boolean networks (known also as *logic models*) depict the biological systems as a network of Boolean functions, i.e. functions describing binary relations between inputs and outputs.^{39,40} These networks presume that the observed chemical species can take only two possible values, i.e. absent (0) or present (1). Boolean networks are thus only a rough and approximate description of the system under study, but circumvent several problems of the approaches mentioned before. Boolean models can be established without any knowledge of kinetic parameter values and, when experimental data describing the system's response in different conditions are available, also without the knowledge of exact mechanistic description of the system under study. Their structure can be in many cases inferred solely from the characterization of the system's dynamical response (see e.g.^{41,42}).

Genome-scale metabolic models (GEMs) describe the *in silico* relations between the organism's genome and its metabolic phenotype.³⁸ In these models, the organism's genome and its annotations are applied to the reconstruction of stoichiometric description of the metabolism.⁴³ GEMs have already been established for simple prokaryotic organisms (see e.g.⁴⁴) as well as for humans¹⁷ and other eukaryotes (see e.g.⁴⁵ and⁴⁶). These models represent the general metabolism encoded within the genome of the organism under study and can be further refined to reflect experimental data observed in different environmental conditions, in different cell strains (see e.g.⁴⁶), in different tissues (see e.g.⁴⁷), organs (see e.g.⁴⁸), diseases (see e.g.⁴⁹), as well as within specific individuals (see e.g.⁵⁰), using dedicated computational algorithms, such as GIMME⁵¹, mCADRE⁴⁷ and CODA⁵². GEMs can be used to assess the *metabolic fluxes* that bring the observed metabolic network into an *optimal steady-state* under given criteria and optimisation function, such as maximal biomass production. *Flux-balance analysis* (FBA)⁵³ and other constraint-based approaches under the hood of COBRA

methodologies⁵⁴ can be applied for this purpose. These methodologies require the definition of optimisation criteria as well as upper and lower limits of metabolic fluxes, i.e. *constraints*, through observed reactions, and do not rely on the evaluation of exact values of kinetic parameters. They are, however, limited solely to the observation of the metabolic phenotype within the steady state of the system and without direct interactions with other cellular processes, such as gene regulation and protein-protein interactions.

The integration of GEMs with other cellular networks into *integrated models* have also been reported in recent years (see e.g.⁵⁵ and⁵⁶). The most comprehensive version of these model are so called *whole-cell models* (WCMs), which integrate the GEMs with the large-scale models of gene regulatory networks, signalling networks, protein-protein networks and other cellular processes.⁵⁷ WCM has already been established for *Mycoplasma genitalium*.¹⁸ This model integrates 28 different submodels into a unified WCM that is able to describe the cellular dynamics in the time-span of one cellular division.¹⁸ Even though this model seems extremely promising, the methodology used in its establishment is hardly scalable.²⁹ There are several challenges and problems that currently obstruct the application of WCMs to more complex organisms.⁵⁸ One of the main problems these models are facing is again the evaluation of realistic parameter values, their distributions and uncertainties in order to describe the dynamics of observed systems accurately.²⁹ Moreover, the integration of models of different cellular processes as well WCMs with their environment into comprehensive models that bridge the gaps between multiple scales still needs to be addressed sufficiently.⁵⁸

While WCMs try to give an accurate description of all cellular processes, models that are currently being applied to the analysis of intra- or inter-cellular dynamics mostly base on the descriptions of the selected processes that seem to be vital for the analysed aspects of cellular dynamics. These models are usually based on the simplifications that combine and reduce the number of observed biochemical reactions thus reducing also the number of parameters that need to be evaluated.⁵⁹ Since the number of observed biochemical entities is drastically reduced, the ODE- or SSA-based approaches can be applied again.

These models can be integrated into multicellular models describing bacterial populations, tissues or organs with the coupling of differential equations and accounting for spatial as well as temporal dynamics of the system's response (see e.g. ⁶⁰, ⁶¹ and ⁶²). An alternative approach that accounts for the spatial aspects of the systems under study is so called *agent-based modelling* (ABM). ABM describes the dynamics of different individual agents, i.e. in our case cells, that follow predefined rules (describing e.g. cellular motility, growth and basic cellular processes) and communicate using cellular communication mechanisms.¹⁵ Different *easy-to-use* computational tools that allow straightforward ABM modelling have been proposed recently

(see⁶³ for a recent review of these tools and frameworks). These allow computational modelling of bacterial populations (see e.g.⁶⁴) as well as computational modelling of tissues and organs (see e.g.⁶⁵, ⁶⁶ and⁶⁷). The main problem of these approaches is again in their inability to scale up, in the context of increasing the modelling accuracy as well as observed population size⁶³. Moreover, large computational complexity of these models usually needs to be addressed with an expensive computer hardware.^{63,68}

An alternative to the approaches described above is *object-oriented modelling* that is based on the systems biology (*SysBio*) library that was built at the University of Ljubljana.⁶⁹ *SysBio* library was initially used to construct the first integrated human metabolic model *SteatoNet* with multi-layered regulation.⁷⁰ This model describes the interaction between multiple tissues and accounts for metabolic reactions as well as for transcriptional and post-transcriptional regulation.⁷⁰ Most of the parameters that describe the dynamics of the observed system can be omitted from the model representation due to the observation of the normalised steady-state of the system's response. Object-oriented modelling approach that is applied here allows us to construct complex models by connecting the objects corresponding to basic biological entities in a meaningful and straightforward way.⁷⁰ Since the number of parameters that need to be incorporated into the model is small, this prevents several problems, such as parameter estimation problems as well as the problem of model overfitting. On the other hand parameters that are used at the end allow us to easily adapt the models to specific data, such as personalised or gender specific data as described in²⁰.

4. Large-scale Computational Models of Liver Metabolism

Changes in health, which may lead to the development and progression of different diseases, are caused by abnormal modifications of metabolism. Identification and characterization of these modifications have potentials for various applications, which include drug discovery and identification of new biomarkers.⁷¹ The majority of metabolic disorders occurs in the liver.^{72,73} The study of liver disorders improves the understanding of their physiological and pathological consequences. Computational models present an indispensable tool for the prediction of the effects of metabolic, genetic or chemical perturbations in liver metabolism and consequently in liver-related disease development and progression.¹³ Traditional methods fail to conduct the analyses in the same scope as *in silico* methods or can be conducted only under unfeasible costs. They need to be, however, complemented with the computational approaches.¹⁵ Finally, combination of experimental work, clinical work and computational modelling can be used for understanding the disease mechanisms, for eval-

uating the clinical efficacy and cost-effectiveness of existing diagnostic methods, for the development of new diagnostic methods and for the proposal of new drugs⁷³ (see Figure 2).

The liver is a key organ maintaining the metabolic homeostasis in the human body *via* synthesis, storage, and degradation of metabolites.⁷⁶ The use of computational models in liver research has been increasingly growing in

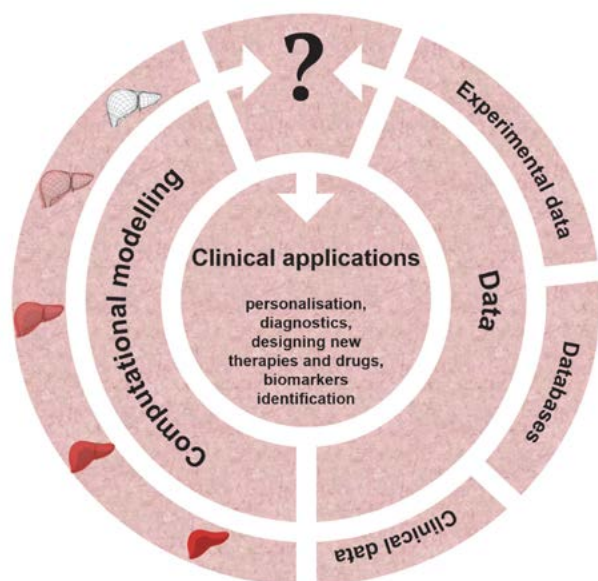


Figure 2: Computational models are complemented with experimental, literature and clinical data, which allows their transition towards clinical applications.

recent years (see Table 2). Most computational liver models are focused to the isolated liver (hepatic) metabolic mechanisms. For example, a detailed kinetic model of glycolysis, gluconeogenesis, and glycogen metabolism in human hepatocytes under the hormonal control of insulin, glucagon, and epinephrine, presents a tool for understanding the role of the liver in glucose homeostasis under normal conditions, in patients with diabetes or with glycogen storage diseases.⁷⁷ Different models are used to analyse different specific aspects of liver metabolism, such as energy metabolism⁷⁸, fat accumulation⁷⁹, iron metabolism⁸⁰ and xenobiotic metabolism⁸¹. Even though liver exhibits a large dynamical complexity, their microscopic architecture is remarkably uniform. The uniformity of the liver structure makes the modelling of the hepatic architecture relatively easy, which is indicated by several *in silico* models of hepatic structural architecture.^{82,83} These models help us to explain how cells form functional tissues, as for example in the 3-dimensional computational model of liver regeneration.⁸⁴

To date, only selected computational approaches of hepatic metabolism have been shifted to clinical application.⁴³ Individualized options for medical care of patients with HCC are not available yet, but there are large efforts to develop personalized systems care for them.⁸⁵ HCC presents a global health problem because it is the seventh most common cancer in the world and the third leading cause of cancer-related deaths.⁸⁶ Research in personalized approaches in hepatology has delivered different examples of successful application of systems biology such as HCC GEMs, which improved the HCC stratification and sug-

Table 2: State-of-the-art computational models used in the liver research. Only major large-scale computational models are included within the table. Abbreviations: GEM – genome scale metabolic models, HCC – hepatocellular carcinoma, NAFLD – non-alcoholic fatty liver disease, NASH – non-alcoholic steatohepatitis, *SteatoNet* – steatosis network.

	Type	Description and applications	Reference
<i>HepatoNet1</i>	GEM	first hepatic GEM; explained the relations between the available oxygen levels and the nutrients availability in the hepatic detoxification of ammonia	74
<i>iHepatocyte2322</i>	GEM	composed of the hepatocyte, the uptake and secretion of VLDL, LDL and HDL lipoproteins, and the formation and/or degradation of lipid droplets; used to simulate the progression of NAFLD to NASH; identified the potential therapeutic targets for treatment of NASH	48
<i>HCC GEM</i>	GEM	personalised <i>iHepatocyte2322</i> model to HCC patients; identified 101 antimetabolites with tumour suppression effect in the HCC; identified t-carnitine as suppressor of HCC progression by inhibiting β -oxidation	50
<i>iHCC2578</i>	GEM	reconstructed from the proteome and transcriptome of 361 HCC tumors and 49 noncancerous liver samples; used to study acetate utilization and HCC; identified deregulation of fatty acid oxidation as a vital process for cell proliferation in HCC	75
<i>SteatoNet</i>	OOM	integrated human metabolic model with multi-layered regulation; used to explain the relations between the liver and other organs in the development of NAFLD; identified ketone body metabolism, cholesterol transport and regulatory functions of FXR, LXR and SREBP2 as crucial steps in NAFLD development and progressions	70
<i>LiverSex</i>	OOM	adaptation of <i>SteatoNet</i> to gender-specific models; used to investigate gender-dependent complex liver pathologies; identified the partition of fatty acids into different pathways as a possible NAFLD protective mechanisms in females; identified PGC1A, PPAR α , FXR and LXR as regulatory factors for gender dependent personalized treatment of NAFLD	20

gested new targets for personalized treatments.^{50,75,87} Different GEMs have been focused on the human liver metabolism. *HepatoNet1*⁷⁴ is a product of the liver adaptation of the human metabolic network *Recon1*⁸⁸ using the extensive knowledge and databases for hepatocyte representation. *HepatoNet1* has been used to explain the relations between the available oxygen levels and the nutrients availability in the hepatic detoxification of ammonia. *HepatoNet1* presents a starting point for the reconstruction of other hepatocyte-specific GEMs, for example *iLJ1046*⁸⁹, *iAB676*⁹⁰, *iHepatocyte1154*⁹¹ and *iHepatocyte2322*⁴⁸. *iHepatocyte2322* currently presents the most powerful liver-related GEM. It was established with the combination of various clinical, biochemical and genetic studies. Its main aim was to provide the identification of novel biomarkers and therapeutic targets for NAFLD. Simulation of NAFLD progression to NASH has exposed serine deficiency as the main cause in NASH patients. *iHepatocyte2322* was used to show that increasing serine level in hepatocytes as a consequence of the serine uptake as a dietary supplement could prevent NASH progression. Phosphoserine phosphatase and hydroxymethyltransferases 1

as well as branched chain amino-acid transaminase 1 were identified as potential therapeutic targets for the treatment of NASH.⁴⁸

*SteatoNet*⁷⁰ presents an OOM model, which was established to increase the understanding of the relations between the liver and other organs in the development of NAFLD. *SteatoNet* was used to identify the interactions between liver and adipose tissue as critical for the pathogenesis of NAFLD. Ketone body metabolism, cholesterol transport, and regulatory functions of farnesoid X receptor, liver X receptor and sterol regulatory element-binding protein 2 were recognized as novel crucial steps of NAFLD development and progressions. However, the liver is well known as one of the most sexually dimorphic non-reproductive organs⁹², which is also indicated by sex differences in liver-related disease prevalence and progression.⁹³ Hepatic large-scale metabolic models are, on the other hand, uniform models and do not differentiate between genders. They are constructed and validated mostly on male data, also because of the lack of liver transcriptome-based studies that would take into account both genders.⁹⁴ With the goal to investigate differences in NAFLD progression be-

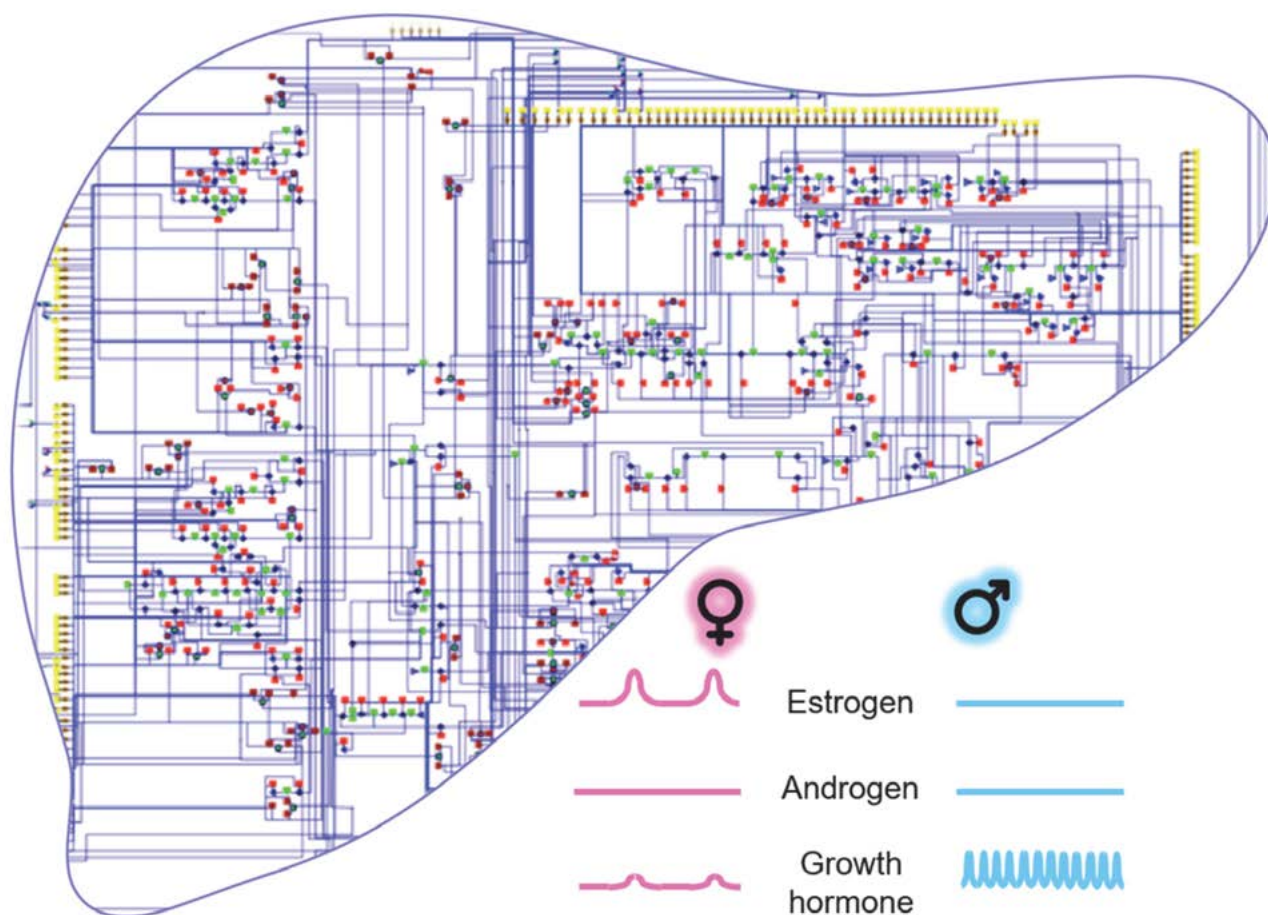


Figure 3: *LiverSex* presents the gender-based adaptation of the *SteatoNet* model, and is able to provide detailed insights into gender-dependent complex liver pathologies. The adaptation was performed with the addition of androgen and estrogen receptor responses, the addition of connections between sex steroids and growth hormone, and the addition of gender-based growth hormone release (see²⁰).

tween genders, we developed the *LiverSex* model²⁰, the first gender-based, multi-tissue and multi-level liver metabolic computational model (see Figure 3). *SteatoNet* was reused and adapted to gender-based hormonal regulation of liver. The key step in the adaptation of liver metabolism to gender was the addition of androgen and estrogen receptor responses to relevant hormones, the additions of connections between sex steroids and growth hormone, and the addition of specific gender-based growth hormone release to the model. Hormonal regulation in *LiverSex* was simplified to a level that still ensures normal function. Hormones were organized into 3 groups: androgen, estrogens and growth hormone. Androgen and estrogen groups represent steroid hormones that regulate the development and maintenance of sex characteristics in mammals by binding to their corresponding receptors.⁹² The growth hormone has a daily oscillatory behaviour in males and has a constant concentration in females, which was also included in the model.⁹⁵ The dynamics of estrogen in the female model was described with the monthly estrous cycle that cannot be found in males.⁹⁶ With these alterations, *LiverSex* was able to provide detailed insights into gender dependent complex liver pathologies in the liver-related disease development and progression. The model identified the cardinal gender dependent metabolic pathways such as partition of fatty acids to ketone body production, VLDL synthesis, and fatty acids oxidation, together with deposition of triglycerides as lipid droplets, which are involved in accumulation of triglyceride as one of the initial steps of NAFLD. Later was recognized as substantially more sensitive in females in response to a high-fat diet challenge. The ability to partition fatty acids into different pathways might be one of the possible protective mechanisms in females leading to delayed NAFLD progression compared to males. In the same way, PGC1A, PPAR α , FXR and LXR were identified as regulatory factors, which could become influential in gender dependent personalized treatment of NAFLD.

5. Future Perspectives

In systems medicine, computational models can be applied for diagnostics, for prediction of disease progression, and for optimal selection of suitable therapeutic strategies. They give us the opportunity to personalise the clinical care to the patients' anatomy, physiology, genomic background, etc. In addition, systems medicine approaches highlight patient specific aspects on the development and progression of the diseases.

The liver has a major physiological role in the fine-tuning of metabolic pathways, including functions associated with health and disease. A comprehensive characterization of liver maintenance and disruptions might be crucial in preventive medicine and in the design of safer and more efficient therapeutic approaches. Systems medi-

cine may help with finding preventive approaches for diseases of hepatic metabolism.

Computational models complement experimental data and can be used for diagnostic purposes, for identification of drug targets and for personalized care of patients with liver diseases. There is an urgent need for new therapies in hepatology, as the mortality and morbidity in many liver diseases is still high. End-stage liver diseases and cancers share a similar dismal prognosis.

The aim of personalised medicine is to adapt the diagnosis and clinical care to each individual patient. With the reduction of the probability of wrong diagnoses as well as the application of wrong therapies, personalized medicine has all the potentials to drastically reduce the costs of health care as well as global health risks. Personalized medicine, however, still needs an approval from the general audience of physicians as well as from the wider population. Making big data work for patients is still a challenge from the decision making to the data management as well as ethical and legal perspective.⁹⁷ The consent policies need to be clear. The data and its interpretations need to be integrated into a comprehensive health care system that would have practical benefits for all participants, i.e. patients, clinicians and researchers. Other challenges that limit the bridging of personalized medicine to market include current costs of multiomics experimental approaches and lack as well as inconsistencies of internationally accepted best practice standards.⁹⁸

The majority of current personalized medicine approaches is directed towards the diagnosis and treatment of cancer. In comparison to the recent progress of personalized medicine in oncology, personalized medicine in hepatology still remains in its infancy. Several liver diseases, such as progression of NAFLD to HCC via NASH, are still hard to characterize in the context of their predictive outcome. We still do not fully understand the sex-dependent mechanisms that lead the development and progression of liver related diseases and which might be crucial for their diagnosis and treatment. We speculate these mechanisms are driven by growth hormone as well as sex hormones and their influences on gene expression patterns. In the future, broad molecular profiling of liver diseases, their integration in computational models and their validation in clinical trials, in females and males could improve the current treatment options with individualized care. These computational models will not only progress in their accuracy and prediction power of describing the dynamics of the metabolism of isolated organs or reactions networks. Current trends of systems biology in hepatology go towards the integration of different network types with multilayered omics data to obtain integrative models, which will accurately simulate whole-body metabolic functions.⁹⁹

Scientific society has entered a new era in which computational methods and technologies have a key role in investigation of the human body. EuroPhysiome¹⁰⁰⁻¹⁰²

is an European project, which created a framework for modelling the human body using computational methods which incorporate the biochemistry, biophysics, and anatomy of cells, tissues and organs known as *Homo sapiens in silico*. These methods aim to design a computational version of the human body within the next 20 years.¹⁰³ This will provide the comprehensive insights into the dynamics of the human body and development and progression of complex diseases, and increase their treatment potentials in the context of preventive and personalized medicine.

In conclusion, despite spectacular advances in the post-genome era, there is a gap between experimental data and medical knowledge, and an even greater gap between new knowledge in terms of clinical utility and benefits to the patients. We still suffer from multifactorial disorders that affect large-scale populations and we are unable to guide the epidemics due to the knowledge gaps. Progressive liver diseases arising from metabolic causes are a typical example where the classical approaches have not lead to sufficient progress. It is thus timely to introduce multi-disciplinary approaches and tackle NAFLD by combining biochemical experimentation with the state-of-the-art modelling. There are no approved therapies for NAFLD and the compounds currently in Phase III clinical trials may very likely face safety and efficacy issues. Further research and more individualized disease progression monitoring is also affected by a current lack of reliable non-invasive biomarkers. It is thus evident that in addition to experimental and clinical work we also need models to help us decrease the burden of liver pathologies.

Acknowledgments

Supported by the resources of FP7 CASyM (Coordinating Action Systems Medicine Europe, grant no. 305033), by Slovenian Research Agency grants P1-0390, P2-0359, and by the infrastructure grant ELIXIR.

Author biographies

Tanja Cvitanović Tomaš is a PhD student at the Faculty of Medicine, University of Ljubljana, Slovenia. She received her MSc from the Biotechnical Faculty, University of Ljubljana, Slovenia in 2012. Her research work is focused on interdisciplinary bridging between medicine, biochemistry and computational modelling. Her recent work is directed towards the applications of computational approaches to gain the insights into hot topics in hepatology.

Miha Moškon received his BSc and PhD degree in computer science from the Faculty of Computer and Information Science, University of Ljubljana, Slovenia in 2007 and 2012, where he holds the position of an assistant professor. His research work is focused on computational approaches in systems medicine, systems biology and synthetic biology. His main research interests have been re-

cently directed towards accurate quantitative modelling and analysis of metabolic and gene regulatory networks and towards the computational design of synthetic biological systems.

Miha Mraz received his BSc, MSc and PhD degree in computer science from the Faculty of Computer and Information Science, University of Ljubljana, Slovenia in 1992, 1995 and 2000, where he leads the Computational biology group, and holds the position of a full professor. His research interests include unconventional processing methods and applications of computational approaches to systems biology, systems medicine and synthetic biology.

Damjana Rozman received her BSc at Faculty of Chemistry and Chemical Technology, University of Ljubljana, MSc and PhD degree at Faculty of Medicine, University of Ljubljana and post-doctoral training at Vanderbilt University in USA. She holds the position of full professor at Institute of Biochemistry and is the head of the Centre for Functional Genomics and Bio-chips at Faculty of Medicine. In her research she applies functional genomics and systems medicine approaches to decipher how the cholesterol homeostasis cross-talks with other liver metabolic pathways and how this influences liver health and transformation to disease.

6. References

1. Younossi, Z.; Henry, L. Contribution of Alcoholic and Nonalcoholic Fatty Liver Disease to the Burden of Liver-Related Morbidity and Mortality. *Gastroenterology* **2016**, *150*, 1778–1785. DOI:10.1053/j.gastro.2016.03.005
2. Naik, A.; Košir, R.; Rozman, D. Genomic Aspects of NAFLD Pathogenesis. *Genomics* **2013**, *102*, 84–95. DOI:10.1016/j.ygeno.2013.03.007
3. Blagotinšek, K.; Rozman, D. Targeting Signalling Pathways in Hepatocellular Carcinoma. *Curr. Pharm. Des.* **2017**, *23*, 170–175.
4. Ačimovič, J.; Rozman, D. Steroidal Triterpenes of Cholesterol Synthesis. *Molecules* **2013**, *18*, 4002–4017. DOI:10.3390/molecules18044002
5. Seliskar, M.; Rozman, D. Mammalian Cytochromes P450 -Importance of Tissue Specificity. *Biochim Biophys Acta* **2007**, *1770*, 458–466.
6. Fink, M.; Acimovic, J.; Rezen, T.; Tansek, N.; Rozman, D. Cholesterogenic Lanosterol 14 α -Demethylase (CYP51) Is an Immediate Early Response Gene. *Endocrinology* **2005**, *146*, 5321–5331. DOI:10.1210/en.2005-0781
7. Kosir, R.; Prosenc Zmrzljak, U.; Korencic, A.; Juvan, P.; Acimovic, J.; Rozman, D. Mouse Genotypes Drive the Liver and Adrenal Gland Clocks. *Sci. Rep.* **2016**, *6*, 31955. DOI:10.1038/srep31955
8. Lorbek, G.; Perše, M.; Jeruc, J.; Juvan, P.; Gutierrez-Mariscal, F. M.; Lewinska, M.; Gebhardt, R.; Horvat, S.; Björkhem, I.;

- Rozman, D. Lessons from Hepatocyte-Specific Cyp51 Knockout Mice: Impaired Cholesterol Synthesis Leads to Oval Cell-Driven Liver Injury. *Sci. Rep.* **2015**, *5*, 8777. DOI:10.1038/srep08777
9. Keber, R.; Motaln, H.; Wagner, K. D.; Debeljak, N.; Ras-soulzadegan, M.; Ačimovič, J.; Rozman, D.; Horvat, S. Mouse Knockout of the Cholesterogenic Cytochrome P450 Lanosterol 14 α -Demethylase (Cyp51) Resembles Antley-Bixler Syndrome. *J. Biol. Chem.* **2011**, *286*, 29086–29097. DOI:10.1074/jbc.M111.253245
10. Urlep, Ž.; Lorbek, G.; Perše, M.; Jeruc, J.; Juvan, P.; Matz-Soja, M.; Gebhardt, R.; Björkhem, I.; Hall, J. A.; Bonneau, R. Disrupting Hepatocyte Cyp51 from Cholesterol Synthesis Leads to Progressive Liver Injury in the Developing Mouse and Decreases RORC Signalling. *Sci. Rep.* **2017**, *7*, 40775. DOI:10.1038/srep40775
11. Kovač, U.; Rozman, D. Genetics of Non-alcoholic Fatty Liver Disease. In *eLS*; John Wiley & Sons, Ltd, 2015.
12. Skubic, C.; Drakulić, Ž.; Rozman, D. Pharmacogenetic Considerations for Personalized Therapy When Tackling Nonalcoholic Fatty Liver Disease: The Perspective of Genes, Drugs, and the Sex. *Submitted 2018*.
13. Cvitanović, T.; Reichert, M. C.; Moškon, M.; Mraz, M.; Lam-mert, F.; Rozman, D. Large-Scale Computational Models of Liver Metabolism: How Far from the Clinics? *Hepatology* **2017**, *66*, 1323–1334. DOI:10.1002/hep.29268
14. Duffy, D. J. Problems, Challenges and Promises: Perspectives on Precision Medicine. *Brief. Bioinform.* **2016**, *17*, 494–504. DOI:10.1093/bib/bbv060
15. Wolkenhauer, O. Why Model? *Front. Physiol.* **2014**, *5*, 21. DOI:10.3389/fphys.2014.00021
16. Mengel, B.; Hunziker, A.; Pedersen, L.; Trusina, A.; Jensen, M. H.; Krishna, S. Modeling Oscillatory Control in NF-KB, P53 and Wnt Signaling. *Curr. Opin. Genet. Dev.* **2010**, *20*, 656–664. DOI:10.1016/j.gde.2010.08.008
17. Brunk, E.; Sahoo, S.; Zielinski, D. C.; Altunkaya, A.; Dräger, A.; Mih, N.; Gatto, F.; Nilsson, A.; Preciat Gonzalez, G. A.; Aurich, M. K.; et al. Recon3D Enables a Three-Dimensional View of Gene Variation in Human Metabolism. *Nat. Biotechnol.* **2018**, *36*, 272–281. DOI:10.1038/nbt.4072
18. Karr, J. R.; Sanghvi, J. C.; MacKlin, D. N.; Gutschow, M. V.; Jacobs, J. M.; Bolival, B.; Assad-Garcia, N.; Glass, J. I.; Covert, M. W. A Whole-Cell Computational Model Predicts Phenotype from Genotype. *Cell* **2012**, *150*, 389–401. DOI:10.1016/j.cell.2012.05.044
19. Hoehme, S.; Friebel, A.; Hammad, S.; Drasdo, D.; Hengstler, J. G. Creation of Three-Dimensional Liver Tissue Models from Experimental Images for Systems Medicine. *Methods Mol. Biol.* **2017**, *1506*, 319–362. DOI:10.1007/978-1-4939-6506-9_22
20. Cvitanović Tomaš, T.; Urlep, Ž.; Moškon, M.; Mraz, M.; Rozman, D. LiverSex Computational Model: Sexual Aspects in Hepatic Metabolism and Abnormalities. *Front. Physiol.* **2018**, *9*, 360. DOI:10.3389/fphys.2018.00360
21. Ingalls, B. P. *Mathematical Modelling in Systems Biology: An Introduction*; MIT Press, 2014.
22. Kærn, M.; Blake, W. J.; Collins, J. J. The Engineering of Gene Regulatory Networks. *Annu. Rev. Biomed. Eng.* **2003**, *5*, 179–206. DOI:10.1146/annurev.bioeng.5.040202.121553
23. Turner, T. E.; Schnell, S.; Burrage, K. Stochastic Approaches for Modelling in Vivo Reactions. *Comput. Biol. Chem.* **2004**, *28*, 165–178. DOI:10.1016/j.compbiolchem.2004.05.001
24. Gillespie, D. T. Deterministic Limit of Stochastic Chemical Kinetics. *J. Phys. Chem. B* **2009**, *113*, 1640–1644. DOI:10.1021/jp806431b
25. Karlebach, G.; Shamir, R. Modelling and Analysis of Gene Regulatory Networks. *Nat. Rev. Mol. Cell Biol.* **2008**, *9*, 770–780. DOI:10.1038/nrm2503
26. De Jong, H. Modeling and Simulation of Genetic Regulatory Systems: A Literature Review. *J. Comput. Biol.* **2002**, *9*, 67–103. DOI:10.1089/10665270252833208
27. Gillespie, D. T. Exact Stochastic Simulation of Coupled Chemical Reactions. *J. Phys. Chem.* **1977**, *81*, 2340–2361. DOI:10.1021/j100540a008
28. Petroni, M.; Zimic, N.; Mraz, M.; Moškon, M. Stochastic Simulation Algorithm for Gene Regulatory Networks with Multiple Binding Sites. *J. Comput. Biol.* **2015**, *22*, 218–226. DOI:10.1089/cmb.2014.0064
29. Babbie, A. C.; Stumpf, M. P. H. How to Deal with Parameters for Whole-Cell Modelling. *J. R. Soc. Interface* **2017**, *14*, 20170237. DOI:10.1098/rsif.2017.0237
30. Ashyraliyev, M.; Fomekong-Nanfack, Y.; Kaandorp, J. A.; Blom, J. G. Systems Biology: Parameter Estimation for Biochemical Models. *FEBS J.* **2009**, *276*, 886–902. DOI:10.1111/j.1742-4658.2008.06844.x
31. Gábor, A.; Banga, J. R. Robust and Efficient Parameter Estimation in Dynamic Models of Biological Systems. *BMC Syst. Biol.* **2015**, *9*, 74. DOI:10.1186/s12918-015-0219-2
32. Zhan, C.; Yeung, L. F. Parameter Estimation in Systems Biology Models Using Spline Approximation. *BMC Syst. Biol.* **2011**, *5*, 14. DOI:10.1186/1752-0509-5-14
33. Sun, J.; Garibaldi, J. M.; Hodgman, C. Parameter Estimation Using Metaheuristics in Systems Biology: A Comprehensive Review. *IEEE/ACM Trans. Comput. Biol. Bioinforma.* **2012**, *9*, 185–202.
34. Lillacci, G.; Khammash, M. Parameter Estimation and Model Selection in Computational Biology. *PLoS Comput. Biol.* **2010**, *6*, e1000696. DOI:10.1371/journal.pcbi.1000696
35. Penas, D. R.; González, P.; Egea, J. A.; Doallo, R.; Banga, J. R. Parameter Estimation in Large-Scale Systems Biology Models: A Parallel and Self-Adaptive Cooperative Strategy. *BMC Bioinformatics* **2017**, *18*, 1–24. DOI:10.1186/s12859-016-1452-4
36. Rozman, D. From Nonalcoholic Fatty Liver Disease to Hepatocellular Carcinoma: A Systems Understanding. *Dig. Dis. Sci.* **2014**, *59*, 238–241. DOI:10.1007/s10620-013-2998-x
37. Saadatpour, A.; Réka, A. Boolean Modeling of Biological Regulatory Networks: A Methodology Tutorial. *Methods* **2013**, *62*, 3–12. DOI:10.1016/j.ymeth.2012.10.012
38. O'Brien, E. J.; Monk, J. M.; Palsson, B. O. Using Genome-Scale Models to Predict Biological Capabilities. *Cell* **2015**, *161*, 971–987. DOI:10.1016/j.cell.2015.05.019

39. Wynn, M. L.; Consul, N.; Merajver, S. D.; Schnell, S. Logic-Based Models in Systems Biology: A Predictive and Parameter-Free Network Analysis Method. *Integr. Biol.* **2012**, *4*, 1323. DOI:10.1039/c2ib20193c
40. Le Novere, N. Quantitative and Logic Modelling of Molecular and Gene Networks. *Nat. Rev. Genet.* **2015**, *16*, 146–158. DOI:10.1038/nrg3885
41. Ivanov, I. Boolean Models of Genomic Regulatory Networks: Reduction Mappings, Inference, and External Control. *Curr. Genomics* **2009**, *10*, 375–387. DOI:10.2174/138920209789177584
42. Martin, S.; Zhang, Z.; Martino, A.; Faulon, J. L. Boolean Dynamics of Genetic Regulatory Networks Inferred from Microarray Time Series Data. *Bioinformatics* **2007**, *23*, 866–874. DOI:10.1093/bioinformatics/btm021
43. Rejc, Ž.; Magdevska, L.; Tršelič, T.; Osolin, T.; Vodopivec, R.; Mraz, J.; Pavliha, E.; Zimic, N.; Cvitanović, T.; Rozman, D.; et al. Computational Modelling of Genome-Scale Metabolic Networks and Its Application to CHO Cell Cultures. *Comput. Biol. Med.* **2017**, *88*, 150–160. DOI:10.1016/j.compbiomed.2017.07.005
44. Orth, J. D.; Conrad, T. M.; Na, J.; Lerman, J. A.; Nam, H.; Feist, A. M.; Palsson, B. A Comprehensive Genome-Scale Reconstruction of Escherichia Coli Metabolism. *Mol. Syst. Biol.* **2011**, *11*, 535.
45. Sánchez, B. J.; Nielsen, J. Genome Scale Models of Yeast: Towards Standardized Evaluation and Consistent Omic Integration. *Integr. Biol.* **2015**, *7*, 846–858. DOI:10.1039/C5IB00083A
46. Hefzi, H.; Ang, K. S.; Hanscho, M.; Bordbar, A.; Ruckerbauer, D.; Lakshmanan, M.; Orellana, C. A.; Baycin-Hizal, D.; Huang, Y.; Ley, D.; et al. A Consensus Genome-Scale Reconstruction of Chinese Hamster Ovary Cell Metabolism. *Cell Syst.* **2016**, *3*, 434–443. DOI:10.1016/j.cels.2016.10.020
47. Wang, Y.; Eddy, J. A.; Price, N. D. Reconstruction of Genome-Scale Metabolic Models for 126 Human Tissues Using MCADRE. *BMC Syst. Biol.* **2012**, *6*, 153. DOI:10.1186/1752-0509-6-153
48. Mardinoglu, A.; Agren, R.; Kampf, C.; Asplund, A.; Uhlen, M.; Nielsen, J. Genome-Scale Metabolic Modelling of Hepatocytes Reveals Serine Deficiency in Patients with Non-Alcoholic Fatty Liver Disease. *Nat. Commun.* **2014**, *5*, 1–11. DOI:10.1038/ncomms4083
49. Ghaffari, P.; Mardinoglu, A.; Nielsen, J. Cancer Metabolism: A Modeling Perspective. *Front. Physiol.* **2015**, *6*, 382. DOI:10.3389/fphys.2015.00382
50. Agren, R.; Mardinoglu, A.; Asplund, A.; Kampf, C.; Uhlen, M.; Nielsen, J. Identification of Anticancer Drugs for Hepatocellular Carcinoma through Personalized Genome-Scale Metabolic Modeling. *Mol. Syst. Biol.* **2014**, *10*, 721. DOI:10.1002/msb.145122
51. Becker, S. A.; Palsson, B. O. Context-Specific Metabolic Networks Are Consistent with Experiments. *PLoS Comput. Biol.* **2008**, *4*, e1000082. DOI:10.1371/journal.pcbi.1000082
52. Schultz, A.; Qutub, A. A. Reconstruction of Tissue-Specific Metabolic Networks Using CORDA. *PLoS Comput. Biol.* **2016**, *12*, 1–33. DOI:10.1371/journal.pcbi.1004808
53. Orth, J. D.; Thiele, I.; Palsson, B. Ø. What Is Flux Balance Analysis? *Nat. Biotechnol.* **2010**, *28*, 245–248. DOI:10.1038/nbt.1614
54. Heirendt, L.; Arreckx, S.; Pfau, T.; Mendoza, S. N.; Richelle, A.; Heinken, A.; Haraldsdóttir, H. S.; Wachowiak, J.; Keating, S. M.; Vlasov, V.; et al. Creation and Analysis of Biochemical Constraint-Based Models: The COBRA Toolbox v3.0. *Dev. Biol.* **2017**, *276*, 391–402.
55. Lee, S.; Zhang, C.; Kilcarslan, M.; Piening, B. D.; Bjornson, E.; Hallström, B. M.; Groen, A. K.; Ferrannini, E.; Laakso, M.; Snyder, M.; et al. Integrated Network Analysis Reveals an Association between Plasma Mannose Levels and Insulin Resistance. *Cell Metab.* **2016**, *24*, 172–184. DOI:10.1016/j.cmet.2016.05.026
56. Lee, S.; Mardinoglu, A.; Zhang, C.; Lee, D.; Nielsen, J. Dysregulated Signaling Hubs of Liver Lipid Metabolism Reveal Hepatocellular Carcinoma Pathogenesis. *Nucleic Acids Res.* **2016**, *44*, 5529–5539. DOI:10.1093/nar/gkw462
57. Karr, J. R.; Takahashi, K.; Funahashi, A. The Principles of Whole-Cell Modeling. *Curr. Opin. Microbiol.* **2015**, *27*, 18–24. DOI:10.1016/j.mib.2015.06.004
58. Widmer, L. A.; Stelling, J. Bridging Intracellular Scales by Mechanistic Computational Models. *Curr. Opin. Biotechnol.* **2018**, *52*, 17–24. DOI:10.1016/j.copbio.2018.02.005
59. Apri, M.; De Gee, M.; Van Mourik, S.; Molenaar, J. Identifying Optimal Models to Represent Biochemical Systems. *PLoS One* **2014**, *9*, e83664. DOI:10.1371/journal.pone.0083664
60. Nikolaev, E. V.; Sontag, E. D. Quorum-Sensing Synchronization of Synthetic Toggle Switches: A Design Based on Monotone Dynamical Systems Theory. *PLoS Comput. Biol.* **2016**, *12*, e1004881. DOI:10.1371/journal.pcbi.1004881
61. Chen, Y.; Kim, J. K.; Hirning, A. J.; Josić, K.; Bennett, M. R. Emergent Genetic Oscillations in a Synthetic Microbial Consortium. *Science* **2015**, *349*, 986–989. DOI:10.1126/science.aaa3794
62. Ricken, T.; Werner, D.; Holzhütter, H. G.; König, M.; Dahmen, U.; Dirsch, O. Modeling Function–perfusion Behavior in Liver Lobules Including Tissue, Blood, Glucose, Lactate and Glycogen by Use of a Coupled Two-Scale PDE–ODE Approach. *Biomech. Model. Mechanobiol.* **2015**, *14*, 515–536. DOI:10.1007/s10237-014-0619-z
63. Gorochoowski, T. E. Agent-Based Modelling in Synthetic Biology. *Essays Biochem.* **2016**, *60*, 325–336. DOI:10.1042/EBC20160037
64. Matyjaszkiewicz, A.; Fiore, G.; Annunziata, F.; Grierson, C. S.; Savery, N. J.; Marucci, L.; Di Bernardo, M. BSim 2.0: An Advanced Agent-Based Cell Simulator. *ACS Synth. Biol.* **2017**, *6*, 1969–1972. DOI:10.1021/acssynbio.7b00121
65. Swat M H, Thomas G L, Belmonte J M, Shirinifard A, Hmeljak D, G. J. A. Multi-Scale Modeling of Tissues Using CompuCell3D. *Methods Cell Biol.* **2012**, *110*, 325–366. DOI:10.1016/B978-0-12-388403-9.00013-8

66. Friebel, A.; Neitsch, J.; Johann, T.; Hammad, S.; Hengstler, J. G.; Drasdo, D.; Hoehme, S. TiQuant: Software for Tissue Analysis, Quantification and Surface Reconstruction. *Bioinformatics* **2015**, *31*, 3234–3236. DOI:10.1093/bioinformatics/btv346
67. Dutta-Moscato, J.; Solovyev, A.; Mi, Q.; Nishikawa, T.; Soto-Gutierrez, A.; Fox, I. J.; Vodovotz, Y. A Multiscale Agent-Based in Silico Model of Liver Fibrosis Progression. *Front. Bioeng. Biotechnol.* **2014**, *2*, 18. DOI:10.3389/fbioe.2014.00018
68. Wolkenhauer, O.; Auffray, C.; Brass, O.; Clairambault, J.; Deutsch, A.; Drasdo, D.; Gervasio, F.; Preziosi, L.; Maini, P.; Marciniak-Czochra, A.; et al. Enabling Multiscale Modeling in Systems Medicine. *Genome Med.* **2014**, *6*, 4–6. DOI:10.1186/gm538
69. Belič, A.; Ačimovič, J.; Naik, A.; Goličnik, M. Analysis of the Steady-State Relations and Control-Algorithm Characterisation in a Mathematical Model of Cholesterol Biosynthesis. *Simul. Model. Pract. Theory* **2013**, *33*, 18–27. DOI:10.1016/j.simpat.2011.12.010
70. Naik, A.; Rozman, D.; Belič, A. SteatoNet: The First Integrated Human Metabolic Model with Multi-Layered Regulation to Investigate Liver-Associated Pathologies. *PLoS Comput Biol* **2014**, *10*, e1003993. DOI:10.1371/journal.pcbi.1003993
71. Ayers, D.; Day, P. J. Systems Medicine: The Application of Systems Biology Approaches for Modern Medical Research and Drug Development. *Mol. Biol. Int.* **2015**, *2015*, 1–8.
72. Guildler, L.; Pula, S.; Pierre, G. Metabolic Disorders Presenting as Liver Disease. *Paediatr. Child Heal. (United Kingdom)* **2017**, *27*, 533–539. DOI:10.1016/j.paed.2017.07.007
73. Hafezi-Bakhtiari, S.; Adeyi, O. A. Metabolic Disorders of the Liver. *Diagnostic Histopathol.* **2014**, *20*, 125–133. DOI:10.1016/j.mpdhp.2014.01.012
74. Gille, C.; Bölling, C.; Hoppe, A.; Bulik, S.; Hoffmann, S.; Hübner, K.; Karlstädt, A.; Ganeshan, R.; König, M.; Rother, K.; et al. HepatoNet1: A Comprehensive Metabolic Reconstruction of the Human Hepatocyte for the Analysis of Liver Physiology. *Mol. Syst. Biol.* **2010**, *6*, 411. DOI:10.1038/msb.2010.62
75. Björnson, E.; Mukhopadhyay, B.; Asplund, A.; Pristovsek, N.; Cinar, R.; Romeo, S.; Uhlen, M.; Kunos, G.; Nielsen, J.; Mardinoglu, A. Stratification of Hepatocellular Carcinoma Patients Based on Acetate Utilization. *Cell Rep.* **2015**, *13*, 2014–2026. DOI:10.1016/j.celrep.2015.10.045
76. Klover, P. J.; Mooney, R. A. Hepatocytes: Critical for Glucose Homeostasis. *Int. J. Biochem. Cell Biol.* **2004**, *36*, 753–758. DOI:10.1016/j.biocel.2003.10.002
77. König, M.; Bulik, S.; Holzhütter, H.-G. Quantifying the Contribution of the Liver to Glucose Homeostasis: A Detailed Kinetic Model of Human Hepatic Glucose Metabolism. *PLoS Comput. Biol.* **2012**, *8*, e1002577. DOI:10.1371/journal.pcbi.1002577
78. Ashworth, W. B.; Davies, N. A.; Bogle, I. D. L. A Computational Model of Hepatic Energy Metabolism: Understanding Zonated Damage and Steatosis in NAFLD. *PLoS Comput. Biol.* **2016**, *12*, e1005105. DOI:10.1371/journal.pcbi.1005105
79. Schleicher, J.; Dahmen, U.; Guthke, R.; Schuster, S. Zonation of Hepatic Fat Accumulation: Insights from Mathematical Modelling of Nutrient Gradients and Fatty Acid Uptake. *J. R. Soc. Interface* **2017**, *14*, 20170443. DOI:10.1098/rsif.2017.0443
80. Mitchell, S.; Mendes, P. A Computational Model of Liver Iron Metabolism. *PLoS Comput. Biol.* **2013**, *9*, e1003299. DOI:10.1371/journal.pcbi.1003299
81. Sluka, J. P.; Fu, X.; Swat, M.; Belmonte, J. M.; Cosmanescu, A.; Clendenon, S. G.; Wambaugh, J. F.; Glazier, J. A. A Liver-Centric Multiscale Modeling Framework for Xenobiotics. *PLoS One* **2016**, *11*, e0162428. DOI:10.1371/journal.pone.0162428
82. Drasdo, D.; Hoehme, S.; Hengstler, J. G. How Predictive Quantitative Modelling of Tissue Organization Can Inform Liver Disease Pathogenesis. *J. Hepatol.* **2014**, *61*, 951–956. DOI:10.1016/j.jhep.2014.06.013
83. Naito, Y. A Computational Model of the Hepatic Lobule. In *E-Cell System*; Springer: New York, 2013; pp 143–155. DOI:10.1007/978-1-4614-6157-9_9
84. Hoehme, S.; Brulport, M.; Bauer, A.; Bedawy, E.; Schormann, W.; Hermes, M.; Puppe, V.; Gebhardt, R.; Zellmer, S.; Schwarz, M.; et al. Prediction and Validation of Cell Alignment along Microvessels as Order Principle to Restore Tissue Architecture in Liver Regeneration. *Proc. Natl. Acad. Sci.* **2010**, *107*, 10371–10376. DOI:10.1073/pnas.0909374107
85. Chan, S. L.; Wong, A. M.; Lee, K.; Wong, N.; Chan, A. K. C. Personalized Therapy for Hepatocellular Carcinoma: Where Are We Now? *Cancer Treat. Rev.* **2016**, *45*, 77–86. DOI:10.1016/j.ctrv.2016.02.008
86. Yang, J. D.; Roberts, L. R. Hepatocellular Carcinoma: A Global View. *Nat. Rev. Gastroenterol. Hepatol.* **2010**, *7*, 448–458. DOI:10.1038/nrgastro.2010.100
87. Folger, O.; Jerby, L.; Frezza, C.; Gottlieb, E.; Ruppin, E.; Shlomi, T. Predicting Selective Drug Targets in Cancer through Metabolic Networks. *Mol. Syst. Biol.* **2011**, *7*, 501. DOI:10.1038/msb.2011.35
88. Duarte, N. C.; Becker, S. A.; Jamshidi, N.; Thiele, I.; Mo, M. L.; Vo, T. D.; Srivas, R.; Palsson, B. O. Global Reconstruction of the Human Metabolic Network Based on Genomic and Bibliomic Data. *Proc. Natl. Acad. Sci.* **2007**, *104*, 1777–1782. DOI:10.1073/pnas.0610772104
89. Jerby, L.; Shlomi, T.; Ruppin, E. Computational Reconstruction of Tissue-Specific Metabolic Models: Application to Human Liver Metabolism. *Mol. Syst. Biol.* **2010**, *6*, 401. DOI:10.1038/msb.2010.56
90. Bordbar, A.; Feist, A. M.; Usaite-Black, R.; Woodcock, J.; Palsson, B. O.; Famili, I. A Multi-Tissue Type Genome-Scale Metabolic Network for Analysis of Whole-Body Systems Physiology. *BMC Syst. Biol.* **2011**, *5*, 180. DOI:10.1186/1752-0509-5-180
91. Agren, R.; Bordel, S.; Mardinoglu, A.; Pornputtapong, N.; Nookaew, I.; Nielsen, J. Reconstruction of Genome-Scale Active Metabolic Networks for 69 Human Cell Types and 16 Cancer Types Using INIT. *PLoS Comput. Biol.* **2012**, *8*, e1002518. DOI:10.1371/journal.pcbi.1002518

92. Roy, A. K.; Chatterjee, B. Sexual Dimorphism in the Liver. *Annu. Rev. Physiol.* **1983**, *45*, 37–50. DOI:10.1146/annurev.ph.45.030183.000345
93. Durazzo, M.; Belci, P.; Collo, A.; Prandi, V.; Pistone, E.; Martorana, M.; Gambino, R.; Bo, S. Gender Specific Medicine in Liver Diseases: A Point of View. *World J. Gastroenterol.* **2014**, *20*, 2127–2135. DOI:10.3748/wjg.v20.i9.2127
94. Zhang, Y.; Laz, E. V.; Waxman, D. J. Dynamic, Sex-Differential STAT5 and BCL6 Binding to Sex-Biased, Growth Hormone-Regulated Genes in Adult Mouse Liver. *Mol. Cell Biol.* **2012**, *32*, 880–896. DOI:10.1128/MCB.06312-11
95. Waxman, D. J.; O'Connor, C. Growth Hormone Regulation of Sex-Dependent Liver Gene Expression. *Mol. Endocrinol.* **2006**, *20*, 2613–2629. DOI:10.1210/me.2006-0007
96. Gui, Y.; Silha, J. V.; Murphy, L. J. Sexual Dimorphism and Regulation of Resistin, Adiponectin, and Leptin Expression in the Mouse. *Obes. Res.* **2004**, *12*, 1481–1491. DOI:10.1038/oby.2004.185
97. Cordeiro, J. V. Ethical and Legal Challenges of Personalized Medicine: Paradigmatic Examples of Research, Prevention, Diagnosis and Treatment. *Rev. Port. Saúde Pública* **2014**, *32*, 164–180. DOI:10.1016/j.rpsp.2014.10.002
98. Knowles, L.; Luth, W.; Bubela, T. Paving the Road to Personalized Medicine: Recommendations on Regulatory, Intellectual Property and Reimbursement Challenges. *J. Law Biosci.* **2017**, *4*, 453–506. DOI:10.1093/jlb/lxx030
99. Mardinoglu, A.; Boren, J.; Smith, U.; Uhlen, M.; Nielsen, J. Systems Biology in Hepatology: Approaches and Applications. *Nat. Rev. Gastroenterol. Hepatol.* **2018**, *15*, 365–377. DOI:10.1038/s41575-018-0007-8
100. Fenner, J. W.; Brook, B.; Clapworthy, G.; Coveney, P. V.; Feipel, V.; Gregersen, H.; Hose, D. R.; Kohl, P.; Lawford, P.; McCormack, K. M.; et al. The EuroPhysiome, STEP and a Roadmap for the Virtual Physiological Human. *Philos. Trans. R. Soc. A Math. Phys. Eng. Sci.* **2008**, *366*, 2979–2999. DOI:10.1098/rsta.2008.0089
101. Hunter, P.; Coveney, P. V.; de Bono, B.; Diaz, V.; Fenner, J.; Frangi, A. F.; Harris, P.; Hose, R.; Kohl, P.; Lawford, P.; et al. A Vision and Strategy for the Virtual Physiological Human in 2010 and Beyond. *Philos. Trans. R. Soc. A Math. Phys. Eng. Sci.* **2010**, *368*, 2595–2614. DOI:10.1098/rsta.2010.0048
102. Hunter, P.; Chapman, T.; Coveney, P. V.; De Bono, B.; Diaz, V.; Fenner, J.; Frangi, A. F.; Harris, P.; Hose, R.; Kohl, P.; et al. A Vision and Strategy for the Virtual Physiological Human: 2012 Update. *Interface Focus* **2013**, *3*, 20130004. DOI:10.1098/rsfs.2013.0004
103. Kolodkin, A.; Boogerd, F. C.; Plant, N.; Bruggeman, F. J.; Goncharuk, V.; Lunshof, J.; Moreno-Sanchez, R.; Yilmaz, N.; Bakker, B. M.; Snoep, J. L.; et al. Emergence of the Silicon Human and Network Targeting Drugs. *Eur. J. Pharm. Sci.* **2012**, *46*, 190–197. DOI:10.1016/j.ejps.2011.06.006

Povzetek

Računski modeli presnove jeter postajajo vse bolj pomembni in prepoznavni v raziskavah na področju sistemske medicine. V zadnjih letih so se pojavile tudi njihove prve klinične aplikacije v kontekstu personalizirane medicine. V pričujočem prispevku predstavimo pregled eksperimentalnih in računskih modelov, ki jih lahko uporabimo pri opisovanju in razumevanju presnovnih procesov *in silico*. Pregledamo zadnje trende pri razvoju obsežnih računskih modelov presnove jeter, kjer se osredotočimo na objektno-orientirane pristope modeliranja, ki predstavljajo eno od glavnih usmeritev naših raziskav. Prednosti objektno-orientiranih pristopov so v relativno enostavnem opisovanju interakcij med tkivi, kot je npr. interakcija presnove jeter z okoliškimi tkivi preko krvi. V nasprotju z alternativnimi pristopi modeliranja objektno-orientirani pristopi omogočajo neposredno vključitev tako transkripcijske kot tudi post-translacijske regulacije presnovnih reakcij. Na koncu prispevka opredelimo obstoječe in potencialne klinične aplikacije obsežnih računskih modelov presnove jeter ter opredelimo potenciale tako modelov presnovne kot tudi modelov ostalih celičnih procesov na področju sistemske in translacijske medicine.

Scientific paper

The Antioxidant Response System in Wheat Exposed to Pesticides and its Combined-induced Oxidative Damage

Nilgün Candan Yücel,^{1,*} Elif Hakli Heybet² and Ozay Ozgür Gokmen³

¹ Chemistry Department, Dokuz Eylül University, Faculty of Science, Buca, 35160, Izmir, Turkey

² Biology Department, Cukurova University, Faculty of Science and Art, 01150, Sarıçam, Balcalı, Adana, Turkey

³ Maize Research Institute, Arifiye, Sakarya

* Corresponding author: E-mail: nilgun.candan@deu.edu.tr

Tel: +90 232 301 95 40

Received: 26-05-2017

Abstract

The aim of the present study was to analyze the alterations in the, antioxidant enzyme activities (such as superoxide dismutase (SOD), catalase (CAT), glutathione peroxidase (GSH-Px) and level of glutathione (GSH) and lipid peroxidation (LPO) of wheat acutely treated with CP and DM treatments at low, high doses and their combination. CP and DM were administered to wheat in different doses of 1, 1.5, 5 and 35 mg kg⁻¹ given alone and combination. After 3 weeks, antioxidant enzyme activities, and the level of GSH and LPO were recorded and analyzed. Antioxidative defense mechanisms and LPO in wheat display different responses depending on different pesticide treatments and doses. Biochemical analysis showed that exposure of the CP and DM cause plant tissue damage. It is suggested that appropriate ecotoxicological risk assessment should be made in the areas where DM is proposed to be used in pest control when compared to CP. In the present study, we also concluded that the effect of the combined of CP and DM on the oxidative stress may be synergistic.

Keywords: Antioxidant enzymes; lipid peroxidation; pesticide mixture; wheat

1. Introduction

With the rapid development of global agriculture, the pesticide risk is receiving increasing consideration. Throughout world, there is a considerable plant exposure to pesticides due to several factors: bioaccumulation and excessive use of pesticides in the agriculture wastes.¹

From the pesticides, chlorpyrifos (CP, an organophosphate) belongs to the phosphorothioate class of organophosphorus insecticides.² CP, used worldwide (for use in nearly 100 countries and is applied to approximately 8.5 million crop acres each year) unfortunately is a known developmental neurotoxicant. There is increasing evidence that organophosphorus compounds also induce oxidative stress through generation of free oxygen radicals and cause an imbalance between formation and removal of free radicals, leading to LPO and DNA damage.³

Oxidative damage has been recognized as one of the primary causes of subcellular toxicity of pesticides.⁴ Studies on CP and DM exposure have also suggested a putative

role for free radicals in LPO and other oxidative stress-mediated injuries.^{5,6} Also, synthetic pyrethroids (DM, a pyrethroid pesticide) have emerged as a new class of agricultural pesticides and have found wide use over organochlorine and organophosphate pesticides. The use of pyrethroids as insecticidal and anti-parasitic formulations has markedly increased in last 2 decades.⁷ The main advantages of their use are their photostability, high efficacy.⁸ Pyrethroid class of pesticide, such as DM, is globally used in crop protection and control of malaria and other vector-borne diseases.

Insecticides may cause oxidative stress in plant cells, affecting the various metabolic activities and growth components in plants.⁸ It has been well documented that oxidative stress can occur in the cells of plants suffering from severe external environment stress like pesticides. For protection, plants have multiple complex enzymatic and non-enzymatic antioxidant systems including SOD, CAT, and POD.

However, no information is available on the combined effect of CP and DM on the response defense systems

in plants. The present study was designed to explore the effects of CP, DM and their combination on wheat plant and their relation to free-radical mediated membrane LPO and the influence of the antioxidant defense systems.

2. Experimental

2.1. Plants

Wheat sterilized seed cultivar (*Triticum durum* Desf. cv. Yelken) were kept in 1% sodium hypochloride about 15 min for sterilizing. Wheat plants were germinated in perlite moistened with saturated CaSO_4 solution. Germinated seedlings were bundled in five, fixed with a sponge stripe and transferred to plastic pots containing 2.7 L of the following continuously aerated nutrient solution: 0.7 mM K_2SO_4 , 2.0 mM $\text{Ca}(\text{NO}_3)_2$, 0.2 mM KH_2PO_4 , 0.75 mM MgSO_4 , 0.1 mM KCl, 100 μM FeEDTA, 1 μM H_3BO_3 , 0.5 μM MnSO_4 , 0.2 μM CuSO_4 , and 0.02 μM $(\text{NH}_4)_6\text{Mo}_7\text{O}_{24}$. Each treatment was replicated three times. Plants were grown in a climate chamber set to light-dark cycles of 16–8 h with a photosynthetic photon flux density of 450 $\mu\text{mol m}^{-2}\text{s}^{-1}$ at plant height during the light cycle and a temperature regime of 24–20°C during the light-dark cycles. Nutrient solutions were renewed every three days.

Seven-day-old seedlings were subjected to foliar application of five concentrations of CP, DM and their combination.

After 3 weeks of treatment, plant MDA level and SOD, GSH-Px, and CAT activities were determined.

Tissue extracts of wheat plants were prepared for enzyme activity determinations. One g material was homogenized in 4 ml 20 mM phosphate buffer (pH 7.4). The homogenate was then centrifuged at 15000 $\times g$ for 15 min. The supernatant was used for enzyme analysis. All operations (until the enzyme determination) were done at 4 °C.

2.2. Enzymatic Assays

The SOD assay was based on the inhibitory effects of SOD on the spontaneous autoxidation of 6-hydroxydopamine.⁹ One IU is the amount of SOD required to inhibit the initial rate of 6-hydroxydopamine autoxidation by 50%. CAT activity was assayed in a reaction mixture containing 25 mM phosphate buffer (pH 7.0) 10.5 mM H_2O_2 , and enzyme. The decomposition of H_2O_2 was followed at 240 nm ($E = 39.4 \text{ mM}^{-1} \text{ cm}^{-1}$).¹⁰ One IU of enzyme activity is the amount of the enzyme, which decomposes 1 μmol H_2O_2 per min at 25 °C. The determination of GSH-Px activity was based on the method of Paglia and Valentine.¹¹ GSH-Px catalyses the oxidation of GSH by cumene hydroperoxide. In the presence of GSH reductase and NADPH, the oxidized glutathione is immediately converted to the reduced form with a concomitant oxidation of NADPH to NADP^+ . The decrease in absorbance of NADPH was measured at 340 nm.

2.3. Non-enzymatic Assays

GSH was estimated based on Ellman 5,5'-Dithiobis(2-nitrobenzoic acid) (DTNB) reactivity. Samples were evaluated for colored component production using a spectrophotometric assay for DTNB at 412 nm.¹²

LPO was estimated based on thiobarbituric acid (TBA) reactivity. Samples were evaluated for MDA production using a spectrophotometric assay for TBA.¹³ The extinction coefficient of 153 $\text{mM}^{-1} \text{ cm}^{-1}$ at 532 nm for the chromophore was used to calculate the MDA-like TBA.

The total protein content was determined by the method of Bradford using bovine serum albumin (BSA) as standard (data not shown).¹⁴

Data are given as mean \pm standard deviation. Statistical analysis of data was performed on computer by using SPSS Version 11.0. Kruskal Wallis was used for comparison of six groups. If a difference was detected by using Kruskal Wallis test, the Bonferonni-corrected Mann-Whitney U test was used to determine which two groups were significantly different.

2.4. Fresh Weight and Shoots Length

The fresh weight of whole seedlings (roots included) and shoot length was measured at 7th, 14th and 21th days.

3. Results and Discussion

Antioxidative defense mechanism and LPO in wheat tissues display different responses depending on different pesticide treatments (CP as an organophosphate, DM as a pyrethroid pesticide) and doses. All the results from various treatment groups have been compared to each other and to control.

Biochemical analysis showed that there was a significant increase in MDA level of plant after low- and high-doses pesticide (CP, DM) treatments compared to control (Fig. 1). At high doses of DM and CP, the wheat showed remarkable increase LPO levels compared to those of low dose of DM and CP treatments ($p < 0,001$). The highest LPO levels in plant were observed as 295.17% in high dose CP treatment and as 226.03% in high dose DM treatment when compared with control plant. DM and CP combination group of plants showed significant maximum LPO level (308.97%) respect to control.

The results of the present study clearly demonstrate that CP, DM and their combination produced adverse effects on wheat plants, the major symptoms were reduced growth, disruption of the antioxidant system and significantly increased of LPO level.

However, the relative responses of LPO affected by CP were more pronounced than in case of DM. According to the present experiments, we concluded that LPO may be one of the molecular mechanisms involved in CP and DM-induced toxicity. Also the same mechanism may be operated for DM treatment caused the LPO induction.

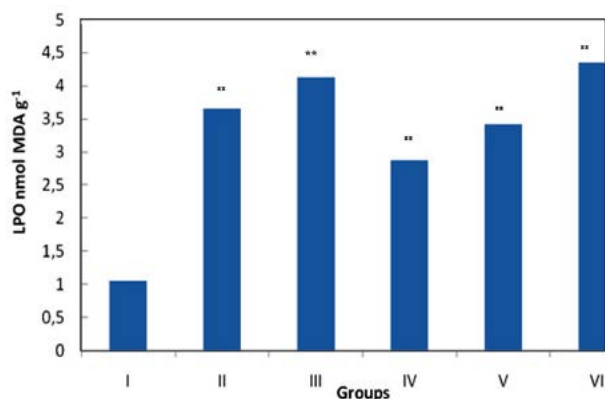


Figure 1. Effect of chlorpyrifos and deltamethrin on the wheat plant lipid peroxidation as measured by MDA value. CP and DM were administered in different doses. Group I (control group), group II (1 mg kg⁻¹ CP group), group III (15 mg kg⁻¹ CP group), group IV (5 mg kg⁻¹ DM group), group V (35 mg kg⁻¹ DM group), group VI (combination group of 1 mg kg⁻¹ CP and 5 mg kg⁻¹ DM). Values are represented as means ** significantly different from control at P < 0.001.

The observed activities of antioxidative enzymes such as SOD (a scavenger of superoxides), CAT (a scavenger of H₂O₂) and GSH-Px are shown in Table 1.

Table 1. Effect of CP and DM on the SOD, CAT and GSH-Px activities of wheat plant. Values are represented as means S.D. of eight plants in each group. ** Significantly different from control at P < 0.001.

Groups	Antioxidant Enzyme Activities		
	SOD (IU/mg)	CAT (IU/mg)	GSH-Px 10 ³ (IU/mg)
I	61.43	132.23	51.31
II	96.87**	211.36**	59.30
III	82.18	150.62	29.03**
IV	76.14	147.79	78.68**
V	116.51**	306.41**	71.27
VI	118.09**	160.00	64.53

SOD activities were significantly increased in both pesticide treatment groups (Table 1). While SOD activities in the CP treatment group showed a negative correlation with CP concentration, DM treatment group displayed a positive correlation with the concentration. The maximum SOD activity was observed in DM and CP combination group of plants as 88.74% (p < 0.001).

GSH-Px activities were significantly increased in wheat tissues except for high dose CP treatment group (Table 1). GSH-Px activities in plants showed a negative correlation with CP and DM concentrations. The maximum GSH-Px activity was observed in low dose DM group of plants as 53.34% (p < 0.001).

CAT activities were significantly increased in all groups (Table 1). While CAT activities in wheat showed a

negative correlation with CP concentration, a positive correlation was observed due to the DM concentration. The maximum increase was observed in high dose DM group as 131.62% (p < 0.001).

GSH levels in wheat plants were decreased in all groups except for low dose CP treatment group showed a negative correlation with CP and DM concentrations (Fig. 2).

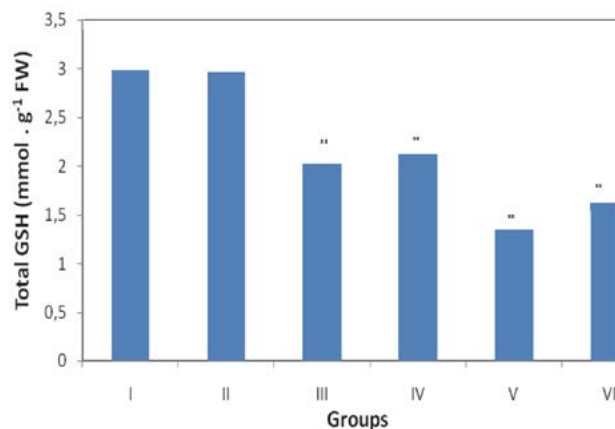


Figure 2. Effect of chlorpyrifos and deltamethrin on the wheat GSH level. CP and DM were administered in different doses. Group I (control group), group II (1 mg kg⁻¹ CP group), group III (15 mg kg⁻¹ CP group), group IV (5 mg kg⁻¹ DM group), group V (35 mg kg⁻¹ DM group), group VI (combination group of 1 mg kg⁻¹ CP and 5 mg kg⁻¹ DM). Values are represented as means ± S.D. of eight plants in each group. ** Significantly different from control at P < 0.001.

Fresh weight and shoot length in wheat plants were decreased in all groups and the maximum decreases were observed in DM and CP combination group of plants as 86.64% and 83.64%, respectively (p < 0.001) (Table 2.).

It appears that the cells under stress increase the production of antioxidant enzymes that scavenge the free radicals.¹⁵ Once free radicals are formed, the cells start some physiological defense mechanisms to prevent the damage. SOD, CAT and GSH-Px activities at 1 mg kg⁻¹ increased activities, while 15 mg kg⁻¹ decreased those. It is highly likely that 3 weeks of treatment with 15 mg kg⁻¹ of CP caused more wheat tissue injury than did 1 mg kg⁻¹. The negative correlation could be a reflection of tissue loss due to the toxic action of these pesticides. Some studies indicated that superoxide radicals can inhibit GSH-Px¹⁶ and CAT activities¹⁷, and singlet oxygen and peroxy radicals can inhibit SOD and CAT activities.¹⁸ As pointed out by Oncu et al., if CP inhibits GSH-Px and CAT significantly via ROS induced by CP, H₂O₂ will accumulate.¹⁹ The increased H₂O₂ could cause SOD inhibition, so that superoxide radicals would increase. The increased superoxide radicals would inhibit both CAT and GSH-Px so that H₂O₂ would accumulate in the medium, causing SOD inhibition and increased superoxide radicals. The observed inhibitions of SOD, CAT and GSH-Px may be due to the direct effect of CP or due to the effect of ROS induced by CP or both.

Table 2. Growth parameters: Fresh weight and % Germination of wheat for different treatments

Growth parameters	Treatments (% + mM)	Plant growth (in days)		
		7	14	21
Fresh weight (mg)	I	60 ± 2	150 ± 2	189 ± 3
	II	52 ± 2	110 ± 2 ^δ	183 ± 8 ^ε
	III	45 ± 2	102 ± 2 ^δ	173 ± 9 ^ε
	IV	50 ± 2	130 ± 2 ^δ	162 ± 5 ^ε
	V	40 ± 2	120 ± 09 ^ε	140 ± 4 ^ε
	VI	30 ± 2	95 ± 11 ^δ	119 ± 11 ^ε
Shoot length (cm)	I	5.2 ± 2	11.3 ± 2	20.2 ± 2
	II	4.9 ± 2	10.5 ± 2	19.2 ± 2
	III	4.6 ± 2	9.9 ± 2	18.1 ± 2
	IV	3.9 ± 2	9.5 ± 2	16.5 ± 2
	V	3.5 ± 2	9.4 ± 2	16.4
	VI	2.9 ± 2	8.7 ± 2	14.4

Data are 'mean ± S.D' the mean ± SD of three independent experiments.

^δ p < 0.05 (probably significant) ^ε p < 0.01 (definitely significant)

In the present study, significant elevations in the SOD and CAT activities were indicated in DM-toxicated plants with increasing dose. These results show that SOD and CAT display co-operative functions for preventing a partial protection of membrane lipid against oxidative stress under DM treatment compared to CP treatment.

GSH is an important antioxidant system of most aerobic cells.²⁰ It plays a key role as a cofactor with a variety of enzymes including GSH-Px. GSH depletion has been shown to intensify LPO and predispose cells to oxidant damage.²¹ This study demonstrates that enhanced CP and DM concentrations effect on GSH loss and LPO elevation in wheat plants. When the relative responses of LPO and GSH were compared, effects of these pesticides were more pronounced in case of decrease in GSH than the LPO induction in wheat plants. Thus, it is concluded that endogenous GSH plays an important protective role against CP than DM and induced oxidative damage in vivo.

Groten et al., suggest that a simple mixture should be evaluated by testing each individual compound separately, and thereafter different combinations of the compounds.²² Testing mixture in this way, it would be possible to identify the compound(s) responsible for possible interactions. As mixture models improve, more precise data throughout the toxicity range could be required. More research on pesticide mode of toxic action and secondary physiological effects caused by pesticides would provide a platform for understanding the physiology of mixture effects, lead to better predictive models, and allow for rational experimental design. We believe that these types of studies are critical for realistic estimations of toxicity, because rarely are organisms exposed to only a single chemical in the field. In the present study, the two pesticides (CP and DM) were tested individually, and one combination group. It was shown that inhibition of GSH level in the combination group induced LPO level. These observations suggest that

the effect of combination of CP and DM on the oxidative stress may be synergistic.

Pesticides before authorized and registered to be used in European Union (EU), member states undergo extensive chemical, biological (effectiveness), toxicological and environmental behaviour scrutiny investigations in the field of water policy.²³ According to this prioritization approach 71 pesticides were identified as being pollutants in the Pinios River Basin of Central Greece reflecting the current situation of land use and agricultural practices.²⁴ CP ranked first potential hazardous candidate for the Pinios River basin and DM did not rank as a potential hazardous. In the present study, we also concluded that the effect of the combined of CP and DM biochemical behavior scrutiny may be much better than DM alone.

4. Conclusions

These data present evidence that, CP and DM treatments lead to enhanced toxicity in wheat plant in relation to dose. The enhancements of LPO suggest the involvement of free radicals intermediates in these pesticide toxicities. The existence of an inducible antioxidant system may reflect an adaptation by the organism. Increased antioxidant defense system of wheat resulted in partial protection of membrane lipid against oxidative stress under DM treatment compared to CP.

5. References

1. C. G. Castillo, M. Montante, L. Dufour, M. Martinez, M. E. Jimenez-Capdeville, *Neurotoxic. Teratol* **2002**, *24*, 797–804.
DOI:10.1016/S0892-0362(02)00268-4
2. R. J. Richardson, T. B. Moore, U. S. Kayyali, J. H. Fowke, J. C.

- Randall, *Fundam. Appl. Toxicol.* **1993**, *20*, 273–279.
DOI:10.1006/faat.1993.1036
3. D. Bagchi, M. Bagchi, E. A. Hassoun, S. J. Stohs, *Toxicol* **1995**, *104*, 129–40. DOI:10.1016/0300-483X(95)03156-A
4. L. Liang, Y. L. Lu, H. Yang, **2012**, *Environ. Sci. Pollut. R.* *19*, 2044–2054. DOI:10.1007/s11356-011-0698-7
5. M. I. Yousef, T. I. Awad, E. H. Mohamed, *Toxicol.* **2006**, *227*, 240–247. DOI:10.1016/j.tox.2006.08.008
6. S. P. Bradburry, J. R. Coast, *Rev. Environ. Contam. Toxicol.* **1989**, *108*, 134–77. DOI:10.1007/978-1-4613-8850-0_4
7. Y. Shukla, A. Arora, A. Singh, *Toxicol.* **2001**, *163*, 1–9.
DOI:10.1016/S0300-483X(00)00416-9
8. F. Bashir, T. O. Siddiqi, Mahmooduzzafar, M. Iqbal, *Environ. Pollut.* **2007**, *147*, 94–100. DOI:10.1016/j.envpol.2006.08.013
9. N. Crosti, T. Servedi, J. Bajera, A. Sera, *J. Clin. Chem. Clin. Biochem.* **1987**, *25*, 265–267.
10. H. E. Aebi, **1983**, Catalase, In: *Methods of Enzymatic Analysis*, 3rd Ed., Deerfield Beach, Florida: Verlag Chemic, pp. 273–286.
11. D. E. Paglia, W. N. Valentine, *J. Lab. Clin. Med.* **1967**, *70*, 158–169.
12. F. Tietze, *Anal. Biochem.* **1969**, *27*, 502–522.
DOI:10.1016/0003-2697(69)90064-5
13. H. H. Draper, M. Hadley, *Methods. Enzymol.* **1990**, *186*, 421–431. DOI:10.1016/0076-6879(90)86135-1
14. M. M. Bradford, *Anal. Biochem.* **1976**, *72*, 248–252.
DOI:10.1016/0003-2697(76)90527-3
15. B. D. Banerjee, V. Seth, R. S. Ahmed, *Rev. Environ. Health.* **2001**, *16*, 1–40. DOI:10.1515/REVEH.2001.16.1.1
16. D. Debnath, T. K. Mandal, *J. Applied. Toxicol.* **2000**, *20*, 197–204. DOI:10.1002/(SICI)1099-1263(200005/06)20:3<197::AID-JAT634>3.0.CO;2-7
17. J. L. Freeman, M. W. Persans, K. Nieman, *Plant Cell* **2004**, *16*, 2176–2191. DOI:10.1105/tpc.104.023036
18. F. Gultekin, M. Ozturk, M. Akdogan, *Arch. Toxicol.* **2000**, *74*, 533–538, 2000. DOI:10.1007/s002040000167
19. J. A. Escobar, M. A. Rubio, E. A. Lissi, *Free Radic Biol Med.* **1996**, *20*, 285–290. DOI:10.1016/0891-5849(95)02037-3
20. D. Dolphin, R. Poulson, R. Avramovic, **1998**, *Glutathione: chemical, biochemical and medical aspects*, Willey, New York, NY Parts A and B.
21. R. G. Nath, J. E. Ocanda, J. P. Richie, F. L. Chung, *Chem Res Toxicol.* **1997**, *10*, 1250–1253. DOI:10.1021/tx9701079
22. J. P. Groten, V. J. Feron, J. Sühnel, *Trends. Pharmacol.* **2001**, *31*, 316–321. DOI:10.1016/S0165-6147(00)01720-X
23. European Commission (EU) **2013**. Decision 2013/39/EC on environmental quality standards in the field of water policy. *Off. J. Eur. Communities* (2013), L 226/1 (12.08.2013).
24. A. Tsaoulas, E. N. Papadakis, Z. Vryzas, A. Kotopoulou, K. Kintzikoglou, *Environ. Inter.* **2016**, *91*, 78–93.
DOI:10.1016/j.envint.2016.02.008

Povzetek

Cilj te študije je bil analizirati spremembe v aktivnostih antioksidantnih encimov (kot so superoksid dismutaze (SOD), katalaze (CAT), glutation peroksidaze (GSH-Px) in stopnje peroksidacije glutationa in lipidov (LPO) pšenice akutno zdravljenje s klorpirifosom in deltametrinskim zdravljenjem pri nizkih in visokih odmerkih in njihovi kombinaciji. Klorpirifos (CP) in deltametrin (DM) so dajali pšenici v različnih odmerkih po 1, 1,5, 5 in 35 mg kg⁻¹, samostojno in v kombinaciji. Po 3 tednih so bile zabeležene in analizirane stopnje antioksidantnih encimov ter ravni glutationa GSH, askorbata in lipidov. Antioxidativni obrambni mehanizmi in peroksidacija lipidov pri pšenici kažejo različne odzive, odvisno od različnih pesticidov in odmerkov. Biokemijske analize so pokazale, da klorpirifos in deltametrin povzročata poškodbe rastlinskega tkiva. Predlagamo, da se ustrezno oceni ekotoksikološko tveganje na območjih, kjer se deltametrin uporablja za zatiranje škodljivcev v primerjavi s klorpirifosom. V tej študiji smo ugotovili tudi, da je lahko učinek kombinacije klorpirifosa in deltametrina sinergističen.

Scientific paper

Simultaneous Sensitive Detection of Lead(II), Mercury(II) and Silver Ions Using a New Nucleic Acid-Based Fluorescence Sensor

Yuan Deng,¹ Yinran Chen² and Xiaodong Zhou^{2,*}¹ Institute of Scientific Research & Development, Wuhan University, Wuhan 430072, PR China.² College of Chemistry and Molecular Sciences, Wuhan University, Wuhan 430072, PR China.* Corresponding author: E-mail: Email: zhouxd@whu.edu.cn
Phone: +86 027 68752439 fax: +86 027 68752136

Received: 07-06-2017

Abstract

A new nucleic acid-based fluorescence sensor is reported for simultaneous detection of Pb²⁺, Ag⁺, and Hg²⁺ based on the specific catalytic activity of Pb²⁺ for a particular DNAzyme, specific regulation of Ag⁺ on “C-Ag⁺-C” complex, and stable complex formed by Hg²⁺ and rhodamine B isothiocyanate (RBITC). Three fluorescence dyes, aminomethylcoumarin acetic acid (AMCA), 5-carboxyfluorescein (FAM), and RBITC, were modified on the probes and served as fluorescent donors. Upon DNA interaction with these metal ions and AuNP fluorescence quenching effect on the fluorescence dyes, the fluorescence recovery of RBITC and the fluorescence quenching of AMCA and FAM were monitored to detect Hg²⁺, Pb²⁺, and Ag⁺, separately, without the need of using any masking reagents. This sensor exhibited high sensitivity and selectivity. The limit of detection (LOD) is 0.48 nM for Pb²⁺, 0.23 nM for Ag⁺, and 0.17 nM for Hg²⁺. Finally, this sensor was successfully applied for simultaneous detection of Pb²⁺, Ag⁺, and Hg²⁺ in real sample.

Keywords: Fluorescent sensor; Au nanoparticles (AuNPs); DNAzyme; simultaneous detection; metal ions

1. Introduction

With the ever increasing pollution from modern industry, heavy metal contaminants have posed severe adverse effects on human health and ecosystems due to their high and persistent toxicities.^{1,2} Therefore, it is quite necessary and urgent to rapidly and accurately detect these metal ions. Traditional methods, such as atomic absorption spectrometry (AAS),³ inductively coupled plasma mass spectrometry (ICP-MS),⁴ and anodic stripping voltammetry (ASV),⁵ have high sensitivity and selectivity but require specialized instrumentation and extensive sample pretreatment processes which limit their applications for *in situ* analysis.^{6,7}

In recent years, much effort has been devoted toward design of DNA-based sensors to detect heavy metal ions, especially Ag⁺, Hg²⁺, and Pb²⁺, which are three of the most toxic heavy metals.⁸ The detection of Pb²⁺ relies on the specific catalytic activity of Pb²⁺ for the particular DNAzyme. For Pb²⁺ detection, most detectors were based on the Pb²⁺-dependent DNAzyme^{9,10} and Pb²⁺-stabilized

G-quadruplex.^{11,12} As for Hg²⁺ and Ag⁺, the detections relies on the selective capture of Hg²⁺ by T-T mismatches to form T-Hg(II)-T base pairs,^{13,14} and the exclusive recognition of Ag⁺ by C-C mismatches to form C-Ag(I)-C complex.^{15,16} Accordingly, various detection techniques, such as colorimetry,^{17–19} electrochemistry,^{10,20,21} and fluorescence,^{15,22,23} were applied to selectively detect Pb²⁺, Ag⁺, or Hg²⁺. Given that metal ions usually coexist in several samples, some researches have been focused on the simultaneous detection of two or more metal ions at trace level, such as Pb²⁺ and Hg²⁺,^{24,25} as well as Hg²⁺ and Ag⁺.^{26–28}

However, with regard to the sensors designed for the simultaneous detection of three metal ions, there are only a few relevant reports. Zhang et al.²⁹ developed a colorimetric assay for parallel detection of Cd²⁺, Ni²⁺, and Co²⁺ utilizing peptide modified gold nanoparticles as a sensing element based on its unique surface plasmon resonance properties. Hien et al.³⁰ designed a fluorescent chemosensor based on dimethylaminocinnamaldehyde-aminothiourea and applied it for simultaneous detection of Ag⁺, Hg²⁺, and Pb²⁺. Lin et al.³¹ reported an unlabeled immobilized DNA-

based sensor for simultaneous detection of Pb^{2+} , Ag^+ , and Hg^{2+} by electrochemical impedance spectroscopy (EIS) with $[\text{Fe}(\text{CN})_6]^{4-/3-}$ as redox probe. However, they have some limitations including poor selectivity, insufficient sensitivity, or the need of using the masking reagent.

In this paper, we designed a DNA-based sensor to achieve a rapid, simple and simultaneous detection of Pb^{2+} , Ag^+ , and Hg^{2+} based on the DNA interaction with these metal ions and AuNP fluorescence quenching effect on the fluorescence dyes. Three fluorescence dyes, aminomethylcoumarin acetic acid (AMCA), 5-carboxyfluorescein (FAM), and rhodamine B isothiocyanate (RBITC), were introduced in this assay to detect Pb^{2+} , Ag^+ , and Hg^{2+} , respectively. Consequently, no masking reagent was needed in this method so that the detection process was simplified and speeded up. Fluorescence spectra were used at trace level due to its high sensitivity.

2. Experimental

2.1. Materials and Instrumentation

Reagents including AgNO_3 , $\text{Hg}(\text{NO}_3)_2$, $\text{Pb}(\text{NO}_3)_2$, $\text{Ca}(\text{NO}_3)_2$, $\text{Mg}(\text{NO}_3)_2$, $\text{Al}(\text{NO}_3)_3$, $\text{Co}(\text{NO}_3)_2$, $\text{Cu}(\text{NO}_3)_2$, $\text{Cr}(\text{NO}_3)_3$, $\text{Zn}(\text{NO}_3)_2$, $\text{Ni}(\text{NO}_3)_2$, KNO_3 , NaNO_3 , $\text{Cd}(\text{NO}_3)_2$, trisodium citrate, 1% HAuCl_4 , K_2CO_3 , RBITC, High Performance Liquid Chromatography (HPLC) purified oligonucleotides (aDNA:5'-FAM-ACCCCTC-3', bDNA:5'-ATGTCACTT-3'-SH-, cDNA: 5'-AMCA-AAGTGACA TrAGGACGATCACCCCT-3'-SH-, dDNA:5'- ATCGTCTC-CGAGCCGGTCGAAATGTC-3') were purchased from Shanghai Sangon Biotechnology Co., Ltd. Deionized water (18.2 M Ω cm resistivity) from a Millipore Milli-Q system was used throughout this work.

Fluorescence spectra were recorded by F-4600 fluorescence spectrophotometer (Hitachi, Japan) with the excitation and emission slit widths 5.0 nm and 10.0 nm, voltage 700 V, and excitation and emission wavelengths of 495 nm and 517 nm for FAM-ssDNA, 530 nm and 580 nm for RBITC, and 353 nm and 450 nm for AMCA, respectively.

2.2. Preparation of Functionalized AuNPs Probe and Analytical Procedure

cDNA (5 μM) and dDNA (5 μM) were mixed uniformly, reacting for 5 min in 90 $^\circ\text{C}$ water bath. Then the mixture was gradually cooled to room temperature to form double-stranded "cDNA+dDNA".

RBITC solution (1 mM, 10 μL) was added into AuNPs suspension (13 nm, 1 mL); the mixture was incubated at room temperature for 2 h, and then centrifuged. The filter cake was added to double-stranded "cDNA+dDNA" solution (5 μM) and bDNA solution (5 μM), respectively, to synthesize cDNA+dDNA-AuNP and bDNA-AuNP probes. Next, the solution containing cDNA+dDNA-AuNP and bDNA-AuNP probes was mixed uniformly with the

same volume of aDNA solution. All the prepared mixtures were stored at 4 $^\circ\text{C}$ for later use.

For Pb^{2+} sensing, Pb^{2+} solutions of different concentrations (10, 50, 100, 300, 500, 700 and 1000 nM) were prepared and added into the sensor solution prepared as described above, reacting at room temperature for 20 min. The concentration of both Ag^+ and Hg^{2+} were 10 μM in these solutions. Afterwards, the fluorescence emission spectra were measured at excitation wavelength of 353 nm. For Ag^+ and Hg^{2+} detection, similar procedures were followed to those described for Pb^{2+} .

For the selectivity measurement, other metal ions solution (10 μM) were added into the sensor solution, and the fluorescence spectra were monitored at excitation wavelengths of 353 nm, 495 nm, and 530 nm, respectively.

The real sample was collected from East Lake in Wuhan City and used after being filtered, and the sample was spiked with different concentrations of Pb^{2+} , Ag^+ , and Hg^{2+} to implement the recovery test.

3. Results and Discussion

3.1. Sensing Strategy

Fig. 1 depicts the process of simultaneous detection. Three fluorescent dyes, AMCA, FAM, and RBITC, served as fluorescent donors for detection of Pb^{2+} , Ag^+ , and Hg^{2+} , respectively. The newly synthesized AuNPs were selected as fluorescent receptor owing to their advantages, such as: small particle size, large specific surface area, strong adsorption capacity and excellent water-solubility. RBITC was initially combined with AuNP (recorded as AuNP-RBITC), resulting in fluorescence quenching at 580 nm. AMCA was specially designed to label at one end of the substrate strand of 8-17 DNAzyme, and the other end was combined with AuNP, emitting fluorescence signal at 450 nm. FAM was combined with ACCCCTC-3' (aDNA), and this FAM-aDNA fluoresced at 520 nm. In addition, the surfaces of some AuNPs were modified with 5'-ATGTCACTT-3'-SH-(bDNA). Then when adding Pb^{2+} , Ag^+ , and Hg^{2+} into the bulk solution, the fluorescence intensity would change due to the interaction between these metal ions and the DNA sequences labeled by fluorescent dye. Pb^{2+} cleaved the substrate strand of DNAzyme at the ribonucleic adenosine (rA) base, releasing two kinds of DNA fragments: AuNP-cDNA and AMCA-dDNA. dDNA complementarily paired with bDNA-AuNP, to shorten the distance between AMCA and the surface of AuNPs, resulting in fluorescence quenching of AMCA. Simultaneously, Ag^+ prompted AuNP-cDNA and aDNA to form a strong double-stranded DNA via the stable "C-Ag+-C" complex, resulting in fluorescence quenching of FAM. There is also a limitation in our sensor that Ag^+ cannot be detected in the absence of Pb^{2+} . If there is no Pb^{2+} in the system, a slight amount of Pb^{2+} should be introduced to trigger the subsequent reactions.

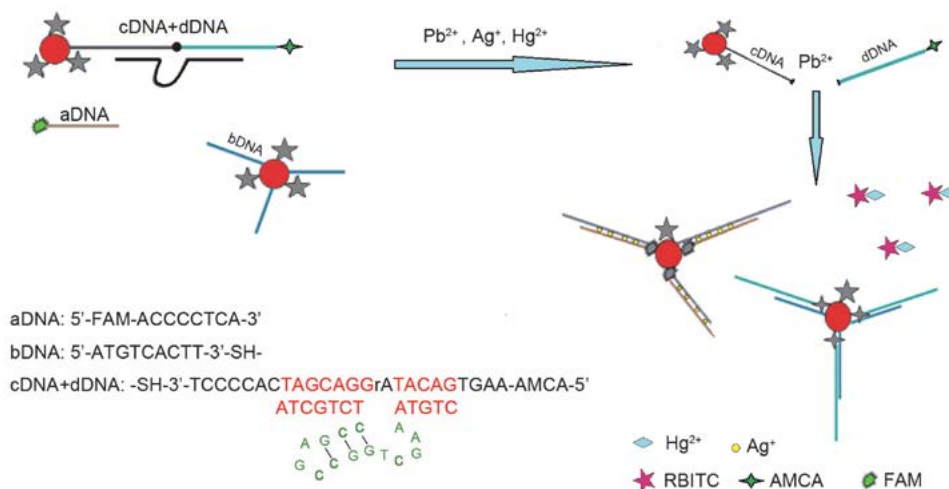


Fig. 1. Schematic of simultaneous detection of Ag⁺, Hg²⁺, and Pb²⁺ using AuNP-based fluorescent sensors.

As for Hg²⁺, owing to the larger stability constant of the complex formed by Hg²⁺ and RBITC than that of the complex formed by AuNPs and RBITC, RBITC would displace from the surface of AuNPs and combine with Hg²⁺, leading to fluorescence recovery of RBITC.

3. 2. Simultaneous Detection of Pb²⁺, Ag⁺, and Hg²⁺

Fig. 2 shows the fluorescence emission spectra of the AuNP probe solution before and after adding Pb²⁺, Ag⁺, and Hg²⁺. As illustrated in Fig. 2(A), the presence of Pb²⁺ in the AuNP-bDNA and AuNP-cDNA+dDNA-AMCA solution leads to ~95% fluorescence quenching of AMCA (compare Curves 3 with 1 or 2), due to the complementary pairing of AuNP-bDNA with the released AMCA-dDNA caused by Pb²⁺-induced cleavage. In Fig. 2(B), fluorescence of FAM quenched ~70% with the addition of Ag⁺ into FAM-aDNA and AuNP-cDNA-dDNA-AMCA (compare Curves 6 with 4 or 5) owing to the Ag⁺-introduced combination of FAM-aDNA and AuNP-cDNA released after Pb²⁺-induced cleavage. In Fig. 2(C), the significant

fluorescence recovery of RBITC (compare Curves 7 and 8) proves the strong binding of Hg²⁺ and RBITC, which impelled the RBITC's departing from surface of AuNPs and caused fluorescence recovery.

In Fig.2(A), the coincidence of Curve 1 and 2 shows that fluorescence signal was almost unchanged when AuNPs-bDNA was added into AuNP-cDNA+dDNA-AMCA, indicating dDNA and bDNA would not pair in the absence of Pb²⁺, which can guarantee the precision for Pb²⁺. Similarly, fluorescence signal of FAM remained almost unchanged when aDNA was added into AuNP-cDNA+dDNA-AMCA (compare Curve 4 with 5). It is because cDNA part of the DNzyme substrate strand was specially designed to be rich in an odd number of C bases arranged asymmetrically, so as to avoid the combination of "C-Ag⁺-C" complex by aDNA itself in the presence of Ag⁺ and improve the precision of detection of Ag⁺. In order to further ensure the precision of this detection method, we analyzed the mutual impacts among the three metal ions during the detection process. As shown in Fig. 3, the detection results remained unchanged in the presence of all three metal ions or only one of these metal ions, proving

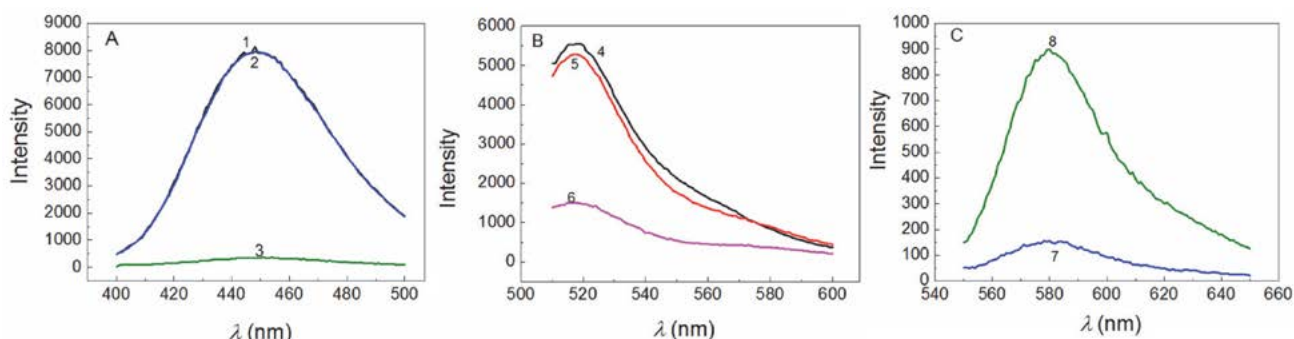


Fig. 2. Fluorescence emission spectra of the detection of (A) Pb²⁺ ($\lambda_{ex} = 353$ nm, $\lambda_{em} = 450$ nm), (B) Ag⁺ ($\lambda_{ex} = 495$ nm, $\lambda_{em} = 517$ nm), (C) Hg²⁺ ($\lambda_{ex} = 530$ nm, $\lambda_{em} = 580$ nm) in the solution containing (1) AuNP-cDNA-dDNA-AMCA, (2) AuNP-cDNA-dDNA-AMCA + AuNP-bDNA, (3) AuNP-cDNA-dDNA-AMCA + AuNP-bDNA + Pb²⁺, (4) FAM-aDNA, (5) FAM-aDNA + AuNP-cDNA, (6) FAM-aDNA + AuNP-cDNA + Ag⁺, (7) AuNP-RBITC, (8) AuNP-RBITC + Hg²⁺.

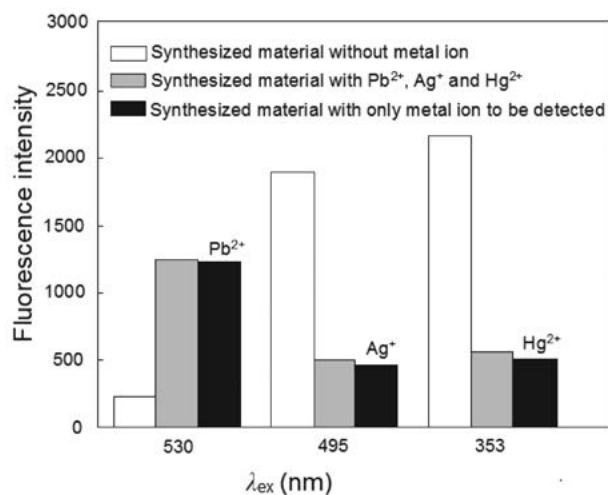


Fig. 3. Mutual impacts among the three metal ions during the detection process.

that the detection of these three metal ions was independent from each other.

Furthermore, fluorescence intensity changes rapidly in response to the addition of the metal ions. As shown in Fig. 4, the reactions reached equilibrium after about 600 s for Pb²⁺, 200 s for Ag⁺, and 200 s for Hg²⁺. The results indicated that this sensor allows a rapid detection of three heavy metal ions with high stability.

3. 3. Sensitivity and Selectivity of Simultaneous Detection for Pb²⁺, Ag⁺, and Hg²⁺

In order to evaluate the sensitivity of the sensor for Pb²⁺, Ag⁺, and Hg²⁺, different concentrations of these metal ions were added into the sensor solution under the optimized conditions such as pH = 8.0, RBITC concentration is 1 mM and DNA concentration is 5 μM.

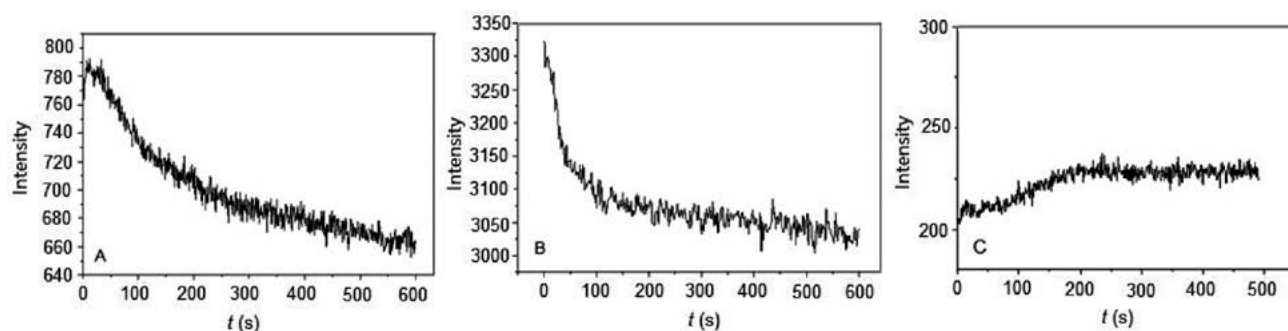


Fig. 4. Fluorescence intensity changes vs. time after adding (A) Pb²⁺, (B) Ag⁺, and (C) Hg²⁺.

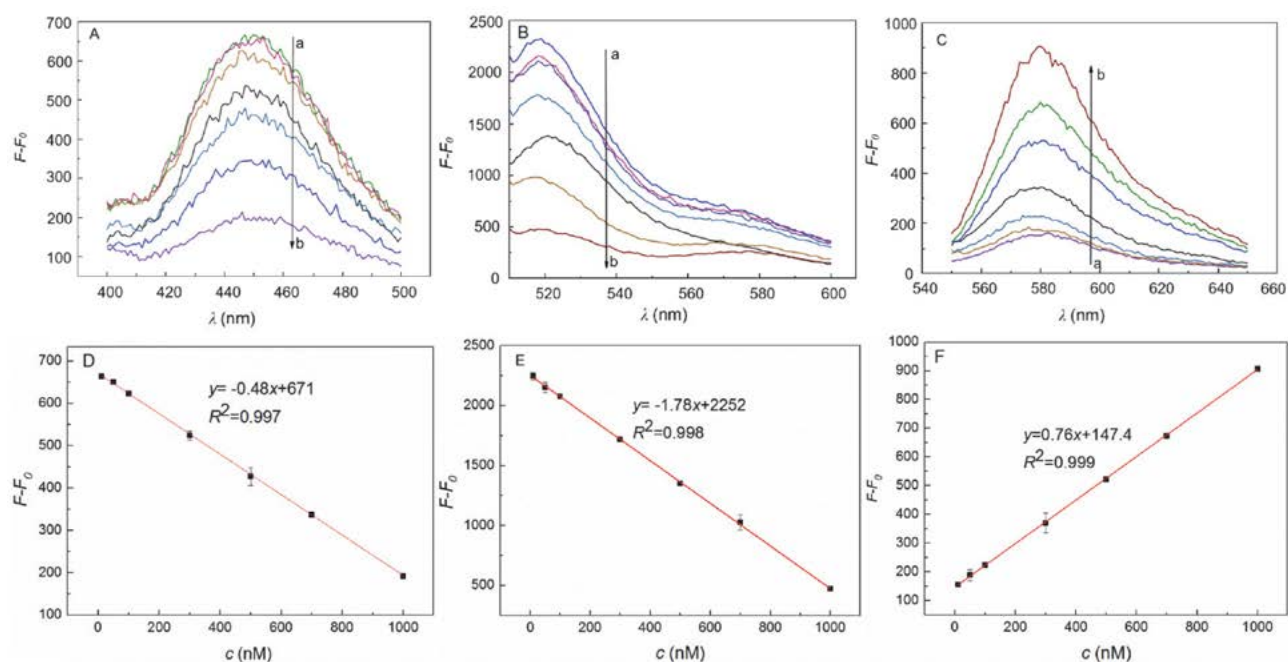


Figure 5. Fluorescence emission spectra of (A) Pb²⁺ (λ_{ex} = 353 nm, λ_{em} = 450 nm), (B) Ag⁺ (λ_{ex} = 495 nm, λ_{em} = 517 nm), and (C) Hg²⁺ (λ_{ex} = 530 nm, λ_{em} = 580 nm), and standard curves of (D) Pb²⁺, (E) Ag⁺, and (F) Hg²⁺ in the concentration of (a~b) 10, 50, 100, 300, 500, 700, 1000 nM. *F* is measured fluorescence intensity, *F*₀ is background fluorescence intensity.

As shown in Fig. 5, the fluorescence spectra changed regularly. The intensity of AMCA ($\lambda_{\text{ex}} = 353 \text{ nm}$, $\lambda_{\text{em}} = 450 \text{ nm}$) and FAM ($\lambda_{\text{ex}} = 495 \text{ nm}$, $\lambda_{\text{em}} = 517 \text{ nm}$) gradually decreased with increased concentration of Pb^{2+} and Ag^+ , respectively; while the intensity of RBITC ($\lambda_{\text{ex}} = 530 \text{ nm}$, $\lambda_{\text{em}} = 580 \text{ nm}$) increased with the increased concentration of Hg^{2+} , which proved the fluorescence quenching caused by Pb^{2+} and Ag^+ , and the fluorescence recovery caused by Hg^{2+} . The LOD (limit of detection) of this assay was 0.48 nM, 0.23 nM and 0.17 nM for Pb^{2+} , Ag^+ , and Hg^{2+} , respectively. The linear range was 10 nM~1000 nM for the three ions.

The selectivity of the sensing system was also explored: the fluorescence spectra were monitored upon adding other metal ions (such as 10 μM Mg^{2+} , Ca^{2+} , Fe^{3+} , Co^{2+} , Ni^{2+} , Zn^{2+} , Cd^{2+} , Al^{3+} , Cr^{3+} , Cu^{2+}) to the sensing system in the presence of 1 μM Ag^+ , Hg^{2+} , and Pb^{2+} . As shown in Fig. 5, Only Pb^{2+} , Ag^+ , and Hg^{2+} caused considerable changes in the intensity of fluorescent signals while other ions have little effect on this system. These results illustrated that the sensor was specifically responding to the three metal ions.

The comparison of the proposed sensor with other methods for simultaneous determination of three metal

ions is listed in Table 1. As it can be seen, the proposed sensor has a comparable and even higher sensitivity to the previous reports, and no masking reagent was used in this method, indicating that this sensor was an appropriate platform for the determination of these metal ions.

3. 4. Detection of Pb^{2+} , Hg^{2+} , and Ag^+ in Real Samples

This sensor's application in real samples (water of the East Lake) were investigated by Standard Recovery Test. the sample of the East Lake water was filtered through a 0.45 μm cellulose acetate filter membrane, and then the water sample (10 μL) was added to the prepared sensor. Afterwards, the standard solution of three metal ions was added to reach the final concentration of 10 nM. The fluorescence intensities were detected at 450 nm, 580 nm and 517 nm. The fluorescent quenching responding to Pb^{2+} and Ag^+ , and recovery responding to Hg^{2+} were also observed in East Lake water (as indicated in Fig. 7), and Table 2 shows that the satisfactory recoveries were obtained for the real samples. The average recoveries are

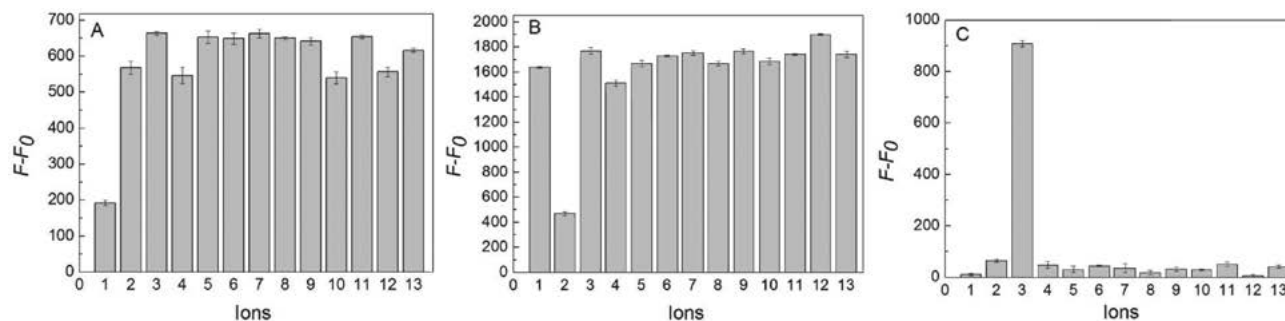


Figure 6. Selective detection of three metal ions at (A) $\lambda_{\text{ex}} = 353 \text{ nm}$, $\lambda_{\text{em}} = 450 \text{ nm}$; (B) $\lambda_{\text{ex}} = 495 \text{ nm}$, $\lambda_{\text{em}} = 517 \text{ nm}$; (C) $\lambda_{\text{ex}} = 530 \text{ nm}$, $\lambda_{\text{em}} = 580 \text{ nm}$. 1-13: Pb^{2+} , Ag^+ , Hg^{2+} , Mg^{2+} , Ca^{2+} , Fe^{3+} , Co^{2+} , Ni^{2+} , Zn^{2+} , Cd^{2+} , Al^{3+} , Cr^{3+} , Cu^{2+} . The concentrations of Pb^{2+} , Ag^+ , Hg^{2+} to be measured were 1 μM , and the concentrations of other metal ions were 10 μM . F is measured fluorescence intensity, F_0 is background fluorescence intensity.

Table 1. The comparison of our sensor with other methods for simultaneous determination of three metal ions.

Method	Ions detected and its LOD	Using masking reagent	Ref.
peptide modified gold nanoparticles probe	Cd^{2+} (0.05 mM) Ni^{2+} (0.3 mM) Co^{2+} (2 mM)	Y	[29]
fluorescent chemosensor based on dimethylaminocinnamaldehyde-aminothiourea	Ag^+ (1.0 ppb) Hg^{2+} (2.8 ppb) Cu^{2+} (0.8 ppb)	Y	[30]
DNA-based sensor	Ag^+ (10 nM) Hg^{2+} (0.1 nM) Pb^{2+} (10 pM)	Y	[31]
DNA-based sensor	Ag^+ (0.23 nM) Hg^{2+} (0.17 nM) Pb^{2+} (0.48 nM)	N	Our method

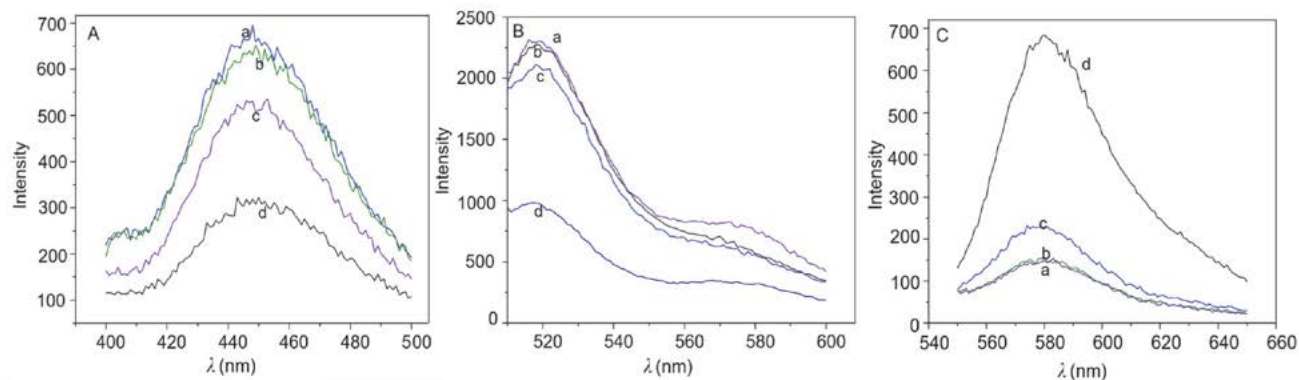


Figure 7. Fluorescence curves of (A) Pb^{2+} (with added standard concentration of (a) 0, (b) 50 nM, (c) 300 nM, and (d) 700 nM), (B) Ag^+ (with added standard concentration of (a) 0, (b) 10 nM (c) 100 nM, and (d) 700 nM), and (C) Hg^{2+} (with added standard concentration of (a) 0, (b) 10 nM (c) 100 nM, and (d) 700 nM) in East Lake water.

Table 2. Standard Recovery Test for detection of the metal ions in East Lake water.

Metal ions	Sample	Measured concentration in test sample /nM	Added standard concentrations /nM	Measured concentration after adding standard concentrations / nM	Recovery /%
Pb^{2+}	1	9.79	50	67.71	115.8
	2	9.79	300	331.04	107.1
	3	9.79	700	726.46	102.4
Ag^+	1	1.12	10	12.36	112.4
	2	1.12	100	105.62	104.5
	3	1.12	700	719.72	102.7
Hg^{2+}	1	1.45	10	11.32	98.7
	2	1.45	100	105.39	103.9
	3	1.45	700	707.76	100.9

108.43% for Pb^{2+} , 106.53% for Ag^+ and 101.17% for Hg^{2+} . These results confirmed that the proposed sensor can be successfully used to detect Pb^{2+} , Ag^+ , and Hg^{2+} in real samples.

4. Conclusions

In this paper, we have described a successful design of a new and simple fluorescent sensor for simultaneous detection of Pb^{2+} , Ag^+ , and Hg^{2+} based on the specific catalytic activity of Pb^{2+} for a particular DNzyme, specific regulation of Ag^+ on “C- Ag^+ -C” complex, stable complex formed by Hg^{2+} and RBITC, and AuNP fluorescence quenching effect on fluorescence dyes. Fluorescence quenching of AMCA and FAM, and the fluorescence recovery of RBITC indicated the presence of Pb^{2+} , Ag^+ , and Hg^{2+} , and the intensity changed corresponding to concentration of these ions. The detection limits of three metal ions were 0.48 nM for Pb^{2+} , 0.23 nM for Ag^+ and 0.17 nM for Hg^{2+} . It has been proven that this sensor is characterized by good stability, high sensitivity and selectivity, fast detection speed, and easy operation, and has successfully produced satisfactory detection results in real samples. These attributions suggest that our approach

provides a well suitable method to simultaneous detection of a variety of heavy metal ions in environmental monitoring.

5. Acknowledgements

This work is supported by the National Natural Science Foundation of China (NSFC) (Grant No. 41273093, 81471696) and the Project of Experimental technology of Wuhan University (Grant No. WHU-2014-SYJS-09). Financial support from the Fundamental Research Funds for the Central Universities is acknowledged.

6. References

- G. C. Zhu and C. Y. Zhang, *Analyst* **2014**, *139*, 6326–6342. DOI:10.1039/C4AN01069H
- T. Li, E. K. Wang, S. J. Dong, *Chem. Commun.* **2009**, *5*, 580–582. DOI:10.1039/B815814B
- Y. Miyake, H. Togashi, M. Tashiro, H. Yamaguchi, S. Oda, M. Kudo, Y. Tanaka, Y. Kondo, R. Sawa, T. Fujimoto, T. Machinami, A. Ono, *J. Am. Chem. Soc.* **2006**, *128*, 2172–2173. DOI:10.1021/ja056354d

4. A. Ataro, R. I. McCrindle, B. M. Botha, C. M. E. McCrindle, P. P. Ndirbewu, *Food Chem.* **2008**, *111*, 243–248. DOI:10.1016/j.foodchem.2008.03.056
5. D. W. Pan, Y. E. Wang, Z. P. Chen, T. T. Lou, W. Qin, *Anal. Chem.* **2009**, *81*, 5088. DOI:10.1021/ac900417e
6. S. J. Lee, M. Moskovits, *Nano Lett.* **2011**, *11*, 145–150. DOI:10.1021/nl1031309
7. Y. X. Du, R. Y. Liu, B. H. Liu, S. H. Wang, M. Y. Han, Z. P. Zhang, *Anal. Chem.* **2013**, *85*, 3160–3165. DOI:10.1021/ac303358w
8. A. Sett, S. Das, U. Bora, *Biochem. Biotechnol.* **2014**, *174*, 1073–1091. DOI:10.1007/s12010-014-0990-3
9. J. Li, Y. Lu, *J. Am. Chem. Soc.* **2000**, *122*, 10466–10467. DOI:10.1021/ja0021316
10. Y. Xiao, A. A. Rowe, K. W. Plaxco, *J. Am. Chem. Soc.* **2007**, *129*, 262–263. DOI:10.1021/ja067278x
11. T. Li, S. J. Dong, E. K. Wang, *J. Am. Chem. Soc.* **2010**, *132*, 13156–13157. DOI:10.1021/ja105849m
12. T. Li, E. K. Wang, S. J. Dong, *Anal. Chem.* **2010**, *82*, 1515–1520. DOI:10.1021/ac902638v
13. Y. Tanaka, S. Oda, H. Yamaguchi, Y. Kondo, C. Kojima, A. Ono, *J. Am. Chem. Soc.* **2007**, *129*, 244–245. DOI:10.1021/ja065552h
14. Y. Miyake, H. Togashi, M. Tashiro, H. Yamaguchi, S. Oda, M. Kudo, Y. Tanaka, Y. Kondo, R. Sawa, T. Fujimoto, T. Machinami, A. Ono, *J. Am. Chem. Soc.* **2006**, *128*, 2172–2173. DOI:10.1021/ja056354d
15. A. Ono, S. Cao, H. Togashi, M. Tashiro, T. Fujimoto, T. Machinami, S. Oda, Y. Miyake, I. Okamoto, Y. Tanaka, *Chem. Commun.* **2008**, *39*, 4825–4827. DOI:10.1039/b808686a
16. H. Torigoe, Y. Miyakawa, N. Nagasawa, T. Kozasa, A. Ono, *Nucleic Acids. Symp. Ser.* **2006**, *50*, 225–226. DOI:10.1093/nass/nrl112
17. B. Rajam, P. Ramasamy, U. Mahalingam, *Acta Chim. Slov.* **2017**, *64*, 186–192. DOI:10.17344/acsi.2016.3054
18. T. Li, S. J. Dong, E. K. Wang, *Anal. Chem.* **2009**, *81*, 2144–2149. DOI:10.1021/ac900188y
19. J. J. Du, L. Jiang, Q. Shao, X. G. Liu, R. S. Marks, J. Ma, X. D. Chen, *Small* **2013**, *9*, 1467–1481. DOI:10.1002/smll.201200811
20. M. B. Gumpu, S. Sethuraman, U. M. Krishnan, J. B. B. Rayapan, *Sensor Actuat B-Chem.* **2015**, *213*, 515–533. DOI:10.1016/j.snb.2015.02.122
21. G. Mor-Piperberg, R. Tel-Vered, J. Elbaz, I. Willner, *J. Am. Chem. Soc.* **2010**, *132*, 6878–6879. DOI:10.1021/ja1006355
22. J. W. Liu, *Anal. Chem.* **2014**, *58*, 99–111.
23. A. Ceylan, S. Z. Bas, M. Bayrakcl, S. Ertul, A. Uysal, *Acta Chim. Slov.* **2012**, *59*, 656–663
24. X. L. Shi, X. Y. Gao, L. L. Zhang, Y. C. Li, *Analyst* **2015**, *140*, 2608–2612. DOI:10.1039/C5AN00120J
25. S. J. Wu, N. Duan, Z. Shi, C. C. Fang, Z. P. Wang, *Talanta* **2014**, *128*, 327–336. DOI:10.1016/j.talanta.2014.04.056
26. C. Y. Lin, C. J. Yu, Y. H. Lin, W. L. Tseng, *Anal. Chem.* **2010**, *82*, 6830–6837. DOI:10.1021/ac1007909
27. G. C. Zhu, Y. Li and C. Y. Zhang, *Chem. Commun.* **2014**, *50*, 572–574. DOI:10.1039/C3CC46884D
28. Y. R. Chen, K. Mao, X. D. Zhou, A. G. Shen, J. M. Hu, *Wuhan University Journal of Natural Sciences* **2016**, *21*, 499–504. DOI:10.1007/s11859-016-1202-5
29. M. Zhang, Y. Q. Liu, B. C. Ye, *Analyst* **2012**, *137*, 601–607. DOI:10.1039/C1AN15909G
30. N. K. Hien, N. C. Bao, N. T. A. Nhung, N. T. Trung, P. C. Nam, T. Duong, J. S. Kim, D. T. Quang, *Dyes and Pigments* **2015**, *116*, 89–96. DOI:10.1016/j.dyepig.2015.01.014
31. Z. Z. Lin, X. H. Li, H. B. Kraatz, *Anal. Chem.* **2011**, *83*, 6896–6901. DOI:10.1021/ac2014096

Povzetek

Poročamo o novem fluorescenčnem senzorju na osnovi nukleinskih kislin za simultano detekcijo Pb^{2+} , Ag^+ in Hg^{2+} ionov. Osnovan je na specifični katalitski aktivnosti Pb^{2+} ionov za določen DNA encim; na specifični regulaciji Ag^+ na »C-Ag⁺-C« kompleksu; na stabilnem kompleksu, ki ga tvorita Hg^{2+} in rodamin B izotiocianat (RBITC). Tri fluorescenčna barvila: aminometilkumarin očetna kislina (AMCA), 5-karboksifluorescein (FAM) in RBITC, smo dodali raztopinam in so služila kot donorji fluorescence. Zaradi interakcije DNA s temi kovinskimi ioni in efekta dušenja fluorescence, ki so ga imeli AuNP delci na fluorescenčna barvila, smo lahko spremljali povečanje fluorescence RBITC za detekcijo Hg^{2+} ter dušenje fluorescence pri AMCA in FAM za ločeno detekcijo Pb^{2+} in Ag^+ , ne da bi bilo treba uporabljati maskirne reagente. Senzor je pokazal visoko občutljivost in selektivnost. Meja zaznave (LOD) je 0,48 nM za Pb^{2+} , 0,23 nM za Ag^+ in 0,17 nM za Hg^{2+} . Na koncu smo senzor uspešno uporabili za hkratno detekcijo Pb^{2+} , Ag^+ in Hg^{2+} ionov v realnem vzorcu.

Scientific paper

A Highly Selective DNA Sensor Based on Graphene Oxide-Silk Fibroin Composite and AuNPs as a Probe Oligonucleotide Immobilization Platform

Ali Benvidi,^{1,*} Zohreh Abbasi,¹ Marzieh Dehghan Tezerjani,¹ Maryam Banaei,¹ Hamid Reza Zare,¹ Hossein Molahosseini² and Shahriar Jahanbani¹

¹ Department of Chemistry, Faculty of Science, Yazd, Yazd, I. R. Iran

² Department of Textile Engineering, Isfahan University of Technology, Isfahan, Iran

* Corresponding author: E-mail: abenvidi@yazd.ac.ir, benvidi89@gmail.com
Tel.: +98 353 812 2645; Fax: +98-353-8210644

Received: 25-06-2017

Abstract

In this study, a simple and novel electrochemical biosensor based on a glassy carbon electrode (GCE) modified with a composite of graphene oxide (GO) – silk fibroin nanofibers (SF) and gold nanoparticles (MCH/ssDNA/AuNPs/SF/GO/GCE) was developed for detection of DNA sequences. The fabrication processes of electrochemical biosensor were characterized by scanning electron microscopy (SEM), FT-IR and electrochemical methods. Some experimental conditions such as immobilization time of probe DNA and MCH incubation time, time and temperature of hybridization were optimized. The designed biosensor revealed a wide linear range of 1.0×10^{-16} – 1.0×10^{-8} mol L⁻¹ and a low detection limit (3.3×10^{-17} mol L⁻¹) for detection of BRCA1 5382 mutation by EIS technique. The designed biosensor revealed high selectivity for discrimination of the complementary (P1C) sequences from various non-complementary sequences of (P1nC1, P1nC2 and P1nC3). Also, the biosensor revealed a high reproducibility (RSD of 7.5% (n = 4)) and high stability (92% of its initial response after 8 days). So, the fabricated biosensor has a suitable potential to be applied for detection of breast cancer sequences in the initial stages of the cancer.

Keywords: DNA biosensor; immobilization; composite; silk nanofibers; graphene oxide nanosheets

1. Introduction

Breast cancer like other cancers initiates continuous process of aberrant chromosomal changes and consequently leads to damage to DNA.^{1–3} As known, there are various clinical methods for detection of breast cancer such as mammography, magnetic resonance imaging (MRI) and breast biopsy tests.⁴ Besides that up to now, lots of techniques such as surface plasmon resonance,^{5,6} optical fiber,⁷ quartz crystal microbalance,⁸ micro cantilever and electrochemical methods have been developed for detection of cancers because the cancer detection in the initial stages is so important.^{9–13} Most of the optical methods are indirect and need a labeling of target DNA. So, the electrochemical biosensors based on electrochemical techniques such as cyclic voltammetry (CV), differential pulse voltammetry (DPV) and electrochemical impedance spectroscopy (EIS) have been developed for detection of low

concentrations of DNA sequences.^{14,15} Some great advantages of electrochemical biosensors compared to other types of biosensors are miniaturization, high sensitivity, low cost and fast detection.¹⁶

The immobilization step of the DNA probe on the electrode surface is important in determining the overall performance of an electrochemical DNA biosensor.¹⁷ To have a good immobilization process, some materials such as polymer, ionic liquid and nanoparticles have been used as the biosensing interface.^{18–21} Up to now, lots of nanoparticles have been applied for fabrication of biosensors due to some unique properties such as high surface-to-volume ratio, high conductivity and suitable biological compatibility.²² Graphene is a one-atom-thick 2D carbon nanomaterial. Graphene oxide is a water dispersible version of graphene with oxygen-containing functional groups such as hydroxyl, carboxyl and epoxy groups.²³ Its nanosheets can adsorb single-stranded DNA (ssDNA) via

non-covalent p-stacking interactions between the hexagonal cells of graphene and the ring structure of nucleobases.²⁴ Graphene oxide (GO) has a key role in the construction of biosensors due to its unique characteristics such as good dispensability and simple surface functionality, high electronic, thermal and mechanical properties.^{25–26} So, in the present work graphene oxide nanosheets were used for immobilization and hybridization processes of DNA strands at the electrode surface.

Another used nanomaterial in this study is silk nanofiber. Silk fibroin (SF) is a macromolecular protein with molecular weight about 350 kDa which can be extracted from silkworm cocoon. It is highly biocompatible and due to its porous structure allows the growing of cells, growth factors and the production of extracellular matrix (ECM) to enable communication between the cells. Fibroin is extremely versatile and can be processed in very different forms.^{27–30} One of the most interesting polymers that could be combined with graphene is silk fibroin (SF). In addition to having an excellent and well known biocompatible properties,³¹ fibroin is a protein with a secondary molecular structure in the form of a beta-sheet that combines well with graphene.^{32,33} However, there are other configurations of fibroin scaffolds that could be improved after combination with graphene.

Recently, lots of electrochemical sensors based on various nanomaterials have been developed for detection of different targets.^{34–39} For instance, S. M. Ghoreishi et al. designed an electrochemical method for determination of acetaminophen in different pharmaceutical forms using gold nanoparticles carbon paste electrode.⁴⁰ B. Bozzini group investigated the electro deposition of Co/CoO nanoparticles onto graphene for electrocatalysis of oxygen reduction reaction by a multi-technique approach.⁴¹ Also, B. Mahltig and coworkers fabricated an antimicrobial agent by using the silver nanoparticles in SiO₂ microspheres.⁴²

As known, voltammetric methods are simple, sensitive, selective and time-saving.⁴³ A DNA biosensor based on using electrochemical impedance spectroscopy (EIS) technique is a device that transduces changes in interfacial properties between the electrode and the electrolyte surface to an electrical signal. DNA biosensors based on EIS detection are label-free and it means that it is not necessary to use some labels such as fluorophore,^{44–46} magnetic beads,⁴⁷ or an enzyme for detection of target.⁴⁸ Thus, some advantages of this kind of DNA biosensor are: low cost, simplicity, and ease of miniaturization. Also, when the differences in current are not significant in a low target concentration range, the EIS technique is more suitable than other electrochemical detection techniques.

Following our previous works,^{4,49,50} in the present research an electrochemical biosensor for detection of BRCA1 sequences was designed. This biosensor is based on nano composite of graphene oxide – silk nanofibers and gold nanoparticles as a platform at the glassy carbon electrode (GCE). The fabrication processes of the designed

sensor were followed by electrochemical impedance spectroscopy (EIS) and cyclic voltammetry (CV) methods. Under optimum conditions, the fabricated biosensor (MCH/ssDNA/AuNPs/SF/GO/GCE) revealed a wide linear range (1.0×10^{-16} to 1.0×10^{-8} mol L⁻¹) and a low detection limit of 3.3×10^{-17} mol L⁻¹ using EIS method. The designed biosensor revealed a high selectivity for discrimination of complementary from different non-complementary sequences. Briefly, some advantages of MCH/ssDNA/AuNPs/SF/GO/GCE biosensor are: detecting DNA without using additional labels, easy preparation, possessing high selectivity, sensitivity, reproducibility and stability.

2. Experimental

2.1. Reagents and Instruments

The used primers and probes were designed based on the breast cancer cells obtained from the Gen Bank database. 6-Mercapto-1-hexanol (MCH) was purchased from Aldrich. HAuCl₄ and all other chemicals were of analytical grade and obtained from Merck Company. All of the chemicals were used as received without further purification. The sequences of the used probe and complementary were as follows:

Probe sequence (P1):

5'-AAGCGAGCAAGAGAATTCCAG-3'

Complementary sequence (P1C):

5'- GTGAAAGTATCTAGCACTGCTGGAATTCTCTTGCTCGCTT-3'

Non-complementary sequence (P1nC1):

5'-TGTGAAAGTATCTAGCACTGTGGGAAT-TCTCTTGCTCGCT-3'

Non-complementary sequence (P1nC2):

5'-GAGAAACATCTGGGATA-3'

Non-complementary sequence (P1nC3):

5'-CACTTTATTTGGGATG-3

For electrochemical measurements an Autolab potentiostat/galvanostat model PGSTAT 302 N (Eco Chem, Utrecht, Netherlands) and NOVA 1.7 software at laboratory temperature (25 ± 1 °C) were used. The used three-electrode system was composed of a modified glassy carbon electrode as working electrode, an Ag/AgCl (1.0 mol L⁻¹ KCl) and a platinum wire as reference and auxiliary electrodes, respectively. A Metrohm model 691 pH/mV meter was applied for pH measurements. The graphene nanosheets were synthesized according to the procedure given in the literature.²⁵

2.2. Preparation of Nano Silk Fibroin

The natural silk fibers were purchased in a silk worm cocoon from Iran-Mazandaran area and then were cut into small pieces. To separate Srysyn gum, the small pieces of silk worm cocoon were boiled in the sodium carbonate solution (0/5% w/w) for 30 min two times. The resulting

fibers were rinsed with distilled water. The obtained silk fibroin was dried at room temperature and then dissolved in a solution containing calcium chloride/ethanol/water (molar ratio of 8/2/1) for 4 h at 60 °C. The resulting solution was purified using filtration process and dialyzed using a cellulose dialysis bag (12000) for 3 days at room temperature in the deionized water solution. The obtained solution as the diluted pure fibroin solution was dried at room temperature in a petri dish and the resulting film was converted to a powder. For preparation of fibroin nanoparticles, the physical method of ball mill grinding was applied for 12 h. The obtained FT-IR spectra of the resulting fibroin nanoparticles indicated a good agreement with other reported FT-IR of fibroin nanoparticles.⁵¹

2. 3. Preparation of MCH/ssDNA/SF/GO/GCE Biosensor

The fabrication processes of ssDNA/SF/GO/GCE biosensor include the steps as follows: at first, non-modified glassy carbon electrode (GCE) was polished by 0.05 μm alumina slurry to a mirror-like appearance, and then the mirror GCE was washed with anhydrous alcohol and water by ultrasonication for 30 min, respectively. At the second step, 20 μL of homogeneously dispersed solution of SF/GO (0.015/0.035 g/mL) nano composite was placed on the working electrode surface and dried under ambient conditions and this electrode was named SF/GO/GCE electrode. At the third step, gold nanoparticles (1.5 mmol L^{-1}) were deposited electrochemically on the surface of SF/GO/GCE electrode to prepare AuNPs/SF/GO/GCE (the applied experimental conditions: the potential range and the number of scans were -0.2 V to $+0.9\text{ V}$ and 40, respectively). Fourth step contained dropping 20 μL of the DNA probe solution (1 $\mu\text{mol L}^{-1}$) at the surface of AuNPs/SF/GO/GCE for 12 h in a wet chamber to prepare ssDNA/AuNPs/SF/GO/GCE electrode. At the last step, the prepared electrode was immersed in a MCH (1 mol L^{-1}) solu-

tion as a blocker of surface to fill the bare areas of the ssDNA/AuNPs/SF/GO/GCE surface which have not been covered by DNA strands and remove nonspecific adsorption of DNA (MCH/ssDNA/AuNPs/SF/GO/GCE). After each step the electrode was rinsed with a buffer and the modification steps were followed by using EIS and CV techniques.

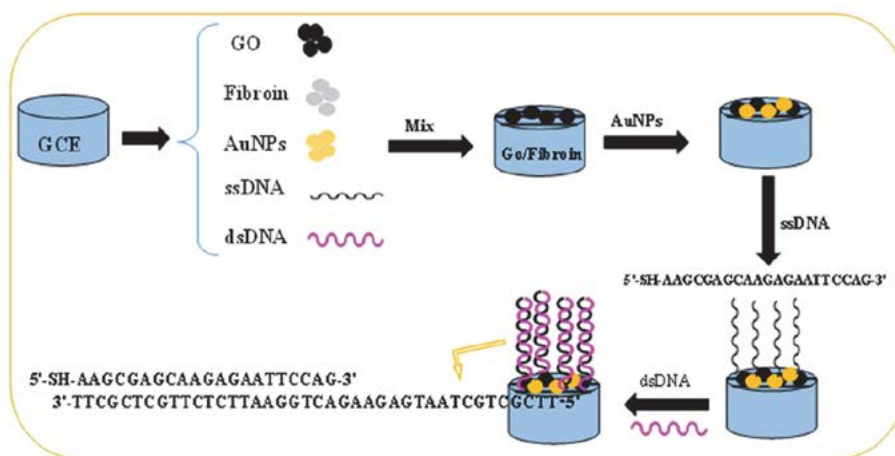
2. 4. The Solutions Preparation Procedure

The probe and complementary solutions provided from the Gen Bank database were dissolved in water and were kept frozen at $-20\text{ }^{\circ}\text{C}$ to form stock solution of primers (18.5 $\mu\text{mol L}^{-1}$). For preparation of solutions, deionized water (DI: 18 M Ω cm resistivity) was used. The solutions of DNA probe (1 $\mu\text{mol L}^{-1}$) and various concentration of complementary (1.0 $\times 10^{-16}$ mol L^{-1} to 1.0 $\times 10^{-8}$ mol L^{-1}) were prepared by sequential dilution of the stock solution of primers. Also, for preparation of SF/GO suspension, GO and SF (0.035 g, 0.015 g, respectively) was weighed and diluted with 1 mL of distilled water. Then, this suspension was sonicated for 1 h to prepare the solution of SF/GOI which was placed on the electrode surface. The probe DNA immobilization and hybridization were monitored in a solution containing $[\text{Fe}(\text{CN})_6]^{3-/4-}$ (1:1) (1.0 mmol L^{-1}) and KCl (0.1 mol L^{-1}) mixture as the redox active probe (Scheme 1).

3. Results and Discussion

3. 1. Characterization of the Fabricated Biosensor

As shown in Fig. 1, the surface morphology of bare glassy carbon electrode (A), the modified glassy carbon with graphene oxide nanosheets (B), the silk nanofibers (C), nano composite of graphene oxide – silk fibroin (D),



Scheme 1. The schematic diagram of the fabrication of MCH/ssDNA/AuNPs/SF/GO/GCE biosensor

the nano composite of graphene oxide – silk fibroin and nanoparticle AuNPs (E) was examined by scanning electron microscopy (SEM) technique. According to Fig. 1A, the bare glassy carbon electrode has a smooth surface area. Fig. 1B indicates the petal-like structure of graphene oxide nanosheets with a large surface area.⁵² Fig. 1C shows the SEM of silk nanofibers compared with smooth surface of bare glassy carbon electrode.⁵³ Fig. 1D, shows the SEM of the modified glassy carbon electrode with nanosheets of

graphene oxide – silk nanofibers which can provide a suitable platform for DNA sensing by increasing the electrode surface area. As shown in Fig 1E, the SEM of the modified glassy carbon electrode with nanosheets of graphene oxide – silk nanofibers and gold nanoparticles (AuNPs) can provide a suitable platform for sensing of thiolated DNA strands via the formation of Au–S bond.

For characterization of the used compounds for modification of the electrode surface the FT-IR spectroscopy

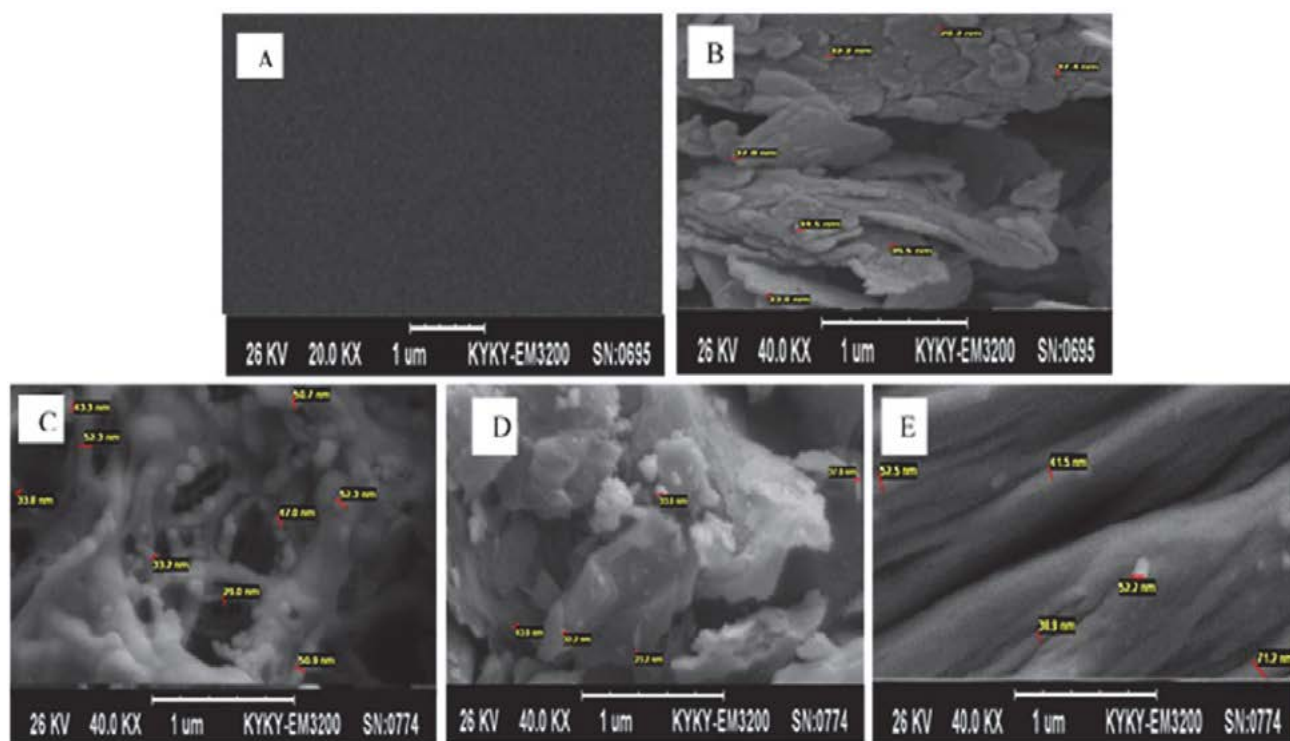


Figure 1. The SEM images of A) bare GCE, B) GO/GCE, C) SF/GCE, D) SF/GO/GCE and E) AuNPs/SF/GO/GCE electrodes

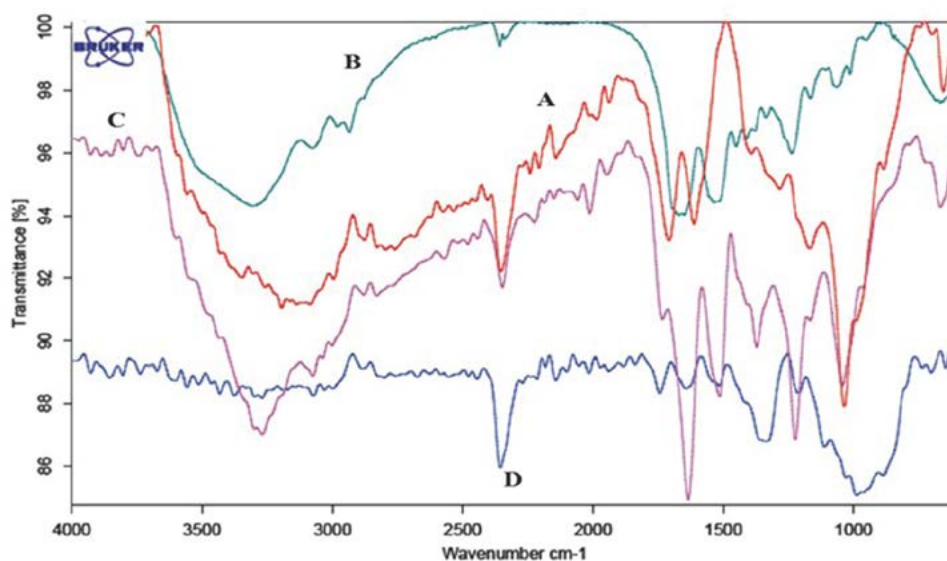


Figure 2. FT-IR spectrum of A) GO, B) SF, C) SF/GO composite and D) AuNPs/SF/GO.

copy technique was used. The FT-IR spectrum of graphene oxide reveals a C-O stretch at 1222 cm^{-1} , an O-H stretch at $3500\text{--}3300\text{ cm}^{-1}$, and a C=O stretch at $1720\text{--}1690\text{ cm}^{-1}$ (Fig. 2A). Also, the FT-IR spectrum of silk nanofibers shows a hydrogen bond at 3300 cm^{-1} , a C-N stretch at 1444 cm^{-1} , C=O stretch at $1640\text{--}1620\text{ cm}^{-1}$, a C-N stretch at 1230 cm^{-1} (Fig. 2B). The FT-IR spectrum of SF/GO composite indicates the related peaks of both graphene oxide and silk fibroin in the SF/GO composite (Fig. 2C). After electro-deposition of gold nanoparticles on the SF/GO surface, a NH peak which is shifted to low energy is ob-

served in the SF/GO/AuNPs spectrum and this can be related to the interaction between the AuNPs and composite of SF/GO (see Fig. 2D). These observations denote that the modification of electrode surface was performed well.

Also, the modification processes of electrode were monitored with electrochemical techniques (cyclic voltammetry (CV) and impedance (EIS)). Fig. 3 indicates the obtained cyclic voltammograms of different electrodes in a solution containing $[\text{Fe}(\text{CN})_6]^{3-/4-}$ (1.0 mol L^{-1}) at a scan rate of 100 mV/s . According to this figure, after introduction of SF/GO composite at the surface of bare glassy

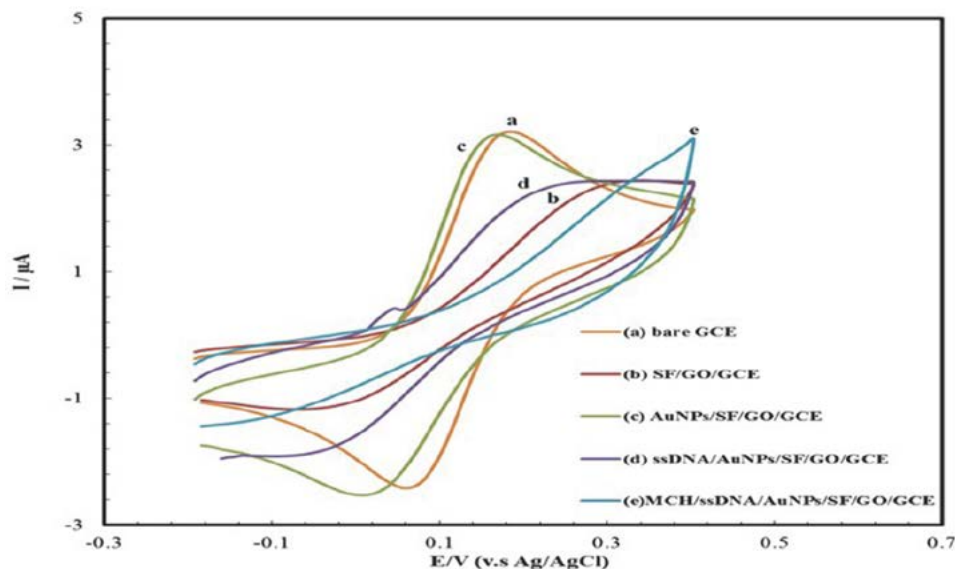


Figure 3. Cyclic voltammograms obtained for a 1.0 mmol L^{-1} $[\text{Fe}(\text{CN})_6]^{3-/4-}$ and 0.1 mol L^{-1} KCl solution at the surfaces of (a) bare GCE, (b) SF/GO/GCE, (c) AuNPs/SF/GO/GCE, (d) ssDNA/AuNPs/SF/GO/GCE, (e) MCH/ssDNA/AuNPs/SF/GO/GCE (CV condition: scan rate 50 mV s^{-1}).

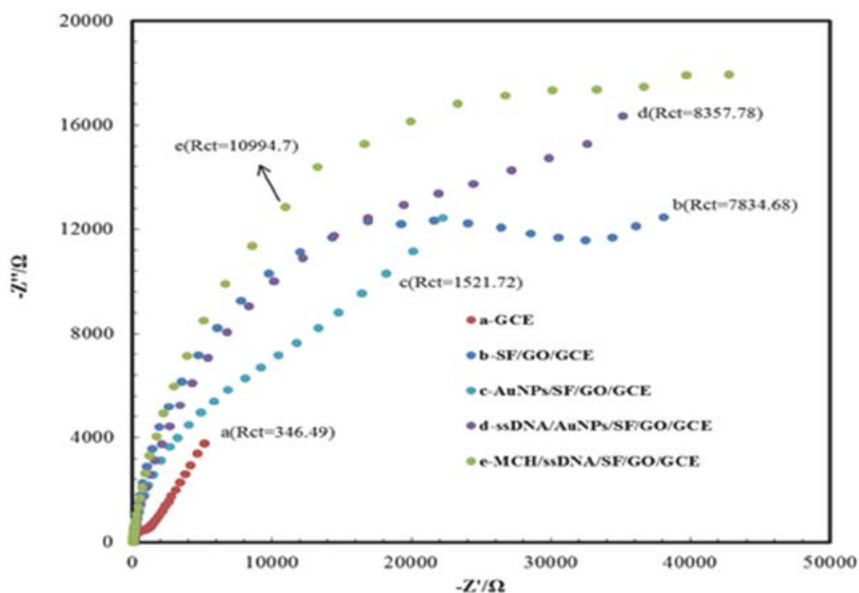


Figure 4. Electrochemical impedance spectroscopy (EIS) signals obtained for a 1.0 mmol L^{-1} $[\text{Fe}(\text{CN})_6]^{3-/4-}$ and 0.1 mol L^{-1} KCl solution at the surfaces of (a) bare GCE, (b) GO/SF/GCE, (c) AuNPs/GO/SF/GCE, (d) ssDNA/AuNPs/GO/SF/GCE, (e) MCH/ssDNA/AuNPs/GO/SF/GCE (EIS conditions: initial ac potential 0.20 V with an AC amplitude of 5 mV and frequency range 10 kHz to 0.1 Hz).

carbon electrode, the peak current (i_p) of SF/GO/GCE electrode is decreased compared with the CV response of the bare GCE (curves a and b). This observation can be related to the insulation of the SF layer.⁵⁵ By electrodeposition of gold nanoparticles on SF/GO/GCE surface, the peak current value is increased due to high conductivity of gold nanoparticles (curves b and c). It is noticeable that the existence of the gold nanoparticles at the modified electrode surface leads to more attachment of ss-DNA strands at the electrode surface (curve c). By immobilization of probe at the surface of the AuNPs/SF/GO/GCE, the peak current is decreased due to the repulsion of $[\text{Fe}(\text{CN})_6]^{3-/4-}$ by the negatively charged phosphate backbone of probe DNA and also the saturation of the electrode surface by probe DNA to prevent $[\text{Fe}(\text{CN})_6]^{3-/4-}$ ions from reaching the electrode surface (curve c and d). After blocking the electrode surface by MCH (1.0 mmol L^{-1}) as a blocker surface at the ss-DNA/AuNPs/SF/GO/GCE, the peak current is decreased (curve e).

In addition, the fabrication process of MCH/ssDNA/AuNPs/SF/GO/GCE was followed with EIS method (Fig. 4). The modification of the bare glassy carbon electrode surface with SF/GO composite causes an increase of the semicircle diameter (R_{ct}) compared to bare GCE (curves a, b). After electrodeposition of gold nanoparticles on the modified electrode surface with SF/GO composite, the val-

ue of R_{ct} is decreased due to the high conductivity of gold nanoparticles (curves b and c). By immobilization of the ss-DNA probe at the AuNPs/SF/GO/GCE surface, R_{ct} value is increased (curve d). Finally, using MCH solution as a blocker agent of electrode surface (ssDNA/AuNPs/SF/GO/GCE) leads to an increase in the value of R_{ct} (curve e). These results reveal that the fabrication process of MCH/ssDNA/AuNPs/SF/GO/GCE biosensor is performed well.

3. 2. Optimization of Experimental Conditions

3. 2. 1. Optimization of the Percentages of GO in the SF/GO Composite, Immobilization Time of Probe DNA and MCH Incubation Time

For increasing the sensitivity of the designed electrochemical sensor (ssDNA/SF/GO/GCE), some experimental parameters such as the percentages of GO in the SF/GO composite was optimized. The influence of the GO percentage in SF/GO composite was examined in the range of 30 to 90% w/w. The results revealed that the ΔR_{ct} values are increased by increasing the percentages of GO in the composite up to 70% w/w and after that, by increasing the percentages of GO the ΔR_{ct} values are nearly constant. So, the

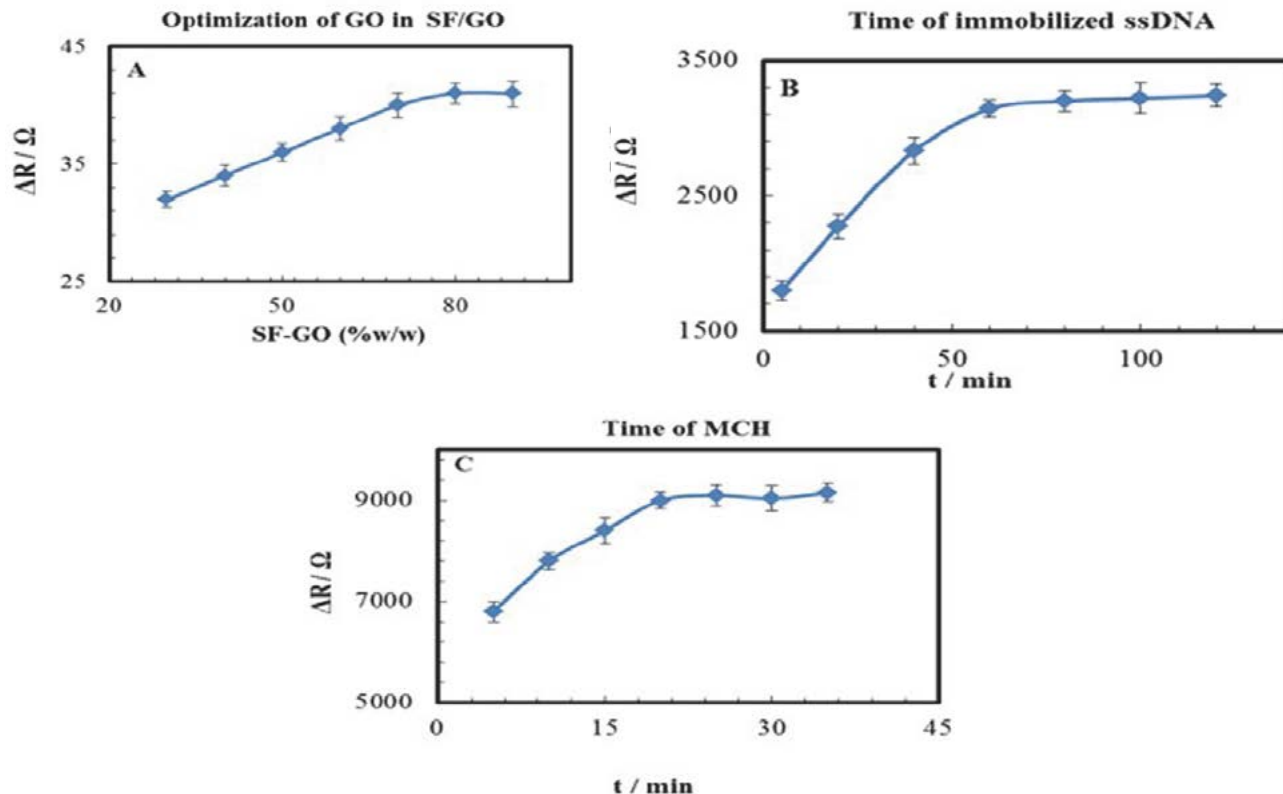


Figure 5. Optimization of operating conditions in a solution containing 0.5 mmol L^{-1} $[\text{Fe}(\text{CN})_6]^{3-/4-}$ and 0.1 mol L^{-1} KCl (the number of independent experiments $n = 3$): (A) the percentages of GO in the composite of SF/GO, (B) the effect of immobilization time of ssDNA ($1.0 \times 10^{-6} \text{ mol L}^{-1}$), (C) the effect of MCH incubation time.

GO percentage of 70% *w/w* was chosen as the optimum percentage value of GO in the SF/GO composite (see Fig. 5A).

For investigation of immobilization time of probe DNA, 20 μL of the probe DNA solution ($1 \times 10^{-6} \text{ mol L}^{-1}$) was introduced at the electrode surface from 5 min to 2 h. According to Fig. 5B, it is observed that by increasing time, ΔR_{ct} values are increased until 1 h and then, ΔR_{ct} values remain constant. So, an immobilization time of 1 h was selected as an optimum immobilization time of probe DNA for further experiments (Fig. 5B). Also, for enhancement of selectivity and sensitivity of the proposed DNA biosensor, the MCH incubation time was investigated. As mentioned before, MCH incubation has an important role to remove the nonspecifically adsorbed probe molecules from the electrode surface. So, ssDNA/AuNPs/SF/GO/GCE electrode was immersed in a solution of MCH (1 mol L^{-1}) for a specific time. MCH can bind to the electrode surface and consequently prevents the absorption of complementary DNA sequences to the electrode surface. After incubation of the fabricated sensor in a solution containing MCH (1 mol L^{-1}), the ΔR_{ct} values are increased until 20 min and then the ΔR_{ct} values are constant (Fig. 5C). Based on these observations, the optimum time of 20 min was selected for the incubation of MCH.

3. 2. 2. Optimization of Time and Temperature of Hybridization

Other parameters which were optimized in this research are the effects of time and temperature of hybridization. The effect of hybridization time was investigated over the range of 5 min to 60 min while temperature and ssDNA concentration were kept constant at $25 \text{ }^\circ\text{C}$ and $1.0 \times 10^{-16} \text{ mol L}^{-1}$, respectively. According to obtained results in Fig. 6A, 40 min was selected as the optimum hybridization time for further experiments.

Also, due to the importance of the temperature of hybridization for hybridization reaction, the temperature of hybridization was optimized. Hybridization temperature was changed from 25 to $65 \text{ }^\circ\text{C}$ while keeping hybridization time and complementary concentration constant at 50 min and $1.0 \times 10^{-16} \text{ mol L}^{-1}$, respectively. As shown in Fig. 6B, the ΔR_{ct} values are constant up to $35 \text{ }^\circ\text{C}$ and then rapidly decrease by increasing the temperature due to replacement of some molecules from the electrode surface. Thus, the temperature of $25 \text{ }^\circ\text{C}$ was selected as the optimum hybridization temperature.

3. 3. Investigation of Sensitivity of MCH/ssDNA/AuNPs/SF/GO/GCE Biosensor

The sensitivity of MCH/ssDNA/AuNPs/SF/GO/GCE biosensor was investigated by electrochemical impedance spectroscopy (EIS) technique. Fig. 7 reveals the impedance signals of the fabricated biosensor versus various concentrations of complementary target DNA sequences. Inset (A) of Fig. 7 reveals that the ΔR_{ct} values versus various target concentrations have a linear relationship in the range from $1.0 \times 10^{-16} \text{ mol L}^{-1}$ to $1.0 \times 10^{-8} \text{ mol L}^{-1}$ with a regression equation of $\Delta R_{\text{ct}} = 698.6 \log C (\text{mol L}^{-1}) + 18480$ ($R = 0.9914$). The detection limit based on $3s_{\text{bl}}$ (where the s_{bl} was the standard deviation of 10 replicate measurements of MCH/ssDNA/AuNPs/SF/GO/GCE in $[\text{Fe}(\text{CN})_6]^{3-/4-}$ solution) was calculated to be $3.3 \times 10^{-17} \text{ mol L}^{-1}$. Inset (B) of this figure indicates the used Randles equivalent circuit in this study while R_s is the electrolyte ($1.0 \text{ mmol L}^{-1} [\text{Fe}(\text{CN})_6]^{3-/4-}$ and $0.1 \text{ mol L}^{-1} \text{ KCl}$) resistance, CPE is constant phase element, W_{01} is Warburg impedance resulting from the diffusion of ions and R_{ct} is the electron transfer resistance. Due to the significant influence of electron transfer process between $[\text{Fe}(\text{CN})_6]^{3-/4-}$ and electrode surface during the modification and hybridization processes, the R_{ct} values are used. The obtained

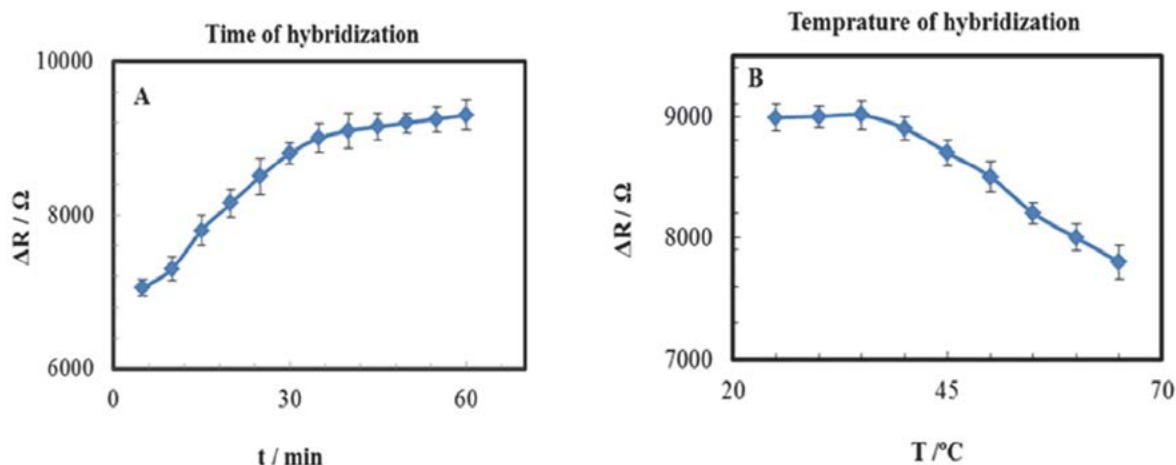


Figure 6. Optimization of operating conditions in a solution containing $[\text{Fe}(\text{CN})_6]^{3-/4-}$ (0.5 mmol L^{-1}) and KCl (0.1 mol L^{-1}) and the number of independent experiments is 3 ($n=3$): (A) the influence of target DNA ($1 \times 10^{-12} \text{ mol L}^{-1}$) interaction time and (B) the effect of hybridization temperature.

results reveal that using the nano composite of GO and SF in the structure of MCH/ssDNA/AuNPs/SF/GO/GCE biosensor leads to increasing the sensitivity of the designed biosensor due to the unique properties of GO such as possessing lots of carboxylic acid groups, increasing the surface area, good biocompatibility and electron mobility at room temperature⁵⁶ and also some specific properties of SF like tensile strength and elasticity, good thermal stability, hygroscopicity, microbial resistance and biocompatibility.⁵⁷ Also, Table 1 reveals the comparison of some charac-

teristics of ssDNA/SF/GO/GCE biosensor with some other reported electrodes.^{58–62} According to Table 1, the obtained detection limit and linear range in this work are better than in other works. It is noticeable that the ssDNA/SF/GO/GCE biosensor has a good sensitivity for detection of BRCA 1 sequences but it has some disadvantages like: (i) EIS is used for DNA detection which is so sensitive towards the electrode surface changes but its selectivity is lower than in some other electrochemical techniques such as differential pulse voltammetry; (ii) the proposed meth-

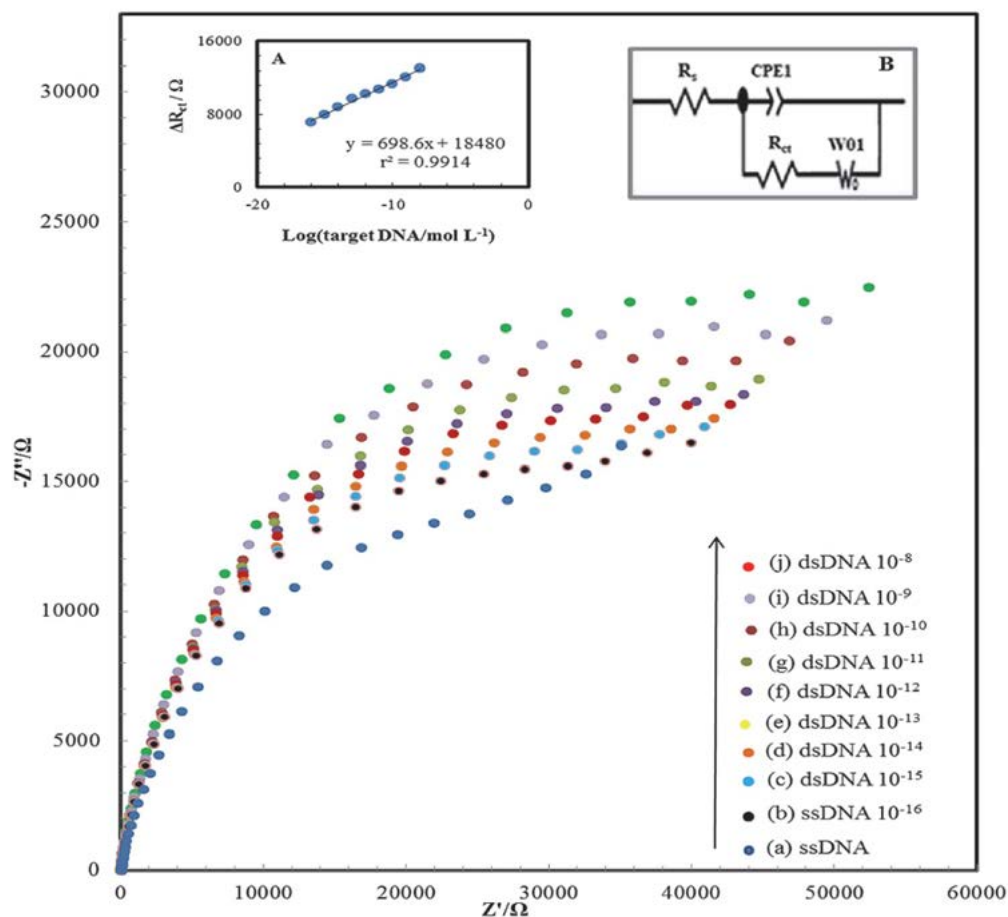


Figure 7. The obtained EIS signals for various concentrations of complementary DNA. Inset A: the applied Randles equivalent circuit, Inset B: the dependence of ΔR_{ct} versus the logC of target (DNA).

Table 1. Comparison of analytical performances of the MCH/ssDNA/AuNPs/SF/GO/GCE biosensor with several reported electrochemical DNA sensors for detection of breast cancer.

Electrode	Detection technique	Linear range (mol L ⁻¹)	Detection limit (mol L ⁻¹)	Ref.
MWCNTs/GCE	DPV	$0.1 \times 10^{-9} - 1000 \times 10^{-9}$	5.0×10^{-11}	[58]
GCE	DPV	$2 \times 10^{-10} - 5 \times 10^{-8}$	1.0×10^{-10}	[59]
DNA/PICA/GCE	EIS	$1 \times 10^{-9} - 2 \times 10^{-8}$	5×10^{-10}	[60]
Polypyrrole/DNA/MWCNT	CV	$3.3 \times 10^{-9} - 1.06 \times 10^{-8}$	1.0×10^{-9}	[61]
PPy/DNA/CNT/GCE	DPV	$1.0 \times 10^{-10} - 1.0 \times 10^{-8}$	8.5×10^{-11}	[62]
MCH/ssDNA/AuNPs/SF/GO/GCE	EIS	$1.0 \times 10^{-16} - 1.0 \times 10^{-8}$	3.3×10^{-17}	This work

od is quite time consuming; and (iii) it was not applied to a real sample although we believe that the fabricated biosensor has a good potential for detection of breast cancer in the near future.

3. 4. The Selectivity Investigation of the Fabricated Biosensor

As known, the selectivity is explained as the recognition of differences between the target DNA sequences from others. For investigation of the selectivity of the ssDNA/SF/GO/GCE biosensor, the fabricated biosensor was hybridized with complementary PIC and different non-complementary sequences of P1nC1, P1nC2 and P1nC3. The obtained results are shown in Fig. 8. According to this figure, ssDNA/SF/GO/GCE biosensor reveals different EIS signals after hybridization with 1.0×10^{-13} mol L⁻¹ of complementary PIC (6400 k Ω) and 1.0×10^{-13} mol L⁻¹ of various non-complementary DNA sequences P1nC1, P1nC2 and P1nC3 (690, 600 and 580 k Ω , respectively). These observations indicate that the fabricated biosensor has a high selectivity and also it can be suggested that the designed biosensor will be applied in the future for real samples.

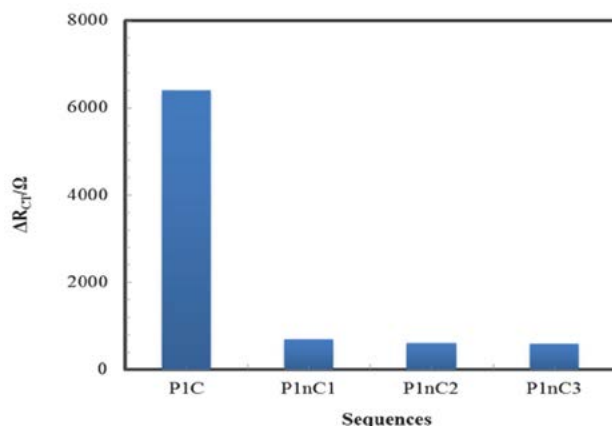


Figure 8. The specificity test using the MCH/ssDNA/AuNPs/SF/GO/GCE biosensor responses to different targets of complementary (PIC) and non-complementary (P1nC1, P1nC2 and P1nC3) sequences.

3. 5. Reproducibility and Stability of the MCH/ssDNA/AuNPs/SF/GO/GCE Biosensor

The reproducibility and stability of MCH/ssDNA/AuNPs/SF/GO/GCE biosensor were examined. For reproducibility investigation of the designed biosensor, three ssDNA/SF/GO/GCE electrodes were fabricated and then hybridized with target DNA (1.0×10^{-13} mol L⁻¹). It is noticeable that independent DNA sensors were prepared in the similar conditions like suspension concentration of SF/GO composite, ssDNA immobilization and hybridization

of complementary sequences. The obtained results revealed a relative standard deviation (RSD) of 7.5% ($n = 4$) for ΔR where $\Delta R = R_{\text{final}} - R_{\text{initial}}$, and R_{final} is EIS response after hybridization and R_{initial} is EIS signal before hybridization. Thus, the obtained results reveal a satisfactory reproducibility of this electrochemical biosensor. The stability of the MCH/ssDNA/AuNPs/SF/GO/GCE biosensor was also investigated during 8 days. The proposed biosensor was stored in a 0.1 mol L⁻¹ phosphate buffer solution (pH 7.4) in the refrigerator at 4 °C and after 8 days the response of the ssDNA/SF/GO/GCE biosensor retained about 92% of its initial response. These observations prove the high stability of the fabricated DNA sensor.

4. Conclusions

In this paper, a DNA electrochemical biosensor based on graphene oxide nanosheets – silk fibroin composite as probe oligonucleotide immobilization platform was designed for breast cancer sequences detection. The modification processes of electrode were followed by scanning electron microscopy (SEM), FT-IR and electrochemical techniques of cyclic voltammetry (CV) and impedance (EIS). Some experimental parameters of the designed biosensor like the percentages of GO in the SF/GO composite, immobilization time of probe DNA and MCH incubation time, time and temperature of hybridization processes were optimized. Under optimum conditions, this electrochemical biosensor revealed a suitable dynamic range (1.0×10^{-16} mol L⁻¹ to 1.0×10^{-8} mol L⁻¹) and a low detection limit (3.3×10^{-17} mol L⁻¹) for target DNA by EIS technique. The obtained results revealed high sensitivity of the fabricated biosensor. This method was successful in detection of BRCA 1 sequences containing complementary PIC sequences and various non-complementary sequences of P1nC1, P1nC2 and P1nC3. Briefly, this designed biosensor possesses some advantages such as suitable selectivity and sensitivity, high reproducibility and being not expensive. This biosensor like other designed sensors has some disadvantages such as being quite time consuming and was not applied to real samples. We hope that our explorations may present a basis for further advancement in modified electrochemical DNA biosensors applied to various science fields.

5. Acknowledgements

We gratefully acknowledge the support of this work by Yazd University research council.

6. References

1. R. Sager, *Cancer Res.* **1986**, 46, 1573–1580.
2. J. H. Ray and J. German, *Chromosome mutation and neoplasia*, **1983**, 135–167.

3. J. D. Rowley, *Chromosomes and cancer: from molecules to man*, Academic Pr, 1983.
4. A. Benvidi, N. Rajabzadeh, M. Mazloun-Ardakani, M. M. Heidari and A. Mulchandani, *Biosens. Bioelectron.* **2014**, *58*, 145–152. DOI:10.1016/j.bios.2014.01.053
5. S. Maheswaran, L. V. Sequist, S. Nagrath, L. Ulkus, B. Brannigan, C. V. Collura, E. Inserra, S. Diederichs, A. J. Iafrate and D. W. Bell, *N Engl. J. Med.* **2008**, *359*, 366–377. DOI:10.1056/NEJMoa0800668
6. Y.-T. Long, C.-Z. Li, T. C. Sutherland, H.-B. Kraatz and J. S. Lee, *Anal. chem.* **2004**, *76*, 4059–4065. DOI:10.1021/ac049482d
7. F. J. Steemers, J. A. Ferguson and D. R. Walt, *Nat. Biotechnol.* **2000**, *18*, 91–94. DOI:10.1038/72006
8. M. Duman, R. Saber and E. Pişkin, *Biosens. Bioelectron.* **2003**, *18*, 1355–1363. DOI:10.1016/S0956-5663(03)00087-3
9. J. Wang and A. J. Bard, *Anal. chem.* **2001**, *73*, 2207–2212. DOI:10.1021/ac001344a
10. L. A. Thompson, J. Kowalik, M. Josowicz and J. Janata, *J. Am. Chem. Soc.* **2003**, *125*, 324–325. DOI:10.1021/ja027929z
11. H. Korri-Youssoufi and A. Yassar, *Biomacromolecules*, **2001**, *2*, 58–64. DOI:10.1021/bm0000440
12. J. Wang, *Chem. Eur. J.* **1999**, *5*, 1681–1685. DOI:10.1002/(SICI)1521-3765(19990604)5:6<1681::AID-CHEM1681>3.0.CO;2-U
13. K. Kerman, M. Kobayashi and E. Tamiya, *Meas. Sci. Technol.* **2003**, *15*, R1. DOI:10.1088/0957-0233/15/2/R01
14. A. Benvidi, M. D. Tezerjani, A. D. Firouzabadi, M. Mazloun-Ardakani and S. M. Moshtaghioun, *JICS*. **2016**, *13*, 2135–2142. DOI:10.1007/s13738-016-0931-x
15. H. Karimi-Maleh, F. Tahernejad-Javazmi, N. Atar, M. L. t. Yola, V. K. Gupta and A. A. Ensafi, *Ind. Eng. Chem. Res.* **2015**, *54*, 3634–3639. DOI:10.1021/ie504438z
16. C. Tlili, H. Korri-Youssoufi, L. Ponsonnet, C. Martelet and N. J. Jaffrezic-Renault, *Talanta* **2005**, *68*, 131–137. DOI:10.1016/j.talanta.2005.04.069
17. S. Cheraghi, M. A. Taher, H. Karimi-Maleh, E. Faghhi-Mirzaei, *New J. Chem.* **2017**, *41*, 4985–4989. DOI:10.1039/C7NJ00609H
18. A. Benvidi, M. D. Tezerjani, S. M. Moshtaghioun and M. Mazloun-Ardakani, *Microchim. Acta* **2016**, *183*, 1797–1804. DOI:10.1007/s00604-016-1810-y
19. N. Zhu, Z. Chang, P. He and Y. Fang, *Electrochim. Acta* **2006**, *51*, 3758–3762. DOI:10.1016/j.electacta.2005.10.038
20. Z. Liu, B. Zhao, Y. Shi, C. Guo, H. Yang and Z. Li, *Talanta* **2010**, *81*, 1650–1654. DOI:10.1016/j.talanta.2010.03.019
21. M. O'hare and E. Nice, *J. Chromatogr. A* **1979**, *171*, 209–226. DOI:10.1016/S0021-9673(01)95300-2
22. R. Vaidyanathan, S. Dey, L. G. Carrascosa, M. J. Shiddiky, M. Trau, *Biomicrofluidics*, **2015**, *9*, 061501. DOI:10.1063/1.4936300
23. Y.-T. Cheng, C.-C. Pun, C.-Y. Tsai and P.-H. Chen, *Sens. Actuators, B* **2005**, *109*, 249–255. DOI:10.1016/j.snb.2004.12.072
24. K. S. Novoselov, A. K. Geim, S. V. Morozov, D. Jiang, Y. Zhang, S. V. Dubonos, I. V. Grigorieva and A. A. Firsov, *science* **2004**, *306*, 666–669.
25. D. C. Marcano, D. V. Kosynkin, J. M. Berlin, A. Sinitskii, Z. Sun, A. Slesarev, L. B. Alemany, W. Lu and J. M. Tour, *ACS nano*, **2010**, *4*, 4806–4814. DOI:10.1021/nn1006368
26. J. Lee, Y.-K. Kim and D.-H. Min, *Anal. chem.* **2011**, *83*, 8906–8912. DOI:10.1021/ac201298r
27. Y. Yang, X. Chen, F. Ding, P. Zhang, J. Liu and X. Gu, *Biomaterials*, **2007**, *28*, 1643–1652. DOI:10.1016/j.biomaterials.2006.12.004
28. L. Soffer, X. Wang, X. Zhang, J. Kluge, L. Dorfmann, D. L. Kaplan and G. Leisk, *J. Biomater. Sci., Polym. Ed.* **2008**, *19*, 653–664. DOI:10.1163/156856208784089607
29. M. K. Hota, M. K. Bera, B. Kundu, S. C. Kundu, C. K. Maiti, *Adv. Funct. Mater.* **2012**, *22*, 4493–4499. DOI:10.1002/adfm.201200073
30. S. Aznar-Cervantes, M. I. Roca, J. G. Martínez, L. Meseguer-Olmo, J. L. Cenis, J. M. Moraleda and T. F. Otero, *Bioelectrochemistry*, **2012**, *85*, 36–43. DOI:10.1016/j.bioelechem.2011.11.008
31. S. Aznar-Cervantes, J. G. Martínez, A. Bernabeu-Esclapez, A. A. Lozano-Pérez, L. Meseguer-Olmo, T. F. Otero and J. L. Cenis, *Bioelectrochemistry*, **2016**, *108*, 36–45. DOI:10.1016/j.bioelechem.2015.12.003
32. K. Hu, M. K. Gupta, D. D. Kulkarni and V. V. Tsukruk, *Adv. Mater* **2013**, *25*, 2301–2307. DOI:10.1002/adma.201300179
33. S. Ling, C. Li, J. Adamcik, S. Wang, Z. Shao, X. Chen and R. Mezzenga, *ACS Macro Letters*, **2014**, *3*, 146–152. DOI:10.1021/mz400639y
34. H. Karimi-Maleh, M. Hatami, R. Moradi, M. A. Khalilzadeh, S. Amiri, H. Sadeghifar, *Microchim. Acta* **2016**, *183*, 2957–2964. DOI:10.1007/s00604-016-1946-9
35. H. Karimi-Maleh, A. F. Shojaei, K. Tabatabaeian, F. Karimi, Sh. Shakeri, R. Moradi, *Biosens. Bioelectron.* **2016**, *86*, 879–884. DOI:10.1016/j.bios.2016.07.086
36. H. Karimi-Maleh, F. Amini, A. Akbari, M. Shojaei, *J. Colloid Interf. Sci.* **2017**, *495*, 61–67. DOI:10.1016/j.jcis.2017.01.119
37. S. Cheraghi, M. A. Taher, H. Karimi-Maleh, *J. Food Compost. Anal. J.* **2017**, *62*, 254–259. DOI:10.1016/j.jfca.2017.06.006
38. S. Cheraghi, M. A. Taher, H. Karimi-Maleh, *Appl. Surf. Sci.* **2017**, *420*, 882–885. DOI:10.1016/j.apsusc.2017.05.218
39. M. Shabani-Nooshabadi, M. Roostaei, H. Karimi-Maleh, *J. Iran. Chem. Soc.* **2017**, *14*, 955–961. DOI:10.1007/s13738-016-1045-1
40. S. M. Ghoreishi, M. Behpour, S. Sadeghzadeh and M. Golestaneh, *Acta Chim. Slov.* **2011**, *58*, 69–74.
41. B. Bozzini, P. Bocchetta, A. Gianoncelli, C. Mele and M. Kiskinova, *Acta Chim. Slov.* **2014**, *61*, 263–271.
42. B. Mahltig, H. Haufe, K. Muschter, A. Fischer, Y. H. Kim, E. Gutmann, M. Reibold, D. C. Meyer, T. Textor and C. W. Kim, *Acta Chim. Slov.* **2010**, *57*, 451–457.
43. M. Kaushik, S. Mahendru, M. Kumar, S. Chaudhary and S. Kukreti, *Advanced Techniques in Biology & Medicine*, **2016**, 1–6.
44. J. Liu, Z. Cao and Y. Lu, *Chem. Rev.* **2009**, *109*, 1948–1998. DOI:10.1021/cr030183i

45. J. N. Wilson, Y. N. Teo and E. T. Kool, *J. Am. Chem. Soc.* **2007**, *129*, 15426–15427. DOI:10.1021/ja075968a
46. J.-Y. Park and S.-M. Park, *Sensors*, **2009**, *9*, 9513–9532. DOI:10.3390/s91209513
47. D. R. Baselt, G. U. Lee, M. Natesan, S. W. Metzger, P. E. Sheehan, R. J. Colton, *Biosens. Bioelectron.* **1998**, *13*, 731–739. DOI:10.1016/S0956-5663(98)00037-2
48. S.-y. Niu, Q.-y. Li, R. Ren and S.-s. Zhang, *Biosens. Bioelectron.* **2009**, *24*, 2943–2946. DOI:10.1016/j.bios.2009.02.022
49. A. Benvidi, N. Rajabzadeh, M. Mazloum-Ardakani and M. M. Heidari, *Sens. Actuators, B* **2015**, *207*, 673–682. DOI:10.1016/j.snb.2014.10.043
50. M. D. Tezerjani, A. Benvidi, M. Rezaeinasab, S. Jahanbani, S. M. Moshtaghioun, M. Youssefi and K. Zarrini, *Anal. Methods*, **2016**, *8*, 7507–7515. DOI:10.1039/C6AY01524G
51. C. Zhao, J. Yao, H. Masuda, R. Kishore and T. Asakura, *Biopolymers*, **2003**, *69*, 253–259. DOI:10.1002/bip.10350
52. R. Jain, A. Sinha and A. L. Khan, *Mater. Sci. Eng., C* **2016**, *65*, 205–214. DOI:10.1016/j.msec.2016.03.115
53. B. Kundu, R. Rajkhowa, S. C. Kundu and X. Wang, *Adv. Drug Deliv. Rev.* **2013**, *65*, 457–470. DOI:10.1016/j.addr.2012.09.043
54. J. R. Lomeda, C. D. Doyle, D. V. Kosynkin, W.-F. Hwang and J. M. Tour, *J. Am. Chem. Soc.* **2008**, *130*, 16201–16206. DOI:10.1021/ja806499w
55. H. Yin, Y. Zhou, J. Xu, S. Ai, L. Cui and L. Zhu, *Anal. Chim. Acta* **2010**, *659*, 144–150. DOI:10.1016/j.aca.2009.11.051
56. A. Benvidi, A. D. Firouzabadi, S. M. Moshtaghiun, M. Mazloum-Ardakani and M. D. Tezerjani, *Anal. Biochem.* **2015**, *484*, 24–30. DOI:10.1016/j.ab.2015.05.009
57. Y.-Q. Zhang, *Biotechnol. Adv.* **1998**, *16*, 961–971. DOI:10.1016/S0734-9750(98)00012-3
58. Y. Xu, Y. Jiang, H. Cai, P.-G. He and Y.-Z. Fang, *Anal. Chim. Acta*, **2004**, *516*, 19–27. DOI:10.1016/j.aca.2004.04.013
59. H. Cai, X. Cao, Y. Jiang, P. He and Y. Fang, *Anal. Bioanal. Chem.* **2003**, *375*, 287–293. DOI:10.1007/s00216-002-1652-9
60. X. Xu, X. Weng, A. Liu, Q. Lin, C. Wang, W. Chen and X. Lin, *Anal. Bioanal. Chem.*, **2013**, *405*, 3097–3103. DOI:10.1007/s00216-013-6715-6
61. X. Li, J. Xia and S. Zhang, *Anal. Chim. Acta*, **2008**, *622*, 104–110.
62. H. Qi, X. Li, P. Chen and C. Zhang, *Talanta* **2007**, *72*, 1030–1035. DOI:10.1016/j.talanta.2006.12.032

Povzetek

V tej študiji smo razvili preprost nov elektrokemični biosenzor za detekcijo DNA sekvenc, osnovan na steklasti ogljikovi elektrodi (GCE), modificirani s kompozitom iz grafenovega oksida (GO) in nanovlaken svilenega fibroina (SF) ter z zlatimi nanodelci (MCH/ssDNA/AuNPs/SF/GO/GCE). Procese izdelave elektrokemičnega biosenzorja smo spremljali z vrstično elektronsko mikroskopijo (SEM), FT-IR in z elektrokemičnimi metodami. Optimizirali smo nekatere eksperimentalne pogoje, kot so: čas imobilizacije DNA in čas inkubacije z MCH, čas in temperatura hibridizacije. Pripravljeni biosenzor je izkazal široko linearno območje od $1,0 \times 10^{-16}$ do $1,0 \times 10^{-8}$ mol L⁻¹ ter nizko mejo zaznave ($3,3 \times 10^{-17}$ mol L⁻¹) za detekcijo mutacije BRCA1 5382 s tehniko EIS. Izkazal je tudi visoko selektivnost za ločevanje med komplementarnimi (PIC) sekvencami in različnimi nekomplementarnimi sekvencami (P1nC1, P1nC2 in P1nC3). Biosenzor je imel tudi visoko obnovljivost (RSD 7,5% (n = 4)) in visoko stabilnost (92% začetnega odziva po 8 dnevih). Pripravljeni biosenzor ima torej ustrezen potencial za uporabo pri odkrivanju sekvenc raka na dojki v začetnih stopnjah.

Scientific paper

Interaction of HF, HBr, HCl and HI Molecules with Carbon Nanotubes

Wiem Felah Gtari¹ and Bahoueddine Tangour^{1,*}

¹ Université de Tunis El Manar, Research Unit of Modeling in Fundamental Sciences and Didactics, Team of Theoretical Chemistry and Reactivity, BP 244, 2092, El Manar 2, Tunisia

* Corresponding author: E-mail: bahoueddine.tangour@ipeiem.utm.tn
Tel: +216 98 817468

Received: 13-07-2017

Abstract

The present work applies the density functional theory (DFT) to study the interactions between armchair (n,n) single walled carbon nanotubes (SWCNTs) and hydrogen halides confined along the nanotube axis and perpendicular to it. Calculations are performed using the CAM-B3LYP functional. According to the hydrogen halides orientation and the internal diameter of CNTs hollow space, HF, HCl, HBr and HI behave differently. The nanoconfinement alters the charge distribution and the dipolar moment. The encapsulated hydrogen fluoride (HF) molecule is stable along and perpendicular to the nanotubes (5,5) and (6,6) axis. The hydrogen chloride (HCl), hydrogen bromide (HBr) and hydrogen iodide (HI) form stable systems inside the nanotube (6,6) only at the perpendicular orientation. In addition, other phenomena are observed such as leaving the nanotube or decreasing the bond length of the molecule and even the creation of covalent bond between the guest molecule and the host nanotube.

Keywords: Carbon nanotubes; hydrogen halides storage; confinement energy; van der Waals interactions; Mulliken analysis population; DFT/CAM-B3LYP.

1. Introduction

Single walled carbon nanotubes (SWCNTs) attract researchers' interest since their discovery¹ in industry and academy, thanks to their unique electrical and mechanical properties and their potential applications in several fields. The greatest advantage of this SWCNTs is their hollow space which could confine numerous molecules in order to storage them^{2–6} or to contain chemical reactions.⁷ They are used to remove heavy metals in wastewater treatment⁸ and in drug delivery.^{9–15} Carbon nanotubes are known to have a great surface of reactivity outside and inside them.

Doping of the exterior surface of a nanotube or the adsorption of atoms or molecules inside it offers the possibility to create exceptional materials with new properties. In particular, the confinement processes modifies the properties of the confined molecules in different ways.^{16–20} In previous studies, we investigated the local influence of CNT's walls on small molecules H₂^{21,22} and F₂.²³ The former molecule H₂ allowed us to study the effect of the confinement on the electron of the single bond H–H. Some differences have been detected on H₂ behavior between its confinement in CNTs and their boron-nitrogen homo-

logues.²² The latter molecule F₂, even apolar in nature, introduced the lone pair effect. This studies focus on the comprehension of the intermolecular interactions nature in endohedral complexes. Differences in behavior of each one of those molecules are CNT's diameter dependent and were rationalized invoking the relatives areas under atomic or van der Waals radii control. The purpose of this paper is to study the interaction between polar molecules that are hydrogen halides (hydrogen fluoride HF, hydrogen chloride HCl, hydrogen bromide HBr and hydrogen iodide HI) and the interior of carbon nanotubes of different diameters.

Hydrogen fluoride HF is toxic and strongly corrosive; it dissolves most minerals (oxides, silicates), metals and plastics. Fluoride ions F⁻ penetrate into deep tissue and react highly with magnesium and calcium. However, HF is a potential fuel generator. It reacts in solution with alkali and light metals by releasing hydrogen (H₂). Its storage inside carbon nanotubes would constitute, on the one hand, an adequate way to avoid its corrosion and its toxicity. On the other hand, it would represent an interesting way of controlling production of dihydrogen.

Another application concerns environmental area. Different techniques exist to uptake the excess fluoride

from wastewater. Among them, nanotube supported alumina could highlight a great potential to adsorb and remove fluoride from water.²⁴

Produced carbon nanotubes still contain impurities like amorphous carbon, and catalytic metal particles. Further physical and chemical applications of CNTs require their removal. Hydrochloric acid (HCl) solution is very often used to purify carbon nanotubes. This in-situ presence of HCl may allow insertion of this gas inside the nanotube generating a doping phenomenon. Such property generated considerable interest because of the possible use of CNTs as gas sensors.^{25–27}

The aim of this work is twofold. First, to extend and to deepen the knowledge of the encapsulation phenomena inside carbon nanotubes, by including an additional layer of difficulty which is the intervention of the permanent dipole moment. Second, to make a contribution to potential applications of HX acids confinement (X = F, Cl, Br and I).

Unfortunately, there is a lack of study focusing on the encapsulation of these molecules inside or outside carbon nanotubes. The encapsulation of HF dimer inside (n,n) CNTs is recently investigated by Roztoczyńska and al. using the M06-2X exchange–correlation functional.²⁸ This work was limited to using a series of energy scans to highlight the orientation influence of HF dimers with respect to carbon nanotubes. Liang and al. revealed the stability of HCl molecule inside the CNT (14,0)²⁹ by studying the electronic and band structure for this complex. There is also few works related to the encapsulation of hydrogen halides inside fullerenes.^{30–32}

2. Methodology

In the present paper, we carried out geometry optimizations for armchair (n,n) carbon nanotubes with n = 3,4, 5 and 6 with HF, HCl, HBr and HI molecules inside using the density functional theory. To gain insight into the interaction between these molecules and carbon nanotubes, we perform quantum calculation using the new hybrid exchange–correlation function CAM-B3LYP presented by Yanai and al.³³ and STO-3G basis set. STO-3G basis

set³⁴ is a minimal basis set, but in term of calculating energy, it gives trusted results^{21,23} without consuming a long calculation time. Carbon nanotubes were produced involving three unit cells with TubeGen 3.4 program.³⁵

Terminal carbon atoms are hydrogenated to saturate their valence. The formulas of the considered (3,3), (4,4), (5,5) and (6,6) carbon nanotubes are : C₃₆H₁₂, C₄₈H₁₆, C₆₀H₂₀ and C₇₂H₂₄ respectively. The optimized diameters of the chosen nanotubes are varying from 5.49 Å to 8.23 Å. All electronic structure calculations were realized using Gaussian 09 suite of programs.³⁶ Kohn–Sham density functional (DFT) is extensively used since its cheap cost and the possibility to employ it to explore several chemical, physical and biological systems. The coulomb attenuated method CAM-B3LYP is an improved version of the B3LYP functional by the inclusion of long range dispersion energy and it is appropriate to describe the noncovalent interactions.³³ This function gives a better description of the energy when the charge transfer is involved.

3. Results and Discussion

Former studies demonstrated that the orientation of a confined molecule affects notably the interaction between the guest molecule and the nanotube.^{22–23,37–40} For that reason, two orientations of hydrogen halides molecules were considered: parallel (//) and perpendicular (⊥) to the CNT's axis as shown in figure 1 and will be noted respectively HX(//)@CNT(n,n) and HX(⊥)@CNT(n,n).

The binding energy (E_{bind}) of the hydrogen halides and the nanotube is calculated as following: $E_{bind} = E(\text{HX@CNT}(n,n)) - E(\text{H-CNT}(n,n)) - E(\text{HX})$

Where $E(\text{HX@CNT}(n,n))$, $E(\text{H-CNT}(n,n))$, $E(\text{HX})$ indicate the energy of the inclusion complex, the hydrogenated CNTs and the isolated HX molecules respectively. The calculated confinement energies were corrected to the basis set superposition error (BSSE).^{41,42} Figure 2 depicts the final situation of each introduced molecule versus CNT's diameter. Depending on the CNT's diameter and the halogens radius, halogen halides exhibit different behavior as summered in table 1. To better explain each phenomenon, we will focus on each nanotube separately. First

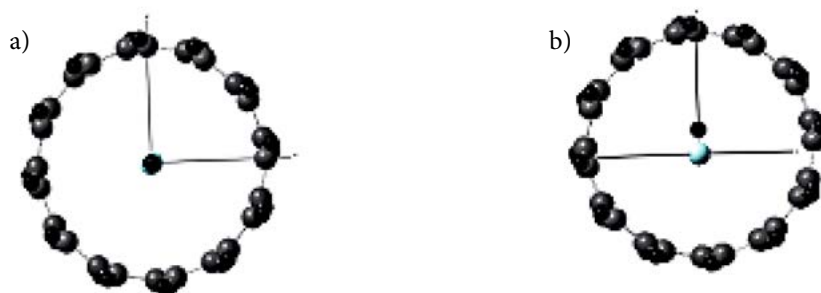


Figure 1. HX studied orientations inside SWNT a) parallel to the nanotube axis noted HX(//)@CNT(n,n) b) perpendicular to the nanotube axis noted HX(⊥)@CNT(n,n)

we discuss the wider nanotube (3,3) which diameter is 4.12 Å. HF and HCl, placed in parallel position along the (3,3) nanotube axis, keep their orientation (Figure 2: a1 and b1). All values of the studied parameters are far from the parameters of the unconfined molecules. When they are placed perpendicular to the (3,3) nanotube axis, we notice a reorientation of these two molecules to the parallel position (Figure 2: a2 and b2). The obtained values of energies, bond lengths and dipolar moment are in the same range of the obtained values at parallel position (Table 2). Roztoczyńska and al. obtained an energy up to +200 kcal mol⁻¹ for HF dimer enclosed inside the nanotube (3,3).²⁸ This result proves the importance of the repulsion forces inside the wider nanotubes in general, in presence of molecules with large radius. HBr and HI sited parallel and perpendicular to the CNT (3,3) axis react with its cage and establish covalent bonds with it (Figure 2: c1, d1, c2, d2). Those figures display the presence of covalent bonds made by the hydrogen atoms. We expected that this result does not have any chemical significance and shows the limits of the computational chemistry of such systems under constraint. In fact, the electronegativity induces a negative charge accumulation from the halogen atoms side, so we can estimate that they present a radius greater than the radius of the isolated atoms. Br and I atoms almost get into the area under the atomic radius of the carbon atoms and set up real chemical bonds with them (Figure 3: 3a and 3e). However, the charge distribution is more destabilized inside the nanotube (3,3). Despite the fact that the Mulliken electric charge is dependent of the method and basis set because it is a local observable, it gives an idea about the charges of each atom.

As seen in table 2, the charges observed on F, Cl and Br atoms are negative, the charges of H atoms are positive. However, in the case of HI molecule, Mulliken gives a negative charge on H atom and positive charge on I atom. This result is due to the choice of the basis of calculation which should be more suitable for iodine atom. In the case of the encapsulation of

HBr and HI inside the CNT (3,3), H, Br and I atoms are linked to the carbons of the nanotube's cavity, that's why their atomic charges are different from the atomic

charges of unconfined HBr and HI molecules. Starting from the CNT (4,4), all the studied molecules introduced at the parallel position are kept inside the nanotubes (Figure 2: a3, b3, c3 and d3). As shown in table 2, HF molecule forms a stable system with the nanotubes (5,5) and (6,6) since the confinement energies values are negative or very weak equal to -0.9276 kcal mol⁻¹ and 0.0290 kcal mol⁻¹ respectively. Theoretical studies which investigated the encapsulation of HF molecule inside the fullerene showed that this molecule forms a stable system. Shameema and al, for example reveal a stabilization energy equal to -2.5 kcal mol⁻¹ using the HF/6-31G method.³¹ The authors of this study explain that the encapsulation of polar guest molecules polarizes the cage in a way that the carbon atoms placed near the positively charged atoms of the guest species turn into negatively charged and those close to the negatively charged atoms become positively charged. Inside the wider nanotubes, the charge distribution has not a significant change in comparison with the unconfined molecules.

That is why there is a decrease in the net dipole moment of these systems. According to this study, the dipole moment of the free HF molecule is 2.3 Debye, and its dipole moment inside C60 is 0.54 Debye.³¹ As a general rule, when the diameter of the CNT increases, the confinement energy value is lower. Values of confinement energies inside the nanotube (6,6), are under 0.001 kcal mol⁻¹ in all the studied cases showing the attenuation of the interaction between the guest species and the host cage. In fact, figures 3 a, b, c and d illustrate the interaction between the van der Waals radii of the carbon atoms and the guest molecules. When the nanotube diameter is bigger, the overlap between vdW radii becomes lower, especially with the fluorine, chlorine and bromine atoms.

At the perpendicular position, only HF molecule (Figure 2a) remains inside the nanotube (4,4), HCl, HBr and HI guest molecules leave it (Figure 2b, 2c, 2d). Outside the nanotube, HCl molecule is re-oriented at the parallel position. Despite the negative energy equal to -3.5 kcal mol⁻¹, the bond length is stretched to 1.3495 Å, signifying that even outside the nanotube, HCl molecule is under the influence of van der Waals radii of terminal hydrogen at-

Table 1. Observed phenomena inside the studied nanotubes at parallel and perpendicular orientations

Orientation	Molecule	CNT (3,3)	CNT (4,4)	CNT (5,5)	CNT (6,6)
Parallel	HF	Destabilized binding	Inside shortness of the bond length	Stabilization	Stabilization
	HCl	Destabilized binding	Destabilized binding	Confinement	Confinement
	HBr	Covalent interaction	Destabilized binding	Confinement	Confinement
	HI	Covalent interaction	Destabilized binding	Confinement	Confinement
Perpendicular	HF	Re-orientation	Inside shortness of the bond length	Stabilization	Stabilization
	HCl	Re-orientation	Leaving CNT	Confinement	Stabilization
	HBr	Covalent interaction	Leaving CNT	Confinement	Stabilization
	HI	Covalent interaction	Leaving CNT	Leaving CNT	Confinement

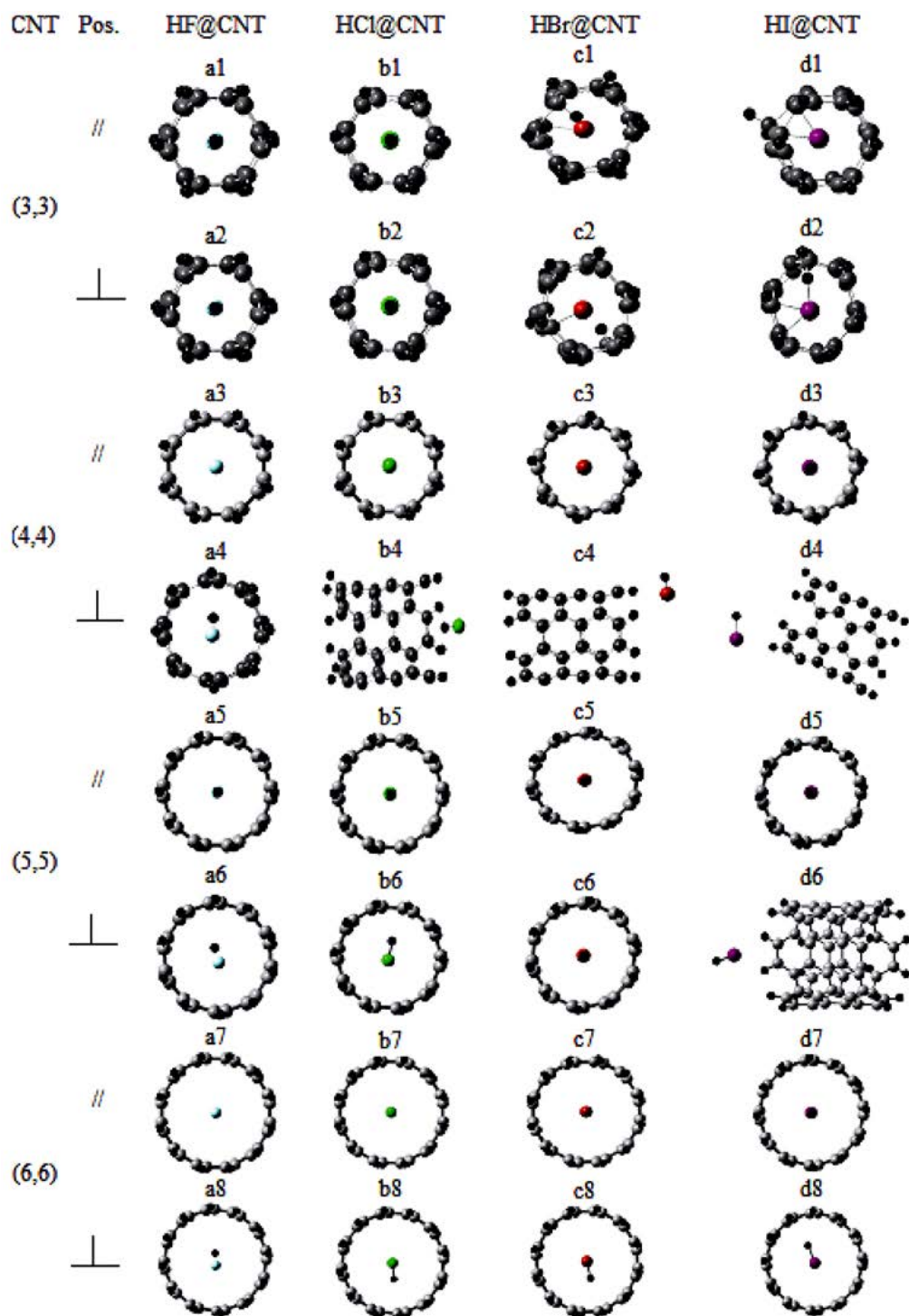


Figure 2. Interaction of HX molecules with the (3,3), (4,4), (5,5) and (6,6) CNT's at both parallel and perpendicular orientations

oms. Figure 3.e shows a significant overlap between the vdW radii of halogens and the carbon atoms of the wall of the CNT. As a result, those molecules are “chased” outside the CNT in order to decrease the electrostatic forces involved. HBr and HI molecules are also expelled outside the nanotube (4,4). Their bond lengths and dipolar moments values are higher than those of unconfined molecules (Ta-

ble 2). The charge distribution is highly affected. We notice that when the van der Waals radius of the halogen atom is greater than the radii of the nanotube, the molecule is expelled out of it. In fact, the halogen halide in this condition is trapped inside a repelled area. The same phenomena was observed for water which flow rate varies when the CNT diameter changes.⁴³

tioned above are under the values of the dipolar moments of the free molecules. There is an important overlap (figure 3g and 3h) between van der Waals radii of the hydrogen halides molecules and the carbon atoms: this overlap has a destabilising and repulsive nature for the HI molecule and it has a stabilising and attractive nature for HF, HCl and HBr molecules.

5. Conclusion

Theoretical calculations have been made to investigate the encapsulation of HF, HCl, HBr and HI molecules inside carbon nanotubes (3,3), (4,4), (5,5) and (6,6). Calculations are made using DFT/CAM-B3LYP functional with STO-3G basis sets. Dipolar moments of all confined molecules are affected. At the parallel and perpendicular directions, HF molecule forms a stable system with the nanotubes (5,5) and (6,6). HCl, HBr and HI molecules placed perpendicular, form a stable complex with the CNT (6,6). In all those cases, the bond lengths and the atomic charge of confined molecules reach the values obtained for the unconfined molecules.

6. References

1. F. S. Ijima, *Nature* **1991**, 354, 56–58.
DOI:10.1038/354056a0
2. E. Bichoutskaia, N.C. Pyper, *J. Chem. Phys.* **2008**, 129, 154701(1)–15.
3. M. Milko, C. Ambrosch-Draxel, *Phys. Review B* **2011**, 84, 085437(1)–7.
4. J. Xiao, X. Pan, F. Zhang, H. Li, X. Bao, *Chem. Sci.* **2016**, 8(1):278–283. DOI:10.1039/C6SC02298G
5. E. I. Calixte, O. N. Samoylova, K. L. Shuford, *Phys. Chem. Chem. Phys.* **2016**, 18, 12204–12212.
DOI:10.1039/C5CP04446D
6. F. Cao, W. Ren, X. Xu, Y-X Tong, C. Zhao, *Chem. Phys. Lett.* **2011**, 512, 81–86. DOI:10.1016/j.cplett.2011.07.010
7. S. A. Miners, G. A. Rance, A. N. Khlobystov, *Chem. Soc. Rev.* **2016**, 45, 4727–4746. DOI:10.1039/C6CS00090H
8. Y. H. Li, Y. M. Zhao, W. B. Hu, I. Ahmad, Y. Q. Zhu, X. J. Peng, Z. Luan, *J. of Phys.: Conf. Ser.* **2007**, 61, 698–702.
DOI:10.1088/1742-6596/61/1/140
9. S. K. S. Kushwaha, S. Ghoshal, A. K. Rai, S. Singh, *Braz. Jour. Pharma. Sci.* **2013**, 49 (4), 629–643.
DOI:10.1590/S1984-82502013000400002
10. Y. Belmiloud, M. Ouraghi, M. Brahim, A. Benaboura, D. Charqaoui, B. Tangour, *Jour. Comput. Theor. Nanosci.* **2012**, 9, 1101–1108. DOI:10.1166/jctn.2012.2150
11. R. Bessrou, Y. Belmiloud, Z. Hosni, B. Tangour, *AIP Conference Proceedings* **2012**, 1456, 229–239.
DOI:10.1063/1.4730664
12. Z. Hosni, R. Bessrou, B. Tangour, *J. Comput. Theor. Nanosci.* **2014**, 11, 318–323. DOI:10.1166/jctn.2014.3354
13. A. Kumari, R. Singla, A. Guliani, S. Y. Kumar, *Excli Jour.* **2014**, 13, 265–286.
14. A. Mejri, D. Vardanega, B. Tangour, T. Gharbi, F. Picaud, *J. Phys. Chem. B* **2015**, 119, 604–611.
DOI:10.1021/jp5102384
15. L. M. Dutra, O. V. de Oliveira, J. D. dos Santos, *Aust. J. Chem.* **2016**, 70(3), 252–257. DOI:10.1071/CH16165
16. K. V. Agrawal, S. Shimizu, L. W. Drahushuk, D. Kilcoyne, M. S. Strano, *Nat. Nanotech.* **2016**, 12, 267–273.
DOI:10.1038/nnano.2016.254
17. S. Dargouthi, S. Boughdiri, B. Tangour, *J. Comput. Theor. Nanosci.*, **2014**, 11, 1258–1263.
DOI:10.1166/jctn.2014.3491
18. L. B. da Silva, *J. Nanostruct. Chem.* **2014**, 4:104.
19. S. Dargouthi, S. Boughdiri, B. Tangour, *Acta Chim. Slov.* **2015**, 62, 445–451. DOI:10.17344/acsi.2014.1080
20. A. Gannouni, M. Ouraghi, S. Boughdiri, R. Bessrou, A. Benaboura, B. Tangour *J. Comput. Theor. Nanosci.* **2012**, 9 (3), 379–383. DOI:10.1166/jctn.2012.2034
21. W. F. Gtari, B. Tangour, *Int. J. Quantum Chem.* **2013**, 113(21), 2397–2404.
22. Y. Belmiloud, W. Djitli, H. Abdeljebar, M.L Abdelatif, B. Tangour, M. Brahim, *Super. and Micro.* **2017**, 101, 547–558.
DOI:10.1016/j.spmi.2016.10.081
23. W. F. Gtari, B. Tangour, *Can. J. chem.* **2016**, 94, 15–19.
DOI:10.1139/cjc-2015-0235
24. Y. H. Li, S. Wang, X. Zhang, J. Wei, C. Xu, Z. Luan, D. Wu and B. Wei, *Environmental Technology*, **2008**, 24:3, 391–398.
DOI:10.1080/09593330309385572
25. P. G. Collins, K. Bradley, M. Ishigami and A. Zettl, *Science*, **2000**, 287, 1801. DOI:10.1126/science.287.5459.1801
26. J. Kong, N. R. Franklin, C. Zhou, M. G. Chapline, S. Peng, K. Cho and H. Dai, *Science*, **2000**, 287, 622.
DOI:10.1126/science.287.5453.622
27. J. Abraham, A. Vencelová, T. Seyller, F. Hennrich, M. M. Kappes, A. Hirsch and L. Ley, *Phys. Chem. Chem. Phys.*, **2003**, 5, 5472–5476. DOI:10.1039/B311016H
28. A. Roztoczyńska, J. Kozłowska, P. Lipkowski, W. Bartkowiak, *Phys Chem Chem Phys.* **2016**, 18, 2417–2427.
DOI:10.1039/C5CP04153H
29. T. Liang, W-X. Li, H. Zhang, *J. of Mol. Struct. : Theochem* **2009**, 905, 44–47. DOI:10.1016/j.theochem.2009.03.007
30. C. I. Williams, M. A. Whitehead, L. Pang, *J. Phys. Chem.* **1993**, 97, 11652–11656.
31. O. Shameema, C. N. Ramachandraan, N. Sathyamurthy, *J. of Phys. Chem. A Let.* **2006**, 110, 2–4.
32. Y-F Chang, B. Hong, L-L. Sun, S-W Tang, R-S. Wang, *Chem. Res. In Chin. Univ.* **2008**, 24, (2):220–222.
DOI:10.1016/S1005-9040(08)60045-8
33. T. Yanai, D. Tew, N. Handy, *Chem. Phys. Lett.* **2004**, 393, 51–57. DOI:10.1016/j.cplett.2004.06.011
34. J. B. Collins, P. v. R. Schleyer, J. S. Binkley, J. A. Pople, *J. Chem. Phys.* **1976**, 64, 5142–5151. DOI:10.1063/1.432189
35. J. T. Frey, D. J. Doren TubeGen 3.4 University of Delaware, Newark DE, **2011**. <http://turin.nss.udel.edu/research/tube-genonline.html>. Accessed on 2014.

36. Gaussian 09, Revision D.01, M. J. Frisch, G. W. Trucks, H. B. Schlegel, G. E. Scuseria, M. A. Robb, J. R. Cheeseman, G. Scalmani, V. Barone, B. Mennucci, G. A. Petersson, H. Nakatsuji, M. Caricato, X. Li, H. P. Hratchian, A. F. Izmaylov, J. Bloino, G. Zheng, J. L. Sonnenberg, M. Hada, M. Ehara, K. Toyota, R. Fukuda, J. Hasegawa, M. Ishida, T. Nakajima, Y. Honda, O. Kitao, H. Nakai, T. Vreven, J. A. Montgomery, Jr., J. E. Peralta, F. Ogliaro, M. Bearpark, J. J. Heyd, E. Brothers, K. N. Kudin, V. N. Staroverov, R. Kobayashi, J. Normand, K. Raghavachari, A. Rendell, J. C. Burant, S. S. Iyengar, J. Tomasi, M. Cossi, N. Rega, J. M. Millam, M. Klene, J. E. Knox, J. B. Cross, V. Bakken, C. Adamo, J. Jaramillo, R. Gomperts, R. E. Stratmann, O. Yazyev, A. J. Austin, R. Cammi, C. Pomelli, J. W. Ochterski, R. L. Martin, K. Morokuma, V. G. Zakrzewski, G. A. Voth, P. Salvador, J. J. Dannenberg, S. Dapprich, A. D. Daniels, Ö. Farkas, J. B. Foresman, J. V. Ortiz, J. Cioslowski, D. J. Fox, Gaussian, Inc., Wallingford CT, 2009.
37. S. S. Han, H.M. Lee, *Carbon* **2004**, *42*, 2169–2177. DOI:10.1016/j.carbon.2004.04.025
38. J. Sloan, G. Matthewman, C. Dyer-Smith, A-Y. Sung, Z. Liu, K. Suenaga, A. I. Kirkland, E. Flahaut, *ACS Nano* **2008**, *2*, 966–976. DOI:10.1021/nn7002508
39. D. Henwood, J. D. Carey, *Phys. Rev. B* **2007**, *75*, 245413: 1–10.
40. C. N. Ramachandran, D. De Fazio, N. Sathyamurthy, V. Aquilanti, *Chem. Phys. Lett.* **2009**, *473*, 146–150. DOI:10.1016/j.cplett.2009.03.068
41. H. B. Jansen, P. Ros, *Chem. Phys. Lett.* **1969**, *3*, 140–143. DOI:10.1016/0009-2614(69)80118-1
42. S. F. Boys, F. Bernardi, *Molec. Phys.* **1970**, *19*, 553–566. DOI:10.1080/00268977000101561
43. A. T. John, A. J. H. McGaughey, *Phy. Rev. Lett.* **2009**, *102*, 184502: 1–4.ww

Povzetek

V tem delu smo s teorijo gostotnega funkcionala (DFT) preučevali interakcije med armchair (n,n) enojnimi panelnimi ogljikovimi nanocevkami (SWCNT)s in vodikovimi halogenidi, ujetimi vzdolž osi nanocevk in pravokotno nanjo. Izračune smo izvedli z uporabo CAM-B3LYP funkcionala. V skladu z orientacijo vodikovih halogenidov in notranjim premerom praznin CNTs, se HF, HCl, HBr in HI različno obnašajo, ker ujetost v nano praznino spremeni porazdelitev naboja in dipolni moment. Inkapsulirana molekula vodikovega fluorida (HF) je stabilna vzdolž in pravokotno na osi (5,5) in (6,6) nanocevk. Vodikov klorid (HCl), vodikov bromid (HBr) in vodikov jodid (HI) tvorijo stabilne sisteme znotraj (6,6) nanocevk le v navpični smeri. Poleg tega opazimo druge pojave, kot so zapuščanje nanocevke ali zmanjšanje dolžine vezi molekule in celo tvorbo kovalentne vezi med molekulo in nanocevko.

Scientific paper

Theoretical Study of Ability of Boron Nitride Nanocone to Oxidation of Sulfur Monoxide

Xuewu Zuo,¹ Kouros Behradfar,² Jia-Bao Liu,^{3,*}
Milad Janghorban Lariche^{4,*} and Meysam Najafi^{5,*}

¹ Department of Common Course Teaching, Anhui Xinhua University, Hefei 230088, Anhui, P. R. China

² Department of Chemical Engineering, Quchan Branch, Islamic Azad University, Quchan, Iran.

³ Jia-Bao Liu, School of Mathematics and Physics, Anhui Jianzhu University, Hefei 230601, P.R. China

⁴ Abadan School of Medical Sciences, Abadan, IRAN.

⁵ Medical Biology Research Center, Kermanshah University of Medical Sciences, Kermanshah 67149-67346, Iran

* Corresponding author: E-mail: liujiabaoad@163.com, janghorban@abadanums.ac.ir
and meysamnajafi2016@gmail.com

Received: 18-10-2017

Abstract

In recent years, the discovery of suitable catalyst to oxidation of sulfur monoxide (SO) in normal temperature is a major concern in the industry. In this study, in first step; the boron nitride nanocone (BNNC) with Ge were doped and the surface of Ge-BNNC by using of the O₂ molecule were activated. In second step; oxidation of SO on surface of Ge-BNNC through the Langmuir Hinshelwood (LH) and Eley Rideal (ER) mechanisms was investigated. Calculated data reveal that surface of O₂-Ge-BNNC oxide the SO molecule with Ge-BNNC-O-O* + SO → Ge-BNNC-O-O*-SO → Ge-BNNC-O* + SO₂ and Ge-BNNC-O* + SO → Ge-BNNC + SO₂ reactions. It can be concluded, the energy barrier of LH mechanism to oxidation of SO on Ge-BNNC is lower than ER mechanism. Finally, the Ge-BNNC is acceptable catalyst with low price and high performance to oxidation of SO in normal temperature.

Keywords: Catalyst; nanostructure; metal adoption; oxidation reaction; adsorption energy

1. Introduction

Refiners, industries, mines and factories product the toxic gases that removing of produced toxic gases by oxidation reactions are important to reduce air pollution.^{1–3} In recent years, researchers were done various works to oxidation of the toxic gases via catalysts with high performance.^{4–6}

In industry, catalysts containing various metals have great activity, proper performance and high sensitivity and dispersed metal catalysts were used in vital chemical reactions, generally.^{7–9} Previous works about oxidation of important toxic gases via metal catalysts proved that metal catalysts were expensive and they have great energy barrier and also they needed high temperature to have appropriate efficiency.^{10–12}

In order to overcome mentioned problems and discover the novel catalyst with low price, high stability and high action in normal temperature; the nano clusters and nanostructures as catalysts of oxidation reactions of important toxic gases were used.^{13–18}

Recently many of nanostructures because of their remarkable properties such as big surface-to-volume relationship, comfort of adopting and functionalization, high

efficiency in normal temperature were used as sensor of toxic gases.^{19–21} Previous studies show that functionalization of nanostructures via organic groups and doping of nanostructures via suitable metal atoms can improve the physical and chemical properties of nanostructures. The functionalization and adoption of nanostructures can improve the response and sensitivity of nanostructures to toxic gases.^{22–27}

The oxidation of sulfur monoxide (SO) as deadly gas can reduce the environmental complications, significantly. Commonly, nanostructures as catalyst can oxide the SO molecule via Langmuir–Hinshelwood (LH) and Eley–Rideal (ER) mechanisms.^{28–30} In previous studies, oxidation of toxic gases on metal-adopted nanostructure surfaces via LH and ER mechanisms were investigated. Results show that oxidation mechanism of toxic gases depends on the type of nanostructures and adopted metals. Results indicated that adopted-metals on the nanostructure surface can improve the rate and quality of oxidation reaction of toxic gases, significantly.^{31–33}

In LH mechanism the oxygen molecule (O₂) and SO were adsorbed on surface of catalyst and also in surface of catalyst an intermediate state were formed and finally sulfur dioxide (SO₂) were separated. In ER mechanism, strai-

ghtforward reaction between the pre-adsorbed O₂ and adsorbed SO were performed.^{34–36}

In previous studies, the potential of metal-adopted nanostructure as catalysts of toxic gases oxidation via LH and ER mechanisms were investigated. Results proved that metal-adopted nanostructures were acceptable catalysts with high performance and lower energy barrier.^{37–40} Therefore, metal-adopted nanostructures can propose the novel high performance and low price catalysts for toxic gases oxidation at normal temperature.^{41–43}

In this study, the surface of boron nitride nanocone were adopted by Ge atom and the SO oxidation on Ge-adopted BNNC low price as catalyst via LH and ER mechanisms were investigated by theoretical methods. The main questions that were answered in this work are: (1) How much adoption energy is needed to adoption of Ge on BNNC surface? (2) How much adsorption energy is needed to O₂ and SO adsorption on Ge-BNNC surface? (3) Can Ge-BNNC be a low price catalyst for SO oxidation in normal temperature? (4) How much barrier and adsorption energies are needed to SO oxidation on Ge-BNNC surface? (5) Which mechanisms are more appropriate for SO oxidation on Ge-BNNC surface?

1. 1. Computational Details

In this study the geometry optimization and frequency calculations of studied nanostructures and their complexes with SO and O₂ were done by DFT/ M06-2X method and 6-311G (2d, 2p) basis set in GAMESS software.^{44–48} In this study, the unsaturated border effects by adding the hydrogen atoms to Ge-BNNC and corresponding studied complexes were avoided. The adsorption energy (E_{ad}) values of studied molecules on Ge-BNNC surfaces were equal with difference in energies between of complexes and corresponding monomers.^{49,50}

2. Results and Discussions

2. 1. The Ge Adoption of BNNC and Adsorption of SO and O₂ on Ge-BNNC Surface

Gao et al.⁵¹ determined the reverse eccentric connectivity index of one family of pentagonal carbon nanocones and three infinite families of fullerenes based on graph analysis and computation derivation, and their results suggested the theoretical basis for material properties.

Gao et al.⁵² investigated the oxidation of CN on surface of the Ge-CNT via the Langmuir Hinshelwood and the Eley Rideal mechanisms. Their results show that oxidation of CN on surface of Ge-CNT via the LH mechanism has lower energy barrier than ER mechanism. Their results shown that reveal that Ge-CNT is acceptable catalyst with high performance for CN oxidation.

Gao et al.⁵³ by means of graph structure analysis and edge dividing technology, formulate for calculating the fifth geometric arithmetic index of bridge graph was given. They presented the fifth geometric-arithmetic index of carbon nanocones.

In previous studies, results show that adoption of BNNCs with metal atoms can modify their electrical properties, chemical activity and reaction potential, efficiently.^{22–27} In this study, first the structure of BNNC and Ge-BNNC were optimized and their binding distances were reported in figure 1.

In figure 1, the Ge atom was adopted to BNNC and Ge atom was formed three bonds by bordering C atoms. Figure 1 show that, average of calculated bond lengths of Ge atom with three bordering N atoms is ca 1.91 Å. Calculated bond length of each N atom with three bordering B atoms is ca 1.40 Å. These growth in the Ge–N rather than B–N were interpreted by forcing of bordering N atoms via the Ge atom and so the locations of the Ge atom and bordering N atoms were perturbed toward out of the main plane.

Table 1. Obtained parameters for Ge adoption of BNNC and calculated parameters for SO and O₂ adsorption on Ge-BNNC surface.

Nanoparticles	ΔE_{ad} (eV)	ΔH_{ad} (eV)	ΔG_{ad} (eV)	q (e)	E_{HLG} (eV)
Ge-BNNC	-1.22	-1.18	-0.75	0.64	2.35
Ge-BNNC-SO	-0.43	-0.37	0.32	0.11	2.36
Ge -BNNC-O ₂	-1.32	-1.28	-0.64	0.79	2.98

The adoption energy (ΔE_{ad}), enthalpy (ΔH_{ad}), Gibbs free energy (ΔG_{ad}) and energy of HOMO–LUMO gap (E_{HLG}) of Ge-BNNC were calculated. The transferred charge (q) between Ge atom and BNNC surface were calculated and obtained results reported in table 1. Results shown that, the calculated ΔE_{ad} , ΔH_{ad} , ΔG_{ad} , E_{HLG} and q values of Ge-BNNC were -1.22, -1.18, -0.75, 2.35 eV and 0.64 electron, respectively. The large energy and charge transfer values were proved that in Ge-BNNC there are three strong covalent bonds between Ge atom and bordering N atoms.

The study of SO and O₂ adsorption on Ge-BNNC surface has high important in order to investigation of SO oxidation. In this step the adsorption ability of SO and O₂ on Ge-BNNC surface were investigated and the most stable Ge-BNNC-SO and Ge-BNNC-O₂ complexes from the energy viewpoint were shown in figure 1.

Structure of Ge-BNNC-SO complex in figure 1 show that the distance between SO and Ge-BNNC was 3.53 Å. The adsorption parameters in table 1 show that, the calculated ΔE_{ad} , ΔH_{ad} , ΔG_{ad} values of Ge-BNNC-SO were -0.43, -0.37 and 0.32 eV, respectively. The calculated q value for interaction between SO and Ge-BNNC is ca 0.11 electron. Additionally, E_{HLG} parameter in order to determination of changing in electronic properties of Ge-BNNC after SO adsorption was calculated and obtained results reported in table 1.

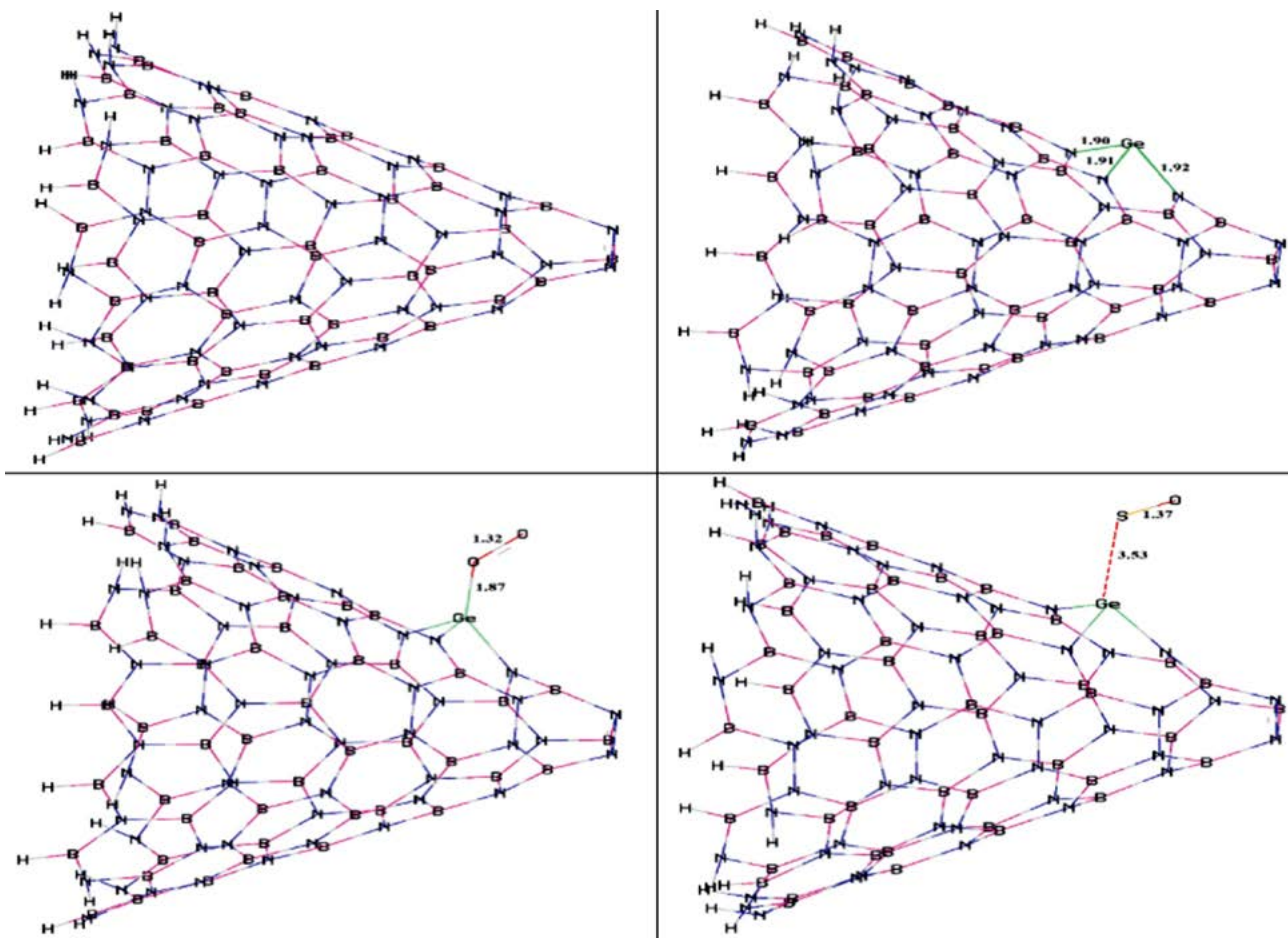


Figure 1. Structures of BNNC, Ge-BNNC, Ge-BNNC-O₂ and Ge-BNNC-SO (bond distances (Å)).

Results indicated that Ge-BNNC and Ge-BNNC-SO have same E_{HLG} values. The low charge transfer from Ge-BNNC to SO show that SO adsorption on Ge-BNNC surface cannot modify the activity of Ge-BNNC, significantly. The low ΔE_{ad} and ΔH_{ad} values and positive ΔG_{ad} values of Ge-BNNC-SO show that interactions SO with Ge-BNNC were weakly and SO adsorption on Ge-BNNC surface was impossible from energy viewpoint.

As seen in figure 1, in Ge-BNNC-O₂ the distance between of O₂ and Ge-BNNC was 1.87 Å. The adsorption parameters in table 1 show that, the calculated ΔE_{ad} , ΔH_{ad} , ΔG_{ad} values of Ge-BNNC-O₂ were -1.32, -1.28 and -0.64 eV, respectively. The large calculated ΔE_{ad} , ΔH_{ad} and ΔG_{ad} values confirm that O₂ and Ge-BNNC have appropriate chemical interactions.

The O₂ bond length in Ge-BNNC-O₂ is 1.32 Å that is longer than bond length in single O₂ ca 0.11 Å. Results show, when Ge-BNNC-O₂ is formed the O₂ bond length is elongated and O₂ on Ge-BNNC surface is activated. The obtained q value of chemical interaction between O₂ and Ge-BNNC is ca 0.79 electron. Calculated E_{HLG} value show that Ge-BNNC-O₂ has higher E_{HLG} values rather than Ge-BNNC ca 0.63 eV. Therefore results show that O₂ adsorption on Ge-BNNC surface can modify the chemical

structure of Ge-BNNC and O₂ adsorption improve the chemical activity of Ge-BNNC, efficiently.

In finally, results in table 1 show that O₂ adsorption on Ge-BNNC surface improve the chemical properties of Ge-BNNC because of large q , ΔE_{ad} and ΔH_{ad} values. Also results confirm that when the equal amount of SO and O₂ molecules were in nearby of Ge-BNNC structure the Ge-BNNC surface covered by adsorbed O₂ molecule exactly. So the Ge-BNNC-O₂ formation can be considered as first step in SO oxidation process.

2. 2. SO Oxidation on Activated Ge-BNNC Surface via ER and LH Mechanisms

As illustrious in introduction the ER and LH were possible mechanisms to SO oxidation on surface of nanostructures. In ER mechanism, SO molecule was neared to surface of activated Ge-BNNC, but in LH mechanism first SO and O₂ groups adsorbed and then oxidation done on Ge-BNNC surface. In previous studies, the ER and LH mechanisms for toxic gas oxidation on metal-adopted nanostructures were investigated and results show that metal-adopted nanostructures were acceptable catalyst to toxic gas oxidation.^{28–36}

In this section the potential of Ge-BNNC surface for SO oxidation were investigated and energy path ways for SO oxidation in both ER and LH mechanisms were examined. The SO oxidation path ways on Ge-BNNC surface in figures 2 and 3 were shown. The calculated activation energies (E_{ac}) and thermodynamic indexes (ΔE_{ad} , ΔH_{ad} and ΔG_{ad}) of studied path ways were reported in table 2.

Results in table 2 show that, energy barrier of SO oxidation on O_2 activated Ge-BNNC surface via LH mechanism was lower than corresponding value of ER mechanism. Therefore, the LH mechanism were considered in two following reactions; first reaction is $Ge-BNNC-O-O^* + SO \rightarrow Ge-BNNC-O-O-SO \rightarrow Ge-BNNC-O^* + SO_2$, and second reaction is $Ge-BNNC-O^* + SO \rightarrow Ge-BNNC + SO_2$. The important structures in path way of two above reactions were geometry optimized and corresponding structures involving the initial state (IS), final state (P) and transition state (TS) structures were shown in figures 2 and 3.

In first reaction ($Ge-BNNC-O-O^* + SO \rightarrow Ge-BNNC-O-O-SO \rightarrow Ge-BNNC-O^* + SO_2$) the $Ge-BNNC-O-O^*-SO$, $Ge-BNNC-O^*$ and $Ge-BNNC-O-O^*$ were TS, P and IS

structures, respectively (structures were shown in figure 2). Calculated results in table 2 show that, E_{ac} , ΔE_{ad} , ΔH_{ad} and ΔG_{ad} values of first reaction were 0.85, -3.43 , -3.37 and -3.28 eV, respectively.

Figure 2 show that in IS structure the SO was neared to $Ge-BNNC-O-O^*$ and the O–O was lengthened from 1.32 to 1.48 Å and in IS structure the distance between SO and O_2 was 2.99 Å. Figure 2 indicated that in TS structure the $Ge-BNNC-O-O^*-SO$ was designed and the O–O^{*} and O^{*}–S were 1.59 and 1.44 Å, respectively. Therefore results in first reaction show that a SO_2 molecule was formed at room temperature because the interaction of $Ge-BNNC-O^*$ with SO_2 was weakly.

In second reaction ($Ge-BNNC-O^* + SO \rightarrow Ge-BNNC + SO_2$) the $Ge-BNNC-O^*-SO$, $Ge-BNNC$ and $Ge-BNNC-O^*$ were TS, P and IS structures, respectively (structures were shown in figure 3). Calculated results in table 2 show that, E_{ac} , ΔE_{ad} , ΔH_{ad} and ΔG_{ad} values of second reaction were 0.18, -2.99 , -2.92 and -2.84 eV, respectively.

Figure 3 show that in IS structure the SO was neared to $Ge-BNNC-O^*$ and the O^{*}–S and $Ge-O^*$ bonds were 2.95 and 1.80 Å, respectively. Figure 3 indicated that in TS structure the $Ge-BNNC-O^*-SO$ was designed and the $Ge-O^*$

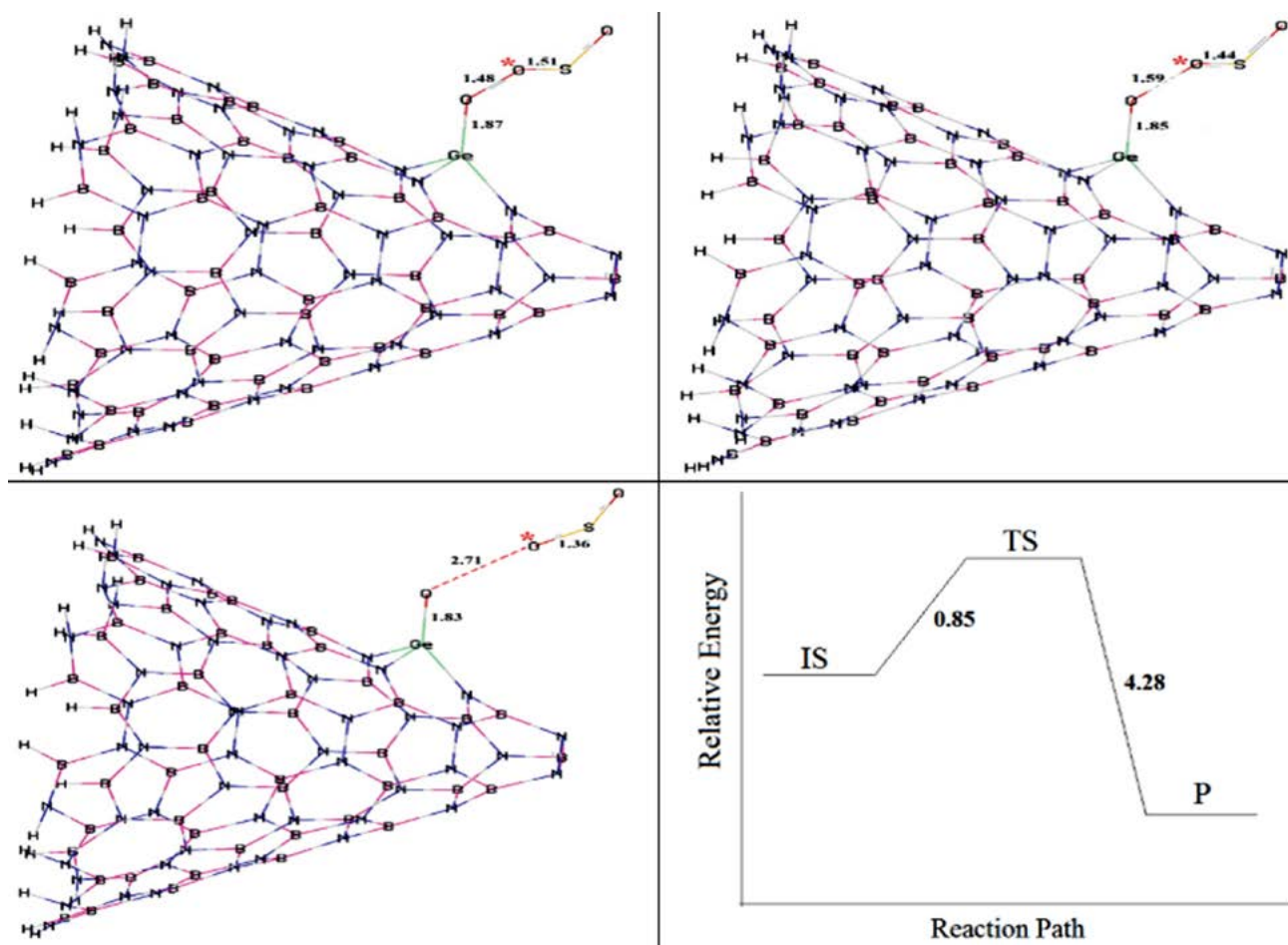


Figure 2. Plan of $Ge-BNNC-O-O^* + SO \rightarrow Ge-BNNC-O + SO_2$ reaction (Bond distances (Å) and relative energies (eV)).

Table 2. Obtained parameters for $\text{Ge-BNNC-O-O}^* + \text{SO} \rightarrow \text{Ge-BNNC-O} + \text{SO}_2$ and $\text{Ge-BNNC-O}^* + \text{SO} \rightarrow \text{Ge-BNNC} + \text{SO}_2$ reactions.

Reactions	E_{ac} (eV)	ΔE_{ad} (eV)	ΔH_{ad} (eV)	ΔG_{ad} (eV)
$\text{Ge-BNNC-O-O}^* + \text{SO} \rightarrow \text{Ge-BNNC-O} + \text{SO}_2$	0.85	-3.43	-3.37	-3.28
$\text{Ge-BNNC-O}^* + \text{SO} \rightarrow \text{Ge-BNNC} + \text{SO}_2$	0.18	-2.99	-2.92	-2.84

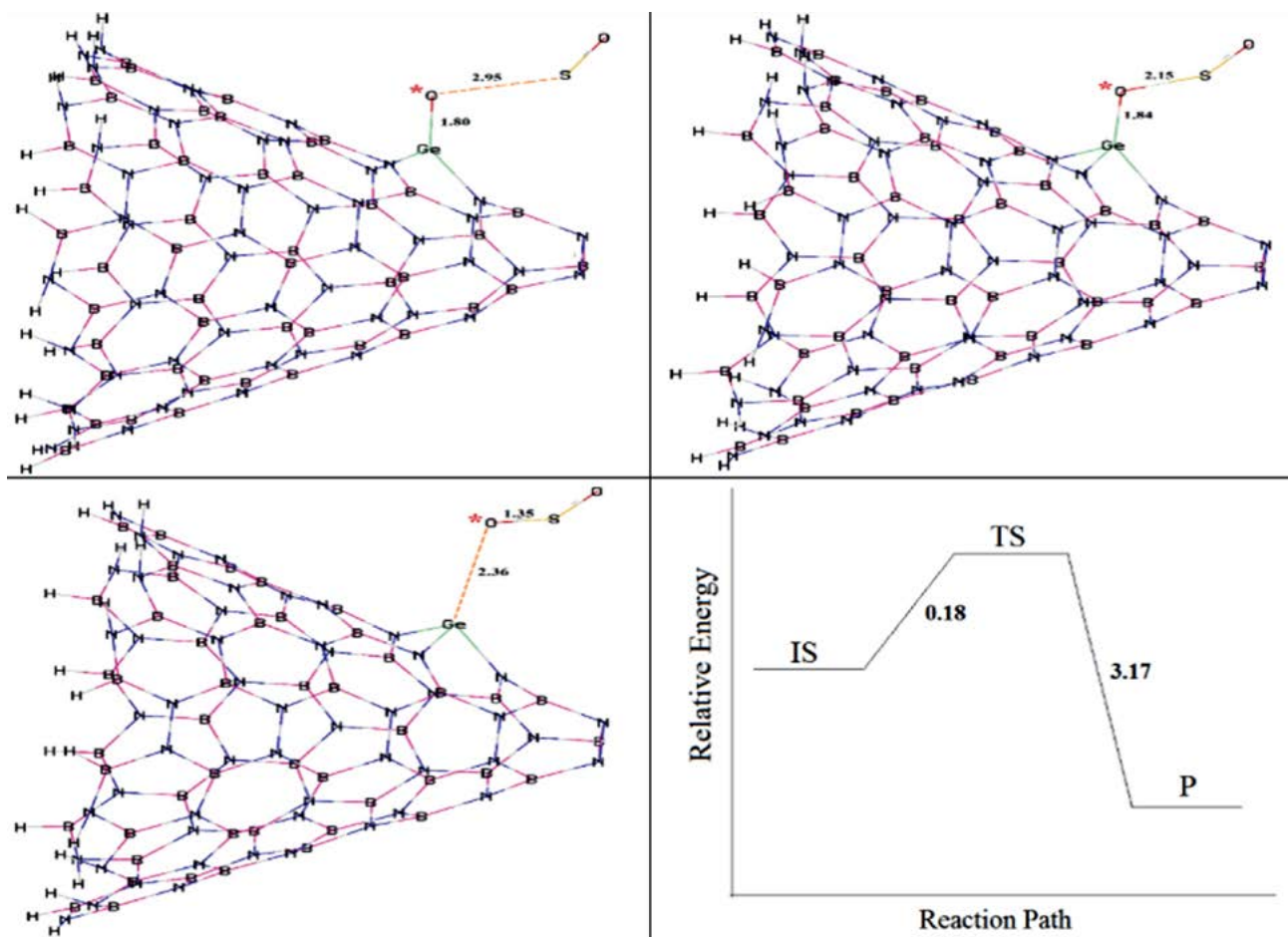


Figure 3. Plan of $\text{Ge-BNNC-O}^* + \text{SO} \rightarrow \text{Ge-BNNC} + \text{SO}_2$ reaction (Bond distances (Å) and relative energies (eV)).

and O^*-S were 1.84 and 2.15 Å, respectively. Therefore results show that in second reaction a SO_2 molecule was formed at room temperature because the interaction of Ge-BNNC with SO_2 was weakly.

That is remarkable that two investigated reactions ($\text{Ge-BNNC-O-O}^* + \text{SO} \rightarrow \text{Ge-BNNC-O-O-SO} \rightarrow \text{Ge-BNNC-O}^* + \text{SO}_2$ and $\text{Ge-BNNC-O}^* + \text{SO} \rightarrow \text{Ge-BNNC} + \text{SO}_2$) in figures 2 and 3 were exothermic. The calculated ΔG_{ad} in table 2 propose that the two studied reactions were negative in normal temperature and so the SO oxidation via Ge-BNNC- O^* and Ge-BNNC-O- O^* was favorable from thermodynamic view point. Finally results show that, Ge-BNNC can be remarkable catalyst for SO oxidation via LH mechanism with high efficiency due to low barrier energy in normal temperature.

3. Conclusion

The DFT method used to SO oxidation on activated Ge-BNNC surface via LH and ER mechanisms. Results indicated that Ge-BNNC can be an efficient catalyst to SO oxidation with low cost in normal temperature. Results show that O_2 adsorption on Ge-BNNC surface cause greater effects on properties of Ge-BNNC. Results show that ΔE_{ad} and q values of Ge-BNNC- O_2 were higher than Ge-BNNC-SO. Results show when the SO and O_2 reached to Ge-BNNC the Ge-BNNC surface surround with O_2 , concurrently. Results show that SO oxidation on Ge-BNNC surface via the LH mechanism has lower energy barrier than ER mechanism. Finally, results propose that O_2 activated Ge-BNNC can be a novel catalyst

to SO oxidation with high efficient and low price in normal temperature.

4. Acknowledgment

The authors would like to thank all chemistry teachers for scientific supports.

5. References

1. A. Kiani, P. Haratipour, M. Ahmadi, R. Zare-Dorabei, A. Mahmoodi, *J. Water Supply. Res.* **2017**, *66*, 239–248.
2. Z. Parsaee, P. Haratipour, M. Janghorban Lariche, A. Vojood, *Ultrason. Sonochem.* **2018**, *41*, 337–349. DOI:10.1016/j.ultsonch.2017.09.054
3. P. Haratipour, A. Baghban, A. H. Mohammadi, S. H. Hosseini Nazhad, A. Bahadori, *J. Mol. Liq.* **2017**, *242*, 146–159. DOI:10.1016/j.molliq.2017.06.123
4. M. H. Doranehgard, H. Samadyar, M. Mesbah, P. Haratipour, S Samiezade, *Fuel*, **2017**, *202*, 29–35. DOI:10.1016/j.fuel.2017.04.014
5. A. Baghban, J. Sasanipour, P. Haratipour, M. Alizad, M. Vafae Ayouri, *Chem. Eng. Res. Des.* **2017**, *126*, 67–75. DOI:10.1016/j.cherd.2017.08.007
6. W. Gao, P. Haratipour, M. R. R. Kahkha, A. Tahvili, *Ultrason. Sonochem.* **2018**, *44*, 152–161. DOI:10.1016/j.ultsonch.2018.02.020
7. H. J. Freund, G. Meijer, M. Scheffler, *Angew. Chem.* **2011**, *50*, 10064–10094. DOI:10.1002/anie.201101378
8. R. S. Johnson, A. DeLaRiva, V. Ashbacher, *Phys. Chem. Chem. Phys.* **2013**, *15*, 7768–7776. DOI:10.1039/c3cp00126a
9. H. Y. Su, M. M. Yang, X. H. Bao, W. X. Li, *J. Phys. Chem. C* **2008**, *112*, 17303–17310. DOI:10.1021/jp803400p
10. M. S. Chen, Y. Cai, Z. Yan, *Surf. Sci.* **2007**, *601*, 5326–5331. DOI:10.1016/j.susc.2007.08.019
11. S. Piccinin, M. Stamatakis, *ACS Catal.* **2014**, *4*, 2143–2152. DOI:10.1021/cs500377j
12. W. Liu, Y. Zhu, J. Lian, Q. Jiang, *J. Phys. Chem. C* **2007**, *111*, 1005–1009. DOI:10.1021/jp0661488
13. D. J. Liu, *J. Phys. Chem. C* **2007**, *111*, 14698–14706. DOI:10.1021/jp071944e
14. W. T. Wallace, R. L. Whetten, *J. Am. Chem. Soc.* **2002**, *124*, 7499–7505. DOI:10.1021/ja0175439
15. C. Chang, C. Cheng, C. Wei, *J. Chem. Phys.* **2008**, *128*, 124710–124710. DOI:10.1063/1.2841364
16. J. Du, G. Wu, J. Wang, *J. Phys. Chem. A* **2010**, *114*, 10508–10514. DOI:10.1021/jp106321s
17. Sharifian S, Harasek M, Haddadi B, *Chem. Prod. Process Mod.* **2016**, *11*, 67–72.
18. Sharifian S, Miltner M, Harasek M, *Chem. Eng. Trans.* **2016**, *52*, 565–570.
19. Sharifian S, Harasek M, *Chem. Eng. Trans.* **2015**, *45*, 409–414.
20. Sharifian S, Harasek M, *Chem. Eng. Trans.* **2015**, *45*, 1003–1008.
21. L. Ci, Z. Xu, L. Wang, W. Gao, F. Ding, *Nano Res.* **2008**, *1*, 116–122. DOI:10.1007/s12274-008-8020-9
22. C. Lee, X. Wei, J. W. Kysar, J. Hone, *Science* **2008**, *321*, 385–388. DOI:10.1126/science.1157996
23. K. S. Novoselov, A. K. Geim, S. Morozov, *Science* **2004**, *306*, 666–669. DOI:10.1126/science.1102896
24. A. K. Geim, K. S. Novoselov, *Nat. Mater.* **2007**, *6*, 183–191. DOI:10.1038/nmat1849
25. S. Morozov, K. Novoselov, M. KatGeelson, *Phys. Rev. Lett.* **2008**, *100*, 016602. DOI:10.1103/PhysRevLett.100.016602
26. A. K. Geim, *Science* **2009**, *324*, 1530–1534. DOI:10.1126/science.1158877
27. K. R. Ratinaç, W. Yang, S. P. Ringer, F. Braet, *Environ. Sci. Technol.* **2010**, *44*, 1167–1176. DOI:10.1021/es902659d
28. A. Hornes, A. B. Hungria, *J. Am. Chem. Soc.* **2010**, *132*, 34–37. DOI:10.1021/ja9089846
29. X. Hu, Y. Wu, Z. Zhang, *J. Mater. Chem.* **2012**, *22*, 15198–15205. DOI:10.1039/c2jm33490a
30. Y. Tang, X. Dai, Z. Yang, Z. Liu, L. Pan, D. Ma, Z. Lu, *Carbon* **2014**, *71*, 139–143. DOI:10.1016/j.carbon.2014.01.022
31. Y. Li, Z. Zhou, G. Yu, W. Chen, Z. Chen, *J. Phys. Chem. C* **2010**, *114*, 6250–6255. DOI:10.1021/jp911535v
32. E. H. Song, Z. Wen, Q. Jiang, *J. Phys. Chem. C* **2011**, *115*, 3678–3683. DOI:10.1021/jp108978c
33. Y. Tang, Z. Yang, X. Dai, *Phys. Chem. Chem. Phys.* **2012**, *14*, 16566–16569. DOI:10.1039/c2cp41441d
34. Y. Tang, Z. Liu, X. Dai, Z. Yang, W. Chen, Z. Lu, *Appl. Surf. Sci.* **2014**, *308*, 402–407. DOI:10.1016/j.apsusc.2014.04.189
35. S. Lin, X. Ye, J. Huang, *Phys. Chem. Chem. Phys.* **2015**, *17*, 888–893. DOI:10.1039/C4CP05007J
36. S. A. Tawfik, X.Y. Cui, D.J. Carter, C. Stampfl, *Phys. Chem. Chem. Phys.* **2015**, *17*, 62–69.
37. A. G. Davies, *Organotin Chemistry*, 2nd edition, Wiley-VCH, Weinheim, **2004**. DOI:10.1002/3527601899
38. H. Song, L. Zhang, C. He, Y. Qu, Y. Tian, Y. Lv, *J. Mater. Chem.* **2011**, *21*, 5972–5975. DOI:10.1039/c0jm04331a
39. Q. Zhou, C. Wang, Z. Fu, Y. Tang, H. Zhang, *Comput. Mater. Sci.* **2014**, *83*, 398–402. DOI:10.1016/j.commatsci.2013.11.036
40. A.V. Krashennnikov, P.O. Lehtinen, A.S. Foster, *Phys. Rev. Lett.* **2009**, *102*, 400–430. DOI:10.1103/PhysRevLett.102.126807
41. F. Li, J. Zhao, Z. Chen, *J. Phys. Chem. C* **2012**, *116*, 2507–2514. DOI:10.1021/jp209572d
42. X. Wang, X. Li, L. Zhang, Y. Yoon, P.K. Weber, *Science* **2009**, *324*, 768–771. DOI:10.1126/science.1170335
43. A. L. M. Reddy, A. Srivastava, S.R. Gowda, H. Gullapalli, *ACS Nano* **2010**, *4*, 6337–6342. DOI:10.1021/nn101926g
44. Y. Zhao, D.G. Truhlar, *Theor. Chem. Acc.* **2008**, *120*, 215–241. DOI:10.1007/s00214-007-0310-x
45. J. Andzelm, C. Kolmel, *J. Chem. Phys.* **1995**, *103*, 9312–9320. DOI:10.1063/1.469990
46. L. H. Gan, J. Q. Zhao, *Physica E* **2009**, *41*, 1249–1252. DOI:10.1016/j.physe.2009.02.014
47. S. F. Boys, F. Bernardi, *Mol. Phys.* **1970**, *19*, 553–566. DOI:10.1080/00268977000101561

48. L. Ma, J. M. Zhang, K. W. Xu, V. Ji, *Appl. Surf. Sci.* **2015**, *343*, 121–127. DOI:10.1016/j.apsusc.2015.03.068
49. T. Zhang, Q. Xue, M. Shan, Z. Jiao, *J. Phys. Chem. C* **2012**, *116*, 19918–19924. DOI:10.1021/jp3073359
50. M. Wu, C. Cao, J. Jiang, *J. Phys.* **2010**, *12*, 063020–063024.
51. W. Gao, M. R. Farahani, *J. Nanotechnol.* **2016**, *2016*, 1–6.
52. W. Gao, S. M. Abrishamifar, G. E. Rajaei, R. Razavi, M. Najafi, *Chem. Phys. Lett.* **2018**, *695*, 44–50. DOI:10.1016/j.cplett.2018.01.056
53. W. Gao, W. F. Wang, *J. Differ. Equations Appl.* **2017**, *23*, 100–109. DOI:10.1080/10236198.2016.1197214

Povzetek

V zadnjih letih se industrija veliko ukvarja z razvojem učinkovitih in poceni katalizatorjev za oksidacijo žvepovega monoksida (SO) pri normalni temperaturi. S tem namenom smo preučevali nanostožec borovega nitrda (BNNC) dopiranega z Ge, čigar površino smo aktivirali z molekulo O₂. Nato smo z uporabo Langmuir Hinshelwood (LH) in Eley Rideal (ER) mehanizmov raziskali oksidacijo SO na aktivirani površini Ge-BNNC. Rezultati kažejo, da tako aktivirana površina Ge-BNNC oksidira molekulo SO ter da ta proces lahko opišemo z zaporedjem reakcij Ge-BNNC-OO* + SO → Ge-BNNC-OO* -SO → Ge-BNNC-O* + SO₂ in Ge-BNNC-O* + SO → Ge-BNNC + SO₂. Izkazalo se je, da oksidacija SO na aktivirani površini Ge-BNNC pri uporabi LH mehanizma poteka pri nižji energetski barieri kot pri ER mehanizmu. Izračunani parametri kažejo, da je aktiviran Ge-BNNC sprejemljiv katalizator z nizko ceno in visoko zmogljivostjo za oksidacijo SO pri normalni temperaturi.

Scientific paper

Possibility of C_{38} and $Si_{19}Ge_{19}$ Nanocages in Anode of Metal Ion Batteries: Computational Examination

Rong-Jun Bie,¹ Muhammad Kamran Siddiqui,² Razieh Razavi,^{3,*}
Milad Taherkhani⁴ and Meysam Najafi^{5,*}

¹ School of Mathematics and Physics, Anhui Jianzhu University, Hefei 230601, China

² Department of Mathematics, Comsats Institute of Information Technology Sahiwal, Pakistan

³ Department of Chemistry, Faculty of Science, University of Jiroft, Jiroft, Iran

⁴ Department of Chemical Engineering, Amirkabir University of Technology (Tehran Polytechnic), Tehran, Iran

⁵ Medical Biology Research Center, Kermanshah University of Medical Sciences, Kermanshah 67149-67346, Iran

* Corresponding author: E-mail: R.Razavi@ujiroft.ac.ir and meysamnajafi2016@gmail.com
Phone: +98-8337243181 Fax: +98-8337243181

Received: 18-10-2017

Abstract

In this study, the potential of C_{38} and $Si_{19}Ge_{19}$ as anode electrodes of Li-ion, Na-ion and K-ion batteries via density functional theory was investigated. Obtained results showed that $Si_{19}Ge_{19}$ as anode electrode in metal-ion batteries has higher potential than C_{38} ca 0.18 V. Calculated results illustrated that K-ion battery has higher cell voltage and higher performance than Li-ion and Na-ion batteries ca 0.15 and 0.31 V, respectively. Results showed that halogen adoption increased the cell voltage of studied metal-ion batteries ca 1.5–2.2 V. Results show that, V_{cell} values of studied metal-ion batteries in water are higher than gas phase ca 0.46 V. Finally it can be concluded that F-doped $Si_{18}Ge_{19}$ as anode electrode in K-ion battery has the highest performance and it can be proposed as novel metal-ion batteries with high performance.

Keywords: Battery; nanocage; adoption; voltage; anode and halogen

1. Introduction

A rechargeable battery is a kind of electronic battery that has many electro-chemical various cells and it can be recharged several times. The cost of buying the rechargeable cells are higher than disposable cells, though rechargeable cells have lower destructive effects on environment. The rechargeable batteries have been used in starter of car, consumer devices and battery reservoir center.^{1–6}

In lithium-ion battery (LIB) there are two processes; in charging process the lithium ions transferred from the positive to negative electrode and in discharge process the motion of lithium ions is the reverse of charge process. LIBs have high energy compression, high storage capacity, small memory effect and small self-evacuation.^{7–12} The LIBs are expensive at actual, and a leakage of Lithium employed in LIBs can convert to an important issue in future.^{13–18} The novel metal-ion batteries as the electrical

storage batteries must have high capacity, high performance and high rate in charge and discharge processes.^{18–23} The graphite due to low cost, cyclic durability, high energy stability has been used for anode electrode. In previous works, potential of some compounds such as germanium, transition metals and silicon for anode electrode have been examined.^{24–33} In previous works the potential and capacities of nanoelectrodes have been investigated and obtained results shown that nanotubes and nanocages have higher valences and energy capacitor than the graphite.^{34–44} In previous studies, results confirmed that hydrogenation, adoption and functionalization of nanostructures improved their performances as anode materials in metal-ion batteries.^{45–52} Due to positive effects of hydrogenation, adoption and functionalization of nanostructures on potentials of metal-ion batteries, many works have been done on usage of nanostructures as anode electrodes in metal-ion batteries.^{52–55}

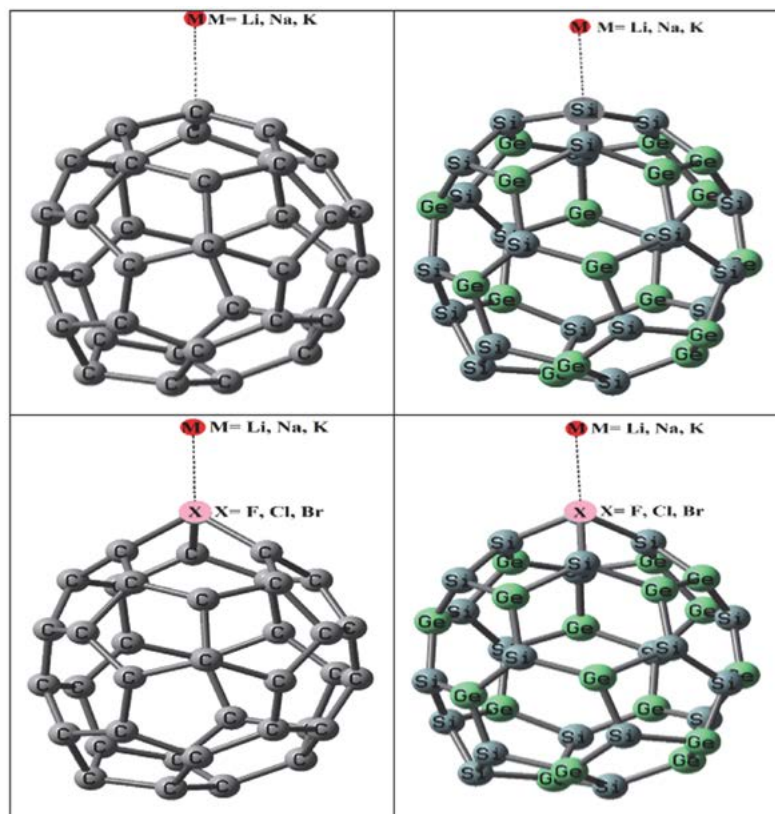


Figure 1. Structures of studied complexes.

In this study, in first step; the potential of C_{38} and $Si_{19}Ge_{19}$ nanocages as anode electrode in Li-ion battery via density functional theory was investigated. In second step; the C_{38} and $Si_{19}Ge_{19}$ nanocages doped with halogen atoms and effects of these adoptions on ability of Li-ion battery were examined. In third step; the potential of sodium-ion battery (NIB) and potassium-ion battery (KIB) were compared with Li-ion battery. In fourth step; the effects of halogen adoption on potential of studied NIBs and KIBs were investigated. In fifth step; novel metal-ion battery with high performance to use in industry will be proposed.

The main questions have been answered in this work are: (1) How much dose cell voltages of LIBs C_{38} and $Si_{19}Ge_{19}$ as anode electrodes? (2) Can NIBs and KIBs be suitable batteries with high performance? (3) Can halogen adoption increase the cell voltage of LIBs? (4) Which metal-ion batteries have high performance?

2. Computational Details

In this study, the geometries of C_{38} and $Si_{19}Ge_{19}$ were optimized via GAMESS software via DFT/ M06-2X theory and 6-311+G (2d, 2p) basis set. The adsorption of C_{38} and $Si_{19}Ge_{19}$ with halogen atoms ($X = F, Cl, Br$) were investigated and geometries of $X-C_{38}$ and $X-Si_{19}Ge_{19}$ complexes were optimized at mentioned level of computational.

In this study the vibrational frequency calculations of all studied via DFT/M06-2X theory and 6-311+G (2d, 2p) basis set were done in order to evidence that all of the optimized geometries are factual local minima and also thermodynamic parameters of studied reactions were calculated by using of vibrational frequency analysis.^{56–58}

The Gibbs free energy of process of adsorption of halogen atom ($X = F, Cl, Br$) on studied nanostructures were calculated via: $G_{ad} = G(X\text{-nanostructure}) - G(\text{nanostructure}) - 0.5 G(X_2)$, where $X\text{-nanostructure}$ corresponds to the Gibbs free energy of complexes of nanostructure with halogen atom, $G(X_2)$ is the Gibbs free energy of the halogen molecule and $G(\text{nanostructure})$ is the Gibbs free energy of the nanostructure.^{59–61}

The Gibbs free energy of adsorption of metal on nanostructure surfaces were calculated via: $G_{ad} = G(M\text{-nanostructure}) - G(\text{nanostructure}) - G(M)$; where $G(M\text{-nanostructure})$ corresponds to the Gibbs free energy of complexes of nanostructure with metal and $G(M)$ is the Gibbs free energy of the metal and $G(\text{nanostructure})$ is Gibbs free energy of the nanostructure.^{62–64}

In this study, the energies of the basis set superposition error (E_{BSSE}) for studied interactions between nanostructures and metals were calculated by using of counterpoise correction method and obtained results showed that E_{BSSE} values are ca 0.05 Kcal/mol.

The energy difference between the highest occupied molecular orbital (HOMO) and the lowest unoccupied molecular orbital (LUMO) of studied nanostructures defined as HOMO–LUMO Gap (E_{HLG}) and it calculated via ($E_{\text{HLG}} = E_{\text{LUMO}} - E_{\text{HOMO}}$); where E_{LUMO} and E_{HOMO} are energies of LUMO and HOMO of studied nanostructures.^{65–67}

In the cathode and anode of LIBs, NIBs and KIBs with hypothetical nanostructure anode it can be expressed the anode reaction is ($M/\text{nanostructure} \leftrightarrow M^+ + e^-$) and cathode reaction is ($M^+ + e^- \leftrightarrow M$). The complete reaction for the LIBs, NIBs and KIBs can be defined via ($M^+ + M/\text{nanostructure} \leftrightarrow M^+/\text{nanostructure} + M + \Delta G_{\text{cell}}$). Finally, in order to calculate the cell voltage (V_{cell}) the Nernst equation are $V_{\text{cell}} = -\Delta G_{\text{cell}} / zF$; where F is the Faraday constant (96,500 C/mol) and z is the charge of M^+ .^{68–70}

3. Results and Discussion

3.1. C_{38} and $Si_{19}Ge_{19}$ as Anode in Metal-ion Batteries

Peyghan et al.⁷¹ investigated the viability of using a BN nanotube for detection of para-chloroaniline molecule by means of density functional theory calculations. Their results showed that the molecule prefers to be adsorbed on the intrinsic BN nanotube from its N atom, releasing energy of 0.65 eV without significant effect on the electrical conductivity of the tube. Their results showed that Si-doped tube detected its presence because of the drastic increase of the electrical conductivity of the tube. Peyghan et al.⁷² investigated the adsorption of two anions (F and Cl) and two cations (Li and Na) on the surface of aluminum nitride nanotubes (AlNNTs) by density functional theory. Their results showed that adsorption of anions may facilitate the electron emission from the AlNNT surface by reducing the work function due to the charge transfer occurs from the anions to the tube.

Hosseini et al.⁷³ investigated the performance of $B_{12}N_{12}$, and its structurally manipulated forms as anode materials for Li-ion batteries (LIBs) by means of density functional theory calculations. Their results shown that encapsulating a fluoride inside the $B_{12}N_{12}$ significantly increased the electrochemical cell voltage (V_{cell}) of $B_{12}N_{12}$.

Najafi et al.⁷⁴ examined the applications of $B_{30}N_{30}$, $B_{36}N_{36}$, BNNT (8, 0) and BNNT (10, 0) as anode materials for lithium-ion batteries by density functional theory. Their results shown that V_{cell} of BNNT (8, 0) and BNNT (10, 0) were higher than $B_{30}N_{30}$ and $B_{36}N_{36}$. Their results shown that F functionalization of studied BN-nanostructures improved the potential of anode materials of lithium-ion batteries.

Nejati et al.⁷⁵ investigated the potential of $B_{12}N_{12}$ nanocages as anode in Na-ion batteries by density func-

tional theory. Their results shown that encapsulation of different halides ($X = F^-, Cl^-, Br^-$) into BN nanocage increased the cell voltage.

Hosseini et al.⁷⁶ investigated the potential of BN nanosheets in anode of Na-ion batteries by means of density functional theory. Their results shown that replacing three N atoms of the hexagonal ring with larger P atoms increased the performance of the BN nanosheet as an anode of a Na-ion battery but the replacement of B by Al decreased its performance.

Ruiz et al.⁷⁷ proven that DFT/M06-2X method can describe the structure and energetics of hybrid inorganic-organic systems with high accuracy. Their results showed that calculated energy error bar values for hybrid inorganic-organic systems correspond to typical experimental error estimates. Their results showed that DFT/M06-2X method has the most accurate results for the binding distance and adsorption energy.

Zhao et al.⁷⁸ compared the accuracy and energy error bar of M06-2X functional with 12 other functionals and Hartree Fock theory for 403 energetic data in 29 diverse databases. They recommend M06-2X functional for calculate the thermochemistry, noncovalent interactions and electronic excitation energies to valence and Rydberg states. They suggested the M06-2X functional with high accurate for application in organometallic and inorganometallic chemistry and for noncovalent interactions.

Mahmood et al.⁷⁹ examined the performance of 26 combinations of DFT functionals and basis sets were evaluated for the calculation of the activation energy of methylation reactions of nitronates. Their results showed that DFT method and M06-2X functional provided the most accurate results.

Wheeler et al.⁸⁰ calculated the enthalpies for bond-forming reactions by using of six DFT functionals and reaction enthalpies were decomposed into contributions from changes in bonding and other intramolecular effects via the hierarchy of homodesmotic reactions. Their results showed that M06-2X has most accurate performance for studied reactions and M06-2X is one of the more accurate functionals for the underlying bond transformations.

Hohenstein et al.⁸¹ showed that M06-2X provide significant improvements over traditional density functionals for the noncovalent interactions. Their results showed that M06-2X correction greatly increases the accuracy of calculations without increasing the computational cost in any significant way. Therefore in previous studies, it can be concluded that DFT/M06-2X method was used for calculation of interactions and energies of various organic and inorganic systems and results showed that DFT/M06-2X has high accuracy.^{77–81}

In this section the potential of C_{38} and $Si_{19}Ge_{19}$ as anodes in LIB, NIB and KIB via DFT method was investigated and novel metal-ion batteries with higher performance were identified. The structures of complexes of C_{38}

Table 1. Calculated G_{ad} (kcal/mol) and bond length (Å) values of studied complexes.

Complex	G_{ad}	Complex	G_{ad}	Complex	G_{ad}
F-C ₃₇	-39.99	Cl-C ₃₇	-37.84	Br-C ₃₇	-35.70
F-Si ₁₈ Ge ₁₉	-45.98	Cl-Si ₁₈ Ge ₁₉	-43.52	Br-Si ₁₈ Ge ₁₉	-41.06
Complex	Bond	Length	Complex	Bond	Length
Li-C ₃₈	Li-----C	2.33	Li-Si ₁₉ Ge ₁₉	Li-----Si	2.73
Na-C ₃₈	Na-----C	2.47	Na-Si ₁₉ Ge ₁₉	Na-----Si	2.86
K-C ₃₈	K-----C	3.15	K-Si ₁₉ Ge ₁₉	K-----Si	3.55
Li-F-C ₃₇	Li-----F	2.13	Li-F-Si ₁₈ Ge ₁₉	Li-----F	2.16
Na-F-C ₃₇	Na-----F	2.25	Na-F-Si ₁₈ Ge ₁₉	Na-----F	2.29
K-F-C ₃₇	K-----F	2.43	K-F-Si ₁₈ Ge ₁₉	K-----F	2.43
Li-F-C ₃₇	F-----C	1.37	Li-F-Si ₁₈ Ge ₁₉	F-----Ge	1.78
Na-F-C ₃₇	F-----C	1.34	Na-F-Si ₁₈ Ge ₁₉	F-----Ge	1.76
K-F-C ₃₇	F-----C	1.36	K-F-Si ₁₈ Ge ₁₉	F-----Ge	1.77
Li-Cl-C ₃₇	Li-----Cl	2.51	Li-Cl-Si ₁₈ Ge ₁₉	Li-----Cl	2.54
Na-Cl-C ₃₇	Na-----Cl	2.65	Na-Cl-Si ₁₈ Ge ₁₉	Na-----Cl	2.65
K-Cl-C ₃₇	K-----Cl	3.36	K-Cl-Si ₁₈ Ge ₁₉	K-----Cl	3.34
Li-Cl-C ₃₇	Cl-----C	1.73	Li-Cl-Si ₁₈ Ge ₁₉	Cl-----Ge	2.18
Na-Cl-C ₃₇	Cl-----C	1.77	Na-Cl-Si ₁₈ Ge ₁₉	Cl-----Ge	2.17
K-Cl-C ₃₇	Cl-----C	1.75	K-Cl-Si ₁₈ Ge ₁₉	Cl-----Ge	2.16
Li-Br-C ₃₇	Li-----Br	2.66	Li-Br-Si ₁₈ Ge ₁₉	Li-----Br	2.67
Na-Br-C ₃₇	Na-----Br	2.87	Na-Br-Si ₁₈ Ge ₁₉	Na-----Br	2.86
K-Br-C ₃₇	K-----Br	3.47	K-Br-Si ₁₈ Ge ₁₉	K-----Br	3.89
Li-Br-C ₃₇	Br-----C	1.93	Li-Br-Si ₁₈ Ge ₁₉	Br-----Ge	2.34
Na-Br-C ₃₇	Br-----C	1.92	Na-Br-Si ₁₈ Ge ₁₉	Br-----Ge	2.32
K-Br-C ₃₇	Br-----C	1.91	K-Br-Si ₁₈ Ge ₁₉	Br-----Ge	2.34

and Si₁₉Ge₁₉ with Li, Na and K were presented in figure 1. The bond lengths in Å of Li, Na and K with C₃₈ and Si₁₉Ge₁₉ were reported in table 1.

The calculated values of the Gibbs free energy (G_{ad}) in kcal/mol of adsorbed metals and metal ions on surfaces of C₃₈ and Si₁₉Ge₁₉ were presented in table 2. Results show that, all calculated G_{ad} values were negatives and so the studied adsorption were possible from thermodynamic view point. Results show that G_{ad} value of K-C₃₈ is higher than G_{ad} values of Li-C₃₈ and Na-C₃₈. Also G_{ad} value of K-Si₁₉Ge₁₉ is higher than G_{ad} values of Na-Si₁₉Ge₁₉ and Li-Si₁₉Ge₁₉. Results show that G_{ad} values of Li, Na and K on Si₁₉Ge₁₉ are higher than G_{ad} values on C₃₈.

Results show that, G_{ad} values of metal ions on C₃₈ and Si₁₉Ge₁₉ are higher than G_{ad} values of metal on C₃₈ and Si₁₉Ge₁₉ and the G_{ad} values for studied metal and metal ions have same trends. The G_{ad} values of metal-nanostructure complexes were decreased as following: Li-C₃₈ < Na-C₃₈ < Li-Si₁₉Ge₁₉ < K-C₃₈ < Na-Si₁₉Ge₁₉ < K-Si₁₉Ge₁₉ and for metal ion-nanostructure complexes were decreased as following: Li⁺-C₃₈ < Na⁺-C₃₈ < Li⁺-Si₁₉Ge₁₉ < K⁺-C₃₈ < Na⁺-Si₁₉Ge₁₉ < K⁺-Si₁₉Ge₁₉. So it can be concluded that K or K⁺-Si₁₉Ge₁₉ and Li or Li⁺-C₃₈ have the highest and the lowest G_{ad} absolute values, respectively.

The calculated E_{HOMO} , E_{LUMO} and E_{HLG} values in eV of complexes of Li, Na and K with C₃₈ and Si₁₉Ge₁₉ were reported in table 3. Results show that, E_{HOMO} value of

K-C₃₈ is lower than E_{HOMO} values of Li-C₃₈ and Na-C₃₈. Also E_{HOMO} value of K-Si₁₉Ge₁₉ is lower than E_{HOMO} values of Li-Si₁₉Ge₁₉ and Na-Si₁₉Ge₁₉. Results display that E_{HOMO} values of Li, Na and K on Si₁₉Ge₁₉ are lower than E_{HOMO} values on C₃₈.

Results in table 3 show that, E_{HLG} value of K-C₃₈ is lower than E_{HLG} values of Li-C₃₈ and Na-C₃₈. Also E_{HLG} value of K-Si₁₉Ge₁₉ is lower than E_{HLG} values of Li-Si₁₉Ge₁₉ and Na-Si₁₉Ge₁₉. Results show that, the E_{HLG} values of studied metal-nanostructures were decreased as following: Li-C₃₈ > Na-C₃₈ > K-C₃₈ > Li-Si₁₉Ge₁₉ > Na-Si₁₉Ge₁₉ > K-Si₁₉Ge₁₉. So it can be concluded that K-Si₁₉Ge₁₉ and Li-C₃₈ have the lowest and the highest E_{HLG} values, respectively.

Hosseini et al.⁷³ investigated the E_{HLG} values of B₁₂N₁₂ and H₁₂B₁₂N₁₂ via B3LYP functional and 6-31G (d) basis set and their results shown that E_{HLG} values of B₁₂N₁₂ and H₁₂B₁₂N₁₂ were 6.84 and 2.51 eV, respectively. Also they calculated the E_{HLG} values of complexes of B₁₂N₁₂ and H₁₂B₁₂N₁₂ with Li atom and their results shown that the E_{HLG} values of Li-B₁₂N₁₂ and Li-H₁₂B₁₂N₁₂ were 6.10 and 2.38 eV, respectively.

Nejati et al.⁷⁵ calculated the E_{HLG} value of B₁₂N₁₂ cage via B3LYP functional and 6-31G (d) basis set in GAMESS software and their results shown that E_{HLG} values of B₁₂N₁₂ and Na-B₁₂N₁₂ were 6.84 and 1.59 eV, respectively. The E_{HLG} values of complexes of F-B₁₂N₁₂, Cl-

$B_{12}N_{12}$ and $Br-B_{12}N_{12}$ with Na atom and their results shown that the E_{HLG} values of $Na-F-B_{12}N_{12}$, $Na-Cl-B_{12}N_{12}$ and $Na-Br-B_{12}N_{12}$ were 1.67, 1.65 and 2.01 eV, respectively.

Hosseinian et al.⁷⁶ calculated the E_{HLG} values of BN-nanosheets via B3LYP functional and 6-31G (d) basis set and their results shown that E_{HLG} values of BN-nanosheet, Al-BN-nanosheet and P-BN-nanosheet were 5.88, 4.98 and 5.38 eV, respectively. Also they calculated the E_{HLG} values of complexes of nanosheets with Na atom and their results shown that the E_{HLG} values of Na-BN-nanosheet, Na-Al-BN-nanosheet and Na-P-BN-nanosheet were 1.64, 2.09 and 1.17 eV, respectively.

The calculated V_{cell} in V of complexes of Li, Na and K with C_{38} and $Si_{19}Ge_{19}$ were reported in table 2. Results show that, V_{cell} value of $K-C_{38}$ is higher than V_{cell} values of $Li-C_{38}$ and $Na-C_{38}$. Also V_{cell} value of $K-Si_{19}Ge_{19}$ is higher than V_{cell} values of $Li-Si_{19}Ge_{19}$ and $Na-Si_{19}Ge_{19}$. Results display that V_{cell} values of Li, Na and K on $Si_{19}Ge_{19}$ are higher than V_{cell} values on C_{38} . Results show that, the V_{cell} values of studied complexes were decreased as following: $Li-C_{38} < Na-C_{38} < K-C_{38} < Li-Si_{19}Ge_{19} < Na-Si_{19}Ge_{19} < K-Si_{19}Ge_{19}$. So it can be concluded that $K-Si_{19}Ge_{19}$ and $Li-C_{38}$ have the highest and the lowest V_{cell} values, respectively.

Finally, it can be concluded: (1) the $Si_{19}Ge_{19}$ as anode in metal-ion batteries has higher potential than C_{38} ca 0.18 V (2) the KIB has higher V_{cell} and higher performance than NIB and KIB ca 0.15 and 0.31 V, respectively.

3. 2. Halogen Adoption of C_{38} and $Si_{19}Ge_{19}$

Hosseini et al.⁷³ calculated the G_{cell} and V_{cell} values of $B_{12}N_{12}$ and $F-B_{12}N_{12}$ as anode electrodes of Li-ion battery. Their results shown that encapsulating a fluoride inside the BN nanocage can be considered as suitable strategy to improvement the performance of BN nanocage as anode electrode of Li-ion batteries.

Nejati et al.⁷⁵ calculated the G_{cell} and V_{cell} values of $B_{12}N_{12}$ as anode electrode of Na-ion battery. Their results shown that the G_{cell} values of $F-B_{12}N_{12}$, $Cl-B_{12}N_{12}$ and $Br-B_{12}N_{12}$ were -85.3 , -87.9 and -90.5 kcal/mol, respectively.

In this section the effects of F, Cl and Br adoption on performance of C_{38} and $Si_{19}Ge_{19}$ as anodes of metal-ion batteries via DFT method were investigated. The calculated G_{ad} values of F-, Cl- and Br-doped C_{38} and $Si_{19}Ge_{19}$ were presented in table 1. Results show that, all calculated G_{ad} values were negatives and so the adoption of C_{38} and $Si_{19}Ge_{19}$ with F, Cl and Br were possible from thermodynamic view point.

Results show that G_{ad} value of $F-C_{37}$ is higher than G_{ad} values of $Cl-C_{37}$ and $Br-C_{37}$. Also G_{ad} value of $F-Si_{19}Ge_{19}$ is higher than G_{ad} values of $Cl-Si_{18}Ge_{19}$ and $Br-Si_{18}Ge_{19}$. Results show that, adoption of C_{38} and $Si_{19}Ge_{19}$ with F atom are possible processes from thermodynamic view point and $F-C_{37}$ and $F-Si_{18}Ge_{19}$ can be suitable candidates as anodes of metal-ion batteries.

In this section the potential of F-, Cl- and Br-doped C_{37} and $Si_{18}Ge_{19}$ as anodes in LIB, NIB and KIB via DFT

Table 2. Calculated G_{ad} (kcal/mol) and V_{cell} (V) values of studied complexes.

Complex	G_{ad}	V_{cell}	Complex	G_{ad}	V_{cell}
K- C_{38}	-7.96	1.44	K- $Si_{19}Ge_{19}$	-9.16	1.66
Na- C_{38}	-7.11	1.29	Na- $Si_{19}Ge_{19}$	-8.18	1.48
Li- C_{38}	-6.35	1.15	Li- $Si_{19}Ge_{19}$	-7.30	1.32
K-F- C_{37}	-17.84	3.23	K-F- $Si_{18}Ge_{19}$	-20.51	3.71
Na-F- C_{37}	-15.93	2.88	Na-F- $Si_{18}Ge_{19}$	-18.31	3.31
Li-F- C_{37}	-14.22	2.57	Li-F- $Si_{18}Ge_{19}$	-16.35	2.96
K-Cl- C_{37}	-16.88	3.05	K-Cl- $Si_{18}Ge_{19}$	-19.41	3.51
Na-Cl- C_{37}	-15.07	2.73	Na-Cl- $Si_{18}Ge_{19}$	-17.33	3.14
Li-Cl- C_{37}	-13.46	2.43	Li-Cl- $Si_{18}Ge_{19}$	-15.48	2.80
K-Br- C_{37}	-15.93	2.88	K-Br- $Si_{18}Ge_{19}$	-18.31	3.31
Na-Br- C_{37}	-14.22	2.57	Na-Br- $Si_{18}Ge_{19}$	-16.35	2.96
Li-Br- C_{37}	-12.70	2.30	Li-Br- $Si_{18}Ge_{19}$	-14.60	2.64
K ⁺ - C_{38}	-41.14		K ⁺ - $Si_{19}Ge_{19}$	-47.32	
Na ⁺ - C_{38}	-36.73		Na ⁺ - $Si_{19}Ge_{19}$	-42.25	
Li ⁺ - C_{38}	-32.80		Li ⁺ - $Si_{19}Ge_{19}$	-37.72	
K ⁺ -F- C_{37}	-92.16		K ⁺ -F- $Si_{18}Ge_{19}$	-105.98	
Na ⁺ -F- C_{37}	-82.29		Na ⁺ -F- $Si_{18}Ge_{19}$	-94.62	
Li ⁺ -F- C_{37}	-73.47		Li ⁺ -F- $Si_{18}Ge_{19}$	-84.49	
K ⁺ -Cl- C_{37}	-87.22		K ⁺ -Cl- $Si_{18}Ge_{19}$	-100.30	
Na ⁺ -Cl- C_{37}	-77.87		Na ⁺ -Cl- $Si_{18}Ge_{19}$	-89.55	
Li ⁺ -Cl- C_{37}	-69.53		Li ⁺ -Cl- $Si_{18}Ge_{19}$	-79.97	
K ⁺ -Br- C_{37}	-82.29		K ⁺ -Br- $Si_{18}Ge_{19}$	-94.62	
Na ⁺ -Br- C_{37}	-73.47		Na ⁺ -Br- $Si_{18}Ge_{19}$	-84.49	
Li ⁺ -Br- C_{37}	-65.60		Li ⁺ -Br- $Si_{18}Ge_{19}$	-75.44	

method was investigated. The structures of complexes of halogen- C_{37} and halogen- $Si_{18}Ge_{19}$ with Li, Na and K were presented in figure 1. The bond lengths of Li, Na and K with halogen- C_{37} and halogen- $Si_{18}Ge_{19}$ and also bond lengths of halogen atoms with bordering C or Ge atoms were reported in table 1.

The calculated G_{ad} values of complexes of metals with halogen- C_{37} and halogen- $Si_{18}Ge_{19}$ were presented in table 2. Results show that, all calculated G_{ad} values were negatives and so the studied adsorption were possible from thermodynamic view point. Results show that G_{ad} value of K-halogen- C_{37} are higher than G_{ad} values of Li-halogen- C_{37} and Na-halogen- C_{37} . Also G_{ad} value of K-halogen- $Si_{18}Ge_{19}$ are higher than G_{ad} values of Na-halogen- $Si_{18}Ge_{19}$ and K-halogen- $Si_{18}Ge_{19}$. Results display that G_{ad} values of Li, Na and K on halogen- $Si_{18}Ge_{19}$ are higher than G_{ad} values on halogen- C_{37} .

Results show that G_{ad} values of F- $Si_{18}Ge_{19}$ and F- C_{37} are higher than G_{ad} values of Cl or Br- $Si_{18}Ge_{19}$ and Cl or Br- C_{37} . The G_{ad} values of complexes of metals with halogen- C_{37} and halogen- $Si_{18}Ge_{19}$ were decreased as following: M-Br- C_{37} < M-Cl- C_{37} < M-F- C_{37} < M-Br- $Si_{18}Ge_{19}$ < M-Cl- $Si_{18}Ge_{19}$ < M-F- $Si_{18}Ge_{19}$. So it can be concluded that K-F- $Si_{18}Ge_{19}$ and Li-Br- C_{38} have the highest and the lowest G_{ad} absolute values, respectively.

The calculated E_{HOMO} , E_{LUMO} and E_{HLG} values in eV of complexes of Li, Na and K with halogen- C_{37} and halogen- $Si_{18}Ge_{19}$ were reported in table 3. Results show that, E_{HOMO} value of K-halogen- C_{37} are lower than E_{HOMO} values of Li-halogen- C_{37} and Na-halogen- C_{37} . Also E_{HOMO} value of K-halogen- $Si_{18}Ge_{19}$ are lower than E_{HOMO} values of Li-halogen- $Si_{18}Ge_{19}$ and Na-halogen- $Si_{18}Ge_{19}$. Results display that E_{HOMO} values of Li, Na and K on halogen- $Si_{18}Ge_{19}$ are lower than E_{HOMO} values of halogen- C_{37} .

Results show that, E_{HLG} value of K-halogen- C_{37} are lower than E_{HLG} values of Li-halogen- C_{37} and Na-halogen- C_{37} . Also E_{HLG} value of K-halogen- $Si_{18}Ge_{19}$ are lower than E_{HLG} values of Li-halogen- $Si_{18}Ge_{19}$ and Na-halogen- $Si_{18}Ge_{19}$. Results show that, the E_{HLG} values of studied complexes were decreased as following: Li-halogen- C_{37} <

Na-halogen- C_{37} < K-halogen- C_{37} < Li-halogen- $Si_{18}Ge_{19}$ < Na-halogen- $Si_{18}Ge_{19}$ < K-halogen- $Si_{18}Ge_{19}$. So it can be concluded that K-F- $Si_{18}Ge_{19}$ and Li-Br- C_{37} have the lowest and the highest E_{HLG} values, respectively.

The calculated V_{cell} of complexes of Li, Na and K with halogen- C_{37} and halogen- $Si_{18}Ge_{19}$ were reported in table 2. Results show that, V_{cell} value of K-halogen- C_{37} are higher than V_{cell} values of Li-halogen- C_{37} and Na-halogen- C_{37} . Also V_{cell} value of K-halogen- $Si_{18}Ge_{19}$ are higher than V_{cell} values of Li-halogen- $Si_{18}Ge_{19}$ and Na-halogen- $Si_{18}Ge_{19}$. Results display that V_{cell} values of Li, Na and K on halogen- $Si_{18}Ge_{19}$ are higher than V_{cell} values on halogen- C_{37} . Results show that, the V_{cell} values of studied structures were decreased as following: Li-halogen- C_{37} < Na-halogen- C_{37} < K-halogen- C_{37} < Li-halogen- $Si_{18}Ge_{19}$ < Na-halogen- $Si_{18}Ge_{19}$ < K-halogen- $Si_{18}Ge_{19}$. So it can be concluded that K-F- $Si_{18}Ge_{19}$ and Li-Br- C_{37} have the highest and the lowest V_{cell} values, respectively.

Table 3. Calculated V_{cell} (V) values of studied complexes in water.

Complex	V_{cell}	Complex	V_{cell}
K- C_{38}	1.71	K- $Si_{19}Ge_{19}$	1.97
Na- C_{38}	1.53	Na- $Si_{19}Ge_{19}$	1.75
Li- C_{38}	1.36	Li- $Si_{19}Ge_{19}$	1.56
K-F- C_{37}	3.83	K-F- $Si_{18}Ge_{19}$	4.39
Na-F- C_{37}	3.41	Na-F- $Si_{18}Ge_{19}$	3.92
Li-F- C_{37}	3.04	Li-F- $Si_{18}Ge_{19}$	3.51
K-Cl- C_{37}	3.61	K-Cl- $Si_{18}Ge_{19}$	4.16
Na-Cl- C_{37}	3.24	Na-Cl- $Si_{18}Ge_{19}$	3.72
Li-Cl- C_{37}	2.87	Li-Cl- $Si_{18}Ge_{19}$	3.33
K-Br- C_{37}	3.41	K-Br- $Si_{18}Ge_{19}$	3.92
Na-Br- C_{37}	3.04	Na-Br- $Si_{18}Ge_{19}$	3.51
Li-Br- C_{37}	2.73	Li-Br- $Si_{18}Ge_{19}$	3.13

Finally, it can be concluded: (1) the halogen adoption of nanostructures increased the V_{cell} of studied metal-ion batteries ca 1.5-2.2 V; (2) the F-doped metal-ion batteries have higher V_{cell} than Cl- and Br-doped metal-ion batteries 0.3 and 0.6 V, respectively; (3) K-F- $Si_{18}Ge_{19}$ can

Table 3. Calculated E_{HOMO} , E_{LUMO} and E_{HLG} (eV) values of studied complexes.

Complex	E_{HOMO}	E_{LUMO}	E_{HLG}	Complex	E_{HOMO}	E_{LUMO}	E_{HLG}
K- C_{38}	-4.09	-1.15	2.94	K- $Si_{19}Ge_{19}$	-3.78	-1.31	2.48
Na- C_{38}	-4.20	-1.03	3.16	Na- $Si_{19}Ge_{19}$	-3.88	-1.17	2.72
Li- C_{38}	-4.30	-0.92	3.38	Li- $Si_{19}Ge_{19}$	-3.98	-1.04	2.94
K-F- C_{37}	-3.55	-2.58	0.96	K-F- $Si_{18}Ge_{19}$	-3.39	-2.78	0.62
Na-F- C_{37}	-3.79	-2.31	1.48	Na-F- $Si_{18}Ge_{19}$	-3.50	-2.65	0.85
Li-F- C_{37}	-4.02	-2.05	1.97	Li-F- $Si_{18}Ge_{19}$	-3.69	-2.35	1.34
K-Cl- C_{37}	-3.67	-2.44	1.23	K-Cl- $Si_{18}Ge_{19}$	-3.47	-2.65	0.82
Na-Cl- C_{37}	-3.90	-2.18	1.72	Na-Cl- $Si_{18}Ge_{19}$	-3.59	-2.50	1.09
Li-Cl- C_{37}	-4.11	-1.95	2.17	Li-Cl- $Si_{18}Ge_{19}$	-3.78	-2.23	1.54
K-Br- C_{37}	-3.79	-2.31	1.48	K-Br- $Si_{18}Ge_{19}$	-3.55	-2.54	1.01
Na-Br- C_{37}	-4.02	-2.05	1.97	Na-Br- $Si_{18}Ge_{19}$	-3.69	-2.35	1.34
Li-Br- C_{37}	-4.22	-1.83	2.38	Li-Br- $Si_{18}Ge_{19}$	-3.87	-2.10	1.77

be proposed as novel metal-ion batteries with highest performance.

3.3. Solvent Effects on Potential of Studied Metal-ion Batteries

In this section the effects of water as polar solvent on performance of C_{38} , $Si_{19}Ge_{19}$, and their halogen-doped nanostructures as anode electrodes of metal-ion batteries via DFT/ M06-2X theory, 6-311+G(2d, 2p) basis set and polarized continuum model (PCM) as solvent model were investigated.^{56–61} The calculated V_{cell} values of metal-ion batteries with C_{38} , $Si_{19}Ge_{19}$, and their halogen-doped nanostructures as anode electrodes were presented in table 3.

Results show that, V_{cell} value of K- C_{38} is higher than V_{cell} values of Li- C_{38} and Na- C_{38} in water. Results display that V_{cell} values of Li, Na and K on $Si_{19}Ge_{19}$ are higher than V_{cell} values on C_{38} in water. Results show that in water, V_{cell} value of K-halogen- C_{37} are higher than V_{cell} values of Li-halogen- C_{37} and Na-halogen- C_{37} . Also V_{cell} value of K-halogen- $Si_{18}Ge_{19}$ are higher than V_{cell} values of Li-halogen- $Si_{18}Ge_{19}$ and Na-halogen- $Si_{18}Ge_{19}$ in water. Results display that V_{cell} values of Li, Na and K on halogen- $Si_{18}Ge_{19}$ are higher than V_{cell} values on halogen- C_{37} in water. Results show that, V_{cell} values of studied metal-ion batteries in water are higher than gas phase ca 0.46 V.

4. Conclusion

In this study, the potential of C_{38} and $Si_{19}Ge_{19}$ as anode electrode of Li-ion, Na-ion and K-ion batteries via density functional theory was investigated. Also the effects of halogen adoption of C_{38} and $Si_{19}Ge_{19}$ on ability of metal-ion battery were examined. Obtained results in preset paper are: (1) the $Si_{19}Ge_{19}$ as anode in metal-ion batteries has higher potential than C_{38} ca 0.18 V; (2) the KIB has higher V_{cell} and higher performance than NIB and KIB ca 0.15 and 0.31 V, respectively; (3) the halogen adoption increased the V_{cell} of studied metal-ion batteries ca 1.5–2.2 V; (4) the F-doped metal-ion batteries have higher V_{cell} and higher performance than Cl- and Br-doped metal-ion batteries; (5) K-F- $Si_{18}Ge_{19}$ can be proposed as novel metal-ion batteries with high performance; (6) Results show that, V_{cell} values of studied metal-ion batteries in water are higher than gas phase ca 0.46 V.

5. Acknowledgment

Thanks for all teachers.

6. References

- M. D. Slater, D. Kim, E. Lee, C. S. Johnson, *Adv. Funct. Mater.* **2013**, *23*, 947–958. DOI:10.1002/adfm.201200691
- Z. Parsaee, P. Haratipour, M. Janghorban Lariche, A. Vojood, *Ultrason. Sonochem.* **2018**, *41*, 337–349. DOI:10.1016/j.ultsonch.2017.09.054
- J. Barker, M. Y. Saidi, J. L. Swoyer, *Electrochem. Solid-State Lett.* **2003**, *6*, 1–4. DOI:10.1149/1.1523691
- D. Er, J. Li, M. Naguib, *ACS Appl. Mater. Interfaces* **2014**, *6*, 11173–11179. DOI:10.1021/am501144q
- Z. Parsaee, P. Haratipour, M. J. Lariche, A. Vojood, *Ultrason. Sonochem.* **2018**, *41*, 337–349. DOI:10.1016/j.ultsonch.2017.09.054
- W. Gao, P. Haratipour, M. R. R. Kahkha, A. Tahvili, *Ultrason. Sonochem.* **2018**, *44*, 152–161. DOI:10.1016/j.ultsonch.2018.02.020
- V. Palomares, P. Serras, I. Villaluenga, *Energy Environ. Sci.* **2012**, *5*, 5884–5901. DOI:10.1039/c2ee02781j
- B. J. Landi, M. J. Ganter, C. D. Cress, *Energy Environ. Sci.* **2009**, *2*, 638–643. DOI:10.1039/b904116h
- A. A. Peyghan, *Struct. Chem.* **2012**, *23*, 1567–1572. DOI:10.1007/s11224-012-9970-9
- A. Rahimi, M. Sepehr, M. J. Lariche, M. Mesbah, A. Kasaiepoor, E. H. Malekshah, *Physica E: Low Dimens. Syst. Nanostruct.* **2018**, *97*, 347–362. DOI:10.1016/j.physe.2017.12.003
- O. Baris, Malcioglu, S. Erkoç, *J. Mol. Graphics Modell.* **2005**, *23*, 367–371. DOI:10.1016/j.jmkgm.2004.11.002
- Z. Bagheri, A. A. Peyghan, *Comp. Theor. Chem.* **2013**, *1008*, 20–26. DOI:10.1016/j.comptc.2012.12.011
- N. L. Hadipour, A. Ahmadi Peyghan, *J. Phys. Chem. C* **2015**, *119*, 6398–6404. DOI:10.1021/jp513019z
- A. Khataee, G. Bayat, J. Azamat, *J. Mol. Graphics Modell.* **2017**, *71*, 176–183. DOI:10.1016/j.jmkgm.2016.11.017
- A. Afshar, M. Salami Hosseini, E. Behzadfar, *Sci. Iran. Trans. C* **2014**, *21*, 2107–2115.
- W. An, X. Wu, X. C. Zeng, *J. Phys. Chem. C* **2008**, *112*, 5747–5755. DOI:10.1021/jp711105d
- Z. Mahdavi, *J. Mol. Graphics Modell.* **2014**, *54*, 32–45. DOI:10.1016/j.jmkgm.2014.08.006
- J. Beheshtian, A. Ahmadi Peyghan, *Physica E* **2012**, *44*, 1963–1968. DOI:10.1016/j.physe.2012.06.003
- X. Wu, W. An, X. C. Zeng, *J. Am. Chem. Soc.* **2006**, *128*, 12001–12006 DOI:10.1021/ja063653+
- J. Beheshtian, *Monatshfte für Chemie/Chemical Monthly* **2012**, *143*, 1623–1626.
- H. Guo, N. Lu, J. Dai, X. Wu, X. C. Zeng, *J. Phys. Chem. C* **2014**, *118*, 14051–14059 DOI:10.1021/jp505257g
- J. Beheshtian, H. Soleymanabadi, *Appl. Surf. Sci.* **2012**, *268*, 436–441. DOI:10.1016/j.apsusc.2012.12.119
- P. Lu, X. Wu, W. Guo, X. C. Zeng, *Phys. Chem. Chem. Phys.* **2012**, *14*, 13035–13040. DOI:10.1039/c2cp42181j
- E. Vessally, S. Soleimani-Amiri, *Appl. Surf. Sci.* **2017**, *396*, 740–745. DOI:10.1016/j.apsusc.2016.11.019
- J. Beheshtian, A. A. Peyghan, Z. Bagheri, *Appl. Surf. Sci.* **2012**, *258*, 8980–8984. DOI:10.1016/j.apsusc.2012.05.134
- Y. Gao, N. Shao, Y. Pei, Z. Chen, X. C. Zeng, *ACS nano* **2011**, *5*, 7818–7829. DOI:10.1021/nn201817b
- A. A. Peyghan, M. Noei, M. B. Tabar, *J. Mol. Model.* **2013**, *19*, 3007–3014. DOI:10.1007/s00894-013-1832-x

28. W. Zhou, J. Zhou, J. Shen, C. Ouyang, *J. Phys. Chem. Solids* **2012**, *73*, 245–251. DOI:10.1016/j.jpms.2011.10.035
29. M. Jeong, T. Ahn, H. Nara, T. Momma, *Nano Energy* **2016**, *28*, 51–62. DOI:10.1016/j.nanoen.2016.08.022
30. Q. Jiang, Z. Zhang, S. Yin, Z. Guo, *Appl. Surf. Sci.* **2016**, *379*, 73–82. DOI:10.1016/j.apsusc.2016.03.204
31. D. Shao, D. Tang, J. Yang, Y. Li, *J. Power Sources* **2015**, *297*, 344–350. DOI:10.1016/j.jpowsour.2015.08.037
32. P. Subalakshmi, A. Sivashanmugam, *J. Alloys Compd.* **2017**, *690*, 523–531. DOI:10.1016/j.jallcom.2016.08.157
33. B. Chen, S. Chu, R. Cai, S. Wei, R. Hu, *Comput. Mater. Sci* **2016**, *123*, 44–51. DOI:10.1016/j.commatsci.2016.06.007
34. A. A. Peyghan, M. Noei, *J. Mex. Chem. Soc.* **2014**, *58*, 46–51.
35. A. Gurung, R. Naderi, *Electrochim. Acta* **2016**, *211*, 720–725. DOI:10.1016/j.electacta.2016.06.065
36. S. W. Lee, N. Yabuuchi, *Nat. Nanotechnol.* **2010**, *5*, 531–537. DOI:10.1038/nnano.2010.116
37. M. Li, Y.-J. Liu, J.-x. Zhao, *Appl. Surf. Sci.* **2015**, *345*, 337–343. DOI:10.1016/j.apsusc.2015.03.144
38. L. Qie, W. M. Chen, Z. H. Wang, *Adv. Mater.* **2012**, *24*, 2047–2050. DOI:10.1002/adma.201104634
39. Z.-S. Wu, W. Ren, L. Xu, F. Li, *ACS Nano* **2011**, *5*, 5463–5471. DOI:10.1021/nn2006249
40. Y. Liu, V. I. Artyukhov, M. Liu, *J. Phys. Chem. Lett.* **2013**, *4*, 1737–1742. DOI:10.1021/jz400491b
41. R. P. Hardikar, D. Das, S. S. Han, *Phys. Chem. Chem. Phys.* **2014**, *16*, 16502–16508. DOI:10.1039/C4CP01412J
42. A. A. Peyghan, M. Noei, S. Yourdkhani, *Superlattices Microstruct.* **2013**, *59*, 115–122. DOI:10.1016/j.spmi.2013.04.005
43. X. Ouyang, M. Lei, S. Shi, C. Luo, D. Liu, *J. Alloys Compd.* **2009**, *476*, 462–465. DOI:10.1016/j.jallcom.2008.09.028
44. A. A. Peyghan, Z. Bagheri, *Struct. Chem.* **2013**, *24*, 1565–1570. DOI:10.1007/s11224-012-0189-6
45. S. Shi, P. Lu, Z. Liu, Y. Qi, L. G. Hector, *J. Am. Chem. Soc.* **2012**, *134*, 15476–15487. DOI:10.1021/ja305366r
46. A. A. Peyghan, A. Soltani, A. A. Pahlevani, *Appl. Surf. Sci.* **2013**, *270*, 25–32. DOI:10.1016/j.apsusc.2012.12.008
47. S. Shi, C. Ouyang, M. Lei, W. Tang, *J. Power Sources* **2007**, *171*, 908–912. DOI:10.1016/j.jpowsour.2007.07.005
48. A. Ahmadi, J. Beheshtian, M. Kamfiroozi, *J. Mol. Model.* **2012**, *18*, 1729–1734. DOI:10.1007/s00894-011-1202-5
49. S. Shi, J. Gao, Y. Liu, Y. Zhao, Q. Wu, W. Ju, *Chin. Phys. B* **2015**, *25*, 018212. DOI:10.1088/1674-1056/25/1/018212
50. A. Soltani, A. Ahmadi Peyghan, Z. Bagheri, *Physica E* **2013**, *48*, 176–180. DOI:10.1016/j.physe.2013.01.007
51. L. Safari, E. Vessally, A. Bekhradnia, L. Edjlali, *Thin Solid Films* **2017**, *623*, 157–163. DOI:10.1016/j.tsf.2017.01.006
52. A. A. Peyghan, M. T. Baei, M. Moghimi, *Comp. Theor. Chem.* **2012**, *997*, 63–69. DOI:10.1016/j.comptc.2012.07.037
53. D. Golberg, Y. Bando, Y. Huang, *ACS Nano* **2010**, *4*, 2979–2993. DOI:10.1021/nn1006495
54. X. Chen, P. Wu, M. Rousseas, D. Okawa, *J. Am. Chem. Soc.* **2009**, *131*, 890–891. DOI:10.1021/ja807334b
55. M. Kamfiroozi, Z. Bagheri, *Chin. J. Chem. Phys.* **2012**, *25*, 60–64. DOI:10.1088/1674-0068/25/01/60-64
56. Y. Zhao, D. G. Truhlar, *Theor. Chem. Acc.* **2008**, *120*, 215–241. DOI:10.1007/s00214-007-0310-x
57. J. Andzelm, C. Kolmel, *J. Chem. Phys.* **1995**, *103*, 9312–9320. DOI:10.1063/1.469990
58. L. H. Gan, J. Q. Zhao, *Physica E* **2009**, *41*, 1249–1252. DOI:10.1016/j.physe.2009.02.014
59. S. F. Boys, F. Bernardi, *Mol. Phys.* **1970**, *19*, 553–566. DOI:10.1080/00268977000101561
60. L. Ma, J. M. Zhang, K. W. Xu, V. Ji, *Appl. Surf. Sci.* **2015**, *343*, 121–127. DOI:10.1016/j.apsusc.2015.03.068
61. J. Beheshtian, H. Soleymanabadi, *J. Mol. Model.* **2012**, *18*, 2343–2348. DOI:10.1007/s00894-011-1256-4
62. Z. Bagheri, M. Kamfiroozi, *Struct. Chem.* **2012**, *23*, 653–657. DOI:10.1007/s11224-011-9911-z
63. A. A. Peyghan, Z. Bagheri, *Comput. Mater. Sci.* **2012**, *62*, 71–74. DOI:10.1016/j.commatsci.2012.05.041
64. R. R. Q. Freitas, G. K. Gueorguiev, *Chem. Phys. Lett.* **2013**, *583*, 119–124. DOI:10.1016/j.cplett.2013.07.077
65. M. T. Baei, A. A. Peyghan, Z. Bagheri, *Chin. Chem. Lett.* **2012**, *23*, 965–968. DOI:10.1016/j.ccl.2012.06.027
66. M. Baei, H. Mohammadian, *Bulg. Chem. Commun* **2014**, *46*, 735–742.
67. J. Beheshtian, Z. Bagheri, M. Kamfiroozi, *J. Mol. Model.* **2011**, *42*, 1400–1403.
68. J. Beheshtian, Z. Bagheri, M. Kamfiroozi, *J. Mol. Model.* **2012**, *18*, 2653–2658. DOI:10.1007/s00894-011-1286-y
69. J. Hosseini, A. Rastgou, R. Moradi, *J. Mol. Liq.* **2017**, *225*, 913–918. DOI:10.1016/j.molliq.2016.11.025
70. L. Saw, Y. Ye, A. Tay, *Appl. Therm. Eng.* **2014**, *73*, 154–161. DOI:10.1016/j.applthermaleng.2014.06.061
71. M. Eslami, V. Vahabi, A. A. Peyghan, *Physica E*, **2016**, *76*, 6–11. DOI:10.1016/j.physe.2015.09.043
72. M. Samadzadeh, S. F. Rastegar, A. A. Peyghan, *Physica E*, **2015**, *69*, 75–80. DOI:10.1016/j.physe.2015.01.021
73. J. Hosseini, A. Rastgou, R. Moradi, *J. Mol. Liq.* **2017**, *225*, 913–918. DOI:10.1016/j.molliq.2016.11.025
74. M. Najafi M, *Can. J. Chem.* **2017**, *95*, 687–690. DOI:10.1139/cjc-2017-0070
75. K. Nejati, A. Hosseinian, A. Bekhradnia, E. Vessally, *J. Mol. Graph. Mod.* **2017**, *74*, 1–7. DOI:10.1016/j.jm.2017.03.001
76. A. Hosseinian, S. Soleimani, S. Arshadi, E. Vessally, *Phys. Lett. A* **2017**, *381*, 2010–2015. DOI:10.1016/j.physleta.2017.04.022
77. T. H. Dunning, *J. Phys. Chem. A* **2000**, *104*, 9062–9065. DOI:10.1021/jp001507z
78. V. G. Ruiz, W. Liu, E. Zojer, A. Tkatchenko, *Phys. Rev. Lett.* **2012**, *108*, 146103–146107. DOI:10.1103/PhysRevLett.108.146103
79. Y. Zhao, D. G. Truhlar, *Theor. Chem. Account* **2008**, *120*, 215–218. DOI:10.1007/s00214-007-0310-x
80. A. Mahmood, R. L. Longo, *Phys. Chem. Chem. Phys.* **2014**, *87*, 1–7.
81. S. E. Wheeler, A. Moran, S. Pieniazek, K. Houk, *J. Phys. Chem. A* **2009**, *113*, 10376–10381. DOI:10.1021/jp9058565
82. E. G. Hohenstein, S. T. Chill, C. D. Sherrill, *J. Chem. Theory Comput.* **2008**, *4*, 1996–22001. DOI:10.1021/ct800308k

Povzetek

S teoretičnimi raziskavami na podlagi teorije gostotnega potenciala (DFT) smo preučevali C_{38} in $Si_{19}Ge_{19}$ kot materiala, ki bi lahko bila primerena za anode v litij-ionskih, natrij-ionskih in kalij-ionskih baterijah. Dobljeni rezultati so pokazali, da ima $Si_{19}Ge_{19}$ kot anoda v baterijah za približno 0,18 V višji potencial kot C_{38} . Rezultati kalkulacij tudi kažejo, da ima kalij-ionska baterija višjo napetost celice kot litij-ionska baterija (približno 0,15 V) in kaliji-ionska baterija (približno 0,31 V). Dodatek halogena naj bi povečal napetost celice v primerih preučevanih baterij za 1,5 do 2,2 V. Izračunana napetost celice v preučevanih sistemih je za približno 0,46 V višja v vodnem mediju kot v plinski fazi. Glede na rezultate kalkulacij v tem sistemu lahko zaključimo, da dodatek fluora v nanokletke $Si_{18}Ge_{19}$ v kalij-ionskih baterijah najbolj izboljša lastnosti baterije in bi ga lahko predlagali kot nov material na tem področju.

Scientific paper

Effect of Copper Alloying on Electro-Catalytic Activity of Nickel for Ethanol Oxidation in Alkaline Media

Niloufar Bahrami Panah,^{1,*} Iman Danaee,² Mahmood Payehghadr¹
and Afrooz Madahi¹

¹Department of Chemistry, Payame Noor University, P.O.BOX 19395-3697, Tehran, Iran

²Abadan Faculty of Petroleum Engineering, Petroleum University of Technology, Abadan, Iran

* Corresponding author: E-mail: bahramipanah@pnu.ac.ir

Tel.: +982634209515 Fax: +982634209525

Received: 03-11-2017

Abstract

In this research, the electro-catalytic activity of nickel-copper (Ni-Cu) alloy towards oxidation of ethanol and its possible redox process were investigated in alkaline solution. For this purpose, cyclic voltammetry, chronoamperometry and electrochemical impedance spectroscopy techniques were employed. According to the cyclic voltammetry studies, Ni-Cu alloy compared to pure nickel can demonstrate a significantly higher response for ethanol oxidation. So, the enhancement of the anodic peak current corresponding to the oxidation of nickel hydroxide was accompanied with attenuated cathodic current in the presence of ethanol. The anodic peak currents have a linearly dependence on the square root of scan rate which is the characteristic of diffusion-controlled processes. Based on the chronoamperometry measurements, the reaction exhibited a Cottrellian behavior and the diffusion coefficient of ethanol was found to be $1.26 \times 10^{-5} \text{ cm}^2 \text{ s}^{-1}$. The impedance spectroscopy declared electro-catalytic behavior of Ni-Cu electrode for oxidation of ethanol and showed that the charge transfer resistance decreases by increasing the ethanol concentration.

Keywords: Electro-catalytic activity; nickel-copper alloy; ethanol; impedance

1. Introduction

Recently, direct ethanol fuel cells (DEFCs) have attracted much interest for different applications.^{1,2} The reason is that they can provide convenient operation, storage and distribution. However, DEFCs require further development compared to hydrogen based fuel cells.³ One of the unresolved problems of DEFCs is slow anodic rate of ethanol oxidation.⁴ In this respect, considerable researches have been devoted to study ethanol electro-oxidation at high pH values. Utilizing alkaline solution has many advantages in fuel cells. For example, it can enhance fuel cell efficiency, reduce corrosion, enable the application of many electrode materials, promote efficiency of the processes occurred at both anode and cathode, eliminate sensitivity to the surface structure and decrease poisoning effects.^{5–8}

In electrochemical oxidation of ethanol, selection of an appropriate material for the anode is very crucial for obtaining an electro-catalyst of high efficiency. Some studies have reported a significant increase in fuel utilization

and power density through optimizing different factors related to fuel cells.^{9,10} For the electrode, different materials have been employed to catalyze the electrochemical oxidation of ethanol.^{11,12} One of the well-established electrode materials is nickel which poses proper surface oxidation properties. Nickel and its complexes have been commonly applied in electro-catalysis to proceed both anodic and cathodic reactions in water electrolysis and organic synthesis.^{13–17} One of the remarkable applications of nickel is catalyzing the ethanol oxidation. Several studies regarding to electro-oxidation of alcohols on nickel electrode have been reported.^{18–20}

For obtaining a synergistic electro-catalytic system, the nickel alloys specifically nickel-copper can be used.^{21–23} In addition, alloy electrodes compared to other electro-catalysts can offer further advantages such as long-term stability and ease of preparation. The crystal structures of pure Ni and Cu metals are similar and they possess face-centered cubic structures with similar lattice parameters. Therefore, it is possible to make a wide range of Ni-Cu alloy ratios.^{24–27}

The aim of present work is to study the electrochemical oxidation of ethanol on Ni-Cu alloy (70/30) electrode in alkaline solution and compare its catalytic activity with pure Ni electrode via electrochemical techniques of cyclic voltammetry, chronoamperometry and impedance spectroscopy.

2. Experimental

All chemicals used in this work [Sodium hydroxide and ethanol in analytical grade] were of Merck origin (Germany) and used without further purification. Double distilled water was employed to prepare the solutions. Nickel and nickel-copper alloy were prepared from Rooyingran Sanaat Company. The electrochemical measurements were carried out in a one-compartment three-electrode cell powered by a Metrohm-Autolab potentiostat/galvanostat (model 12/30/302, The Netherlands). The disk of Ni-Cu alloy (70/30) of 1 cm² area was employed as working electrode. Before each measurement, the electrode was polished with emery paper of 1000 grit and rinsed in double distilled water and acetone. Counter and reference electrodes were platinum and KCl-saturated Ag/AgCl electrode (Metrohm, The Netherlands), respectively. All the electrochemical studies were done at 22 ± 1 °C.

The electrochemical impedance experiments were carried out in a frequency range of 100 kHz to 10 MHz and modulation amplitude of 10 mV with respect to open circuit potential. The experimental impedance spectroscopy data were fitted to the proposed equivalent circuit using a home written least square software. This software was programmed according to the method of Marquardt for optimization of functions and Macdonald weighting for the real and imaginary parts of the experimental impedance data.^{28,29}

3. Results and Discussion

Figure 1 displays consecutive cyclic voltammograms of the Ni-Cu electrode in 1 M NaOH solution recorded after 50 cycles at scan rate of 100 mV s⁻¹. Upon the first scan, a pair of redox peak is observed at 463 and 295 mV which is attributed to the Ni²⁺/Ni³⁺ redox couple. In the subsequent cycles, the anodic and cathodic peaks shift to the negative direction and stabilize at 378 and 310 mV, respectively. This behavior is consistent with the data reported in previous electrochemical studies related to formation of the nickel oxide film on the surface and inter-conversion of α-Ni(OH)₂ and β-phases, conversion of Ni(OH)₂ to NiOOH and enrichment of Ni³⁺ species around the surface of the electrode.^{30,31} During the next cycles, a negative shift of the anodic peak and its stabilization are evident, which refer to higher potential energies required for NiOOH nucleation. In the first cycle, the baseline current is

higher which corresponds to the oxidation of Ni to Ni²⁺. An increase in peak currents with the number of cycles demonstrates a continuous enrichment of electrode's surface by accessible Ni²⁺ and Ni³⁺ electro-active species. Figure 2 shows the cyclic voltammograms of the Ni, Cu and Ni-Cu electrode in 1 M NaOH solution recorded at scan rate of 10 mV s⁻¹. As can be seen, the oxidation behavior of Ni and Ni-Cu electrode is the same and the Ni²⁺/Ni³⁺ redox couple is observed. No considerable anodic peak for Cu³⁺ is shown in cyclic voltammogram of Cu electrode, but the cathodic peak is clear in inset of Figure 2.

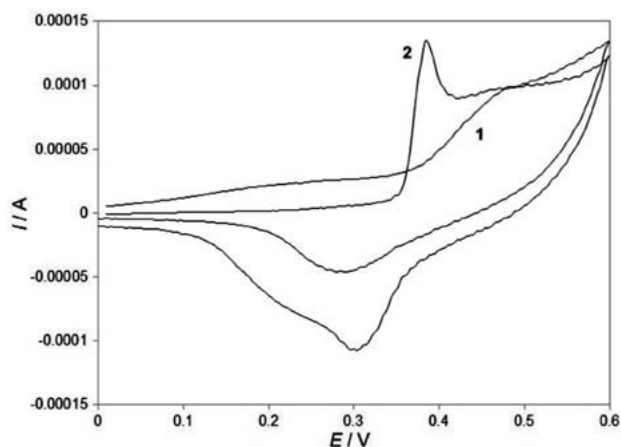


Figure 1. Consecutive cyclic voltammogram of Ni-Cu electrode oxidation in 1 M NaOH (1) first and (2) fiftieth cycle at a scan rate of 100 mV s⁻¹.

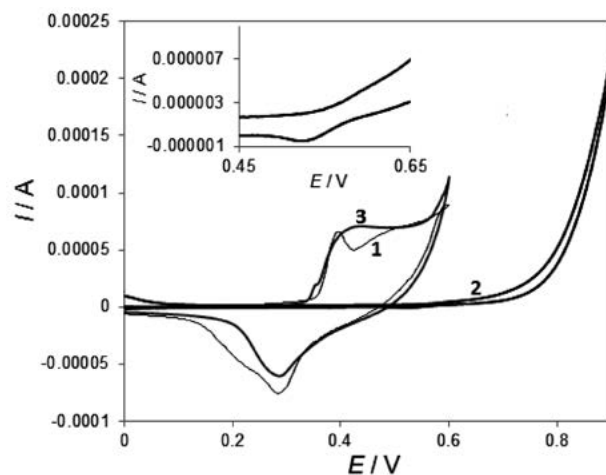


Figure 2. Cyclic voltammogram of (1) Ni, (2) Cu and (3) Ni-Cu electrode oxidation in 1 M NaOH at a scan rate of 10 mV s⁻¹. Inset: Cyclic voltammogram of Cu electrode in the potential range of 0.45 and 0.65 V.

Figure 3a illustrates the typical cyclic voltammograms of a Ni-Cu electrode at various scan rates (2–2500 mV s⁻¹) in 1 M NaOH solution. Figure 3b shows that the anodic peak currents increase proportional to the lower

scan rate values (2–200 mV s^{-1}). This behavior is expected for the electrochemical activity of redox couples that their voltammetric responses are sensitive to the low concentration of surface-confined electro-active species.³² In this process, only the nickel oxide layer produced on electrode surface participates in the redox reaction.³³ Surface coverage of the redox species, Γ^* , can be calculated according to the slope of the lines shown in Figure 3b:³³

$$I_p = \left(\frac{n^2 F^2}{4RT} \right) v \Gamma^* \quad (1)$$

where I_p , n , and v is peak current, electron transfer number and potential scan rate, respectively. The Γ^* value is calculated to be about $8.15 \times 10^{-8} \text{ mol cm}^{-2}$ which is related to the presence of ca. 80 monolayers of surface species on Ni-Cu electrode. Figure 3c presents the proportionality of anodic peak current to square root values of higher scan rates (350–2500 mV s^{-1}). It shows that the oxidation reaction is a diffusion-controlled process at higher scan rate³³ and the reaction is limited by diffusion of hydroxide ion from bulk of solution to the electrode surface according to following equation:

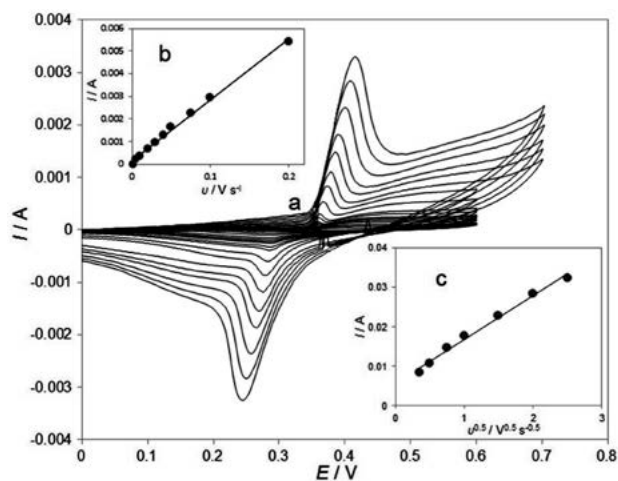


Figure 3. (a) Typical cyclic voltammograms of Ni-Cu electrode in 1 M NaOH at different scan rates of 2–2500 mV s^{-1} , (b) The dependency of anodic peak currents to the scan rate at lower values (2–200 mV s^{-1}), (c) The proportionality of anodic peak currents to the square roots of scan rate at higher values (350–2500 mV s^{-1}).

Figure 4 depicts cyclic voltammograms of pure Ni, pure Cu and Ni-Cu electrodes in 1 M NaOH solution containing 0.5 M ethanol at scan rate of 10 mV s^{-1} . As seen, Ni-Cu electrode provides a higher current density for ethanol electro-oxidation in alkaline solution. The reason can be related to higher atomic radius of Cu compared to Ni which can enhance ethanol adsorption on the electrode surface. Furthermore, electro-catalytic activity of Cu elec-

trode is high for ethanol oxidation, but it is at higher anodic over-potentials. As it can be seen, the measured anodic potentials of Ni-Cu and Ni electrodes are the same, but the anodic peak current of Ni-Cu is higher than that in Ni electrode. Consequently, the high electro-catalytic activity of Cu electrode is responsible for electro-catalytic activity of Ni-Cu electrode.

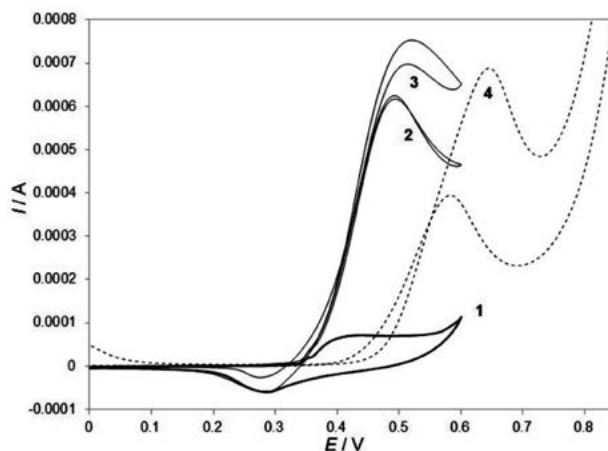


Figure 4. Cyclic voltammograms in the (1) absence and (2) presence of 0.5 M ethanol on Ni, (3) Ni-Cu (4) Cu electrode in 1 M NaOH solution. Scan rate: 10 mV s^{-1} .

Figure 5a exhibits the cyclic voltammograms of Ni-Cu electrode in a solution of 1 M NaOH and different concentrations of ethanol at scan rate of 10 mV s^{-1} . It is declared that the oxidation of ethanol on Ni-Cu electrode has a typical electro-catalytic response. The anodic current increases around the potential of 350 mV. The oxidation of ethanol and Ni^{2+} oxidation to Ni^{3+} starts simultaneously. The anodic to cathodic charge ratio in the presence of 0.5 M ethanol is obtained to be 92/8 while it is 55/45 in the absence of ethanol. The charge values are calculated through integrating the background corrected anodic and cathodic peaks.

In the positive sweep, the measured anodic current is proportional to the bulk concentration of ethanol. An increase in ethanol concentration up to 0.6 M caused a linear increase in the anodic current (Figure 5b). Based on these evidences, catalytic electro-oxidation of ethanol on Ni-Cu electrode is confirmed. Zhang et al. investigated the ethanol oxidation on Ni-B amorphous alloy nanoparticles modified nanoporous Cu in alkaline medium.³⁴ They reported that ethanol oxidation at the Ni-B modified porous Cu electrode had a negative shift of 52 mV in the onset oxidation potential and the oxidation peak current increased in comparison with the bulk Ni. Kakaei and Marzang studied the electro-catalytic activity of nitrogen doped reduced graphene oxide with Ni-Co nanoparticles for ethanol oxidation in alkaline media.³⁵ The fabricated alloy electro-catalyst exhibited a remark-

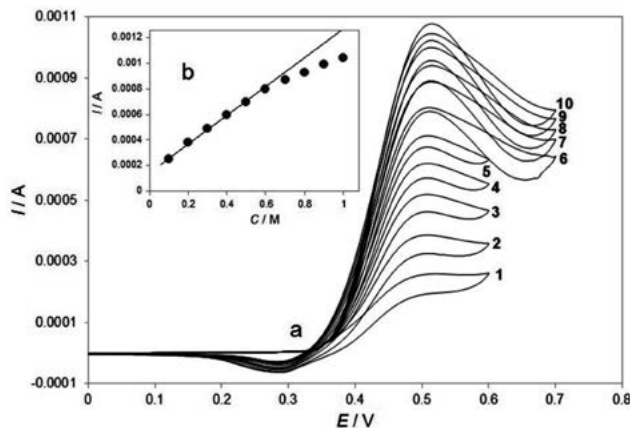


Figure 5. (a) Cyclic voltammograms of the Ni-Cu electrode in 1 M NaOH solution in the presence of (1) 0.1, (2) 0.2, (3) 0.3, (4) 0.4, (5) 0.5, (6) 0.6, (7) 0.7, (8) 0.8, (9) 0.9 and (10) 1 M of ethanol. Scan rate: 10 mV s⁻¹. (b) Dependency of the anodic peak current on the concentration of ethanol.

able electro-catalytic activity and high stability for the ethanol oxidation reaction in comparison with fabricated Ni and Co.

The decrease in cathodic current that occurs in the negative potential scan verifies the involvement of ethanol in the rate determining step. It also indicates that the process is incapable of reducing all high-valence nickel species that have formed in the anodic half cycle. Along with the oxidation of Ni²⁺ species to Ni³⁺, the adsorbed ethanol molecules oxidize on the surface at higher over-potentials. The products or intermediates of the reaction poison the electrode surface and reduces the number of available sites for ethanol adsorption. Consequently, the anodic current approaches a maximum in the positive potential scan and then the overall rate of ethanol oxidation decreases. Electro-catalytic oxidation of ethanol also continues in the early stages of the cathodic half cycle and the current tends to a maximum since some active sites for adsorption of ethanol regenerate due to removal of the adsorbed intermediates and products.

Figure 6 shows the cyclic voltammograms of Ni-Cu electrode in the presence of 0.5 M ethanol at various potential scan rates (2–350 mV s⁻¹) and also the scan rate proportionality of the anodic peak current. The anodic peak potential appears at 0.5 V as a result of ethanol oxidation on the nickel active sites. The variation of anodic peak current vs. the square root of scan rate values shows a linear relationship which represents that the oxidation of ethanol on Ni-Cu electrode is controlled by diffusion of ethanol species from solution to the redox sites accessible on the electrode's surface (Figure 6b). Although, the cathodic peak of Ni³⁺ reduction is negligible at low scan rates, but it appears at higher scan rates. This observation implies that the electro-oxidation of nickel species is much faster than catalytic oxidation of ethanol at higher scan rates. Therefore, oxidation of ethanol on nickel surface is a slow process.

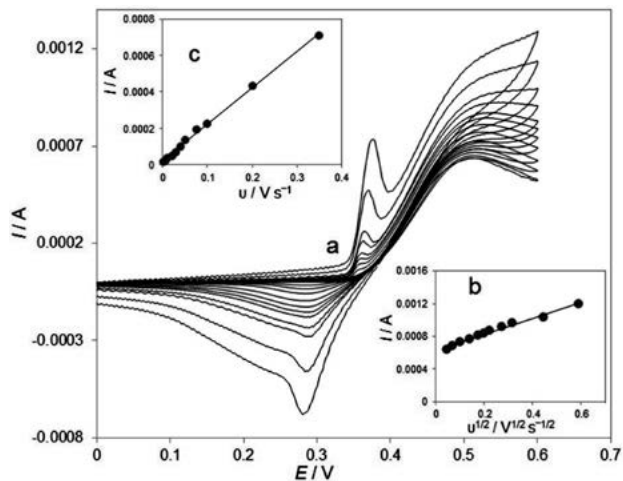
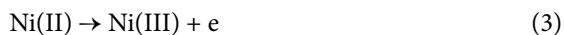


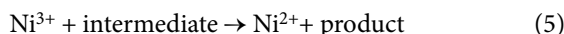
Figure 6. (a) Typical cyclic voltammograms of the Ni-Cu in 1 M NaOH in the presence of 0.5 M ethanol at various scan rates of 2, 5, 10, 20, 30, 40, 50, 75, 100, 200 and 350 mV s⁻¹. (b) Dependence of anodic peak current at 530 mV on the square root of scan rate. (c) Dependence of anodic peak current at 370 mV on the scan rate.

At higher scan rates, the oxidation peak of Ni(OH)₂ to NiOOH rises at potentials that are considerably more negative than the potential of ethanol oxidation (≈ 370 mV). This peak is insignificant at low scan rates but enhances at higher scan rate values. Figure 6c illustrates a linear dependency of the current peak on the scan rate which proposes the presence of surface-confined electro-active species. According to the high current density observed in the presence of ethanol and also the appearance of two oxidation peaks for Ni²⁺ and ethanol, it is appeared that one of the anodic current can be attributed to the oxidation of ethanol by NiOOH since the NiOOH reduction peak disappears during the negative scan. The other one can be assigned to the direct electro-oxidation of ethanol on the surface of the oxide layer.

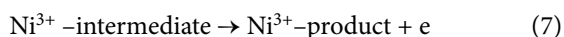
The following redox reaction of the nickel species is expected:



while ethanol oxidizes on the alloy surface through the following reaction^{23,36,37}:



In Eqs. (4) and (5), ethanol oxidation occurs through the reduction of NiOOH sites. The Ni³⁺ sites can be regenerated by the power source or via direct electro-oxidation on Ni³⁺ oxide surface as follows:



In Eqs. (6) and (7), Ni^{3+} provides an active site for direct ethanol oxidation. Also, Eqs. (3), (6) and (7) refer to two anodic peaks of ethanol and Ni^{2+} oxidation.

Figure 7a displays the chronoamperograms recorded for Ni-Cu in 1 M NaOH solution containing (0.1–0.8 M) ethanol at the potential step of 500 mV. Figure 7b identifies a linear behavior of the net current changes (after elimination of the background current) vs. the inverse square root of time. So, a diffusion-controlled process is dominant in this electrochemical process. The diffusion coefficient of ethanol is calculated $1.26 \times 10^{-5} \text{ cm}^2 \text{ s}^{-1}$ by substitution of the line slope of Figure 7b into Cottrell equation³³ (Eq. 8).

$$I = nFAD^{1/2}C\pi^{-1/2}t^{-1/2} \quad (8)$$

The catalytic rate constant of ethanol oxidation on Ni-Cu alloy is evaluated according to Eq. (9) which is introduced by Pariente et al.³⁸

$$\frac{I_{\text{catal}}}{I_d} = \gamma^{1/2} \left(\pi^{1/2} \text{erf}(\gamma^{1/2}) + \frac{\exp(-\gamma)}{\gamma^{1/2}} \right) \quad (9)$$

Where I_{catal} and I_d stand for Ni-Cu electrode currents in the presence and absence of ethanol, respectively. $\gamma = kCt$ is the related error function in which k is the catalytic rate constant, C is the bulk concentration of ethanol and t is the elapsed time. When $\gamma > 1.5$, $\text{erf}(\gamma^{1/2})$ equals to unity approximately and Eq. (9) simplifies to:

$$\frac{I_{\text{catal}}}{I_d} = \gamma^{1/2} \pi^{1/2} = \pi^{1/2} (kCt)^{1/2} \quad (10)$$

Based on the slope of I_{catal}/I_d vs. $t^{1/2}$ plot, the obtained mean catalytic rate constant was $865.5 \text{ cm}^3 \text{ mol}^{-1} \text{ s}^{-1}$ for ethanol concentration of 0.1–0.8 M (Figure 7c).

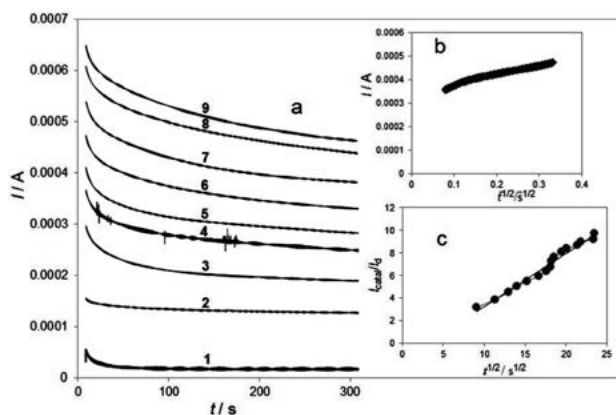


Figure 7. (a) Chronoamperograms of Ni-Cu electrode in 1 M NaOH solution with different concentration of ethanol: (1) blank, (2) 0.1, (3) 0.2, (4) 0.3, (5) 0.4, (6) 0.5, (7) 0.6, (8) 0.7 and (9) 0.8 M at potential step of 500 mV. (b) Dependency of transient current on $t^{-1/2}$. (c) Dependence of I_{catal}/I_d vs. $t^{1/2}$ derived from the data of chronoamperograms.

Figure 8 represents the Nyquist diagrams of Ni-Cu electrode recorded at the anodic peak potential as the dc-offset in 1 M NaOH solution containing different concentration of ethanol. These diagrams contain two depressed semicircles that are overlapped. The high frequency depressed semicircle corresponds to a combination of a charge transfer resistance and the double layer capacitance and the low frequency semicircle can be due to the adsorption of reaction intermediate on the surface of Ni-Cu electrode.^{39,40}

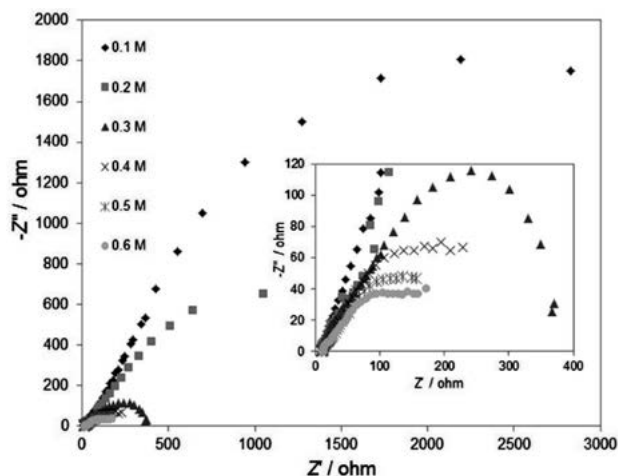


Figure 8. Nyquist diagrams of Ni-Cu electrode in 1 M NaOH solution containing different concentration of ethanol at an anodic potential of 500 mV. Inset: high frequency part of the Nyquist diagram.

Figure 9 shows the equivalent circuit in the presence of ethanol which is compatible with Nyquist diagram. The capacitor C should be replaced with a constant phase element (CPE), Q , in the equivalent circuit. The CPE behavior is due to the microscopic roughness of the electrode that causes an inhomogeneous distribution in the solution resistance and the double-layer capacitance.^{41,42} In Figure 9, R_s , Q_{dl} and R_{ct} are solution resistance, a constant phase

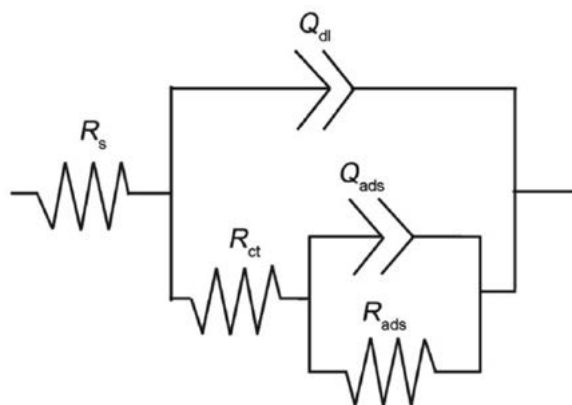


Figure 9. Equivalent circuit compatible with the experimental impedance data in Figures 8 for ethanol electro-oxidation on Ni-Cu electrode.

Table 1. Equivalent circuit parameters of electro-oxidation of ethanol on Ni-Cu electrode in 1 M NaOH solution.

Concentration / M	R_s / Ω	R_{ct} / Ω	Q_{dl} / F	n_1	R_{ads} / Ω	Q_{ads} / F	n_2
0.1	11.9	105	0.0018	0.79	4224	0.008	0.9
0.2	11.5	78	0.0024	0.79	1671	0.018	0.75
0.3	11.7	45	0.0026	0.77	361	0.018	0.68
0.4	10.3	21	0.0025	0.67	274	0.02	0.56
0.5	10.5	19	0.003	0.66	196	0.025	0.58
0.6	10.9	18	0.003	0.67	181	0.03	0.57

element related to the double layer capacitance and charge transfer resistance, respectively. Also, Q_{ads} and R_{ads} are the electrical elements corresponding to the adsorption of reaction intermediates.

The experimental data were fitted to the equivalent circuit to obtain the circuit elements. Table 1 represents the equivalent circuit parameters for the impedance spectra of ethanol electro-oxidation. The charge transfer resistance value decreases as the ethanol concentration increases. It approves the catalytic activity of Ni-Cu alloy for ethanol oxidation. n_1 and n_2 are the constant phase element exponent and show the extent of difference between capacitance and the constant phase element.

4. Conclusions

In this study, the electro-oxidation of ethanol was investigated on the nickel oxide film formed on the surface of Ni-Cu alloy electrode in an alkaline solution. The results confirmed that Ni-Cu alloy is electro-catalytically active for ethanol oxidation at a potential of ≈ 500 mV. The catalytic response obtained for electro-oxidation of ethanol on Ni-Cu electrode is greater than the one observed for pure nickel. The anodic peak currents for ethanol oxidation are linearly proportional to square root of scan rates. The chronoamperograms revealed the dominance of a diffusion-controlled process in presence of ethanol species. The diffusion coefficient of ethanol was calculated $1.26 \times 10^{-5} \text{ cm}^2 \text{ s}^{-1}$. The charge transfer resistance for various concentrations of ethanol was evaluated and highlighted an effective catalytic activity of Ni-Cu alloy for oxidation of ethanol in alkaline solutions.

5. References

1. Y. Li, Z. Wang, X. Li, T. Yin, K. Bian, F. Gao, D. Gao, *J. Power Sources* **2017**, *341*, 183–191.
DOI:10.1016/j.jpowsour.2016.12.006
2. Q. Zhang, F. Zhang, X. Ma, Y. Zheng, S. Hou, *J. Power Sources* **2016**, *336*, 1–7. DOI:10.1016/j.jpowsour.2016.10.028
3. Z. Xiong, B. Yan, K. Zhang, C. Wang, S. Li, H. Xu, Y. Du, C. Zhai, *J. Taiwan Inst. Chem. E.* **2017**, *75*, 12–17.

- DOI:10.1016/j.jtice.2017.03.008
4. Y. Xie, H. Zhang, G. Yao, S. A. Khan, X. Cui, M. Gao, Y. Lin, *J. Energy Chem.* **2017**, *26*, 193–199.
DOI:10.1016/j.jechem.2016.11.014
 5. J. L. Tan, A. M. De Jesus, S. L. Chua, J. Sanetuntikul, S. Shanmugam, B. J. V. Tongol, H. Kim, *Appl. Catal. A- Gen.* **2017**, *531*, 29–35. DOI:10.1016/j.apcata.2016.11.034
 6. C. Peng, W. Yang, E. Wu, Y. Ma, Y. Zheng, Y. Nie, H. Zhang, J. Xu, *J. Alloy Compd.* **2017**, *698*, 250–258.
DOI:10.1016/j.jallcom.2016.12.198
 7. Y. H. Qin, Z. Y. Xiong, J. Ma, L. Yang, Z. Wu, W. Feng, T. L. Wang, W. G. Wang, C. W. Wang, *Int. J. Hydrogen Energ.* **2017**, *42*, 1103–1112. DOI:10.1016/j.ijhydene.2016.09.060
 8. T. Li, G. Fu, J. Su, Y. Wang, Y. Lu, X. Zou, X. Zhu, L. Xu, D. Sun, Y. Tang, *Electrochim. Acta* **2017**, *231*, 13–19.
DOI:10.1016/j.electacta.2017.02.044
 9. X. Hu, C. Lin, L. Wei, C. Hong, Y. Zhang, N. Zhuang, *Electrochim. Acta* **2016**, *187*, 560–566.
DOI:10.1016/j.electacta.2015.11.100
 10. C. Du, X. Gao, Z. Zhuang, C. Cheng, F. Zheng, X. Li, W. Chen, *Electrochim. Acta* **2017**, *238*, 263–268.
DOI:10.1016/j.electacta.2017.03.198
 11. P. Kanninen, N. D. Luong, L. H. Sinh, J. Flórez-Montaña, H. Jiang, E. Pastor, J. Seppälä, T. Kallio, *Electrochim. Acta* **2017**, *242*, 315–326. DOI:10.1016/j.electacta.2017.05.019
 12. K. Ding, P. Wang, J. Zhao, Y. Li, Y. Chen, Y. Zhang, B. Wei, Y. Sun, J. Pan, *Int. J. Hydrogen Energ.* **2017**, *42*, 9766–9774.
DOI:10.1016/j.ijhydene.2017.01.210
 13. I. Danaee, M. Jafarian, F. Forouzandeh, F. Gopal, *Int. J. Chem. Kinet.* **2012**, *44*, 712–721. DOI:10.1002/kin.20721
 14. J. Guo, Y. Hou, B. Li, E. Duan, *Mater. Lett.* **2017**, *200*, 90–93.
DOI:10.1016/j.matlet.2017.04.111
 15. I. Danaee, M. Jafarian, M. Sharafi, F. Gopal, *J. Electrochem. Sci. Technol.* **2012**, *3*, 50–56. DOI:10.5229/JECST.2012.3.1.50
 16. W. Shi, Q. Wang, F. Qin, J. Yu, M. Jia, H. Gao, Y. Zhang, Y. Zhao, G. Li, *Electrochim. Acta* **2017**, *232*, 332–338.
DOI:10.1016/j.electacta.2017.02.164
 17. W. Shi, H. Gao, J. Yu, M. Jia, T. Dai, Y. Zhao, J. Xu, G. Li, *Electrochim. Acta* **2016**, *220*, 486–492.
DOI:10.1016/j.electacta.2016.10.051
 18. S. J. Zhang, Y. X. Zheng, L. S. Yuan, L. H. Zhao, *J. Power Sources* **2014**, *247*, 428–436.
DOI:10.1016/j.jpowsour.2013.08.129
 19. N. A. M. Barakat, H. M. Moustafa, M. M. Nassar, M. A. Ab-

- delkareem, M.S. Mahmoud, A. A. Almajid, K. A. Khalil, *Electrochim. Acta* **2015**, *182*, 143–155. DOI:10.1016/j.electacta.2015.09.079
20. K. Kakaei, K. Marzang, *J. Colloid Interf. Sci.* **2016**, *462*, 148–153. DOI:10.1016/j.jcis.2015.09.072
21. I. Pötzelberger, A. I. Mardare, A. W. Hassel, *Appl. Surf. Sci.* **2017**, *417*, 48–53. DOI:10.1016/j.apsusc.2016.12.193
22. I. Danaee, M. Jafarian, F. Forouzandeh, F. Gobal, M. G. Mahjani, *Int. J. Hydrogen Energy* **2008**, *33*, 4367–4376. DOI:10.1016/j.ijhydene.2008.05.075
23. I. Danaee, M. Jafarian, F. Forouzandeh, F. Gobal, M. G. Mahjani, *Int. J. Hydrogen Energy* **2009**, *34*, 859–869. DOI:10.1016/j.ijhydene.2008.10.067
24. M. Jafarian, T. Rostami, M. G. Mahjani, F. Gobal, *J. Electroanal. Chem.* **2016**, *763*, 134–140. DOI:10.1016/j.jelechem.2015.12.031
25. S. J. Zhang, Y. X. Zheng, L. S. Yuan, L. H. Zhao, *J. Power Sources* **2014**, *247*, 428–436. DOI:10.1016/j.jpowsour.2013.08.129
26. L. Wang, X. Lu, Y. Ye, L. Sun, Y. Song, *Electrochim. Acta* **2013**, *114*, 484–493. DOI:10.1016/j.electacta.2013.10.125
27. X. Tarrús, M. Montiel, E. Vallés, E. Gómez, *Int. J. Hydrogen Energ.* **2014**, *39*, 6705–6713. DOI:10.1016/j.ijhydene.2014.02.057
28. J. R. Macdonald, *Solid State Ionics* **1984**, *13*, 147–149. DOI:10.1016/0167-2738(84)90049-3
29. I. Danaee, S. Noori, *Int. J. Hydrogen Energ.* **2011**, *36*, 12102–12111. DOI:10.1016/j.ijhydene.2011.06.106
30. F. Hahn, B. Beden, M. J. Croissant, C. Lamy, *Electrochim. Acta* **1986**, *31*, 335. DOI:10.1016/0013-4686(86)80087-1
31. A. A. El-Shafei, *J. Electroanal. Chem.* **1999**, *471*, 89–95. DOI:10.1016/S0022-0728(99)00235-1
32. R. Barnard, C. F. Randell, *J. Appl. Electrochem.* **1983**, *13*, 89–95. DOI:10.1007/BF00615892
33. A. J. Bard, L. R. Faulkner (Ed.): *Electrochemical Methods: Fundamentals and Applications*, Wiley, New York, **2001**, pp. 591.
34. S. J. Zhang, Y. X. Zheng, L. S. Yuan, L. H. Zhao, *J. Power Sources* **2014**, *247*, 428–436. DOI:10.1016/j.jpowsour.2013.08.129
35. K. Kakaei, K. Marzang, *J. Colloid Interf. Sci.* **2016**, *462*, 148–153. DOI:10.1016/j.jcis.2015.09.072
36. I. Danaee, M. Jafarian, F. Forouzandeh, F. Gobal, M. G. Mahjani, *Electrochim. Acta* **2008**, *53*, 6602–6609. DOI:10.1016/j.electacta.2008.04.042
37. I. Danaee, M. Jafarian, F. Forouzandeh, F. Gobal, M. G. Mahjani, *J. Phys. Chem. B* **2008**, *112*, 15933–15940. DOI:10.1021/jp8069173
38. F. Pariente, E. Lorenzo, F. Tobalina, H. D. Abruna, *Anal. Chem.* **1995**, *67*, 3936–3944. DOI:10.1021/ac00117a019
39. I. Danaee, M. Jafarian, F. Gobal, M. Sharafi, M. G. Mahjani, *Chem. Res. Chinese U.* **2012**, *28*, 19–25.
40. M. Jafarian, A. Mirzapoor, I. Danaee, A. A. Shahnazi Sangachin, F. Gobal, *Sci. China Chem.* **2012**, *55*, 1819–1824. DOI:10.1007/s11426-012-4731-6
41. H. Jafari, I. Danaee, H. Eskandari, M. Rashvand Avei, *J. Mater. Sci. Technol.* **2014**, *30*, 239–252. DOI:10.1016/j.jmst.2014.01.003
42. A. R. Hosein Zadeh, I. Danaee, M. H. Maddahy, *J. Mater. Sci. Technol.* **2013**, *29*, 884–892. DOI:10.1016/j.jmst.2013.06.006

Povzetek

V tej raziskavi smo v alkalni raztopini raziskali elektrokatalitsko aktivnost elektrode iz zlitine nikelj-baker (Ni-Cu) za oksidacijo etanola in njegovega morebitnega procesa redukcije. V ta namen smo uporabili ciklično voltometrijo, kronoamperometrijo in tehniko elektrokemijske impedančne spektroskopije. Rezultati študije ciklične voltometrije kažejo na povečano oksidacijo etanola v primeru uporabe zlitine Ni-Cu v primerjavi z uporabo samo nikljeve elektrode. Povečanje anodnega vrha, ki ustreza oksidaciji nikljevega hidroksida, spremlja zmanjšan katodni vrh v prisotnosti etanola. Anodni vrhovi imajo linearno odvisnost od kvadratnega korena stopnje skeniranja, ki je značilna za difuzijsko nadzorovane procese. Na osnovi kronoamperometričnih meritev je reakcija pokazala Cottrellianovo vedenje, difuzijski koeficient etanola pa je bil $1,26 \times 10^{-5} \text{ cm}^2 \text{ s}^{-1}$. S pomočjo impedančne spektroskopije smo prikazali elektrokatalitsko aktivnost elektrode Ni-Cu v primeru oksidacije etanola in pokazali, da se upornost napram prenosu naboja zmanjša s povečanjem koncentracije etanola.

Scientific paper

Solvothermal Synthesis of ZnO-Nitrogen Doped Graphene Composite and its Application as Catalyst for Photodegradation of Organic Dye Methylene Blue

Rajinder Singh, Manesh Kumar, Heena Khajuria, Jigmet Ladol,
and Haq Nawaz Sheikh*

Department of Chemistry, University of Jammu, Jammu Tawi, 180 006 India.

* Corresponding author: E-mail: hnsheikh@rediffmail.com

Received: 10-11-2017

Abstract

A facile one step solvothermal method is designed for the synthesis of visible light-sensitive ZnO-nitrogen doped graphene (ZNG) nano photocatalysts using ethylene glycol as a solvent as well as an agent to prevent aggregation of graphene layers. The deposition of ZnO nanoparticles onto the NG layers was confirmed by high resolution transmission electron microscope (HR-TEM), scanning electron microscope (SEM), powder X-ray diffraction (XRD), and Fourier transform infrared spectroscopy (FTIR). UV-Vis spectroscopy (UV-Vis) was used to study the enhanced photocatalytic activity, which shows the red-shift of the band-edge as compared to ZnO nano particles. The enhancement in photocatalytic activity is possibly due to the synergistic effect of improved adsorptivity of dyes, enhanced visible light absorption and effective charge separation.

Keywords: ZnO; photocatalysis; methylene blue; nitrogen doped graphene

1. Introduction

The visible light degradation of organic pollutants have attracted the attention of the scientific community worldwide due to the various reasons such as better efficiency, easy to operate and non toxic byproducts.^{1–6} The process of photocatalysis takes place by the absorption of light by the photocatalysts such as ZnO and TiO₂ and thereby promoting the electrons from valence band to the conduction band and forming the electron and hole pairs in the structure.^{7–9} The produced electron-hole pairs can move and start the various redox reactions involving water and oxygen and thus cause the degradation of organic molecules. However, the recombination of electrons and holes can lower the performance of photocatalyst ZnO.¹⁰ In order to make the catalyst more effective, the recombination of electron and hole must be hindered. Various experiments have been conducted to prevent the recombination of electron and hole by combining the photocatalyst with the other materials such as non reactive metals^{11,14} and semiconductors.^{15,16} In addition, it has been found that deposition of semiconductor photocatalysts on a co-adsorbent surface such as mesoporous materials, zeolites, alumina, silica or carbon based materials may en-

hance the photocatalytic activity of photocatalysts.^{17–21} Among the various materials, carbon based materials are of great importance due to their excellent electronic properties, adsorption capacity and unique structure. The carbon based materials include activated carbon, graphene and carbon nanotubes.^{21–27} Graphene is a two-dimensional monolayer network of conjugated carbon atoms having sp²-hybridization between the atoms.^{28–32} Graphene has many advantages as compared to the carbon nanotubes (CNTs) such as high surface area and excellent adsorption on the surface of adsorbent. Graphene possesses the excellent electrical, thermal and mechanical properties by virtue of which it is used in the diverse areas and also as electrode materials for electrochemical capacitor.^{31–34} However, despite all these facts graphene has to undergo some structural transformation to be used for many other applications.³⁵ The doping of graphene with the heteroatom (i.e. N-atom) can enhance the electron mobility and causes the larger capacitance. All these properties are attributed to the atomic size and strong valence bonds of nitrogen atoms.³⁶ In the recent years, nitrogen doped graphene (NG) has received much importance^{37,38} Thus, it is favored to synthesize the N-doped graphene based nano

materials using simple techniques with enhanced physical and chemical properties that can have applications in diverse fields. Various analysis techniques have been focused on the application of graphene based composites in capacitors,³⁹ biosensors,⁴⁰ solar cells⁴¹ and liquid crystalline displays.⁴² It has been thought that composite of ZnO with graphene is a perfect candidate to have the excellent photocatalytic performance due to the conjugated structure of graphene which help in the separation of charge in the photocatalysis process. ZnO-graphene nanohybrids have been synthesized having regularly arranged ZnO nanorods on the graphene sheets possessing the high electrical property and excellent optical transmittance.⁴³ Lv and co-workers have proposed ZnO-RGO hybrid composites by using a microwave synthesis system, resulting in improved degradation of methylene blue dye.⁴⁴ Zheng et al. have employed chemical vapour deposition technique to synthesize the ZnO-graphene composite with exceptional field emission properties.⁴⁵ ZnO-graphene thin films have the good capacitive properties which are prepared by ultrasonic spray pyrolysis.⁴⁶ However, the conditions that are used in all these processes are complex and can be carried out at high temperature only. The solution based processes are proved better as compared to the physical methods as they are cost effective for the fabrication of ZnO nanoparticles and its graphene based composites.^{20,47} Here in this study, a simple one step synthetic approach is explored for the synthesis of ZnO-NG nano composites with the varying amounts of NG using ethylene glycol as a solvent. The ethylene glycol inhibits the aggregation of reduced nitrogen doped graphene sheets. In the further study, the photocatalytic activity of the ZnO-NG for degradation of organic dye methylene blue was investigated and the obtained results were compared with naked ZnO nano particles. The effect of concentration of NG on the photocatalytic property of ZnO-NG composites for degradation of methylene blue dye was investigated in detail.

2. Experimental

2. 1. Synthesis of Graphene Oxide (GO)

Graphene oxide (GO) was synthesized from 99.99% pure natural graphite powder flakes, by modified Hummer's method.⁴⁸ In this method, 3 g graphite powder flakes were added into 40 mL mixture of concentrated H_2SO_4 and H_3PO_4 (9:1) maintained at 0 °C. To this mixture, 18g KMnO_4 was added in small installments under vigorous stirring. The reaction mixture was stirred for 2 h below 10 °C and then for another 1 h at 35 °C. After that the mixture was diluted with 100 mL of deionised water (DI) and stirred for 1 h in an ice bath to prevent overheating of reaction mixture. Then the residual KMnO_4 present in the reaction mixture was reduced by adding 20 mL of 30% H_2O_2 . The brilliant yellow colored solution was obtained. The reaction mixture was washed with 5% HCl

aqueous solution to remove the metal ions followed by washing with deionised water to counteract the acidic nature of the solution until its pH value reaches 6. The reaction mixture was centrifuged and obtained product was further purified by sonicating its dispersion in deionised water for 1 h. Finally, the product was centrifuged and dried at 60 °C for 24 h.

2. 2. Synthesis of Nitrogen Doped Graphene (NG)

Nitrogen doped graphene (NG) was synthesized by the pyrolysis of prepared graphene oxide (GO). 0.5 g GO and 0.6 g urea were dissolved in 30 mL ethanol and sonicated for 30 min to form the homogenous solution. Then the solution was heated at 60 °C to evaporate the solvent. The as obtained black mixture was grounded finely and heated at 350 °C in the muffle furnace at a heating rate of 5 °C/min for 12 h. The obtained black powder was washed with ethanol and dried in oven at 60 °C for 24 h.

2. 3. Synthesis of Zinc Oxide/Nitrogen Doped Graphene Composites (ZnO-NG)

ZnO-NG composites were prepared via hydrothermal method by varying the content of NG as 10, 20, 30, 40 and 50 mg. Briefly, purified NG with different weight contents as mentioned were dispersed in 15 mL of ethylene glycol (EG) by ultrasonication treatment for 2 h, labelled as solution A. Two separate solutions of zinc acetate [$\text{Zn}(\text{CH}_3\text{COO})_2$] and sodium hydroxide (NaOH) were prepared by dissolving 20 mg $\text{Zn}(\text{CH}_3\text{COO})_2$ and 10 mg NaOH in 10 mL of EG, labelled as solution B and C respectively. Solution B and C are added to solution A and stirred for 1 h to obtain a homogenous suspension. The suspension was transferred to a 50 mL Teflon-lined stainless steel autoclave and maintained at 160 °C for 24 h for the deposition of ZnO simultaneously. Finally, the resultant composite was centrifuged and washed with DI water followed by ethanol and dried at 70 °C for 24 h. Pure ZnO was also prepared by the same method under similar conditions. The as-prepared ZnO-NG composites with 20, 30, 40, 50 mg of NG were labelled as ZNG-1, ZNG-2, ZNG-3 and ZNG-4 respectively.

2. 4. Spectroscopic and Microscopic Measurements

The phase and size of the as prepared samples were determined from powder X-ray diffraction (PXRD) using D8 X-ray diffractometer (Bruker) at a scanning rate of $12^\circ \text{ min}^{-1}$ in the 2θ range from 10° to 80° , with Cu K α radiation ($\lambda = 0.15405 \text{ nm}$). Scanning electron microscopy (SEM) micrographs of the samples were recorded on FEI Nova Nano SEM 450. High Resolution Transmission Electron Microscopy (HRTEM) was recorded on Tecnai G2 20

S-TWIN Transmission Electron Microscope with a field emission gun operating at 200 kV. The samples for TEM measurements were prepared by evaporating a drop of the colloid onto a carbon coated copper grid. The infrared spectra were recorded on Shimadzu Fourier Transform Infrared Spectrometer (FT-IR) over the range of wave number $4000\text{--}400\text{ cm}^{-1}$ and the standard KBr pellet technique was employed. All the measurements were performed at room temperature.

2. 5. Photocatalytic Measurements

The catalytic activity of the as synthesized sample was performed by degradation of organic dye methylene blue (MB) under the irradiation of visible light. For the photo irradiation 500 W xenon lamp was used fitted with UV cut-off filters (JB450) in order to completely remove any radiation below 420 nm ensuring the exposure to only visible light. The whole procedure was performed at 25 °C. A 100 mL of MB dye solution was prepared (20 mg/L concentration) and 0.025 g of photocatalyst was mixed with dye solution. The resulting mixture was stirred for 1 h before illumination in order to establish the adsorption and desorption equilibrium between MB and catalyst surface. At the same time instant of time 5 mL of dye-catalyst mixture was taken out and concentration of the residual dye was determined with the help of UV-vis spectroscopy by measuring the absorption at 664 nm. The absorbance of dye in presence of different catalysts (ZNG-1, ZNG-2, ZNG-3 and ZNG-4) at 664 nm was monitored after fixed intervals of time. The absorbance of dye in presence of pure ZnO at same time intervals was also recorded for reference.

3. Results and Discussion

3. 1. PXRD Measurements

The structural characterization of the nanoparticles has been carried out by Powder X-ray diffraction technique using $\text{CuK}\alpha$ radiation. The PXRD spectrum of GO, NG, ZnO, ZNG-1, ZNG-2, ZNG-3 and ZNG-4 composite materials are shown in the Figure. 1 and Figure. 2. Figure. 1a, b show the differences of phase composition between GO and NG. The doping of nitrogen in GO can be shown easily by PXRD spectrum. The X-ray diffraction pattern of GO (Figure. 1a) shows one characteristic peak (2θ) at 10.3° . The PXRD pattern of NG shown in Figure. 1b has three characteristic peaks (2θ) at 26.3° (002), 31.92° (002) and 42.63° (004). The results obtained for NG are in well agreement with literature (JCPDS Card No. 75-1621)⁴⁴. The characteristic absorption peak of GO at 10.3° was not found in PXRD spectrum of the NG which shows nitrogen doping of graphene oxide framework. The PXRD patterns of ZnO, ZnO/NG composites (Figure 2) there are following main peaks at $2\theta = 31.7^\circ, 34.4^\circ, 36.2^\circ,$

$47.5^\circ, 56.6^\circ, 62.9^\circ, 66.3^\circ, 67.9^\circ, 69.2^\circ, 77.0^\circ$ which corresponds to the (1 0 0), (0 0 2), (1 0 1), (1 0 2), (1 1 0), (1 0 3), (2 0 0), (1 1 2), (2 0 1) and (2 0 2) planes of ZnO nano crystals respectively (JCPDS No. 36-1451).⁴⁹ The reduction of nitrogen doped graphene takes place by the alcohol in the hydrothermal conditions so no peak corresponding to (002) plane is visible in the composite. It can also be attributed to efficient exfoliation of the NG sheets in the resultant composites so this reason can be given disappearance of the NG patterns in the XRD spectrum of ZnO/NG composites.

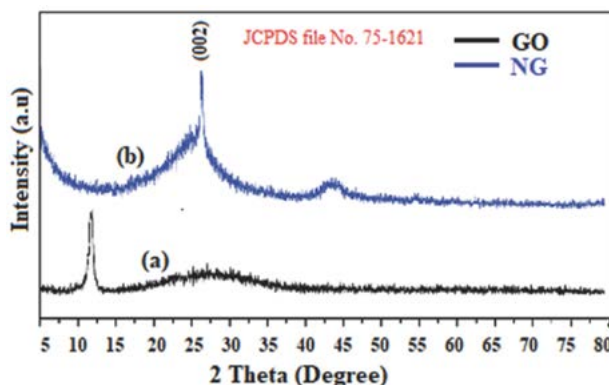


Figure 1. PXRD patterns of (a) GO (b) NG

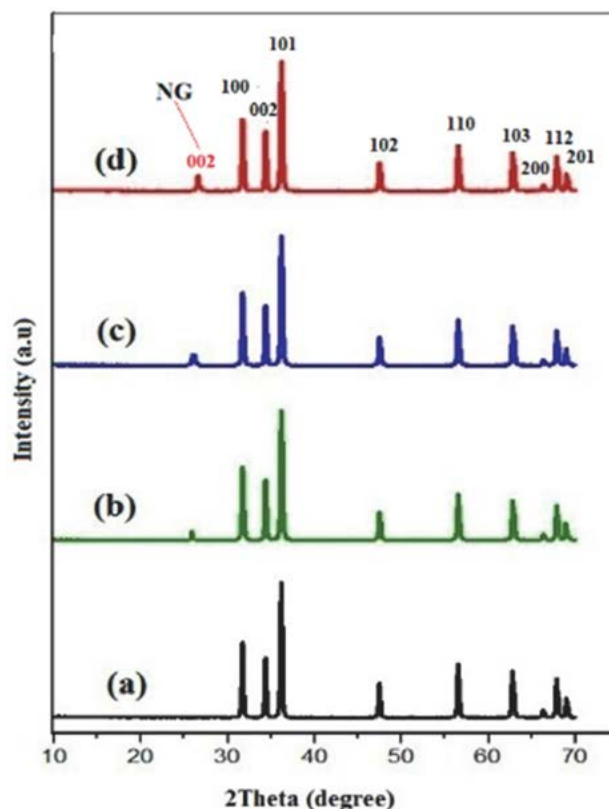


Figure 2. PXRD patterns of (a) ZnO (b) ZG-1 (c) ZG-2 (c) ZG-3 (d) ZG-4

The average crystallite size of these nanoparticles was calculated according to the Scherrer's equation.

$$\beta = \frac{K\lambda}{L\cos\theta} \quad (1)$$

where, L (nm) is the crystallite size, λ (nm) is the wavelength of the Cu K α radiant, $\lambda = 0.15405$ nm, β ($^\circ$) is the full-width at half-maximum (FWHM) of the diffraction peak, θ is the diffraction angle and K is the Scherrer constant equal to 0.89. All the major peaks were used to calculate the average crystallite size of the ZnO and ZnO/NG nanoparticles. The estimated average crystallite sizes of nanoparticles are in the range of 80–120 nm.

3. 2. FT-IR Characterization

FTIR spectra of GO, NG was shown in Figure. 3a, b. There are many O-containing groups that exist on GO sheets, such as hydroxyl, epoxy, and carboxyl groups. Majority of the O-containing groups will disappear after reduction. FTIR bands at 1050, 1220, 1405 and 1730 cm^{-1} were observed for GO. These bands correspond to C–O stretching, C–O–C stretching, O–H deformation vibra-

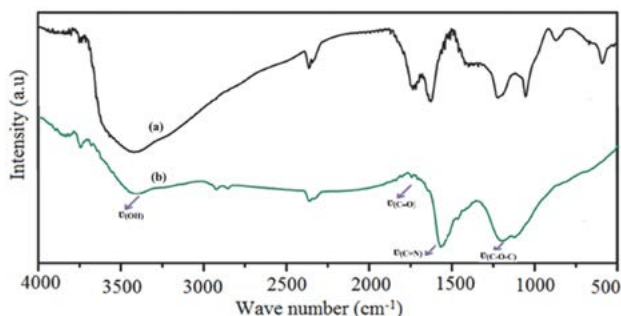


Figure 3. FTIR spectra of (a) GO (b) NG

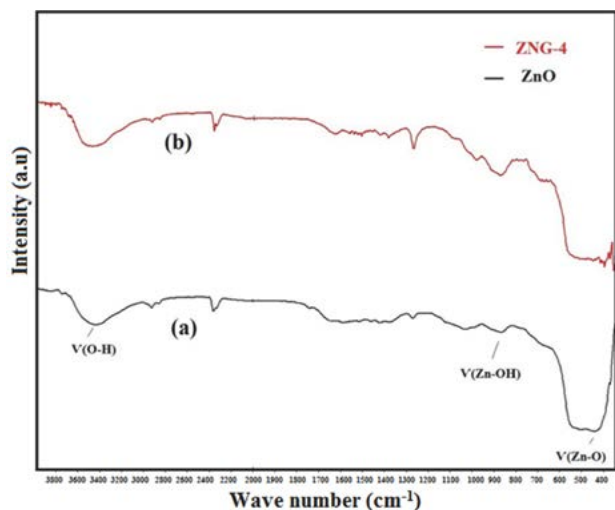


Figure 4. FTIR of (c) ZnO (d) ZNG-4.

tion and C=O carbonyl stretching.⁵⁰ FTIR bands at 1400 cm^{-1} due to C=C stretching is observed in NG and the $\nu_{\text{(C=O)}}$ band at 1730 cm^{-1} completely disappeared due to reduction. The bands located at 1180 and 1565 cm^{-1} in Figure. 3b are assigned to the $\nu_{\text{(C-N)}}$ and $\nu_{\text{(C=C)}}$ respectively. The FTIR spectra suggest nitrogen doping of GO. Figure. 4a, b shows the FT-IR bands of ZnO and ZnO-NG. The absorption band at 450 cm^{-1} is attributed to the stretching modes of Zn–O. Furthermore, it is observed that almost all the characteristic bands of oxygen containing functional groups (C=O, O–H, C–OH and C–O–C) disappeared in the FT-IR spectrum of ZnO-NG suggesting the nitrogen doping of graphene oxide and uniform anchoring of ZnO onto the surface of NG⁵¹. The results above show the heteroatom N was entered in the graphene structure and the ZnO–NG composites were prepared favourably.

3. 3. Raman Analysis

The Raman spectrum of the as synthesized NG and ZNG-4 are shown in Figure 5a and 5b respectively. In the Figure. 5 two noticeable peaks at 1340 and 1600 cm^{-1} indicating the D and G band respectively. The ratio of the intensity of D and G band indicates disorder, as revealed by the sp^2/sp^3 carbon proportion. The G band indicates in (plane bond(stretching motion of pairs of sp^2 C atoms. The D band (“disordered” band) is the breathing mode of the sp^2 rings of the graphene layer which corresponds to a range of defects: bond angle disorder, bond length disorder

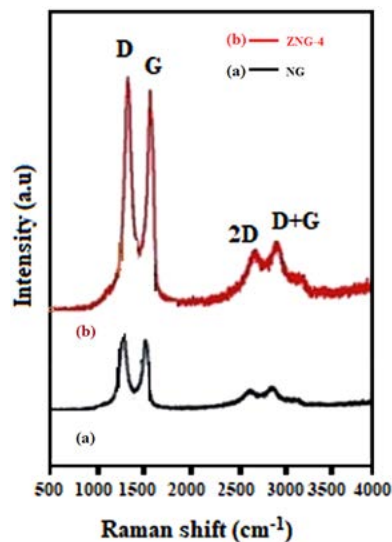


Figure 5. Raman spectrum of (a) NG (b) ZNG-4.

der and hybridization caused by heteroatom (nitrogen/oxygen) doping and structure defects. Therefore, the relatively increased intensity of the D band for NG indicates that the content of disordered carbon increases, particularly by nitrogen doping.

3. 4. SEM and TEM Analysis

Figure. 6a and 7a depicts scanning electron microscopy and transmission electron microscopy images of as prepared GO respectively. The scanning electron microscopy, suggested layered structure and crumpled surface

morphology of as synthesized graphene oxide. Furthermore, by analysing the TEM image (Figure. 7a) it was revealed that GO has stacked layer by layer structure and has morphology like the wrinkled paper. The morphological changes can be attributed to excessive carboxylic, phenolic

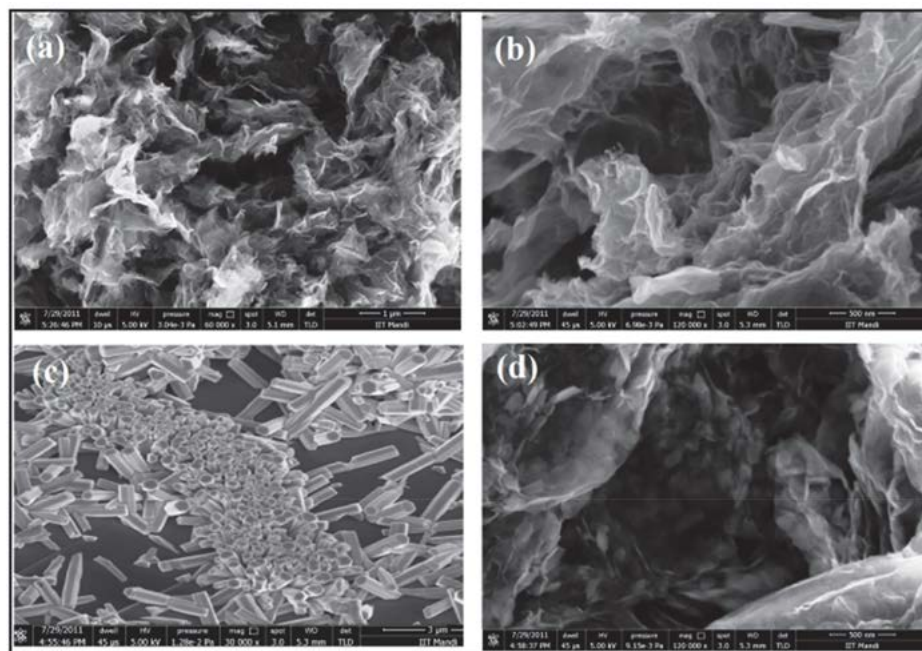


Figure 6. SEM micrographs of (a) GO (b) NG (c) ZnO (d) ZNG-4.

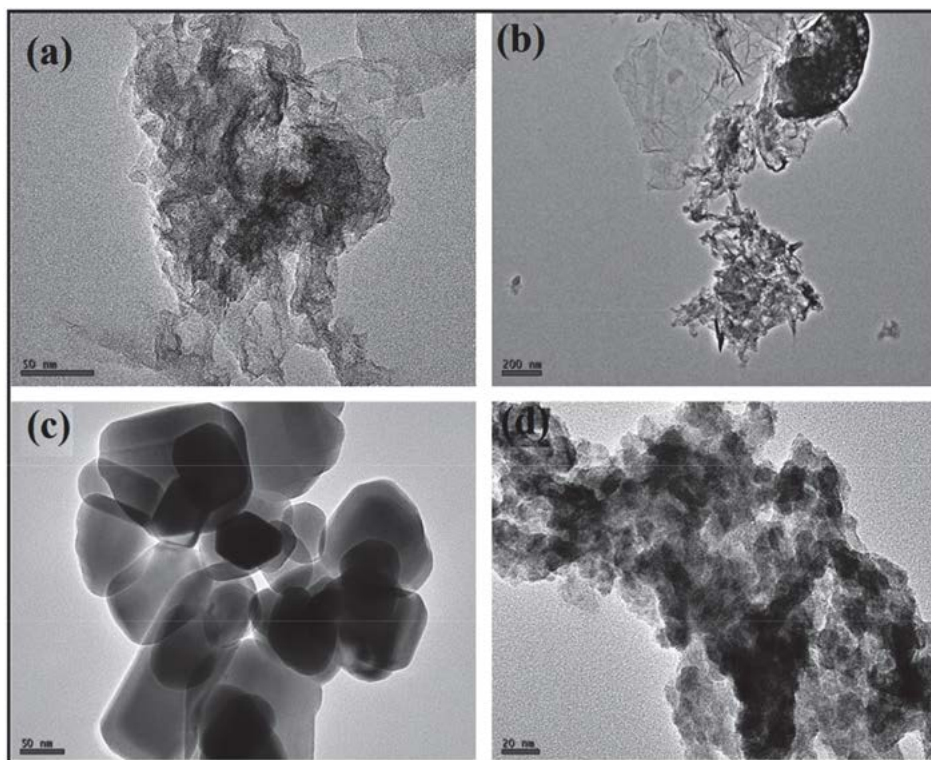


Figure 7. TEM micrographs of (a) GO (b) NG (c) ZnO (d) ZNG-4

and epoxy functional groups on the basal plane of GO. The curled and overlapped nanosheets of GO can be clearly observed. Figure. 6b and Figure. 7b represent nitrogen-doped graphene nano-sheets which shows a highly wrinkled topology, by virtue of stable thermodynamic bending.^{45,46} SEM image of the ZnO is shown in Figure. 6c which suggested rectangular rods like morphology of the prepared sample. Figure. 6d is SEM image of ZNG-4 sample which clearly shows a uniform distribution of ZnO on the surface of NG. Furthermore the SEM results are supported by TEM analysis of ZnO and ZNG-4 as shown in Figure. 7c and d respectively. The morphological features of prepared nanostructures are in close agreement with reported literature.⁵² The particle size data obtained from TEM data by using *Image J software* are in very close agreement to the size calculated from the Debye–Scherrer method.

3. 5. Photocatalytic Measurements

The photocatalytic decomposition of organic dye MB under the visible light was helpful to show the photocatalytic performance at 25 °C of the prepared ZnO, ZNG-1, ZNG-2, ZNG-3, ZNG-4. The photocatalytic degradation profile of MB solution (concentration of MB, $C = 0.075$ M and path length, $l = 1$ cm) in the presence of different composites was shown in the Figure. 7. It has been found that the MB dye (blank solution) was not decomposed even after 90 min exposure to the visible light. The ZnO-NG composites shows better photocatalytic activity than ZnO. The decomposition rate of MB for ZnO was found 58% but on the introduction of nitrogen doped graphene the decomposition rate was increased to 76%, 88%, and 93% corresponding to ZNG-1, ZNG-2, ZNG-3 respectively. And for the ZNG-4 it reaches a maximum value of 99.5%. These results shows that the

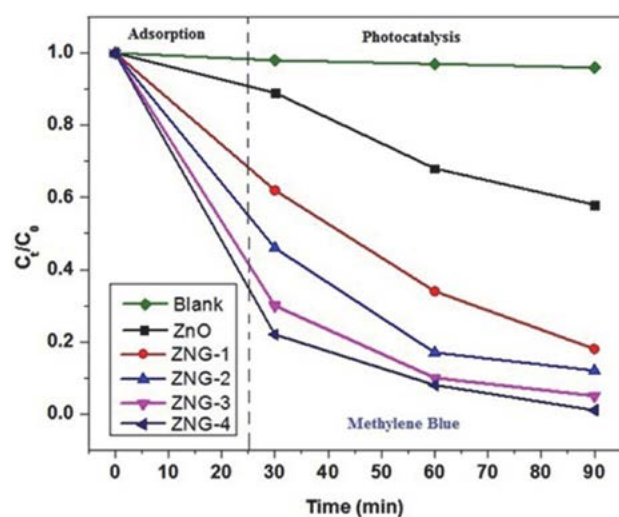


Figure 8. The kinetics of photodegradation of MB.

presence of nitrogen doped graphene has vital importance in the photocatalytic process and can be shown by the plot of C_t/C_0 versus time (min). The degradation process for the various photocatalysts was shown in the Figure. 7.

3. 6 Mechanism of Photocatalysis

A possible mechanism of photocatalytic degradation of MB over the ZnO-NG nanocomposite has been suggested based on the photocatalytic studies as shown in Figure. 9. Upon the visible light irradiation, the electrons are excited in the valence band (VB) to the conduction band (CB) of ZnO nanoparticles, thus generating holes (h^+) in the VB. The electron produced transferred to the CB of carbon layers of nitrogen doped graphene and which discharge the photogenerated electrons which get reacted with the oxygen (O_2) to produce super oxide anion radicals ($O_2^{\cdot-}$). The huge separation rate of h^+ easily reacts with water molecules (H_2O) to generate the hydroxyl radicals (OH^{\cdot}). The presence of the above radicals results into the degradation of the adsorbed MB dye onto the surface of ZnO-NG nanocomposite. The effective electron transfer process with nitrogen doped graphene layers as electron receiver and transporter leads to the enhanced photocatalytic activity of the ZnO-NG nanocomposite under the visible light irradiation. Nitrogen doped graphene prevents electron–hole pairs recombination onto the surface of ZnO nanoparticles (NPs).^{53–55} So, the enhancement of photocatalytic activity was given to the synergistic effect between ZnO NPs and nitrogen doped graphene layers. Furthermore the role of NG in in photodegradation of MB might be double fold;

1. Nitrogen doped graphene (NG) increases adsorption of tested dyes (MB) on the surface of ZNG photocatalyst(s), as result of π – π conjugation between aromatic region of the dye and nanosheets of nitrogen doped graphene.^{56, 57}
2. It is also helpful in suppression of recombination of charges in ZnO, as NG acts as photoelectron ac-

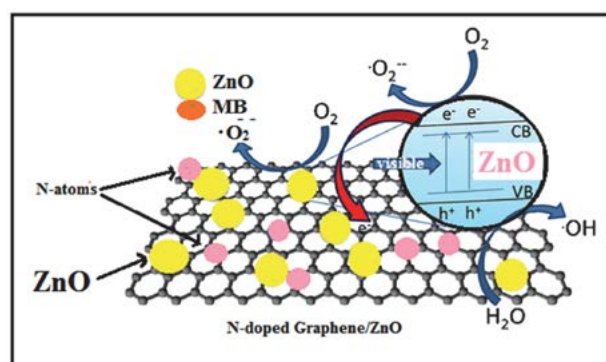


Figure 9. Proposed mechanism of photodegradation process MB dye.

ceptor and there by facilitate a higher photocatalytic activity of prepared nanocomposites.^{58, 59}

3. 7. Recyclability and Reusability of As-Synthesised Photocatalyst (ZNG-4)

For a greener-ecofriendly approach and practical applications, reuse and recyclability of a photocatalyst is prime requirement. This makes the process cost effective and free of waste. The reusability and recycling efficiency of as-synthesized photocatalyst (ZNG-4) was tested against photodegradation of methylene blue (MB). It can be noted that photocatalyst (ZNG-4) shows appreciable activity even after the five cycles. The results are shown in Figure. 10.

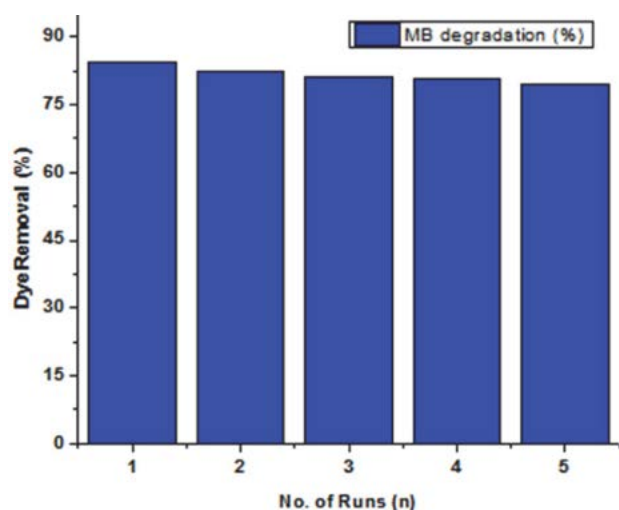


Figure 10. Recyclability of ZNG-4 in Photodegradation of MB dye (upto 5 cycles).

4. Conclusions

In conclusion, we have reported the structural, photocatalytic properties of ZnO, ZnO-NG nanocomposites prepared by hydrothermal method. PXRD patterns are in well agreement with the ZnO and nitrogen doped graphene structure. SEM and TEM images reveal the morphological and topological features of nitrogen doped graphene, ZnO, ZnO-NG respectively. The crystallite size of synthesized nanocomposites as calculated from PXRD and TEM analysis was found to be in the range of 80-120 nm. The photocatalytic results show that photodegradation of MB in presence of nanocomposites was enhanced compared to bare ZnO.

5. Acknowledgement

We would like to acknowledge SAIF, Panjab University for their technical support. We thank Indian Institute

of Technology Mandi for powder X-ray diffraction study. One of the authors (R. S.) is thankful to UGC-Delhi for the financial support.

6. References

- Z. Liu, W. Xu, J. Fang, X. Xu, S. Wu, X. Zhu, Z. Chen, *Appl. Surf. Sci.* **2012**, 259, 441–447. DOI:10.1016/j.apsusc.2012.07.063
- W. Xu, G. Zhou, J. Fang, Z. Liu, Y. Chen, C. Cen. *Int. J. Photoenergy.* **2013**, 2013, Aug 7. DOI:10.1155/2013/234806
- W. Xu, Z. Liu, J. Fang, G. Zhou, X. Hong, S. Wu, X. Zhu, Y. Chen, C. Cen *Int. J. Photoenergy.* **2013**, 2013, jul 29. DOI:10.1155/2013/394079
- Y. Liao, W. Que, Z. Tang, W. Wang, W. Zhao, *J Alloys Compd.* **2011**, 509, 1054–1059. DOI:10.1016/j.jallcom.2010.09.175
- N. R. Khalid, E. Ahmed, Z. Hong, M. Ahmad, *Appl. Surf. Sci.* **2012**, 263, 254–259. DOI:10.1016/j.apsusc.2012.09.039
- J. Wang, D. N. Tafen, J. P. Lewis, Z. L. Hong, A. Manivannan, M. J. Zhi, M. Li, N. Q. Wu, *J. Am. Chem. Soc.* **2009**, 131, 12290–12297. DOI:10.1021/ja903781h
- C. Wang, J. Yan, X. Wu, Y. Song, G. Cai, H. Xu, J. Zhu, H. Li, *Appl. Surf. Sci.* **2013**, 273, 159–166. DOI:10.1016/j.apsusc.2013.02.004
- M. Li, Z. L. Hong, Y. N. Fang, F. Q. Huang, *Mater. Res. Bull.* **2008**, 43, 2179–2186. DOI:10.1016/j.materresbull.2007.08.030
- M. Li, P. S. Tang, Z. L. Hong, M. Q. Wang, *Colloids Surf., A.* **2008**, 318, 285–290. DOI:10.1016/j.colsurfa.2008.01.001
- R. M. Asmussen, M. Tian, A. Chen, *Environ. Sci. Technol.* **2009**, 43, 5100–5105. DOI:10.1021/es900582m
- T. Hirakawa, P. V. Kamat, *J. Am. Chem. Soc.* **2005**, 127, 3928–3934. DOI:10.1021/ja042925a
- P. V. Kamat, M. Flumiani, A. Dawson *Colloids and surf. A.* **2002**, 202, 269–279. DOI:10.1016/S0927-7757(01)01071-8
- K. Vinodgopal, P. V. Kamat, *Environ. Sci. Technol.* **1995**, 29(3), 841–485. DOI:10.1021/es00003a037
- V. Subramanian, E. E. Wolf, P. V. J. Kamat, *J. Am. Chem. Soc.* **2004**, 126, 4943–4950. DOI:10.1021/ja0315199
- S. H. Elder, F. M. Cot, Y. Su, S. M. Heald, A. M. Tyryshkin, M. K. Bowman, Y. Gao, A. G. Joly, M. L. Balmer, A. C. Kolwaite, K. A. Magrini, D. M. Blake, *J. Am. Chem. Soc.* **2000**, 122, 5138–5146. DOI:10.1021/ja992768t
- T. Tatsuma, S. Saitoh, P. Ngaotrakanwivat, Y. Ohko, A. Fujishima, *Langmuir* **2002**, 18, 7777–7779. DOI:10.1021/la026011i
- J. Aguado, R. V. Grieken, M. J. Lopez-Munos, J. Marugan, *Appl. Catal.* **2006**, 312, 202–212. DOI:10.1016/j.apcata.2006.07.003
- B. Li, H. Cao, *J. Mater. Chem.* **2011**, 21, 3346–3349. DOI:10.1039/C0JM03253K
- J. Matos, A. Garcia, T. Cordero, J. M. Chovelon, C. Ferronato, *Catal. Lett.* **2009**, 130, 568–574. DOI:10.1007/s10562-009-9989-8

20. K. Woan, G. Pyrgiotakis, W. Sigmund, *Adv. Mater.* **2009**, *21*, 2233–2239. DOI:10.1002/adma.200802738
21. M. Li, S. F. Zhou, Y. W. Zhang, G. Q. Chen, Z. L. Hong, *Appl. Surf. Sci.* **2008**, *254*, 3762–3766. DOI:10.1016/j.apsusc.2007.11.047
22. Y. Yang, Liu, *Appl. Surf. Sci.* **2011**, *257*, 8950–8954. <https://doi.org/10.1016/j.apsusc.2011.05.070>
23. H. Zhang, X. Lv, Y. Li, Y. Wang, J. Li, *ACS Nano*, **2010**, *4*, 380–386. DOI:10.1021/nn901221k
24. X. Zhou, T. Shi, H. Zhou, *Appl. Surf. Sci.* **2012**, *258*, 6204–6211. DOI:10.1016/j.apsusc.2012.02.131
25. N. R. Khalid, Z. L. Hong, E. Ahmed, Y. W. Zhang, H. Chan, M. Ahmad, *Appl. Surf. Sci.* **2012**, *258*, 5827–5834. DOI:10.1016/j.apsusc.2012.02.110
26. A. A. Casaos, I. Tacchini, A. Unzue, M. T. Martinez, *Appl. Surf. Sci.* **2013**, *270*, 675–684. DOI:10.1016/j.apsusc.2013.01.120
27. N. R. Khalid, E. Ahmed, Z. L. Hong, Y. W. Zhang, M. Ahmad, *Curr. Appl. Phys.* **2012**, *12*, 1485–1492. DOI:10.1016/j.cap.2012.04.019
28. K. S. Novoselov, A. K. Geim, S. V. Morozov, D. Jiang, M. I. Katsnelson, I. V. Grigorieva, S. V. Dubonos, A. A. Firsov, *Nature*, **2005**, *438*, 197–200. DOI:10.1038/nature04233
29. A. K. Geim, K. S. Novoselov, *Nat. Mater.* **2007**, *6*(3), 183–191. DOI:10.1038/nmat1849
30. A. C. Neto, F. Guinea, N. M. Peres, K. S. Novoselov, A. K. Geim, *Rev. Mod. Phys.* **2009**, *81*(1), 109–155. DOI:10.1103/RevModPhys.81.109
31. Y. P. Zhang, C. Z. Luo, W. P. Li; C. X. Pan, *Nanoscale*, **2013**, *5*, 2616–2619. DOI:10.1039/C3NR34141K
32. Y. P. Zhang, D. L. Li, X. J. Tan, B. Zhang, X. F. Ruan, H. J. Liu, C. X. Pan, L. Liao, T. Zhai, Y. Bando, S. S. Chen, W. W. Cai, R. S. Ruo, *Carbon*, **2013**, *54*, 143–148. DOI:10.1016/j.carbon.2012.11.012
33. D. F. Sun, X. B. Yan, J. W. Lang, Q. J. Xue, *J. Power Sources*, **2013**, *222* 52–58. DOI:10.1016/j.jpowsour.2012.08.059
34. Y. Huang, J. J. Liang, Y. S. Chen, *Small*, **2012**, *8*, 1805–1834. DOI:10.1002/sml.201102635
35. X. S. Du, C. F. Zhou, H. Y. Liu, Y. W. Mai, G. X. Wang, *J. Power Sources*, **2013**, *241*, 460–466. DOI:10.1016/j.jpowsour.2013.04.138
36. W. Fan, Y. Y. Xia, W. W. Tjiu, P. K. Pallathadka, C. B. He, T. X. Liu, *J. Power Sources* **2013**, *243*, 973–981. DOI:10.1016/j.jpowsour.2013.05.184
37. H. M. Jeong, J. W. Lee, W. H. Shin, Y. J. Choi, H. J. Shin, J. K. Kang, J. W. Choi, *Nano Lett.* **2011**, *11*, 2472–2477. DOI:10.1021/nl2009058
38. G. X. Luo, L. Z. Liu, J. F. Zhang, G. B. Li, B. L. Wang, J. J. Zhao, *ACS Appl. Mater. Interfaces*, **2013**, *5*, 11184–11193. DOI:10.1021/am403427h
39. X. Chen, C. Fu, W. Yang, *Analyst*, **2009**, *134*, 2135–2140. DOI:10.1039/B910754A
40. N. L. Yang, J. Zhai, D. Wang, Y. S. Chen, L. Jiang, *ACS Nano* **2010**, *4*, 887–894. DOI:10.1021/nn901660v
41. P. Blake, P. D. Brimicombe, R. R. Nair, T. J. Booth, D. Jiang, F. Schedin, L. A. Ponomarenko, S. V. Morozov, H. F. Gleeson, E. W. Hill, A. K. Geim, K. S. Novoselov, *Nano Lett.* **2008**, *8*, 1704–1708. DOI:10.1021/nl080649i
42. X. Y. Zhang, H. P. Li, X. L. Cui, Y. Lin, *J. Mater. Chem.* **2010**, *20*, 2801–2806. DOI:10.1039/B917240H
43. J. M. Lee, Y. B. Pyun, J. Yi, J. W. Choung, W. I. Park, *J. Phys. Chem. C* **2009**, *113*, 19134–19138. DOI:10.1021/jp9078713
44. T. Lv, L. Pan, X. Liu, T. Lu, G. Zhu, Z. Sun, *J. Alloys Compd.* **2011**, *509*, 10086. DOI:10.1016/j.jallcom.2011.08.045
45. W. T. Zheng, Y. M. Ho, H. W. Tian, M. Wen, J. L. Qi, Y. A. Li, *J. Phys. Chem. C* **2009**, *113*, 9164–9168. DOI:10.1021/jp900881q
46. Y. Zhang, H. Li, L. Pan, T. Lu, Z. Sun, *J. Electroanal. Chem.* **2009**, *634*, 68–71. DOI:10.1016/j.jelechem.2009.07.010
47. B. Li, T. Liu, Y. Wang, Z. Wang, *J. Colloid Interface Sci.* **2012**, *377*, 114–121. DOI:10.1016/j.jcis.2012.03.060
48. W. S. Hummers, R. E. Offeman, *J. Am. Chem. Soc.* **1958**, *80*, 1339–1339.
49. M. Ahmad, E. Ahmed, Z. L. Hong, J. F. Xua, N. R. Khalida, A. Elhissi, W. Ahmed *Appl. Surf. Sci.* **2013**, *274* 273–281. DOI:10.1016/j.apsusc.2013.03.035
50. M. Acik, C. Mattevi, C. Gong, G. Lee, K. Cho, M. Chhowalla, *ACS Nano* **2010**, *10*, 5861–5868. DOI:10.1021/nn101844t
51. A. K. Mageed, A. B. DR, A. Salmiaton, S. Izhar, M. A. Razak, H. M. Yusoff, F. M. Yasin, S. Kamarudin *International Journal of Applied Chemistry*, **2016**, *12*(1), 104–8.
52. W. Zou, J. Zhu, Y. Sun, X. Wang, *Mater. Chem. Phys.* **2011**, *125*, 617–620. DOI:10.1016/j.matchemphys.2010.10.008
53. B. Li, T. Liu, Y. Wang, Z. Wang, *J. Colloid Interface Sci.* **2012**, *377*, 114–121. DOI:10.1016/j.jcis.2012.03.060
54. R. Atchudan, T.N.J.I. Edison, S. Perumal, M. Shanmugam, Y. R. Lee, *J. Photochem. Photobiol. A*, **2017**, *337*, 100–111. DOI:10.1016/j.jphotochem.2017.01.021
55. R. Cai, J. Wu, L. Sun, Y. Liu, T. Fang, S. Zhu, S. Li, Y. Wang, L. Guo, C. Zhao, A. Wei, *Mater. Des.* **2016**, *90*, 90839–844. <http://10.1016/j.matdes.2015.11.020>
56. P. Chen, T. Y. Xiao, H. H. Li, J. J. Yang, Z. Wang, H. B. Yao, S. H. Yu, *ACS Nano*, **2011**, *6*, 712–719. DOI:10.1021/nn204191x
57. M. Kumar, R. Singh, H. Khajuria, H. N. Sheikh, *J. Mater. Sci. Mater. Electron.*, **2017**, *28*, 9423–9434. DOI:10.1007/s10854-017-6684-1
58. K. Gopalakrishnan, H. M. Joshi, P. Kumar, L. S. Panchakarla, C. N. R. Rao, *Chem. Phys. Lett.*, **2011**, *511*, 304–308. DOI:10.1016/j.cplett.2011.06.033
59. R. Singh, M. Kumar, H. Khajuria, J. Ladol, H. N. Sheikh, *Chemical Papers*, **2018**, *1-12*. DOI:10.1007/s11696-018-0385-y

Povzetek

S preprostim enostopenjskim solvotermalnim sinteznim postopkom smo pripravili nano fotokatalizator na osnovi ZnO na grafenu, dopiranem z dušikom (ZNG). V sinteznem postopku smo uporabili etilen glikol kot topilo, ki hkrati preprečuje agregacijo plasti grafena. Depozicijo nanodelcev ZnO na plasti grafena dopiranega z dušikom smo potrdili s presevno elektronsko mikroskopijo visoke ločljivosti (HR-TEM), vrstično elektronsko mikroskopijo (SEM), rentgensko praškovno difrakcijo (XRD) in infrardečo spektroskopijo (FTIR). UV-Vis spektroskopijo smo uporabili za preučevanje fotokatalitične aktivnosti, ki je višja v primerjavi s samimi nanodelci ZnO. Višjo fotokatalitično aktivnost lahko pripišemo sinergističnim učinkom povečane absorpcije barvila, povišane absorpcije vidne svetlobe in učinkovite ločitve naboja.

Scientific paper

DFT Study of the Reaction Mechanism of *N*-(Carbomylcarbamoithiyl) Benzamide

Felix Odame

Department of Chemistry, Nelson Mandela University, P.O. Box 77000, Port Elizabeth 6031, South Africa

* Corresponding author: E-mail: felixessah15@gmail.com(FO)

Tel.: +27836660784, Fax: +2741 504 4236.

Received: 13-11-2017

Abstract

The reaction mechanism for the formation of *N*-(carbomylcarbamoithiyl)benzamide has been successfully computed with the B3LYP/6-31g(d) functional and basis set and compared with ¹H NMR monitoring of the progress of the reaction with time. The reaction is proposed to proceed through two transition states: **Ts1** (the rate-determining step) with highly unstable species (with a requisite orientation for the reaction to proceed), and **Ts2** with a lower energy leading to the product. Computation of the reaction pathway was also carried out using the B3PW91/6-31G(d), M06/6-31G(d) and Wb97XD/6-31G(d) functionals and basis set. These results do not present a clear reaction pathway compared to that given by the B3LYP/6-31G(d).

Keywords: Transition state; imaginary frequency; urea, reaction mechanism; benzoyl isothiocyanate.

1. Introduction

The use of Density functional theory (DFT) in computation in most branches of chemistry over the years has been extensive,¹⁻³ and various methods have been used in that regard,⁴⁻⁸ the methods used include local density approximation (LDA), generalized gradient approximation (GGA), meta GGA, hybrid GGA, hybrid-meta GGA, and double-hybrid GGA, various empirical corrections such as dispersion, have been successfully implemented in many popular computational codes. By the use of standard functional approximation and standard basis set, the theoretical calculation of the electronic structure and energetics of chemical interest are easily computed. B3LYP, which is a global hybrid GGA and has been used extensively in most areas of chemistry. It is a hybrid of exact Hartree-Fock exchange with local and semi-local exchange and correlation terms on the basis of the adiabatic connection,⁹⁻¹⁴ In this work, the use of different DFT methods to compute the reaction mechanism for the synthesis of *N*-(carbomylcarbamoithiyl) benzamide has been explored.

The mechanisms for the oxidation of thiophene by OH radicals under inert conditions (Ar) have been studied using density functional theory in conjunction with various exchange-correlation functionals.¹⁵ A density functional theory (DFT) study has been performed to explore

the mechanisms of the acid catalyzed decarboxylation reaction of salicylic acids using the B3LYP method with 6-31++G(d,p) basis set in both gas phase and aqueous environment.¹⁶ Density functional theory (DFT) has been used to study the cobalt(I)-catalyzed enantioselective intramolecular hydroacylation of ketones and alkenes. Hydrogen migration was both the rate determining and chirality-limiting step, and this step was endothermic. Reductive elimination was the rate-determining step, but the chirality-limiting step was hydrogen migration, which occurred easily. The results also indicated that the alkene hydroacylation leading to (S)indanone formation was more energetically favourable than the ketone hydroacylation that gave (R)-phthalide, both thermodynamically and kinetically.¹⁷

The reaction mechanisms of H₂ with OCS have been investigated theoretically by using density function theory method. Three possible pathways leading to major products CO and H₂S, as well as two possible pathways leading to by-product CH₄ have been proposed and discussed. The structure parameters, vibrational frequencies and energies for each stationary point were calculated, and the corresponding reaction mechanism given by the potential energy surface determined from the relative energies.¹⁸ Though a lot of computational effort has been expended on different reaction systems much has not been done on the reaction mechanisms of thiones with amines.

In this work we present the computed reaction mechanism and the DFT transition state studies of the formation of *N*-(carbomylcarbamothioyl) benzamide, the transition states that contribute to the formation of products as well as the intermediates in the reaction pathway have been computed and discussed.

2. Computational Details

The reactants, transition states, intermediates and products structures were fully optimized at the B3LYP/6-31G(d). When compared with other levels of theory, the B3LYP method was sufficiently accurate for predicting reliable geometries and frequencies of the stationary points.^{19–22} Computation of vibrational frequency based on the optimized geometry of each reactant, transition structure, intermediate and product was carried out. All reactants, intermediates and products had no imaginary frequencies, whereas each transition state had one and only one imaginary frequency. The intrinsic reaction coordinate (IRC)^{23–25} calculations, were performed at the same level of theory to ensure that the transition states lead to the expected reactants and products. The computations were carried out using the GAUSSIAN 09 program package,²⁶ with Gausview 4.1 as the software for preparing the files whilst the HOMO–LUMO diagrams were generated using Avogadro.

3. Results and Discussion

The species used for the computations are defined as follows.

I1 = initial starting material

Ts1 = first transition state and highest energy specie

P1 = Intermediate

TS1 = Second transition state

P2 = final product.

The predicted reaction pathway proceeds by the coming together of urea and benzoyl isothiocyanate (I1), it was obtained by optimising the starting material to a minimum and also tracing the reverse intrinsic reaction coordinate (IRC) path of the transition state **TS1**. The starting materials were initially minimized using the B3LYP functional and the 6–31g(d) basis set. The two species (I1) together have no charge and a dipole moment of 2.1286 Debye. At the onset of the attack of the thiocyanate carbon by an amine group of urea, the distance between the carbon of the thione and the amine was 3.70191 Å. In the determination of energy profile, I1 was used as the point of reference. A transition state **Ts1** was computed using both the B3LYP functional at the 6–31g(d) basis set, this gave a dipole moment of 10.2126 Debye and a relative free energy of +40.23 kcal/mol. **TS1** is singlet species of no charge, It is a saddle point with a single imaginary frequency, obtained according to the Berny algorithm and subsequent vibrational analysis. The high energy barrier of **Ts1** is consistent with the fact that it is the rate determining step. This is the step that involves attaining the right orientation for attack of the thione carbon by the lone pair of electrons on the nitrogen of the urea. A forward IRC computation and optimization of the species obtained gave **P1** which is a singlet species of no charge with a dipole moment of 3.7226 Debye. The relative free energy of **P1** is –0.66 kcal/mol. The formation of the C–N bond in **P1** using the thione carbon leads to the formation of **TS2** which is also a singlet species with a charge of 2 and a dipole moment of 9.3700 Debye. **TS2** is a saddle point with a single imaginary frequency. The relative free energy of **TS2** is 13.62 kcal/mol. A forward IRC pathway from **TS2** gives **P2** which is a singlet species of no charge, and an imaginary

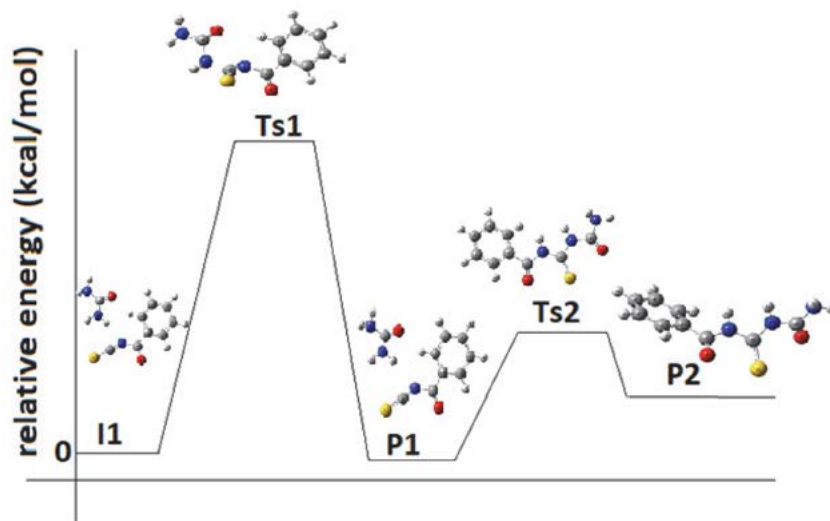


Figure 1. The potential energy surface of the formation of *N*-(carbomylcarbamothioyl) benzamide computed using the B3LYP/6-31g(d) level of theory.

frequency of zero. The dipole moment of **P2** is 7.7072 Debye. **P2** is the product of the reaction and this consistent with experimentally obtained product. The relative free energy of **P2** was 10.04 kcal/mol. **Figure 1** gives the potential energy surface of the formation of *N*-(carboxylcarbamothioyl)benzamide computed using the B3LYP functional and 6-31g(d) basis set and the corresponding optimized conformation of the intermediates and transition states in gas phase for the formation of *N*-(carboxylcarbamothioyl)benzamide. All the other functionals used for this computation (B3PW91, M06 and wB97XD) gave inconsistent results hence a good potential energy surface could not be obtained.

The bond length has been computed for all the species. Table 1 gives the bond angles of starting species, intermediates, transition states and the products for the re-

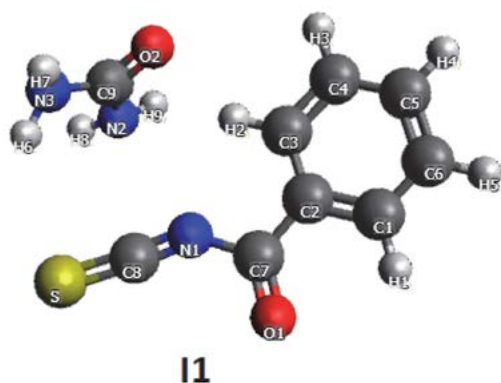


Figure 2. Structure of **I1** with enlarged numbering for clarity.

action. The bond distances of the atoms in the aromatic range are approximately equal whilst the bond lengths of the groups that are at the site of activity or directly attached to the site of activity undergo significant changes in most cases. Whilst table 2 gives the compiled results of the computed reaction pathway using the B3PW91/6-31G(d), M06/6-31G(d) and Wb97XD/6-31G(d) functionals and basis set. These results do not present a clear reaction pathway as given by the B3LYP/6-31G(d).

Figure 2 gives the structure of **I1** with enlarged numbering for clarity.

Table 1. Comparison of the bond lengths of the starting species, intermediates, transition states and products.

Bond length/Å	I1	Ts1	P1	Ts2	P2
O2-C9	1.23	1.20	1.23	1.21	1.21
C8-S	1.58	1.67	1.57	1.64	1.634
N3-C9	1.39	1.36	1.39	1.40	1.39
C4-C3	1.39	1.39	1.39	1.40	1.40
C4-C5	1.40	1.40	1.40	1.40	1.40
C3-C2	1.40	1.40	1.40	1.40	1.40
C8-N1	1.20	1.27	1.21	1.40	1.40
C5-C6	1.40	1.40	1.40	1.40	1.40
N1-C7	1.43	1.41	1.44	1.41	1.41
C2-C7	1.48	1.49	1.48	1.50	1.50
C2-C1	1.41	1.40	1.41	1.40	1.41
C7-O1	1.21	1.22	1.21	1.21	1.21
C6-C1	1.39	1.39	1.39	1.39	1.39
C9-N2	1.38	1.51	1.39	1.42	1.42
N2-C8	3.70	1.66	3.66	1.401	1.39

Table 2. Compiled results from the computation of the reaction mechanism using the B3PW91/6-31G(d), M06/6-31G(d) and Wb97XD/6-31G(d) functionals and basis set.

Species	Dipole moment	Imaginary frequency	Free Energies	Change in entropy (hartrees)	Change in entropy (kcal/mol)
B3PW91/6-31G(d)					
I1	4.89	0	-1060.862	0	0
TS1	10.39	1	-1060.798	0.063	39.69
P1	5.16	0	-1060.819	0.043	27.07
TS2	9.24	1	-1060.844	0.017	10.82
P2	12.29	0	-1060.877	-0.015	-9.28
M06/6-31G(d)					
I1	2.83	0	-1060.734	0	0
Ts1	3.52	1	-1060.717	0.017	10.42
P1	5.37	0	-1060.676	0.057	35.88
Ts2	9.25	1	-1060.701	0.033	20.67
P2	12.05	0	-1060.734	-0.0003	-0.19
Wb97XD/6-31G(d)					
I1	3.74	0	-1060.940	0	0
Ts1	10.73	1	-1060.865	0.075	46.97
P1	2.11	0	-1060.941	0.001	-0.684
Ts2	6.19	1	-1060.933	0.007	4.18
P2	9.33	0	-1060.932	0.008	5.09

4. HOMO-LUMO Analysis

Table 3 gives the frontier orbitals for all the species in the reaction pathway computed using the B3LYP functional at the 6-31g(d) basis set. The HOMO–LUMO gaps showed that there is consistency in the information obtained from the HOMO–LUMO gaps of the different species. For **II** the gap was 0.17727 eV this is consistent with high energy barrier hence heat or any other source of energy to help to form the **Ts1** with a HOMO–LUMO gap of 0.17424 eV, the HOMO–LUMO gap obtained for **P1** was 0.17881 eV this narrows to 0.13336 eV in **Ts1** with the final product **P2** giving a HOMO–LUMO gap of 0.14175 eV.

Table 3. Frontier orbitals of reacting species, transition states, intermediates and product computed using B3LYP/6-3

	II/eV	Ts1/eV	P1/eV	Ts2/eV	P2/eV
LUMO+4	-0.044	0.010	0.043	0.035	0.040
LUMO+3	-0.005	0.005	-0.004	0.022	0.027
LUMO+2	-0.013	-0.006	-0.013	-0.022	-0.021
LUMO+1	-0.041	-0.033	-0.047	-0.031	-0.034
LUMO	-0.081	-0.034	-0.080	-0.064	-0.069
HOMO	-0.258	-0.208	-0.259	-0.198	-0.210
HOMO-1	-0.261	-0.213	-0.261	-0.240	-0.237
HOMO-2	-0.264	-0.240	-0.262	-0.266	-0.265
HOMO-3	-0.269	-0.241	-0.270	-0.274	-0.271
HOMO-4	-0.276	-0.242	-0.277	-0.277	-0.274
HOMO-LUMO GAP (eV)	0.177	0.174	0.179	0.133	0.142

Figure 3 gives the ^1H NMR monitoring of the reaction over a 3 hour period at 30 minute intervals. The amino group gets attached after 30 minutes with the amino group changing environment upon attachment hence the disappearance of the signal at 4.50 ppm with time, whilst the signal at 12.00 ppm increases in intensity with time.

5. Conclusion

The reaction mechanism of *N*-(carbomylcarbamothioyl)benzamide has been successfully computed with B3LYP/6-31g(d). The reaction is proposed to proceed through two transition states **Ts1** (the rate determining

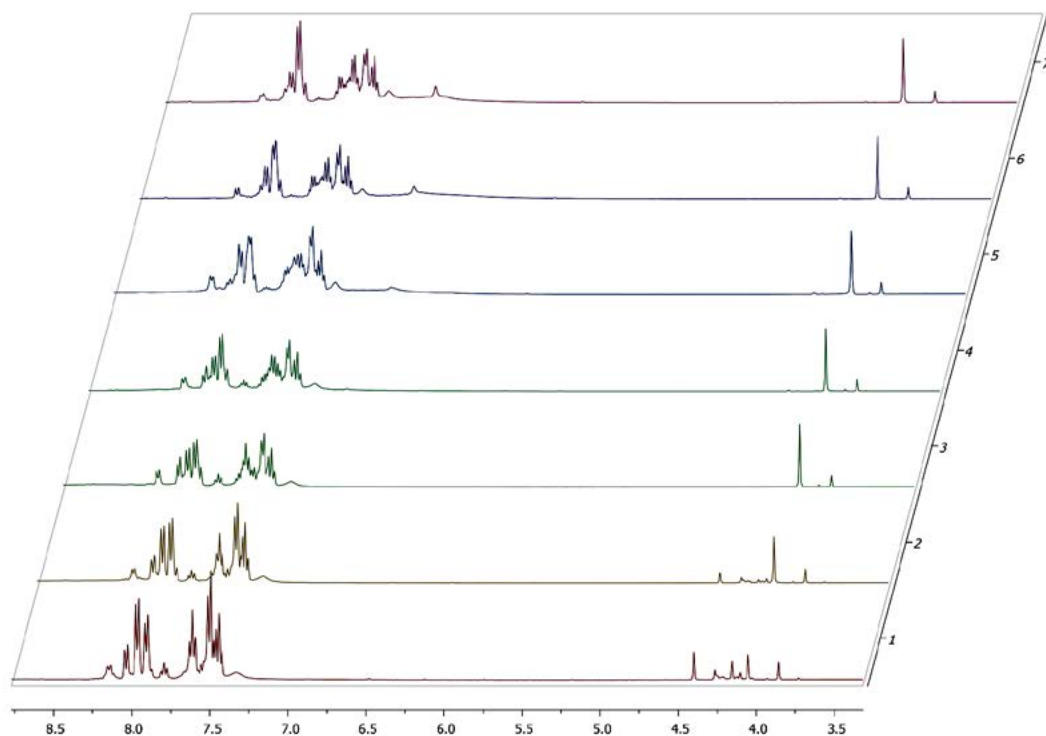


Figure 3. ^1H NMR monitoring of the progress of the reaction with time at 30 minute intervals

step) which is a high energy species. **Ts2** which is the second transition state has a lower energy hence it easily leads to the product. The HOMO-LUMO gaps showed the transition states have narrower HOMO-LUMO gaps compared to the starting materials, intermediate and products. The narrower HOMO-LUMO gaps confirms the ease of their transitions and hence their high reactivity.

6. Acknowledgements

I would like to thank the National Research Foundation (South Africa) for awarding me a postdoctoral fellowship.

7. References

1. L. Lu, H. Hu, H. Hou, B. Wang, *Comput & Theo Chem.* **2013**, *1015*, 64–71. DOI:10.1016/j.comptc.2013.04.009
2. W. Kohn, A. D. Becke, R. G. Parr, *J. Phys. Chem.* **1996**, *100*, 12974–12980. DOI:10.1021/jp960669l
3. K. Burke, *J. Chem. Phys.* **2012**, *136*, 150901. DOI:10.1063/1.4704546
4. S. F. Sousa, P. A. Fernandes, M. J. Ramos, *J. Phys. Chem. A* **2007**, *111*, 10439–10452. DOI:10.1021/jp0734474
5. M. Korth, S. Grimme, *J. Chem. Theory. Comput.* **2009**, *5*, 993–1003. DOI:10.1021/ct800511q
6. K. E. Riley, B. T. Holt, K. M. Merz, *J. Chem. Theory. Comput.* **2007**, *3*, 407–433. DOI:10.1021/ct600185a
7. C. J. Cramer, D. G. Truhlar, *Phys. Chem. Chem. Phys.* **2009**, *11*, 10757–10816. DOI:10.1039/b907148b
8. L. Goerigk, S. Grimme, *Phys. Chem. Chem. Phys.* **2011**, *13*, 6670–6688. DOI:10.1039/c0cp02984j
9. J. Harris, *Phys. Rev. A* **1984**, *29*, 1648–1659. DOI:10.1103/PhysRevA.29.1648
10. E. K. U. Gross, C. R. Proetto, *J. Chem. Theory Comput.* **2009**, *5*, 844–849. DOI:10.1021/ct9000334
11. A. D. Becke, *J. Chem. Phys.* **1993**, *98*, 1372–1377. DOI:10.1063/1.464304
12. A. D. Becke, *J. Chem. Phys.* **1993**, *98*, 5648–5652. DOI:10.1063/1.464913
13. R. H. Hertwig, W. Koch, *Chem. Phys. Lett.* **1997**, *268*, 345–351. DOI:10.1016/S0009-2614(97)00207-8
14. G. E. Scuseria, V. N. Staroverov, Progress in the development of exchange–correlation functionals, in: C. E. Dykstra, G. Frenking, K. S. Kim, G. E. Scuseria (Eds.), *Theory and Applications of Computational Chemistry: The First 40years*, Amsterdam, Elsevier, 2005, pp. 669–724. DOI:10.1016/B978-044451719-7/50067-6
15. A. Shiroudi, M. S. Deleuze, *J. Mol. Model* **2015**, *21*, 301. DOI:10.1007/s00894-015-2839-2
16. Y. Hu, L. Gao, Z. Dai, G. Sun, T. Zhang, S. Jia, Y. Dai, X. Zhang, *J. Mol. Model* **2016**, *22*, 56. DOI:10.1007/s00894-016-2923-2
17. Q. Meng, F. Wang, *J. Mol. Model* **2016**, *22*, 60. DOI:10.1007/s00894-016-2930-3
18. R. Zhang, L. Ling, B. Wang, *J. Mol. Model* **2010**, *16*, 1911–1917. DOI:10.1007/s00894-010-0686-8
19. A. D. Becke, *J. Chem. Phys.* 1993, *98*, 5648–5652. DOI:10.1063/1.464913
20. C. Lee, W. Yang, R. G. Parr, *Phys. Rev. B* 1988, *37*, 785–789. DOI:10.1103/PhysRevB.37.785
21. P. J. Stephens, F. J. Devlin C. F. Chabalowski, M. J. Frisch, *J. Phys. Chem.* 1994, *98*, 11623–11627. DOI:10.1021/j100096a001
22. W. J. Zhang, Y. Y. Zhu, D. H. Wei, M. S. Tang, *J. Comput. Chem.* **2012**, *33*, 715–722. DOI:10.1002/jcc.22906
23. Y. Zhu, Z. F. Chen, Z. J. Guo, Y. Wang, G. J. Chen. *J. Mol. Model.* **2009**, *15*, 469–479. DOI:10.1007/s00894-008-0432-7
24. K. Fukui, *Acc. Chem. Res.* 1981, *14*, 363–368. DOI:10.1021/ar00072a001
25. C. Gonzalez, H. B. Schlegel, *J. Chem. Phys.* 1989, *90*, 2154–2161. DOI:10.1063/1.456010
26. C. Gonzalez, H. B. Schlegel, *J. Phys. Chem.* 1990, *94*, 5523–5527. DOI:10.1021/j100377a021

Povzetek

S teorijo gostotnega funkcionala smo z uporabo B3LYP / 6-31g (d) funkcionalnega in baznega seta preučevali mehanizem tvorbe N- (karbomilkarbamotioil) benzamida in rezultate primerjali s podatki, dobljenimi iz časovnega spremljanja poteka reakcije z ¹H NMR spektroskopijo. Ugotovili smo, da za potek reakcije lahko predlagamo dve prehodni stanji: **Ts1** (stopnja, ki določa hitrost reakcije) z izredno nestabilnimi delci, ki za nadaljevanje reakcije zahtevajo določeno orientacij in **Ts2** z nižjo energijo, ki vodi do produkta. Računanje reakcijska pot je bila izvedena tudi z uporabo B3PW91 / 6-31G (d), M06 / 6-31G (d) in Wb97XD / 6- 31G (d) funkcionalnih in baznih setov, a dobljeni rezultati ne dopuščajo zanesljive napovedi reakcijske poti.

Scientific paper

Biological Significance of Hetero-Scaffolds Based Gold(III) Complexes

Darshana N. Kanthecha,¹ Dilip B. Raval,² Vasudev R. Thakkar²
and Mohan N. Patel^{1,*}

¹ Department of Chemistry, Sardar Patel University, Vallabh Vidyanagar–388 120,
Gujarat, India, Phone number: (+912692) 226856*218

² B. R. Doshi School of Bioscience, Sardar Patel University, Vallabh Vidyanagar-388 120, Gujarat, India

* Corresponding author: E-mail: jeenen@gmail.com

Received: 18-11-2017

Abstract

Synthesized ligands and complexes, $[\text{Au}(\text{L}^n)\text{Cl}_2]\text{Cl}$, have been characterized by various techniques such as elemental analysis, LC-MS, FT-IR, UV-Vis, ^1H and ^{13}C NMR spectroscopy, conductance measurement and magnetic moments measurement. The experimental results show that complexes exhibit higher antibacterial activity against Gram^(+ve) and Gram^(-ve) microorganisms than free ligands. The *in vitro* cytotoxicity and cellular level cytotoxicity suggest that Au(I-II) complexes show better activity than corresponding ligands. The DNA interaction study has been evaluated using absorption titration. The experimental evidence indicates ($K_b = 1.08 - 3.44 \cdot 10^5 \text{ M}^{-1}$) that all the complexes have been bind to HS-DNA by intercalation mode. To further verify the nature of interaction viscosity measurement and molecular modeling have been carried out which suggest the intercalation binding between complex and DNA. The *Schizosaccharomyces pombe* cell DNA cleavage has been performed using agarose gel and their photographic images of complexes show smearing of DNA due to DNA cleavage from the nucleus.

Keywords: Gold(III) complexes; DNA interaction; molecular modeling; antibacterial activity; *Schizosaccharomyces pombe* cell

1. Introduction

A recent discovery is focused on metal based chemotherapeutics targeting the double-helix DNA, due to the interesting structural diversity of metal complexes caused by different coordination numbers and types of ligands. DNA binding study with metal complexes expand knowledge in molecular biology, which show the possibilities of specifically targeting therapeutically related proteins or enzymes.^{1–3} It is a challenging task to design a metal-based drug, which may be applicable to various medical treatments. The successful use of *cisplatin* as drug in medicine raises the interest in the study of metal complexes and their various biomedical applications.⁴ Complexes with square planar geometry (d^8 system), isoelectronic and isostructural to platinum(II) complexes have been designed as potential alternatives for binding with DNA.⁵ DNA binding has gained main attention on biological activities because DNA contains exact genetic data for maintaining the function of cell growth. DNA replication is essential for the life cycle of

biological organisms. The alteration of the DNA replication occurs when the drugs bind to the site of the DNA, which leads to the inhibition of the DNA replication. The drugs that exhibit such types of alteration in DNA are known as anticancer agents. Also, metal complexes can interact with biomolecules irreversibly and enhanced the effectiveness and lower the dosages for *in vivo* application. Cytotoxicity of drugs is habitually associated with their DNA-binding properties.^{6,7} Therefore, DNA interaction study has a great importance for the design of new transition-metal drugs and their biological applications.⁸ Application of gold(III) complexes are interesting and developing topics in the area of nanomaterial, nanotechnology, and catalyst.⁹ In the last decade, new studies of gold(III) complexes have been focused on the treatment of cancer,¹⁰ rheumatoid arthritis,¹¹ HIV,¹² malaria¹³ and antiproliferative action.¹⁴ Comparatively, metals, including nickel, cadmium, chromium, and arsenic, can prompt carcinogenesis and hence are less favorable to the body. These limitations have triggered a search for platinum/gold-based compounds that show low-

er toxicity, higher selectivity and a broader spectrum of activity.¹⁵ By following the interactions between gold complexes and various biological targets, much progress can be made in understanding the mode of action of gold complexes. The low doses on a daily basis for capacity oral administration are the main challenge for a new gold-based drug, in addition to improved cytotoxicity and pharmacological profile.¹⁶ While developing new gold-based anti-cancer drugs, it is essential to design a drug that would target a specific biological site, resulting in minimizing or no unwanted side effects.¹⁷ Gold(III) complexes are promising anticancer agents with enhanced stability, having a superior chemotherapeutic index in terms of increased bio-availability, higher cytotoxicity, and promising selectivity associated with lower toxicity towards healthy tissues. Therefore, *in vitro* screening should be mandatory and should be followed by relevant *in vivo* studies, which remain the most important evaluation of drug effectiveness in preclinical sites.¹⁸ In comparison to *cisplatin*, gold(I) and gold(III) complexes represent a class of compounds that have shown to possess both *in vitro* and *in vivo* cytotoxicity, antimicrobial activity and different mode of action, and have received great attention among medicinal inorganic chemists.^{19,20} Anticipated *in vivo* reduction of gold(III) complexes in the mammalian environment, selection of N-coordinating bidentate and polydentate chelating ligands can satisfactorily stabilize complexes under physiologically relevant conditions. Some complexes possess equal or higher cytotoxicity than *cisplatin*.^{21–24}

The N-coordinating hydrazone and their metal complexes have been investigated earlier demonstrating potential biological application.^{25–27} Various derivatives of Schiff bases based on pyridine, pyrimidine, coumarin, quinoline, benzoxazole, indole, purine, pyrrole, furan, benzofuran and triazoles moieties have been reported earlier for their biological activities, such as antibacterial, antitubercular, anti-inflammatory, anthelmintic, antiviral and antioxidant activities.^{28,29} Gold(III) complexes are the great promise as new pharmacological agents. Therefore, to examine the biological activity of gold(III) complexes, synthesis and characterization of gold(III) complexes have been carried out. The interaction of gold(III) complexes with HS-DNA has been investigated using UV-Vis spectroscopy, viscosity measurement and molecular modeling. The *in vitro* cytotoxicity and *in vivo* cytotoxicity of gold(III) complexes examined with a brine shrimp bioassay and *S. pombe* cell, respectively. The antibacterial activity of the synthesized complexes was determined by determining their MIC (minimum inhibitory concentration) values against five different microorganisms.

2. Materials and Method

2.1. Materials and Reagents

All analytical grade chemicals and solvent were purchased commercially and used as received without further

purification. $\text{HAuCl}_4 \cdot 3\text{H}_2\text{O}$ was purchased from S.D. Fine-Chem Ltd. (India.). 2,2-Dipyridylketone, 2-pyridine-carboxaldehyde, 2-acetylpyridine, phenylhydrazine, benzhydrazide, HS-DNA and EDTA were purchased from Sigma Aldrich Chemical Co. (India). Agarose, Luria Broth (LB), ethidium bromide (EtBr), Tris-acetyl-ESTA (TAE) and bromophenol blue were purchased from Himedia (India). Culture for antibacterial activity *Bacillus subtilis* (*B. subtilis*-7193), *Staphylococcus aureus* (*S. aureus*-3160), *Pseudomonas aeruginosa* (*P. aeruginosa*-1688), *Escherichia coli* (*E. coli*-433) and *Serratia marcescens* (*S. marcescens*-7103) were purchased from the Institute of Microbial Technology (Chandigarh, India).

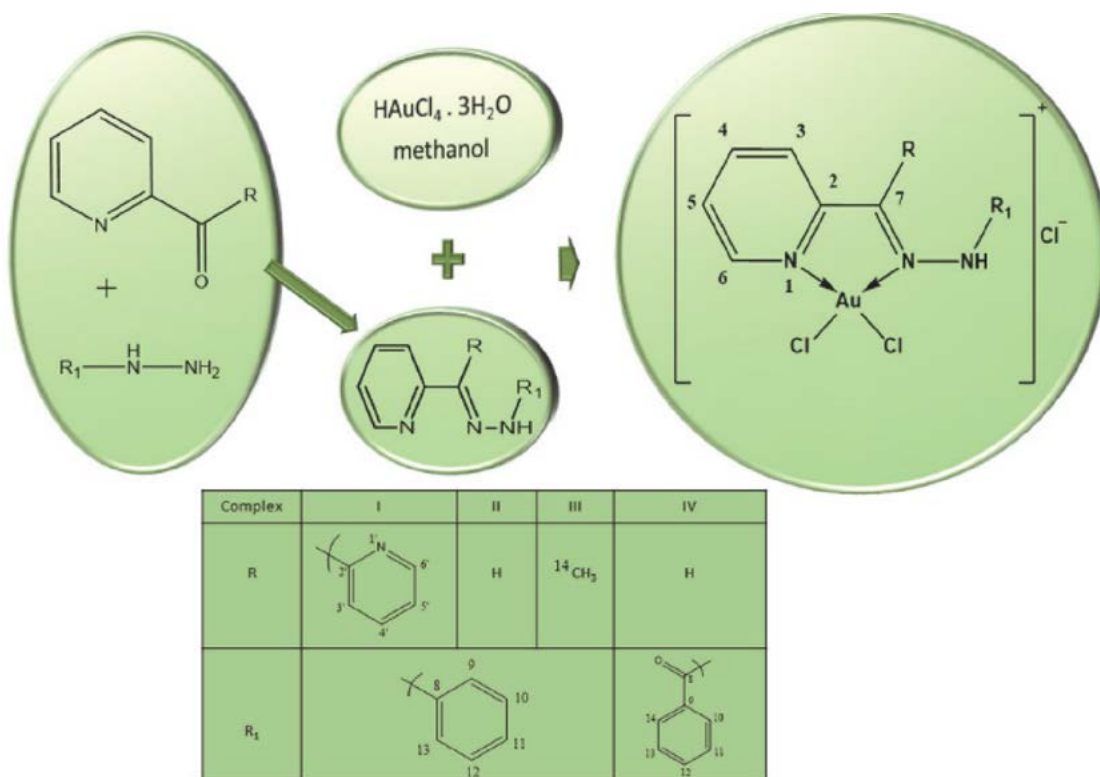
2.2. Physical Measurement

The ^1H and ^{13}C NMR spectra were recorded with a Bruker Avance (400 MHz) spectrometer using deuterated dimethyl sulfoxide and deuterated chloroform solvent. FT-IR Shimadzu spectrophotometer was used for IR spectra in the range 4000–300 cm^{-1} . C, H, and N elemental analysis were performed with a model Perkin-Elmer 240 elemental analyser. Melting points were determined in open capillaries on hermoCal10 melting point apparatus (Analab Scientific Pvt. Ltd, India). The LC-MS spectra were recorded using Thermo scientific mass spectrometer (USA). The electronic spectra of metal complexes were recorded on a UV-160A UV-Vis spectrophotometer, Shimadzu, Kyoto (Japan). The Gouy's method used for magnetic measurement of metal complexes taking mercury tetrathiocyanatocobaltate(II) as the calibrant ($\chi_g = 16.44 \cdot 10^{-6}$ cgs units at 20 °C), citizen balance. Antibacterial study was carried out by means of laminar air flow cabinet Toshiba, Delhi (India). AlphaDigiDoc™ RT. Version V.4.0.0 PC-Image software, CA (USA) used for the Photo quantization of the DNA cleavage activity.

2.3. Synthesis and Spectral Characterization of Ligands

Generally, Schiff base was prepared by condensation of ketone/aldehyde with an amine as per earlier reported literature method.²⁵ The reaction mixture of substituted pyridyl ketone (0.05 mol), substituted hydrazine (0.05 mol) and 4–5 drops of conc. HCl (as a catalyst) in methanol (15 mL) were refluxed with stirring for 6 h. After completion of the reaction, the reaction mixture was cooled to room temperature and the resulting yellow solids were collected by filtration, washed with ethanol and dried in vacuo. General reaction scheme for the synthesis of ligand and complexes is shown in Scheme 1.

2,2'-((2-Phenylhydrazono)methylene)dipyridine (L^1) It has been synthesized according to the above procedure using 2,2'-dipyridyl ketone and phenylhydrazine. Yield: 72%, m.p. 186 °C, mol. wt. 274.33 g mol^{-1} ; Anal. Calc. for



Scheme 1. Synthesis of ligands (L¹-L⁴) and their gold(III) complexes (I-IV).

C₁₇H₁₄N₄: calc. (found) (%): C, 74.43 (74.23); H, 5.14 (5.17); N, 20.42 (20.45). ¹H NMR (400 MHz, CDCl₃-d₁) δ/ppm: 6.93–6.98 (1H, m, H₁₁), 7.25–7.36 (6H, m, H_{5,5',9,10,12,13}), 7.74–7.83 (3H, m, H_{3,4,4'}), 8.02 (1H, d, *J* = 8.0 Hz, H₃), 8.59 (1H, d, *J* = 4.8 Hz, H₆), 8.75 (1H, d, *J* = 4.8 Hz, H₆), 13.83 (1H, s, NH). ¹³C NMR (100 MHz, CDCl₃-d₁) δ/ppm: 113.7 (CH C_{9,13}), 122.3 (CH C₁₁), 123.5 (CH C_{3,3'}), 125.4 (CH C_{5,5'}), 129.2 (CH C_{10,12}), 136.6 (CH C_{4,4'}), 144.4 (C_{quaternary} C₈), 147.9 (CH C_{6,6'}), 153.2 (C_{quaternary} C_{2,2'}), 157.8 (C_{quaternary} C₇). FT-IR (KBr, 4000–400 cm⁻¹): 3270 ν(N-H)_{stretching}; 3047 ν(C-H)_{stretching}; 1589 ν(C=N); 1427 ν(C=C); 1149 ν(C-N); 794 ν(C-H)_{bending}. LC-MS (*m/z*, %): 275 (100) [M⁺].

2-((2-Phenylhydrazono)methyl)pyridine (L²) It has been synthesized according to the above procedure using 2-pyridinecarboxaldehyde and phenylhydrazine. Yield: 68%, m.p. 195 °C, mol. wt. 197.24 g mol⁻¹. Anal. Calc. for C₁₂H₁₁N₃: calc. (found) (%): C, 73.07 (73.21); H, 5.62 (5.40); N, 21.30 (21.15). ¹H NMR (400 MHz, CDCl₃-d₁) δ/ppm: 6.91–6.95 (1H, m, H₁₁), 7.15–7.20 (3H, m, H_{5,9,13}), 7.29–7.34 (2H, m, H_{10,12}), 7.70 (1H, dd, *J* = 1.6, 6.0 Hz, H₄), 7.82 (1H, s, H₃), 8.02 (1H, d, *J* = 8.0 Hz, H₆), 8.18 (1H, s, H₇), 8.55 (1H, s, NH). ¹³C NMR (100 MHz, CDCl₃-d₁) δ/ppm: 113.0 (CH C_{9,13}), 119.6 (CH C₃), 120.7 (C₁₁), 122.5 (CH C₅), 129.3 (CH C_{10,12}), 136.2 (CH C₄), 137.2 (CH C₇), 144.1 (C_{quaternary} C₈), 149.0 (CH C₆), 154.5 (C_{quaternary} C₂). FT-IR (KBr, 4000–400 cm⁻¹): 3271 ν(N-H)_{stretching}; 3086

ν(C-H)_{stretching}; 1527 ν(C=N); 1465 ν(C=C); 1149 ν(C-N); 750 ν(C-H)_{bending}. LC-MS (*m/z*, %): 197 (100) [M⁺].

2-(1-(2-Phenylhydrazono)ethyl)pyridine (L³) It has been synthesized according to the above procedure using 2-acetylpyridine and phenylhydrazine. Yield: 75%, m.p. 166 °C, mol. wt. 211.27 g mol⁻¹. Anal. Calc. for C₁₃H₁₃N₃: calc. (found) (%): C, 73.91 (73.85); H, 6.20 (6.30); N, 19.89 (19.93). ¹H NMR (400 MHz, CDCl₃-d₁) δ/ppm: 2.47 (3H, s, H₁₄), 7.23 (1H, t, *J* = 6.0 Hz, H₁₁), 7.39 (1H, d, *J* = 7.2 Hz, H₉), 7.48 (1H, d, *J* = 6.8 Hz, H₁₃), 7.66 (1H, t, *J* = 8.0 Hz, H₅), 7.92 (2H, dd, *J* = 7.2, 10.4 Hz, H_{10,12}), 8.08 (1H, t, *J* = 3.6 Hz, H₄), 8.48 (2H, d, *J* = 10.4 Hz, H_{3,6}), 10.92 (1H, s, N-H). ¹³C NMR (100 MHz, CDCl₃-d₁) δ/ppm: 12.7 (CH₃ C₁₄), 121.3 (CH C_{9,13}), 124.3 (CH C₃), 127.6 (CH C₁₁), 128.6 (CH C₅), 132.1 (CH C_{10,12}), 132.7 (C_{quaternary} C₈), 136.7 (CH C₄), 148.3 (C_{quaternary} C₇), 149.1 (CH C₆), 152.9 (C_{quaternary} C₂). FT-IR (KBr, 4000–400 cm⁻¹): 3255 ν(N-H)_{stretching}; 3024 ν(C-H)_{stretching}; 2823 ν(CH₃)_{stretching}; 1604 ν(C=N); 1450 ν(C=C); 1373 ν(C-C); 1172 ν(C-N); 779 ν(C-H)_{bending}. LC-MS (*m/z*, %): 211 (100) [M⁺].

2-((2-Phenylhydrazono)methyl)pyridine (L⁴) It has been synthesized according to the above procedure using 2-pyridinecarboxaldehyde and benzhydrazide. Yield: 75%, m.p. 142 °C, mol. wt. 225.25 g mol⁻¹. Anal. Calc. for C₁₃H₁₁ON₃: calc. (found) (%): C, 69.32 (69.22); H, 4.92 (4.97); N, 18.66 (18.69); O, 7.10 (7.20). ¹H NMR (400 MHz, CDCl₃-d₁) δ/

ppm: 7.21 (1H, t, $J = 6.0$ Hz, H_{12}), 7.34 (2H, t, $J = 6.0$ Hz, $H_{11,13}$), 7.44 (1H, t, $J = 8.0$ Hz, H_5), 7.64 (1H, t, $J = 6.0$ Hz, H_4) 7.72–8.05 (2H, m, $H_{3,6}$), 8.12 (1H, s, H_7) 8.53 (2H, d, $J = 4.4$ Hz, $H_{10,14}$), 11.21 (1H, s, N-H). ^{13}C NMR (100 MHz, $\text{CDCl}_3\text{-d}_1$) δ /ppm: 121.3 (CH C_3), 124.3 (CH C_4), 127.2 (CH $C_{10,14}$), 128.5 (CH $C_{11,12}$), 132.1 (CH C_{13}), 132.7 ($C_{\text{quaternary}} C_9$), 136.7 (CH C_4), 148.3 (CH C_7), 149.0 (CH C_6), 152.9 ($C_{\text{quaternary}} C_2$), 167.1 (C=O C_8). FT-IR (KBr, 4000–400 cm^{-1}): 3271 $\nu(\text{N-H})_{\text{stretching}}$; 3032 $\nu(\text{C-H})_{\text{stretching}}$; 1689 $\nu(\text{C=O})$; 1604 $\nu(\text{C=N})$; 1450 $\nu(\text{C=C})$; 1165 $\nu(\text{C-N})$; 794 $\nu(\text{C-H})_{\text{bending}}$. LC-MS (m/z , %): 226 (100) [M^+].

2. 4. Synthesis and Spectral Characterization of Gold Complexes

The prepared methanolic solution of a ligand ($\text{L}^1\text{-L}^4$) (0.25 mmol) was added dropwise into $\text{HAuCl}_4 \cdot 3\text{H}_2\text{O}$ (0.25 mmol) in methanol (5 mL) with stirring at room temperature for 10 min and the reaction mixture was refluxed for further 2 h. After complete complexation orange precipitate has appeared and filtered, washed with diethyl ether and dried in vacuo.

[Au(L^1)Cl $_2$]Cl (I) It has been synthesized using 2,2'-(2-phenylhydrazono)methylene)dipyridine (L^1). Yield: 59%, m.p. >250 °C, mol. wt.: 577.64 g mol $^{-1}$; Anal. Calc. for $\text{C}_{17}\text{H}_{14}\text{AuCl}_3\text{N}_4$: calc. (found) (%): C, 35.35 (36.76); H, 2.44 (2.24); N, 9.70 (10.11). ^1H NMR (400 MHz, DMSO- d_6) δ /ppm: 7.69 (1H, t, $J = 6.0$ Hz, H_{11}), 7.89 (3H, d, $J = 5.6$ Hz, $H_{3,10,12}$), 8.01 (2H, d, $J = 7.6$ Hz, $H_{9,13}$), 8.05 (1H, d, $J = 7.2$ Hz, H_3), 8.12–8.16 (1H, m, H_5), 8.38 (2H, dd, $J = 8.0, 9.2$ Hz, $H_{5,6}$), 8.93 (1H, d, $J = 4.8$ Hz, H_4), 9.30 (1H, d, $J = 8.8$ Hz, H_4), 9.35 (1H, d, $J = 7.2$ Hz, H_6), 12.60 (1H, s, N-H). ^{13}C NMR (100 MHz, DMSO- d_6) δ /ppm: 122.1(CH $C_{9,13}$), 123.0(CH C_{11}), 124.3(CH C_3), 125.5(CH C_5), 126.0(CH C_5), 127.8(CH $C_{10,12}$), 131.2(CH C_3), 133.3(CH C_4), 133.6($C_{\text{quaternary}} C_8$), 134.5($C_{\text{quaternary}} C_2$), 135.9(CH C_6), 138.8(CH C_4), 140.2($C_{\text{quaternary}} C_7$), 147.8($C_{\text{quaternary}} C_2$), 150.7(CH C_6). FT-IR (KBr, 4000–400 cm^{-1}): 3271 $\nu(\text{N-H})_{\text{stretching}}$; 3062 $\nu(\text{C-H})_{\text{stretching}}$; 1581 $\nu(\text{C=N})$; 1481 $\nu(\text{C=C})$; 1126 $\nu(\text{C-N})$; 825 $\nu(\text{C-H})_{\text{bending}}$; 416 $\nu(\text{Au-N})$; 347 $\nu(\text{Au-Cl})$. LC-MS (m/z , %): 541 (100) [M^+].

[Au(L^2)Cl $_2$]Cl (II) It has been synthesized using 2-(1-(2-phenylhydrazono)ethyl)pyridine (L^2). Yield: 62%, m.p. >250 °C, mol. wt. 465.11 g mol $^{-1}$; Anal. Calc. for $\text{C}_{12}\text{H}_{11}\text{AuCl}_2\text{N}_3$: calc. (found) (%): C, 30.99 (30.95); H, 2.38 (2.42); N, 9.03 (8.89). ^1H NMR (400 MHz, DMSO- d_6) δ /ppm: 7.15 (1H, d, $J = 4.8$ Hz, H_{11}), 7.27 (1H, d, $J = 5.6$ Hz, H_3), 7.40 (1H, d, $J = 5.2$ Hz, H_4), 7.50–7.67 (3H, m, $H_{7,9,13}$), 7.92–8.22 (3H, m, $H_{6,10,12}$), 8.62–8.72 (1H, m, H_5), 10.63 (1H, s, NH). ^{13}C NMR (100 MHz, DMSO- d_6) δ /ppm: 122.8 (CH $C_{9,13}$), 127.9 (CH C_{11}), 128.9 (CH C_3), 129.7 (CH $C_{10,12}$), 131.3 (CH C_5), 132.6 (CH C_6), 133.3 ($C_{\text{quaternary}} C_8$), 138.3 (CH C_7), 146.0 (CH C_4), 149.1 ($C_{\text{quaternary}}$

C_2). FT-IR (KBr, 4000–400 cm^{-1}): 3290 $\nu(\text{N-H})_{\text{stretching}}$; 3055 $\nu(\text{C-H})_{\text{stretching}}$; 1597 $\nu(\text{C=N})$; 1427 $\nu(\text{C=C})$; 1134 $\nu(\text{C-N})$; 748 $\nu(\text{C-H})_{\text{bending}}$; 509 $\nu(\text{Au-N})$; 354 $\nu(\text{Au-Cl})$. LC-MS (m/z , %): 430 (100) [M^+].

[Au(L^3)Cl $_2$]Cl (III) It has been synthesized using N' -(di(pyridin-2-yl)methylene)benzohydrazide (L^3). Yield: 57%, m.p. >250 °C, mol. wt. 479.13 g mol $^{-1}$; Anal. Calc. for $\text{C}_{13}\text{H}_{13}\text{AuCl}_2\text{N}_3$: calc. (found) (%): C, 32.59 (32.43); H, 2.73 (2.81); N, 8.77 (8.85). ^1H NMR (400 MHz, DMSO- d_6) δ /ppm: 2.38 (3H, s, H_{14}), 6.92 (1H, t, $J = 7.2$ Hz, H_{11}), 7.05 (1H, d, $J = 8.0$ Hz, H_5), 7.18 (1H, s, H_3), 7.31 (2H, t, $J = 6.8$ Hz, $H_{10,12}$), 7.51 (2H, d, $J = 7.6$ Hz, $H_{9,13}$), 8.24 (1H, t, $J = 4.0$ Hz, H_4), 8.67 (1H, d, $J = 5.6$ Hz, H_6), 10.18 (1H, s, N-H). ^{13}C NMR (100 MHz, DMSO- d_6) δ /ppm: 12.9 (CH $_3$ C_{14}), 114.4 (CH $C_{9,13}$), 123.6 (CH C_{11}), 124.2 (CH C_5), 127.36 (CH $C_{10,12}$), 132.0 (CH C_3), 133.6 ($C_{\text{quaternary}} C_7$), 137.3 (CH C_6), 147.4 ($C_{\text{quaternary}} C_8$), 148.2 (CH C_4), 156.1 ($C_{\text{quaternary}} C_2$). FT-IR (KBr, 4000–400 cm^{-1}): 3286 $\nu(\text{N-H})_{\text{stretching}}$; 3001 $\nu(\text{C-H})_{\text{stretching}}$; 2893 $\nu(\text{CH}_3)_{\text{stretching}}$; 1604 $\nu(\text{C=N})$; 1494 $\nu(\text{C=C})$; 1435 $\nu(\text{C-C})$; 1157 $\nu(\text{C-N})$; 825 $\nu(\text{C-H})_{\text{bending}}$; 510 $\nu(\text{Au-N})$; 339 $\nu(\text{Au-Cl})$. LC-MS (m/z , %): 443 (100) [M^+].

[Au(L^4)Cl $_2$]Cl (IV) It has been synthesized using 2-(2-phenylhydrazono)methylpyridine (L^4). Yield: 55%, m.p. >250 °C, mol. wt. 493.12 g mol $^{-1}$; Anal. Calc. for $\text{C}_{13}\text{H}_{11}\text{AuCl}_2\text{N}_3\text{O}$: calc. (found) (%): C, 31.66 (31.50); H, 2.25 (2.18); N, 8.52 (8.90). ^1H NMR (400 MHz, DMSO- d_6) δ /ppm: 7.07 (1H, d, $J = 2.4$ Hz, H_{12}), 7.20 (1H, d, $J = 2.0$ Hz, H_3), 7.33 (1H, s, H_7), 7.52 (2H, t, $J = 7.6$ Hz, $H_{11,13}$), 7.60 (1H, t, $J = 4.4$ Hz, H_5), 7.66 (1H, t, $J = 2.8$ Hz, H_4), 7.93 (2H, d, $J = 11.6$ Hz, $H_{10,14}$), 8.13 (1H, dd, $J = 7.6, 12$ Hz, H_6), 11.50 (1H, s, N-H). ^{13}C NMR (100 MHz, DMSO- d_6) δ /ppm: 122.8 (CH $C_{10,14}$), 127.9 (CH C_5), 128.2 (CH $C_{11,13}$), 128.9 (CH C_3), 129.7 (CH C_{12}), 130.0 (CH C_6), 132.3 (CH C_4), 133.0 ($C_{\text{quaternary}} C_9$), 138.4 (CH C_7), 149.1 ($C_{\text{quaternary}} C_2$), 165.9 (C=O C_8). FT-IR (KBr, 4000–400 cm^{-1}): 3270 $\nu(\text{N-H})_{\text{stretching}}$; 3093 $\nu(\text{C-H})_{\text{stretching}}$; 1720 $\nu(\text{C=O})$; 1597 $\nu(\text{C=N})$; 1481 $\nu(\text{C=C})$; 1157 $\nu(\text{C-N})$; 748 $\nu(\text{C-H})_{\text{bending}}$; 417 $\nu(\text{Au-N})$; 347 $\nu(\text{Au-Cl})$. LC-MS (m/z , %): 458 (100) [M^+].

3. Biological Screening of Synthesized Compounds

3. 1. UV-Vis Absorbance Titration

Binding mode and interaction strength of DNA with metal complexes have been examined effectively by electronic absorption spectra (UV-Vis absorbance titration) using Herring Sperm DNA (HS-DNA) with $\epsilon = 12858 \text{ dm}^3 \text{ mol}^{-1} \text{ cm}^{-1}$ in phosphate buffer solution (pH 7.2). The stock solutions of the complexes were prepared in DMSO. The absorption titration has been performed by the con-

centration of complex keeping constant (20 μM) and continuous adding the volume of DNA (100 μL), and incubated for 10 min at room temperature. By using absorption spectral titration data K_b value have been determined from the ratio of the slope to intercept from the plot of $[\text{DNA}]/(\epsilon_a - \epsilon_f)$ versus $[\text{DNA}]$.³⁰

3. 2. Viscosity Measurement

An Ubbelohde viscometer maintained at a constant temperature of 27 ± 0.1 °C in a thermostatic jacket. It was used to measure the flow time of HS-DNA in phosphate buffer (pH 7.2) with a digital stopwatch. Flow time measurements of each compound were carried out three times to calculate average flow time. Data were presented as relative specific viscosity ($(\eta/\eta_0)^{1/3}$) versus binding ratio ($[\text{Drug}]/[\text{DNA}]$),³¹ where η and η_0 is the viscosity of DNA in the presence of complex and viscosity of DNA alone, respectively. Viscosity values have been calculated from the observed flow time of DNA containing solutions ($t > 100$ s), corrected for the flow time of buffer alone (t_0), $\eta \propto (t - t_0)$.³²

3. 3. Molecular Docking Study

The interaction between DNA and complexes at the molecular level were studied by advanced computational technique. The rigid molecular docking study has been executed using HEX 8.0 software to conclude the orientation of the Au(III) complexes binding to DNA. The most stable configuration was selected as the input for investigation. Mole file of coordinates of metal complexes was prepared for optimized structure and was rehabilitated to .pdb format using CHIMERA 1.5.1 software. HS-DNA used in the experimental, the structure of the DNA of sequence (5'-d(CGCGAATTCGCG)-3')₂ (PDB id: 1BNA, a familiar sequence used in oligodeoxynucleotide study) obtained from the Protein Data Bank (<http://www.rcsb.org/pdb>). All calculations were carried out on an Intel CORE i5, 2.20 GHz based machine running MS Windows 8.1 64 bit as the operating system. The default parameters were used for the docking calculation with correlation type shape only, FFT mode at the 3D level, grid dimension of 6 with receptor range 180 and ligand range 180 with twist range 360 and distance range 40.³³

3. 4. In vitro Cytotoxicity

The toxicity of bioactive compounds were carried out using brine shrimp (*Artemia* cysts) lethality bioassay.³⁴ Brine shrimp (*Artemia* cysts) eggs were hatched in a shallow rectangular plastic dish (22 × 32 cm), filled with artificial seawater, which was prepared by dissolving sea salt in double distilled water. An unequal partition was made in the plastic dish with the help of a perforated device. Approximately 50 mg of eggs were sprinkled into the large compartment and was opened to ordinary light. After two

days, nauplii were collected by a pipette from the lighted side. A sample of the test compound was prepared by dissolving 10 mg of each compound in 10 mL of DMSO. From these stock solutions, solutions were transfer to 18 vials to make final concentration 2, 4, 8, 12, 16, and 20 mg mL⁻¹ (three sets for each dilutions were used for each test sample and mean of three sets was used for LC₅₀ calculation), and three vials were kept as control having same amount of DMSO only. When the nauplii were ready, 1 mL of seawater and 10 shrimps were added to each vial, and the volume was adjusted with seawater to 2.5 mL per vial. After 24 h, the number of survivors was counted. Data were analyzed by simple logit method to determine the LC₅₀ values, in which log of concentration of samples were plotted against percentage of mortality of nauplii.

3. 5. Cellular Level Cytotoxicity Assay

Eukaryotic *Schizosaccharomyces pombe* was an important organism for the study of effects of the metal complexes at cellular level (cytotoxicity) to the DNA damage (genotoxicity). *S. pombe* were grown in liquid yeast extract media in 150 mL Erlenmeyer flask containing 50 mL of yeast extract media. To acquire the enough growth of *S. pombe*, flask was incubated at 30 °C on shaker at 150 rpm (24 to 30 h). Then the cell culture was treated with synthesized ligands, complexes and DMSO (as control) at different concentrations (2, 4, 6, 8, 10 mg mL⁻¹), further allowed to growth for 16–18 h. Next day, the treated and control cells were centrifuged at 10,000 rpm for 10 min to remove the media and wash the cells with phosphate buffer saline (PBS) three times. Cells were resuspend in 500 μL of PBS. Take the 10 μL of cells suspension and 10 μL 0.4% trypan blue dye in vial and incubate for 5 min. at room temperature, then 10 μL from the above mixture were put on glass slide and observed in a microscope (40X). The treated cells were observed as colourless or blue in colour, dead cells permitting the entry of trypan blue dye in the cells and appear as blue, whereas the live cells resisted the entry of dye and appear as colourless. Percentage viability was counted in triplicate where number of dead cells and number of live cells were counted in three microscopic fields and calculated average percentage of live cells.³⁵

3. 6. Antibacterial Activity

All of the newly synthesized gold(III) complexes (I–IV) were screened for their antibacterial activity using *Staphylococcus aureus*, *Bacillus subtilis*, *Serratia marcescens*, *Pseudomonas aeruginosa* and *Escherichia coli* micro-organisms. The broth dilution technique has been used to determine the bactericidal effect by minimum inhibitory concentration (MIC) in terms of μM . MIC is the lowest concentration that prevents the microbial growth incubated at 37 ± 1 °C for 24 h. MIC was determined in liquid media containing 0.2–3500 μM of the tested compound. A precul-

ture of bacteria was grown in Luria broth overnight at 37 °C. First culture was used as a control to examine normal growth and second culture 20 μL of the bacteria and compound at the desired concentration were added to monitor bacterial growth by measuring turbidity of the culture after 18 h. If a certain concentration of a compound inhibit bacterial growth, half of the concentration of the compound was tested. This procedure was carried out up to the concentration that inhibited the growth of bacteria. All equipment and culture media were sterilized.

3. 7. DNA Cleavage Study

Effect of compounds on the integrity of *S. pombe* cell's DNA were studied by agarose gel electrophoresis. The *S. pombe* cells were grown and treated as in cellular level cytotoxicity assay. After treatment, cells were harvested by centrifugation 10,000 rpm for 10 min than washed with PBS three times. Cells were resuspended in 0.5 μL of distilled water after removing supernatant, then transferred to screw-cap microfuge tube containing 0.2 mL of lysis buffer (2% Triton X-100, 1% sodium dodecyl sulphate, 100 mM NaCl, 10 mM Tris-HCl (pH 8.0) and 1 mM EDTA (pH 8.0)), 0.2 mL mixture of phenol/chloroform/isoamyl alcohol (25:24:1) and glass beads. Vortex the screw-cap having cells to break the cells for 1 min to 3–4 times with alternating cooling. It was centrifuged for 5 min and transferred the upper aqueous layer to other tube followed by the addition of 3 M sodium acetate (1/10 volume) and 100% ethanol (2.5 volume) and centrifuged again for 5 min. Pellet were collected and wash with 70% ethanol. Then 20–30 μL Tris-EDTA buffer was added in the vial contain pellet. Agarose gel electrophoresis were carried out using 0.8% agarose, Tris-acetate-EDTA buffer and staining with ethidium bromide (0.5 mg mL^{-1}) at 100 V. Image was captured by a CCD camera and Alpha Digi Doc system was used for analysing gel.³⁶

4. Result and Discussion

4. 1. NMR and IR Spectra of Synthesized Compound

The NMR and IR spectra of the synthesized ligands and gold(III) complexes are represented in supplementary material and data are shown in the experimental section. The ^1H NMR spectra of compounds show a downfield shift of the C-6 proton next to the coordinating nitrogen from 0.19 to 0.76 ppm, this indicates that the ligand coordinate to the gold ion. The δ ppm values for the NH hydrogen in complexes I and III show upfield shift by 1.23 and 0.76 ppm, whereas complexes II and IV show downfield shift from 2.08 to 0.3 ppm, respectively, due to different environment near to N–H hydrogen. The δ values of phenyl ring protons in the ligands (L^1 – L^4) are observed at

6.92–7.35 ppm and after the coordination with gold metal ion they are shifted to 6.94–8.61 ppm. Infrared spectra of the ligands show intense band for $\nu(\text{C}=\text{N})_{\text{ar}}$, $\nu(\text{C}-\text{N})_{\text{ar}}$, $\nu(\text{C}-\text{H})_{\text{ar}}$, $\nu(\text{C}=\text{C})_{\text{ar}}$, $\nu(\text{N}-\text{H})$ at 1527–1604 cm^{-1} , 1149–1172 cm^{-1} , 3024–3086 cm^{-1} , 1427–1465 cm^{-1} and 3255–3271 cm^{-1} , respectively. In gold(III) complexes band are slightly shifted for $\nu(\text{C}=\text{N})_{\text{ar}}$, $\nu(\text{C}-\text{N})_{\text{ar}}$, $\nu(\text{C}-\text{H})_{\text{ar}}$, $\nu(\text{C}=\text{C})_{\text{ar}}$, $\nu(\text{N}-\text{H})$ at 1581–1604 cm^{-1} , 1126–1157 cm^{-1} , 3001–3093 cm^{-1} , 1427–1481 cm^{-1} , 3270–3290 cm^{-1} , respectively and intense band for $\nu(\text{Au}-\text{N})$ appear in the region 416–510 cm^{-1} and $\nu(\text{Au}-\text{Cl})$ in the region 339–354 cm^{-1} .³⁷ According to these data we can conclude that ligands coordinate to the gold ion.

4. 2. Magnetic Moments, Electronic Spectra and Conductance Measurements

Magnetic moments measurement of gold(III) complexes has been carried out at room temperature. The μ_{eff} value of gold(III) complexes are zero B.M, which corresponds to all paired electron in low-spin 5d^8 configuration and confirms that gold complexes have +3 oxidation states with low-spin $t_{2g}^6 e_g^2$ configuration. The electronic spectra (Fig. 1) of all the complexes in DMSO exhibit intra-ligand charge transfer band (π – π^*) and MLCT band (n – π^*) at 254–274 nm and 290–327 nm, respectively. The molar conductivity value of the gold(III) complexes are in the range of 83–102 $\text{cm}^2 \Omega^{-1} \text{mol}^{-1}$ at room temperature, which suggests the electrolytic nature of metal complexes having one counter ion outside the coordination sphere. So, we conclude that all synthesized gold(III) complexes having chlorine as counter ion and square-planar geometry. The single-crystal structure of similar square-planer gold(III) with bidentate N, N/N, C ligation have also been reported.^{38–40}

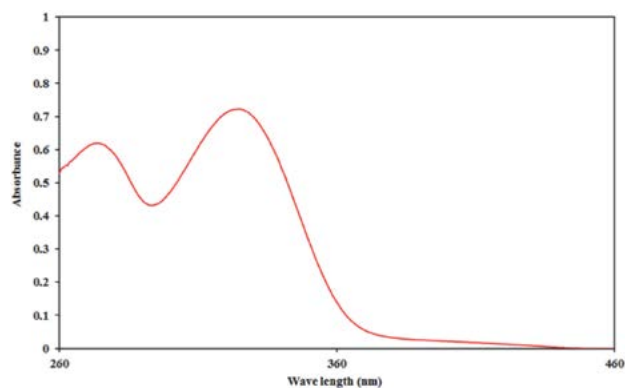


Figure 1. UV absorption spectra of representative complex I in DMSO

4. 3. Binding Behaviour of Complex with HS DNA

Electronic absorption titration is one of the technique to investigate the binding mode of metal complexes

with DNA and provides intrinsic DNA binding constants (K_b) using Herring Sperm DNA (HS-DNA) with $\epsilon = 12858 \text{ dm}^3 \text{ mol}^{-1} \text{ cm}^{-1}$ in phosphate buffer solution (pH 7.2). Strong stacking interaction among chromophore of complex and DNA base pair result in hypochromic shift and red shift (bathochromic shift) in absorption spectra which generally indicate that intercalation binding.^{41,42} The increase in DNA volume leads to hypochromic shift with bathochromic shift (Fig. 2), and concludes the intercalation mode of binding between compounds and DNA base pair. The plot of $[DNA]/(\epsilon_a - \epsilon_f)$ versus $[DNA]$ were analyzed to evaluate K_b determined from the spectroscopic titration data from the following equation:

$$\frac{[DNA]}{[\epsilon_a - \epsilon_f]} = \frac{[DNA]}{[\epsilon_b - \epsilon_f]} + \frac{1}{K_b(\epsilon_b - \epsilon_f)} \quad (1)$$

K_b values for gold(III) complexes I–IV (Fig. 2) are $3.05 \cdot 10^5 \text{ M}^{-1}$, $3.44 \cdot 10^5 \text{ M}^{-1}$, $1.08 \cdot 10^5 \text{ M}^{-1}$ and $2.75 \cdot 10^5 \text{ M}^{-1}$, respectively. Complex II shows higher binding affinity towards HS-DNA in comparison to other complex.

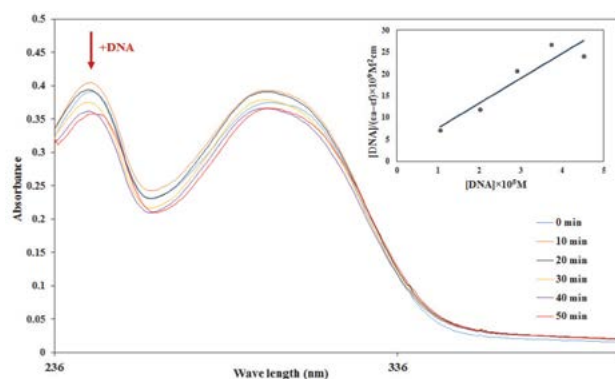


Figure 2. Absorption spectra of complex I with increasing concentration of HS-DNA after incubation for 10 min for each addition at 37 °C in phosphate buffer (pH 7.2). Inset: Plots of $[DNA]/(\epsilon_a - \epsilon_f)$ versus $[DNA]$ for the titration of DNA with gold(III) complexes.

4. 4. Hydrodynamic Volume Measurement

Viscosity measurement is the most useful study of DNA interaction in the absence of X-ray crystallographic data.³¹ Interaction of complex moiety with DNA alters the length of DNA duplex and directly influences on the intrinsic viscosity. The intrinsic viscosity depends on the mode of interaction with concentration of complexes. This phenomenon may be explained by insertion of the complex between base pairs, leading to an increase in the separation of base pairs at the intercalation sites and thus an increase in overall DNA length.⁴³ The increase in viscosity confirms that the Au(III) complexes are bound to HS-DNA by intercalation. Plot of relative specific viscosity $(\eta/\eta_0)^{1/3}$ versus $[\text{complex}]/[\text{DNA}]$ in Fig. 3 shows increase in viscosity of the DNA with the addition of complexes.

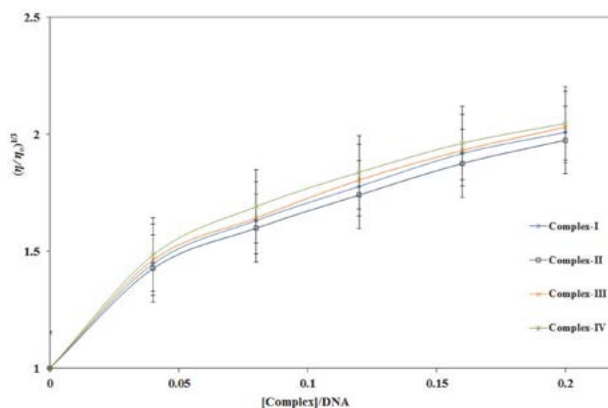


Figure 3. Effect on relative viscosity of HS DNA under the influence of increasing amount of complexes at $37 \pm 0.1 \text{ }^\circ\text{C}$ in phosphate buffer (pH 7.2) with standard deviation.

4. 5. Orientation of Docked Structure

Docking study was implemented to determine the orientation and to calculate binding energy of the gold(III) complexes with DNA using HEX 8.0 software. Molecular docking study of the complexes with the B-DNA (PDB ID: 1BNA) duplex of sequence $(5'\text{-d}(\text{CGCGAATTCGCG})\text{-}3')_2$ was performed to investigate binding site along with the preferred orientation of complex inside the DNA helix. The study show that the complexes under investigation interact with DNA via an intercalation mode involving outside edge stacking interaction with oxygen atom of the phosphate back bone. From the ensuing docked structures, it is clear that the complexes fit well into the intercalative mode of the targeted DNA and A–T rich region stabilized by van der Waal's interaction and hydrophobic contacts.⁴⁴ The theoretically found binding energies of

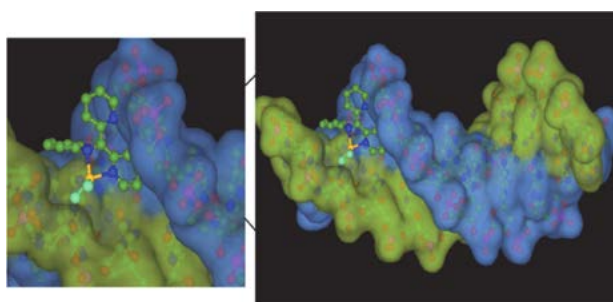


Figure 4. Docked structure of complex I with the HS-DNA duplex of sequence $(5'\text{-d}(\text{CGCGAATTCGCG})\text{-}3')$

docked complexes I–IV are -264.01 , -229.63 , -261.34 and $-261.19 \text{ kJ mol}^{-1}$, respectively. The more negative values of the binding energy, more effective binding between DNA and target molecules.⁴⁵ The docking study is shown preferential intercalation binding when complexes interact with DNA. Results obtained by molecular docking suggest similar binding as determined by viscosity measurements and absorption titrations.

4. 6. Brine Shrimp Lethality Bioassay

For the discovery and isolation of bioactive compounds with significant cytotoxic potential, the simple and inexpensive methodology employed was Brine shrimp (*Artemia cysts*) lethality bioassay.³⁴ By this activity, we can discover commercially important bioactive compounds. Data were analyzed by the log concentration of sample vs % mortality of nauplii that gives LC₅₀ values. LC₅₀ values of synthesized ligands and gold(III) complexes in the range of 12.0–26.2 µg/mL and 7.1–12.5 µg/mL, respectively. The obtained results were compared with the standard drug cisplatin (LC₅₀ = 3.13 µg/mL).⁴⁶ Cytotoxicity of synthesized ligand and complexes are shown in Fig. 5, which suggest that tested compounds exhibit strong ability to interact with the biological model system and the effectiveness of the compound is ordered as follows: cisplatin > I > IV > II > III > L¹ > L⁴ > L³ > L². Most of the drugs exert their pharmacological effects by interaction with the biological system through receptors, subcellular components and enzyme. The brine shrimp assay had served the purpose of exploration of numerous pharmacological properties of natural products as well as synthesized compound to serve as a potential candidate for the preparation of effective medicines against various diseases.⁴⁷

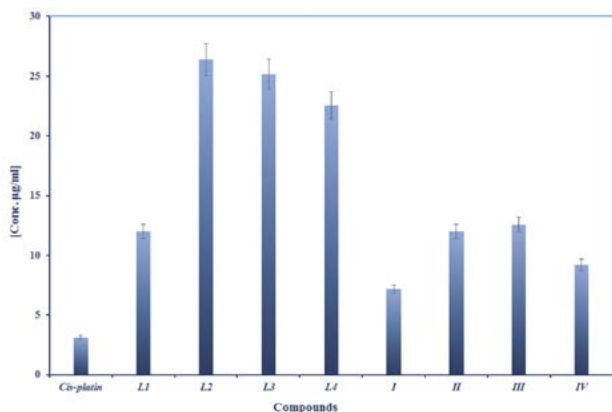


Figure 5. Cytotoxicity of synthesized ligand and complexes by brine shrimp assay.

4. 7. In vivo Cytotoxicity

Cytotoxic study of synthesized compounds at a cellular level has been carried out through eukaryotic *Schizosaccharomyces pombe* (*S. pombe*) cell.⁴⁴ A comparative cytotoxicity of free ligand and their complexes was carried out by trypan blue assay. After 17 hours of the treatment, many of the *S. pombe* cells were killed due to toxic nature of the compound. The observed cytotoxicity data of ligands and complexes are in the range of 76–95% and 60–88%. From the data recorded, complex I is the most potent amongst all the compounds. From Fig. 6, it is concluded that the synthesized complexes are the good cytotoxic agent than that of respective ligands. The order of potency

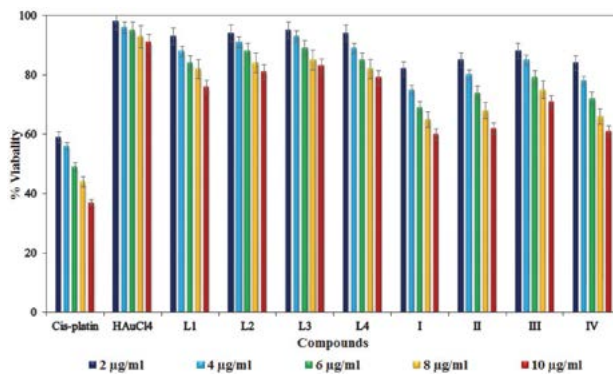


Figure 6. *S. pombe* cell viability represents as the percentage with standard deviation for three independent experiments of synthesized compounds.

of compounds is cisplatin > I > IV > II > III > L¹ > L⁴ > L³ > L² > HAuCl₄. A general reflection of the result is that toxicity varies with the N-donor moiety and as the concentration of compounds increased the cytotoxicity was also increased.

4. 8. Antibacterial Activity

Bioactivation potentials were evaluated using minimum inhibition concentration (MIC). MIC value is a minimum concentration of compounds that induced a complete growth inhibition. All the synthesized gold(III) complexes (I–IV) have been screened for their antibacterial activity against two Gram^(+ve) (*Bacillus subtilis* (*B. subtilis*-7193) and *Staphylococcus aureus* (*S. aureus*-3160)) and three Gram^(-ve) (*Pseudomonas aeruginosa* (*P. aeruginosa*-1688), *Escherichia coli* (*E. coli*-433) and *Serratia marcescens* (*S. marcescens*-7103)) bacteria. A comparative study of *in vitro* antibacterial activity of the ligands and their complexes indicates that the metal complexes increase activity against five different bacteria. Reason for this enhancing of antibacterial activity of complexes may be considered in the light of an Overton's concept⁴⁴ and chelation theory.⁴⁸ As summarized in Figure 7, MIC values of li-

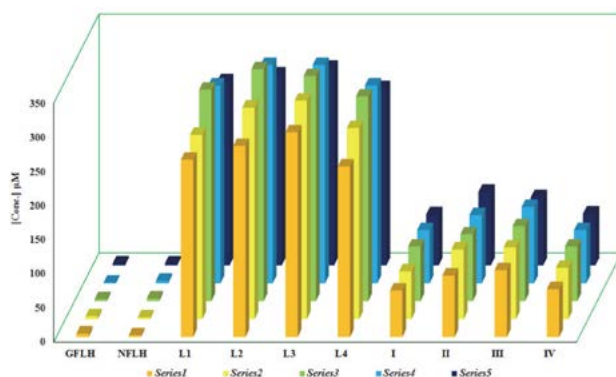


Figure 7. Minimum inhibition concentration (MIC) values of synthesized compounds given in µM.

gands and complexes are in the range of 250–340 μM and 68–112 μM , respectively. The results show that the complexes are more effective compared to the ligands but less effective compared to the standard drugs gatifloxacin (GFLH) and norfloxacin (NFLH). The complex I and IV are comparatively potent than complex II and III against all bacteria. Antimicrobial activity of cisplatin drug has been reported earlier against *S. aureus*, *P. aeruginosa* and *E. coli*, and comparable results suggest that synthesized gold(III) complexes are more effective on bacteria.⁴⁹

4. 9. Effect of the Compound on the Integrity of *S. pombe* Cell's DNA

DNA extraction has been carried out from *S. pombe* cells for the study of DNA cleavage by agarose gel electrophoresis.³⁶ The effects of the compound on the integrity of DNA are shown in Figure 8.

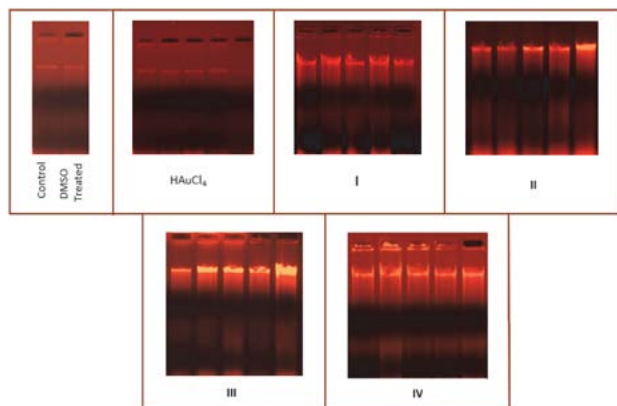


Figure 8. Photogenic view of cleavage of *S. pombe* DNA ($1 \mu\text{g L}^{-1}$) with series of compounds using 1% agarose gel containing $0.5 (\mu\text{g L}^{-1})$ EtBr. All reactions were incubated in TE buffer (pH 8) at a final volume of $10 \mu\text{g L}^{-1}$ for 24 h at 37°C .

The smearing of DNA in agarose gel suggests that the damage occurs due to the toxic nature of the compound, whereas control cell DNA appeared in the intact band. The complexes exhibit good genotoxicity compare to metal salt and ligands. So, the complexes are toxic at the cellular level and break the DNA from the nucleus to express their toxic effect. The general observation from the Fig. 8 is that the smearing of DNA is increases with the increase in the amount of complexes, which suggests the cytotoxic nature of the complexes.

5. Conclusion

In this study, pyridyl moiety based hydrazone N-coordinating ligand and gold(III) based complexes have been synthesized and characterized by ^1H NMR, ^{13}C NMR and IR spectroscopy and LC-MS. The observed values

from conductivity measurement and magnetic moment suggest the square planar geometry of gold(III) complexes having one chloride as the counter ion. Electronic absorption titration and viscosity studies suggest intercalation mode of binding between the compound and HS-DNA duplex. Further binding mode verifying by the data generated from docking study promote that intercalating orientation with HS-DNA duplex of sequence $(5\text{'-d}(\text{CGC-GAATTCGCG})\text{-3'})_2$. All complexes show strong *in vitro* and *in vivo* cytotoxicity and antibacterial activity. Result of DNA cleavage by gel electrophoresis shows DNA smearing due to the toxicity of compounds. The all biological experiments illustrate that the gold(III) complexes as potential biologically active agent. So, this study hypothesize that further detailed investigation of these compounds can explore the potential useful pharmacological effects.

6. Conflict of Interest

The authors report no conflicts of interest. The authors alone are responsible for the content and writing of the paper.

7. Acknowledgments

The authors thankful to the Head, Department of Chemistry, Sardar Patel University, Vallabh Vidyanagar, Gujarat, India, for providing the laboratory facilities, SAIF Panjab university for C, H, N and ESI-MS analysis, DST-PURSE Sardar Patel University, Vallabh Vidyanagar for LC-MS analysis. U.G.C. New Delhi for providing financial assistance of UGC-BSR grant No. C/2013/BSR/Chemistry/1573.

8. References

1. K. C. Nicolaou, D. Rhoades, Y. Wang, R. Bai, E. Hamel, M. Aujay, J. Sandoval, J. Gavriluyuk, *J. Am. Chem. Soc.* **2017**, *139*, 7318–7334. DOI:10.1021/jacs.7b02655
2. H.-J. Zhong, L. Lu, K.-H. Leung, C. C. L. Wong, C. Peng, S.-C. Yan, D.-L. Ma, Z. Cai, H.-M. David Wang, C.-H. Leung, *Chem. Sci.* **2015**, *6*, 5400–5408. DOI:10.1039/c5sc02321a
3. C. Yang, W. Wang, J.-X. Liang, G. Li, K. Vellaisamy, C.-Y. Wong, D.-L. Ma C.-H. Leung, *J. Med. Chem.* **2017**, *60*, 2597–2603. DOI:10.1021/acs.jmedchem.7b00133
4. T. Yang, C. Tu, J. Zhang, L. Lin, X. Zhang, Q. Liu, J. Ding, Q. Xu, Z. Guo, *Dalton Trans.* **2003**, 3419–3424. DOI:10.1039/B305109A
5. N. Pantelić, B. B. Zmejkovski, J. Trifunović-Macedoljan, A. Savić, D. Stanković, A. Damjanović, Z. Juranić, G. N. Kaluderović, T. J. Sabo, *J. Inorg. Biochem.* **2013**, *128*, 146–153. DOI:10.1016/j.jinorgbio.2013.08.002

6. M. N. Patel, B. S. Bhatt, P. A. Dosi, *Spectrochim. Acta, Part A* **2013**, *110*, 20–27. DOI:10.1016/j.saa.2013.03.037
7. S. Tabassum, S. Yadav, *Inorg. Chim. Acta* **2014**, *423*, 204–214. DOI:10.1016/j.ica.2014.07.056
8. R. Vafazadeh, A. C. Willis, M. M. Heidari, N. Hasanzade, *Acta Chim. Slov.* **2014**, *62*, 122–129. DOI: 10.17344/acsi.2014.797
9. V. Amani, A. Abedi, S. Ghabeshi, H. R. Khavasi, S. M. Hosseini, N. Safari, *Polyhedron* **2014**, *79*, 104–115. DOI:10.1016/j.poly.2014.04.064
10. C. D. Sanghvi, P. M. Olsen, C. Elix, S. Peng, D. Wang, Z. Chen, D. M. Shin, K. I. Hardcastle, C. E. MacBeth, J. F. Eichler, *J. Inorg. Biochem.* **2013**, *128*, 68–76. DOI:10.1016/j.jinorgbio.2013.07.014
11. A. E. Finkelstein, D. T. Walz, V. Batista, M. Mizraji, F. Roisman, A. Misher, *Ann. Rheum. Dis.* **1976**, *35*, 251–257.
12. P. N. Fonteh, F. K. Keter, D. Meyer, *J. Inorg. Biochem.* **2011**, *105*, 1173–1180. DOI:10.1016/j.jinorgbio.2011.05.011
13. K. Fourmy, M. Gouygou, O. Dechy-Cabaret, F. Benoit-Vical, *C. R. Chim.* **2017**, *20*, 333–338. DOI:10.1016/j.crci.2016.06.008
14. T. V. Serebryanskaya, A. S. Lyakhov, L. S. Ivashkevich, J. Schur, C. Frias, A. Prokop, I. Ott, *Dalton Trans.* **2015**, *44*, 1161–1169. DOI:10.1039/C4DT03105A
15. U. Ndagi, N. Mhlongo, M. E. Soliman, *Drug. Des. Devel. Ther.* **2017**, *11*, 599–616. DOI:10.2147/DDDT.S119488
16. V. Milacic, Q. P. Dou, *Coord. Chem. Rev.* **2009**, *253*, 1649–1660. DOI:10.1016/j.ccr.2009.01.032
17. C. Marzano, L. Ronconi, F. Chiara, M. C. Giron, I. Faustinelli, P. Cristofori, A. Trevisan, D. Fregona, *Int. J. Cancer* **2011**, *129*, 487–496. DOI:10.1002/ijc.25684
18. C. Nardon, G. Boscutti, D. Fregona, *Anticancer Res.* **2014**, *34*, 487–492.
19. C. Martín-Santos, E. Michelucci, T. Marzo, L. Messori, P. Szumlas, P. J. Bednarski, R. Mas-Ballesté, C. Navarro-Raninger, S. Cabrera, J. Alemán, *J. Inorg. Biochem.* **2015**, *153*, 339–345. DOI:10.1016/j.jinorgbio.2015.09.012
20. B. D. Glisic, M. I. Djuran, *Dalton Trans.* **2014**, *43*, 5950–5969. DOI:10.1039/C4DT00022F
21. S. Iwashita, Y. Saito, H. Ohtsu, K. Tsuge, *Dalton Trans.* **2014**, *43*, 15719–15722. DOI:10.1039/C4DT02279C
22. S. J. Sabounchei, P. Shahriary, S. Salehzadeh, Y. Gholiee, D. Nematollahi, A. Chehregani, A. Amani, *New J. Chem.* **2014**, *38*, 1199–1210. DOI:10.1039/C3NJ01042B
23. K. N. Kouroulis, S. K. Hadjikakou, N. Kourkoumelis, M. Kubicki, L. Male, M. Hursthouse, S. Skoulika, A. K. Metsios, V. Y. Tyurin, A. V. Dolganov, E. R. Milaeva, N. Hadjiliadis, *Dalton Trans.* **2009**, 10446–10456. DOI:10.1039/B909587J
24. S. Wang, W. Shao, H. Li, C. Liu, K. Wang, J. Zhang, *Eur. J. Med. Chem.* **2011**, *46*, 1914–1918. DOI:10.1016/j.ejmech.2011.02.031
25. M. Bakir, O. Green, M. Wilmot-Singh, *J. Mole. Struct.* **2010**, *967*, 174–182. DOI:10.1016/j.molstruc.2010.01.005
26. G. Tamasi, L. Chiasserini, L. Savini, A. Segal, R. Cini, *J. Inorg. Biochem.* **2005**, *99*, 1347–1359. DOI:10.1016/j.jinorgbio.2005.03.009
27. A. A. R. Despaigne, J. G. d. Silva, A. C. M. d. Carmo, F. Sives, O. E. Piro, E. E. Castellano, H. Beraldo, *Polyhedron* **2009**, *28*, 3797–3803. DOI:10.1016/j.poly.2009.07.059
28. V. T. Angelova, V. Valcheva, N. G. Vassilev, R. Buyukliev, G. Momekov, I. Dimitrov, L. Saso, M. Djukic, B. Shivachev, *Biorg. Med. Chem. Lett.* **2017**, *27*, 223–227. DOI:10.1016/j.bmcl.2016.11.071
29. K. El-mahdy, A. El-Kazak, M. Abdel-Megid, M. Seada, O. Farouk, *Acta Chim. Slov.* **2016**, *63*, 18–25. DOI:10.17344/acsi.2015.1555
30. P. A. Dosi, M. N. Patel, B. S. Bhatt, *Acta Chim. Slov.* **2012**, *59*, 622–631.
31. G. Cohen, H. Eisenberg, *Biopolymers* **1969**, *8*, 45–55. DOI:10.1002/bip.1969.360080105
32. S. Mondal, B. Pakhira, A. J. Blake, M. G. B. Drew, S. K. Chattopadhyay, *Polyhedron* **2016**, *117*, 327–337. DOI:10.1016/j.poly.2016.05.052
33. M.-L. Liu, M. Jiang, K. Zheng, Y.-T. Li, Z.-Y. Wu, C.-W. Yan, *J. Coord. Chem.* **2014**, *67*, 630–648. DOI:10.1080/00958972.2014.884218
34. B. N. Meyer, N. R. Ferrigni, J. E. Putnam, L. B. Jacobsen, D. E. Nichols, J. L. McLaughlin, *Planta Med.* **1982**, *45*, 31–34. DOI:10.1055/s-2007-971236
35. J. V. Mehta, S. B. Gajera, M. N. Patel, *J. Biomole. Struct. Dyn.* **2016**, *1*–9. DOI:10.1080/07391102.2016.1189360
36. P. B. Patel, V. Thakkar, *Asian J. Cell Biol.* **2013**, *8*, 22–32. DOI:10.3923/ajcb.2013.22.32
37. R. Křikavová, J. Hošek, P. Suchý, J. Vančo, Z. Trávníček, *J. Inorg. Biochem.* **2014**, *134*, 92–99. DOI:10.1016/j.jinorgbio.2014.02.002
38. R. W.-Y. Sun, C.-M. Che, *Coord. Chem. Rev.* **2009**, *253*, 1682–1691. DOI:10.1016/j.ccr.2009.02.017
39. M. Frik, J. Fernández-Gallardo, O. Gonzalo, V. Mangas-Sanjuan, M. González-Alvarez, A. Serrano del Valle, C. Hu, I. González-Alvarez, M. Bermejo, I. Marzo, M. Contel, *J. Med. Chem.* **2015**, *58*, 5825–5841. DOI:10.1021/acs.jmedchem.5b00427
40. A. N. Wein, A. T. Stockhausen, K. I. Hardcastle, M. R. Saadein, S. Peng, D. Wang, D. M. Shin, Z. Chen, J. F. Eichler, *J. Inorg. Biochem.* **2011**, *105*, 663–668. DOI:10.1016/j.jinorgbio.2011.01.006
41. S. Mistri, H. Puschmann, S. C. Manna, *Polyhedron* **2016**, *115*, 155–163. DOI:10.1016/j.poly.2016.05.003
42. M. Gaber, H. A. El-Ghamry, S. K. Fathalla, *Spectrochim. Acta, Part A* **2015**, *139*, 396–404. DOI:10.1016/j.saa.2014.12.057
43. M. N. Patel, M. R. Chhasatia, D. S. Gandhi, *Biorg. Med. Chem. Lett.* **2009**, *19*, 2870–2873. DOI:10.1016/j.bmcl.2009.03.078
44. J. V. Mehta, S. B. Gajera, P. Thakor, V. R. Thakkar, M. N. Patel, *RSC Adv.* **2015**, *5*, 85350–85362. DOI:10.1039/C5RA17185G
45. N. Deepika, C. S. Devi, Y. P. Kumar, K. L. Reddy, P. V. Reddy, D. A. Kumar, S. S. Surya, S. Satyanarayana, *J. Photochem. Photobiol., B* **2016**, *160*, 142–153. DOI: 10.1016/j.jphotobiol.2016.03.061
46. M. V. Lunagariya, K. P. Thakor, D. N. Kanthecha, M. N. Patel, *J. Organomet. Chem.* **2018**, *854*, 49–63. DOI:10.1016/j.jorganchem.2017.11.012

47. M. N. Ahmed, K. A. Yasin, K. Ayub, T. Mahmood, M. N. Tahir, B. A. Khan, M. Hafeez, M. Ahmed, I. ul-Haq, *J. Mol. Struct.* **2016**, *1106*, 430–439. DOI:10.1016/j.molstruc.2015.11.010
48. B. Tweedy, *Phytopathology* **1964**, *55*, 910–914.
49. N. Chowdhury, T. L. Wood, M. Martínez-Vázquez, R. García-Contreras, T. K. Wood, *Biotechnol. Bioeng.* **2016**, *113*, 1984–1992. DOI:10.1002/bit.25963

Povzetek

Sintetizirane ligande in komplekse, $[\text{Au}(\text{L}^n)\text{Cl}_2]\text{Cl}$, smo okarakterizirali z različnimi tehnikami, kot so elementna analiza, LC-MS, FT-IR, UV-Vis, ^1H in ^{13}C NMR spektroskopija, merjenje prevodnosti in magnetnega momenta. Eksperimentalni rezultati kažejo, da imajo kompleksi višjo antibakterijsko aktivnost proti Gram(+) in Gram(-) mikroorganizmom kakor prosti ligandi. *In vitro* citotoksičnost in citotoksičnost na celičnem nivoju kažeta, da imajo Au(III) kompleksi boljše aktivnosti kakor ligandi. Študija interakcij z DNA je bila izvedena z absorpcijsko titracijo. Na podlagi eksperimentalnih podatkov ($K_b = 1.08 - 3.44 \cdot 10^5 \text{ M}^{-1}$) sklepamo, da se vsi kompleksi interkalirajo na HS-DNA. Za dodatno potrditev narave interakcij smo izvedli meritve viskoznosti in tudi molekulske modeliranje. Spremljali smo tudi cepitev DNA pri *Schizosaccharomyces pombe* na agarose gelu, pri čemer posnetki kažejo cepitev DNA.

Scientific paper

Polypropylene Blends with m-EPR Copolymers: Mechanical and Rheological Properties

Iztok Švab,^{1,*} Anđela Pustak,^{2,*} Matjaž Denac,³ Andrijana Sever Škapin,⁴
Mirela Leskovac,⁵ Vojko Musil^{3,6} and Ivan Šmit²

¹ ISOKON, Production and Processing of Thermoplastics, Ltd, Mestni trg 5a, 3210 Slovenske Konjice, Slovenia

² Ruđer Bošković Institute, Division of Materials Chemistry, Bijenička 54, 10002 Zagreb, Croatia

³ University of Maribor, FEB Maribor, Institute of Technology, Razlagova 14, 2000 Maribor, Slovenia

⁴ Slovenian National Building and Civil Engineering Institute, Department of Materials, Laboratory for polymers, Dimičeva 12, 1000 Ljubljana, Slovenia

⁵ University of Zagreb, Faculty of Chemical Engineering and Technology, Savska 16, 10 000 Zagreb, Croatia

⁶ Faculty of polymer technology, Ozare 19, 2380 Slovenj Gradec, Slovenia

* Corresponding author: E-mail: Iztok.Svab@isokon.si

phone: ++386 (0)3 757 11 37; fax: ++386 (0)3 757 10 63

apustak@irb.hr

phone: ++ 385 1 457 1255

Received: 22-11-2017

Abstract

The effects of two metallocene ethylene-propylene-based elastomers (m-EPR1 and m-EPR2) differing in molecular mass and viscosity on mechanical, rheological and interfacial properties were compared. The m-EPR elastomers were added to iPP in 2.5, 5, 10, 15, and 20 vol.%. Torque values, elongation at break and impact strength measured of the iPP/m-EPR1 blends were higher than the iPP/m-EPR2 blends due to higher molten viscosity of m-EPR1 than m-EPR2 copolymer. Slight differences in Young moduli as well as in tensile strength at yield and at break might indicate that tensile properties of iPP/m-EPR blends were not significantly affected by difference in viscosity or molecular mass, miscibility and spherulite size. Optimization diagrams indicated the metallocene m-EPR copolymers are efficient impact modifiers for polypropylene and showed good balancing of mechanical properties in iPP/m-EPR blends.

Keywords: Isotactic polypropylene; metallocene ethylene-propylene-based elastomers; blends; mechanical properties; adhesion parameters

1. Introduction

The addition of different types of specially designed elastomers to isotactic polypropylene is the common way to increase the toughness and to improve impact properties of the polypropylene. The blending of the semi-crystalline isotactic polypropylene by melt mixing with different elastomeric rubbers have been studied for three decades now.¹⁻¹² The most frequent used elastomers in modification of isotactic polypropylene are ethylene propylene diene monomer (EPDM),²⁻³ ethylene-propylene rubber (EPR),^{4,5,6,7} styrene-butadiene-styrene triblock copolymer (SBS),^{8,9} or

styrene-ethylene/butylene-styrene triblock copolymer (SEBS)^{9,10} and elastomer PEOC, copolymer of ethylene and octene (PEOC).¹¹ The prior role of this elastomers is to modify/improve the impact properties of polyolefins and to achieve certain level of compatibility (e.g. partial miscibility or co-crystallinity if possible) with polymeric matrix to additionally improve other properties as well.

The investigation of polypropylene-based copolymers or ethylene-propylene elastomers with polyolefins, was mostly oriented on achieving better optimization of mechanical properties and consequently other properties as well.

Zhang and coworkers studied the influence of copolymerization on structure and mechanical properties of iPP/EPR random copolymer in situ blends. The investigation showed that the mechanical properties of the blends, including the impact strength and flexural modulus, depended on copolymerization conditions. The impact strength was influenced also by the amount of random copolymer.¹²

Nitta et al. investigated the mechanical properties for the binary blends of isotactic polypropylene (iPP) and random copolymers of ethylene–propylene (EP).¹³ The iPP/EP blends were partly miscible in the melt. The addition of the novel EP copolymers played an important role in the modification of mechanical properties of iPP and final morphology.¹³ Grain et al. studied the influence of the molecular weight of dispersed phase in ethylene–propylene rubber in modified isotactic polypropylene (iPP/EPR) blend.¹⁴ The ductile–brittle transitions did not correlate linearly with M_w , suggesting the macroscopic behavior of the blend is controlled by the morphology of the EPR particles. Dynamical mechanical analysis (DMA) showed relationship between molecule relaxation processes and mechanical properties. Similar investigation was done by Oracio and coworkers¹⁵ who studied the rubber molecular relaxations with DMA and obtained information about mechanical characteristics and the deformation mechanisms for the investigated iPP/EPR materials.¹⁵ Oracio and coworkers showed that the iPP phase is more effective in stiffening the matrix and provide better tensile elastic behaviour than EPR based materials.¹⁵

An iPP/EPR blend in-situ synthesized by spherical Ziegler-Natta catalyst has also been investigated by the same investigation group.¹⁶ The synergistic effect between random copolymer and copolymer has been found to be the key factor for high impact strength at low temperature. The thermal study clearly shows that, polyethylene PE segments of different lengths in the segmented copolymer fractions can form crystalline lamellae of different thickness.¹⁶

The influence of the nucleation (agents) of ethylene–propylene rubber modified isotactic polypropylene on ductile–brittle transition of iPP/EPR blends was studied by Grein and coworker and have found positive effects on mechanical properties.¹⁷

Trongtorsak and coworkers also reported improvement of mechanical properties of iPP/m-EPR blends with

the addition of calcium stearate as β -nucleation agent, especially the improvement of notched Izod and strength.¹⁸

Thereby, metallocene EPR copolymers (m-EPR) with propylene being the major component (> 80 wt% according to producer) were applied as impact modifiers for polypropylene in our investigation. Two chosen Vistamaxx™ thermoplastic elastomers, signed as m-EPR1 and m-EPR2, are actually specialty co/terpolymers of propylene balanced with ethylene and other α -olefins with different viscosity (e.g. different molecular mass) and compatible with various polyolefins in different extent.^{19,20}

The goal was to study the mechanical properties of iPP/m-EPR blends and to compare the experimental and calculated results using some custom models for mechanical properties. Comprehensive study of interaction in iPP/m-EPR blends with different content of elastomer was also performed to estimate the influence of interactivity and possible miscibility of m-EPR elastomers with isotactic polypropylene primarily on mechanical properties.

2. Experimental Part

2.1. Materials

Isotactic polypropylene (trade name Moplen) used as polymer matrix was supplied by LyondellBasell, Netherlands. Two metallocene propylene–ethylene copolymers with different viscosity are used from Exxon Mobil producer.^{19,20} The properties of used polymers and fillers are listed in Table 1.

2.2. Sample Preparation

Binary iPP/m-EPR blends were prepared in a Brabender Plasti-Corder kneading chamber. The content of m-EPR copolymers in blends was 2.5, 5, 10, 15 and 20 vol.%. The components were kneaded for 7 min, in a chamber preheated to 200 °C, with a rotor speed of 50 min^{-1} . After kneading, the melt was rapidly transferred to a preheated laboratory press and compression moulded into 1- and 4-mm thick plates. The pressing temperature was 220 °C, the pressure 100 bar and the pressing time 14 min for 1-mm, and 11.5 min for 4-mm thick plates. The plates were used for specimen preparation for morphology observation and mechanical testing.

Table 1. The properties of used materials

Polymer	Commercial name	Density (g cm^{-3})	MFI ($\text{g } 10^{-1} \text{min}^{-1}$)	M_n (g mol^{-1})	M_w/M_n
iPP	Moplen HP501L	0.90	6.0 ^a	120.000 ^c	5.40
m-EPR1	Vistamaxx-VM-1100	0.863	4.5 ^b	92.900 ^c	3.40
m-EPR2	Vistamaxx-VM-1120	0.863	20	48.100 ^c	2.66

a) according to ISO 1133 (230 °C/2.16 kg) b) according to ISO 1133 (200 °C/5 kg) c) measured with exclusion chromatography with PS standard

2. 3. Testing Methods

2. 3. 1. Steady State Torque (τ_M)

The torque value (τ_M) of iPP/m-EPR blends was determined from the diagram of kneading in the Brabender kneading chamber. The average τ_M value was calculated on the basis of 5 measurements carried out for each sample with the same filling volume.

2. 3. 2. Tensile Tests

Tensile properties of iPP/m-EPR blends (Young's modulus, yield stress and strain, tensile strength at break, elongation at break) were measured according to ISO 527 standard using Zwick 147,670 Z100/SN5A apparatus at 23 °C and strain rate of 2 mm/min. For each sample, 5 measurements were carried out.

2. 3. 3. Notched Impact Strength

Notched impact strength of iPP/m-EPR blends was measured by Zwick apparatus at 25 °C according to Charpy test (DIN 53453). For each sample, 12 measurements were carried out.

2. 3. 4. Contact Angle Measurement

Surface free energies of used polymers, as well as their corresponding dispersive and polar components, were determined by measuring contact angle. Contact angles of the isotactic polypropylene and propylene-ethylene copolymers were measured on a contact angle goniometer DataPhysics OCA 20 Instrument at temperature of 23 °C. Sessile drops (2 μ L) of test liquids: water (distilled twice $\lambda = 1.33 \mu\text{Lcm}^{-1}$), formamide (p.a. 99.5%, Fluka) and diiodomethane (p.a. 99%, Aldrich) were used for the advancing contact angle measurements at 23 °C. The surface tensions of the test liquids used for contact angle measurements are presented in Table 2. The average values of at least five drops at different places of the same sample were taken and the standard deviation was always less than 2%.

Surface free energies of the iPP and elastomers (γ_l) were calculated using harmonic mean equation according to Wu's model presented with equation (1):²¹

$$\gamma_l(1 + \cos \theta) = \frac{4\gamma_s^d \gamma_l^d}{\gamma_s^d + \gamma_l^d} + \frac{4\gamma_s^p \gamma_l^p}{\gamma_s^p + \gamma_l^p} \quad (1)$$

where γ^p was the dispersive and γ^d the polar component of the surface free energy (surface tension), γ_l and γ_s were the surface tension of liquid and surface free energy of solid, respectively.

Surface free energies of the iPP and elastomers were presented in Table 4. The interfacial free energy, γ_{AB} , work

Table 2. Surface free energy (γ), dispersion (γ^d) and polar components (γ^p) of surface free energy of test liquids used for contact angle measurements

Test liquids	$\gamma(\text{mJm}^{-2})$	$\gamma^d(\text{mJm}^{-2})$	$\gamma^p(\text{mJm}^{-2})$
Water	72.8	21.8	51.0
Formamide	58.0	39.0	19.0
Diiodomethane	50.8	50.8	0.0

of adhesion, W_{AB} , and spreading coefficient, S_{AB} , of all polymer/elastomer blend pairs were calculated from obtained γ values using equations (2–4) and presented in Table 5:

$$\gamma_{AB} = \gamma_A + \gamma_B - \frac{4\gamma_A^d \gamma_B^d}{\gamma_A^d + \gamma_B^d} + \frac{4\gamma_A^p \gamma_B^p}{\gamma_A^p + \gamma_B^p} \quad (2)$$

$$W_{AB} = \gamma_A + \gamma_B - \gamma_{AB} \quad (3)$$

$$S_{AB} = \gamma_B - \gamma_A - \gamma_{AB} \quad (4)$$

where subscripts *A* and *B* correspond to the phases in blends (*A*-matrix, *B*- elastomer) and superscripts *d* and *p* mean dispersed and polar components of interfacial free energy γ . The results from Table 4 and Table 5 are presented in *Adhesion parameters of iPP/m-EPR blends* section.

3. Results and Discussion

3. 1. The Mixing Torque Values of the iPP/m-EPR Blends

The mixing torque values (τ_M) provide information how toughening elastomeric m-EPR modifier affect processability of the iPP/m-EPR blends. The torque values can be considered as a measure of the viscosity under the same mixing conditions, including the same filling volume. The torque τ_M increases by adding components in batch mixer and decreases after the polypropylene melting and reaches constant value around sixth minute of mixing (τ_M values in Figure 1 are measured at 7th min) due to process of homogenization and equalized viscosity of blends.²²

The τ_M values of two blend systems begun to diverge already at minimal addition of m-EPR's (2.5 vol.% showed in Figure 1): the blends with m-EPR1 exhibit the trends of somewhat higher τ_M values than with m-EPR2 (especially at 20 vol.% of added m-EPR's) due to significantly higher viscosity of m-EPR1 than m-EPR2 copolymer (see MFI values in Table 1). Moreover, the τ_M values of blends with m-EPR1 (MFI = 4.5 g 10⁻¹min⁻¹) were somewhat higher than plain polypropylene (MFI = 6.0 g 10⁻¹min⁻¹) due to somewhat higher viscosity of m-EPR1 than plain iPP.

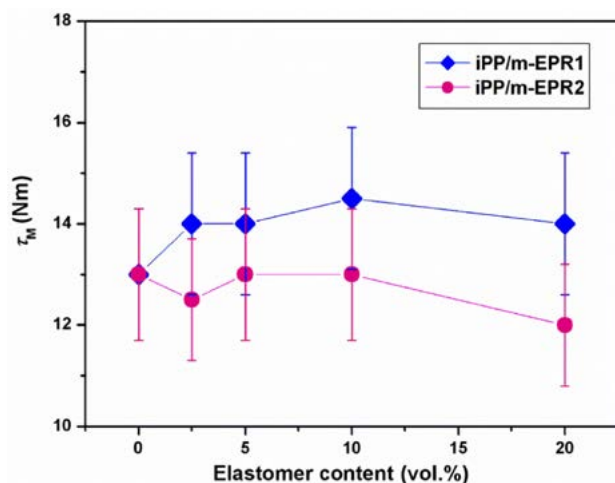


Figure 1. Steady state torque of the iPP/m-EPR blends in dependence on volume content of added elastomers

3. 2. Tensile Test

3. 2. 1. Young's Modulus

The addition of both m-EPR elastomers to iPP matrix decreases Young's modulus steadily and almost linearly due to toughening effect of elastomers (Figure 2).^{7–9,23}

An almost linear decrease of close E values is in accordance with the parallel model with linear combination of plastic and elastomeric components.²⁴ Although m-EPR2 elastomer has significantly lower viscosity than m-EPR1 (MFI = 20 g 10⁻¹min⁻¹ in comparison to 4.5 g 10⁻¹min⁻¹ for m-EPR1) due to lower molecular mass (M_n = 48.100 in comparison to 92.900 g mol⁻¹ for m-EPR1) the blends with m-EPR2 exhibit just minor decline of the E values than blends with m-EPR1 elastomer.

For a further analysis of the E data, the experimental values were compared with the values calculated by the different theoretical models based on the modulus-concentra-

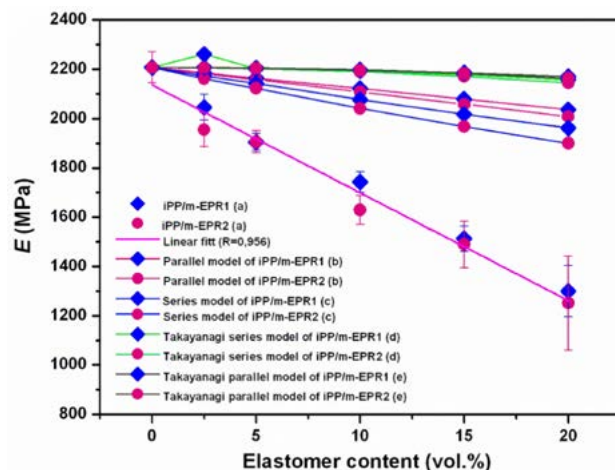


Figure 2. Young's modulus of the iPP/m-EPR blends as a function of the m-EPR content compared to the theoretical predictions: (a) experimental values, (b) parallel model, (c) series model, (d) Takayanagi parallel model, (e) Takayanagi series model

tion dependence of two-phase polymeric materials. The elastic moduli of stiffness of a material is affected by the elastic moduli of all components, fraction of components, the morphology and the interactions between the components. The E models usually presume the idealization about perfect adhesion between the phases, spherical particles and perfectly distributed minor phase through the matrix.^{25,26} The most simple of all models for predicting the moduli of a composite or a blend is known as the parallel model and has been considered as the upper limit of elastic modulus:

$$E_{1,2} = E_1\varphi_1 + E_2\varphi_2 \quad (5)$$

where the $E_{1,2}$ is the elastic modulus of compound, E_1 and E_2 are the elastic modulus of components. The series model represents the lower limit of elastic modulus:

$$\frac{1}{E_{1,2}} = \frac{\varphi_1}{E_1} + \frac{\varphi_2}{E_2} \quad (6)$$

Takayanagi developed a combined series-parallel model for the tensile property E , by introducing a degree of parallelinity into the series model.^{27,28} It was assumed that the two-phase material can be treated as a combination of series and parallel elements. The equation for Takayanagi parallel model is given as:

$$E_{1,2} = \left[\frac{\varphi}{(1-\lambda)E_1 + \lambda E_2} + \frac{1-\varphi}{E_1} \right]; \quad (7)$$

and for series model:

$$E_{1,2} = \lambda \left[\frac{\varphi}{E_2} + \frac{1-\varphi}{E_1} \right]^{-1} + (1-\lambda)E_1. \quad (8)$$

where the E_1 is the property of the matrix phase; E_2 is the property of the dispersed phase. Quantities λ and φ are geometry factors representing phase morphology in the Takayanagi model, whereas the product $\lambda\varphi$ is the volume fraction of the dispersed phase, and is related to the degree of series parallel coupling. Parameters λ and φ vary with composition and with the change in the state of dispersion. For spherical particles independently and homogeneously dispersed in a matrix, it can be assumed that λ is equal to φ .^{27,28} The Figure 2 showed that calculated models have higher values than measured experimental values for iPP/m-EPR blends. Both Takayanagi's models showed almost the same behavior as classic series and parallel model in this case. The divergence can be related with partial miscibility of phases in blends (not only with interfacial adhesion), geometry and dispersion of added phase in polymer matrix and other factors.^{25–28}

3. 2. 2. Yield stress and Strain (Tensile Strength and Elongation at Yield)

Yield stress gives additional information on polymer matrix-elastomer interactions in binary blends besides how the elastomers affect yield stress as impact modifiers.^{2,3} Steady, monotonous decrease of σ_y values with addition of both, m-EPR1 and m-EPR2 elastomers (Figure 3) indicates gradually increase of toughening similarly to gradually reduced stiffness (Figure 2) with increased elastomer content. Slightly higher σ_y values of the iPP/m-EPR2 than iPP/m-EPR1 blends at higher elastomer contents might be ascribed to different factors and will be discussed at *Tensile strength and elongation at break* section.

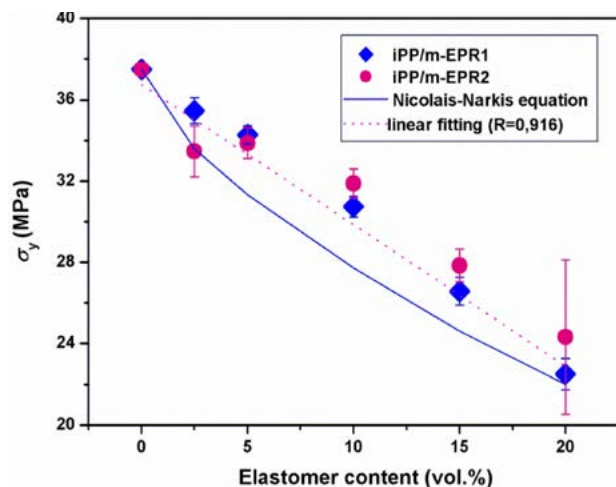


Figure 3. Tensile strength at yield of the iPP/m-EPR blends in dependence on volume content of added elastomers and Nicolais-Narkis model for yield strength

Nicolais and Narkis developed a model for yield strength of polymeric materials containing spherical particles for class of polymer systems based on the interphase properties.²⁹ According to Nicolais–Narkis model, when interfacial adhesion does not exist between polymer and elastomer, the particles in matrix cannot bear the stress and it could be carried only through the matrix. Nevertheless, when a good interfacial adhesion is provided between matrix and dispersed phase the interfacial layer can transfer a fraction of stress from matrix to dispersed phase. So in this case the yield strength includes both matrix and dispersed phase contributions so the simplified equation can be expressed:

$$\sigma_b = \sigma_m(1 - 1.21\phi_f^{2/3}) \quad (9)$$

where σ_b and σ_m are yield strength of blend and matrix and ϕ_f is the volume fraction of particles, assuming that dispersed particles in polymer matrix are spherical and there is a good adhesion. This model corresponds well to iPP/m-

EPR blends containing spherical particles of m-EPR with proved good adhesion, and exhibits somewhat lower values comparing to experimental values (Figure 3).³⁰

The extent of yield strain, ϵ_y , of neat semicrystalline iPP primarily depends on the strengthening of tie molecules in amorphous interlayer (intercrystalline links) and interspherulitic links. Whereas the addition of m-EPR1 affects the elongation at yield negligibly, the addition of m-EPR2 increases yield strain steadily (Figure 4). Stronger strengthening effect of m-EPR2 than m-EPR1 elastomer has been also observed at ternary iPP/silica/m-EPR and composites.³¹ It could be ascribed to better stress transfer from softer m-EPR2 particles as bumpers and better miscibility of m-EPR2 than m-EPR1 with iPP matrix, and might also lead to higher elongations with regard to stiffer m-EPR1 particles. However, more significant divergence in strain behavior in present case could be reasonable due to more effective stretching in simpler binary blend system (without filler).

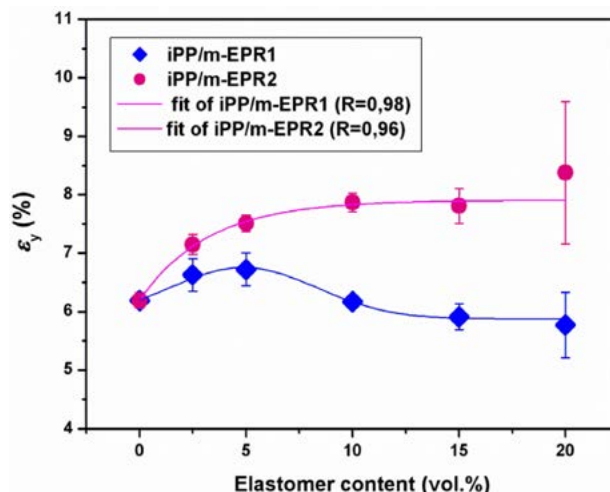


Figure 4. Elongation at yield of the iPP/m-EPR blends in dependence on volume content of added elastomers

3. 2. 3. Tensile Strength and Elongation at Break

Although the incorporation of elastomeric modifiers into iPP matrix might have complex influence to the tensile strength at break, σ_b values of the iPP/m-EPR blends monotonously decrease with increased elastomer content (Figure 5) similarly to steady decrease of E (Figure 2) and σ_y (Figure 3) values. Somewhat higher σ_y and σ_b values of the iPP/m-EPR2 than for iPP/m-EPR1 blends at higher m-EPR2 contents, has been primarily conducted (driven) by the difference in molecular weights of elastomers analogous to similar yield stress behavior.

Higher values of iPP/m-EPR2 might also be ascribed to higher crystallinity and spherulite size, compatibility or miscibility of the iPP/m-EPR2 than iPP/m-EPR1 blends and to stronger interfacial effect (interfacial free energy) at iPP–m-EPR2 interface. However, the effects of mentioned

factors could not be resolved and ascribed to any of mentioned influencing factors due to slight difference in σ_b and ε_b values between these two m-EPR elastomers.

Higher viscosity iPP/m-EPR2 ratio than iPP/m-EPR1 (Figure 1) leads to smaller size of dispersed m-EPR2 than m-EPR1 particles.³¹ Moreover, prolonged crystallization of iPP matrix with additions of both m-EPR's was affected by migration of iPP chains from the remained melt islands of both elastomers, i.e. by solidification effect.³¹ However, higher partial miscibility of the iPP with m-EPR2 than m-EPR1 (proved exactly by DMA³¹) as well as m-EPR2 with lower molecular mass and higher mobility of macromolecules than m-EPR1 macromolecules may more easily diffuse into the iPP interlamellar amorphous layer where they may form domains more or less interconnected with the amorphous iPP phase, thus increasing its thickness.¹⁶

This statement was proved by higher spherulite size of blends with m-EPR2 than m-EPR1 elastomer.³¹ Intra-spherulitically accommodated smaller m-EPR's dispersed particles beside their interspherulitically accommodation may indicate better stress transfer from softer m-EPR2 particles as bumpers and might also lead to higher elongations additionally.

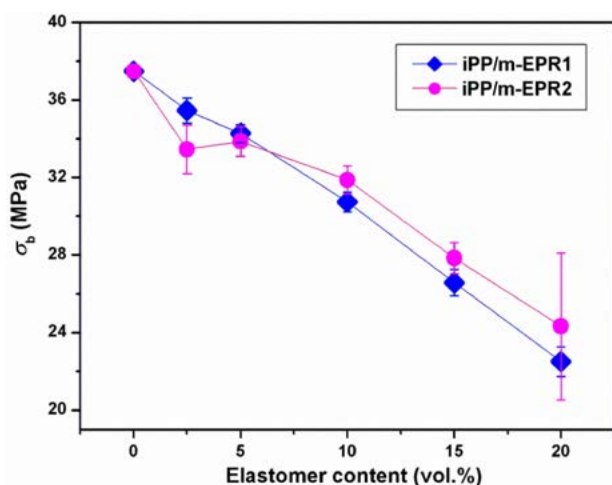


Figure 5. Tensile strength at break of the iPP/m-EPR blends in dependence on volume content of added elastomers

The elongation at break, ε_b , usually behaves inversely to the tensile strength at break, σ_b . Indeed, the ε_b values increases with increased m-EPR1 and m-EPR2 content almost linearly after 2.5 vol.% of elastomer (Figure 6). However, in distinct to σ_b values behavior, ε_b values of both blend systems are very close in whole concentration range. The elongation at break, ε_b after 5 vol.% increases exceptionally fast with respect to pure isotactic polypropylene. The reason for such profound increase is probably the plasticization effect caused by addition of the m-EPR elastomer that has great impact on elongation properties of blends acting like plasticizers dissolved in the matrix phase

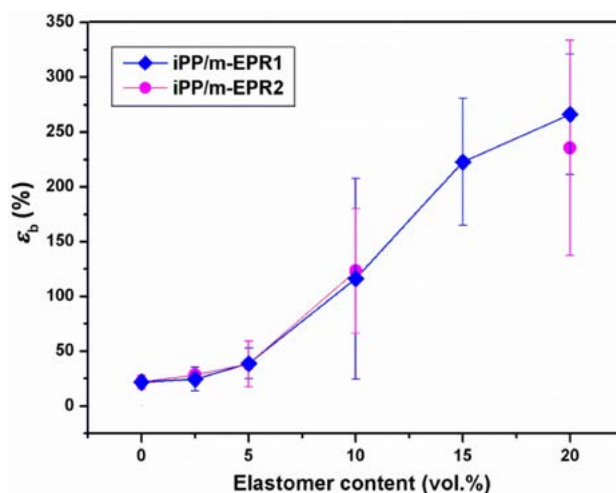


Figure 6. Elongation at break of the iPP/m-EPR blends in dependence on volume content of added elastomer

in large concentration range. The slopes of ε_b iPP/m-EPR for both added elastomers are very similar because of very similar structure of both elastomers.

3. 3. Impact Properties

The incorporation of the m-EPR elastomers toughens plastomeric iPP matrix and increases impact strength, a_K , values almost exponentially (Figure 7). The both m-EPR's considerably improve a_K at additions higher than 10 vol.% of m-EPR's analogously to similar behavior with addition of poly(styrene-*b*-ethylene-*co*-propylene) in iPP.²⁸

These results proved that both m-EPR's have efficient rubber-toughening characteristics for polypropylene. It is known that the phase separation is essential for producing impact-resistant blends for many polymeric systems. The m-EPR elastomer dissolved in the matrix phase can act as a plasticizer, reducing the glass-transition temperature and stiffness of the matrix without increasing its toughness.³²

However, other important facts influencing the impact strength of the iPP must be considered in addition to the afore mentioned facts: (non)existence of β -phase iPP, stiffness reduction, particle-matrix adhesion (or miscibility), etc. The iPP/m-EPR's blends exhibited mainly monoclinic α -form of the iPP in iPP/m-EPR blends,³³ in distinct to the appearing of β -phase in iPP/SEP blends with poly(styrene-*b*-ethylene-*co*-propylene),²⁸ with superior impact resistance to α -phase iPP in present iPP/m-EPR blends.³⁴ However, the toughness of the iPP/m-EPR blends is commensurable with the iPP/SEP blends.²⁸ This fact indicates that new metallocene m-EPR copolymers exhibit higher toughening effect in comparison to SEP elastomer as custom SBC copolymer toughening agents.²⁸ Although the iPP/m-EPR2 blend exhibited doubtless higher degree of miscibility than iPP/m-EPR1 blends,³³ higher a_K values of the iPP/m-EPR1 than for iPP/m-EPR2 blend could be observed in whole concentration range (Figure 7). This fact

could be explained by almost twice higher molecular weight of m-EPR1 than m-EPR2, e.g. by MFI value of m-EPR1 commensurable with the iPP (Table 1) that might affect impact strength in two ways. First, dispersed particles of copolymer with longer macromolecules exhibit higher toughness. Secondly, longer macromolecules or longer olefins segments similar to this one of the iPP chains may provide stronger mutual entanglements improving thus the notched impact strength (Figure 7). Similar difference in toughening effects of these two m-EPR's copolymers has been observed in composites of the iPP/wollastonite and iPP/silica.^{31,35}

Obviously, the effect of macromolecular length prevails the effect of miscibility in toughening of iPP/m-EPR blends.

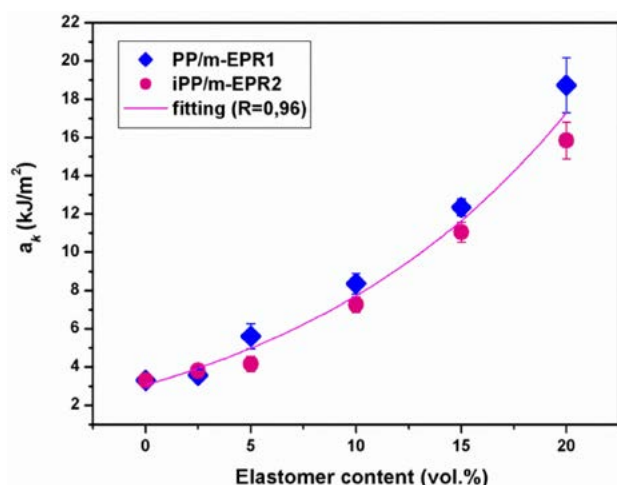


Figure 7. Notched impact strength of the iPP/m-EPR blends in dependence on volume content of added elastomers

3. 4. iPP Matrix-elastomer Interactions

3. 4. 1. Parameter Interactivity B of iPP/m-EPR Blends

The strength of polymer-elastomer interactions can be quantitatively described using Pukanszky's model for particle-based composites, as described in equation (10).³⁶ More specifically, equation (10) allows to investigate a linear relationship existing between the natural logarithm:

$$\ln\left(\frac{\sigma_{yc}}{\sigma_{yp}} \frac{1 + 2,5\varphi_d}{1 - \varphi_d}\right) = \ln \sigma_{yrel} = B\varphi_d \quad (10)$$

where σ_{yc} is the yield stress of elastomer and σ_{yp} is the yield stresses of matrix, respectively; B is a term corresponding to the load carrying capability of the elastomer and depends on elastomer-matrix interactions; φ_d is the elastomer volumetric fraction within polymer matrix. If $\ln[\sigma_{yc}(1 + 2,5\Phi_f)/(\sigma_{yp}(1 - \Phi_f))]$ of fraction value is plotted against of elastomer, parameter B can be calculated as a line slope, with intercept in cross section of coordinate parameter

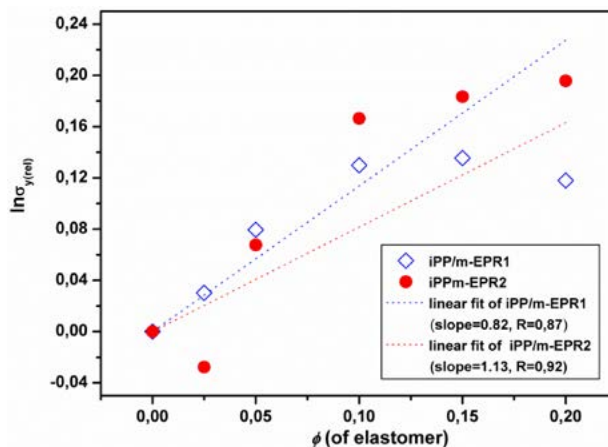


Figure 8. Presentation of calculated $\ln \sigma_{rel}$ values in dependence on elastomer content

Table 3. Interaction parameter B for iPP/m-EPR blends

Blend iPP/m-EPR	Interaction parameter B
iPP/mEPR-1	0.82
iPP/mEPR-2	1.13

axes. This assumes a tensile yield stress of matrix (σ_{yp}) to be constant.

Calculated $\ln \sigma_{rel}$ values were presented in Figure 8 in dependence on elastomer content and proportional to values of Pukanszky's³⁶ interaction parameter showed in Table 3. Higher interaction parameter B value for iPP/m-EPR2 (1.13) than for iPP/m-EPR1 blend (0.82) corresponds to higher σ_y values for iPP/m-EPR2 blend. This fact corresponds well with proved higher miscibility of iPP/m-EPR2 than iPP/m-EPR1 blends.³³

3. 4. 1. Adhesion Parameters of iPP/m-EPR Blends

Interfacial properties may also affect the strength of polymer-elastomer interactions. The results of the studies on the effective adhesion for a given system indicate some conditions as optimal: thermodynamic work of adhesion as a maximal, spreading coefficient as a positive value and interfacial free energy as a minimal (tends to null) (Table 3).^{21,37,38} The surface free energy of the polypropylene and elastomers are showed in Table 4.

Table 4. The surface free energy (γ) of the iPP and elastomers and their dispersive (γ^d) and polar component values (γ^p) evaluated by using the Wu's model²¹

Polymer	The surface free energies (mJ/m ²)		
	γ^d	γ^p	γ
iPP	31.5	1.3	32.8
mEPR-1	26.7	4.7	31.4
mEPR-2	25.3	1.4	26.7

Table 5. Adhesion parameters γ_{AB} , W_{AB} , S_{AB} of the iPP/m-EPR blends

Possible adhesion pairs	Adhesion parameters (mJ/m ²)		
	Interfacial free energy γ_{AB}	Work of adhesion W_{AB}^*	Spreading coefficient S_{AB}^*
iPP/m-EPR1	2.32	62.9	-2.7
iPP/m-EPR2	0.78	59.2	-6.4

* γ_{mf} for calculation according to Wu's equation

Higher interfacial free energy for EPR-1 than for EPR-2 were calculated with Wu's equation (1) (Table 4). The surface free energy for m-EPR1 elastomer is close to value for iPP. The ethylene-propylene copolymers m-EPR1 and m-EPR2 differed in polar component of surface free energy and the m-EPR1 is more polar than m-EPR2 and iPP with almost similar polarity.

Interfacial free energy, γ_{AB} , work of adhesion, W_{AB} , and spreading coefficient, S_{AB} , of all polymer/elastomer pairs for the iPP/m-EPR blends were calculated according to equations (2–4) (Table 5).

However, higher interfacial free energy for iPP-m-EPR1 ($\gamma = 2.32$ mJ/m²) than for iPP-m-EPR2 ($\gamma = 0.78$ mJ/m²) indicates contrary – stronger interfacial effect of the iPP-m-EPR2 than for iPP-m-EPR1 interface. In this case the interfacial free energy, as the inversely proportioned to the strength of intermolecular interactions in polymer blends, would be more relevant for such ambiguous systems.^{39,40,41} Higher interaction parameter B value for the iPP/m-EPR2 than for iPP/m-EPR1 blend seemed to confirm this ambiguous fact.

3. 5. Miscibility/Compatibility and Interactivity

Better miscibility of the iPP/m-EPR2 than iPP/m-EPR1 blend was confirmed with Dinamic Mechanical Analysis, DMA (one mutual intermediary maximum in E''/T curve of the iPP/m-EPR2 blend comparison to two overlapped β -relaxation maxima of the iPP/m-EPR1 blend) in our previous paper.³³ The DMA results as well as biphasic morphology observed by all microscopy techniques suggests that m-EPR2 molecules are not completely dissolved into the iPP amorphous region, i.e. partial miscibility and compatibility between m-EPR2 particles and iPP matrix is better than with m-EPR1.³³ The higher crystallinity due to crystallization across phase boundary at dispersed m-EPR2 particles and increased spherulite size in the iPP/m-EPR2 may affect the yield stress of semicrystalline polymers besides higher miscibility/ compatibility.^{42,43}

The effect of spherulite size on yield stress depends on its position on summary curve tensile strength as a function of spherulite size related to the intraspherulite yield.³¹ Intraspherulitical location of both dispersed m-EPR particles in the iPP matrix had been observed by polarized optical micrographs³¹ interspherulitical accom-

modation. Homogeneous distribution of dispersed m-EPR1 particles (some in radial directions) in TEM micrograph of iPP/m-EPR1 80/20 blend in Figure 9 also indicates intraspherulitical location of m-EPR1 particles.³³

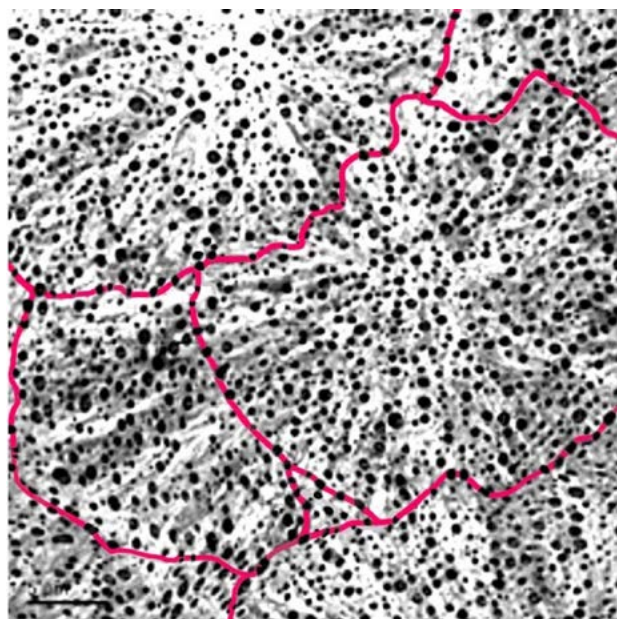


Figure 9. TEM picture of iPP/m-EPR1 80/20 with marked spherulites boundaries indicating intraspherulitical besides interspherulitical accommodation of m-EPR particles

The difference is only in somewhat thinner dispersed m-EPR2 (up to 1,2 μ m) than m-EPR1 particles (up to 2.5 μ m) due to Jordhamo law.⁴⁴ It is well known that dispersed particle size and distribution may affect yield properties. It was proved that the particle size of the elastomer significantly affects the deformation and failure processes in polypropylene toughened with olefinic elastomer being small particle favouring shear yielding while coarser dispersion promotes crazing due to difference in an average surface-to-surface interparticle distance.^{45,46,47}

3. 6. Optimization Diagrams of Mechanical Properties of iPP/m-EPR Blends

Mechanical properties are one of the most respected criteria for choosing right materials for some end-use pur-

pose. Schematic diagrams show the change in some important materials' mechanical properties by introducing one or two components in polymer matrix. The optimization diagrams of such designed materials were used for comparing their mechanical parameters with the pure isotactic polypropylene.

The addition of propylene-ethylene elastomers in isotactic polypropylene decreased the Young's modulus as expected due to toughening effect of elastomers. The yield strength and strength at break also decrease by addition of elastomers and the values are higher for the blends with m-EPR2 elastomer with smaller molecular mass. The few times bigger increase in impact strength in comparison to iPP is the result of addition of soft elastomers in large concentration so the role of impact modifier is completely fulfilled. Higher a_K values of the iPP/m-EPR1 than for iPP/m-EPR2 blend could be explained by almost twice higher molecular weight (longer macromolecules) of m-EPR1 than m-EPR2. Optimization diagram (Figure 10) indicate good balancing of mechanical properties besides efficient effect of metallocene m-EPR copolymers as impact modifiers for polypropylene.

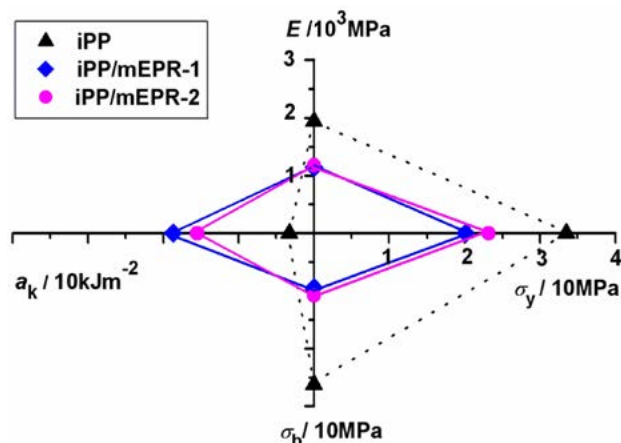


Figure 10. Optimization diagram of mechanical properties of iPP/m-EPR blends with 20 vol.% of added elastomers

4. Conclusions

The effects of two metallocene ethylene-propylene-based elastomers with varied contents (2,5–20 vol.% of m-EPR1 and m-EPR2) differing in molecular mass (viscosity) on mechanical, rheological and interfacial properties of the iPP/m-EPR blends were investigated. While Young's modulus, tensile strength and yield and break of the iPP/m-EPR's blends decreased, impact strength and elongation at break increased with increased elastomer content. Such behavior of presented iPP/m-EPR blends resulted primarily by prevailed toughening or plastification effect caused by spherically shaped dispersed m-EPR particles. Thereby, elongation at break and impact strength as

well as torque values of the iPP/m-EPR1 blends were higher of the iPP/m-EPR2 blends due to higher molecular mass, e.g. higher molten viscosity of m-EPR1 than m-EPR2 copolymer. However, slight divergence of almost linearly decreased E , σ_y and σ_b values of the iPP/m-EPR's blends could be ascribed to different factors (difference in crystallinity and spherulite size, compatibility or miscibility of the iPP with m-EPR's, and interfacial effect at iPP-m-EPR interface) which could not be resolved. So the behavior of these values could not be ascribed to any of mentioned influencing factors particularly; it could be only concluded that the difference in viscosity or molecular length between two m-EPR's does not affect E , σ_y and σ_b values. Somewhat divergence of yield strain values resembles to similar divergence of torque values but in inverse mode. Whereas this divergence in torque values was governed by difference in molten viscosity of copolymers, the divergence of ε_y values was governed by difference in miscibility of m-EPR's with iPP matrix and by difference in stress transfer from m-EPR particles differently soft. Moreover, optimization diagrams indicated beside efficient effect of metallocene m-EPR copolymers as impact modifiers for polypropylene also its balancing effect of mechanical properties.

5. Acknowledgements

Financial support of the Ministry of Science, Education and Sports of the Republic of Croatia and the Ministry of Higher Education, Science and Technology of the Republic of Slovenia is acknowledged.

6. References

- H. G. Karian, in: H. G. Karian (Ed.): Handbook of polypropylene and polypropylene composites, Marcel Dekker, New York, USA, **2003**. DOI:0.1201/9780203911808
- G. Wypych, in: G. Wypych (Ed.): Handbook of fillers, ChemTec Publishing, Toronto, Canada, **2000**.
- R. N. Rotheron, in: R. N. Rotheron (Ed.): Particulate-Filled Polymer Composites, Smithers Rapra Press, Shawbury, UK, **2006**.
- J. Karger-Kocsis, S. Fakirov, in: J. Karger-Kocsis, S. Fakirov (Eds.): Nano- and micromechanics of polymer blends and composites, Carl Hanser Verlag, Munich, Germany, **2010**.
- R. N. Rotheron, in: M. Xanthos (Ed.): Functional Fillers for Plastics, Wiley-VCH Verlag, Weinheim, Germany, **2010**.
- X. Chen, G. Ma, J. Li, S. Jiang, X. Yuan, J. Sheng, *Polym.* **2009**, *50*, 3347–3360. DOI:10.1016/j.polymer.2009.04.069
- D. N. Bikiaris, G. Z. Papageorgiou, E. Pavlidou, N. Vouroutzis, P. Palatzoglou, G.P. Karayannidis, *J. Appl. Polym. Sci.* **2006**, *100*, 2684–2696. DOI:10.1002/app.22849
- M. Z. Rong, M. Q. Zhang, Y. X. Zheng, H. M. Zeng, R. Walter, K. Friedrich, *Polym.* **2001**, *42*, 167–183. DOI:10.1016/S0032-3861(00)00325-6

9. C. L. Wu, M. Q. Zhang, M. Z. Rong, K. Friedrich, *Compos. Sci. Technol.* **2002**, 62, 1327–1340. DOI:10.1016/S0266-3538(02)00079-9
10. T. H. Zhou, W. H. Ruan, Y. L. Mai, M. Z. Rong, M. Q. Zhang, *Compos. Sci. Technol.* **2008**, 68, 2858–3066. DOI:10.1016/j.compscitech.2007.10.002
11. A. Vassiliou, D. N. Bikiaris, E. Pavlidou, *Macromol. React. Eng.* **2007**, 1, 488–501. DOI:10.1002/mren.200700006
12. Y.-Q. Zhang, Z.-Q. Fan, L.-X. Feng, *J. Appl. Polym. Sci.* **2002**, 84, 445–453. DOI:10.1002/app.10415
13. K. Nitta, A. Tanaka, *Polym.* **2001**, 42, 1219–1226. DOI:10.1016/S0032-3861(00)00418-3
14. C. Grein, K. Bernreitner, M. Gahleitner, *J. Appl. Polym. Sci.* **2003**, 87, 1702–1712. DOI:10.1002/app.11696
15. L. D’Orazio, G. Cecchin, *Polym.* **2001**, 42, 2675–2684. DOI:10.1016/S0032-3861(00)00631-5
16. L. D’Orazio, C. Mancarella, E. Martuscelli, G. Sticotti, G. Cecchin, *J. Appl. Polym. Sci.* **1999**, 72, 701–719. DOI:10.1002/(SICI)1097-4628(19990502)72:5<701::AID-APP11>3.0.CO;2-U
17. C. Grein, M. Gahleitner, *Express. Polym. Lett.* **2008**, 2, 392–397. DOI:10.3144/expresspolymlett.2008.47
18. K. Trongtorsak, P. Supaphol, S. Tantayanon, *Polym. Test.* **2004**, 23, 533–539. DOI:10.1016/j.polymertesting.2003.11.006
19. The use of Vistamaxx™ specialty elastomers in Thermoplastic Compounds & Blends, <http://www.baixii.com/upload/files/2015/3/2621142284.pdf> (accessed March 30, 2017).
20. S. Datta, S. Srinivas, G. Racine, in: Novel Propylene-Based Specialty Elastomers- Structure and Properties, ANTEC 62nd annual technical conference, Chicago, USA, **2004**, p. 422.
21. S. Wu, *J. Adhes.* **1973**, 5, 39–55.
22. H. N. Hemmati, H. Nazokdast, H. S. J. Panahi, *J. Appl. Polym. Sci.* **2001**, 82, 1129–1137. DOI:10.1002/app.1947
23. A. Pustak, M. Leskovic, M. Denac, I. Švab, J. Pohleven, M. Makarovič, V. Musil, I. Šmit, *J. Reinf. Plast. Compos.* **2014**, 33, 851–861. DOI:10.1177/0731684413518827
24. U. W. Gedde, in: *Polymer Physics*, Springer Science+Business Media, Dordrecht, Netherlands, **1995**.
25. M. Haghghat, A. Zadhoush, S. Nouri Khorasani, *J. Appl. Polym. Sci.* **2005**, 96, 2203–2211. DOI:10.1002/app.21691
26. H. W. Zhang, J. B. Wang, X. Guo, *J. Mech. Phys. Solids* **2005**, 53, 1929–1950. DOI:10.1016/j.jmps.2005.05.001
27. J. A. Gopi, G. B. Nando, *Adv. Polym. Sci. Techn.* **2014**, 4, 43–51.
28. G. Radonjič, I. Šmit, *J. Polym. Sci. B. Polym. Phys.* **2001**, 39, 566–580. DOI:10.1002/1099-0488(20010301)39:5<566::AID-POLB1030>3.0.CO;2-P
29. L. Nicolais, M. Narkis, *Polym. Eng. Sci.* **1971**, 11, 194–199.
30. Y. Zare, *Int. J. Adhes. Adhes.* **2016**, 70, 191–195.
31. A. Pustak, M. Denac, A. Sever Škapin, I. Švab, V. Musil, I. Šmit, *J. Polym. Res.* **2016**, 23, 163 (1–13).
32. C. B. Bucknall, in: S. G. Aggarwal (Ed.): *Comprehensive Polymer Science: The Synthesis, Characterization, Reactions and Applications of Polymers*, Pergamon, Oxford, UK, **1989**, pp. 27–34. DOI:10.1016/B978-0-08-096701-1.00205-6
33. A. Pustak, I. Švab, E. Govorčin Bajsić, M. Denac, V. Musil, I. Šmit, *Polym. Plast. Technol. Eng.* **2017**, 57(3), 229–241. DOI:10.1080/03602559.2017.1320720
34. M. Fujiyama, *Int. Polym. Proc.* **1998**, 4, 411–416. DOI:10.3139/217.980411
35. I. Švab, V. Musil, A. Pustak, I. Šmit, *Polym. Compos.* **2009**, 30, 1091–1097. DOI:10.1002/pc.20660
36. B. Pukanszky, *Eur. Polym. J.* **2005**, 41, 645–662. DOI:10.1016/j.eurpolymj.2004.10.035
37. V. Mittal, in: V. Mittal (Ed.): *Polymer Nanotube Nanocomposites: Synthesis, Properties, and Applications*, Wiley&Sons, Inc. Hoboken, New Jersey & Scrivener Publishing LLC, Salem, Massachusetts, USA, **2010**, pp. 449–460.
38. S. Steinmann, W. Gronski, C. Friedrich, *Polymer.* **2002**, 43, 4467–4477. DOI:10.1016/S0032-3861(02)00271-9
39. G. Guerrica-Echevarria, J. I. Eguizabal, J. Nazabal *Polym. Test.* **2000**, 19, 849–854. DOI:10.1016/S0142-9418(99)00055-0
40. G. Biresaw, C. J. Carriere, *Compos. Part. A*, **2004**, 35, 313–320. DOI:10.1016/j.compositesa.2003.09.020
41. H. Liang, R. Xu, B.D. Favis, H.P. Schreiber, *Polymer* **1999**, 40, 4419–4423. DOI:10.1016/S0032-3861(98)00767-8
42. M. Jenkins, N. J. Mills, in: *Plastics: Microstructure and Engineering Applications*, 3rd edition, Butterworth-Heinemann for Elsevier, Oxford, UK, **1993**, pp. 229–249.
43. A. K. Ghosal, *Crystallization of Isotactic Poly(Propylenes) with Enchanted Melt Strength*, Ph. D. Thesis, Florida State University, USA, **2008**.
44. G. M. Jordhamo, J. A. Manson, L. H. Sperling, *Polym. Eng. Sci.* **1986**, 26, 517–524. DOI:10.1002/pen.760260802
45. C. Lotti, C. A. Correa, S. V. Canevarolo, *Mat. Res.* **2000**, 3, 37–44. DOI:10.1590/S1516-14392000000200007
46. C. J. Chou, K. Vijayan, D. Kirby, A. Hiltner, E. Baer, *J. Mater. Sci.* **1988**, 23, 2521–2532. DOI:10.1007/BF01111912
47. J. A. W. van Dommelen, W. A. M. Brekelmans, F. P. T. Baaijens, *Mech. Mater.* **2003**, 35, 845–863. DOI:10.1016/S0167-6636(02)00307-1

Povzetek

V delu smo preučevali vpliv dveh metalocenskih elastomerov na osnovi etilena/propilena (m-EPR1 in m-EPR2), ki sta se razlikovala v molekularni masi in viskoznosti, na mehanske, reološke in medpovršinske lastnosti. V iPP matrici smo dodali 2,5, 5, 10, 15 in 20 vol.% m-EPR elastomera. Ugotovili smo, da imajo mešanice iPP/m-EPR1 višje vrednosti torzijskega momenta mešanja, raztezka ob pretrgu in udarne žilavosti kot mešanice iPP/m-EPR2 zaradi višje viskoznosti taline m-EPR1 kot m-EPR2 elastomera. Manjše razlike v Youngovem modulu, meji plastičnosti in natezni trdnosti pri pretrgu kažejo, da natezne lastnosti mešanic iPP/m-EPR niso v veliki meri odvisne od viskoznosti ali molekulske mase, mešljivosti in velikosti sferolitov. Optimizirani diagrami kažejo, da so m-EPR elastomeri učinkoviti modifikatorji žilavosti za polipropilen in kažejo ugodno ravnotežje mehanskih lastnosti mešanic iPP/m-EPR.

Scientific paper

***Capsicum annuum* Fruit Extract: A Novel Reducing Agent for the Green Synthesis of ZnO Nanoparticles and Their Multifunctional Applications**

**Haraluru Shankraiah Lalithamba,^{1,*} Mahadevaiah Raghavendra,¹ Kogali Uma,¹
Kalanakoppal Venkatesh Yatish,¹ Das Mousumi,² and Govindappa Nagendra³**

¹ Department of Chemistry, Siddaganga Institute of Technology, B.H. Road, Tumakuru - 572 103, Karnataka, India

² Department of Biotechnology, Siddaganga Institute of Technology, B.H. Road, Tumakuru - 572 103, Karnataka, India

³ Fakultät für Chemie und Chemische Biologie, Technische Universität Dortmund, Germany

* Corresponding author: E-mail: lalithambasit@yahoo.co.in

Received: 28-11-2017

**Dedicated to the 111th Birthday (born April 1, 1907) of Dr. Sree Sree Sree Shivakumara
Mahaswamiji, Siddaganga Matt, Tumakuru, Karnataka, India.**

Abstract

A simple, efficient and convenient method for the preparation of zinc oxide (ZnO) nanoparticle was described. Several parameters like size and morphology of the prepared nanoparticles were characterized through a variety of analytical techniques such as XRD, FT-IR, UV-Vis, SEM, and EDX. The prepared ZnO nanoparticles were successfully used as catalyst for the formylation of amino acid esters and biodiesel synthesis. Further, the synthesized formamide esters were well characterized through HRMS, ¹H NMR and ¹³C NMR analysis and subjected for the *in vitro* antibacterial and anti-fungal tests and the results indicated that some of them showed promising activity against targeted bacterial pathogens.

Keywords: Zinc oxide NPs; Solution combustion; Formylation; Biodiesel production; Biological activities

1. Introduction

Zinc oxide is a multifunctional material with its unique physical and chemical properties, such as high chemical stability, high electrochemical coupling co-efficient, high range of radiation absorption and high photostability.¹ ZnO as a catalyst with high specific surface area² finds the potential use in electronics, optoelectronics, laser technology and is made possible because of broad energy band (3.37 eV), high bond energy (60 MeV), thermal and mechanical stability at room temperature.³ ZnO NPs have fascinated the research world through its significant applications in pigment electronics, spintronics and piezoelectricity fields.⁴ Nano structured material ZnO has the ability to generate power, which also finds an extensive application in self-power generating devices for medical, wireless technologies and sensor applications.⁵ ZnO shows diverse group of growth morphologies such as nano rings, nano springs, nano combs, nanowires and nano cages.⁶

These have been synthesized using solid-vapour phase thermal sublimation technique⁷ under specific growth condition. ZnO nanoparticles have drawn attention due to their antimicrobial activity; this finds application in food packaging.⁸ Biocompatibility and biodegradability makes it a material of interest for biomedicine and in pro-ecological systems.⁹ Nano ZnO plays a vital role as a semiconductor photo catalyst for UV-induced degradation of methylene blue¹⁰ and doped ZnO also exhibits good optical and electrical properties.

Dhiman *et al.* reported the synthesis of Fe-doped ZnO nanoparticles by solution combustion method.¹¹ Recently, there are several attempts for the green biosynthesis approach for the preparation of ZnO, SnO₂, silver and reduced graphene oxide-silver (RGO-Ag) nanocomposites using leaf extracts of *Plectranthus amboinicus* and *Corymbia citriodora* as a reducing agent at different temperatures. The synthesized NPs showed a superior photocatalytic, catalytic activity towards dye molecules degradation and

also investigated the electrochemical properties of ZnO, RGO-Ag.^{12–16} It has been widely studied that, ZnO is a highly efficient catalyst for a plethora of organic reactions, such as Friedel–Crafts acylation, Beckmann rearrangements, synthesis of cyclic ureas from diamines, *N*-alkylation of imidazoles and ring-opening of epoxides.¹⁷ Nehal and others synthesized the ZnO nanoparticles and studied the effect of annealing temperature on its particle size.¹⁸ The prepared ZnO NPs were reported to be employed in various functional group transformations. Among the transformations, protection of reactive amino groups is commonly required in organic synthesis using formyl group.¹⁹ Formylation of amine is one of the important protocol in organic synthesis and medicinal chemistry. Various formylating reagents such as formic acid-DCC, formic acid-EDCI, KF-alumina, and ammonium formate were employed.^{20–23} The obtained formamides are the main class of organic intermediates, which act as Lewis bases.²⁴ Synthesis of formamide was also achieved by the reaction of isocyanate and formic acid in the presence of DMAP,²⁵ acetic formic anhydride,²⁶ and metallic zinc.²⁷ Literature survey reveals that, many catalysts were used for the *N*-formylation of amines with formic acid, such as amberlite IR-120,²⁸ TiO₂-P25 or sulfated titania,²⁹ and HEU zeolite.³⁰ *N*-formylation of amines using hydroxylamine hydrochloride as a catalyst under neat condition was reported by Deepali agarwal and co-workers.³¹ Using amine and formic acid in the presence of a catalytic amount of thiamine hydrochloride, formamide derivatives have been synthesized in excellent yields.³² Nano MgO, ZnO, and CeO₂ were also used as catalysts in the synthesis of formamides.^{33–35} Chandra shekhar *et al.* reported the facile *N*-formylation of amines using Lewis acids such as, FeCl₃, AlCl₃, and NiCl₂ as novel catalysts.³⁶ There are various methods to prepare nano structured particles. Some of the methods include chemical vapour deposition,³⁷ hydrothermal,³⁸ precipitation,³⁹ and sol-gel method.⁴⁰ The conventional physical and chemical methods available for the synthesis of NPs have adverse effects like critical temperature conditions and pressure, expensive chemicals, toxic byproducts *etc.*

Herein, green synthesis of zinc oxide nanoparticles using eco-friendly and non-toxic *Capsicum annuum* extract was reported. Capsaicin is an alkaloid found mainly in the fruit of the *Capsicum* genus, which provides spicy flavour and has pharmacological effects to determine specific applications, such as for weight-loss and as an analgesic.⁴¹ Literature survey confirms that the capsaicin has anti-bacterial and anti-diabetic properties.⁴² *Capsicum annuum* is a rich source of ascorbic acid generally known as vitamin C, a very essential antioxidant for human nutrition.⁴³ This method has several benefits such as simple procedure, inexpensive reagents and good stability of nanoparticles. The solid catalyst is of great importance because of its advantages such as non-hazardous nature, requirement in small proportions and easier reaction workup.

Biodiesel is recognized as an alternative fuel due to its similar bearing with diesel fuel. Existing days, research has been intensive to the alternative sources of energy.^{44,45} Commonly, biodiesel is a mixture of fatty acid methyl ester (FAME), which is synthesized from vegetable oil, waste oils and animal fat through transesterification reaction. Homogeneous catalysts such as KOH, NaOH, CH₃OK, and CH₃ONa show a favorable catalytic efficiency with various drawbacks such as generation of waste water, corrosion of equipment.⁴⁶ In display, solid heterogeneous catalysts are favorable for biodiesel synthesis because of environmentally friendly, easy separation, and could be reused many times.⁴⁷ Many solid acid catalysts like zeolite,⁴⁸ WO₃/ZnO₂,⁴⁹ and sulphated zirconia⁵⁰ were suitable for esterification reaction under 60–75 °C. In fact, solid acid catalysts (phosphotungstic acid, 12-tungstophosphoric acid, and ionic liquids) are used for the esterification and transesterification through one pot method. Meanwhile, solid base catalysts such as Ca(OCH₃)₂,⁵¹ CaO⁵², and KOH/Al₂O₃ were used in transesterification reaction at mild condition. Among the transition metal oxides, zinc oxide was reported the best catalyst for transesterification due to its minimum weight loss and high activity in the reaction.⁵³ Currently, application of nano catalysts for biodiesel synthesis has drawn much attention, as a result of easy separation of products, less pollution, higher catalytic activity and reusability.⁵⁴ Recently, nano catalysts such as CaO,⁵⁵ Ti(SO₄)O,⁵⁶ KF/CaO-Fe₃O₄,⁵⁷ Ag/ZnO⁵⁸, and mixed oxide TiO₂-ZnO⁵⁹ were used for biodiesel production. Presently, non-edible oils are used for biodiesel production to reduce edible oil conflict among food and fuel purpose. In this study, *Buteamonosperma* oil (non-edible) is used for biodiesel production and this plant belongs to a fabaceae family which is native to Indian subcontinent and seeds contain 23% of oil.^{60,61}

In the present work, we report the synthesis of ZnO NPs through solution combustion by using *Capsicum annuum* extract as the combustible fuel and the obtained ZnO is employed as catalyst for the *N*-formylation of amino acid esters and biodiesel production. Further, the synthesized formamide derivatives were subjected for biological activities.

2. Experimental Section

2.1. General

All chemicals were purchased from Sigma-aldrich and Merck and used without purification. The pathogenic bacterial strains were procured from National chemical laboratory Pune, India. The *Capsicum annuum* fruits were collected from local market, Tumakuru district, Karnataka, India. TLC analysis was carried out using pre-coated silica gel F₂₅₄. The phase identity and crystalline size of ZnO NPs were characterized through shimadzu powder X-ray diffractometer (PXRD-7000). IR spectra were re-

corded on Bruker Alpha-T FT-IR spectrometer (KBr windows, 2 cm^{-1} resolution), SEM analysis on Hitachi-7000 Scanning Electron Microscopy and elemental analysis was obtained from energy dispersive X-ray diffraction (EDX). UV-Vis diffused reflectance spectra were analyzed through Lambda-35 (Parkin Elmer) spectrophotometer. Mass spectra were recorded on a Micromass Q-ToF Micro Mass Spectrometer. Melting points were taken on open capillaries, ^1H NMR, and ^{13}C NMR spectra of the formamide derivatives were done on a Bruker AMX 400 MHz spectrometer using Me_4Si (tetramethylsilane) as an internal standard and CDCl_3 (deuterated chloroform) as a solvent.

2. 2. Synthesis of Nano Zinc Oxide Particles Through Solution Combustion Method

The *Capsicum annuum* fruit was collected and washed with distilled water. The whole mass was grinded to get the powder and then mixed with distilled water and boiled at $80\text{ }^\circ\text{C}$. After cooling to room temperature, the mixture was filtered using a Whatman filter paper no. 1 to obtain chilli extract. Zinc nitrate as precursor and *Capsicum annuum* fruit extract as fuel in the ratio of 4:1 were used for the synthesis of ZnO NPs through solution combustion method.⁶² The solution was heated to $450\text{ }^\circ\text{C}$ for 30 min and then dried in hot air oven for 4–5 h to obtain ZnO NPs in good yield.

2. 3. General Procedure for the Synthesis of Formamide Esters Using ZnO NPs

The prepared amino acid ester (1.0 mmol) was dissolved in dry DCM (dichloromethane) and neutralized with NMM (*N*-methyl morpholine) (1.5 mmol). To this solution, formic acid (2.0 mmol) was added at room temperature, followed by the addition of nano ZnO (0.5 mmol). The reaction mixture was stirred for 2 to 3 hours. The product was extracted into DCM and the organic layer was washed with hydrochloric acid solution (10 mL), sodium carbonate solution (15 mL), water (15 mL) and brine (15 mL). It was dried over anhydrous sodium sulphate and concentrated under reduced pressure.

2. 4. Synthesis of Biodiesel Using ZnO NPs as a Catalyst

Transesterification reaction was carried out in a three necked round bottom flask equipped with reflux condenser on the middle neck, thermometer on the side neck and placed on the plate of the magnetic stirrer. In the beginning, 100 ml of *B. monosperma* oil was pre heated at $70\text{ }^\circ\text{C}$ then a mixture of 2% wt. ZnO and 9:1 molar ratio of methanol to oil was added. The entire reaction was carried out at $65\text{ }^\circ\text{C}$ for duration of 2 h. After the completion of reaction, the mixture was allowable to phase separation,

the biodiesel (top layer), glycerine (middle layer) and catalyst (bottom layer) phase were separated. Then, the catalyst and glycerine were drained out and unreacted methanol was recovered from biodiesel. The obtained biodiesel was filtered to remove any dissolved zinc oxide catalyst.

3. Results and Discussion

3. 1. Characterization of ZnO NPs

XRD spectrum (Figure 1) has prominent peaks corresponding to the diffraction peaks at $2\theta = 31^\circ, 34^\circ, 36^\circ, 47^\circ, 56^\circ, 62^\circ$ and 67° were indexed with the diffraction planes (100), (002), (101), (102), (110), (103) and (112) approve with JCPDS card no. 36–1451,⁶³ which confirms the hexagonal wurtzite structure of ZnO NPs. Average particle size (D) of synthesized NPs were found to be 33.26 nm using Scherer's formula. From the XRD spectrum, it is concluded that ZnO NPs synthesised by biologically initiated green synthesis conferred uniform size distribution fluctuates between 30 to 40 nm.

The average crystallite size of prepared sample was calculated by Debye-Scherrer's⁶⁴ formula i.e.

$$D = \frac{0.89 \lambda}{\beta \cos \theta} \quad (1)$$

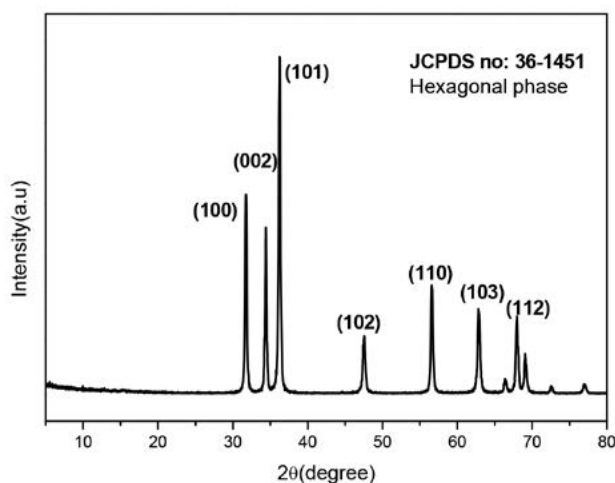


Figure 1. XRD pattern of ZnO NPs.

where, D is crystalline size, λ is X-ray wavelength (0.154 nm), β is full-width at half-maximum and θ is Bragg's angle. The average crystallite size of the ZnO NP was found to be 33.26 nm.

Figure 2(a) and 2(b) show DRS spectra and band gap plot of ZnO nanoparticles respectively. DRS spectrum reveals that the absorption is at $\sim 400\text{ nm}$. The Kubelka – Munk function^{65,66} was utilized to determine the band gap energy (E_g) of ZnO NPs. The intercepts of the tangents to the plots of $[\text{F}(\text{R}_\infty) \text{ hv}]^{1/2}$ versus photon energy (hv) were

shown in Figure 2(a) and 2(b). The Kubelka-Munk function $F(R_{\infty})$ and photon energy ($h\nu$) can be calculated by following Equations (2), (3) and (4):

$$F(R_{\infty}) = \frac{(1 - R_{\infty})^2}{2R_{\infty}} \quad (2)$$

$$R_{\infty} = 10^{-A} \quad (3)$$

$$h\nu = \frac{1240}{\lambda} \quad (4)$$

where R_{∞} ; reflection coefficient of the sample, A ; the absorbance intensity of ZnO nanoparticles and λ ; the absorption wavelength. The energy band gap value was found to be 3.10 eV.

Figure 3 shows the SEM images of as prepared zinc oxide nanoparticles. Figure 3c is the enlarged part of 3b and 3a, which clearly shows that the particles are agglomerated cluster to form spongy cave like structures. The sizes of the particles are found to be in the 500 nm to 1 micrometer.

The Energy Dispersive X-ray Diffractive study was carried out for the prepared ZnO NPs to know about the elemental composition. The EDX spectrum confirms the

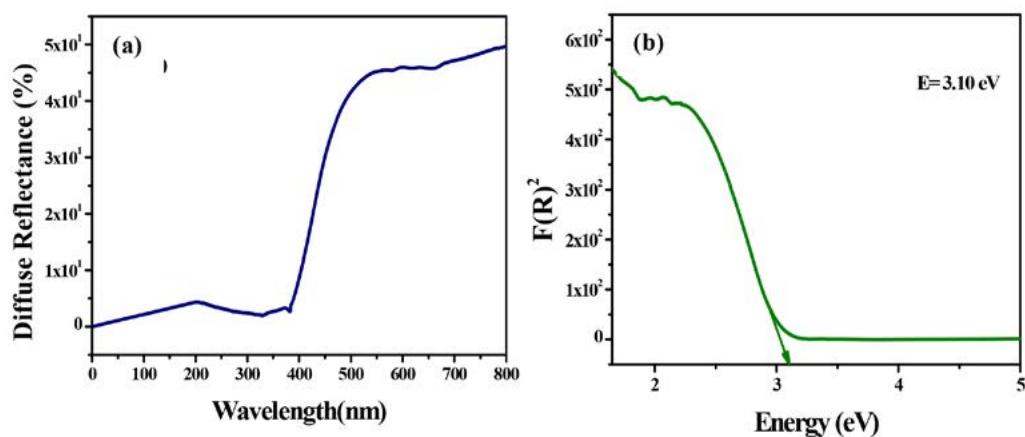


Figure 2. Diffuse reflectance spectrum (a) and direct band gap energy of ZnO (b).

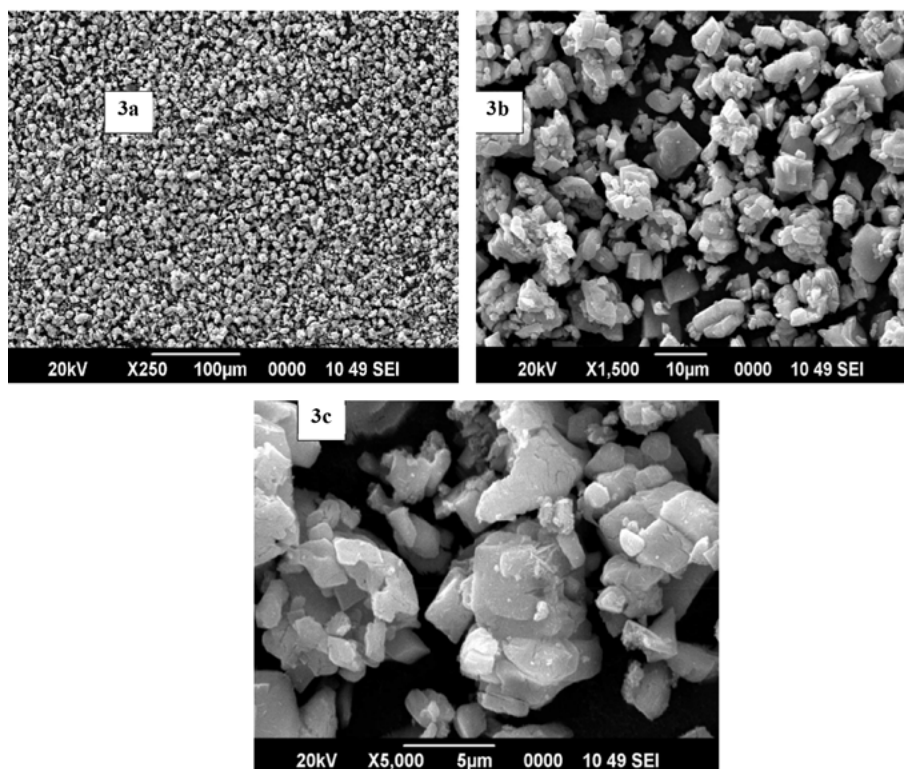


Figure 3. SEM image of ZnO nanoparticles.

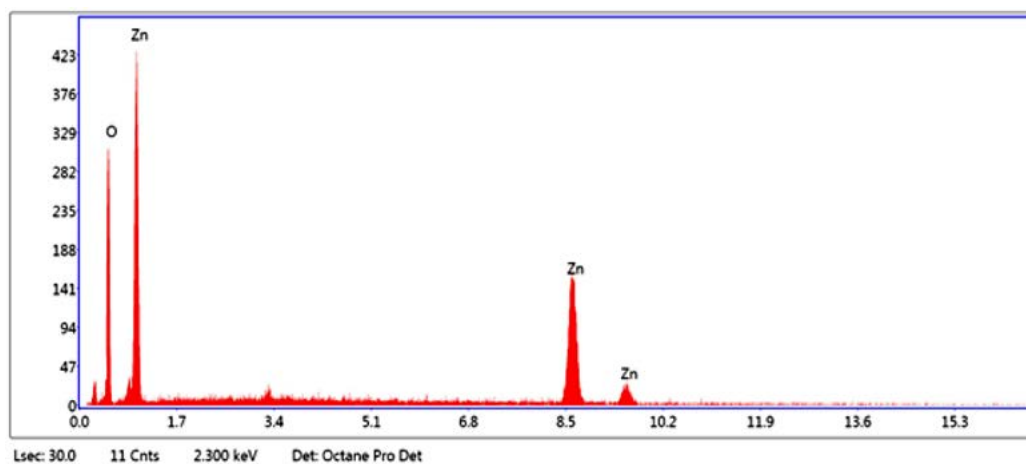


Figure 4. EDX spectrum of ZnO nanoparticles.

presence of zinc and oxygen signals and elemental analysis of the nanoparticle yielded 55.33% of zinc and 44.67% of oxygen.

Figure 5 is the FT-IR spectrum of ZnO NPs and the band in the region of 680–400 cm^{-1} is the characteristic

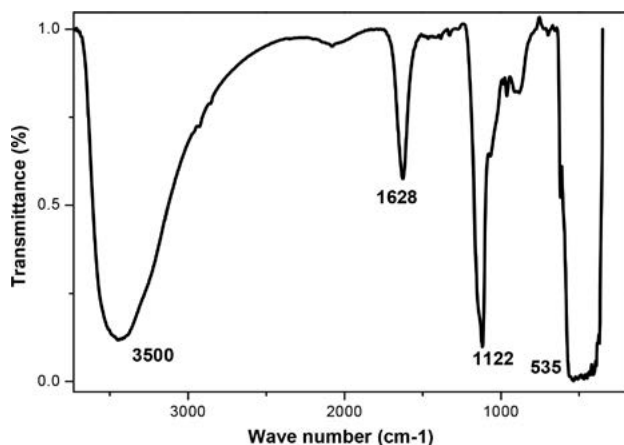


Figure 5. FTIR spectrum of ZnO nanoparticles.

peak of ZnO NPs. Thus, the formation of pure ZnO NPs at 535 cm^{-1} is evidenced by FT-IR⁶⁷ and the peak at 1122 cm^{-1} in FTIR spectrum is due to C-O stretching mode.⁶⁸ The peaks observed at 1628 cm^{-1} and 3500 cm^{-1} were due to the presence of -OH stretching and bending vibrations respectively assigned to the H₂O adsorption on the surface of metal.⁶⁹

Figure 6(a), (b) show the photoluminescence (PL) spectra of ZnO NPs recorded at room temperature. The recombination of photo generated free charge carriers leads to photoluminescence emission in semiconductor materials. The spectrum was recorded under UV excitation (375 nm) using Xenon lamp as source. The result obtained reveals that nano ZnO shows the strong emission peak at 600 nm (Figure 6(a)). The emission spectrum was monitored at 375 nm showed a broad emission at 600 nm was shown in

Figure 6(b). The broad 600 nm peak was due to the transition between single charged oxygen vacancies. The correlated color temperature was one of the essential parameter to know the color appearance of the light emitted by a light source with respect to a reference light source

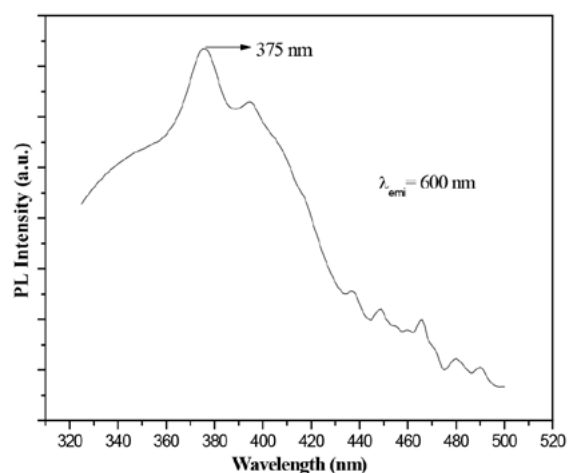
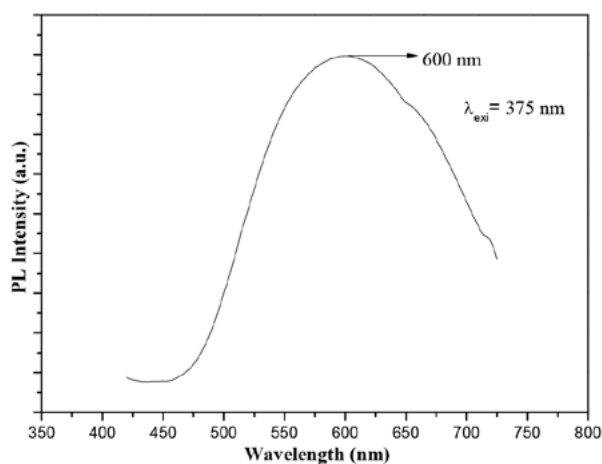


Figure 6. PL emission spectrum (a) and excitation spectrum (b) of nano ZnO.

when heated up to a specific temperature. The color clarity of any luminescent material was expressed in terms of chromaticity coordinates, called Commission International De l'Eclairage (CIE).

3. 2. Application of ZnO NPs as a Catalyst for the Formylation of Amino Acid Esters

In the current years, the use of metaloxides as a catalysts and reaction media has received considerable tremendous interest because of their high level of environmental compatibility, chemo selectivity and availability at low cost. Therefore, we explored the application of nano ZnO powder as an inorganic catalyst to carry out *N*-formylation of amino acid ester (1 mmol) in DCM with aq. 98% formic acid (1.5 mmol) at room temperature. Formamide derivative of amino acid ester was obtained in trace amount in the absence of ZnO catalyst, while good results were obtained with use of 0.5 mmol ZnO catalyst after same reaction conditions as mentioned. But less than 0.5 mmol considerably decreased the percentage of formamide esters and may took longer time for the completion of reaction. Using more than 0.5 mmol of ZnO has less effect on the final yield of the products. Thus, we found that 0.5 mmol of ZnO could efficiently catalyze the reaction for preparation of the desired products and observed that the excellent yield obtained using 1.5 mmol of formic acid. In literature survey Suresh babu *et al.* achieved successful synthesis of formamide derivatives of protected amino acids by the reaction of isocyanate with aqueous formic acid using DMAP as an organo catalyst.⁷⁰ However, this procedure suffers from the difficulties such as expensive reagents, highly toxic and may also require special care. Hence, it is necessary of convenient reagent for the synthesis of stable formamides in terms of economic via-

bility and operational simplicity. Therefore, it is necessary to study this reaction using nano ZnO with a variety of amino acid esters as starting materials which were subjected to formylation reaction and the results were presented in Table 1. For the synthesis of titled compounds (**2a–h**), amino acid ester containing different aryl/alkyl groups prepared from thionyl chloride was dissolved in dry DCM and neutralized with NMM, to which aqueous formic acid was added followed by the addition of nano ZnO. The reaction mixture was stirred till the completion of the reaction (as monitored by TLC). After the simple work-up, desired products were obtained in good yield (Scheme 1). Using this procedure several formamide esters were synthesized from amino acid esters and characterized by their ¹H NMR, ¹³C NMR and mass spectral studies.

3. 3. Spectral Data of the Synthesized Compounds:

N-formyl Ala-OMe (**2a**): % Yield 90, Solid, Melting Point: 162 °C. ¹H NMR (400 MHz, CDCl₃) δ 1.39 (d, *J* = 8 Hz, 3H), 2.02 (s, 1H), 3.46 (s, 3H), 4.55 (m, 1H), 8.20 (s, 1H). ¹³C NMR (100 MHz, CDCl₃) δ 17.5, 46.36, 52.0, 162.3, 170.1. MS: Cald. for C₅H₉NO₃ *m/z*: 131.06, found: 131.0576.

N-formyl Ser-OMe (**2b**): % Yield 80, Gum. ¹H NMR (400 MHz, CDCl₃) δ 1.81 (s, 2H), 3.60 (s, 3H), 4.06 (m, 2H), 4.42 (m, 1H), 8.22 (s, 1H). ¹³C NMR (100 MHz, CDCl₃) δ 51.4, 52.9, 60.5, 160.8, 171.0. MS: Cald. for C₅H₉NO₄ *m/z*: 147.05, found: 147.002.

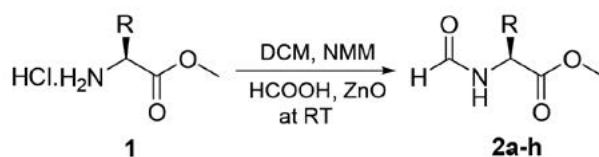
N-formyl Tyr-OMe (**2c**): % Yield 89, Solid, Melting Point: 188 °C. ¹H NMR (400 MHz, CDCl₃) δ 1.88 (s, 1H), 3.04 (m, 2H), 3.45 (s, 3H), 4.78 (m, 1H), 5.06 (s, 1H), 6.68 (d, *J* = 8 Hz, 2H), 6.80 (d, *J* = 8 Hz, 2H), 7.92 (s, 1H). ¹³C NMR (100 MHz, CDCl₃) δ 36.4, 50.8, 51.6, 114.8, 129.3, 131.4, 155.0, 162.6, 171.5. MS: Cald. for C₁₁H₁₃NO₄ *m/z*: 223.08, found: 223.0802.

N-formyl Leu-OMe (**2d**): % Yield 85, Solid, Melting Point: 132 °C. ¹H NMR (400 MHz, CDCl₃) δ 1.06 (d, *J* = 8 Hz, 6H), 1.74–1.80 (m, 3H), 2.0 (s, 1H), 3.47 (s, 3H), 4.46 (m, 1H), 8.10 (s, 1H). ¹³C NMR (100 MHz, CDCl₃) δ 22.4, 22.75, 40.34, 48.2, 51.62, 162.4, 170.8. MS: Cald. for C₈H₁₅NO₃ *m/z*: 173.11, found: 173.0998.

N-formyl Pro-OMe (**2e**): % Yield 79, Gum. ¹H NMR (400 MHz, CDCl₃) δ 1.60 (m, 2H), 1.68 (m, 2H), 2.65 (m, 2H),

Table 1. List of formamide esters prepared using ZnO NPs

Entry	Product	Yield (%)	M.p./ °C
1	2a	90	162
2	2b	80	Gum
3	2c	89	188
4	2d	85	132
5	2e	79	Gum
6	2f	84	Gum
7	2g	85	158
8	2h	88	Gum



R = Amino acid side chains

Scheme 1. Synthesis of *N*-formamide esters

3.53 (t, 1H), 3.62 (s, 3H), 8.0 (s, 1H). ^{13}C NMR (100 MHz, CDCl_3) δ 22.8, 28.4, 43.92, 50.73, 58.02, 162.1, 172.0. MS: Cald. for $\text{C}_7\text{H}_{11}\text{NO}_3$ m/z : 157.07, found: 157.0711.

N-formyl Val-OMe (**2f**): % Yield 84, Gum. ^1H NMR (400 MHz, CDCl_3) δ 1.08 (d, $J = 8$ Hz, 6H), 2.0 (s, 1H), 2.98 (m, 1H), 3.66 (s, 3H), 4.38 (d, $J = 8$ Hz, 1H), 8.0 (s, 1H). ^{13}C NMR (100 MHz, CDCl_3) δ 17.8, 29.92, 51.0, 54.7, 163.4, 171.2. MS: Cald. for $\text{C}_7\text{H}_{13}\text{NO}_3$ m/z : 159.09, found: 159.0898.

N-formyl Phe-OMe (**2g**): % Yield 85, Melting Point: 158 °C. ^1H NMR (400 MHz, CDCl_3) δ 2.0 (s, 1H), 3.02 (m, 2H), 3.48 (s, 3H), 4.75 (t, 1H), 7.08–7.20 (m, 5H), 8.17 (s, 1H). ^{13}C NMR (100 MHz, CDCl_3) δ 37.6, 50.82, 51.7, 126.2, 127.5, 128.0, 138.65, 162.88, 171.1. MS: Cald. for $\text{C}_{11}\text{H}_{13}\text{NO}_3$ m/z : 207.09, found: 207.0930.

N-formyl Met-OMe (**2h**): % Yield 88, Gum. ^1H NMR (400 MHz, CDCl_3) δ 1.86 (s, 1H), 2.04 (s, 3H), 2.20 (m, 2H), 2.38 (t, 2H), 3.55 (s, 3H), 4.40 (t, 1H), 8.11 (s, 1H). ^{13}C NMR (100 MHz, CDCl_3) δ 16.9, 29.64, 31.5, 50.12, 52.3, 163.82, 172.0. MS: Cald. for $\text{C}_7\text{H}_{13}\text{NO}_3\text{S}$ m/z : 191.06, found: 191.0602.

3. 4. Antibacterial and Antifungal Activity of Formamide Derivatives

The synthesized compounds were evaluated for their antibacterial activity against *E. coli* (MTCC 443) and *S.*

Aureus (MTCC 5823). Lack of activity of the tested substances against Gram +ve bacteria could be explained by the differences in the structure of cell walls of Gram +ve and Gram -ve microorganisms. In most Gram +ve bacteria, the cell wall consists of many layers of peptidoglycan, forming a thick, rigid structure. Whereas, the cell walls of Gram -ve bacteria consist of one or a very few layers of peptidoglycan and a lipid-rich outer membrane.⁷¹ Similar type of results employing different type of compounds such as Schiff's bases and amine derived from alkyl 2-(2-formyl-4-nitrophenoxy) alkanooates was recorded by Goszczyn'ska.⁷² A contrasting difference in antibacterial activity employing Gram +ve and Gram -ve strains representing better susceptibility by *E. coli* than *S. aureus* employing novel benzothienopyrimidines compounds was shown.

In this study, the antibacterial screening indicated quite varied results among the tested samples as depicted in Table 2, 3, and 4 exhibiting antibacterial and antifungal activities respectively. For *E. coli* (MTCC 443), formamide ester derivatives of Ala, Tyr, Phe have shown good susceptibility over a wide volume range taken for a fixed concentration of samples (Table 2). Serine derivative has shown best result in comparison

to others at higher volume of fixed concentration of the sample tested. Rest of the samples were found to be resistant against the bacterial strain. A different result has been observed in terms of susceptibility pattern tested against *S. aureus* (MTCC 5823). Derivatives of Ala, Ser,

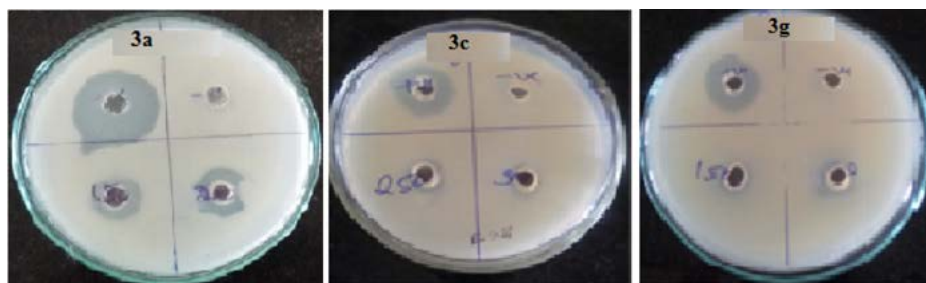


Figure 7. Photographs showing antibacterial activity of the formamides (3a, 3c and 3g) in agar well diffusion method with Gram -ve *Escherichia coli* bacteria.

Table 2. Antibacterial activity of standard and samples employing *E. coli*

Entry	Sample name <i>Escherichia coli</i>	Standard (Gentamicin)	Sample concentration (μl)					
			50	100	150	200	250	300
			Zone of Inhibition (mm)					
3a	OHCHN-Ala-OMe	++++	–	–	+	+	+	+
3b	OHCHN-Ser-OMe	++++	–	–	–	+	+	++
3c	OHCHN-Tyr-OMe	++++	–	–	–	+	+	+
3d	OHCHN-Leu-OMe	++++	–	–	–	–	–	–
3e	OHCHN-Pro-OMe	++++	–	–	–	–	–	+
3f	OHCHN-Val-OMe	++++	–	–	–	–	–	–
3g	OHCHN-Phe-OMe	++++	–	–	+	+	+	+
3h	OHCHN-Met-OMe	++++	–	–	–	–	–	–

Table 3. Antibacterial activity of standard and samples employing *S. Aureus*

Entry	Sample name <i>S. Aureus</i>	Standard (Gentamicin)	Sample concentration (µl)					
			50	100	150	200	250	300
			Zone of Inhibition (mm)					
3a	OHCHN-Ala-OMe	++++	-	-	-	-	-	-
3b	OHCHN-Ser-OMe	++++	-	-	-	-	-	-
3c	OHCHN-Tyr-OMe	++++	-	-	-	-	+	+
3d	OHCHN-Leu-OMe	++++	-	-	-	-	-	+
3e	OHCHN-Pro-OMe	++++	-	-	-	-	-	-
3f	OHCHN-Val-OMe	++++	-	-	-	-	-	+
3g	OHCHN-Phe-OMe	++++	-	-	-	-	-	+
3h	OHCHN-Met-OMe	++++	-	-	-	-	-	-

Zone of Inhibition: (-) 0–3 mm; (+) 4–6 mm, (++) 7–9 mm, (+++) 10–12 mm, (++++) 12 mm

Table 4. Antifungal activity of standard and samples employing *Humicolafuscoatra*

Entry	Sample name <i>Humicolafuscoatra</i>	Standard (Fluconazole)	Sample concentration (µl)					
			50	100	150	200	250	300
			Zone of Inhibition (mm)					
3a	OHCHN-Ala-OMe	+++	+	-	-	+	+	-
3b	OHCHN-Ser-OMe	+++	-	+	+	+	+	+
3c	OHCHN-Tyr-OMe	+++	-	-	-	-	-	+
3d	OHCHN-Leu-OMe	+++	-	+	+	+	-	+
3e	OHCHN-Pro-OMe	+++	-	+	-	+	+	+
3f	OHCHN-Val-OMe	+++	-	+	+	+	+	-
3g	OHCHN-Phe-OMe	+++	-	+	+	+	+	+
3h	OHCHN-Met-OMe	+++	-	+	+	+	+	+

Zone of Inhibition: (-) 0–1 mm; (+) 2–4 mm, (++) 5–7 mm, (+++) 8 mm

Pro and Met were found to be resistant at fixed concentration with different range of volume from 50 to 300 µl. While, Tyr, Leu, Val and Phe derivatives have shown (Table 3) moderate susceptibility in comparison to Gram -ve *E. coli* (MTCC 443). All comparisons were done keeping in record the values of standard tested. Zones of inhibition (in mm) were measured at varying dilutions and depicted in the photographs of the culture plates of the best cases (Figure 7).

Summarization of antifungal activity has shown in Table 4. Derivatives of Ala, Tyr, Leu, Pro and Val have shown some activity in comparison to standard. While the derivatives of Phe, Ser, and Met have also shown good activity over a wide range of volume of samples (50–300 µl)

tested for a fixed concentration. We are also measured the equivalent zones of inhibition (in mm) at varying dilutions and depicted in the photographs of the culture plates for the best cases (Figure 8).

The antimicrobial activity of formamide esters were evaluated against standard MTCC strains of Gram +ve and Gram -ve bacteria (standard strains: *Staphylococcus aureus* MTCC 5823, *Escherichia coli* MTCC 443) and a strain of fungi *Humicolafuscoatra* (MTCC 3938) by agar well diffusion method.⁷³ The optimum turbidity (<1.0) suitable for bacterial inoculum preparation was followed according to McFarland's test⁷⁴ employing Luria Bertani Broth for *E. coli* and Nutrient Broth for *S. aureus*. For fungal inoculum preparation 72 h incubation period was optimized for

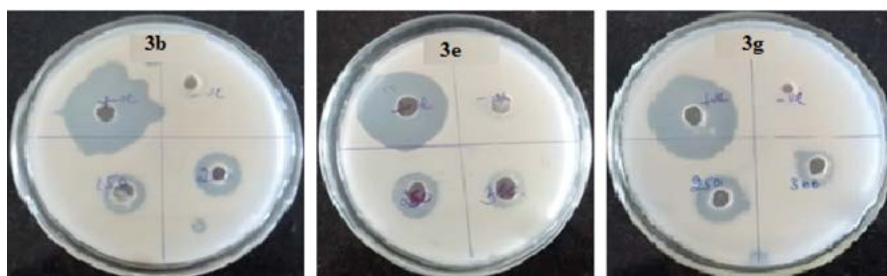


Figure 8. Photographs showing antifungal activity of the formamides (3b, 3e and 3g) in agar well diffusion method with *Humicolafuscoatra* bacteria.

choosing the culture suspension employing Potato dextrose broth pertaining to antifungal activity. The standards used were fluconazole at the conc. of 0.10 mg/ml and gentamicin of 0.003 mg/ml concentration (Plating volume 50 μ l) for antifungal and antibacterial activity respectively. The wells of 6 mm diameter were punched employing a sterile cork borer into the Mueller hinton agar (MHA) having the test microorganisms at concentration about 5×10^6 CFU/ml for bacterial strains and 3×10^5 CFU/ml for fungi. The wells were filled with different volumes in a range from 50 μ l to 300 μ l, at the concentration of 0.10 mg/ml employing DMSO. The plates were incubated for 18 h and 36 h at 35 ± 1 °C for *E. coli* and *S. aureus* respectively. For antifungal activity employing the same method with potato dextrose agar plates were incubated for 72 h at 28 ± 1 °C. Antimicrobial activity was evaluated by measuring the inhibition zone against the test microorganisms us-

ing an antibiogram scale and standard measurement protocol was followed according to CLSI guidelines.^{75,76}

3. 4. Application of ZnO NPs as a Catalyst for the Biodiesel Production

After transesterification of *Buteamonosperma* oil, the yield of biodiesel was found to be 82.7%. In order to evaluate the quality of biodiesel, the fuel properties of the biodiesel were determined according to ASTM D6751 standards as shown in the Table 5. The fuel properties such as kinematic viscosity (4.3 cSt), flash point (151 °C), acid value (0.2 mg KOH/g), calorific value (37790 kJ/kg), density (880 kg/m³) and copper strip corrosion (1a) were within the range of ASTM standard. Schematic diagram of ZnO NPs catalyzed transesterification for the production of biodiesel is shown in the Figure 9.

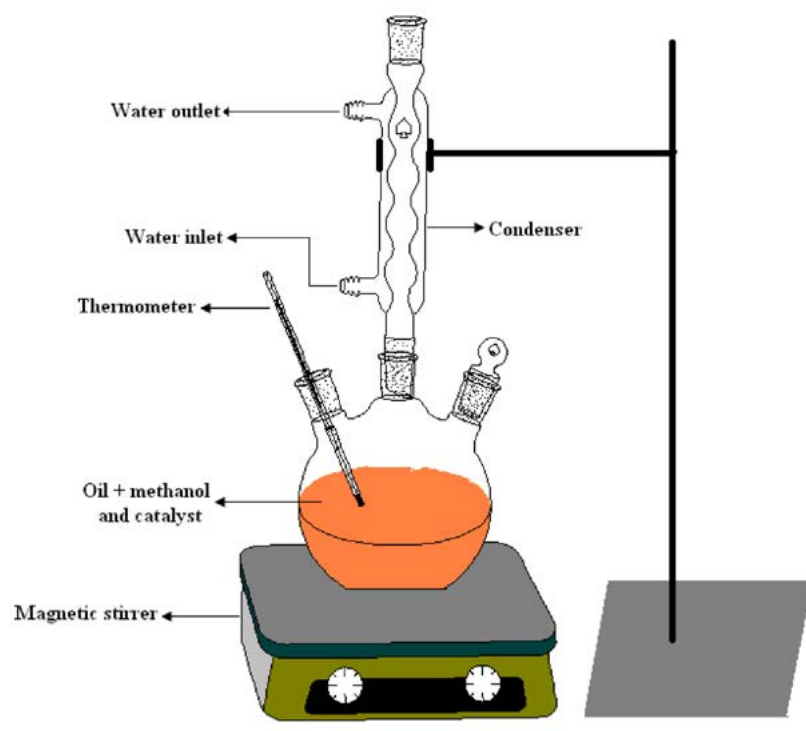


Figure 9. Schematic diagram of transesterification reaction.

Table 5. Fuel properties of *Buteamonosperma* biodiesel

Properties	Units	Testing procedure ASTM	BMME/ biodiesel	Biodiesel standard ASTM D6751
Viscosity at 40 °C	cSt	D445	4.3	1.9–6.0
Flash point	°C	D4052	151	>130
Acid value	mg KOH/g	D664	0.2	0.8 max
Calorific value	kJ/kg	D240	37790	–
Density	kg/m ³	D93	880	870–900
Copper strip corrosion, 50 °C, 3h	–	D130	1a	no. 3 max

BMME = *Buteamonosperma methyl ester*

4. Conclusions

Multifunctional ZnO nanoparticle has been synthesized via a simple solution combustion method using *Cap-sicum annuum* extract as a new fuel. The prepared NPs were characterized by UV-Vis DRS, XRD, SEM, and EDX and also evaluated its photoluminescence property. The method is environmental friendly and overcome the demerits of conventional physical and chemical methods of synthesis. In the presence of nano ZnO catalyst excellent yield of formamide esters and biodiesel have been obtained. The synthesized formamide esters were successfully characterized by ^1H NMR, ^{13}C NMR, and mass spectroscopy analysis. Finally, the formamide esters were subject to biological activities against bacterial pathogens and few of the molecules exhibited considerable biological activities.

5. Acknowledgements

We thank the Principal and Director of Siddaganga Institute of Technology, Tumakuru, Karnataka, for the research facilities. One of the authors (HSL) is thankful to the Vision Group of Science and Technology, Department of Information Technology, Biotechnology and Science & Technology, Government of Karnataka for providing funds under CISEE programme (GRD No. 472) to carry out the present research work by means of a sponsored project.

6. References

- H. G. Reza, P. Ferdos, P. Hossein, B. R. Mosavar, *Oriental J. Chem.* **2015**, *31*, 1219–1221.
- S. M. Hosseini, S. Hashem, *J. Org. Chem.* **2006**, *71*, 6652–6654. DOI:10.1021/jo060847z
- K. R. Agnieszka, J. Teofil, *Materials.* **2014**, *7*, 2833–2881. DOI:10.3390/ma7042833
- D. Gnanasangeetha, T. D. Sarala, *J. Chem. Biol. Phy. Sci.* **2013**, *4*, 238–246.
- D. Indrani, A. Nitin, *Nanomaterials and Nanotech.* **2013**, *3*, 1–16. DOI:10.5772/56188
- Z. W. Lin, *J. Phys. Condens. Matt.* **2004**, *16*, 829–858. DOI:10.1088/0953-8984/16/45/025
- L. Miao, S. Tanemura, Y. Ieda, M. Tanemura, Y. Hayashi, H. Y. Yang, S. P. Lau, B. K. Tay, Y. K. Cao, *Surface Sci.* **2007**, *601*, 2660–2663. DOI:10.1016/j.susc.2006.12.011
- J. J. Velázquez, V. D. Rodríguez, A. C. Yanes, J. del Castillo, J. Méndez-Ramos, *Appl. Phys. A.* **2012**, *108*, 577–583. DOI:10.1007/s00339-012-6929-z
- G. M. Krishna, R. Jagannadha, *J. Engg. Trends and Tech.* **2015**, *26*, 272–275. DOI:10.14445/22315381/IJETT-V26P247
- A. I. Muhammad, A. S. Iqbal, A. K. M. Rahman, A. M. Mah-bubul, S. M. I. Saiful, A. H. Mohammad, *International J. Chemical Reactor Engg.* **2011**, *9*, 1–20.
- P. Dhiman, K. M. Batoo, R. K. Kotnala, M. Singh, *Micro & Nano Lett.* **2012**, *7*, 1333–1335. DOI:10.1049/mnl.2012.0862
- L. Fu, Z. Fu, *Ceramics International.* **2015**, *41*, 2492–2496. DOI:10.1016/j.ceramint.2014.10.069
- L. Fu, Y. Zheng, Q. Ren, A. Wang, B. Deng, *J. Ovonic Res.* **2015**, *11*, 21–26.
- Y. Zheng, Z. Wang, F. Peng, L. Fu, *Revista Mexicana de Ingeni-er'ia Qu'ımica.* **2017**, *16*, 41–45.
- Y. Zheng, A. Wang, W. Cai, Z. Wang, F. Peng, Z. Liu, L. Fu, *Enzyme and Microbial Technology.* **2016**, *95*, 112–117. DOI:10.1016/j.enzmictec.2016.05.010
- Y. Zheng, Z. Wang, F. Peng, L. Fu, *Brazilian Journal of Pharma-ceutical Sciences.* **2016**, *52*, 781–786. DOI:10.1590/s1984-82502016000400023
- Z. Ilona, S. Jakub, M. C. Anna, S. Kamil, L. Janusz, S. Jacinto, *Chem. Science Rev. and Lett.* **2015**, *4*, 735–745.
- A. S. Nehal, M. El-Kemary, M. I. Ebtisam, *Nanoscience and Nanotech.* **2015**, *5*, 82–88.
- S. Mojmir, A. H. E. Adam, H. E. H. Robert, *Org. Lett.* **2011**, *13*, 3952–3955. DOI:10.1021/ol201475j
- J. Waki, J. Meienhofer, *J. Org. Chem.* **1977**, *42*, 2019–2020. DOI:10.1021/jo00431a046
- F. M. F. Chen, N. L. Benoiton, *Synthesis.* **1979**, 709–710. DOI:10.1055/s-1979-28805
- M. Miharam, Y. Ishino, S. Minakata, M. Komatsu, *Synthesis.* **2003**, *15*, 2317–2320.
- P. G. Reddy, G. D. K. Kumar, S. Baskaram, *Tetrahedron.* **2000**, *41*, 9149–9151. DOI:10.1016/S0040-4039(00)01636-1
- H. S. Mona, *Green Chem.-Envi. Benign Appro.* **2012**, *6*, 103–120.
- V. V. Sureshbabu, N. Narendra, *Int. J. Pept. Res. Ther.* **2008**, *14*, 201–207. DOI:10.1007/s10989-008-9127-2
- A. Jafar, H. Malak, S. Mehdi, H. Akbar, *Arkivok.* **2009**, *xi*, 123–129.
- K. Joong-Gon, J. Doo Ok, *Bull. Korean Chem. Soc.* **2010**, *31*, 2989–2991. DOI:10.5012/bkcs.2010.31.10.2989
- R. Madhusudana, T. M. V. Bhojgowda, N. Aatika, A. P. Mo-hamed, *Chinese J. Cat.* **2010**, *31*, 518–520.
- B. Krishnakumar, M. Swaminathan, *J. Mol. Catalysis A: Chem.* **2011**, *334*, 98–102. DOI:10.1016/j.molcata.2010.11.002
- B. Siavash, M. A. Babak, S. Mohammad, Z. Fereshteh, *Bull. Korean Chem. Soc.* **2012**, *33*, 2251–2254. DOI:10.5012/bkcs.2012.33.7.2251
- D. Agarwal, A. Agrwal, A. Bairagi, V. K. Kasana, *Res. J. Chem-ical Sci.* **2014**, *4*, 54–57.
- L. Min, M. Lei, H. Lihong, *Tetrahedron Lett.* **2010**, *51*, 4186–4188. DOI:10.1016/j.tetlet.2010.06.005
- M. M. B. Reddy, S. Ashoka, G. T. Chandrappa, M. A. Pasha, *Catal. Lett.* **2010**, *138*, 82–87. DOI:10.1007/s10562-010-0372-6
- S. S. Mohammad, M. Mehdi, R. Akbar, *Lett. in Org. Chem.* **2014**, *11*, 49–54. 35. M. Raghavendra, K. V. Yatish, H. S. Lali-thamba, *Eur. Phys. J. Plus.* **2017**, *132*, 1–12.
- S. A. Chandra, K. A. Ravi, G. Sathaiah, P. V. Luke, S. Madab-hushi, R. P. Shanthan, *Tetrahedron Lett.* **2009**, *50*, 7099–7101. DOI:10.1016/j.tetlet.2009.10.006

37. R. Namita, *International J. Adv. in Engg. & Tech.* **2015**, *7*, 1806–1881.
38. R. Donya, B. H. Mohd Zobir, T. Y. Yun Hin, *Chm. Central J.* **2013**, *7*, 1–10. DOI:10.1186/1752-153X-7-1
39. H. R. Ghorbani, F. P. Mehr, H. Pazoki, B. M. Rahmani, *Oriental J. Chem.* **2015**, *31*, 1219–1221.
40. S. Jurablu, M. Farahmandjou, T. P. Firoozabadi, *J. Sci. Islamic Republic of Iran.* **2015**, *26*, 281–285.
41. R. E. Maria de Lourdes, G. G. M. Edith, V. T. Erika, *Molecules.* **2011**, *16*, 1253–1270. DOI:10.3390/molecules16021253
42. S. D. Joao, *Food and Nutrition Sci.* **2012**, *3*, 1354–1374. DOI:10.4236/fns.2012.310179
43. A. O. Benin, H. Ahissou, Gbaguidi, F. Sanoussi, A. Hougbe, A. Dansi, A. Sanni, *Int. J. Curr. Microbiol. App. Sci.* **2015**, *4*, 394–403.
44. S. Veena, H. H. Bassim, C. S. Yogesh, *Energy conversion and man.* **2016**, *122*, 52–62.
45. Muhammadi, Shabina, M. Afzal, S. Hameed, *Green Chem. Let. and Rev.* **2015**, *8*, 56–77. DOI:10.1080/17518253.2015.1109715
46. Z. Quan, Z. Heng, C. Fei, L. Hu, P. Hu, X. Wei, H. De-Yu, Y. Song, *J. Industrial and Engg. Chem.* **2015**, *31*, 385–392. DOI:10.1016/j.jiec.2015.07.013
47. E. M. Shahid, Y. Jamal, *Renewable and Sustainable Energy Rev.* **2011**, *15*, 4732–4745. DOI:10.1016/j.rser.2011.07.079
48. Y. M. Park, J. Y. Lee, S. H. Chung, I. S. Park, S. Y. Lee, D. K. Kim, J. S. Lee, K. Y. Lee, *Bioresource Tech.* **2010**, *101*, S59–S61. DOI:10.1016/j.biortech.2009.04.025
49. K. H. Chung, B. G. Park, *J. Ind. Eng. Chem.* **2009**, *15*, 388–392. DOI:10.1016/j.jiec.2008.11.012
50. X. R. Chen, Y. H. Ju, C. Y. Mou, *J. Phys. Chem. C.* **2007**, *111*, 18731–18737. DOI:10.1021/jp0749221
51. X. Liu, X. Piao, Y. Wang, S. Zhu, H. He, *Fuel.* **2008**, *87*, 1076–1082. DOI:10.1016/j.fuel.2007.05.059
52. X. Liu, H. He, Y. Wang, S. Zhu, X. Piao, *Fuel.* **2008**, *87*, 216–221. DOI:10.1016/j.fuel.2007.04.013
53. S. J. Yoo, H. S. Lee, V. Bambang, J. D. Kim, Y. W. Lee, *Bior. Technol.* **2010**, *101*, 8686–8989.
54. S. Hu, L. Wen, Y. Wang, X. Zhen, H. Han, *Bior. Tech.* **2012**, *123*, 413–418. DOI:10.1016/j.biortech.2012.05.143
55. P. R. Pandit, M. H. Fulekar, *J. Environ. Manage.* **2017**, *198*, 319–329. DOI:10.1016/j.jenvman.2017.04.100
56. G. Jabbar, H. Ali, L. Xiaojun, H. A. Mukhtar, *Appl. catalysis A: general.* **2016**, *527*, 81–95. DOI:10.1016/j.apcata.2016.08.031
57. H. Shengyang, G. Yanping, W. Yun, H. Heyou, *Appl. Energy.* **2011**, *88*, 2685–2690. DOI:10.1016/j.apenergy.2011.02.012
58. G. Nagaraju, Udayabhanu, S. A. Shivaraj, M. S. Prashanth, K. V. Yathish, C. Anupama, D. Rangappa, *Mat. Res. Bull.* **2017**, *94*, 54–63. DOI:10.1016/j.materresbull.2017.05.043
59. M. Rajesh, P. Shakkthivel, *Bior. Tech.* **2013**, *150*, 55–59. DOI:10.1016/j.biortech.2013.09.087
60. A. U. Khan, *Environ. Monit. Assess.* **2010**, *170*, 171–184. DOI:10.1007/s10661-009-1224-y
61. F. Rana, M. Avijit, *Int. J. Rese. Pharm. Chemi.* **2012**, *2*, 1035–1039.
62. M. Raghavendra, H. S. Lalithamba, B. S. Sharath, H. Rajanai-ka, *Scientia Iranica C.* **2017**, *24*, 3002–3013.
63. U. S. Rao, G. Srinivas, T. P. Rao, *Procedia Materials Science.* **2015**, *10*, 90–96.
64. S. P. Vinay, N. Chandrasekhar, *IOSR J. App. Chem.* **2017**, *10*, 57–63.
65. L. Wan, J. F. Li, J. Y. Feng, W. Sun, Z. Q. Mao, *Mater. Sci. Eng. B.* **2007**, *139*, 216–220. DOI:10.1016/j.mseb.2007.02.014
66. J. Zhang, J. Xi, Z. Ji, *J. Mater Chem.* **2012**, *22*, 17700–17708. DOI:10.1039/c2jm32391e
67. S. Yedurkar, C. Maurya, P. Mahanwa, *Open Journal of Synthesis Theory and Applications.* **2016**, *5*, 1–14. DOI:10.4236/ojsta.2016.51001
68. D. Panchavarnam, S. Menaka, A. Anitha, M. Arulmozhi, *Int. J. ChemTech Research.* **2016**, *9*, 308–315.
69. S. N. Rao, M. V. B. Rao, *American Journal of Materials Science.* **2015**, *5*, 66–68.
70. N. S. Sudarshan, N. Narendra, H. P. Hemantha, V. V. Sureshbabu, *J. Org. Chem.* **2007**, *72*, 9804–9807. DOI:10.1021/jo701371k
71. J. B. Terry, *J. bacteriology.* **1999**, *181*, 4725–4733.
72. G. Agata, K. Halina, F. Karol, *Med. Chem. Res.* **2015**, *24*, 3561–3577. DOI:10.1007/s00044-015-1397-6
73. K. Uma, H. S. Lalithamba, M. Raghavendra, V. Chandramohan, C. Anupama, *Arkivoc.* **2016**, *4*, 339–351.
74. W. Irith, H. Kai, E. W. H. Robert, *Nature Proto.* **2008**, *3*, 163–175. DOI:10.1038/nprot.2007.521
75. L. B. Reller, M. Weinstein, J. H. Jorgensen, M. J. Ferraro, *Clin Infect Dis.* **2009**, *49*, 1749–1755. DOI:10.1086/647952
76. S. P. Vinay, N. Chandrasekhar, *App. Nanoscience.* **2017**, *7*, 851–861. DOI:10.1007/s13204-017-0624-5

Povzetek

S preprosto, učinkovito in priročna metodo smo pripravili nanodelce cinkovega oksida ZnO. Različne parametre, kot so velikost in morfologija, tako pripravljenih nanodecev, smo preučevali z naslednjimi metodami: rentgenska praškovna difrakcija (XRD), infrardeča spektroskopija (FT-IR), UV-Vis spektroskopija, vrstično elektronsko mikroskopijo (SEM), in energijsko disperzijsko spektroskopijo rentgenskih žarkov (EDX). Nanodelce ZnO smo uporabili kot katalizatorje pri pripravi estrov aminokislin in v postopku sinteze biodizla. Tako sintetizirane estre smo karakterizirali z masno spektroskopijo (HRMS) in NMR spektroskopijo in z njimi opravili nekaj *in vitro* antibakterijskih in protiglivičnih testov. Nekateri izmed njih so pokazali obetajočo aktivnost proti bakterijskim patogenom.

Scientific paper

Phase Equilibria in the Tl_4PbTe_3 - Tl_9SmTe_6 - Tl_9BiTe_6 Section of the Tl-Pb-Bi-Sm-Te System

Samira Zakir Imamaliyeva,^{1,*} Alakbarzade Ganira Ilgar,²
Mahmudova Matanat Aydin,³ Amiraslanov Imameddin Rajabali³
and Mahammad Baba Babanly¹

¹ Institute of Catalysis and Inorganic Chemistry named after acad. M. Nagiyev, Azerbaijan National Academy of Sciences, 113, H. Javid. ave., AZ-1143, Baku, Azerbaijan

² Azerbaijan State Oil and Industry University, 16/21, Azadlig Ave., AZ-1010, Baku, Azerbaijan

³ Physics Institute, Azerbaijan National Academy of Sciences, 131, H. Javid ave., Az-1143, Baku, Azerbaijan

* Corresponding author: E-mail: samira9597a@gmail.com

Received: 04-12-2017

Abstract

Phase equilibria in the section Tl_4PbTe_3 - Tl_9SmTe_6 - Tl_9BiTe_6 of the Tl-Pb-Bi-Sm-Te system were determined by combination of differential thermal analysis, powder X-ray diffraction methods as well as microhardness measurements. The phase diagrams of the boundary systems Tl_4PbTe_3 - Tl_9SmTe_6 , Tl_9SmTe_6 - Tl_9BiTe_6 , isothermal section at 820 and 840 K, some isopleth sections and as well as liquidus and solidus surfaces projections, were plotted. Unlimited solid solutions, which crystallize in Tl_5Te_3 structure type were found in the system at the solidus temperatures and below.

Keywords: Thallium-lead telluride; thallium-samarium tellurides; thallium-bismuth tellurides; phase equilibria; liquidus and solidus surfaces; solid solutions

1. Introduction

Complex chalcogenides based materials of great interest for many years due to their functional properties such as optic, photoelectric, magnet, thermoelectric et al.¹⁻³ Some of these materials exhibit properties of topological insulators and can use in spintronic devices.⁴⁻⁶ Furthermore, a number of papers present the results of the study of interactions of the rare-earth elements with heavy elements chalcogenides.⁷⁻⁹

Tl_5Te_3 compound crystallizes in tetragonal structure (Sp.gr. $I4/mcm$, $a = 8.930$; $c = 12.598$ Å),^{10,11} and has a number of ternary substitutional analogs of $Tl_4A^{IV}Te_3$ and $Tl_9B^VTe_6$ -type (A^{IV} -Sn, Pb; B^V -Sb, Bi),¹²⁻¹⁴ which also possess a good thermoelectric performance.^{15,16} Moreover, authors¹⁷ found the Dirac-like surface states in the $[Tl_4]TlTe_3$ (Tl_5Te_3) and its non-superconducting tin-doped derivative $[Tl_4](Tl_{1-x}Sn_x)Te_3$.

A new thallium lanthanide tellurides of Tl_9LnTe_6 -type (Ln-Ce, Nd, Sm, Gd, Tb, Tm) were found to be a new structural analog of Tl_5Te_3 .^{18,19} H. Kleinke and co-workers²⁰⁻²²

confirmed the results of the studies,^{18,19} and determined the thermoelectric and magnetic properties for a number Tl_9LnTe_6 -type compounds.

The development of the novel preparative methods for direct synthesis of functional materials requires to provide an accurate study of phase relations and plot the phase diagram.

Early, we presented the results of a study of phase relations for a number of systems including the Tl_5Te_3 compound or its structural analogs.²³⁻²⁵ The formation of unlimited solid solutions was shown for these systems.

In this paper, we continue to study similar systems and present the experimental results on phase equilibria in the Tl_4PbTe_3 - Tl_9SmTe_6 - Tl_9BiTe_6 section of the Tl-Pb-Bi-Sm-Te system.

The initial compounds of above-mentioned system have been studied in a number of papers. Tl_4PbTe_3 and Tl_9BiTe_6 melt congruently at 893 K,²⁶ and 830 K,¹⁴ respectively, while Tl_9SmTe_6 is formed incongruently at 755 K.²⁵ The tetragonal lattice constants of Tl_4PbTe_3 , Tl_9SmTe_6 , and Tl_9BiTe_6 are following: $a = 8.841$, $c =$

13.056 Å, $z = 4^{27}$; $a = 8.888$; $c = 13.013$ Å, $z = 2^{28}$; $a = 8.855$, $c = 13.048$ Å, $z = 2^{25}$

According to Ref.²⁶, the boundary system Tl_4PbTe_3 - Tl_9BiTe_6 is quasi binary and characterized by the formation of unlimited solid solutions (δ) with Tl_5Te_3 -structure.

2. Experimental

2.1. Materials and Syntheses

The following reagents were used as starting components: thallium (granules, 99.999%), lead (ingot, 99.99%), samarium (powder, 99.9%), bismuth (granules, 99.999%), and tellurium (broken ingots 99.999%).

We used protective gloves at all times when working with thallium because thallium and its compounds are highly toxic and contact with skin is dangerous.

Stoichiometric amounts of the starting components were weighed with accuracy ± 0.0001 g. Then they were put into silica tubes of about 20 cm in length and diameter about 1.5 cm and sealed under a vacuum of 10^{-2} Pa. Tl_4PbTe_3 and Tl_9BiTe_6 were synthesized by heating in a resistance furnace at 920 K followed by cooling in the switched-off furnace.

In the case of Tl_9SmTe_6 , the ampoule was graphitized using pyrolysis of toluene in order to prevent the reaction of samarium with quartz. Taking into account the results of the work²⁶, the intermediate ingot of Tl_9SmTe_6 was powdered in an agate mortar, carefully mixed, pressed into a pellet and annealed at 700 K within ~ 700 h.

The resulting ingots were homogeneous polycrystals alloys that were established by the differential thermal analysis (DTA) and X-ray diffraction (XRD).

The alloys of the Tl_4PbTe_3 - Tl_9SmTe_6 - Tl_9BiTe_6 system were prepared by melting of previously synthesized ternary compounds. After synthesis the samples containing $>60\%$ Tl_9SmTe_6 were powdered, carefully mixed, pressed into pellets and annealed at 700 K during ~ 800 h in order to complete the homogenization. The total mass of each ingot is about 1 g.

2.2. Methods

DTA and XRD analyses, as well as microhardness measurements, were used to analyze the samples of the investigated system.

The phase transformation temperatures were determined using a NETZSCH 404 F1 Pegasus differential scanning calorimeter within room temperature and ~ 1400 K at a heating rate of $10 \text{ K} \cdot \text{min}^{-1}$ and accuracy about ± 2 K. The phase identification was performed using a Bruker D8 diffractometer utilizing CuK_α radiation. The powder diagrams of the ground samples were collected at room temperature in the 2θ range of 6 – 75° . The unit cell parameters of intermediate alloys were calculated by indexing of powder patterns using Topas V3.0 software. An accuracy of the crystal lattice parameters is shown in parentheses (Table). Microhardness measurements were done with a microhardness tester PMT-3, the typical loading being 20 g and accuracy about 20 MPa.

3. Results and Discussion

The Tl_4PbTe_3 - Tl_9SmTe_6 - Tl_9BiTe_6 section was plotted based on combined analysis of experimental results and literature data on boundary system Tl_4PbTe_3 - Tl_9BiTe_6 ²⁶ (Fig. 1–6).

Table 1. Experimental data of the DTA, microhardness measurements and parameters of tetragonal lattice for the alloys of the Tl_4PbTe_3 - Tl_9SmTe_6 and Tl_9BiTe_6 - Tl_9SmTe_6 sections of the Tl-Pb-Bi-Sm-Te system

Solid phase compositions	Thermal effects, K	Microhardness, MPa	Tetragonal lattice parameters, Å	
			<i>a</i>	<i>c</i>
Tl_4PbTe_3	893	1120	8.8409(5)	13.0556(6)
$Tl_{8.2}Pb_{1.6}Sm_{0.2}Te_6$	845–875	1160	8.8504(4)	13.0482(9)
$Tl_{8.4}Pb_{1.2}Sm_{0.4}Te_6$	820–850	1180	8.8602(5)	13.0387(8)
$Tl_{8.5}Pb_{1.0}Sm_{0.5}Te_6$	817–845	–	8.8645(6)	13.0343(9)
$Tl_{8.6}Pb_{0.8}Sm_{0.6}Te_6$	790–830	1150	8.8702(6)	13.0298(9)
$Tl_{8.8}Pb_{0.4}Sm_{0.8}Te_6$	775–800; 1190	1140	8.8788(5)	13.0280(9)
$Tl_{8.9}Pb_{0.2}Sm_{0.9}Te_6$	760–775; 1155	–	–	–
Tl_9SmTe_6	755; 1180	1080	8.8882(5)	13.0132(7)
$Tl_9Bi_{0.1}Sm_{0.9}Te_6$	760; 1150	–	–	–
$Tl_9Bi_{0.2}Sm_{0.8}Te_6$	765–775; 1095	1120	8.8810(4)	13.0201(7)
$Tl_9Bi_{0.4}Sm_{0.6}Te_6$	770–790	1140	8.8741(5)	13.0279(8)
$Tl_9Bi_{0.5}Sm_{0.5}Te_6$	780–800	–	8.8710(5)	13.0301(8)
$Tl_9Bi_{0.6}Sm_{0.4}Te_6$	785–810	1110	8.8673(5)	13.0340(9)
$Tl_9Bi_{0.8}Sm_{0.2}Te_6$	810–820	1070	8.8614(5)	13.0410(8)
Tl_9BiTe_6	830	980	8.8545(4)	13.0476(7)

The Table presents the results of DTA, microhardness measurements, and parameters of the tetragonal lattice for starting compounds and some intermediate alloys.

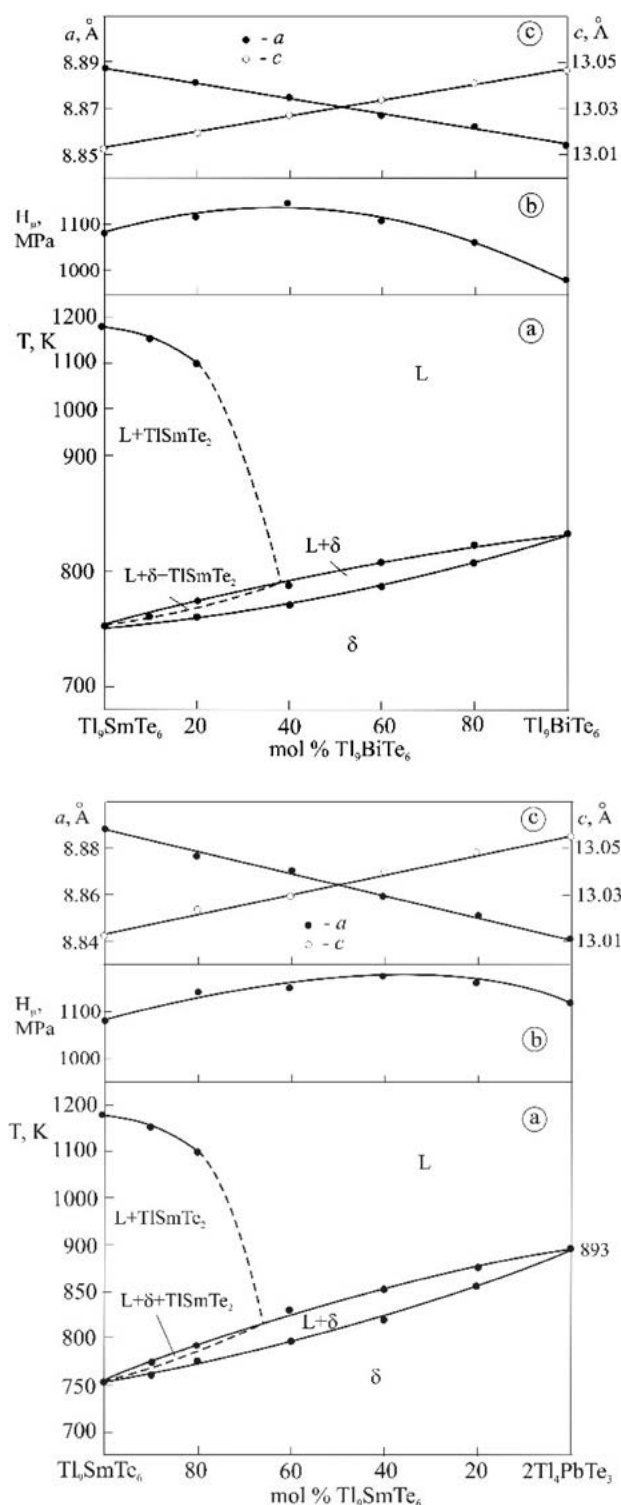


Fig. 1. Polythermal sections (a), concentration dependencies of microhardness (b), and lattice parameters (c) for the alloys of the Tl₉SmTe₆-Tl₉BiTe₆ and Tl₄PbTe₃-Tl₉SmTe₆ sections of the Tl-Pb-Bi-Sm-Te system.

Phase diagrams and the composition dependences of properties are plotted based on these data.

Tl₄PbTe₃-Tl₉SmTe₆ and Tl₉BiTe₆-Tl₉SmTe₆ sections (Fig. 1) are characterized by the formation of unlimited solid solutions (δ) with Tl₅Te₃-structure. But, they are non-quasi-binary sections of the Tl-Pb-Sm-Te and Tl-Bi-Sm-Te quaternary systems due to the peritectic character of melting of Tl₉SmTe₆. As the result, the crystallization of TlSmTe₂ compound occurs in a wide composition interval which leads to the formation of two-phase L+TlSmTe₂ and three-phase L+TlSmTe₂+δ areas. The L+TlSmTe₂+δ area is shown by a dotted line because not fixed experimentally due to a narrow interval of temperatures.

In order to determine the phase constituents, polished surfaces of the intermediate samples were visually observed under the microscope of microhardness meter. The microhardness curves have a flat maximum which is typical for systems with unlimited solid solutions (Fig. 1b).²⁹

The XRD powder patterns for some alloys of the Tl₄PbTe₃-Tl₉SmTe₆ and Tl₉BiTe₆-Tl₉SmTe₆ sections are presented in Fig. 2. Powder diffraction patterns of Tl₄PbTe₃, Tl₉SmTe₆, and Tl₉BiTe₆ as well as intermediate alloys are single-phase and have the diffraction patterns qualitatively similar to Tl₅Te₃ with slight reflections displacement from one compound to another. For example, we present the powder diffraction patterns of alloy with composition 20, 50 and 80 mol% Tl₉SmTe₆ for both systems. Parameters of the tetragonal lattice of solid solutions obey the Vegard's law (Table, Fig. 1c).

Isopleth sections of the Tl₄PbTe₃-Tl₉SmTe₆-Tl₉BiTe₆ system (Fig. 3).

In order to construct a complete T-x-y diagram and to refine the boundaries of areas of primary crystallization of δ-phase and TlSmTe₂, we constructed some isopleth sections. Figs. 3a-c present the isopleth sections Tl₉SmTe₆-[A], Tl₉BiTe₆-[B] and Tl₄PbTe₃-[C] of the Tl₄PbTe₃-Tl₉SmTe₆-Tl₉BiTe₆ system, where A, B, and C are equimolar alloys from the respective boundary system as shown in Fig. 4.

Along the Tl₉SmTe₆-[A] section, the δ-phase crystallizes in the composition area <60 mol% Tl₉SmTe₆. In the Tl₉SmTe₆-rich interval the TlSmTe₂ primary crystallizes, then a monovariant peritectic process L+TlSmTe₂ ↔ δ takes place (Fig. 3a).

Over the entire compositions range of the Tl₉BiTe₆-[B] and Tl₄PbTe₃-[C] sections, crystallization of the δ-phase occurs from the melt (Fig. 3b,c).

The XRD powder patterns for selective alloys on polythermal sections confirmed continuous solid solutions with the Tl₅Te₃-structure.

The liquidus and solidus surfaces projections (Fig. 4)

Projection of liquidus of Tl₄PbTe₃-Tl₉SmTe₆-Tl₉BiTe₆ section consists of two fields of the primary crystallization of TlSmTe₂ and δ- solid solutions. These fields are separated by a monovariant peritectic curve L+TlSmTe₂ ↔ δ (ab curve). The solidus projection (dashed lines) con-

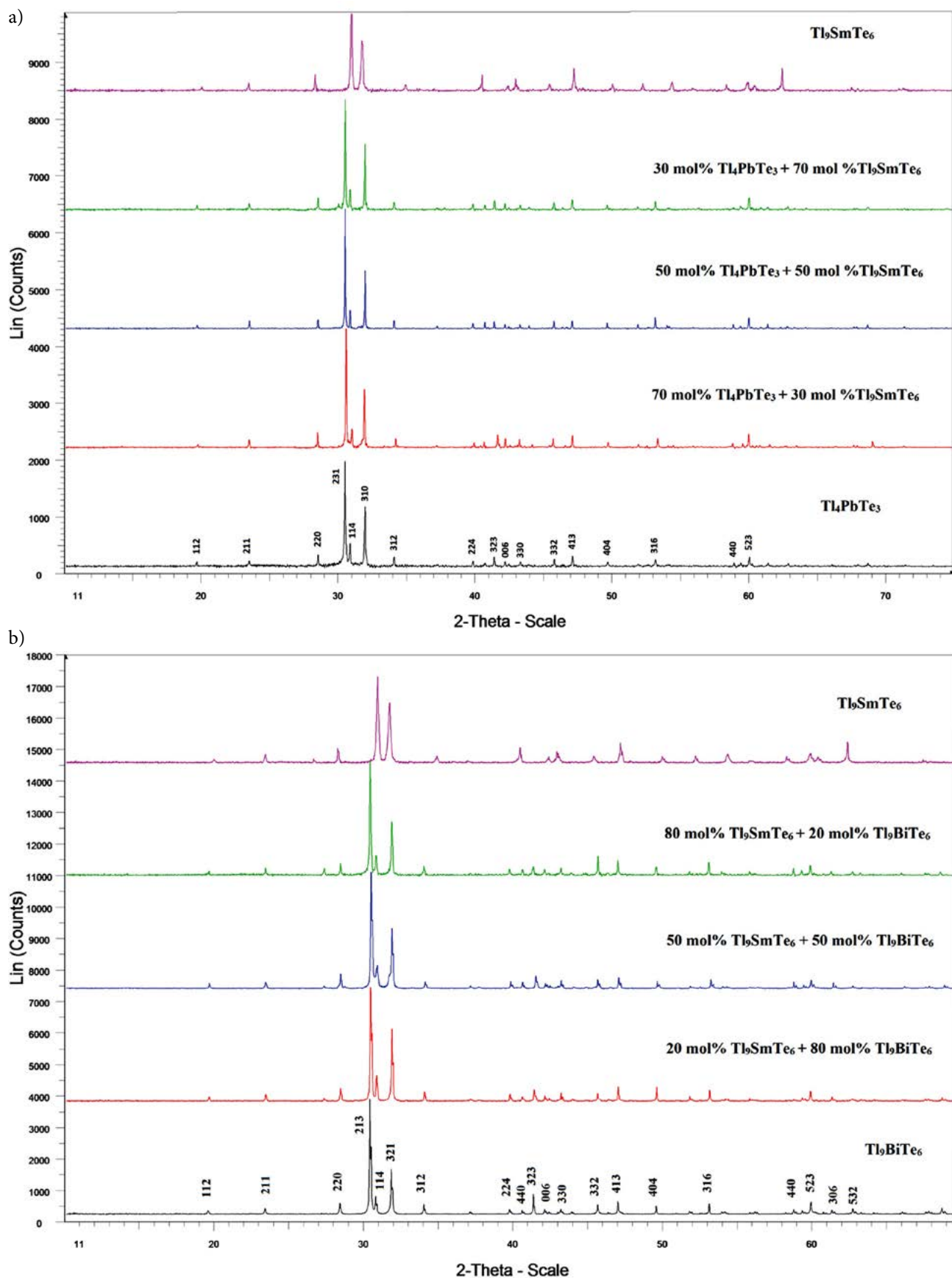


Fig. 2. XRD powder patterns for starting compounds and some alloys of the Tl₄PbTe₃-Tl₉SmTe₆ (a) and Tl₉SmTe₆-Tl₉BiTe₆ (b) systems.

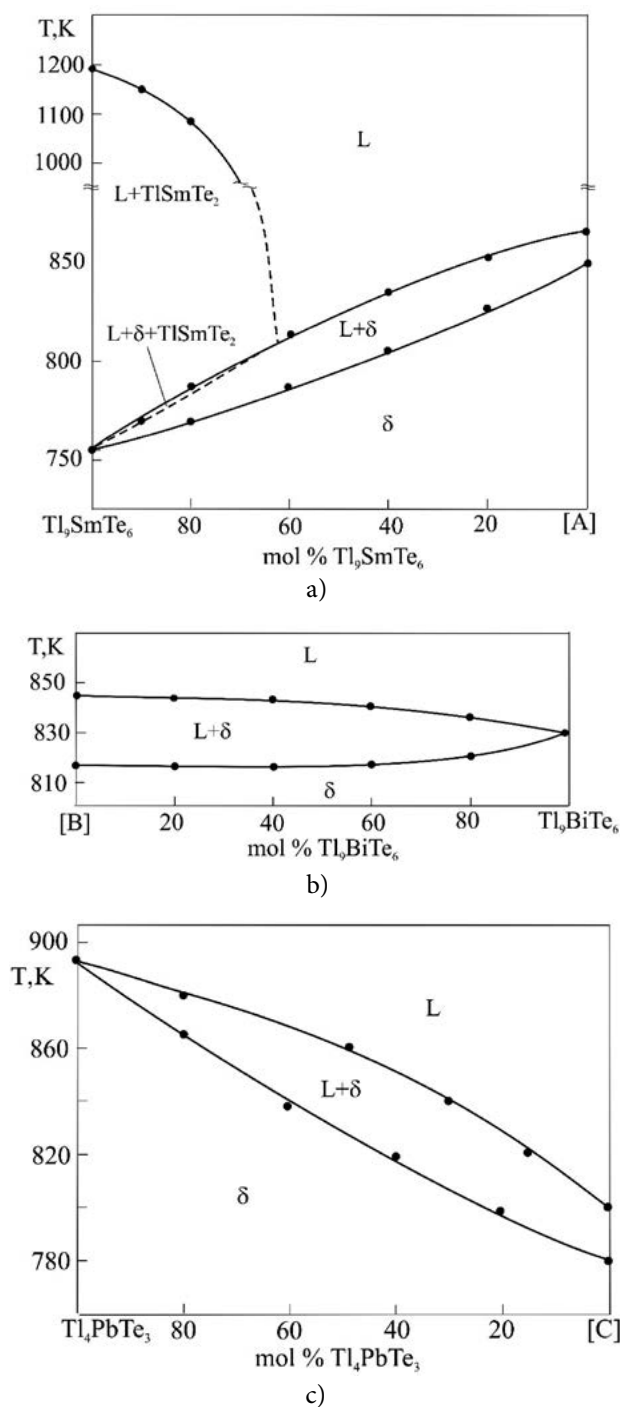


Fig. 3. Polythermal sections Tl₉SmTe₆-[A], Tl₉BiTe₆-[B] and Tl₄PbTe₃-[C] of the phase diagram of the Tl₄PbTe₃-Tl₉SmTe₆-Tl₉BiTe₆ section of the Tl-Pb-Bi-Sm-Te system. A, B, and C are equimolar alloys from the respective boundary system as shown in Fig. 4.

sist of one surface corresponding to the completion of the crystallization of the δ-phase.

Isothermal sections at 820 and 840 K of the Tl₄PbTe₃-Tl₉SmTe₆-Tl₉BiTe₆ section (Fig. 5) are consists of areas of L-, TlSmTe₂ and δ- phases. In alloys <60 mol% Tl₉SmTe₆ in the two-phase L+δ region the directions of the

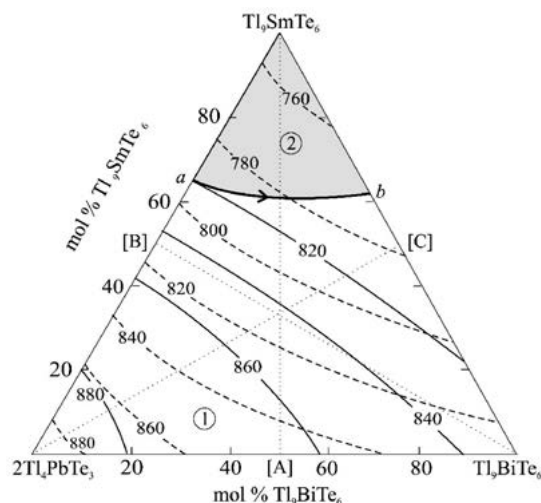


Fig. 4. The liquidus and solidus surfaces projections Tl₄PbTe₃-Tl₉SmTe₆-Tl₉BiTe₆ section of the Tl-Pb-Bi-Sm-Te system. The investigated sections are shown by dash-dot lines. A, B and C are equimolar compositions of the boundary systems. Primary crystallization phases: 1-δ; 2-TlSmTe₂

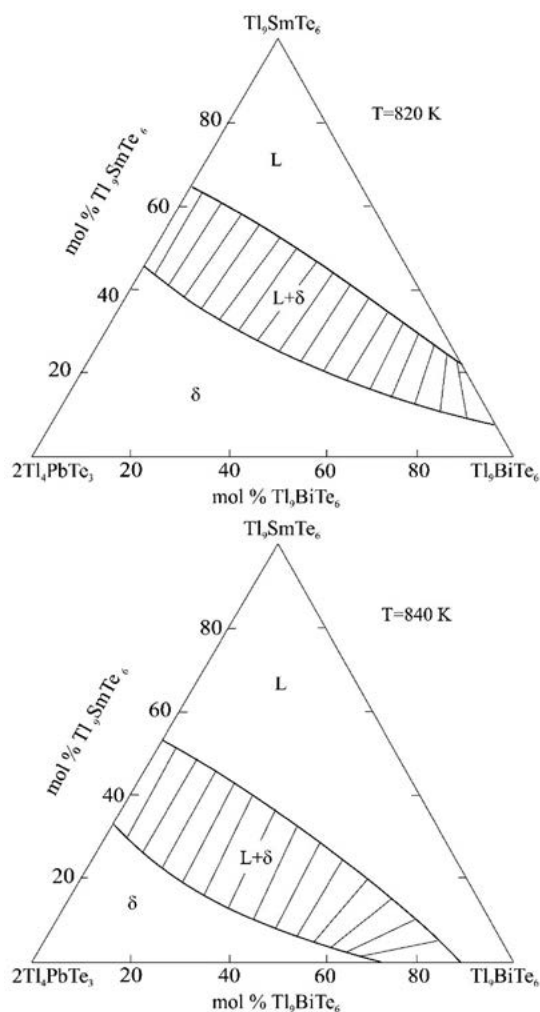


Fig. 5. Isothermal sections at 820 and 840 K in the Tl₄PbTe₃-Tl₉SmTe₆-Tl₉BiTe₆ section of the Tl-Pb-Bi-Sm-Te system.

connodes are on the studied composition plane. It should be noted that comparison of the isopleth sections (Fig. 3) and isothermal sections (Fig. 5) shows that the directions of the connodes in the two-phase region L+ δ deviate from the T - x plane and constantly vary with temperature. Isothermal sections at 820 and 840 K clearly confirm this.

4. Conclusion

A complete phase diagram of the Tl-Pb-Bi-Sm-Te system in the Tl_4PbTe_3 - Tl_9SmTe_6 - Tl_9BiTe_6 composition interval is plotted. Unlimited solubility of components in the solid state is found in the studied section. Obtained experimental results can be used for choosing the composition of solution-melt for the growth of the high-quality crystals of δ - phase which is of interest as thermoelectric material.

5. Acknowledgment

The work has been carried out within the framework of the international joint research laboratory “Advanced Materials for Spintronics and Quantum Computing” (AMSQC) established between Institute of Catalysis and Inorganic Chemistry of ANAS (Azerbaijan) and Donostia International Physics Center (Basque Country, Spain).

6. References

- Applications of Chalcogenides: S, Se, and Te, ed. by Gurinder Kaur Ahluwalia, Springer, 2016.
- A. V. Shevelkov, *Russ. Chem. Rev.*, **2008**, 77, 1–19
DOI:10.1070/RC2008v077n01ABEH003746
- M. G. Kanatzidis, in T. M. Tritt (ed.), *Semiconductors and semimetals*. San Diego; San Francisco; N. Y.; Boston; London; Sydney; Tokyo: Academ. Press. **2001**, 69, 51–98.
- N. Singh and U. Schwingenschlogl, *Phys. Status Solidi RRL*, **2014**, 8, 805–808. DOI:10.1002/pssr.201409110
- Y. L. Chen, Z. K. Liu, J. G. Analytis, J. H. Chu, H. J. Zhang, B. H. Yan et al., *Phys Rev Lett.*, **2010**, 105, 266–401.
DOI:10.1103/PhysRevLett.105.266401
- S. V. Eremeev, Yu. M. Koroteev, E. V. Chulkov, *JETP Lett.*, **2010**, 92, 161–165. DOI:10.1134/S0021364010150087
- C. Zhou, L. Li, *J. Phys. Chem. Solids*, **2015**, 85, 239–244.
DOI:10.1016/j.jpcs.2015.05.021
- B. Yan, H.-J. Zhang, C.-X. Liu, X.-L. Qi, T. Frauenheim and S.-C. Zhang, *Phys. Rev. B*, **2010**, 82, 161–108(R)-7
- O. V. Andreev, V. G. Bamburov, L. N. Monina, I. A. Razumkova, A. V. Ruseikina, O. Yu. Mitroshin, V. O. Andreev, *Phase equilibria in the sulfide systems of the 3d, 4f-elements*. Ekaterinburg: Editorial Publication Department of the UR RAS, **2015**
- I. Schewe, P. Böttcher, H. G. Schnering, *Z. Kristallogr.* **1989**, Bd188, 287–298. DOI:10.1524/zkri.1989.188.3-4.287
- R. Cerny, J. Joubert, Y. Filinchuk, Y. Feutelais, *Acta Crystallogr. C.*, **2002**, 58, 163.
- A. A. Gotuk, M. B. Babanly, A. A. Kuliev, *Inorg. Mater.* **1979**, 15, 1062–1067.
- M. B. Babanly, A. Azizulla, A. A. Kuliev, *Russ. J. Inorg. Chem.* **1985**, 30, 1051–1059.
- M. B. Babanly, A. Azizulla, A. A. Kuliev, *Russ. J. Inorg. Chem.* **1985**, 30, 2356–2359.
- B. Wolfing, C. Kloc, J. Teubner, E. Bucher, *Phys. Rev. Lett.* **2001**, 36, 4350–4353. DOI:10.1103/PhysRevLett.86.4350
- Q. Guo, M. Chan, B. A. Kuropatwa, H. Kleinke, *J. Appl. Phys.*, **2014**, 116, 183702/1–9
- K. E. Arpino, D. C. Wallace, Y. F. Nie, T. Biroli, P. D. C. King, S. Chatterjee, M. Uchida, S. M. Koohpayeh, J.-J. Wen, K. Page, C. J. Fennie, K. M. Shen, and T. M. McQueen, *Phys. Rev. Lett. (PRL)*, **2014**, 112, 017002–5.
DOI:10.1103/PhysRevLett.112.017002
- S. Z. Imamaliyeva, F. M. Sadygov, M. B. Babanly, *Inorg. Mater.* **2008**, 44, 935–938. DOI:10.1134/S0020168508090070
- M. B. Babanly, S. Z. Imamaliyeva, D. M. Babanly, *Azerb. Chem. J.* **2009**, 2, 121–125.
- S. Bangarigadu-Sanasy, C. R. Sankar, P. Schlender, H. Kleinke, *J. Alloys Compd.* **2013**, 549, 126–134.
DOI:10.1016/j.jallcom.2012.09.023
- S. Bangarigadu-Sanasy, C. R. Sankar, P. A. Dube, J. E. Greedan, H. Kleinke, *J. Alloys. Compd.* **2014**, 589, 389–392.
DOI:10.1016/j.jallcom.2013.11.229
- Q. Guo, H. Kleinke, *J. Alloys. Compd.* **2015**, 630, 37–42.
DOI:10.1016/j.jallcom.2015.01.025
- S. Z. Imamaliyeva, T. M. Gasanly, V. A. Gasymov, M. B. Babanly, *Acta Chim. Slov.*, **2017**, 64, 221–226.
DOI:10.17344/acsi.2017.3207
- S. Z. Imamaliyeva, I. F. Mekhdiyeva, V. A. Gasymov, M. B. Babanly, *Mater. Res.*, **2017**, 20, 1057–1062.
DOI:10.1590/1980-5373-mr-2016-0894
- S. Z. Imamaliyeva, V. A. Gasymov, M. B. Babanly, *Chemist*, **2017**, 90, 1–6.
- M. B. Babanly, G. B. Dashdiyeva, F. N. Guseinov, *Chem. Probl.*, **2008**, 1, 69–72.
- S. Bradtmöller, P. Böttcher, *Z. anorg. allg. chem.*, **1993**, 619, 1155–1160. DOI:10.1002/zaac.19936190702
- T. Doert, P. Böttcher, *Z. Kristallogr.*, **1994**, 209, 95.
- V. M. Glazov, V. N. Vigdorovich, *Mikrotverdst’ metallov i poluprovodnikov* (Microhardness of Metals and Semiconductors), Moscow: Metallurgiya, **1969**.

Povzetek

V sistemu Tl-Pb-Bi-Sm-Te smo preučevali fazna ravnotežja dela Tl_4PbTe_3 - Tl_9SmTe_6 - Tl_9BiTe_6 s termično analizo, rentgensko praškovno difrakcijo in meritvami mikrotrdote. Pripravili smo fazne diagrame sistemov Tl_4PbTe_3 - Tl_9SmTe_6 , Tl_9SmTe_6 - Tl_9BiTe_6 , izotermične krivulje pri 820 K in 840 K, nekatere izopletne krivulje ter projekcije tekočinsko trdnih površin. Trdne raztopine kristalizirajo v Tl_5Te_3 kristalnem sistemu pri temperaturah strjavanja in nižjih.

Synthesis, X-ray Structural Characterization, and DFT Calculations of Mononuclear Nickel(II) Complexes Containing Diamine and Methacrylate Ligands

Rasoul Vafazadeh,^{1,*} Mansoor Namazian,¹ Behnoosh Shahpoori-Arani,¹ Anthony C. Willis² and Paul D. Carr

¹ Department of Chemistry, Faculty of Science, Yazd University, Yazd, Iran.

² Research School of Chemistry, Australian National University, Canberra, ACT 2601, Australia.

* Corresponding author: E-mail: rvafazadeh@yazd.ac.ir

Received: 14-12-2017

Abstract

The mononuclear Ni(II) complexes $[\text{Ni}(\text{en})_2(\text{H}_2\text{O})_2](\text{MAA})_2$ (**1**) and $[\text{Ni}(\text{pn})_2(\text{MAA})_2]$ (**2**), where MAA, en and pn are methacrylate, ethylenediamine and 1,3-propylenediamine, respectively, have been synthesized and characterized by elemental analysis, FT-IR and UV-Vis spectroscopy. Structures of the complexes have been determined by single-crystal X-ray diffraction analyses. In the nickel(II) complexes **1** and **2** nickel(II) ion is six-coordinate and has a distorted octahedral geometry. Ni(II) is bonded to four nitrogen atoms of the two diamines and additionally to two oxygen atoms of aqua ligand in **1**, and two oxygen atoms of methacrylate ligands in **2**. The theoretical geometries of the studied compounds have been calculated by means of density functional theory (DFT) at the B3LYP/6-311+G(d,p)/LanL2DZ level and considering effective core potential (ECP). The comparison of the results indicates that the employed DFT method yields good agreement with experimental data.

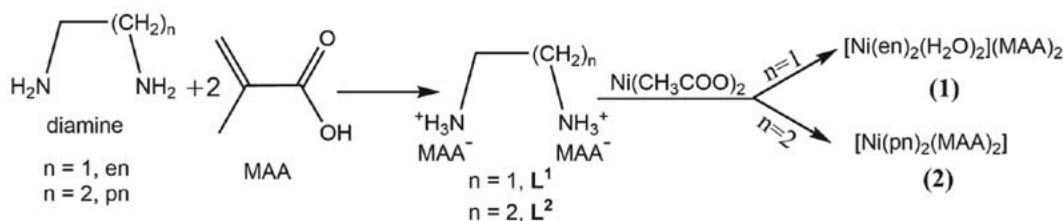
Keyword: Nickel(II) complex; mononuclear; methacrylate; diamine; DFT

1. Introduction

Transition metal complexes containing poly-dentate amine ligands the most widely used in coordination chemistry.^{1–5} There have been numerous of investigation on polydentate amines. These ligands, and in particular diamines such as ethylene diamine (en) and 1,3-propane diamine (pn) find great utility due to ease synthesis and the ability to form stable complexes with first-row transition metal ions.^{5–9} On the other hand, the complexes with organic, inorganic carboxylates and their derivatives are widely used in coordination chemistry. The carboxylates

in the complexes exhibit various possible bonding modes, mono- and bidentate by forming chelation or bridges in coordinating to the transition metal. The coordination mode of the carboxylate ligands depends on metal ion and other ligands employed in the synthesis of the complexes.^{10–15}

In our previous work, we reported the synthesis, spectroscopic characterization, structural aspects and density functional theory (DFT) calculations for two Cu(II) complexes containing diamine, acetate, and methacrylate ligands.¹⁵ In order to investigate the effect of the metal on the structural complexes with these ligands, we



Scheme 1. Synthesis of the complexes **1** and **2**

carried out the synthesis of two Ni(II) complexes by reaction of diaminium-methacrylic acid salt (diamines are ethylenediamine and 1,3-propylenediamine) with Ni(II) acetate (Scheme 1). The structures of the complexes have been determined by single-crystal X-ray diffraction analyses and calculated by density functional theory.

2. Experimental

2. 1. Starting Materials and Physical Measurements

All chemicals were of analytical reagent grade and were used without further purification. Infrared spectra were taken with an Equinox 55 Bruker FT-IR spectrometer using KBr pellets in the 400–4000 cm^{-1} range. Absorption spectra were determined in the solvent of dimethylformamide (DMF) using GBC UV-Visible Cintra 101 spectrophotometer with 1 cm quartz, in the range of 200–800 nm. Elemental analyses (C, H, N) were performed by using a CHNS-O 2400II PERKIN-ELMER elemental analyzer.

2. 2. X-Ray Crystallography

Diffraction images of **1** and **2** were measured at 150 K on Agilent Xcalibur and SuperNova diffractometers using Cu $K\alpha$ ($\lambda = 1.54180 \text{ \AA}$) and Mo $K\alpha$ ($\lambda = 0.71073 \text{ \AA}$) radiation, respectively. Data were extracted using the

Table 1. Crystallographic data and structural refinement for complexes **1** and **2**

Compound	1	2
Empirical formula	$\text{C}_{12}\text{H}_{30}\text{N}_4\text{NiO}_6$	$\text{C}_{14}\text{H}_{30}\text{N}_4\text{NiO}_4$
Formula weight	385.10	377.13
Crystal system	Monoclinic	Monoclinic
Space group	C2/c	P2 ₁ /c
Temperature (K)	150	150
<i>a</i> / \AA	24.4016 (10)	10.0738 (5)
<i>b</i> / \AA	6.9977 (3)	8.3205 (3)
<i>c</i> / \AA	10.7021 (6)	11.1221 (6)
α / $^\circ$	90	90
β / $^\circ$	93.316 (4)	103.659 (3)
γ / $^\circ$	90	90
<i>V</i> / \AA^3	697.29 (9)	1610.89 (6)
<i>Z</i>	4	2
<i>F</i> (000)	824	404
<i>d</i> _{calc} (g cm^{-3})	1.402	1.383
μ (mm $^{-1}$)	1.84	1.10
Measured reflections	9955	10433
Independent reflections	1803	2280
Observed reflections	1710	1868
<i>R</i> _{int}	0.036	0.044
<i>R</i> [$F^2 > 2\sigma(F^2)$]	0.054	0.043
<i>wR</i> (F^2) (all data)	0.159	0.098

CrysAlis PRO package.¹⁶ The structures were solved by direct methods with the use of SIR92.¹⁷ The structures were refined on F^2 by full matrix least-squares techniques using the CRYSTALS program package.¹⁸ Atomic coordinates, bond lengths, and angles and displacement parameters have been deposited at the Cambridge Crystallographic Data Centre. Crystallographic data and refinement details for the complexes are given in Table 1. Details of the refinement procedures for the structures are given in the Supplementary Information.

2. 3. Theoretical Calculations

All computations were performed by means of standard DFT method using the Gaussian09 (G09) program package.^{19,20} The geometries of the studied complexes have been optimized at the B3LYP level of the theory.²¹ The basis set of 6-31G(2df,p) was used for the C, H, N, and O atoms as recommended by Curtiss and his co-workers,²² while the basis set of LanL2DZ was employed for Ni atom considering the size of complexes and hardware limitations.^{23–25} Special care was taken to select the (global) minimum energy conformation *via* systematic conformational searching at this level. The nature of each stationary point was established by frequency calculations at the same level of B3LYP/6-31G(2df,p)/LanL2DZ. The geometry optimizations have been completed in the absence of solvent molecules and other impurities, and the optimized structures were compared with the crystalline structures. Charges on atoms have been calculated using Natural Bond Orbital (NBO) theory at the higher level of B3LYP/6-311+G(2df,p)/LanL2TZf.^{26,27}

2. 4. Syntheses of Compounds **L**¹ and **L**²

The compounds **L**¹ and **L**² were prepared as previously reported elsewhere by us by reaction between two equivalents of methacrylic acid (20 mmol, 1.70 mL) and one equivalent of related diamine, 1,2-ethylenediamine (10 mmol, 0.67 mL) and 1,3-propandiamine (10 mmol, 0.84 mL) in methanol (40 mL), respectively.¹⁵ The resulting bright yellow solution was heated to reflux for two hours. After two days, the solid yellow powder obtained was filtered, washed with acetone and acetonitrile, and dried in air.

2. 5. Synthesis of Nickel(II) Complexes

$\text{Ni}(\text{CH}_3\text{COO})_2 \cdot 4\text{H}_2\text{O}$ (2.00 mmol, 0.496 g) was slowly added to an ethanol solution (40 mL) of the corresponding compound (**L**¹, 2.00 mmol, 0.464 g; **L**², 2.00 mmol, 0.492 g) and the resulting solution was stirred for two hours at room temperature. Two days upon evaporation of the solvents, a blue-green oil formed. The oil form obtained was re-suspended in ether and stirred at room temperature until a precipitate formed. The solid product

was recrystallized from suitable solvents according to the following procedures:

[Ni(en)₂(H₂O)₂](MAA)₂ (**1**)

Yield: 0.36 g (47%). The light violet solid product was recrystallized from dichloromethane/toluene (1:1 v/v). The light violet crystals were filtered and dried in air. Anal. Calc. for C₁₂H₃₀N₄NiO₆ (385.09): C, 37.43; H, 7.85; N, 14.55%. Found: C, 37.62; H, 7.91; N, 14.39%. IR (KBr, cm⁻¹): 3276, 3192, 1628, 1547 and 1450. Electronic spectra for CH₃OH: λ_{max} (log ε) 225 nm (2.93), 284 nm (2.46), 370 nm (2.26), 631 nm (0.93) and 1009 nm (0.93).

[Ni(pn)₂(MAA)₂] (**2**)

Yield: 0.50 g (66%). The blue-green solid product was recrystallized from dichloromethane/n-hexane/toluene (3:1:2 v/v). Blue crystals were filtered and dried in air. Anal. Calc. for C₁₄H₃₀N₄NiO₄ (377.11): C, 44.59; H, 8.02; N, 14.86%. Found: C, 44.82; H, 8.18; N, 14.66%. IR (KBr, cm⁻¹): 3290, 3176, 1632, 1546 and 1451. Electronic spectra for CH₃OH: λ_{max} (log ε) 226 nm (4.60), 284 nm (3.65), 377 nm (3.40), 630 nm (0.71) and 1041 nm (0.46).

3. Results and Discussion

3. 1. Syntheses and Characterization of the Complexes

The diamine-methacrylic acid salt ligands were obtained by reaction of related diamine (ethylenediamine, en, and 1, 3-propylenediamine, pn) and methacrylic acid in methanol under reflux. The reaction of nickel(II) acetate with **L**¹ and **L**² leads to the formation of mononuclear complexes **1** and **2**, while in the reaction of copper(II) acetate with these ligands dinuclear copper complexes were formed.

The most significant IR bands for ligands and complexes are given in the experimental section. In the IR

spectra of the compounds **L**¹ and **L**² two strong bands at 1650 and 1455 cm⁻¹ (for **L**¹) and 1646 and 1455 cm⁻¹ (for **L**²) corresponding to stretching frequencies of the carboxylate group: asymmetric ν_{asym}(COO⁻) and symmetric ν_{sym}(COO⁻), respectively.

In IR spectra of **1**, [Ni(en)₂(H₂O)₂](MAA)₂, the appearance of two bands at 1628 and 1450 cm⁻¹ due to asymmetric ν_{asym}(COO⁻) and symmetric ν_{sym}(COO⁻), respectively, reveal the uncoordinated methacrylate ions. In contrast, complex **2**, [Ni(pn)₂(MAA)₂], shows two strong bands at 1632 and 1381 cm⁻¹ corresponding to stretching frequencies of the carboxylate group: asymmetric ν_{asym}(COO⁻) and symmetric ν_{sym}(COO⁻), respectively. The difference between asymmetric and symmetric frequencies (Δ[ν_{asym}(COO⁻) - ν_{sym}(COO⁻)] > 200 cm⁻¹) indicates a monodentate coordination mode for the methacrylate ion (see the description of X-ray crystal structures section).^{10,12,28,29}

The absorption spectra of the compounds **L**¹ and **L**² in methanol solution show band n-π* transitions at 226 and 216 nm, respectively. Electronic spectra of **1** and **2** show broad bands at 1009 and 631 nm (for **1**) 1041 and 630 nm (for **2**), respectively. These spectral features are consistent with six-coordinate octahedral geometry for Ni(II). These bands arise from spin-allowed d-d transitions of the nickel(II) ion in a distorted octahedral environment where two maxima observed in the visible region result from ³A_{2g}→³T_{1g} and ³A_{2g}→³T_{2g} transitions, respectively.³⁰ The sharp a signal at 370 (for **1**), and 377 nm (for **2**) can be assigned to be charge transfer transition. Two bands at 284 and 225 nm (for **1**) and 284 and 226 nm (for **2**) assigned to intraligand π-π* transitions.

3. 2. Description of X-Ray Crystal Structures

3. 2. 1. Crystal Structures of **1** and **2**

The molecular structure of nickel(II) complexes **1** and **2** are shown in Figs. 1 and 2, respectively. The com-

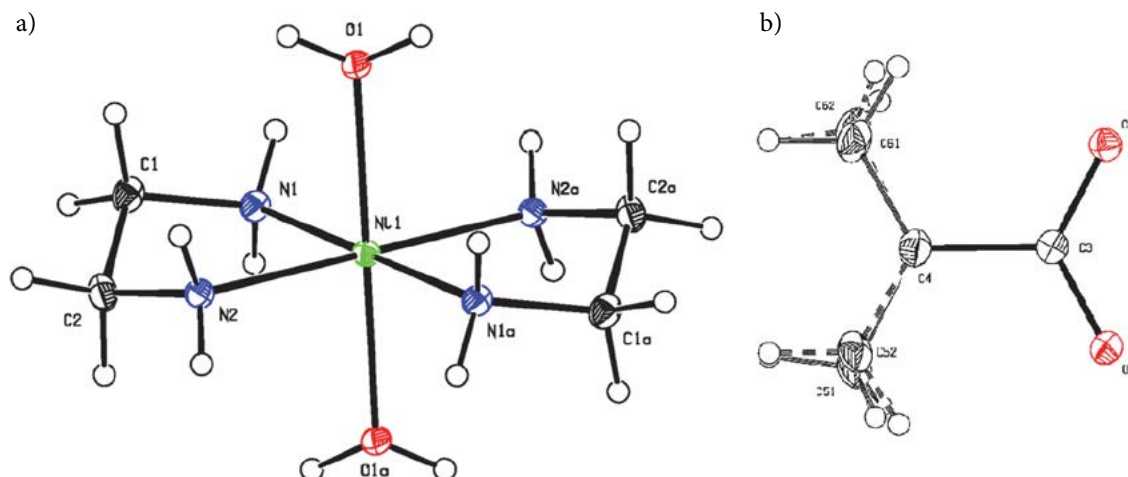


Fig. 1. The ORTEP view of complex **1** (a) with one methacrylate anion (b), showing 30% probability thermal ellipsoids

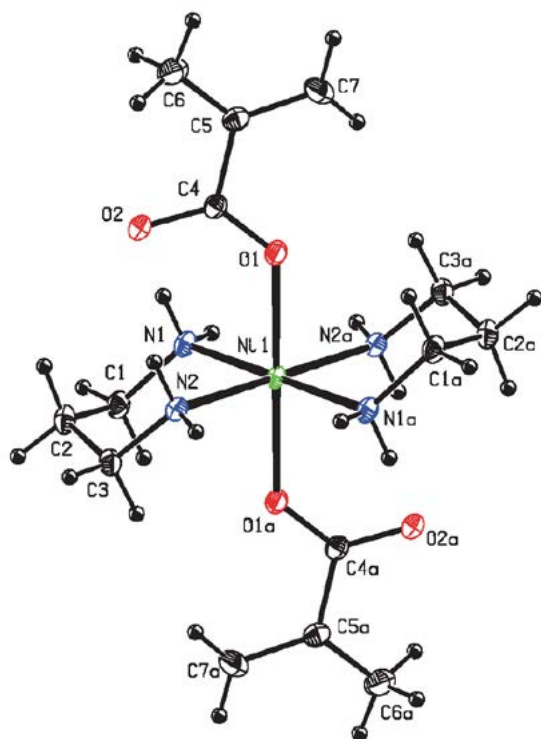


Fig. 2. The ORTEP view of complex 2 showing 30% probability thermal ellipsoids

plexes **1** and **2** crystallizes in monoclinic space group $C2/c$ and monoclinic space group $P2_1/c$ and there are four ($Z = 4$) and two ($Z = 2$) molecules in the unit cell, respectively.

The Ni–O and Ni–N bond lengths of the complexes **1** and **2** have good agreement with Ni(II) complexes previously reported.^{31–33}

In both complexes, the nickel(II) ion is six-coordinate (N_4O_2 donor atoms) and have a distorted octahedral geometry. The equatorial plane is formed by four nitrogen atoms from two diamine ligands (ethylenediamine, **1**, and 1,3-propylenediamine, **2**) coordinates to the metal center. The ethylenediamine and 1,3-propylenediamine ligands form with Ni(II) atom five-membered and six-membered

Table 2. Selected bond lengths (Å) and angles (°) in complexes **1** and **2**

Bond lengths (Å)		Bond angles (°)	
Complex 1			
Ni1–N1	2.088 (3)	N1–Ni1–N2	83.51 (13)
Ni1–N2	2.099 (3)	O1–Ni1–O1 ^a	180
Ni1–O1	2.159 (3)	N1–Ni1–N2 ^a	96.49 (13)
C3–O2	1.261 (5)	N1–Ni1–O1	88.17 (12)
C3–O3	1.264 (5)	O3–C3–O2	124.1 (3)
Complex 2			
Ni1–N1	2.105 (2)	N1–Ni1–N2	86.69 (9)
Ni1–N2	2.104 (2)	O1–Ni1–O1 ^b	180
Ni1–O1	2.1225 (19)	N1–Ni1–N2 ^b	93.31 (9)
C4–O1	1.267 (3)	N1–Ni1–O1	89.47 (8)
C4–O2	1.260 (3)	O1–C4–O2	125.0 (3)

Symmetry codes: $a = -x + 3/2, -y + 3/2, -z + 1$; $b = -x + 2, -y + 1, -z + 1$

chelate rings, respectively. The Ni–N bond lengths in the complex **2** are at distances 2.104(2) and 2.105(2) Å, which are longer than Ni–N bond lengths (2.088(3) and 2.099(3) Å) in the complex **1**, possibly due to the increased chelate rings formed with the Ni(II) atom. The main difference between the two complexes is that in **1** where are two water molecules coordinated to the Ni(II) ion and two methacrylate ions are not coordinated to the Ni(II) ion and acts only as counter anions, whereas in **2** the two methacrylate ions are coordinated to the center ion. The Ni–O bond length of complex **1** (2.159(3) Å) is longer than the corresponding bond of complex **2** (2.1225(19) Å). This variation is consistent with the anionic nature of the methacrylate ligands. The chelating N–Ni–N angle is 83.51(13)° for **1** and 86.69(9)° for **2**, whereas the non-chelating N–Ni–N angles are 96.49(13)° and 93.31(9)° for **1** and **2**, respectively. Selected bond lengths and angles, as well as interatomic distances, are summarized in Table 2.

In **1**, there is a disorder pattern in the packing of the $-C(CH_3)=CH_2$ group over two positions, with relative occupancies of 52%:48% (Fig. 1b). However, in **2** two methacrylate ions are coordinated to the Ni(II) ion.

Table 3. Hydrogen bonding (Å) and angles (°) in complexes **1** and **2**

	D–H...A	D–H	H...A	D...A	D–H...A	Symmetry code
1	N1–H811...O1	0.95 (5)	2.59 (5)	3.337 (4)	135 (4)	$-x + 3/2, y + 1/2, -z + 3/2$
	N1–H811...O2	0.95 (5)	2.44 (5)	3.214 (4)	139 (4)	$x, -y + 1, z + 1/2$
	N1–H812...O3	0.91 (5)	2.15 (5)	3.041 (4)	170 (4)	$x, y + 1, z$
	N2–H821...O3	0.91 (5)	2.19 (5)	3.066 (4)	164 (4)	$x, -y + 1, z - 1/2$
	N2–H822...O2	0.90 (5)	2.17 (5)	2.066 (4)	171 (4)	x, y, z
	O1–H911...O2	0.96 (5)	1.78 (5)	2.731 (4)	172 (4)	$-x + 3/2, -y + 1/2, -z + 1$
	O1–H912...O3	0.84 (6)	1.91 (6)	2.747 (4)	173 (4)	x, y, z
2	N1–H5...O2	0.89 (3)	2.44 (3)	3.144 (4)	136 (1)	x, y, z
	N2–H9...O2	0.88 (3)	2.16 (3)	3.007 (4)	162 (1)	$-x + 2, y - 1/2, -z + 1/2$
	N1–H12...O2	0.91 (3)	2.13 (3)	3.030 (4)	171 (1)	$x, -y + 3/2, z + 1/2$
	N2–H13...O2	0.88 (3)	2.24 (3)	2.989 (4)	142 (1)	x, y, z

Crystal structures of complexes **1** and **2** both show hydrogen bonding interactions. In **1** one hydrogen atom of the coordinated water molecule is involved in an intramolecular hydrogen bonding interaction with the oxygen atom O3 of a methacrylate anion, and the other water H atom is hydrogen bonded to O2A of the methacrylate anion (symmetry code: $x, -y + 1, z + \frac{1}{2}$), with donor(D)–acceptor(A) distances of 2.747(4) and 3.214(4) Å and D–H...A angles of 173(5) and 139(4)°, respectively. Also, there is a hydrogen bonding interaction between the hydrogen atoms of the NH₂ of the ethylenediamine ligands with the oxygen atoms of a methacrylate anion. In **2**, there are hydrogen bonding interaction, between the hydrogen atoms bonded of the 1,3-propylenediamine with oxygen atoms of the methacrylate ligand. Full details of the hydrogen bonding are given in Table 3.

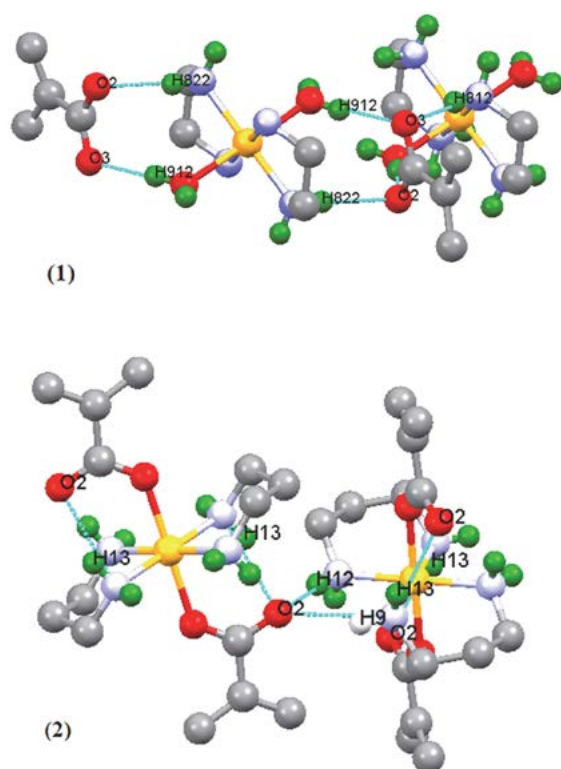


Fig. 3. Various hydrogen bonding interactions in complexes **1** and **2**, other hydrogen atoms are omitted for clarity.

Table 4. Selected geometric parameters from X-ray experiment and DFT-B3LYP calculations

	Bond length (Å)	Expt.	Calc.	\Delta d	Bond angle (°)	Expt.	Calc.	\Delta \theta
1	Ni1–N1	2.09	2.10	0.01	N1–Ni1–N2	83.5	82.11	1.4
	Ni1–N2	2.10	2.14	0.04	O1–Ni1–O1 ^a	180	178.3	1.7
	Ni1–O1	2.16	2.26	0.10	N1–Ni1–O1	88.2	89.1	0.9
2	Ni1–N1	2.10	2.16	0.06	N1–Ni1–N2	86.7	83.6	3.1
	Ni1–N2	2.10	2.16	0.06	O1–Ni1–O1 ^b	180.0	180.0	0.0
	Ni1–O1	2.12	2.10	0.02	N1–Ni1–O1	89.5	89.8	0.3

Symmetry codes: $a = -x + 3/2, -y + 3/2, -z + 1$; $b = -x + 2, -y + 1, -z + 1$

3. 3. DFT Optimized Geometries

The geometry optimization of nickel(II) complexes was carried out in their singlet and triplet spin states. The optimized geometric parameters at their most stable spin states, which are triplet for complexes **1** and **2** is shown in Fig. 4.

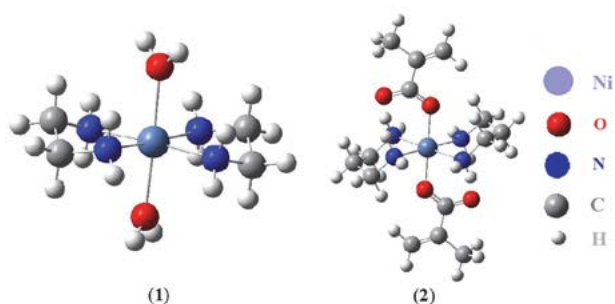


Fig. 4. The optimized structures of the complexes **1** and **2**.

As shown in Table 4, the calculated bond lengths for the studied complexes agree well with the X-ray experimental data.

The differences between optimized geometrical parameters and experiment are less than 0.05 Å (bond distances) and 2° (bond angles) in most cases (Fig. 5).

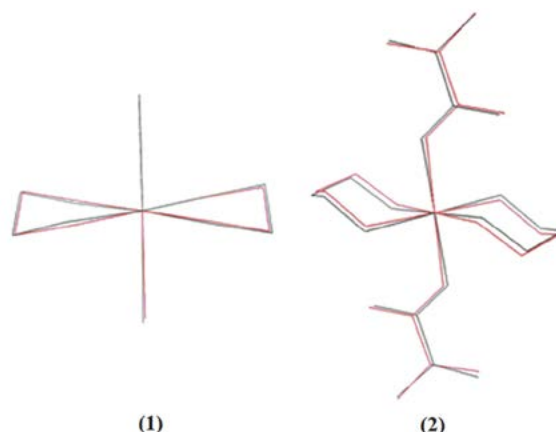


Fig. 5. Atom-by-atom superimposition of the calculated structures (black) over the X-ray structure (red); hydrogen atoms have been removed for clarity.

In general, the predicted bond lengths are slightly longer in comparison with the values based on the X-ray crystal structure data. The geometrical differences might be a result of crystal packing forces which have an influence on the molecules as expected for the experimental ones (solid state), but the calculated geometries are in the gas phase.^{34,35} The crystal packing forces, which have an influence on the molecules, as expected for the experimental parameters (solid state), is a reason for the difference of calculated bond lengths in the gas phase and solid phase.

The vibrational frequency calculations were performed based on the optimized structures of complexes. The calculated and experimental IR spectra of complexes are in good agreement with experimental data (Fig. 6 and Fig. S1).

The energies of the HOMO and LUMO molecular orbitals have been also calculated. The experimental values of HOMO-LUMO gap (Δ) for the complexes of **1** and **2** based on UV-Vis spectra are 5.51 and 5.49 eV, respectively, which corresponds to $n \rightarrow \pi^*$ transitions. The theoretical

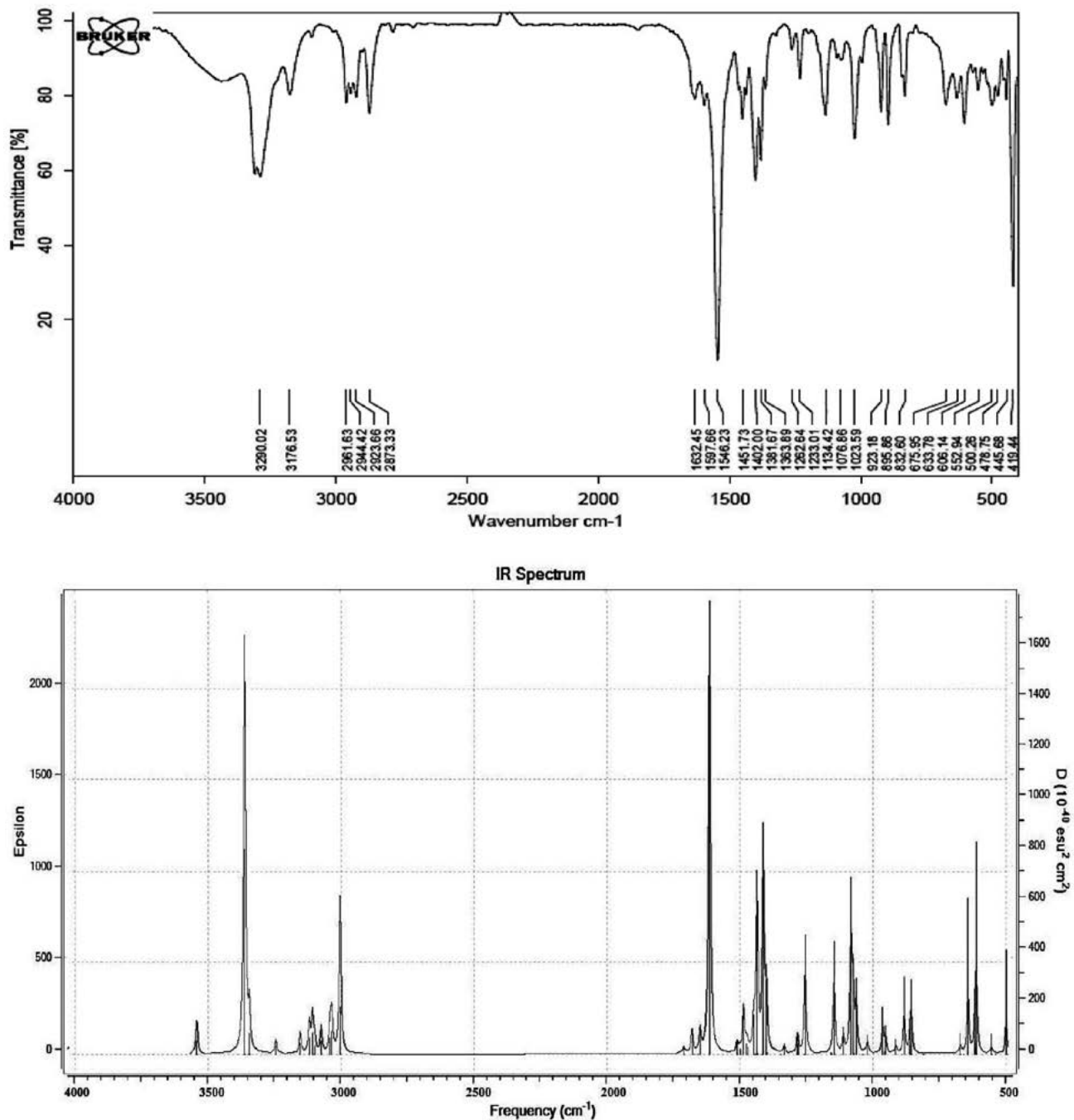


Fig. 6. The experimental (top) and calculated (down) IR spectra of complex 2.

values have been calculated as 6.36 and 5.25 eV, respectively, which are in line with the experimental values with relatively low deviations.

The calculated charges on the metal centers in complexes **1** and **2** are +1.306 and +1.267 respectively, and these values are greatly lower than the formal charge of +2. These differences are as a result of charge donation from the donor atoms of ligands.

4. Conclusion

The reaction of nickel(II) acetate with **L**¹ and **L**² ligands led to the formation of mononuclear complexes **1** and **2**. The crystal structures were determined for two studied complexes. In mononuclear nickel(II) complexes **1** and **2**, metal centers are hexacoordinated with a distorted octahedral geometry. The optimized structure of the complexes has been studied using the B3LYP/6-31G(d)/Lan-L2DZ level of theory. The calculated molecular geometries are in a very good agreement with the experimental data. It has been revealed that the triplet state for nickel(II) complexes **1** and **2** are more stable than their singlet state.

5. Supplementary Material

The deposition numbers of the studied complexes, **1** and **2** are CCDC 1481553 and 1481554, respectively. These data can be obtained free-of-charge via www.ccdc.cam.ac.uk/data_request/cif, by emailing data-request@ccdc.cam.ac.uk, or by contacting The Cambridge Crystallographic Data Centre, 12 Union Road, Cambridge CB2 1EZ, UK; fax +44 1223 336033.

6. Acknowledgement

MN is thankful to Prof. Michelle L. Coote and Research School of Chemistry, The Australian National University for the offer of campus visiting position and for the Gaussian calculations. BS is grateful to the graduate school of Yazd University for the post-graduate scholarships. MN and RV are also grateful to Yazd University and the Australian National University for their valuable support.

7. References

- G. C. Giri, A. Patra, G. Vijaykumar, L. Carrella, M. Bera, *RSC Adv.* **2015**, *5*, 99270–99283.
- P. Bhowmik, S. Biswas, S. Chattopadhyay, C. Diaz, C. J. Gómez-García, A. Ghosh, *Dalton Trans.* **2014**, *43*, 12414–12421
- K. Zheng, L. Jiang, Y. T. Li, Z. Y. Wu, C. W. Yan, *RSC Adv.* **2015**, *5*, 51730–51744.
- X. Sala, E. J. García Suárez, Z. Freixa, J. Benet-Buchholz, P. W. N. M. van Leeuwen, *Eur. J. Org. Chem.* **2008**, 6197–6205.
- H. Shirase, Y. Miura, Y. Fukuda, *Monatsh Chem.* **2009**, *140*, 807–814.
- M. Behrens, S. Scherb, C. Näther, W. Bensch, *Z. Anorg. Allg. Chem.* **2003**, *629*, 1367–1373.
- X. Wang, D. S. Yang, *J. Phys. Chem. A* **2006**, *110*, 7568–7576.
- F. Emmenegger, C. W. Schlaepfer, H. Stoeckli-Evans, M. Piccand, H. Piekarski, *Inorg. Chem.* **2001**, *40*, 3884–3888.
- H. Golchoubian, E. Rezaee, G. Bruno, H. Amiri Rudbari, *Inorg. Chim. Acta*, **2013**, *394*, 1–9.
- L. N. Wang, L. Fu, J. W. Zhu, Y. Xu, M. Zhang, Q. You, P. Wang, J. Qin, *Acta Chim. Slov.* **2017**, *64*, 202–207.
- C. J. Lina, J. L. Qia, Y. Q. Zheng, J. L. Lina, *J. Coord. Chem.* **2013**, *66*, 3877–3890.
- R. Vafazadeh, Z. Moghadas, A. C. Willis, *J. Coord. Chem.* **2015**, *68*, 4255–4271.
- G. T. Musie, X. Li, D. R. Powell, *Inorg. Chim. Acta* **2006**, *359*, 1989–1996.
- S. Singh, D. Saini, S. K. Mehta, D. Choquesillo-Lazarte, *J. Coord. Chem.* **2011**, *64*, 1544–1553.
- R. Vafazadeh, M. Namazian, M. Chavoshiyan, A. C. Willis, P. D. Carr, *Acta Chim. Slov.* **2017**, *64*, 613–620.
- Agilent. CrysAlis PRO. Agilent Technologies Ltd, Yarnton, Oxfordshire, England, **2014**.
- A. Altomare, G. Cascarano, G. Giacovazzo, A. Guagliardi, M. C. Burla, G. Polidori, M. Camalli, *J. Appl. Cryst.* **1994**, *27*, 435–436.
- P. W. Betteridge, J. R. Carruthers, R. I. Cooper, K. Prout, D. J. Watkin, *J. Appl. Cryst.* **2003**, *36*, 1487–1487.
- W. J. Hehre, L. Radom, P. V. R. Schleyer, J. A. Pople, *Ab initio Molecular Orbital Theory*, Wiley, New York, 1986.
- Gaussian 09, Revision D.01, M.J. Frisch, G. W. Trucks, H. B. Schlegel, G. E. Scuseria, M. A. Robb, J. R. Cheeseman, G. Scalmani, V. Barone, B. Mennucci, G. A. Petersson, H. Nakatsuji, M. Caricato, X. Li, H.P. Hratchian, A. F. Izmaylov, J. Bloino, G. Zheng, J. L. Sonnenberg, M. Hada, M. Ehara, K. Toyota, R. Fukuda, J. Hasegawa, M. Ishida, T. Nakajima, Y. Honda, O. Kitao, H. Nakai, T. Vreven, J.A. Montgomery Jr., J.E. Peralta, F. Ogliaro, M. Bearpark, J. J. Heyd, E. Brothers, K. N. Kudin, V. N. Staroverov, T. Keith, R. Kobayashi, J. Normand, K. Raghavachari, A. Rendell, J. C. Burant, S. S. Iyengar, J. Tomasi, M. Cossi, N. Rega, J. M. Millam, M. Klene, J. E. Knox, J. B. Cross, V. Bakken, C. Adamo, J. Jaramillo, R. Gomperts, R. E. Stratmann, O. Yazyev, A. J. Austin, R. Cammi, C. Pomelli, J. W. Ochterski, R. L. Martin, K. Morokuma, V. G. Zakrzewski, G. A. Voth, P. Salvador, J. J. Dannenberg, S. Dapprich, A. D. Daniels, O. Farkas, J. B. Foresman, J. V. Ortiz, J. Cioslowski, D. J. Fox, Gaussian Inc., Wallingford CT, 2010.
- A. D. Becke, *J. Chem. Phys.* **1993**, *98*, 5648–5652.
- L. A. Curtiss, P. C. Redfern, K. Raghavachari, *J. Chem. Phys.* **2007**, *126*, 084108–084120.
- J. B. Foresman, A.E. Frisch, *Exploring Chemistry with Electronic Structure Methods*, Gaussian Inc., Pittsburgh, PA, 1998.
- P. J. Hay, W. R. Wadt, *J. Chem. Phys.* **1985**, *82*, 270–283.

25. P. J. Hay, W. R. Wadt, *J. Chem. Phys.* **1985**, *82*, 284–298.
26. P. J. Hay, W. R. Wadt, *J. Chem. Phys.* **1985**, *82*, 299–310.
27. J. P. Foster, F. Weinhold, *J. Am. Chem. Soc.* **1980**, *102*, 7211–7218.
28. Y. Thio, X. Yang, J. J. Vittal, *Dalton Trans.* **2014**, *43*, 3545–3556.
29. K. Nakamoto, *Infrared and Raman Spectra of Inorganic and Coordination Compounds*, 4th ed., Wiley, New York, 1986.
30. B. Shaabani, A. A. Khandar, M. Dusek, M. Pojarova, F. Mahmoudi, A. Feher, M. Kajnakova, *J. Coord. Chem.* **2013**, *66*, 748–762.
31. R. Vafazadeh, A. Gorji, S. Ansari, A. C. Willis, *Acta Chim. Slov.* **2012**, *59*, 897–903.
32. P. Ghorai, A. Chakraborty, A. Panja, T. K. Mondal, A. Saha, *RSC Adv.* **2016**, *6*, 36020–36030.
33. D. Das, N. Sahu, S. Mondal, S. Roy, P. Dutta, S. Gupta, T. K. Mondal, C. Sinha, *Polyhedron* **2015**, *99*, 77–86.
34. R. Vafazadeh, B. Khaledi, A. C. Willis, M. Namazian, *Polyhedron* **2011**, *30*, 1815–1819.
35. G. Alpaslan, M. Macit, *Spectrochim. Acta A* **2014**, *121*, 372–380.

Povzetek

Sintetizirali smo dva enojedrna Ni(II) kompleksa $[\text{Ni}(\text{en})_2(\text{H}_2\text{O})_2](\text{MAA})_2$ (**1**) in $[\text{Ni}(\text{pn})_2(\text{MAA})_2]$ (**2**), kjer so MAA, en in pn metakrilat, etilendiamin in 1,3-propilendiamin. Okarakterizirali smo ju z elementno analizo, FT-IR in UV-Vis spektroskopijo. Strukture obeh kompleksov smo določili z monokristalno rentgensko analizo. V kompleksih **1** in **2** je okoli nikljevega(II) iona popačena oktaedrična geometrija. Ni(II) je v obeh spojinah vezan na štiri dušikove atome dveh diaminov ter nadalje na dva kisikova atoma aqua liganda v **1** oziroma dva kisikova atoma metakrilatnih ligandov v **2**. Teoretične geometrije proučevanih spojin smo izračunali na podlagi teorije gostotnostnega funkcionala (DFT) na B3LYP/6-311+G(d,p)/LanL2DZ nivoju in ob uporabi učinkovitih potencialov (ECP). Primerjava rezultatov kaže na dobro ujemanje uporabljene DFT metode z eksperimentalnimi podatki.

Scientific paper

Determination of Titanium Dioxide Content in Bauxites Using X-ray Fluorescence Spectrometry by Fusion and by Pressing

Dragana Blagojević,^{1,*} Dragica Lazić,² Dragana Kešelj,² Gordana Ostojić³
and Mugdin Imamović⁴

¹ Department of Chemistry, Faculty of Natural Sciences and Mathematics, University of Banja Luka, Mladena Stojanovića 2, 78 000 Banja Luka, BiH

² Department of Chemical Technology, Faculty of Technology, University of East Sarajevo, Karakaj bb, 75400 Zvornik, BiH

³ Alumina Factory "Alumina" Zvornik, Karakaj, 75400 Zvornik, BiH

⁴ Cement Factory "Lukavac", Lukavačkih brigada bb, 75300 Lukavac, BiH

* Corresponding author: E-mail: dragana_blagojevic@yahoo.com
Tel.: +387 65 870 534

Received: 15-12-2017

Abstract

Bauxites of different deposits were analysed for their content of TiO₂ (mass %), using X-ray fluorescence spectrometry and the reference spectrophotometric method JUS B.G8.514. The samples were prepared in two ways: fusion with a borax technique and pressing, after which beads were formed for the purpose of analysis. Certified reference samples of bauxite were used for producing a calibration curve. The equation for calculating the content of TiO₂ (mass %) in the samples of bauxite was derived from the calibration curve. Results of the XRF method were tested statistically by means of the F-test and the t-test (the standard sample of the bauxite and the reference method). The values obtained from the afore mentioned tests for the fusion beads showed that the XRF method was precise and correct and that there were no systematic errors, whereas for the pressed beads this method showed significant systematic errors.

Keywords: XRF analysis, bauxite, titanium dioxide

1. Introduction

Bauxite is the principal ore for producing aluminium metal via a two-stage process that involves, firstly, the refining of bauxite to alumina through a wet chemical caustic leach process (the Bayer process) and, secondly, the electrolytic reduction of alumina to aluminium metal (the Hall-Heroult process).¹ The remaining bauxite is used in the refractory, abrasive and chemical industries.²

The main minerals that are present in bauxite include several forms of hydrated aluminium oxide: gibbsite (Al₂O₃ · 3H₂O), boehmite (Al₂O₃ · H₂O), and diasporite (Al₂O₃ · H₂O). In addition to these, the rock also contains significant quantities of the following minerals: corundum, goethite, hematite, kaolinite, halloysite, anatase, and rutile.³ This means that, in addition to the aluminium mineral, the

main components of bauxite are the following elements: iron, silicon, titanium, calcium, and magnesium. The mixture may also contain minerals of a series of other elements: Na, K, P, Cr, V, Ga, Zn, Pb, Cu, Ni, Mn, Co, and others.⁴

The mineralogy of bauxite deposits controls the efficacy of the Bayer process. Some of the gangue components, such as clays, fine-grained quartz, and titanium oxides, are deleterious as they react with the leaching solution, which causes caustic soda losses in the Bayer process.¹

Bauxite usually contains 2–4 mass % of TiO₂. TiO₂ exists in the form such as anatase, rutile and brookite minerals.⁵

Various methods have been used for determining titanium content in different types of samples, such as: inductively coupled plasma-atomic emission spectrometry (ICP-AES),⁶ inductively coupled plasma-mass spectrometry (ICP-MS),⁷ graphite furnace atomic absorption spec-

trometry (GFAAS),⁸ catalytic adsorptive stripping voltammetry (CASV),⁹ neutron activation analysis (NAA),¹⁰ spectrophotometry,^{11,12,13} X-ray fluorescence (XRF),¹⁴ and laser induced breakdown spectroscopy (LIBS).¹⁵

Chemical composition of bauxite is usually expressed in the content of Al₂O₃, SiO₂, Fe₂O₃, TiO₂, and CaO, with the loss on ignition at 1075 °C. In the alumina factory “Alumina”, chemical determination of TiO₂ content in bauxite is carried out using the spectrophotometric method JUS B.G8.514.

X-ray fluorescence spectrometry is a technique for the analysis of bulk specimens. It is based on the interaction of X-rays with atoms in the sample.¹⁶ Each of the elements present in a sample produces a set of characteristic fluorescent X-rays (“a fingerprint”) that is unique for that specific element, which is why XRF spectroscopy is an excellent technology for qualitative and quantitative analysis of material composition.¹⁷

XRF is widely used for environmental, industrial, pharmaceutical, forensic, and scientific research applications to determine the presence or absence and, in some cases, to measure the concentration of elemental constituents or contaminants.¹⁸

Some examples in which the XRF technique was used are: determination of the chemical composition of different bauxites,^{19,20} bauxitic-based ceramic proppants,²¹ brown fused alumina,²² red mud (bauxite residue),^{23,24,25} determination of trace elements in rocks, soils, and sediments,²⁶ analysis of ceramic oxide refractories.²⁷

2. Experimental

Bauxites labelled “Brazil”, “Grčka”, and “Mađarska”, prepared in alumina factory “Alumina”, in Zvornik, BiH, were used for the experimental part of the research.

Bauxite samples were first ground to particle size below 200 µm and dried, and then annealed at 1075 °C. The loss on ignition was calculated at that temperature.

In the XRF analysis, for the purpose of the preparation of fused beads, 1 g of the annealed sample was separated and mixed with 8 g of Li₂B₄O₇ in a platinum pot. After gentle stirring, using a glass rod, the pot was mounted on the “VULCAN” fusion system from Fluxana. After 15 min of melting at around 1250 °C, the sample was poured into a heated platinum mould. After cooling for 10 min, the bead obtained in this way was recorded by WDXRF “S8 TIGER” (BRUKER).

For the purpose of preparing pressed beads, 47.5 g of the annealed sample was separated and mixed with 2.5 g of wax and ground in a mill. The sample prepared in this way (10 g) was then transferred to the mould in the press and subjected to the pressure of 150 KN for 10 s.

The calibration curve was obtained based on the certified reference bauxite samples, which were also annealed prior to the process (Table 1).

One series of samples was prepared by fusion and poured into moulds for beads, and the other series was prepared by pressing in the moulds. The samples were recorded afterwards.

The parameters in the process of recording titanium were as follows: Line Ti KAl, Mask: 34 mm, Mode: Vacuum, 50 kV, 60 mA, Filter: None, Crystal (nominal): 2d = 4.026 Å, Collimator aperture (nominal) = 0.46 degrees, Detector: flow counter LLD = 50, ULD = 150 % of nominal peak, Adjusted peak at 86.101 degrees 2-theta, Wavelength = 2.7485 Å.

Spectrophotometric analysis involved the preparation of solutions by fusing the sample with a mixture of Na₂CO₃ and Na₂B₄O₇ (3:1), according to a modified method JUS B.G8. 520/92 and ISO 6994/86. A UV-VIS spectro-

Table 1. Analysis of standard reference bauxite samples according to the certificate (mass %)

Components	69b NBS (Arkansas)	696 NBS (Surinam)	697 NBS (Dominican)	698 NBS (Jamaican)	BXT-09
Al ₂ O ₃	48.80	54.50	45.80	48.20	53.40
BaO	0.008	0.004	0.015	0.008	–
CaO	0.13	0.018	0.71	0.62	0.010
Co	0.0001	0.00009	0.0013	0.0045	–
Cr ₂ O ₃	0.011	0.047	0.100	0.080	0.037
Fe ₂ O ₃	7.14	8.70	20.00	19.60	14.15
MgO	0.085	0.012	0.18	0.058	0.03
MnO	0.110	0.004	0.41	0.38	0.04
P ₂ O ₅	0.118	0.050	0.97	0.37	0.07
K ₂ O	0.068	0.009	0.062	0.010	–
SiO ₂	13.43	3.79	6.81	0.69	7.57
Na ₂ O	0.025	0.007	0.036	0.015	–
SO ₃	0.63	0.21	10.13	0.22	–
TiO ₂	1.90	2.64	2.52	2.38	2.98
V ₂ O ₅	0.028	0.072	0.063	0.064	0.06
Loss on Ignition	27.2	29.9	22.1	27.3	20.8

photometer Lambda 25 Perkin Elmer was used for measurement.

Mineralogical characterization of all the samples of bauxite was carried out using X-ray diffraction (XRD analysis) on a powder diffractometer PHILIPS PW 171. Radiation from the copper anticathode with the wavelength of $\text{CuK}\alpha = 1.54178 \text{ \AA}$ and a graphite monochromator were used for the analysis. The operating voltage on the tube was $U = 40 \text{ kV}$, and the current intensity was $I = 30 \text{ mA}$. Samples were tested in the range $2\theta 5\text{--}50^\circ$ and with time retention of 1s at each step. X'Pert Quantify computer software was used for instrument manipulation, whereas X'Pert HighScore was used for data processing.

3. Results and Discussion

According to XRD analysis and the obtained diffractograms, the standard reference samples of bauxite have the following mineralogical composition:

- Standard NBS 69b is a typical hydrargillite bauxite. In addition to gibbsite, this sample also contains kaolinite, hematite, goethite, and siderite (Figure 1).

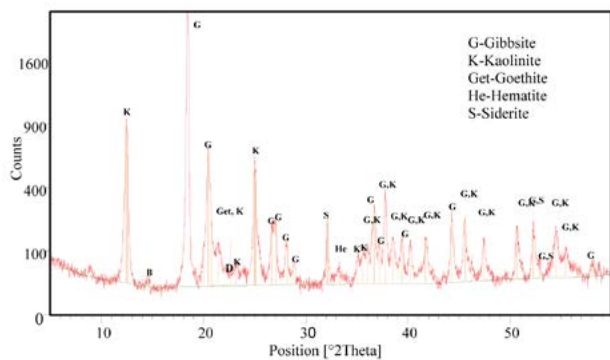


Figure 1. Diffractogram of the standard bauxite sample NBS 69b (Arkansas)

- Standard NBS 696 is a typical hydrargillite bauxite. In addition to gibbsite, this sample of bauxite also contains small traces of hematite, anatase, goethite, kaolinite, and pyrite (Figure 2).

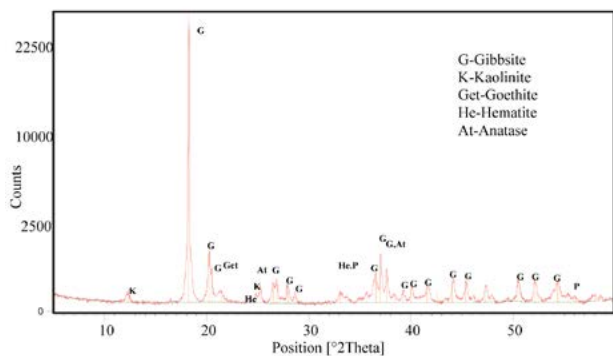


Figure 2. Diffractogram of the standard bauxite sample NBS 696 (Surinam)

- Standard NBS 697 is a combined, gibbsite-boehmite type, with hematite content. In addition to the aforementioned minerals, the sample also contains goethite and kaolinite, whereas anatase and calcite are found in traces (Figure 3).

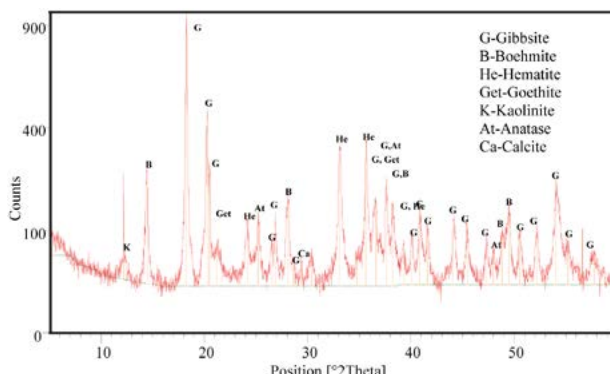


Figure 3. Diffractogram of the standard bauxite sample NBS 697 (Dominican)

- Standard NBS 698 is a hydrargillite bauxite with hematite content. In addition to gibbsite, this sample also contains anatase, goethite, and hematite (Figure 4).

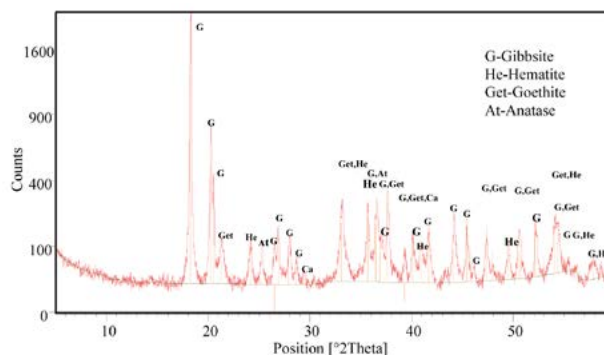


Figure 4. Diffractogram of the standard bauxite sample NBS 698 (Jamaican)

- Standard BXT 09 is a combined gibbsite-boehmite type of bauxite with hematite content. In addition to those

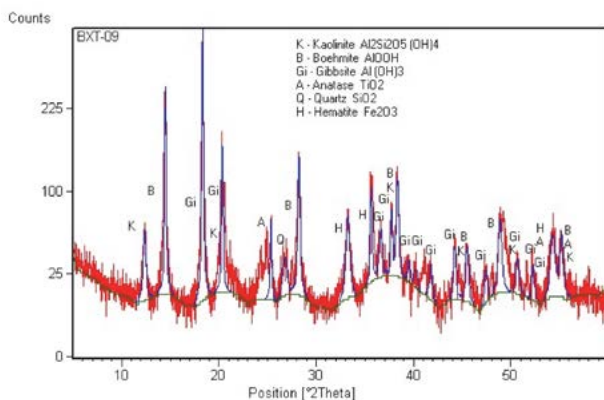


Figure 5. Diffractogram of the standard bauxite sample BXT-09

minerals, the sample also contains kaolinite, whereas anatase and quartz occur in traces (Figure 5).

According to the XRD analysis, the bauxite samples from different deposits (“Brazil”, “Grčka”, and “Mađarska”) have the following mineralogical composition:

- “Brazil” is a typical hydrargillite type of bauxite. In addition to gibbsite, this sample contains boehmite, hematite, anatase, and kaolinite, all in traces (Figure 6).

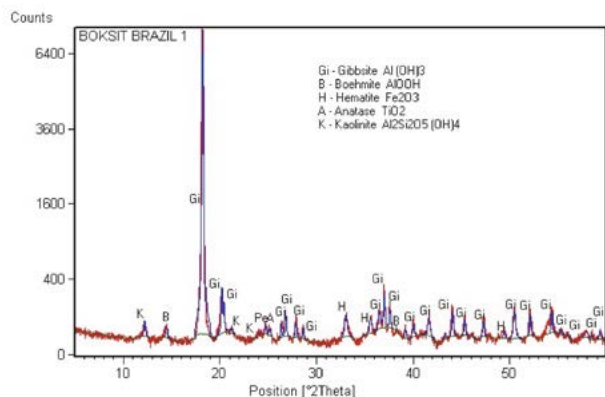


Figure 6. Diffractogram of the bauxite sample “Brazil”

- “Grčka” bauxite is diaspore bauxite with a boehmite and hematite contents. In addition to those minerals, the sample also contains calcite and anatase, whereas quartz, kaolinite, gibbsite, goethite, and rutile are present in traces (Figure 7).

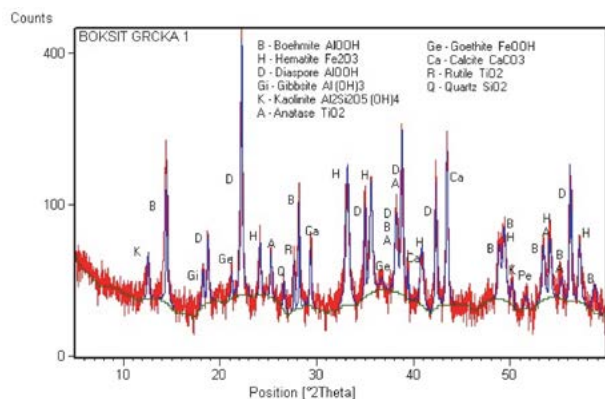


Figure 7. Diffractogram of the bauxite sample “Grčka”

- “Mađarska” is a gibbsite-boehmite combination with hematite and kaolinite contents. In addition to these minerals, the sample also contains goethite and traces of anatase and rutile (Figure 8).

Calibration curves were created based on data for standard certified reference samples of bauxite and the obtained values of intensity (Net) for the samples prepared by fusion and pressing (Figure 9 and Figure 10). The content of TiO_2 , which was taken as the basis for the development of the calibration curve, was calculated for an absolutely annealed sample.

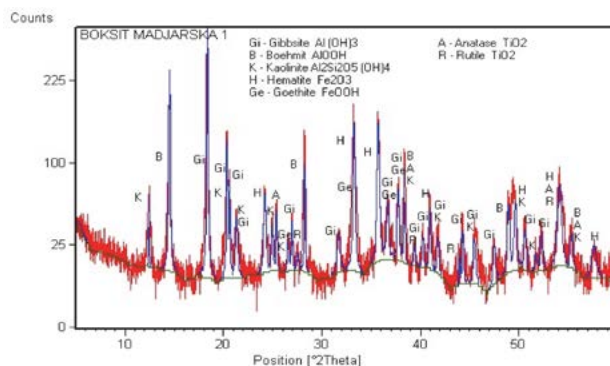


Figure 8. Diffractogram of the bauxite sample “Mađarska”

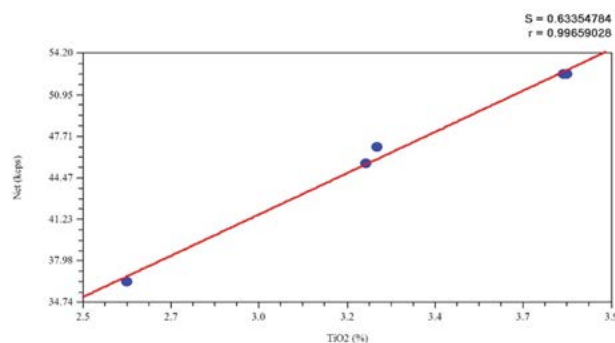


Figure 9. Calibration curve for the beads prepared by fusion

The equation for calculating the percentage (mass %) of titanium dioxide in annealed bauxite was derived based on the calibration curve obtained for the beads resulting from fusion, Eq. (1):

$$\text{TiO}_2(\text{annealed})/\% = 0.071917331 \times \text{Net} - 0.035012049 \quad (1)$$

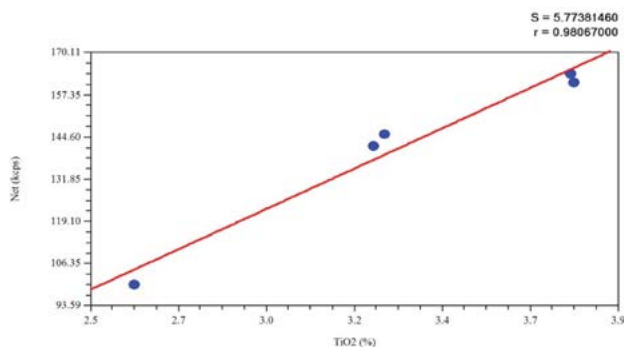


Figure 10. Calibration curve for the beads prepared by pressing

Another equation for calculating the percentage (mass %) of titanium dioxide in annealed bauxite was also derived based on the calibration curve obtained for the beads resulting from the process of pressing, Eq. (2):

$$\text{TiO}_2(\text{annealed})/\% = 0.019017877 \times \text{Net} + 0.621131611 \quad (2)$$

The actual content of titanium dioxide in the samples of bauxite was calculated according to the following equation, Eq. (3):

$$\text{TiO}_2/\% = \text{TiO}_2(\text{annealed})/\% \times \frac{100 - \text{LOI}_{1075^\circ\text{C}}}{100} \quad (3)$$

This calculation is based on the values of the loss on ignition (LOI) at 1075 °C (Table 2).

Table 2. Loss on ignition for bauxites from different deposits

Bauxite	LOI (1075 °C)/%
Brazil	27.84
Grčka	12.12
Mađarska	19.05

On the basis of the calibration curve, the samples of different deposits prepared by fusion and by pressing were recorded, and the content of TiO₂ was calculated according to the above equations (Table 3 and Table 4).

Table 3. The content of TiO₂ in bauxites from different deposits, calculated using a spectrophotometric and XRF method (by fusion)

Bauxite	TiO ₂ (mass %)		Residual value
	Spectrophotometry	XRF	
Brazil	1.267	1.3271	0.0601
Grčka	2.59	2.6219	0.0319
Mađarska	2.113	2.1829	0.0699
\bar{x}	–	–	0.053966667
S	–	–	0.01972849

Table 4. The content of TiO₂ in bauxites from different deposits calculated using spectrophotometric and XRF method (by pressing)

Bauxite	TiO ₂ (mass %)		Residual value
	Spectrophotometry	XRF	
Brazil	1.267	1.5703	0.3033
Grčka	2.59	2.6569	0.0669
Mađarska	2.113	2.3959	0.2829
\bar{x}	–	–	0.2177
S	–	–	0.130994351

The data presented here were obtained as a result of recording ten different beads from every sample, as well as recording a bead from each sample ten times. Moreover, ten samples for every bauxite were prepared for spectrophotometric analysis of the content of TiO₂. The results for “Grčka” bauxite are shown in the tables below (Table 5, Table 6, and Table 7).

In order to check the precision of the XRF method for the beads prepared by fusion, a F-test was conducted,

Table 5. The content of TiO₂ in ten different beads of the “Grčka” bauxite sample calculated using the XRF method (by fusion)

Bead	Intensity (kcps)	TiO ₂ (mass %)	
		annealed	not annealed
1	42.1089	2.99335	2.6304
2	41.9086	2.97894	2.6178
3	41.8425	2.97419	2.6136
4	41.9263	2.98022	2.6189
5	42.0063	2.98597	2.6239
6	42.1625	2.99720	2.6338
7	41.9912	2.98488	2.6229
8	41.9809	2.98414	2.6223
9	41.9748	2.98370	2.6219
10	41.8317	2.97341	2.6129
Min	41.8317	2.97341	2.6129
Max	42.1625	2.99720	2.6338
\bar{x}	41.97337	2.9836	2.6219
S	0.104991	0.007551	0.006622

Table 6. The content of TiO₂ in one bead of the bauxite sample “Grčka” calculated using the XRF method (by fusion)

Number of measurements	Intensity (kcps)	TiO ₂ (mass %)	
		annealed	not annealed
1	42.1986	2.99980	2.6361
2	42.0286	2.98757	2.6254
3	41.9453	2.98158	2.6201
4	42.2673	3.00474	2.6399
5	42.2150	3.00098	2.6371
6	42.2632	3.00444	2.6402
7	41.9801	2.98408	2.6222
8	42.2027	3.00009	2.6364
9	42.2263	3.00179	2.6379
10	42.0353	2.98805	2.6258
Min	41.9453	2.98158	2.6201
Max	42.2673	3.00474	2.6402
\bar{x}	42.13624	2.995312	2.6322
S	0.124065	0.008924	0.00779

Table 7. The content of TiO₂ in ten different samples of “Grčka” bauxite calculated using spectrophotometric method JUS B.G.8.514

Number of analysis	TiO ₂ (mass %)
1	2.69
2	2.59
3	2.54
4	2.42
5	2.58
6	2.66
7	2.55
8	2.64
9	2.64
10	2.59
Min	2.42
Max	2.69
\bar{x}	2.59
S	0.076739096

where the zero hypothesis tested was that the variances in the spectrophotometric method for calculating the content of TiO₂ in bauxites-JUS B.G8.514 and in a non-standard XRF method were equal. The following value of the F-test was obtained:

$$F = \frac{S_1^2}{S_2^2}, F = 101,85, \nu_1 = n_1 - 1, \nu_2 = n_2 - 1 \quad (4)$$

Critical value at $\alpha = 0.05$, $\nu_1 = 9$, $\nu_2 = 9$ is $F_{9,9} = 3.18$. The calculated result is considerably higher than the critical value, which means that the difference between the variances of the two methods is significant, and, with a risk of 5%, the zero hypothesis on the equality of variances can be rejected. The standard method variance is higher than the XRF method variance, which leads to the conclusion that the XRF method is more precise.

The test of accuracy for the XRF method used in determining TiO₂ was performed on the standard bauxite BXT-09, as well as compared to the same reference method. Ten beads of this standard were prepared by fusion and then recorded. The results obtained are given in Table 8.

Table 8. The content of TiO₂ in the certified bauxite sample BXT-09 determined by XRF method (by fusion)

Bead	Intensity (kcps)	TiO ₂ (mass %)	
		annealed	not annealed
1	52.4692	3.73843	2.9608
2	52.9908	3.77595	2.9906
3	52.2886	3.72544	2.9505
4	52.1599	3.71619	2.9432
5	53.0883	3.78296	2.9961
6	52.7425	3.75809	2.9764
7	52.3993	3.73341	2.9569
8	52.8240	3.76395	2.9811
9	52.4176	3.73472	2.9579
10	52.6323	3.75016	2.9701
Min	52.1599	3.71619	2.9432
Max	53.0883	3.78296	2.9961
\bar{x}	52.60125	3.74793	2.9684
S	0.306229	0.022025	0.017461

These results served as a starting point for the t-test, where the hypothesis on the equality of the reference value and the average value of the results was tested.

$$|t| = \left| \frac{\mu - \bar{x}}{s} \right| \times \sqrt{n}, |t| = 2.096, \nu = n - 1, \nu = 9 \quad (5)$$

Critical value at $\alpha = 0.05$, $\nu = 9$ is $t = 2.262$. Since $|t| < |t|_{\text{critical}}$, with the risk of 5%, the zero hypothesis can be accepted, and one can conclude, that the XRF method does not have a systematic error.

Testing the accuracy of the XRF method using the same reference method involved testing the hypothesis of

equality of arithmetic means of the two methods. The following values were calculated for this purpose:

$$t = \frac{(\bar{x}_1 - \bar{x}_2)}{\sqrt{\frac{s_1^2}{N_1} + \frac{s_2^2}{N_2}}}, t = -1,307 \quad (6)$$

$$\nu = \frac{\left(\frac{s_1^2}{N_1} + \frac{s_2^2}{N_2} \right)^2}{\left(\frac{s_1^4}{N_1^2(N_1 - 1)} + \frac{s_2^4}{N_2^2(N_2 - 1)} \right)}, \nu = 9,18 \quad (7)$$

Critical value at $\alpha = 0.05$, $\nu = 9$ is $t = 2.262$. Since in this case $|t| < |t|_{\text{critical}}$ the hypothesis of equality of arithmetic means of the two methods can be accepted and one can conclude, with the risk of 5 %, that the XRF method has no systematic error.

The following tables (Table 9 and Table 10) show results for "Grčka" bauxite sample obtained by measuring the beads prepared by pressing.

Table 9. The content of TiO₂ in ten different beads of "Grčka" bauxite calculated using the XRF method (by pressing)

Bead	Intensity (kcps)	TiO ₂ (mass %)	
		annealed	not annealed
1	126.1713	3.02064	2.6544
2	125.9570	3.01657	2.6508
3	126.4727	3.02637	2.6595
4	126.4312	3.02558	2.6588
5	126.2525	3.02219	2.6558
6	126.6123	3.02903	2.6618
7	126.3718	3.02445	2.6578
8	126.1743	3.02070	2.6545
9	126.4447	3.02584	2.6589
10	126.3210	3.02349	2.6569
Min	125.9570	3.01657	2.6508
Max	126.6123	3.02903	2.6618
\bar{x}	126.3209	3.023486	2.6569
S	0.188271	0.003579	0.003156

Another F-test was conducted in order to test the precision of the XRF method for the beads prepared by pressing and the results were as follows:

$$F = \frac{S_1^2}{S_2^2}, F = 453.93 \quad (8)$$

Again, the calculated value was considerably higher than the critical value, the difference between the variances of the two methods was significant and, with the risk of 5%, the zero hypothesis on equality of the variances had to be rejected. The variance of the standard method was higher than the variance of the XRF method, which again leads to the conclusion that the latter is more precise.

Table 10. The content of TiO₂ in one bead of “Grčka” bauxite calculated using the XRF method (by pressing)

Number of measurements	Intensity (kcps)	TiO ₂ (mass %)	
		annealed	not annealed
1	126.1205	3.01968	2.6536
2	126.1848	3.0209	2.6546
3	126.0728	3.01877	2.6528
4	126.0922	3.01914	2.6531
5	125.9905	3.01720	2.6514
6	125.9390	3.01622	2.6505
7	126.5761	3.02834	2.6612
8	126.4619	3.02617	2.6593
9	126.3677	3.02438	2.6577
10	126.2962	3.02302	2.6565
Min	125.9390	3.01622	2.6505
Max	126.5761	3.02834	2.6612
\bar{x}	126.2102	3.021382	2.6551
S	0.208899	0.003974	0.003499

Table 11. The content of TiO₂ in the reference bauxite sample B 010 calculated using the XRF method (by pressing)

Bead	Intensity (kcps)	TiO ₂ (mass %)	
		annealed	not annealed
1	140.4317	3.29184	2.9245
2	139.7303	3.27851	2.9126
3	140.0871	3.28529	2.9187
4	140.2406	3.28821	2.9212
5	140.3696	3.29066	2.9234
6	140.4510	3.29221	2.9248
7	139.9880	3.28341	2.9169
8	140.3402	3.29010	2.9229
9	140.1154	3.28583	2.9191
10	140.0452	3.28449	2.9179
Min	139.7303	3.27851	2.9126
Max	140.4510	3.29221	2.9248
\bar{x}	140.1799	3.287055	2.9202
S	0.229043	0.004353	0.003881

Testing the accuracy of the XRF method using the same reference method involved testing the hypothesis of equality of arithmetic means of the two methods. The following values were calculated for this purpose:

$$t = \frac{(\bar{x}_1 - \bar{x}_2)}{\sqrt{\frac{s_1^2}{N_1} + \frac{s_2^2}{N_2}}}, \quad t = -2,753 \quad (9)$$

$$v = \frac{\left(\frac{s_1^2}{N_1} + \frac{s_2^2}{N_2}\right)^2}{\left(\frac{s_1^4}{N_1^2(N_1-1)} + \frac{s_2^4}{N_2^2(N_2-1)}\right)}, \quad v = 9,04 \quad (10)$$

Critical value at $\alpha = 0.05$, $v = 9$ is $t = 2.262$. Since in this case $|t| > |t|_{\text{critical}}$, then, with the risk of 5%, the hypothesis of the equality of arithmetic means of the two methods must be rejected. It can be concluded that the XRF method for the beads prepared by pressing does not yield the same average value as the reference method, which means that it shows a systematic error.

The test of accuracy for the XRF method for determining TiO₂ for the beads prepared by pressing was conducted using the reference bauxite B 010. Ten beads were prepared and recorded. The data obtained are given in Table 11.

These values served as the basis for the t-test and the hypothesis on equality of the reference value and the average value of the results investigated.

$$|t| = \frac{|\mu - \bar{x}|}{s} \cdot \sqrt{n}, \quad |t| = 316.389, \quad v = n-1, \quad v = 9 \quad (11)$$

Critical value at $\alpha = 0.05$, $v = 9$ is $t = 2.262$. Since $|t| > |t|_{\text{critical}}$, the zero hypothesis can be rejected, with the risk of

5%, and it can be concluded that the XRF method in this case shows a systematic error.

4. Conclusions

Based on recording the intensities of the beads made from certified reference bauxite samples, prepared by fusion, the calibration curve was obtained with the correlation coefficient of $r = 0.9966$ and the standard deviation of $S = 0.6335$. For the samples prepared by pressing, the calibration curve obtained had the correlation coefficient $r = 0.9807$ and the standard deviation $S = 5.7738$. The calibration curve was the basis for the equation used for calculating the content of TiO₂ (%) in the bauxite samples for both methods of bead preparation. The average residual value between the content of TiO₂ calculated using the XRF method and the reference method JUS B.G8.514 was 0.054, with the standard deviation of 0.019, for the beads obtained by fusion, and 0.218, with the standard deviation of 0.131 for the beads obtained by pressing. The XRF method was then tested for precision and accuracy. The F-test results show, with the risk of 5%, that the zero hypothesis on the equality of variances can be rejected. The standard method variance is higher than the XRF method variance for both fused and pressed beads, which leads to the conclusion that the XRF method is more precise. A t-test was conducted to test the accuracy (using the reference method and the standard bauxite samples BXT-09 and B 010) for the beads obtained by fusion and by pressing. In the case of the beads prepared by fusion, it can be concluded, with the risk of 5%, that the reference values and the average values of the results investigated were equal, that the arithmetic means of the two methods showed no differences, and

that the method did not have any systematic errors. As far as the pressed beads are concerned, it can be concluded, with the risk of 5%, that the arithmetic means of the two methods differed, as well as the reference and the average values of the results investigated, and that the XRF technique for this method of bead preparation showed a systematic error.

Based on the results obtained, it can be concluded that the XRF, as a method for calculating the content of TiO₂ in bauxite, is precise and accurate when beads are prepared by fusion. For the beads prepared by pressing, this method shows a systematic error, which is a consequence of insufficient homogeneity of the sample.

5. References

1. F. M. Meyer, *Nat. Resour. Res.*, **2004**, *13*, 161–172. DOI:10.1023/B:NARR.0000046918.50121.2e
2. M. Authier-Martin, G. Forte, S. Ostap, J. See, *JOM*, **2001**, *53*, 36–40. DOI:10.1007/s11837-001-0011-1
3. J. E. Kogel, R. C. Nikhil, in J. E. Kogel (Ed.): *Industrial Minerals and Rocks: Commodities, markets and Uses*, Elsevier, New York, **2006**, pp. 225–269.
4. R. Vračar, Ž. Živković, *Ekstraktivna metalurgija aluminijuma*, Naučna knjiga, Belgrade, Serbia, **1993**, pp. 1–14.
5. J. Q. Li, Y. Zou, C. Y. Chen, Y. Z. Jia, *Adv Mat Res*, **2013**, *1124*–1127. DOI:10.4028/www.scientific.net/AMR.734–737.1124
6. G. Alkan, C. Schier, L. Gronen, S. Stopic and B. Friedrich, *Metals*, **2017**, *7*, 458. DOI:10.3390/met7110458
7. H. Mahmoud, A. Abdel-Lateef, A. Attiah, *J. Anal. Sci., Methods Instrum.*, **2013**, *3*, 62–66. DOI: 10.4236/jasmi.2013.31007
8. T. M. Sørli, G. Wibetoe, *Anal Bioanal Chem*, **2003**, *376*, 721–727. DOI:10.1007/s00216-003-1938-6
9. M. Gawrys, J. Golimowski, *Analytica Chimica Acta*, **2001**, *427*, 55–61. DOI:10.1016/S0003-2670(00)01183-1
10. R. L. Njinga, M. N. Moyo and S. Y. Abdulmalik, *Int. J. Agron.*, **2013**, *2013*, 1–9. DOI:10.1155/2013/156520
11. R. K. Mondal, P. K. Tarafder, *Microchim. Acta*, **2004**, *148*, 327–333. DOI: 10.1007/s00604-004-0272-9
12. V. Srilalitha, A. R. G. Prasad, K. R. Kumar, V. Seshagiri, L. R. K. R. Ravindranath, *Facta Univ., Ser.: Phys., Chem. Technol.*, **2010**, *8*, 15–24. DOI: 10.2298/FUPCT1001015S
13. H. Z. Mousavi, N. Pourreza, *J. Chin. Chem. Soc.*, **2008**, *55*, 750–754. DOI:10.1002/jccs.200800112
14. B. Xing, X. Liu, Z. Zhang, K. Wang and K. Li, *Commun. Soil Sci. Plant Anal.*, **2005**, *35*, 1839–1850. DOI:10.1081/LCSS-200026803
15. D. N. Stratis, K. L. Eland, S. M. Angel, *Appl. Spectrosc.*, **2000**, *54*, 1719–1726. DOI:10.1366/0003702001948871
16. P. J. Potts, *A Handbook of Silicate Rock Analysis*, Springer, Boston, MA, **1992**, pp. 226–285. DOI:10.1007/978-1-4615-3270-5
17. S. Jagadeeswari, P. D. Devi, *Asian J. Appl. Sci. Technol.*, **2017**, *1*, 196–198.
18. Z. W. Chen., M. W. Gibson, H. Huang, *X-Ray Opt. Instrum.*, **2008**, *8*, 1–10. DOI:10.1155/2008/318171
19. B. K. Gan, Z. Taylor, B. Xu, A. Riessen, R. D. Hart, X. Wang and P. Smith, *Int. J. Miner. Process.*, **2013**, *123*, 64–72. DOI:10.1016/j.minpro.2013.05.005
20. F. S. Oliveira, A. F. D. C. Varajão, C. A. C. Varajão, B. Boulangé, C. C. V. Soares, *Catena*, **2013**, *105*, 29–39. DOI:10.1016/j.catena.2013.01.004
21. A. I. Assem, H. A. Nasr-El-Din, *J. Pet. Sci. Eng.*, **2017**, *158*, 441–453. DOI:10.1016/j.petrol.2017.08.075
22. E. R. Passos, J. A. Rodrigues, *Ceramica*, **2016**, *62*, 38–44. DOI:10.1590/0366-69132016623611960
23. R.-X. Liu, C.-S. Poon, *J. Cleaner Prod.*, **2016**, *112*, 384–391. DOI:10.1016/j.jclepro.2015.09.049
24. F. M. Kaußen, B. Friedrich, *Hydrometallurgy*, **2018**, *176*, 49–61. DOI:10.1016/j.hydromet.2018.01.006
25. N. Yalçın, V. Sevinç, *Ceram. Int.*, **2000**, *26*, 485–493. DOI:10.1016/S0272-8842(99)00083-8
26. A. G. Revenko, *X-Ray Spectrom.*, **2002**, *31*, 264–273. DOI:10.1002/xrs.564
26. M. F. Gazulla, M. P. Gómez, A. Barba and J. C. Jarque, *X-Ray Spectrom.*, **2004**, *33*, 421–430. DOI:10.1002/xrs.743

Povzetek

V boksitih iz različnih depozitov smo določali delež TiO₂ (masni %) z X-žarkovno fluorescenčno spektrometrijo (XRF) in z referenčno spektrofotometrično metodo JUS B.G8.514. Vzorce smo pripravili na dva načina: tehnika fuzije z bokskom in stiskanje, zatem pa smo za namen analize oblikovali kroglice. Za pripravo umeritvene krivulje smo uporabili certificirane referenčne standarde boksita. Enačbo za izračun deleža TiO₂ (masni %) v vzorcih boksita smo izpeljali iz umeritvene krivulje. Rezultate XRF metode smo statistično testirali z uporabo F-testa in t-testa (s standardnim vzorcem boksita in z referenčno metodo). Vrednosti iz zgoraj navedenih testov za kroglice po fuziji so pokazale, da je XRF metoda natančna in pravilna ter da nima sistematskih napak, medtem ko je za kroglice po stiskanju ta metoda pokazala signifikantno sistematsko napako.

Scientific paper

Thin-Layer Chromatography: an Efficient Technique for the Optimization of Dispersive Liquid-Liquid Microextraction

Elena Kupcová,^{1,*} Katarína Reiffová¹ and Yaroslav Bazel¹

¹ Department of Analytical Chemistry, Faculty of Science, Pavol Jozef Šafárik University in Košice,
Moyzesova 11, SK-040 01, Košice, Slovakia

* Corresponding author: E-mail: elena.kupcova@gmail.com
Tel.: +421 908 408 121

Received: 18-12-2017

Abstract

Thin-layer chromatography (TLC) is an often omitted analytical technique due to its lower sensitivity and separation capacity. Even in the era of high-performance liquid chromatography (HPLC), thin-layer chromatography still offers many advantages, such as simplicity, rapidity, and cost-effectiveness, which predict TLC to be the first-choice method for the laborious optimization process requiring analysis of numerous samples. In this work, a thin-layer chromatography method with chemical and densitometric detection was used to optimize a dispersive liquid-liquid microextraction (DLLME) process for the extraction and preconcentration of estradiol in human urine. The chromatographic system consisted of silica gel plates as the stationary phase and toluene-ethanol (9:1; v/v) mixture as the developing solvent. The plates were dyed with 10% phosphomolybdic acid reagent and sequentially evaluated densitometrically at $\lambda = 430$ nm. In the context of DLLME optimization, parameters including the type and volume of extraction and dispersive solvents, centrifugation, salt addition and extraction time, were studied. The proposed DLLME-TLC method was successfully applied to the determination of estradiol in real human urine samples.

Keywords: Thin-layer chromatography; post-chromatographic detection; dispersive liquid-liquid microextraction; estradiol; human urine

1. Introduction

Estrogens are human hormones primarily responsible for the development and function of female gonadal system, regulation of menstrual cycle, and maintenance of pregnancy¹ which also take part in various biochemical processes within the organism in both males and females.² Estrogens originate in steroidogenesis with estradiol (E2) being the primary product and the most potent human estrogen. Urinary estradiol levels are essential for the monitoring of regular pregnancy progress as well as for the diagnosis of reproductive and hormonal diseases.³ Estradiol concentrations in urine are typically low and fluctuate during pregnancy. While mean daily excretion of estradiol in menstruating women is 3.5 μg , it usually elevates up to 259–330 μg per day during pregnancy.⁴ Besides clinical applications, development of new analytical methods for the monitoring of estrogens in environmental and food samples is required due to their adverse effects on living organisms and environment.^{5,6} Chromatographic methods, pri-

marily high-performance liquid chromatography, are the most commonly used for the quantification of estrogens owing to their high sensitivity.^{7,8} Still, sample pretreatment remains a crucial step in the analysis of estrogens because of their low concentrations and complex character of the samples.⁹

Dispersive liquid-liquid microextraction (DLLME) was introduced in 2006¹⁰ as a fast and straightforward sample preparation technique offering high preconcentration factors and recoveries. DLLME is based on a ternary solvent system in which a dispersive solvent causes dispersion of an extraction solvent within the aqueous sample. A mixture of extraction and dispersive solvents is rapidly injected into the aqueous sample with a syringe resulting in the formation of tiny droplets of extraction solvent in the solution thus allowing fast transfer of the desired analyte into the extraction solvent. This state, called cloudy solution, disappears during centrifugation when the aqueous and organic phases are separated. The organic drop sedimented at the bottom of the tube is removed with a mi-

crossyringe and analyzed by the compatible analytical system.¹¹ Although DLLME was initially introduced as an extraction technique for organic compounds from predominantly water samples, it has evolved to be suitable even for the extraction of analytes from more complex matrices, including biological samples.¹² Few DLLME applications for estrogen extraction have been described^{13–17} so far; however, most of them were limited to water samples, except for two DLLME modifications used for the extraction of estrogens from milk¹⁸ and urine.¹⁹

This work describes optimization of a dispersive liquid-liquid microextraction for the extraction and preconcentration of estradiol in human urine samples using thin-layer chromatography (TLC) with chemical and densitometric detection which has, to the best of our knowledge, not been described yet. The main advantage of open planar arrangement over column chromatography lies in the possibility for simultaneous analysis of numerous samples at once, while column arrangement allows analysis of only one sample at a time. This factor significantly decreases the time needed for the analysis itself, making TLC the first-choice method for laborious optimization process, despite its lower sensitivity. Moreover, new aspects regarding the DLLME application to biological sample are presented, emphasizing the effects of centrifugation and salt addition on extraction recovery.

2. Experimental

2.1. Chemicals and Reagents

Standard of 17 β -estradiol ($\geq 98\%$) was purchased from Cayman Chemical (USA). Acetone, methanol, toluene, ethanol, tetrachloromethane, tetrachloroethane, chloroform and phosphomolybdic acid were obtained from Lambda Life (Slovakia), sodium chloride, sodium carbonate and potassium carbonate were from Mikrochem (Slovakia). All reagents were of analytical grade. Distilled water was used throughout all experiments.

2.2 Instrumentation

End-capped plastic 5-mL test tubes, 100- μ L microsyringe (Hamilton, Switzerland), centrifuge MPW-310 (Poland), thermal chamber (Laboratorni pristroje Praha, Czech Republic), 5- μ L microsyringe (Hamilton, Switzerland), alumina-backed TLC plates with silica gel coating ALUGRAM Sil G/ UV 254 (Macherey-Nagel, Germany) and vertical chromatographic chamber (Lublin, Poland) were used throughout the experiments.

2.3 Thin-Layer Chromatography

Chromatographic separation was carried out on alumina-backed silica gel 60 TLC plates (10 \times 10 cm, 0.20 mm) with fluorescent indicator UV₂₅₄. The samples were

applied manually with a 5 μ L microsyringe to the starting line 1 cm from the bottom edge. The TLC plates were placed into the chromatographic chamber saturated with vapors of developing solvent, toluene-ethanol (9:1; *v/v*) mixture, at laboratory temperature. The developing distance was 8 cm and chromatographic separation in this system took 20 min. Developed TLC plates were dried in the stream of air at laboratory temperature for approximately 5 min and subjected to post-chromatographic detection. TLC plates were shortly (1–2 s) immersed in the detection reagent (10% phosphomolybdic acid in methanol²⁰) and then heated in a thermal chamber at 110 °C for approximately 10 min, until dark-blue estradiol spots appeared on a yellow-greenish background. For quantification, the spots were evaluated densitometrically at $\lambda = 430$ nm. The volume of sample applied to the plates was 0.3 μ L.

2.4. Standard Solutions and Calibration Curve

Estradiol stock solution at a concentration of 5 mg mL⁻¹ was prepared in methanol. Working standard solutions were prepared by further dilution of stock solution with methanol. The calibration curve in the range of 0.10 – 5.00 mg mL⁻¹ consisted of the following calibration points ($n = 3$): 0.10, 0.25, 0.50, 0.75, 1.00, 2.50 and 5.00 mg mL⁻¹.

2.5. Urine Samples

Urine samples obtained from healthy individuals were checked with diagnostic strips for the presence of pathological constituents such as blood, sugar, or proteins. The urine samples were frozen and stored at -10 °C. On the day of analysis, the urine samples were thawed in lukewarm water, centrifuged at 10 000 rpm for 5 min and only the supernatants were used for further study.

Urine of a 3-year old boy, spiked with estradiol at concentration of 0.1 mg mL⁻¹, was used as a model urine sample throughout the optimization process. The real urine sample was prepared by blending pregnancy urines obtained from five healthy women in the second half of pregnancy as follows: 5 mL from each urine sample was combined together and diluted to 50 mL with distilled water.

2.6. Dispersive Liquid-Liquid Microextraction

A mixture of tetrachloromethane as an extraction solvent and methanol as a dispersive solvent (500 μ L; 1:9, *v/v*) was rapidly injected into 2 mL urine sample with 1.5 mol L⁻¹ NaCl. After gentle agitation for 30 s, the sample was centrifuged at 10 000 rpm for 5 min. Sedimented organic drop (75 μ L) was removed by a microsyringe and subjected to TLC analysis.

3. Results and Discussion

3.1. Thin-Layer Chromatography

Silica gel aluminum-backed TLC plates were after the application of samples developed in vertical chromatographic chamber previously saturated with the vapors of developing solvent, a mixture of toluene and ethanol (9:1; v/v). After development, estradiol on TLC plate was visualized with 10% phosphomolybdic acid detection reagent as dark-blue spots on greenish background²⁰ and it was quantified densitometrically at wavelength of $\lambda = 430$ nm. TLC chromatogram and densitogram of estradiol standard analyzed in the described chromatographic system are demonstrated in Figure 1.

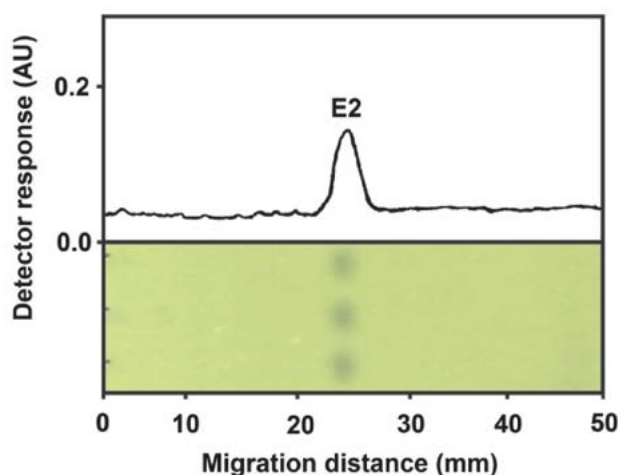


Figure 1. TLC chromatogram and densitogram of estradiol (E2) standard (0.25 mg mL^{-1} ; $n = 3$); stationary phase: silica gel, developing solvent: toluene-ethanol (9:1; v/v), detection reagent: 10% phosphomolybdic acid in methanol, $\lambda = 430$ nm, sample volume: $0.3 \mu\text{L}$.

Qualitative chromatographic parameter – R_f value for estradiol in this system was 0.28 ($n = 3$, $\text{RSD} = 0.23\%$). Optimized TLC method was linear within the concentration range of $0.1 - 5.0 \text{ mg mL}^{-1}$ ($r = 0.9979$) with $\text{LOD} = 0.03 \text{ mg mL}^{-1}$ and $\text{LOQ} = 0.1 \text{ mg mL}^{-1}$. The limit of detection (LOD) and the limit of quantification (LOQ) were calculated based on the standard deviation of response (σ) and slope of calibration curve (b): $\text{LOD} = 3 \sigma/b$ and $\text{LOQ} = 10 \sigma/b$.

3.2. Optimization of Dispersive Liquid-Liquid Microextraction

The efficiency of DLLME procedure is significantly influenced by several factors which were studied in the following manner: (1) type and volume of extraction and dispersive solvents, (2) centrifugation conditions, (3) salt addition, and (4) extraction time. A model urine sample containing 0.1 mg mL^{-1} estradiol was used throughout the optimization process so the influence of real matrix on the extraction efficiency could be assessed.

The selection of dispersive and extraction solvents is crucial in order to attain efficient extraction of the analyte. The requirement for extraction solvent is higher density than water, good extraction capacity for the target analyte and low miscibility in water. On the other hand, high miscibility with dispersive solvent is mandatory. According to these requirements, three halogenated solvents were selected as extraction solvents: chloroform ($\rho = 1.5 \text{ g cm}^{-3}$), tetrachloromethane ($\rho = 1.6 \text{ g cm}^{-3}$) and tetrachloroethane ($\rho = 1.6 \text{ g cm}^{-3}$). The only demand for the dispersive solvent is high miscibility in both extraction solvent and the aqueous phase. Two dispersing solvents were tested in combination with selected extraction solvents: methanol and acetone. Dispersive solvent ($500 \mu\text{L}$) was mixed with $100 \mu\text{L}$ extraction solvent before injection into the model urine sample (2 mL). As a result of the rapid injection, a cloudy solution of a different character was formed, depending mainly on the type of the dispersive solvent: while acetone induced poor dispersion, methanol resulted in fine droplets of extraction solvent scattered within the sample. Consequently, the type of dispersive solvent greatly affected the quality of sedimented organic phase after centrifugation. The sedimented organic phase emerged as a compact drop and was well separated from the solution containing methanol. On the other hand, the sedimented organic phase obtained with acetone was inconsistent and exceeded the initial volume of extraction solvent which suggests that the phase also contained some undesirable portion of the sample or dispersive solvent besides the extraction solvent. According to the obtained results, methanol was selected as a suitable dispersive solvent. The extraction solvents were compared for extraction recovery. Chloroform provided the least extraction potential for estradiol in combination with both methanol and acetone, reaching extraction recoveries of 41% and 40%, respectively. Extraction recoveries obtained with tetrachloroethane and tetrachloromethane in both dispersive solvents ranged from 68% to 74%, reaching their highest level with tetrachloromethane in combination with methanol. Since the requirements for the optimal progress of DLLME procedure were fulfilled with methanol and tetrachloromethane, they were tested in various ratios for adequate development of dispersion, volume of sedimented organic phase and extraction recovery. These demands were met with $500 \mu\text{L}$ tetrachloromethane-methanol (1:9; v/v) mixture which was used throughout the following experiments.

After the selection of extraction and dispersive solvents, the centrifugation conditions were investigated. Although most of the literature published about DLLME so far claims that 4 000 rpm is sufficient for extraction of estrogens in environmental water samples,^{13–17} this study indicated that urine sample requires higher centrifugation speed for adequate separation of phases. Centrifugation causes the separation of phases and is essential for the formation of compact organic drop sedimented on the bot-

tom of the tube. This parameter is of critical importance to the following removal of extraction solvent which should be free of dispersive solvent or sample components. Centrifugation reached optimal conditions for the separation of phases at 10 000 rpm.

The complex character of urine sample resulted in the forming of precipitate which, during centrifugation, covered the sedimented organic drop and hindered the removal for the following analysis. Three types of salts, including potassium carbonate, sodium carbonate, and sodium chloride, were tested in order to prevent the development of this undesired state. Potassium carbonate and sodium carbonate had no influence on the presence of the precipitate. However, the addition of NaCl significantly reduced the amount of precipitation and, moreover, resulted in an unforeseen increase in extraction recovery. This led to further study of the NaCl effect on the extraction efficiency with series of additions ranging from NaCl concentration of 0.5 mol L⁻¹ to 2.0 mol L⁻¹ which is demonstrated in Figure 2. The highest extraction recovery was reached with the NaCl concentration of 1.5 mol L⁻¹ in the sample.

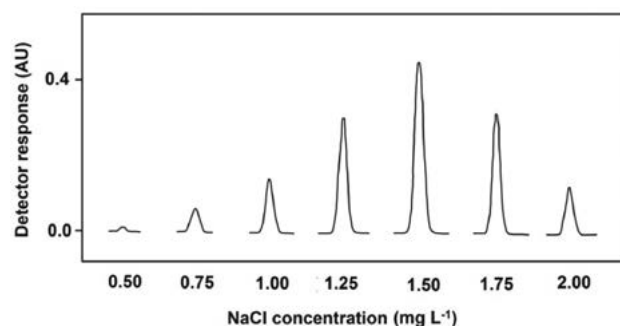


Figure 2. Effect of NaCl concentration on extraction efficiency. Experimental conditions: 2 mL model urine sample containing estradiol (0.1 mg mL⁻¹) with NaCl addition; 500 μ L tetrachloromethane – methanol (1:9; v/v), centrifugation: 5 min, 10 000 rpm

In the final step, the extraction time (time from injection of extraction and dispersive solvents mixture into the sample until the start of centrifugation) was optimized. The initial extraction time in previous experiments was 60 s while the sample was gently agitated to enhance the extraction process. However, the study of the extraction time ranging from 0 to 120 s showed that the extraction efficiency rapidly increases during the first 30 s and does not noticeably change afterwards.

3. 3. Evaluation of Extraction Process

Optimal conditions and characteristics of DLLME procedure for extraction and pre-concentration of estradiol in human urine are summarized in Table 1 and Table 2.

Figure 3 presents the pre-concentration obtained with optimized microextraction technique as the differ-

Table 1. Conditions for optimized DLLME method

Studied parameters	Optimal conditions
Extraction solvent (ES)	Tetrachloromethane
Dispersive solvent (DS)	Methanol
Volume of ES and DS mixture	500 μ L (1 : 9, v/v)
Salt addition	1.5 mol L ⁻¹ NaCl
Extraction time	30 s
Centrifugation conditions	5 min, 10 000 rpm

Table 2. Evaluation of optimized DLLME method with model urine sample spiked with estradiol (0.1 mg mL⁻¹)

Evaluation of DLLME	
Volume of sample	2.0 mL
Volume of organic phase	75 μ L (n=3, RSD = 2.67%)
Pre-concentration factor	25 (n = 3, RSD = 6.81%)
Extraction recovery	93.75% (n = 3, RSD = 6.81%)

ence in estradiol concentration detected in model urine sample before and after DLLME.

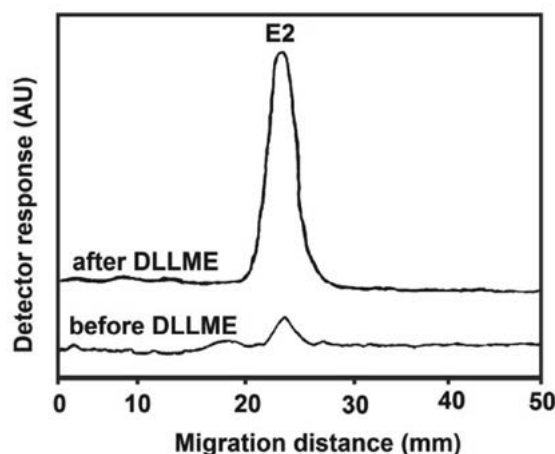


Figure 3. Chromatogram of model urine sample spiked at 0.1 mg mL⁻¹ with estradiol (E2) before and after DLLME. Experimental conditions: 2 mL model urine sample with NaCl addition (1.5 mol L⁻¹); 500 μ L tetrachloromethane – methanol (1:9; v/v) mixture, extraction time: 30 s; centrifugation: 5 min, 10 000 rpm

3. 4. Application to Real Samples

An optimized DLLME-TLC method was applied to the analysis of real urine prepared from five urine samples obtained from women in the second half of pregnancy. The real urine sample was spiked with estradiol at two concentration levels. Table 3 shows found estradiol concentrations in both spiked and non-spiked real urine samples analyzed by the DLLME-TLC method.

Table 3. Extraction recovery (ER) obtained from the determination of estradiol in real urine samples (n = 3)

Spiked (mg mL ⁻¹)	Found (mg mL ⁻¹)	ER (%)	RSD (%)
non-spiked	ND	–	–
0.20	0.18	89%	1.12%
0.10	0.09	91%	1.10%

ER: Extraction recovery; RSD: Relative standard deviation, ND: Not detected

4. Conclusion

Thin-layer chromatography with chemical and densitometric detection was used to optimize a DLLME procedure for the extraction and preconcentration of estradiol in human urine. TLC method enabled fast chromatographic separation of 19 samples within 20 min and, therefore, allowed fast optimization of extraction technique which provided preliminary results for further experiments carried out with HPLC. Optimum conditions for DLLME were reached after rapid injection of 500 µL tetrachloromethane-methanol (1:9; v/v) mixture into 2 mL urine sample containing NaCl (1.5 mol L⁻¹). The samples were after 30 s of gentle agitation centrifuged at 10 000 rpm for 5 min. This study proved TLC to be an efficient method for the laborious optimization process.

5. Acknowledgement

This work was financially supported by the Scientific Grant Agency of the Ministry of Education of the Slovak Republic and of Slovak Academy of Sciences, VEGA 1/0253/16.

6. References

- G. Holder, H. L. J. Makin, H. L. Bradlow, in: H. L. J. Makin, D. B. Gower (Eds.): *Steroid analysis*, Springer, London, UK, **2008**; pp. 605–742.
- K. Wend, P. Wend, S. A. Krum, *Front Endocrinol.* **2012**, *3*, 1–14. DOI:10.3389/fendo.2012.00019
- W. Rosner, S. E. Hankinson, P. M. Sluss, H. W. Vesper, M. E. Wierman, *J. Clin. Endocrinol. Metab.* **2013**, *98*, 1376–1387. DOI:10.1210/jc.2012-3780
- A. C. Johnson, A. Belfroid, A. Di Corcia, *Sci. Total Environment* **2000**, *256*, 163–173. DOI:10.1016/S0048-9697(00)00481-2
- C. G. Campbell, S. E. Borglin, F. B. Green, A. Grayson, E. Wozei, W. T. Stringfellow, *Chemosphere* **2006**, *65*, 1265–1280. DOI:10.1016/j.chemosphere.2006.08.003
- H. Noppe, B. Le Bizec, K. Verheyden, H. F. De Brabander, *Anal. Chim. Acta* **2008**, *611*, 1–16. DOI:10.1016/j.aca.2008.01.066
- W. Yan, J. M. Lin, *Chinese J. Anal. Chem.* **2010**, *38*, 598–606. DOI:10.1016/S1872-2040(09)60038-4
- B. Chen, Y. Huang, M. He, B. Hu, *J. Chromatogr. A* **2013**, *1305*, 17–26. DOI:10.1016/j.chroma.2013.06.029
- Z. Liu, G. Lu, H. Yin, Z. Dang, H. Littier, Y. Liu, *TrAC Trends Anal. Chem.* **2015**, *64*, 149–164. DOI:10.1016/j.trac.2014.09.003
- M. Rezaee, Y. Assadi, M. R. M. Hosseini, E. Aghae, F. Ahmadi, S. Berijani, *J. Chromatogr. A* **2006**, *1116*, 1–9. DOI:10.1016/j.chroma.2006.03.007
- A. Zgola-Grzeskowiak, T. Grzeskowiak, *TrAC Trends Anal. Chem.* **2011**, *30*, 1382–1399.
- M. Rezaee, Y. Yamini, M. Faraji, *J. Chromatogr. A* **2010**, *1217*, 2342–2357. DOI:10.1016/j.chroma.2009.11.088
- X. Du, X. Wang, Y. Li, F. Ye, Q. Dong, C. Huang, *Chromatographia* **2010**, *71*, 405–410. DOI:10.1365/s10337-009-1455-7
- M. R. Hadjmohammadi, S. S. Ghoreishi, *Acta Chim. Slov.* **2011**, *58*, 765–771.
- C. C. Chang, S. D. Huang, *Anal. Chim. Acta* **2010**, *662*, 39–43. DOI:10.1016/j.aca.2010.01.003
- D. L. D. Lima, C. P. Silva, M. Otero, V. I. Esteves, *Talanta* **2013**, *115*, 980–985. DOI:10.1016/j.talanta.2013.07.007
- C. Q. Wu, D. Y. Chen, Y. S. Feng, H. M. Deng, *Anal. Lett.* **2012**, *45*, 1995–2005. DOI:10.1080/00032719.2012.680086
- G. D’Orazio, M. Asensio-Ramos, J. Hernandez-Borges, M. A. Rodriguez-Delgado, S. Fanali, *Electrophoresis* **2015**, *36*, 615–625. DOI:10.1002/elps.201400452
- P. Wang, X. Qiu, Y. Yang, *J. Liq. Chromatogr. Relat. Technol.* **2015**, *38*, 640–646. DOI:10.1080/10826076.2014.913522
- K. Reiffova, E. Kupcova, *J. Planar Chromatogr.-Mod. TLC* **2013**, *26*, 375–378.

Povzetek

Tankoplastna kromatografija (TLC) je zaradi svoje slabše občutljivosti in ločljivosti pogosto spregledana analizna tehnika. Vendar celo v eri visokozmogljive tekočinske kromatografije (HPLC) tankoplastna kromatografija še vedno nudi mnoge prednosti, kot na primer: preprostost, hitrost, cenovno ugodnost; to pa postavlja TLC na prvo mesto pri izbiri metode za delovno intenziven proces optimizacije, ki zahteva analizo številnih vzorcev. V tej raziskavi smo uporabili tankoplastno kromatografijo s kemijsko in denzitometrično detekcijo za optimizacijo disperzivne mikroekstrakcije tekoče-tekoče (DLLME) za ekstrakcijo in predkoncentracijo estradiola iz človeškega urina. Kromatografski sistem je bil sestavljen iz silikagelskih plošč kot stacionarne faze in mešanice toluen-etanol (9:1; v/v) kot topila za razvijanje plošče. Plošče smo orosili z reagentom 10% fosfomolibdensko kislino in nadalje denzitometrično ovrednotili pri $\lambda = 430$ nm. V kontekstu optimizacije DLLME smo preučevali naslednje parametre: tip in volumen ekstrakcijskega in disperzijskega topila, centrifugiranje, dodatek soli ter čas ekstrakcije. Predlagano DLLME-TLC metodo smo uspešno uporabili za določitev estradiola v realnih vzorcih človeškega urina.

Scientific paper

The Accuracy of Macro–Submicro–Symbolic Language of Future Chemistry Teachers

Dušica D. Rodić,¹ Tamara N. Rončević¹ and Mirjana D. Segedinac¹¹ Department of Chemistry, Biochemistry and Environmental Protection, Faculty of Sciences, University of Novi Sad, Trg Dositeja Obradovića 3, Novi Sad, Republic of Serbia* Corresponding author: E-mail: dusica.milenkovic@dh.uns.ac.rs

Received: 24-12-2017

Abstract

The present study is focused on the examination of language accuracy of future chemistry teachers in the macro–submicro–symbolic domain. Since the knowledge at the submicroscopic level is crucial for the understanding of chemical concepts and ideas, the aim of this study was to examine the accuracy of the language of future chemistry teachers while delivering chemical contents at this level. Within this objective, it was examined whether future chemistry teachers make a distinction between submicroscopic and macroscopic levels, as well as between submicroscopic and symbolic levels in their speech. Using qualitative methods of analysis, it was found that the majority of surveyed future chemistry teachers did not have the expected and necessary language accuracy within the examined domain. Most worrying were the attitudes of future chemistry teachers, who perceived the accurate expressions in the macro–submicro–symbolic domain as a redundant complication rather than a necessity.

Keywords: Future chemistry teachers; language accuracy; micro-submicro-symbolic language

1. Introduction

The concept of three levels of chemical representation, or the so-called “triplet relationship”¹ has been attracting the attention of a large number of researchers in the field of chemical education for many years. Although this notion was first mentioned in 1982 it still seems to be very influential and widespread among researchers.² From the basic idea that chemical contents can be taught on three levels, commonly called macroscopic (sensory accessible properties of substance), submicroscopic (particulate level) and symbolic (symbols, formulae, equations), multiple lines of research have been established over time. Nonetheless, most attention has been paid to the problems and misconceptions that occur as a result of misinterpretations regarding the submicroscopic level.^{3–5} Along with the fact that this level is the most abstract one and therefore the most difficult to master, some researchers have suggested that there is an additional issue that further fosters these difficulties, and that is the imprecise use of language.^{6,7} Namely, teachers, textbook writers or scientists are prone to use language in a way that does not maintain the necessary distinction between macroscopic and submicroscopic levels. Thus, it is quite common to hear teachers saying e.g. that ammonia consists of nitrogen and hy-

drogen, that stearic acid has a long chain of C-atoms or that oxygen has a double bond, when in fact they referring to particles of these substances. However, students commonly lack the skill to shift between levels, which further complicates the already heavy and abstract submicroscopic concepts. The same can be said of the writers of school textbooks, who have a fairly inattentive approach to this issue. For example, in textbooks approved by the Ministry of Education of the Republic of Serbia for primary school chemistry, it is possible to find statements such as the following:

Each period, except the first, ends with the element that has 8 electrons in the highest energy level;⁸ electronegativity is the ability of a chemical element to attract the electron pair;⁹ carboxylic acids which have a higher number of carbon atoms are referred to as a higher fatty acid;¹⁰ benzene contains six carbon and six hydrogen atoms.¹¹

The above examples clearly show the use of blurred language concerning macroscopic and submicroscopic. Furthermore, researchers have also pointed out the interference between macroscopic and submicroscopic levels in some presentations of the Periodic table of elements,¹² as some of the data provided, refer to submicroscopic particles (e.g. electron configuration, atomic and mass number), while some of them refer to elementary substances

(e.g. density, state of matter) which leads to confusion among students.

Such inconsistencies, which are likely the result of teachers' or textbook writers' carelessness, may have some severe consequences on students' meaningful understanding. Namely, such approach could be one of the possible causes of the formation of a well-known and scrutinized misconception of transmission of substance macroscopic properties to its submicroscopic particles. Thus, it is not surprising that students believe that molecules of solids are hard unlike molecules of liquids and gasses,¹³ that molecules of water can be hot and cold, that molecules of naphthalene have an odour¹⁴ or that sulphur atoms are coloured yellow¹⁵ given that the macro-submicro terms are used quite often interchangeably during classes.

Besides this flimsy language between macro and submicro domains, inaccurate language can also appear between submicro and symbolic domains. Namely, the symbolic models may appear to be the reality for many students. Chittleborough and Treagust stated that teachers insufficiently emphasize the representational nature of the formulas, saying, for example that CH₄ is methane, instead that it represents the composition of a methane molecule.¹⁶ Kleinman, Griffin, and Kerner reported about a student who believed that bromobenzene has no plane of symmetry since $B \neq r$, which is an obvious example of the fact that some students firmly adhere representations, instead of submicroscopic reality.¹⁷ Furthermore, favouring symbolic visualizations over underlying submicroscopic concepts is commonly present when dealing with chemical equations.¹⁸ It means that student may become very adept at manipulating a chemical equation, without its proper reasoning.

There is an interesting view that the language itself could act as a greater barrier for learning than contents of natural sciences.¹⁹ Namely, the peculiarity of chemistry by which it differs from other natural sciences is the developed system of scientific communication – chemical language. It often happens that words of chemical language are used in everyday life, but with different meaning, which can create difficulties for students. Confusion arises when teachers in explaining some chemical concepts use words that are also used in everyday life (e.g. pure, reduction, etc.), assuming that students will understand them in a chemical way.²⁰ Sometimes in chemistry, even one word can have several meanings (e.g. *neutral oxide*, *pH-neutral*, *neutral atom*), which additionally frustrates students. Studies show that accurate and consistent use of chemical language, especially in describing the substance at the submicroscopic level enhances the students' ability to interpret concepts.¹⁵

Accordingly, it is important that teachers are aware of the significance of accurate and precise expression, which necessarily includes the precise expression in the macro-submicro-symbolic domain. Otherwise, the imprecise use of language, though often unintended, can create barriers to learning.

2. Methodology

2. 1. Aim of Research

Assuming that imprecise and inconsistent use of chemical language in the macro-submicro-symbolic domain by teachers can represent the basis for the formation of biases and misconceptions, the main objective of this study was to examine the precision of future chemistry teachers' language within macro-submicro-symbolic domain. Within this goal, two research tasks have been set:

T1: To determine whether future chemistry teachers make a clear distinction between macroscopic and submicroscopic levels in their explanations.

T2: To determine whether future chemistry teachers make a clear distinction between submicroscopic reality and symbolic representations in their explanations.

2. 2. Context of the Study

In the Republic of Serbia, there are two basic university programs for education of chemistry teachers – bottom-up and concurrent model. At the faculties with a bottom-up model, students opt for teaching programme at the beginning of their studies. At the faculties with a concurrent model, such as the Faculty of Sciences (University of Novi Sad) where the research was conducted, students study compulsory chemistry courses, and to be profiled in the direction of teaching chemistry, students have to acquire a regulated number of credits in educational courses and compulsory school practice, during the studies through elective courses. Within school practice courses, students are required to undergo two main parts: (1) observations of classes performed by licensed mentor-practitioner, without participation in the teaching and (2) teaching under supervision of licensed mentor-practitioner.

At the Department of Chemistry, Biochemistry and Environmental Protection, Faculty of Sciences, there are two courses of school practice: (1) School practice I (8th semester; primary school teaching: 7th and 8th grade) and (2) School practice II (10th semester; secondary school teaching: 9–12th grade). Within the first stage of the School practice (both I and II), students have to observe 25 classes (18.75 hours) performed by experienced mentor-practitioner. In the next stage, students are required to independently hold at least 5 classes under supervision of mentor-practitioner. Additionally, students are required to attend weekly coaching lessons.

2. 3. Participants and Setting

Students who enrolled in the School practice I course at the Department of Chemistry, Biochemistry and Environmental Protection, Faculty of Sciences, Novi Sad in 2014/15 academic year were participants of this study ($N = 16$). All of them were female students majoring in chemistry teaching in their fourth and final year of their Bachelor

degree. Most of the subjects had completed obligatory subject matter courses before selecting the School practice I course. In addition, the majority of them have taken following educational courses as well: Pedagogy, Psychology, Introduction to Teaching Profession, Methods of Teaching Chemistry I and II and Modern Educational Technology in Teaching Chemistry.

The research was conducted in three public, urban schools located in the municipality of Novi Sad, Province of Vojvodina wherein students observed and held classes. Mentors-practitioners were three licensed chemistry teachers (one from each school) who have at least 5 years of work experience in primary school teaching and who have been achieving excellent educational results in their teaching practice.

Prior to conducting the survey, all participants were informed that the lessons will be voice recorded and that the results will be used for research purposes. After the research procedure was explained, all the students gave their consent to voluntarily participate in the research.

2. 4. Study Design

To obtain data, qualitative research methodology was used. Namely, two authors of this paper (university staff) have been present during all the classes that were held independently by students (a total of 80 classes, 60 hours) and marked the errors encountered. The role of university staff was both advisory and assessment similar to other research studies.²¹ In addition, all classes were voice recorded. Since there is no uniform protocol for monitoring school practice, which is in accordance with competency standards for the profession of teachers and their professional development in the Republic of Serbia, in this study we used an internal protocol developed by the authors of this paper. It involved consideration of the fol-

lowing points in line with the mentioned standards: content knowledge, pedagogical knowledge, connection of new information to prior knowledge, correlations to contents of other subjects, use of everyday life examples, classroom management, and literacy. In addition, special attention was paid to monitoring the precision of language in the macroscopic, submicroscopic and symbolic domain, which was the main topic of this study. In addition to observations, after each class, in the five-minute break between classes, the authors conducted brief interviews with the future chemistry teachers to determine their awareness of inaccurate use of language in the macro-submicro-symbolic domain, during teaching.

All teaching topics covered in this study are shown in Table 1.

3. Results and Discussion

3. 1. Macro–Submicro Inaccuracies

Within data interpretation, the field notes as well as voice recordings were carefully analysed and categorised according to two defined research questions.

Since the first task was related to the determination of language accuracy in macro-submicro domain, the first part of this section will be devoted to the analysis of the most frequent linguistic imprecisions that were noticed during the monitoring future teachers' classes. The list of imprecise and unclear statements has been extracted and summarized in Table 2. It is important to note that in addition to the statements specified in Table 2, similar statements have also been recorded, however, to avoid redundant repetition they are not included in the Table 2.

Statements of the type I (Imprecise expression of the particle type; S1–S4 in Table 2) were recorded during the various teaching topics and were constantly repeated by

Table 1. Topics Covered During Data Collection

Grade	Teaching unit	Type of class*
VII	Solubility of substances and percentage composition of the solution	PNMT
VII	Solubility of substances and percentage composition of the solution	R
VII	Water	PNMT
VII	Chemical reactions. Analysis and synthesis	PNMT
VII	Chemical equations	R
VII	The law of conservation of mass	PNMT
VIII	Oxygen containing organic compounds	R
VIII	Physical and chemical properties of carboxylic acids	PNMT
VIII	Physical and chemical properties of carboxylic acids	R
VIII	Esters	PNMT
VIII	Carbohydrates, monosaccharides	PNMT
VIII	Disaccharides and polysaccharides	PNMT
VIII	Fats and oils	PNMT
VIII	Amino acids and proteins	PNMT
VIII	Vitamins	PNMT

*PNMT (Processing new teaching material); R (Revising)

Table 2. List of Imprecise Statements in relation to Macro-Submicro Level

Type	No.	Statement/Question
I	S1	Molecules of sodium chloride
I	S2	On the left side, we have three molecules of sodium hydroxide
I	S3	The molecules of soap can remove the stain
I	S4	On the third carbon atom, OH molecule is located on the left side
II	S5	Which atoms have that sugar?
II	S6	From one molecule of sucrose, glucose and fructose can be obtained
II	S7	Water is composed of two hydrogen atoms and one atom of oxygen
II	S8	The oligosaccharides contain 2–10 monosaccharides
II	S9	When equalizing this equation, we should first counter the number of oxygen
II	S10	How many hydrogens are there on the left side?
III	S11	Compounds with a polar covalent bond can be dissolved in water
III	S12	How are oxygen and hydrogen connected in water?
IV	S13	Tap water is a pure water

the majority of future chemistry teachers. Listening to the voice recordings, it was found that future chemistry teachers often used the expression “molecule” to represent main particles which build ionic compounds. Besides sentence such as: “there are molecules of sodium chloride in this solution”, analogous sentences and questions were also recorded, such as: “on the left side, we have three molecules of sodium hydroxide”, “molecules of soap can remove the stain”, “what do we call a molecule of copper(II) sulphate”, “if we want to obtain a molecule of iron(II) sulphide, we need 7 g of iron, and 4 g of sulphur” etc. Furthermore, while writing formula of glucose molecule, one future chemistry teacher said: “on the third carbon atom, OH molecule is located on the left side”.

Reviewing the literature, we found information on the widespread school-made misconception among students, that the main particles that build the substance sodium chloride are neutral molecules,^{22–25} then CaCl_2 molecules are present in water which contains calcium chloride,²⁶ or students write balanced equations of reactions in which the ionic compounds dissolve as neutral atoms or molecules.²⁷ In the case where students have acquired this misconception, the inattentive speech of a teacher can additionally enhance it.

Statements of the type II (Neglecting particle terms and prevalent use of macroscopic terms; S5–S10 in Table 2) were recorded among the majority of future chemistry teachers. Based on the above examples it can be noted that future chemistry teachers’ expressions in terms of particles are quite imprecise, and very often replaced by analogous macroscopic terms. However, such statements may confuse students who are at the very beginning of their chemical education and who have yet to establish a flexible system of knowledge with firmly incorporated fundamental chemical concepts. Due to the aforementioned statements, students may conclude that the main building blocks of sugars are free atoms (“which atoms have that sugar”), that water is a mixture composed of hydrogen and oxygen

(“water is composed of two hydrogen atoms and one atom of oxygen”) or may neglect the fact that small amounts of some substance contain an enormous number of particles (“from one molecule of sucrose glucose and fructose can be obtained”; “fructose consist of six carbon atoms, ketone carbonyl group and five hydroxyl groups”; “carboxylic acids which have 4–7 carbon atoms are malodorous”). The statements such as: “when equalizing this equation, we should first count the number of oxygen” and “how many hydrogens are there on the left side?”, which are related to chemical equations, should be particularly stated. Namely, it is observed that future chemistry teachers rarely use particulate terms while balancing equations, replacing them with terms such as “one hydrogen on the left side, two oxygens on the right side” and the like.

Within type III (Chemical bond as a feature of elementary substance), two statements were noted (S11 and S12 in Table 2). Namely, a future chemistry teacher asked: “how are oxygen and hydrogen connected in water”, which can make students think that water is made of chemically bonded molecules of hydrogen and molecules of oxygen rather than water molecules. Another such case arises from the statement: “compounds with polar covalent bonds can be dissolved in water”. Likewise, students can conclude that a polar covalent bond occurs between the particles of a compound, and not within the particle.

One statement of the type IV (Mixing chemical terms with everyday life terms; S13 in Table 2: Tap water is a pure water) has been observed in the case of four future teachers during the teaching topic “Water”. Namely, comparing the prepared samples of tap water and water from a local canal, a future teacher used the term “pure water” instead of clear water without considering the fact that chemically pure water has a different meaning. As already mentioned, one of the problems, frequently encountered during teaching of chemistry, is that some words used in everyday life can sometimes be used in chemistry but with a different meaning. In the presented case, the future

teacher was thinking about physically pure water i.e. water that is not contaminated by other substances which may affect its physical appearance. However, the expression pure water in chemical and theoretical sense would mean that the tap water consists of water molecules only, which cannot be concluded merely on the basis of its physical appearance. This led to confusion, as in the final part of the class, during the revision, some students stated tap water as an example of a pure substance.

Taber stated that chemistry teachers use the term pure substance as a technical term thinking of the composition of the substance at the submicroscopic level, while at the same time students are more focused on the external appearance of a substance, which leads to common problems in teaching practice.²⁸ In this case, it can be noted that the future teacher was also thinking about the external appearance of substance, without considering the possible biases that go along with that term.

After interviews with the future chemistry teachers, it was noticed that they do not pay attention to the precise language at the submicroscopic level. Moreover, they do not believe that it could have an impact on creating confusion among students. Some future chemistry teachers even after the interview and the reflection on differences between the two modes of expressions did not consider precise language as required, but rather as complicated. Similarly, Gilbert, and Treagust stated that some authors believe that the introduction of additional submicroscopic terms, with a view to precise language, unnecessarily complicates sentences and does not contribute to the removal of ambiguities among students.¹ Worryingly, some future chemistry teachers in this study could not even comprehend the difference between the two modes of expressions.

3. 2. Submicro–Symbolic Inaccuracies

In this section, we present a table with noted inaccuracies within the submicro-symbolic domain. Recorded

inaccurate statements (S1–S6) as well as graphical representations (G1–G2) are summarised and given in Table 3.

The statement of the type I (Reasoning at symbolic level; S1 in Table 3) was recorded during the teaching topic Esters. Namely, one future chemistry teacher explained the esterification reaction in the following manner: “In the esterification reaction, ester and water are formed. We know that the water is made up of two hydrogen atoms and one oxygen atom. Therefore, we have OH (showing on the condensed structural formula of ethanol), and H (showing on the condensed structural formula of ethanoic acid) and we get water, and all that remains combines into a new compound. So, on the left side we will have CH₃CH₂, and on the right side CH₃COO and one free bond which we can use to connect the left and right side of the compound”. In addition to the inaccurate expression at submicroscopic level and content knowledge flaws (probably substituting esterification with neutralisation reaction), the described situation clearly illustrates an example of reasoning at the symbolic level. Namely, the future teacher has poorly developed concepts of chemical bond and chemical reaction. Reviewing the literature, we came across various misconceptions regarding chemical bond and bonding. This area of research has proved to be one of the most studied one in the last several decades.^{29–33} Researchers, acting in this area, identified some interesting misconceptions, however, this study revealed another interesting misconception. Namely, the future chemistry teacher conceived chemical bond as a tangible strong connection (stick) that can be transferred from one place to another and used to connect the atoms or atomic groups, similar to molecular models. On the other hand, this future chemistry teacher understood the chemical equation as a simple combination of atoms without considering the mechanism of chemical reactions. This is not surprising, given that many researchers in literature reported the students’ ability to write and equate chemical equations without proper submicroscopic reasoning.¹⁸

Table 3. List of Imprecise Statements in relation to Submicro-Symbolic Level

Type	No.	Statement/Graphical representation
I	S1	In the esterification reaction, ester and water are formed. We know that the water is made up of two hydrogen atoms and one oxygen atom. Therefore, we have OH (showing on the condensed structural formula of ethanol), and H (showing on the condensed structural formula of ethanoic acid) and we get water, and all that remains combines in a new compound
II	S2	We will write a reaction of photosynthesis
II	S3	Is there anyone who knows how to balance this reaction?
II	S4	On the left side of the reaction there are ethanol and acetic acid, while on the right side there are ester and water
II	S5	Substance that undergoes chemical change is written on the left side of the reaction
II	S6	We will write glucose
III	G1	$\begin{array}{c} \text{CH}_2\text{—CH—CH}_2 \\ \quad \quad \\ \text{OH} \quad \text{OH} \quad \text{OH} \end{array}$
III	G2	$\text{C}_{12}\text{H}_{22}\text{O}_{11} + \text{H}_2\text{O} \xrightleftharpoons{\text{H}^+} \text{C}_6\text{H}_{12}\text{O}_6 + \text{C}_6\text{H}_{12}\text{O}_6$

Within type II (Mixing symbolic terms and submicroscopic reality) five statements were recorded (S2–S6 in Table 3). Namely, by observing the lessons of future chemistry teachers, we were able to notice that future teachers commonly do not make a distinction between reaction and the chemical equation as its representation in their speech; between a compound and its representation – formula, or between an atom of an element and its representation – symbol. Therefore, we were able to record some very imprecise constructions such as: reaction of photosynthesis, left side of the reaction, we will write glucose, and others listed in Table 3. However, since chemistry is a subject which emphasizes precision and accuracy, the precise use of language also implies.³⁴

The third type of observed inaccuracies was related to imprecise writing of chemical formulas and equations. In the Table 3 we gave two examples, one for a formula and one for an equation, as presented by future chemistry teachers. According to the structure of glycerol presented in Table 3, students could incorrectly conclude that an oxygen atom is directly bonded to a hydrogen atom instead of a carbon atom. After a conversation with one future chemistry teacher, it was found that she does not realize the importance of proper writing of formulas, as she assumed that the students would understand them in the proper way. The second noticed imprecision refers to the writing of arrows in chemical equations. Although double-headed arrow implies the existence of a ‘resonance hybrid’, in this study, future chemistry teachers regularly used it to present an equilibrium condition. This is a well-known misinterpretation, explained by Bucat and Mocerino.⁶

Easy and smooth movement through the levels of representation of knowledge is very important for the development of chemical thinking and the development of proper mental models among students. To make these possible, students should be given the opportunity to meet and explore chemistry contents at all three levels, without neglecting certain levels or favouring others. In-service teachers, even university teachers do not pay sufficient attention to this, because as experts, they know the difference in use between macroscopic level as real and perceptually available and submicroscopic as real, but unavailable to direct sensory perception, or the difference in use between submicroscopic as real and symbolic as representational and assume that students will perceive them in the same way. However, for students, especially for those who have just started to study chemistry, it is difficult to perceive these differences. Therefore, it is important that teachers do not create additional confusion with inconsistent and inaccurate language within the triplet system. In line with that, it is essential that future chemistry teachers, in particular, become aware of the importance of accurate use of language, as being ones who will be in direct contact with novices, helping them to develop proper chemical concepts.

4. Conclusions

This study highlights areas of concern regarding submicro–macro and submicro–symbolic language. The main outcomes of this study are related to findings that future chemistry teachers tend to use imprecise language expressions in terms of particle types, prevalently using the term molecule regardless of the fact whether the compound is a covalent or ionic. It is also found that a vast majority of the covered sample avoided using particle terms, using macroscopic terms instead. Additionally, some concepts that belong to submicroscopic level were transferred to a bulk substance. Finally, concerning submicroscopic–symbolic relations, in one particular case, it was shown that future teachers do not pay the necessary attention to the terms that have different meanings in chemistry and in everyday life. Similarly, several issues in relation to submicroscopic–symbolic transitions were identified. It has been found that there were future chemistry teachers who reasoned at the symbolic level, and who did not have properly developed submicroscopic mental models. Furthermore, certain imprecisions regarding presentations of structural formulas have been noted as well. According to this, we may conclude that future chemistry teachers, which were involved in this study, did not possess adequate language accuracy within a triplet domain.

In light of this, we would like to emphasize the need to introduce students, future chemistry teachers, to the idea of the triplet model of content representation during their initial education. In accordance with that, students majoring in chemistry teaching should become aware of the importance of precise expression in this domain.

Regarding limitations of this study, it should be mentioned that studies with larger samples are needed before making any generalizations. Therefore, the findings of this study should be considered preliminary and additional research should be based on the cooperation with other university centres to be able to reach conclusions that are more general.

5. Acknowledgments

This paper was written with the support of a grant from the Ministry of Education, Science and Technological Development of the Republic of Serbia #179010. The authors would like to thank mentors-practitioners Gordana Gajić, Dragica Krivokuća and Sanja Rodić Rončević, as well as future teachers of chemistry who participated in the study.

6. References

1. J. K. Gilbert, D. F. Treagust, in: J. K. Gilbert, D. F. Treagust (Eds.): *Multiple Representations in Chemical Education*, Springer, Berlin, Germany, 2009, pp. 1–8.

- DOI:10.1007/978-1-4020-8872-8
2. A. H. Johnstone, *Sch. Sci. Rev.* **1982**, *64*, 377–379.
 3. I. Devetak, M. Urbančič, K. Wissiak Grm, D. Krnel, S. Glažar, *Acta Chim. Slov.* **2004**, *51*, 799–814.
 4. I. Devetak, J. Vogrinc, S. A. Glažar, *Res. Sci. Educ.* **2009**, *39*, 157–179. DOI:10.1007/s11165-007-9077-2
 5. M. I. Stojanovska, B. T. Šoptrajanov, V. M. Petruševski, *Creat. Educ.* **2012**, *3*, 619–631. DOI:10.4236/ce.2012.35091
 6. B. Bucat, M. Mocerino, in: J. K. Gilbert, D. F. Treagust (Eds.): *Multiple Representations in Chemical Education*, Springer, Berlin, Germany, **2009**, pp. 11–29. DOI:10.1007/978-1-4020-8872-8_2
 7. B. Van Berkel, A. Pilot, A. M. W. Bulte, in: J. K. Gilbert, D. F. Treagust (Eds.): *Multiple Representations in Chemical Education*, Springer, Berlin, Germany, **2009**, pp. 31–54. DOI:10.1007/978-1-4020-8872-8_3
 8. L. Mandić, J. Korolija, D. Danilović, Hemija za 7. razred osnovne škole, Zavod za udžbenike i nastavna sredstva, Beograd, **2009**, p. 61.
 9. J. Adamov, N. Makivić, S. Olić, Hemija za 7. razred osnovne škole, Gerundijum, Beograd, **2012**, p. 72.
 10. L. Mandić, J. Korolija, D. Danilović, Hemija za 8. razred osnovne škole, Zavod za udžbenike i nastavna sredstva, Beograd, **2010**, p. 129.
 11. T. Nedeljković, D. Anđelković, Hemija 8, Novi Logos, Beograd, **2010**, p. 124.
 12. M. Stojanovska, V. M. Petruševski, B. Šoptrajanov, *Nat. Math. Biotech. Sci.* **2014**, *35*, 37–46.
 13. C. Horton, Student Alternative Conceptions in Chemistry, modeling.asu.edu/modeling/Chem-AltConceptions3-09.doc, (assessed June 24, 2014).
 14. E. Adadan, Promoting High School Students' Conceptual Understandings of the Particulate Nature of Matter through Multiple Representations, Ph.D. Thesis, Ohio State University, **2006**.
 15. G. D. Chittleborough, The Role of Teaching Models and Chemical Representations in Developing Students' Mental Models of Chemical Phenomena, Ph.D. Thesis, Curtin University, **2004**.
 16. G. D. Chittleborough, D. F. Treagust, *Chem. Educ. Res. Pract.* **2007**, *8*, 274–292. DOI:10.1039/B6RP90035F
 17. R. W. Kleinman, H. C. Griffin, N. K. Kerner, *J. Chem. Educ.* **1987**, *64*, 766–770. DOI:10.1021/ed064p766
 18. V. Talanquer, *Int. J. Sci. Educ.* **2011**, *33*, 179–195. DOI:10.1080/09500690903386435
 19. R. Vladušić, R. Bucat, M. Ožić, *Chem. Educ. Res. Pract.* **2016**, *17*, 474–488. DOI:10.1039/C6RP00037A
 20. H. K. Boo, *J. Res. Sci. Teach.* **1998**, *35*, 3–12. DOI:10.1002/(SICI)1098-2736(199805)35:5<569::AID-TEA6>3.0.CO;2-N
 21. K. S. Wissiak Grm, V. Ferik Savec, *Acta. Chim. Slov.* **2014**, *61*, 729–739.
 22. K. S. Taber, *Educ. Chem.* **1994**, *31*, 100–103.
 23. R. M. Kelly, L. L. Jones, *J. Sci. Educ. Technol.* **2007**, *16*, 413–429. DOI:10.1007/s10956-007-9065-3
 24. L. T. Tien, M. A. Teichert, D. Rickey, *J. Chem. Educ.* **2007**, *84*, 175–181. DOI:10.1021/ed084p175
 25. J. Othman, D. F. Treagust, A. L. Chandrasegaran, *Int. J. Sci. Educ.* **2008**, *30*, 1531–1550. DOI:10.1080/09500690701459897
 26. H. D. Barke, *Bull. Chem. Technol. Bosnia Herzeg.* **2013**, *40*, 9–16.
 27. B. M. Naah, M. J. Sanger, *Chem. Educ. Res. Pract.* **2012**, *13*, 186–194. DOI:10.1039/C2RP00015F
 28. K. S. Taber, Chemical axioms, <http://www.rsc.org/learn-chemistry/resource/res00001138/chemical-axioms?cmpid=C-MP00002169>, (assessed December 26, 2016).
 29. R. Peterson, D. F. Treagust, *J. Chem. Educ.* **1989**, *66*, 459–460. DOI:10.1021/ed066p459
 30. K. S. Taber, *Educ. Chem.* **1994**, *31*, 100–103.
 31. K. C. D. Tan, D. F. Treagust, *Sch. Sci. Rev.* **1999**, *81*, 75–83.
 32. R. K. Coll, D. F. Treagust, *J. Res. Sci. Teach.* **2003**, *40*, 464–486. DOI:10.1002/tea.10085
 33. R. Vladušić, R. B. Bucat, M. Ožić, *Chem. Educ. Res. Pract.* **2016**, *17*, 685–699. DOI:10.1039/C6RP00040A
 34. H. K. Boo, in: N. K. Goh, L. S. Chia, H. K. Boo, S. N. Tan, M. F. R. Tsoi (Eds.): *Chemistry Teachers' Network*, Singapore National Institute of Chemistry, Singapore, Singapore, **2000**, pp. 60–63.

Povzetek

Raziskava je osredotočena na pregled jezikovne natančnosti izražanja bodočih učiteljev kemije na področju makro–submikro–simbolnih domen. Ker je znanje na submikroskopskem nivoju ključnega pomena za razumevanje kemijskih konceptov in idej, je namen te raziskave preverjanje natančnosti jezikovnega izražanja bodočih učiteljev kemije na tem nivoju. V okviru tega cilja smo proučevali ali bodoči učitelji kemije med poučevanje pri jezikovnem izražanju razlikujejo med submikroskopskim in makroskopskim nivojem in tudi med submikroskopskim in simbolnim nivojem. Z uporabo kvalitativnih metod analize smo ugotovili, da večina bodočih učiteljev kemije, ki so sodelovali v raziskavi, nima zadosti natančnega načina jezikovnega izražanja glede proučevanih nivojev. Zaskrbljujoče je, ker pogosto bodoči učitelji kemije gledajo na natančnost jezikovnega izražanja na področju makro–submikro–simbolnih domen kot na nepotrebno komplikacijo in ne kot nujnost pri jasnem podajanju snovi.

Scientific paper

Synthesis of Cyclic and Acyclic Pyrimidine Nucleosides Analogues with Anticipated Antiviral Activity

Mohamed F. El-Shehry,^{1,*} Emad M. El Telbani^{2,3}
and Mohamed I. Hegab^{4,5}

¹ Pesticides Chemistry Department, National Research Centre, Dokki, 12622 Giza, Egypt

² Green Chemistry Department, National Research Centre, Dokki, 12622 Giza, Egypt

³ Chemistry Department, Faculty of Science, Jazan University, Jazan, Saudi Arabia

⁴ Photochemistry Department, National Research Centre, Dokki, 12622 Giza, Egypt

⁵ Chemistry Department, Faculty of Science & Arts, Qurayat, Al-Jouf University, Saudi Arabia

* Corresponding author: E-mail: moh_elshehry2000@yahoo.com

Received: 25-12-2017

Abstract

A convenient method for preparation of cyclic and acyclic nucleosides was achieved by alkylation of 6-(2,4-dichlorophenoxy)methylpyrimidine-2,4-dione (**1**) with a variety of acyclic and cyclic activated sugar analogues, namely (2-acetoxyethoxy)methyl acetate (**3**), 2-(acetoxymethoxy)propane-1,3-diyl dibenzoate (**4**), benzyloxymethyl acetate (**5**), 2-acetoxy-5-(benzyloxymethyl)tetrahydrofuran-3,4-diyl dibenzoate (**12**), 5-chloro-2-((4-chlorobenzoyloxy)methyl)tetrahydrofuran-3-yl 4-chlorobenzoate (**13**) and 2-(acetoxymethyl)-6-bromotetrahydro-2H-pyran-3,4,5-triyl triacetate (**14**), respectively. Deprotection of the synthesized nucleosides was achieved by using methanolic ammonia. The structures of the newly synthesized nucleoside analogues were fully characterized by analytical methods (mass spectrometry, ¹H NMR, ¹³C NMR, and elemental analysis).

Keywords: Pyrimidines, nucleosides, vorbrüggen and niedballa's procedure, antiviral activity

1. Introduction

A number of base-modified nucleosides have been playing a vital and important role as therapeutic agents in the treatment of patients infected with different viruses including human immunodeficiency virus (HIV), herpes simplex virus (HSV), hepatitis B virus (HBV), hepatitis C virus (HCV) and cytomegalovirus (CMV) infections.¹ According to U.S. Food and Drug Administration (FDA), many cyclic and acyclic nucleoside analogues, such as 3'-azido-3'-deoxythymidine (AZT), 2',3'-dideoxyinosidine (DDI), 2',3'-dideohydro-3'-deoxythymidine (D4T), 1-[(2-hydroxyethoxy)methyl]-6-(phenylthio)thymine (HEPT), acyclovir, and penciclovir (Fig. 1) are effective in treatment of various viruses.²

Moreover, it is well known that functionalized nitrogen heterocycles play an interesting role in drug chemistry and therefore they have been intensively studied and used as scaffolds for searching and developing new drugs.³ Py-

rimidine-incorporating sugar residues represent an interesting class of nucleosides which have a promising antiviral chemotherapy potential, especially that class in which the cyclic sugar residue is replaced with open-chain "acyclic" sugar moieties. Moreover, heterocycles possessing pyrimidine nucleus are of great interest because they constitute an important class of natural and non-natural products which possess diverse biological activities and medicinal applications.⁴ Additionally, pyrimidine skeleton is also present in many natural products, such as vitamin B1 (thiamine) and a lot of synthetic compounds which possess a wide spectrum of biological activities including polio herpes viruses,⁵ diuretic, anti-HIV, cardiovascular,⁶ antibacterial,⁷⁻⁹ antifungal,^{10,11} antihypertensive,¹² antipyretic,¹³ antiviral,¹⁴⁻¹⁵ antidiabetic,¹⁶ antioxidant,¹⁷⁻¹⁸ anticancer activities,¹⁹⁻²⁰ antileishmanial,²¹ anti-inflammatory,²² analgesic,²³ antiallergic,²⁴ anticonvulsant,²⁵ antihistaminic,²⁶ herbicidal,²⁷ antidepressant,²⁸ and also act as calcium

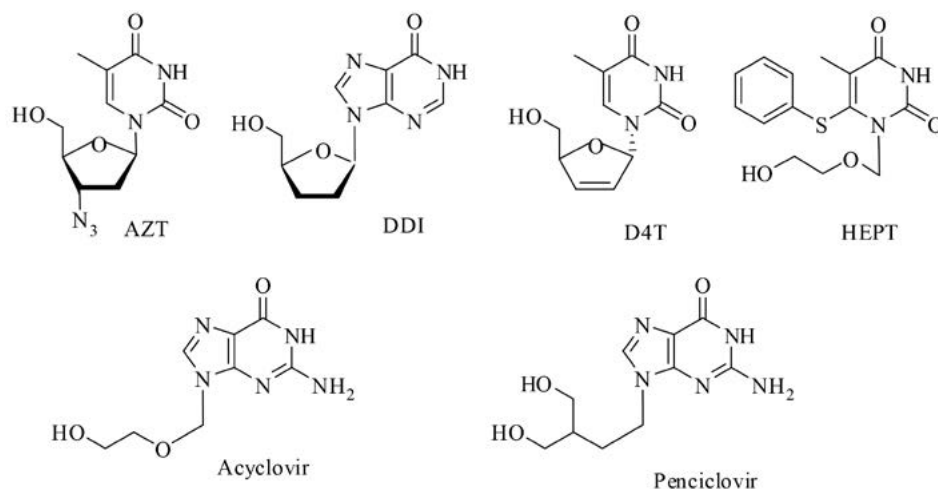


Figure 1: Some examples of cyclic and acyclic antiviral agents

channel blockers.²⁹ On the other side, fusion of pyrimidine moiety with different heterocycle scaffolds gives rise to a new class of hybrid heterocycles possessing improved biological activity. Fused pyrimidines like purines, quinazolines, pteridines, pyridopyrimidines, pyrazolopyrimidines, pyrimidoazepines, triazolopyrimidines, furopyrimidines and pyrrolopyrimidines were studied in the past decade and were found to possess remarkable pharmacological properties, such as antibacterial activity, antifungal activity, anti-cancer agents, antihyperlipidemic activity, blood related disorders, analgesic and anti-inflammatory activities, anti-HIV agents, CNS related agents, and immunosuppressants.³⁰

For the design and search of new drugs, the development of hybrid molecules through the binding of various pharmacophores in one frame could lead to molecules with interesting pharmaceutical properties. Based on above information and in continuations of our interest in the synthesis of bioactive molecules derived from the pyrimidine moiety,^{15,31–33} our investigation aimed to synthesize new cyclic and acyclic nucleosides using available cyclic and acyclic moieties, which will be coupled with pyrimidine base, hoping to increase their antiviral activities. The effective method of protection and deprotection will also be examined.

2. Experimental

2.1. Chemistry

All the reagents were purchased from Sigma-Aldrich and the solvents from Merck and were used without further purification. Melting points were measured on an Apotec apparatus and are uncorrected. NMR spectra were recorded on Bruker AMX400 and Bruker Current AV400 Data spectrometers (400 MHz for ¹H, 100.6 MHz for ¹³C). ESI mass spectra were determined with a Finnigan Thermo Quest MAT 95XL spectrometer and FAB high-resolu-

tion (HR) mass spectra with a VG Analytical 70-250S spectrometer using an MCA method and poly(ethylene glycol) as the support. The reactions were monitored by thin layer chromatography (TLC) using silica gel (60 F254) coated aluminium plates (Merck) which were visualized by UV irradiation (254 nm) and iodine vapours. Column chromatography was performed by using silica gel (60–120 mesh). All reactions were carried out under dry nitrogen. 6-(2,4-Dichlorophenoxy)methylpyrimidine-2,4-dione (**1**) was prepared according to our previous report.¹⁵

2.1.1. Preparation of Nucleosides **6**, **8**, **10**, **11**, **16**, **15**, **17** and **19**

A suspension of uracil derivative **1** (10 mmol) and ammonium sulphate (10 g) in HMDS (50 mL) was stirred and refluxed for 4 h. HMDS in excess was evaporated under reduced pressure to give bis(trimethylsilyl) compound **2**. A solution of acylated acyclic reagents (10 mmol): (2-acetoxyethoxy)methyl acetate (**3**), 2-(acetoxymethoxy)propane-1,3-diyl dibenzoate (**4**), benzyloxymethyl acetate (**5**), 2-acetoxy-5-(benzyloxymethyl)tetrahydrofuran-3,4-diyl dibenzoate (**12**), 5-chloro-2-((4-chlorobenzoyloxy)methyl)tetrahydrofuran-3-yl 4-chlorobenzoate (**13**) and 2-(acetoxymethyl)-6-bromotetrahydro-2H-pyran-3,4,5-triyl triacetate (**14**), in dry acetonitrile (30 mL) and tin(IV) chloride (2 mL) was individually added to the residue of **2** and stirred at –30 °C for 24 h. After addition of pyridine (4 mL) the mixture was filtered to remove inorganic materials. The filtrate was diluted with chloroform (40 mL). The organic layer was washed with a saturated solution of sodium hydrogen carbonate (50 mL), followed by a 1N solution of hydrochloric acid (50 mL), then brine (50 mL) and water successively, dried over anhydrous sodium sulfate and concentrated to dryness under reduced pressure. The resulting crude nucleosides **6**, **8**, **10**, **11**, **15**, **17** and **19** were separated by silica gel column chromatography (graduated mixture of ethyl acetate and petroleum ether, 9:1) as white solid.

2-((6-((2,4-Dichlorophenoxy)methyl)-2,4-dioxo-3,4-dihydropyrimidin-1(2H)-yl)methoxy)ethyl Acetate (6)

Yield 2.8 g (70%), m.p. 166–168 °C. ¹H NMR (DMSO-*d*₆, 400 MHz) δ 2.11 (s, 3H, COCH₃), 3.83, 4.42 (t, 4H, OCH₂CH₂O), 5.45 (s, 2H, CH₂ phenoxy), 5.62 (s, 2H, OCH₂N), 6.10 (s, 1H, CH uracil), 7.48–7.90 (m, 3H, Ar-H), 12.50 (br s, 1H, NH). ¹³C NMR (DMSO-*d*₆, 100 MHz) δ 20.9, 63.2, 65.1, 66.8, 72.1, 100.7, 115.9, 116.0, 122.9, 126.1, 128.6, 129.9, 151.5, 152.1, 162.7, 170.6. MS *m/z* = 402 [M–1]. Anal. Calcd for C₁₆H₁₆Cl₂N₂O₆: C, 47.66; H, 4.00; N, 6.95. Found: C, 47.81; H, 4.09; N, 6.79.

2-((6-((2,4-Dichlorophenoxy)methyl)-2,4-dioxo-3,4-dihydropyrimidin-1(2H)-yl)methoxy)propane-1,3-diyl Dibenzoate (8)

Yield 4.3 g (73%), m.p. 162–164 °C. ¹H NMR (DMSO-*d*₆, 400 MHz) δ 4.20–4.50 (m, 5H, 2CH₂, CH), 5.11 (s, 2H, CH₂ phenoxy), 5.41 (s, 2H, OCH₂N), 5.62 (s, 1H, CH uracil), 7.10–7.93 (m, 13H, Ar-H), 12.10 (br s, 1H, NH). ¹³C NMR (DMSO-*d*₆, 100 MHz) δ 64.1, 64.8, 71.3, 74.3, 100.6, 115.6, 122.8, 125.9, 128.4, 129.0, 129.5, 129.8, 133.8, 151.3, 151.7, 152.2, 162.5, 165.8. MS *m/z* = 599.2 [M⁺]. Anal. Calcd for C₂₉H₂₄Cl₂N₂O₈: C, 58.11; H, 4.04; N, 4.67. Found: C, 58.24; H, 4.13; N, 4.53.

1-(Benzyloxymethyl)-6-((2,4-dichlorophenoxy)methyl)pyrimidine-2,4(1H,3H)-dione (10)

Yield 2.8 g (69%), m.p. 114–116 °C. ¹H NMR (DMSO-*d*₆, 400 MHz): δ 4.62 (s, 2H, CH₂Ph), 5.25 (s, 2H, CH₂ phenoxy), 5.45 (s, 2H, OCH₂N), 5.81 (s, 1H, CH uracil), 7.28–7.81 (m, 8H, Ar-H), 12.01 (br s, 1H, NH). ¹³C NMR (DMSO-*d*₆, 100 MHz): δ 64.8, 70.3, 71.5, 100.6, 115.6, 122.6, 125.7, 127.0, 127.7, 128.1, 128.2, 129.5, 137.3, 150.9, 151.5, 151.6, 158.8. MS: *m/z* = 407.2 [M⁺]. Anal. Calcd for C₁₉H₁₆Cl₂N₂O₄: C, 56.04; H, 3.96; N, 6.88. Found: C, 56.11; H, 3.87; N, 6.97.

1,3-Bis(benzyloxymethyl)-6-((2,4-dichlorophenoxy)methyl)pyrimidine-2,4(1H,3H)-dione (11)

Yield 3 g (58%), m.p. 158–160 °C. ¹H NMR (DMSO-*d*₆, 400 MHz) δ 4.43, 4.45 (2 × s, 4H, 2 × CH₂Ph), 5.24 (s, 2H, CH₂ phenoxy), 5.34 (s, 2H, OCH₂-N¹), 5.46 (s, 2H, OCH₂-N³), 5.91 (s, 1H, CH uracil), 7.25–7.67 (m, 13H, Ar-H). ¹³C NMR (DMSO-*d*₆, 100 MHz) δ 65.1, 70.6, 71.4, 73.1, 100.2, 116.0, 122.9, 126.1, 127.7, 127.8, 128.1, 128.5, 128.6, 129.9, 137.7, 150.8, 152.2, 161.6. MS *m/z* = 527.3 [M⁺]. Anal. Calcd for C₂₇H₂₄Cl₂N₂O₅: C, 61.49; H, 4.59; N, 5.31. Found: C, 61.55; H, 4.51; N, 5.39.

2-(Benzoyloxymethyl)-5-(6-((2,4-dichlorophenoxy)methyl)-2,4-dioxo-3,4-dihydropyrimidin-1(2H)-yl)tetrahydrofuran-3,4-diyl Dibenzoate (15)

Yield 4.5 g (62%), m.p. 113–115 °C. ¹H NMR (DMSO-*d*₆, 400 MHz) δ 4.31–4.40 (m, 2H, H-5';5"), 4.51–4.60 (m, 1H, H-4'), 4.91 (s, 2H, CH₂ phenoxy), 5.71 (s, 1H, CH uracil), 5.90–6.11 (m, 2H, H-2'; H-3'), 6.40 (d, 1H, *J* = 9.10 Hz,

H-1'), 7.10–7.98 (m, 18H, Ar-H), 12.01 (br s, 1H, NH). ¹³C NMR (DMSO-*d*₆, 100 MHz) δ 63.7, 65.7, 70.7, 73.8, 78.2, 98.0, 115.7, 122.9, 125.9, 128.6, 128.8, 128.9, 129.1, 129.5, 129.6, 129.9, 133.7, 134.0, 134.2, 151.1, 152.2, 162.5, 164.9, 165.1, 165.8. MS *m/z* = 730 [M–1]. Anal. Calcd for C₃₇H₂₈Cl₂N₂O₁₀: C, 60.75; H, 3.86; N, 3.83. Found: C, 60.63; H, 3.94; N, 3.75.

(3-(4-Chlorobenzoyloxy)-5-(6-((2,4-dichlorophenoxy)methyl)-2,4-dioxo-3,4-dihydropyrimidin-1(2H)-yl)tetrahydrofuran-2-yl)methyl 4-Chlorobenzoate (17)

Yield 3.9 g (58%), m.p. 85–87 °C. ¹H NMR (DMSO-*d*₆, 400 MHz) δ 2.21–2.30 (m, 2H, H-2';2"), 4.81–4.25 (m, 2H, H-5';5"), 4.72 (m, 1H, H-4'), 4.90 (s, 2H, CH₂ phenoxy), 5.40 (m, 1H, H-3'), 5.61 (s, 1H, CH uracil), 6.51 (m, 1H, H-1'), 7.10–8.00 (m, 11H, Ar-H), 11.93 (br s, 1H, NH). ¹³C NMR (DMSO-*d*₆, 100 MHz) δ 66.4, 67.6, 74.9, 75.6, 79.5, 81.2, 82.3, 98.2, 102.9, 115.6, 128.5, 129.2, 129.8, 129.9, 130.6, 131.1, 131.4, 138.6, 150.4, 150.8, 151.1, 162.8, 163.0, 164.9. MS *m/z* = 678 [M–2]. Anal. Calcd for C₃₀H₂₂Cl₄N₂O₈: C, 52.96; H, 3.26; N, 4.12. Found: C, 52.87; H, 3.31; N, 4.20.

2-(Acetoxymethyl)-6-(6-((2,4-dichlorophenoxy)methyl)-2,4-dioxo-3,4-dihydropyrimidin-1(2H)-yl)tetrahydro-2H-pyran-3,4,5-triyl Triacetate (19)

Yield 4.1 g (67%), m.p. 137–139 °C. ¹H NMR (DMSO-*d*₆, 400 MHz) δ 1.80–2.10 (4×s, 12H, 4 × COCH₃), 3.31 (m, 1H, H-5'), 4.18 (m, 2H, H-6';6"), 5.02 (m, 4H, H-3'; H-4';CH₂ phenoxy), 5.42 (dd, 1H, *J*_{1,2} = 9.50, *J*_{2,3} = 9.10 Hz, H-2'), 5.60 (s, 1H, CH uracil), 6.20 (d, 1H, *J*_{1,2} = 9.50 Hz, H-1'), 7.10–7.81 (m, 3H, Ar-H), 12.01 (br s, 1H, NH). ¹³C NMR (DMSO-*d*₆, 100 MHz) δ 15.5, 20.2, 20.5, 20.7, 62.0, 65.2, 67.9, 73.0, 77.8, 79.5, 96.6, 99.1, 115.7, 122.9, 125.9, 149.8, 151.7, 152.1, 162.1, 162.7, 169.3, 170.3. MS *m/z* = 617.3 [M⁺]. Anal. Calcd for C₂₅H₂₆Cl₂N₂O₁₂: C, 48.64; H, 4.24; N, 4.54. Found: C, 48.59; H, 4.31; N, 4.60.

2. 1. 2. General Procedure for the Preparation of Deprotected Nucleosides 7, 9, 16, 18 and 20

Each protected nucleoside was dissolved individually in methanol saturated with ammonia and stirred for two days at room temperature. Then the solution was concentrated to dryness and the residue recrystallized in methanol to give deprotected nucleosides 7, 9, 16, 18 and 20.

6-((2,4-Dichlorophenoxy)methyl)-1-((2-hydroxyethoxy)methyl)pyrimidine-2,4(1H,3H)-dione (7)

Yield 3 g (83%), m.p. 228–230 °C. ¹H NMR (DMSO-*d*₆, 400 MHz) δ 3.70, 3.76 (2 × t, 4H, HOCH₂CH₂O), 4.90 (br s, 1H, OH), 5.50 (s, 2H, CH₂ phenoxy), 5.56 (s, 2H, OCH₂N), 6.03 (s, 1H, CH uracil), 7.40–7.80 (m, 3H, Ar-H), 11.83 (br s, 1H, NH). ¹³C NMR (DMSO-*d*₆, 100 MHz) δ 60.3, 65.0, 70.7, 72.2, 100.5, 116.0, 122.9, 126.0, 128.6, 129.9, 151.9, 162.7. MS *m/z* = 360 [M–1]. Anal. Calcd for C₁₄H₁₄Cl₂N₂O₅: C, 46.56; H, 3.91; N, 7.76. Found: C, 46.62; H, 3.83; N, 7.84.

6-((2,4-Dichlorophenoxy)methyl)-1-((1,3-dihydroxypropan-2-yloxy)methyl)pyrimidine-2,4(1H,3H)-dione (9)

Yield 3.2 g (84%), m.p. 190–192 °C. ¹H NMR (DMSO-*d*₆, 400 MHz) δ 3.40–3.58 (m, 5H, 2CH₂, CH), 4.53 (m, 2H, OH), 5.33 (s, 2H, CH₂ phenoxy), 5.42 (s, 2H, OCH₂N), 5.69 (s, 1H, CH uracil), 7.31–7.64 (m, 3H, Ar-H), 12.10 (br s, 1H, NH). ¹³C NMR (DMSO-*d*₆, 100 MHz) δ 61.0, 65.1, 70.2, 80.6, 110.1, 115.4, 116.0, 122.8, 125.9, 128.6, 129.8, 151.9, 152.0, 152.2, 163.2. MS *m/z* = 390 [M–1]. Anal. Calcd for C₁₅H₁₆Cl₂N₂O₆: C, 46.05; H, 4.12; N, 7.16. Found: C, 46.14; H, 4.20; N, 7.09.

6-((2,4-Dichlorophenoxy)methyl)-1-(3,4-dihydroxy-5-(hydroxymethyl)tetrahydrofuran-2-yl)pyrimidine-2,4(1H,3H)-dione (16)

Yield 2.7 g (65%), m.p. 128–130 °C. ¹H NMR (DMSO-*d*₆, 400 MHz) δ 3.40–3.44 (m, 2H, H-5',5''), 3.58–3.60 (m, 1H, H-4'), 3.70–3.85 (m, 1H, H-3'), 4.10–4.25 (m, 1H, H-2'), 4.15 (d, 1H, OH), 4.60 (d, 1H, OH), 4.90 (s, 2H, CH₂ phenoxy), 5.13 (m, 1H, OH), 5.72 (s, 1H, CH uracil), 6.08 (d, 1H, *J* = 7.75 Hz, H-1'), 7.20–7.62 (m, 3H, Ar-H), 11.91 (br s, 1H, NH). ¹³C NMR (DMSO-*d*₆, 100 MHz) δ 62.6, 65.7, 70.52, 71.1, 84.7, 87.7, 98.0, 115.6, 122.9, 125.8, 128.5, 129.0, 133.7, 150.6, 152.2. MS *m/z* = 421.1 [M+2]. Anal. Calcd for C₁₆H₁₆Cl₂N₂O₇: C, 45.84; H, 3.85; N, 6.68. Found: C, 45.92; H, 3.93; N, 6.76.

6-((2,4-Dichlorophenoxy)methyl)-1-(4-hydroxy-5-(hydroxymethyl)tetrahydrofuran-2-yl)pyrimidine-2,4(1H,3H)-dione (18)

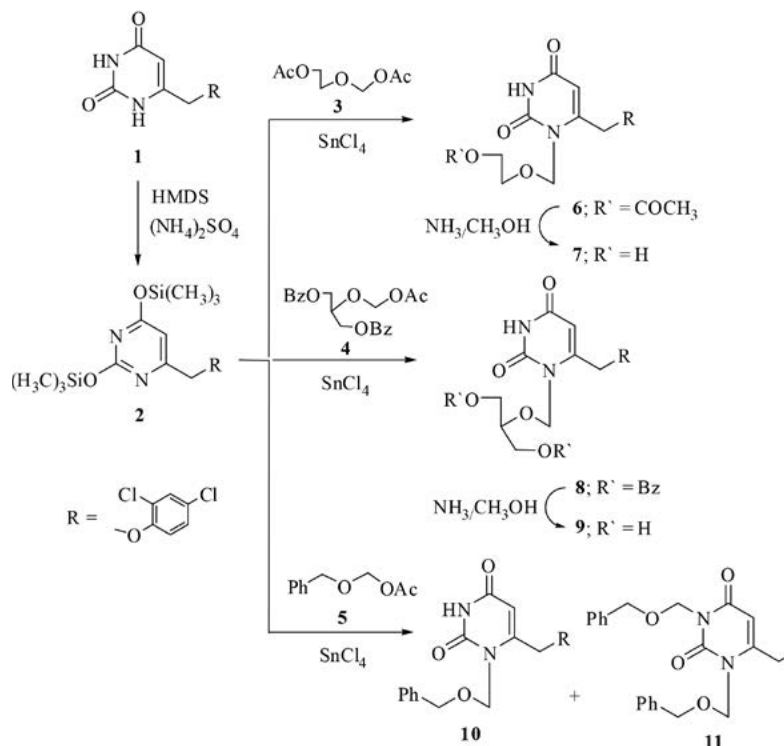
Yield 2.8 g (69.7%), m.p. 195–197 °C. ¹H NMR (DMSO-*d*₆, 400 MHz) δ 2.15–2.21 (m, 2H, H-2',2''), 3.22–3.31 (m, 2H, H-5',5''), 3.81 (br s, 2H, 2 × OH), 4.50 (m, 1H, H-3'), 4.80 (s, 2H, CH₂ phenoxy), 5.08 (m, 1H, H-4'), 5.40 (s, 1H, CH uracil), 5.51 (m, 1H, H-1'), 7.06–7.70 (m, 3H, Ar-H), 12.10 (br s, 1H, NH). ¹³C NMR (DMSO-*d*₆, 100 MHz) δ 61.7, 65.6, 71.5, 81.1, 86.0, 87.7, 98.3, 115.6, 122.9, 125.8, 128.6, 129.9, 150.1, 151.1, 152.2, 163.1. MS *m/z* = 405.2 [M+2]. Anal. Calcd for C₁₆H₁₆Cl₂N₂O₆: C, 47.66; H, 4.00; N, 6.95. Found: C, 47.59; H, 4.05; N, 6.87.

6-((2,4-Dichlorophenoxy)methyl)-1-(3,4,5-trihydroxy-6-(hydroxymethyl)tetrahydro-2H-pyran-2-yl)pyrimidine-2,4(1H,3H)-dione (20)

Yield 2.5 g (55.7 %), m.p. 214–216 °C. ¹H NMR (DMSO-*d*₆, 400 MHz) δ 2.80–2.90 (m, 1H, H-3'), 3.19–3.45 (m, 4H, H-4', H-5', H-6',6''), 4.10 (dd, 1H, *J*_{1,2} = 9.95 Hz, *J*_{2,3} = 9.15 Hz, H-2'), 4.10 (m, 4H, 4 × OH), 4.71 (s, 2H, CH₂ phenoxy), 5.30 (d, 1H, *J* = 9.95 Hz, H-1'), 5.55 (s, 1H, CH uracil), 7.02–7.55 (m, 3H, Ar-H), 8.20 (br s, 1H, NH). ¹³C NMR (DMSO-*d*₆, 100 MHz) δ 61.4, 65.8, 68.4, 70.4, 78.3, 81.2, 83.3, 96.9, 99.1, 115.6, 122.8, 125.7, 128.6, 129.8, 152.2, 163.7, 166.5. MS *m/z* = 451.1 [M+2]. Anal. Calcd for C₁₇H₁₈Cl₂N₂O₈: C, 45.45; H, 4.04; N, 6.24. Found: C, 45.51; H, 4.09; N, 6.17.

3. Results and Discussion

Our strategy to design and synthesize pyrimidine nucleoside analogues was based on the alkylation of si-



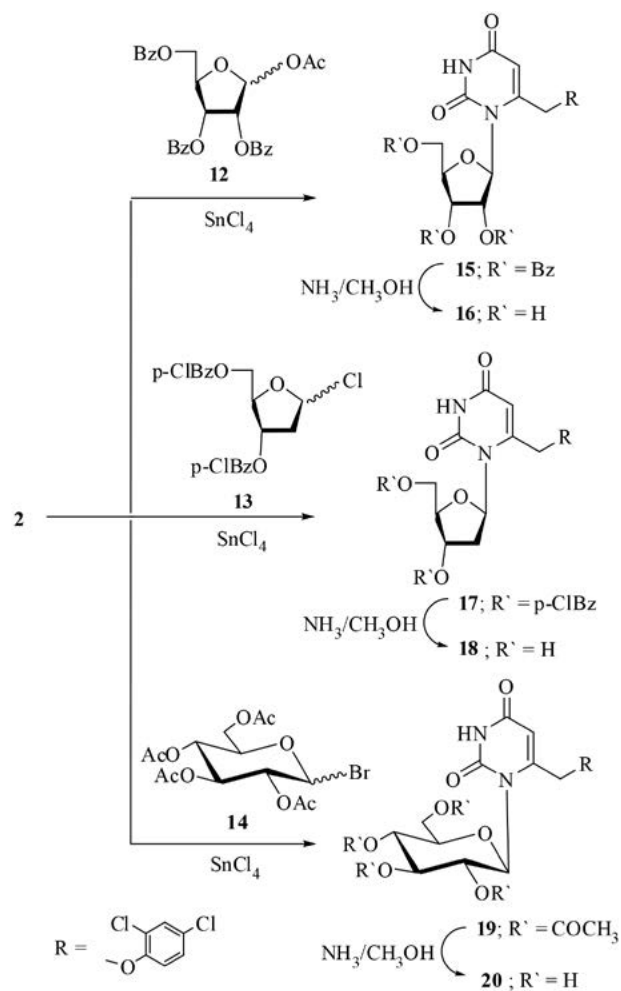
Scheme 1. Synthesis of acyclic nucleoside analogues containing pyrimidine moiety 6–11

lylated pyrimidine following Vorbrüggen and Niedballa's procedure.^{33–35} The intermediate, bis(trimethylsilyl) **2**, was prepared by the silylation of 6-(2,4-dichlorophenoxy)methyl)pyrimidine-2,4-dione (**1**) using hexamethyldisilazane (HMDS) and subjected to react with different acyclic sugar analogues, namely (2-acetoxyethoxy)methyl acetate (**3**), 2-(acetoxymethoxy)propane-1,3-diol dibenzoate (**4**) and benzyloxymethyl acetate (**5**) to afford the corresponding protected nucleosides analogues **6**, **8** and **10**, **11**, respectively (Scheme 1).

Structures of new acyclic nucleoside analogues were fully characterized by analytical and spectral methods (¹H NMR, ¹³C NMR, and elemental analysis). The ¹H NMR showed the disappearance of –NH proton which was detected in the parent compound **1** and instead a new signal appeared at the range δ 5.34–5.62 ppm characteristic for (–OCH₂N) indicative for the acyclic nucleosides formation. It is interesting to note that the reaction of **2** with benzyloxymethyl acetate (**5**) afforded two products **10** and **11**. ¹H NMR showed the disappearance of the two –NH protons of **1** and two new signals appeared at 5.34 and 5.46 ppm at-

tributed to (–OCH₂N¹ and –OCH₂N³), supporting the formation of **11** via double alkylation of **2** (cf. Experimental).

Deprotection of compounds **6** and **8** was achieved by cleavage of the ester blocking group with methanolic ammonia solution to give compounds **7** and **9** in fair to moderate yield, respectively (cf. Experimental). In the continuation of our study, compound **1** was reacted with various activated cyclic sugars, namely 2-acetoxy-5-(benzyloxymethyl)tetrahydrofuran-3,4-diyl dibenzoate (**12**), 5-chloro-2-((4-chlorobenzoyloxy)methyl)tetrahydrofuran-3-yl 4-chlorobenzoate (**13**) and 2-(acetoxymethyl)-6-bromotetrahydro-2*H*-pyran-3,4,5-triyl triacetate (**14**) under the same procedure as previously, giving the protected nucleosides **15**, **17** and **19** as β -anomers. ¹H NMR showed a doublet signal at δ 6.20–6.51 ppm corresponding to the anomeric proton of the sugar moiety with the spin-spin coupling constant ($J_{1,2} = 9.10$ – 9.50 Hz) which can be attributed to the diaxial orientation of H-1 and H-2 protons indicating the presence of β -configuration. Compounds **15**, **17**, and **19** were deprotected by using methanolic ammonia solution at room temperature to give compounds **16**, **18**, and **20**, respectively (Scheme 2).



Scheme 1. Synthesis of acyclic nucleoside analogues containing pyrimidine moiety **6–11**

4. Conclusions

A series of cyclic and acyclic nucleosides were prepared with moderate yields by alkylation of 6-(2,4-dichlorophenoxy)methyl)pyrimidine-2,4-dione with various acyclic and cyclic activated sugars by performing Vorbrüggen and Niedballa's procedure. Deprotection of the synthesized nucleosides was achieved by using methanolic ammonia solution.

5. Acknowledgments

The authors acknowledge Professor Chris Meier and Innovative Research Team in State Key laboratory of Organic Chemistry, Hamburg University, for their help during performing this work.

6. References

1. E. De Clercq, A. Holý, *Nat. Rev. Drug Discovery*. **2005**, *4*, 928–240. DOI:10.1038/nrd1877
2. D. F. Ewing, V. Glaçon, G. Mackenzie, C. Len, *Tetrahedron Lett.* **2002**, *43*, 989–991. DOI:10.1016/S0040-4039(01)02298-5
3. D. Pansuriya, K. Menpara, N. Kachhadiya, J. Menpara, K. Ladva, *J. Appl. Chem.* **2014**, *3*, 2335–2342.
4. R. C. Elderfield, *Heterocyclic compounds*, John Wiley & Sons, Inc., New York, **1957**, Vol. 6, p 744. DOI:10.1002/jps.3030460623
5. A. E. Porter, *Diazines and benzodiazines* (Netherlands: Pre-gamon Press, Elsevier Science) BV 6. Amsterdam, 1979, p.14.

6. C. O. Kappe, *Tetrahedron*. **1993**, *49*, 6937–7168.
DOI:10.1016/S0040-4020(01)87971-07
7. A. L. S. Rodrigues, J. M. Rosa, V. M. Gadotti, *Pharmacol., Biochem. Behav.* **2005**, *82*, 156–162.
DOI:10.1016/j.pbb.2005.08.003
8. J. S. Bradley, R. Guidos, S. Baragona, *Lancet Infect. Dis.* **2007**, *7*, 68–78. DOI:10.1016/S1473-3099(06)70689-2
9. N. M. Thumar, A. A. Kaneria, M. Vadodaria, K. Ladva, *Int. Lett. Chem. Phys. Astron.* **2016**, *65*, 11–26.
DOI:10.18052/www.scipress.com/ILCPA.65.11
10. H. P. Schweizer, *Microbiology Lett.* **2001**, *202*, 1–7.
DOI:10.1111/j.1574-6968.2001.tb10772.x
11. K. Poole, *J. App. Microbiol.* **2002**, *92*, 55–64S.
DOI:10.1046/j.1365-2672.92.5s1.8.x
12. K. Poole, *J. Pharm. Pharmacol.* **2001**, *53*, 283–294.
DOI:10.1211/0022357011775514
13. P. W. Taylor, P. D. Stapleton, J. P. Luzio, *Drug Discov. Today*. **2002**, *7*, 1086–1091.
DOI:10.1016/S1359-6446(02)02498-4
14. Y. Ju, D. Kumar, R. S. Varma, *J. Org. Chem.* **2006**, *71*, 6697–6700. DOI:10.1021/jo061114h
15. M. F. El Shehry, J. Balzarini, C. Meier, *Synthesis*. **2009**, *5*, 841–847. DOI:10.1055/s-0028-1083369
16. Y. Ju, R. S. Varma, *J. Org. Chem.* **2006**, *71*, 135–141.
DOI:10.1021/jo051878h
17. C. A. Zificsak, D. J. Hlasta, *Tetrahedron*. **2004**, *60*, 8991–9016.
DOI:10.1016/j.tet.2004.07.016
18. T. Haino, M. Tanaka, K. Ideta, K. Kubo, A. Mori, Y. Fukazawa, *Tetrahedron Lett.* **2004**, *45*, 2277–2279.
DOI:10.1016/j.tetlet.2004.01.116
19. A. Manlove, M. P. Groziak, *J. Heterocycl. Chem.* **2009**, *21*, 375–414. DOI:10.1016/S0959-6380(9)70040-6
20. R. Singh, A. Chouhan, *World J. Pharm. Pharm. Sci.* **2014**, *3*, 574–597.
21. M. Hassan, D. van der Lelie, D. Springael, U. Römling, N. Ahmed, M. Mergeay, *Gene*. **1999**, *238*, 417–425.
DOI:10.1016/S0378-1119(99)00349-2
22. D. M. Livermore, *Intensive Care Med.* **2000**, *26*, S14–21.
DOI:10.1007/s001340051113
23. L. Jeu, F. J. Piacenti, A. G. Lyakhovetskiy, H. B. Fung, *Voriconazole. Clin. Ther.* **2003**, *25*, 1321–1381.
DOI:10.1016/S0149-2918(03)80126-1
24. P. D. Lokhande, B. Y. Waghmare, S. S. Sakate, *Indian J. Chem. Sect. B.* **2005**, *44*, 2338–2342.
25. G. J. Reddy, D. Manjula, K. S. Rao, M. Khalilullah, D. Latha, *Indian J. Chem. Sect. B.* **2005**, *44*, 2412–2415.
26. M. Garcia-Valverde, T. Torroba, *Molecules*. **2005**, *10*, 318–320.
DOI:10.3390/10020318
27. D. W. Hopper, A. L. Crombie, J. J. Clemens, S. Kwon, *Prog. Heterocycl. Chem.* **2009**, *21*, 330–374.
DOI:10.1016/j.pbb.2005.08.003
28. J. Tani, Y. Yamada, T. Oino, T. Ochiai, R. Ishida, I. Inoue, *J. Med. Chem.* **1979**, *22*, 95–99. DOI:10.1021/jm00187a021
29. B. Kumar, B. Kaur, J. Kaur, A. Parmar, R. D. Anand, H. Kumar, *Indian J. Chem. Sect. B.* **2002**, *41*, 1526–1530.
DOI:10.1155/2014/202784
30. S. V. Dinakaran, B. Bomma, K. K. Spinivasan, *Pharm. Chem.* **2012**, *4*, 255–265.
31. M. A. Abu-Zaied, E. M. El-Telbani, G. H. Elgemeie, G. A. M. Nawwar, *Eur. J. Med. Chem.* **2011**, *46*, 229–235.
DOI:10.1016/j.ejmech.2010.11.008
32. M. F. El Shehry, R. H. Swellem, S. M. Abu-Bakr, E. M. El-Telbani, *Eur. J. Med. Chem.* **2010**, *45*, 4783–4787.
DOI:10.1016/j.ejmech.2010.07.043
33. E. M. El-Telbani, S. M. Ghanem, F. A. El Essawy, A. F. El-Sayed, *Lett. Drug. Des. Discov.* **2011**, *8*, 822–829.
DOI:10.2174/1570180811108090822
34. U. Niedballa, H. Vorbrüggen, *J. Org. Chem.* **1974**, *39*, 3654–3660. DOI:10.1021/jo00939a008
35. U. Niedballa, H. Vorbrüggen, *J. Org. Chem.* **1976**, *41*, 2084–2086. DOI:10.1021/jo00874a002
36. H. Vorbrüggen, K. Kroliekiewicz, B. Bennua, *Chem. Ber.* **1981**, *114*, 1234–1255. DOI:10.1002/cber.19811140404

Povzetek

V članku predstavljamo priročno metodo za pripravo cikličnih in acikličnih nukleozidov s pomočjo alkiliranja 6-(2,4-diklorofenoksimetil)pirimidin-2,4-diona (**1**) s širokim izborom acikličnih in cikličnih aktiviranih analogov sladkorjev: (2-acetoksi)metil acetat (**3**), 2-(acetoksimetoksi)propan-1,3-diil dibenzoat (**4**), benziloksimetil acetat (**5**), 2-acetoksi-5-(benziloksimetil)tetrahidrofuran-3,4-diil dibenzoat (**12**), 5-kloro-2-((4-klorobenzoiloksi)metil)tetrahidrofuran-3-il 4-klorobenzoat (**13**) in 2-(acetoksimetil)-6-bromotetrahidro-2H-piran-3,4,5-triil triacetat (**14**). Odstranitev zaščitne skupine iz tako pripravljenih nukleozidov smo dosegli z uporabo amonijaka v metanolu. Nove nukleozide, ki smo jih na ta načini sintetizirali, smo tudi karakterizirali z analitskimi metodami (masna spektrometrija, ¹H NMR, ¹³C NMR in elementna analiza).

Scientific paper

Investigation of High-Activity Activated Carbon-Supported Co-Cr-B Catalyst in the Generation of Hydrogen from Hydrolysis of Sodium Borohydride

Orhan Baytar

Siirt University, Faculty of Engineering and Architecture, Department of Chemical Engineering, Siirt, 56100, Turkey

* Corresponding author: E-mail: orhanbaytar@siirt.edu.tr

Received: 28-12-2017

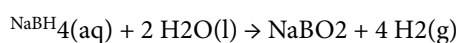
Abstract

In this study, activated carbon-supported Co-Cr-B catalyst was synthesized by chemical impregnation and precipitation method for use in the catalytic hydrolysis of sodium borohydride (NaBH₄). The activity of Co-Cr-B / activated carbon (5–20%) obtained by using different ratios was investigated while synthesizing activated carbon-supported Co-Cr-B catalyst. The effects of some parameters such as NaOH Concentration (0–5%), NaBH₄ concentration (2.5–10%), amount of catalyst (25–100 mg) and solution ambient temperature were investigated in the catalytic hydrolysis of NaBH₄. The hydrogen production rate of Co-Cr-B catalyst without support in hydrolysis of NaBH₄ was found as 6.5 Lg⁻¹ min⁻¹ catalyst while the hydrogen production rate of activated carbon supported Co-Cr-B catalyst was found as 30.2 Lg⁻¹ min⁻¹ catalyst. In presence of activated carbon-supported Co-Cr-B catalyst, the hydrolysis kinetic order and activation energy of NaBH₄ were found as 0.126 and 16.27 kJ/mol, respectively. The results suggest that activated carbon-supported Co-Cr-B catalysts can be used for mobile applications of Proton exchange membrane fuel cell (PEMFCs) systems.

Keywords: Activated carbon; catalyst; Co-Cr-B; NaBH₄

1. Introduction

Depletion of existing fossil fuels, global warming and environmental pollution are increasing demands for a clean and sustainable energy system.¹ Hydrogen can be considered as energy for the future due to clean and zero emission.² Therefore, a safe and practical hydrogen production system is required. Production, storage and consumption of hydrogen are very difficult due to its flammability and storage problem. Therefore, an aqueous solution of metal hydride stabilized can be considered as a suitable material for hydrogen storage.³ Metal hydrides are compounds such as NaBH₄, NaH, CaH₂, MgH₂, Li-AlH₂. Among these metal hydrides, NaBH₄ has some advantages such as high hydrogen storage capacity (10.8%), high stability and non-flammability at high pH, optimum control over the rate of hydrogen production with supported catalysts, acceptable hydrogen production rate even at low temperatures, ease of use and availability.^{4–5} The hydrolysis of NaBH₄ with water is indicated the following reaction.⁶



Self-hydrolysis of NaBH₄ does not occur at high pH values. Therefore, hydrolysis of NaBH₄ takes place in the presence of suitable catalyst. In other words, to be able to perform the hydrolysis of sodium borohydride in a suitable catalyst surface. Many catalysts such as Co-B-P6, Co-W-B7, Co-Cu-B8, Ce0.05-Ni-W9, carbon nanotube supported Co-B10 and carbon supported Ru₃ are used for hydrolysis of NaBH₄.

The activity of the catalyst is directly related to the particle size and surface area, since the catalyst having small particle size and high surface area is in more contact with the reactant. Therefore, higher amounts of catalyst are required to significantly increase the reaction rate. Hence, some materials with high surface area are used as support material.¹¹ Activated carbon,¹¹ carbon,³ Al₂O₃¹² and Pd-TiO₂⁴ can be used as support materials. Activated carbon is more advantageous than other support materials due to its porous, high surface area and functional groups in its structure.¹³ The activated carbon is synthesized by physical or chemical activation method. Physical activation is the process of activation of the raw material at high temperature with a gas such as water vapor or CO₂. Chemical activation is the synthesis process using activators such as

KOH, ZnCl₂, H₃PO₄.¹⁴ The activated carbon is synthesized from raw materials such as pistachio shell,¹⁴ acorn shell,¹⁵ eleagnus angustifolia,¹⁶ carob bean seed husk.¹⁷

In our previous study, activated carbon was synthesized from the eleagnus seed by physical activation method using a mixture of CO₂ and water vapor. In this current study, the synthesized activated carbon was used as support material for the Co-Cr-B catalyst to be used for the hydrolysis of sodium borohydride.¹⁸ The experimental conditions for the NaBH₄ hydrolysis of the synthesized activated carbon supported Co-Cr-B catalyst were optimized. It was found that the activated carbon-supported Co-Cr-B catalyst has high activity in the hydrolysis of NaBH₄.

2. Experimental Part

2.1. Materials

All the chemical substances used in the experiments are in analytical grade purity and have not been subjected to any purification process. In our previous work,¹⁸ the production and properties of activated carbon were given and the BET surface area was determined as 1084 m²/g. NaBH₄ from Merk, CoCl₂ · 6H₂O and CrCl₃ · 6H₂O from Alpha Aesar and ethanol (C₂H₅OH, > 99.9%) from Sigma-Aldrich, were purchased. Pure water was used in our experiments.

2.2. Synthesis of Activated Carbon

The procedure followed for the synthesis of activated carbon is given below. Approximately 10 g of milled spindle core was subjected to physical activation for 60 minutes at 900 °C in the presence of a mixture of CO₂ and water vapor. The activated material cooled to room temperature was first washed with 500 mL of 0.5 M HCl, then

with hot deionized water until the pH of the solution reached 6-6.5. The obtained activated carbon was used as support material for the Co-Cr-B catalyst.

2.3. Preparation of Catalyst

Activated carbon supported Co-Cr-B catalyst was prepared by chemical impregnation and reduction method. The production scheme of the catalyst is given in Figure 1. Catalyst preparation procedure; A certain amount of CoCl₂ · 6H₂O and CrCl₃ · 6H₂O were dissolved in 50 ml of ethanol, then the required amount of activated carbon was added and the metals were adsorbed to activated carbon at room temperature for 24 hours. The ethanol in the medium was then removed at 50 °C and 50 ml of distilled water was added to the metal-impregnated activated carbon, then left in the ice bath. The 50 ml of the NaBH₄ solution, prepared to be 5 times the total metal moles, was added dropwise to the metal impregnated activated carbon in the presence of N₂ gas. The resulting catalyst was filtered and washed several times with distilled water and anhydrous ethanol. The synthesized catalyst was dried in a nitrogen atmosphere at 80 °C for 6 hours. The obtained catalyst was maintained in a closed vessel in a nitrogen atmosphere to use in the hydrolysis of NaBH₄.

2.4. Characterization of Catalyst

Characterization of synthesized activated carbon-supported Co-Cr-B catalyst, Co-Cr-B catalyst and activated carbon was performed with BET surface area, XRD, FTIR and SEM-EDX measurements. Nitrogen adsorption-desorption of BET surface area at 77 K was determined by Quantachrome Nova 1200 series instrument. The structural properties was studied by x-ray diffraction

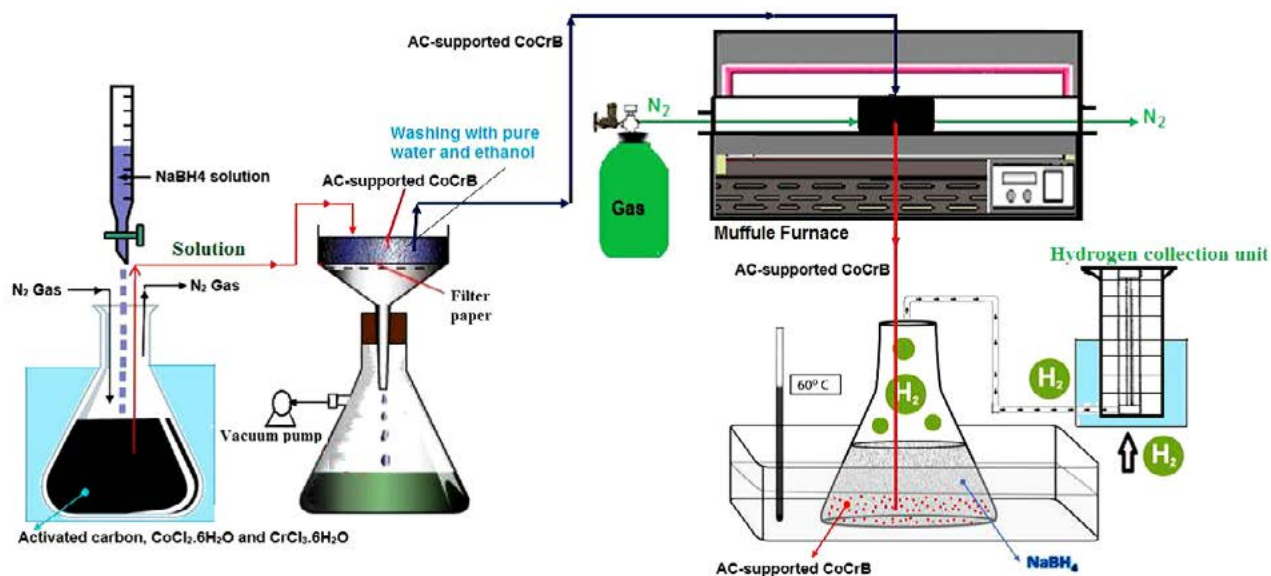


Figure 1: Application steps for production of activated carbon supported Co-Cr-B catalyst and for hydrolysis of NaBH₄.

(XRD) on a Rigaku x-ray diffractometer with Cu K α ($\lambda = 154.059$ pm) radiation. The functional groups of the synthesized materials were determined with a Bruker Vertex 70 FT-IR instrument in the range of 4000–400 cm^{-1} wave number. The surface morphology of the synthesized materials was determined by scanning electron microscopy (SEM) and the percentages were determined by EDX.

2. 5. Determination of Catalyst Activity

The activity of synthesized activated carbon-supported Co-Cr-B catalysts for the hydrolysis of NaBH_4 was determined using the system given in Figure 1. Experimental studies in which catalyst activity was determined,

were carried out in 10 ml of solution containing 2.5–10% NaBH_4 , 0–5% NaOH and 25–100 mg of activated carbon supported Co-Cr-B (5–20% Co-Cr-B catalyst loaded). The temperature was changed between 20 and 60 $^\circ\text{C}$. The released hydrogen was noted cumulatively by time.

3. Results and Discussions

3. 1. SEM and EDX Analysis

The SEM and EDX results of activated carbon, activated carbon supported Co-Cr-B catalyst (15% Co-Cr-B loaded) and Co-Cr-B catalyst used as support materials are shown in Figure 2.

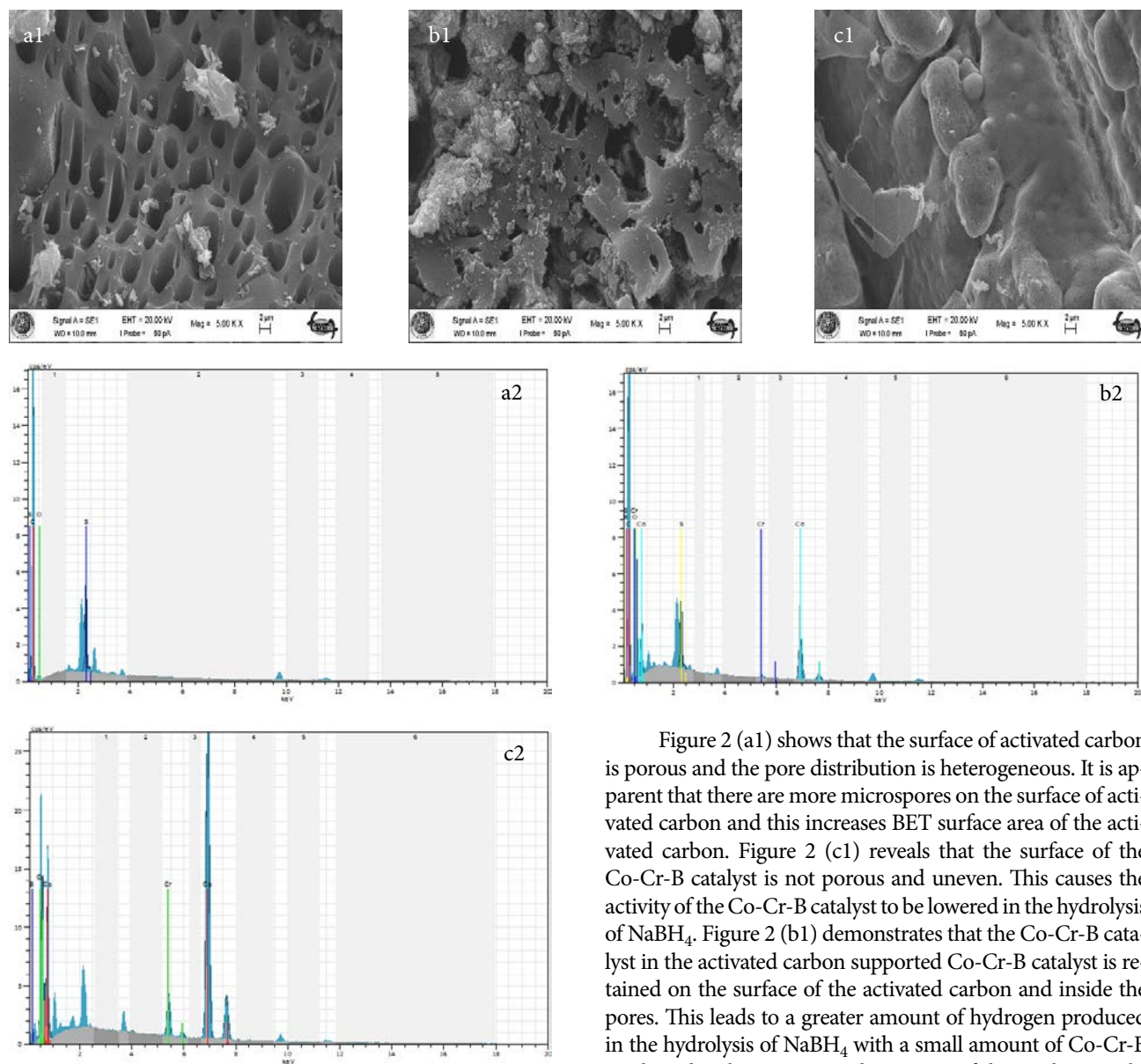


Figure 2: SEM and EDX results; **a1 and a2)** activated carbon, **b1 and b2)** activated carbon-supported Co-Cr-B catalyst, **c1 and c2)** Co-Cr-B catalyst.

Figure 2 (a1) shows that the surface of activated carbon is porous and the pore distribution is heterogeneous. It is apparent that there are more microspores on the surface of activated carbon and this increases BET surface area of the activated carbon. Figure 2 (c1) reveals that the surface of the Co-Cr-B catalyst is not porous and uneven. This causes the activity of the Co-Cr-B catalyst to be lowered in the hydrolysis of NaBH_4 . Figure 2 (b1) demonstrates that the Co-Cr-B catalyst in the activated carbon supported Co-Cr-B catalyst is retained on the surface of the activated carbon and inside the pores. This leads to a greater amount of hydrogen produced in the hydrolysis of NaBH_4 with a small amount of Co-Cr-B catalyst, thereby increasing the activity of the catalyst. Looking at the EDX results, it appears that the Co-Cr-B catalyst is present on the surface of the activated carbon.

3. 2. XRD Analysis

The structure properties of activated carbon, activated carbon supported Co-Cr-B catalyst (15% Co-Cr-B loaded) and Co-Cr-B catalyst were determined by XRD and the obtained results are displayed in Figure 3a, Figure 3b and Figure 3c, respectively.

As can be seen from Figure 3 (a), the characteristic peak of the carbon was observed between $2\theta = 20\text{--}25^\circ$. Zhu et al.¹ found the same results in their study of the synthesis of car-

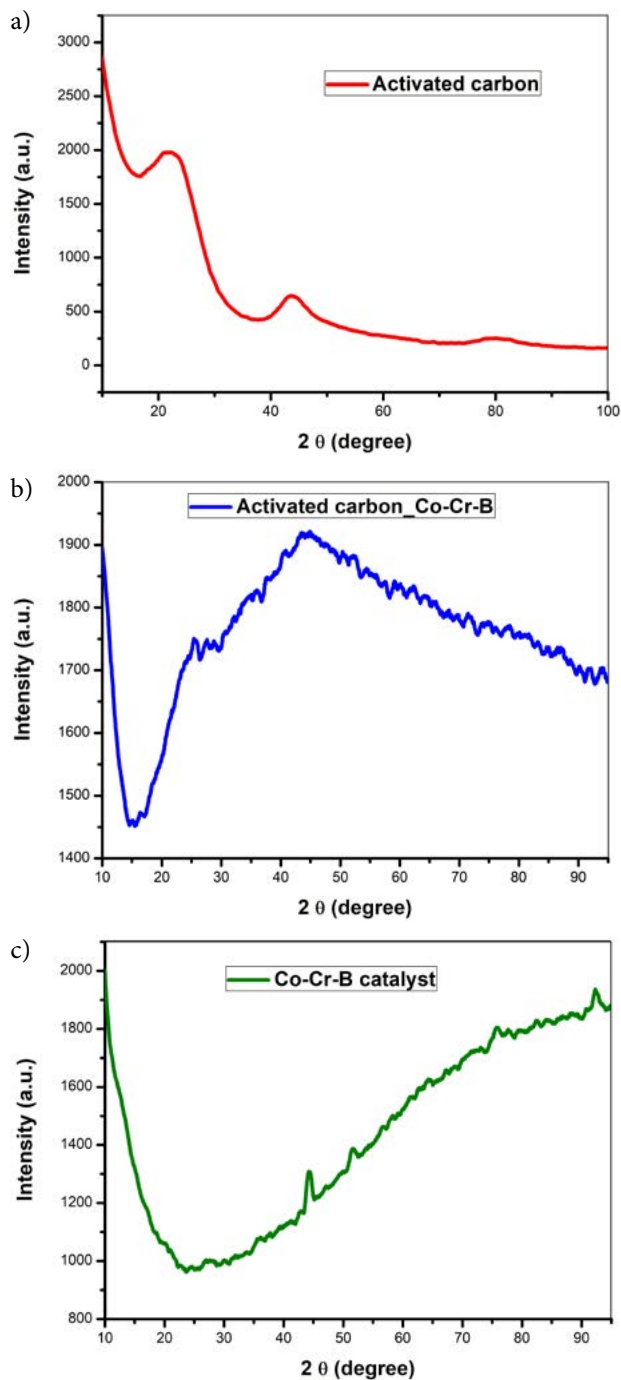


Figure 3: XRD results of a) activated carbon, b) activated carbon supported Co-Cr-B catalyst (15% Co-Cr-B loaded), c) Co-Cr-B catalyst.

bon-supported CoB catalysts. Fernandes et al.²³ reported that the Co-Cr-B catalyst gives a peak at $2\theta = 45^\circ$. A peak at $2\theta = 45^\circ$, is shown in Figure 3 (b-c), also was observed. It is seen that the XRD results are in agreement with the EDX results.

3. 3. FTIR Analysis

The FT-IR spectra of the activated carbon, activated carbon supported Co-Cr-B catalyst (15% Co-Cr-B loaded)

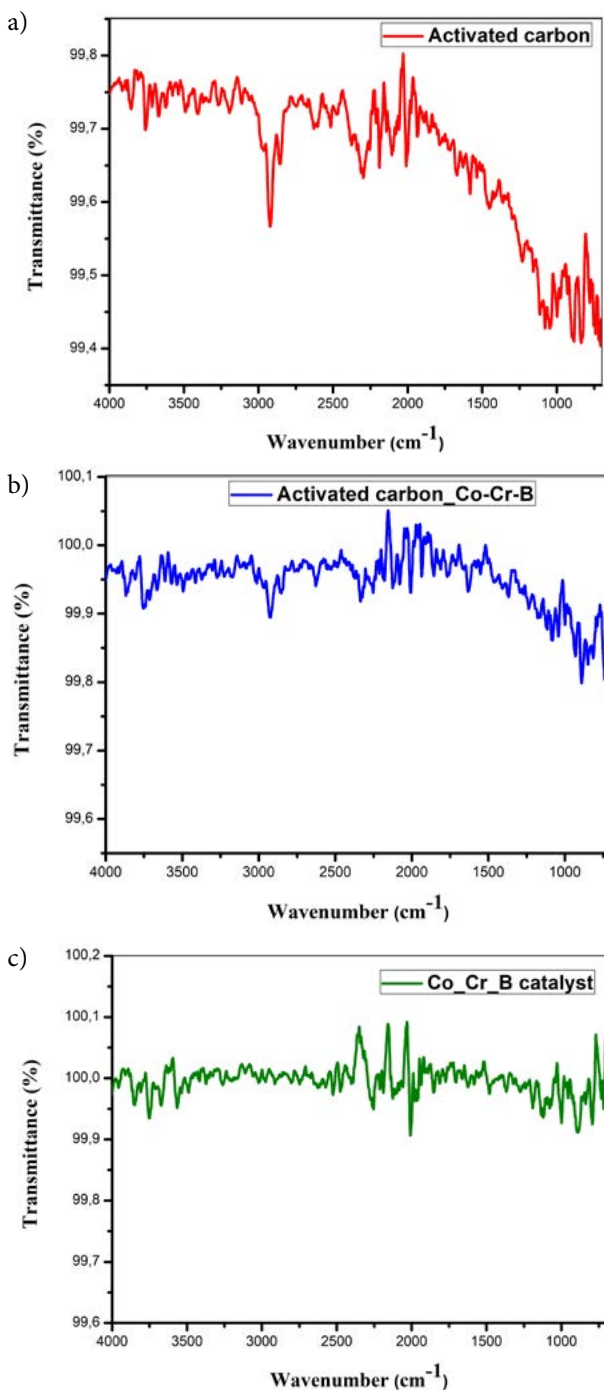


Figure 4: FTIR Results; a) activated carbon b) activated carbon-supported Co-Cr-B catalyst c) Co-Cr-B catalyst.

and Co-Cr-B catalyst are shown in Figure 4a, Figure 4b and Figure 4c, respectively.

As can be seen from Figure 4 (a), the activated carbon structure used as support material has; a peak at 3700 cm^{-1} due to hydroxyl (OH^-) functional groups bound by hydrogen bonds, a peak at 2900 cm^{-1} is related to the functional groups of CH originating from methyl or methylene groups, a peak at 2380 cm^{-1} is associated with the $-\text{C}=\text{C}$ functional groups, a peak at 2100 cm^{-1} is related to the $-\text{COOH}$ functional groups and a peak at 1400 cm^{-1} gives the $-\text{C}-\text{CH}_3$ functional groups. Figure 4 (b) reveals that after the Co-Cr-B catalyst is adsorbed on the activated carbon surface, some functional groups are weakened and others are becoming more visible. It is seen that the peak of OH^- at 3700 cm^{-1} and the peak of $-\text{C}-\text{H}$ at 2900 cm^{-1} in activated carbon structure shown in Figure (3b) are weakened. A large peak at 700 cm^{-1} was observed. The probable cause of this peak formation is due to the newly formed bond between the Co-Cr-B catalyst and activated carbon. BET surface areas of activated carbon, activated carbon supported Co-Cr-B catalyst (loaded with 15% Co-Cr-B) and Co-Cr-B catalyst used as support materials are given in Table 1.

Table 1: BET surface area results

Samples	BET surface area (m^2/g)
Activated carbon	1084
Activated carbon supported Co-Cr-B catalyst	666
Co-Cr-B catalyst	219

As can be seen from Table 1, the surface area of the activated carbon is observed to decrease very seriously by the adsorption of the Co-Cr-B catalyst. The probable cause of this situation is the placement of the Co-Cr-B catalyst in the activated carbon pores, as seen in the SEM images. The BET surface area for Co-Cr-B catalyst was obtained as $219\text{ m}^2/\text{g}$ and this value is the same with result reported by Fernande et al.²³.

3. 4. Effect of the Ratio Between Metal and Activated Carbon

Effect of Co-Cr-B catalyst / activated carbon ratio (5–20% Co-Cr-B loaded) was investigated in the presence of $2.5\% \text{ NaBH}_4 + 2\% \text{ NaOH}$ at $30\text{ }^\circ\text{C}$ and 100 mg of catalyst in 10 ml of the solution. The change in the rate of hydrogen with % Co-Cr-B is given in Figure 5a.

Figure 5a displays that the hydrogen production rate of Co-Cr-B catalyst produced without support in NaBH_4 hydrolysis is $6.5\text{ L g}^{-1}\text{ min}^{-1}\text{ catalyst}$ while the hydrogen production rate of 15% Co-Cr-B loaded on the activated carbon catalyst is $30.226\text{ L g}^{-1}\text{ min}^{-1}\text{ catalyst}$. This is probably due to the increase in the surface area of the Co-Cr-B cat-

alyst with activated carbon and the increase in active sites on the surface of the activated carbon. Baydaroglu et al.¹⁹ found that hydrogen production rate is $21.540\text{ L g}^{-1}\text{ min}^{-1}\text{ catalyst}$ using carbon black supported CoB catalysts while it is $5.670\text{ L g}^{-1}\text{ min}^{-1}\text{ catalyst}$ using an unsupported CoB catalysts. It can be seen from Figure 5 that the rate of hydrogen production increases as the Co-Cr-B / activated carbon percentage increases from 5% to 15% and the rate of hydrogen production decreases after the maximum value reaches 15%. The probable cause of this situation is that as the amount of Co-Cr-B increases, there are multilayers of catalyst layers on the surface of activated carbon and in the pores.

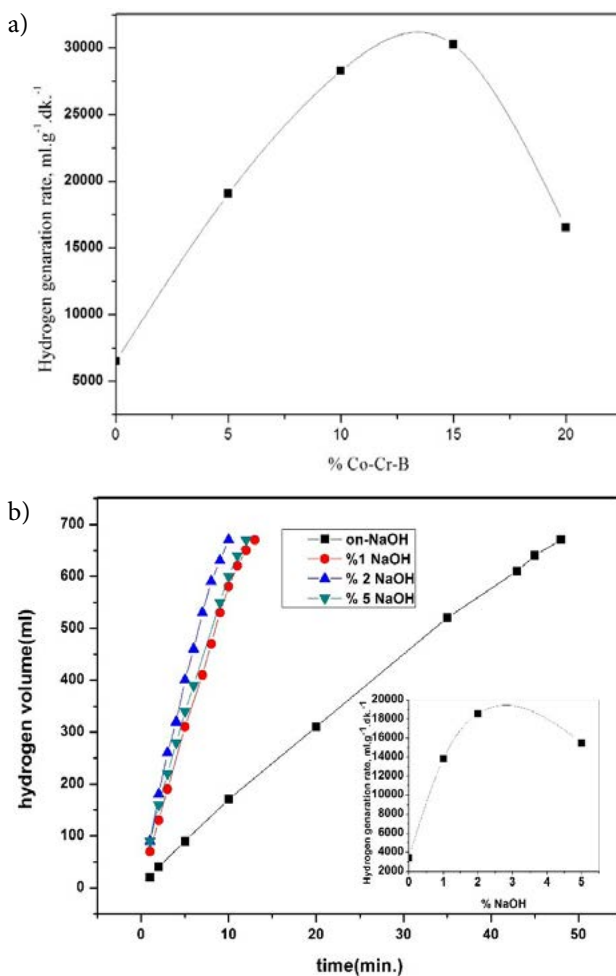


Figure 5: a) Change of hydrogen production rate by the amount of Co-Cr-B loaded on the activated carbon. b) Graph of the change in hydrogen content over time for different NaOH concentrations (V: 10 mL, 2.5% NaBH_4 , 100 mg of catalyst, $30\text{ }^\circ\text{C}$).

3. 5. Effect of NaOH

Since aqueous solutions of NaBH_4 are not hydrolyzed at high pH values, NaOH is used to increase the pH value of the solution. In this part of the study, the effect of 10 ml of solution of 2.5% NaBH_4 , 100 mg (loaded with

15% Co-Cr-B) activated carbon supported catalyst and different NaOH concentrations at 30 °C on the hydrolysis of NaBH₄ was investigated. The volume of hydrogen produced over time at different NaOH concentrations is given in Figure 5b.

As can be seen from Figure 5b, when the concentration of NaOH is increased from 1% to 2%, the rate of hydrogen production is increased whereas when the concentration of NaOH is more than 2%, the rate of hydrogen production is decreased. The probable cause of this behavior is that there are two different effects of OH ions in catalytic hydrolysis reactions. The first of these is the increase in the contact between NaBH₄ and the catalyst that results in increased electrostatic interaction between the activated carbon and the Co-Cr-B catalyst in the reaction solution medium at low NaOH concentrations. Hence, when the NaOH concentration is increased from 1% to 2%, the hydrogen production rate rises. The second is that OH⁻ (more than 2%) ions present in the medium in excess have an inhibitory effect on NaBH₄ hydrolysis. Another possible cause of this situation is that NaOH, which is present in excess in the solution medium, reduces the aqueous solubility of NaBO₂, a by-product of hydrolysis of NaBH₄. Therefore, NaBO₂ in solution will collapse and block the active sites of the catalyst, thereby reducing the hydrogen production rate. Kaya et al.²⁰ found that the NaBO₂ metastatic area narrows with increasing solution pH in the study of NaBO₂ metastatic region. That is, if the concentration of NaOH is high, it accelerates NaBO₂ precipitation. Ye et al.¹² used Al₂O₃-supported CoB catalysts for hydrolysis of NaBH₄ in the presence of different NaOH concentrations and found the same results. The optimum concentration of NaOH for hydrolysis of NaBH₄ was determined as 2% and all subsequent runs were performed at a NaOH concentration of 2%.

3. 6. Effect of Concentration of NaBH₄

Hydrolysis of NaBH₄ is not only dependent on catalyst activity but also on factors such as NaBH₄ concentration, NaOH concentration and temperature. NaBH₄ hydrolysis was investigated at different concentrations in a 10 ml solution medium with 2% NaOH concentration, 100 mg activated carbon supported Co-Cr-B catalyst (loaded with 15% Co-Cr-B) and 30 °C temperature. The time-eluted hydrogen volume at different NaBH₄ concentrations is given in Figure 6a. Hydrogen initial production rates versus different concentrations of NaBH₄ is also given on the same figure.

As can be seen from Figure 6a, as the NaBH₄ concentration increases, the initial rate of hydrogen decreases. Especially, when the NaBH₄ concentration is 10%, there is a very serious decrease in the hydrogen production rate. The likely reason for this is that the solubility in water of the NaBO₂ which is by-product in the hydrolysis of NaBH₄,

is limited. Another reason for this is; The high concentrations of NaBH₄ and NaBO₂ presented in the medium increase the viscosity of the final solution, which slows the mass transfer to the catalyst surface from the NaBH₄ present in the solution medium. Xu et al.²¹ found the same conclusion in their work.

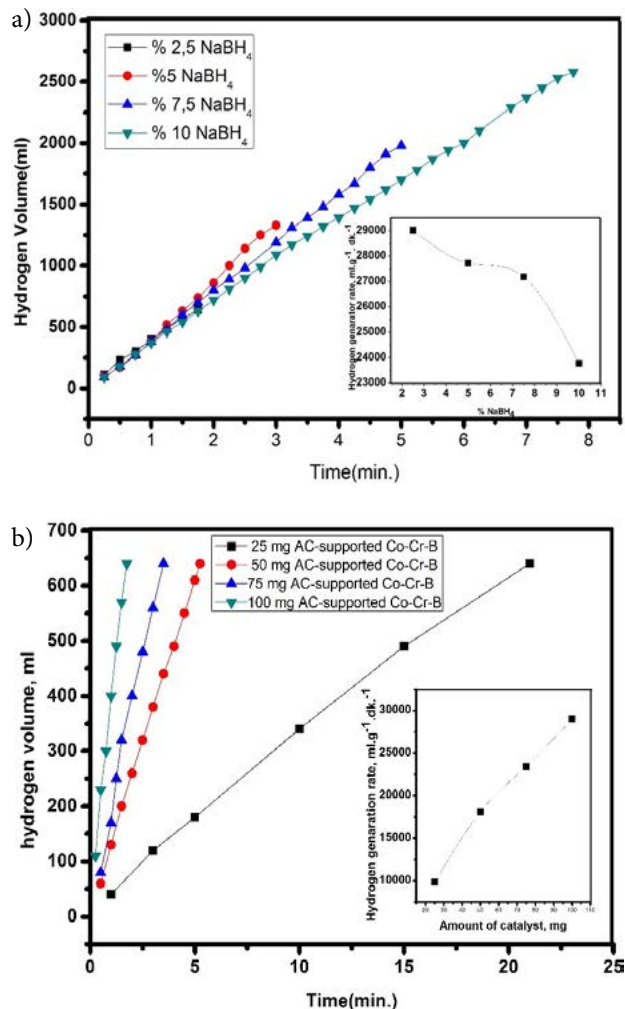


Figure 6: a) The graph of change in hydrogen content over time for different NaBH₄ concentrations (V: 10 mL, 2% NaOH, 100 mg of catalyst, 30 °C). b) The graph of change in hydrogen content with time for different amounts of catalyst (V: 10 ml; 2.5% NaBH₄; 2% NaOH; 30 °C).

3. 7. Effect of Amount of Catalyst

The hydrolysis of NaBH₄ was studied in 10 ml of solution at a concentration of 2.5% NaBH₄ + 2% NaOH, at 30 °C and in different amounts of catalyst. The volume of hydrogen produced with time for different amounts of catalyst is given in Figure 6b.

As shown in the Figure 6b, as the amount of catalyst increases, the hydrogen rate also increases. This suggests that the hydrolysis of NaBH₄ is catalyst-controlled.

3. 8. Effect of Solution Temperature

The effect of the temperature on the hydrolysis of NaBH₄ was investigated. The change in hydrogen volume of produced hydrogen at different temperatures is given in Figure 7a.

As can be seen from Figure 7a, there is a significant increase in the volume of hydrogen obtained in the hydrolysis of NaBH₄ as the temperature increases. 2.5% NaBH₄ hydrolysis takes place in 13 minutes at 20 °C, 1.75 minutes at 30 °C and 1 minute at 60 °C.

One of the most fundamental reasons for measuring the reaction time of any reaction at different temperatures is determining the reaction rate constant and determining the activation energy required for the reaction to take place accordingly. For this reason, first of all, a n-th reaction was used to determine the rate constants at different temperatures and the reaction rate constant for this reaction was determined by the equation given below.

$$\frac{1}{n-1} \left(\frac{1}{c_A^{n-1}} - \frac{1}{c_{A_0}^{n-1}} \right) = kt \quad (1)$$

Equation 2 was obtained if Equation 1 was set.

$$\frac{1}{c_A^{n-1}} = (n-1)kt + \frac{1}{c_{A_0}^{n-1}} \quad (2)$$

According to Equation 2, the slope of $\frac{1}{c_A^{n-1}}$ versus t gives the reaction rate constant (k) for different temperatures.

However, when this equation was applied, the n values were selected in that form, until the regression coefficient was close to 1. After the most suitable n value was determined, k was obtained from the slope of the obtained curve. In this procedure, the graph of $\frac{1}{c_{NaBH_4}^{n-1}}$ versus t is given in Figure 7b.

As you can see in Figure 7b, the selected n values in all temperatures are consistent and linear. Within the

above procedure, the optimum order of rate was found as 0.126. The rate constants at different temperatures are given in Table 2. Activation energy was determined by arhenius equation using these rate constants at different temperatures.

Table 2: The rate constants for different temperatures.

Temperatures (°C)	Rate constants, k (ml g ⁻¹ min ⁻¹ catalyst)	Order
20	0.0518	0.126
25	0.1157	0.126
30	0.4217	0.126
40	0.4919	0.126
50	0.6038	0.126
60	0.7619	0.126

$$k = Ae^{\frac{-E}{RT}} \quad (3)$$

When Equation 3 was linearized, Equation 4 was obtained.

$$\ln(k) = \ln A - \frac{E}{RT} \quad (4)$$

According to Equation 4, when the slope of the graph of lnk versus 1/T (is shown in Figure 8) was used, the activation energy required for the hydrolysis of NaBH₄ in the presence of activated carbon-supported Co-Cr-B catalyst was found as 16.27 kJ/mol. This value is very low and indicates that the activity of the catalyst is very high. The hydrogen production rate of activated carbon-supported Co-Cr-B catalyst in 2.5 ml of NaBH₄ hydrolysis in 10 ml of solution at 30 °C was determined as 30.266 L g⁻¹ min⁻¹ catalyst and the comparison with literature is given in Table 3.

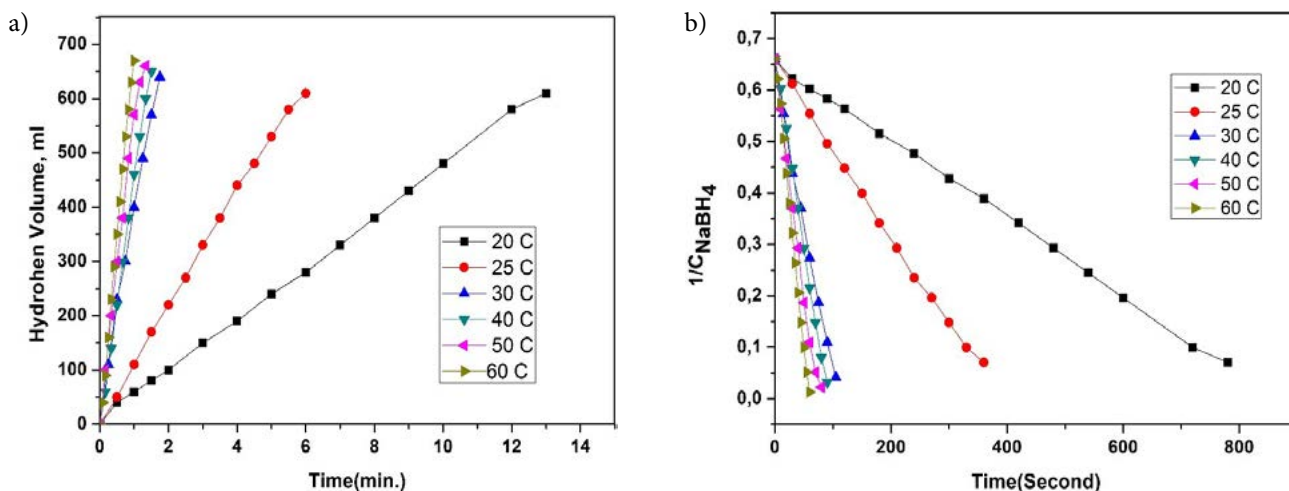
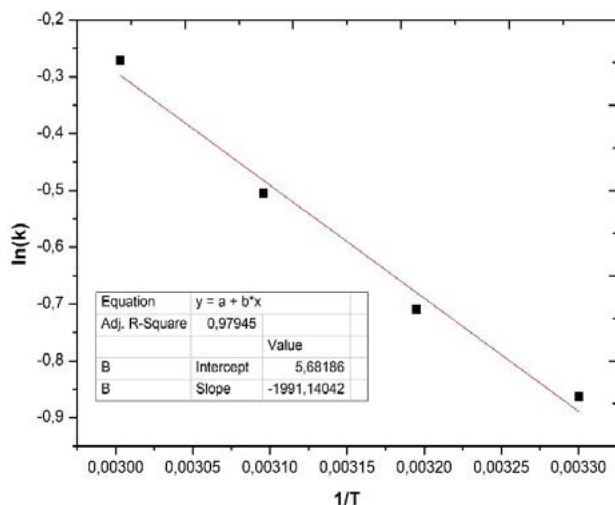


Figure 7: a) The graph of change in hydrogen content with time for different temperatures (V: 10 ml; 2.5% NaBH₄; 2% NaOH; 100 mg of catalyst). b) The graph of 1/C versus t for different temperatures.

Table 3: Hydrogen production rates and activation energies of different catalysts for hydrolysis of NaBH₄ in the literature.

Catalyst	Hydrogen production rate (L g ⁻¹ min. ⁻¹ _{catalyst})	Activation energ, E(kj/mol)	Reference
Carbon supported CoB	2.073	57,8	1
Carbon supported CoB		44,1	21
Clay supported CoB	3.350	56,32	22
Co-Cr-B	3.400	37	23
Reduced Co-Cr-B in plasma medium	1.416	16.17	24
Activated carbon supported Co-Cr-B	30.226	16.27	This study

**Figure 8:** The graph of ln (k) versus 1/T.

4. Conclusions

In this study, activated carbon supported Co-Cr-B catalyst was prepared to use in the hydrolysis of NaBH₄. The hydrogen production rate of synthesized activated carbon-supported Co-Cr-B catalyst was found as 30.226 L g⁻¹ min⁻¹_{catalyst} while the hydrogen production rate unsupported Co-Cr-B catalyst was found as 6.490 L g⁻¹ min⁻¹_{catalyst}. It was determined that the activity of the Co-Cr-B catalyst on the activated carbon surface increases approximately 5-fold. The effect of activated carbon ratio, NaOH concentration, NaBH₄ concentration, catalyst amount and temperature on the activated carbon-supported Co-Cr-B catalyst for the hydrolysis of NaBH₄ was investigated. It was determined that the hydrogen production rate of the 15% Co-Cr-B loaded catalyst was the best when the NaOH concentration was 2%. The increase in the concentration of NaBH₄ reduced the production rate of hydrogen while the increase in the amount of catalyst increased the hydrogen production rate. It was determined that the production rate of hydrogen significantly increased with increasing temperature. The inhibition of hydrolysis kinetic of NaBH₄ and the activation energy in the presence of activated carbon-supported Co-Cr-B catalyst were found to as 0.126 and 16.27 kJ/mol, respectively. According to the re-

sults obtained, activated carbon-supported Co-Cr-B catalyst NaBH₄ can be used in PEMFC mobile systems.

5. References

- J. Zhu, R. Li, W. Niu, Y. Wu, Gou X, *J. Power. Sources*, **2012**, *211*, 33. DOI:10.1016/j.jpowsour.2012.03.051
- W. Luo, P.G. Campbell, L.N. Zakharov, Liu S, *J. Am. Chem. Soc.* **2011**, *133*(48), 19326–19329. DOI:10.1021/ja208834v
- C. Crisafulli, S. Scire`, R. Zito, C. Bongiorno, *Catalysis Letters*, **2012**, *142*, 882–888. DOI:10.1007/s10562-012-0844-y
- M. Rakap, E.E. Kalu, S. Özkar, *Journal of Alloys and Compounds*, **2011**, *509*, 7016–7021. DOI:10.1016/j.jallcom.2011.04.023
- J. Lee, K. Y. Kong, C. R. Jung, E. Cho, S. P. Yoon, *Catalysis Today*, **2007**, *120*, 305–310. DOI:10.1016/j.cattod.2006.09.019
- Ö. Şahin, D. Karakas, M. Kaya, C. Saka, *Journal of the Energy Institute*, **2016**, *90*, 1–10.
- A. Ekinci, Ö. Şahin, C. Saka, T. Avci, *Int. J. Hydrog. Energy*, **2013**, *38*, 15295–15301. DOI:10.1016/j.ijhydene.2013.09.098
- M. S. Izgi, Ö. Şahin, C. Saka, *Int. J. Hydrog. Energy*, **2016**, *41*, 1600–1608. DOI:10.1016/j.ijhydene.2015.11.004
- C. Saka, A. Ekinci, Ö. Şahin, A. Balbay, *Journal of the Energy Institute*, **2016**, *89*, 190–198. DOI:10.1016/j.joei.2015.02.004
- Y. Huang, Y. Wang, R. Zhao., P. K. Shen, Z. Wei, *Int. J. Hydrog. Energy*, **2008**, *33*, 7110–7115. DOI:10.1016/j.ijhydene.2008.09.046
- D. Xu, P. Dai, Q. Guo, X. Yue, *Int. J. Hydrog. Energy*, **2008**, *33*, 7371–7377. DOI:10.1016/j.ijhydene.2008.09.065
- W. Ye, H. Zhang, D. Xu, L. Ma, B. Yi *J. Power Sources*, **2007**, *164*, 544–548. DOI:10.1016/j.jpowsour.2006.09.114
- C. Saka, *Journal of Analytical and Applied Pyrolysis*, **2012**, *95*: 21–24. DOI:10.1016/j.jaap.2011.12.020
- H. Dolas, Ö. Şahin, C. Saka, H. Demir, *Chem. Eng. J.*, **2011**, *166*, 191–197. DOI:10.1016/j.cej.2010.10.061
- Ö. Şahin, C. Saka, *Bioresource Technology*, **2013**, *136*, 163–168. DOI:10.1016/j.biortech.2013.02.074
- Ö. Şahin, C. Saka, A. A. Ceyhan, O. Baytar, *Separation Science and Technology*, **2015**, *50*, 886–891. DOI:10.1080/01496395.2014.966204
- Ö. Şahin, C. Saka, A. A. Ceyhan, O. Baytar, *Energy Sources, Part A: Recovery Utilization And Environmental Effects*, **2016**, *38*, 1756–1762. DOI:10.1080/15567036.2014.956195

18. O. Baytar, Selçuk University Institute of Science, **2015**, 42.
19. F. Baydaroglu, E. Özdemir, A. Hasimoglu, *Int. J. Hydrog. Energy*, **2014**, 39, 1516–1522. DOI:10.1016/j.ijhydene.2013.04.111
20. M. Kaya, A. A. Ceyhan, Ö. Şahin, *Russian Journal of Physical Chemistry*, **2014**, 88, 402–408. DOI:10.1134/S0036024414030182
21. D. Xu, P. Dai, X. Liu, C. Cao, Q. Guo, *J. Power Sources*, **2008**, 182, 616–620. DOI:10.1016/j.jpowsour.2008.04.018
22. H. Tian, Q. Guo, D. Xu, *J. Power Sources*, **2010**, 195, 2136–2142. DOI:10.1016/j.jpowsour.2009.10.006
23. R. Fernandes, N. A. Patel, *Applied Catalysis B: Environmental*, **2009**, 92, 68–74. DOI:10.1016/j.apcatb.2009.07.019
24. F. Hansu, *Journal of the Energy Institute*, **2015**, 88, 266–274. DOI:10.1016/j.joei.2014.09.004

Povzetek

V tem prispevku smo raziskovali katalizator Co-Cr-B na aktiviranem ogljiku, ki smo ga sintetizirali z metodo kemične impregnacije in precipitacije in njegovo uporabo pri katalitski hidrolizi natrijevega borhidrida (NaBH_4). Material smo pripravili z različnimi razmerji Co-Cr-B / aktivnega oglja (5–20%). V procesu katalitske hidrolize NaBH_4 smo preučevali učinke nekaterih parametrov, kot so koncentracija NaOH (0–5%), koncentracija NaBH_4 (2,5–10%), količina katalizatorja (25–100 mg) in temperatura raztopine. Stopnja sproščenega vodika pri hidrolizi NaBH_4 z uporabo katalizatorja Co-Cr-B brez nosilca je bila $6,5 \text{ Lg}^{-1} \text{ min}^{-1}$, medtem ko je bila stopnja nastajanja vodika na katalizatorju Co-Cr-B na aktiviranem ogljiku $30,2 \text{ Lg}^{-1} \text{ min}^{-1}$. V prisotnosti katalizatorja Co-Cr-B na aktiviranem ogljiku, sta bili stopnja katalize in aktivacijska energija hidrolize NaBH_4 0,126 in 16,27 kJ/mol. Rezultati kažejo, da bi lahko katalizator Co-Cr-B na aktiviranem ogljiku uporabili za gorivne celice z membrano za izmenjavo protonov (PEMFC).

Scientific paper

Copper(II) Schiff Base Complexes with Catalyst Property: Experimental, Theoretical, Thermodynamic and Biological Studies

Sheida Esmailzadeh¹ and Elham Zarenezhad^{2,*}¹ Department of Chemistry, Darab branch, Islamic Azad University, Darab, I. R. Iran² Non-communicable Diseases Research Center, School of Medicine, Fasa University of Medical Sciences, Fasa, Iran

* Corresponding author: E-mail: el.zarenezhad.fums@gmail.com

Received: 02-01-2018

Abstract

Two novel copper(II) Schiff base complexes were synthesized and characterized by various physico-chemical and spectroscopic methods, revealing a distorted square planar geometry around the copper atom. The analytical data confirmed the 1:1 metal to ligand stoichiometry of the complexes. B3LYP/(LANL2DZ/6-311G**) density functional theory (DFT) were used to investigate structural and electronic properties of the synthesized compounds in gas phase. The computational results support the conclusion obtained by the experimental studies. Thermodynamic study of complex formation in solution was carried out spectrophotometrically at 25 °C. These compounds were also subjected to study *in vitro* antibacterial screening against some bacteria. Also, click reaction was investigated for its catalytic properties. The synthesized Schiff base copper complexes catalyzed 1,3-dipolar Huisgen cycloaddition of different functionalized β -azido alcohols and alkynes in the presence of ascorbic acid in a solution of THF/H₂O (2:1, V/V) at room temperature.

Keywords: Copper complex; catalytic activity; antibacterial screening; formation constant; DFT calculations

1. Introduction

Schiff bases are an important class of compounds in inorganic chemistry. Research on these compounds has expanded very rapidly over the time and covered several applicative domains. Schiff base ligands and their metal complexes have been employed in areas that include analytical and bioinorganic chemistry, non-linear optics, fluorescence studies, agricultural, pharmaceutical and chemical industries and materials chemistry.^{1–5} Beside the broad range of applications of Schiff base compounds in different field, the metal complexes of Schiff bases are widely used as homogeneous and heterogeneous catalyst in reaction.^{6–8} In recent years, the development of efficient new catalysts for several organic reactions like carbonylation, hydroformylation, reduction, oxidation, epoxidation, hydrolysis have received considerable attention as well as for the use as corrosion inhibitors.^{9–12} Among the transition metals, copper has proved to be particularly useful for catalytic applications. Schiff base copper complexes with various types of ligands have shown to possess effective catalytic ability.^{13–15}

Based on the above catalytic activity importance of Schiff base complexes and in continuation of our recent

work^{16–19} on the Schiff base complexes, in the current investigation, two copper(II) complexes with NNOS coordination sphere have been synthesized and characterized. Catalytic potential have also been explored. The coordination behaviors of the ligands and their complexes, molecular parameter, spectral properties, relative energy and molecular orbital diagrams of all synthesized compounds have been calculated and interpreted with density functional theory (DFT). The antibacterial properties of the compounds against selected kinds of bacteria were also screened and discussed. The thermodynamic parameters of 1:1 complex formation in DMF solvent were determined spectrophotometrically at 25 °C. Due of our interest in the chemistry of azole derivatives^{20–22} we report a new catalyst system based on Cu^{II} and ascorbic acid as reducing agent for regioselective 1,3-dipolar Huisgen cycloaddition reaction to access diverse 1,2,3-triazole cores. 1,2,3-Triazole moieties are attractive compounds in medicinal chemistry because of their wide range of applications including use as HIV protease inhibitors, as well as anticancer, anti-tuberculosis, antifungal and antibacterial agents.²³

2. Experimental

2.1. Instruments and Starting Materials

All chemicals were purchased from Fluka and Merck and were used without further purification. Solvents were purified by standard procedures and stored over 3 Å molecular sieves. Reactions were followed by TLC using SILG/UV 254 silica-gel plates. Column chromatography was performed on silica gel 60 (0.063–0.200 mm, 70–230 mesh; ASTM).

The electronic absorption spectra were measured on Perkin Elmer (LAMBDA 2) double beam spectrophotometer in the range of 250–700 nm in DMF solution at room temperature. The infrared spectra were determined by using KBr pressed disc method on a Shimadzu FTIR 8300 FT-IR spectrophotometer in the 4000–350 cm⁻¹ region. Melting points were recorded on open capillaries with electronic melting point and are uncorrected. The percentages of C, H, N and S in synthesized compounds were obtained with a Termo Finningan-Flash-1200 microanalysis instrument. Mass spectrum performed with Perkin Elmer R MU-6E instrument. The magnetic susceptibilities of the copper complexes were carried out on Sherwood scientific magnetic susceptibility balance calibrated with Hg-Co(NCS)₄. Diamagnetic corrections were calculated from Pascal's constants. Molar conductance values (1 × 10⁻³ M) in DMF solution were determined by means of a Jenway 4310 conductivity meter and a diptype cell with a platinized electrode at room temperature. ¹H and ¹³C NMR spectra were obtained using a Bruker Avance-DPX-400 spectrometer operating at 400/100 MHz, respectively.

2.2. Synthesis of the Ligand

Methyl 2-((1-aminopropan-2-yl)amino)cyclopent-1-enedithioate and two Schiff base ligands methyl 2-((1-((2-hydroxy-5-methoxybenzylidene)amino)propan-2-yl)amino)cyclopent-1-enecarbodithioate, H₂L¹, and methyl 2-((1-((2-hydroxy-5-nitrobenzylidene)amino)propan-2-yl)amino)cyclopent-1-enecarbodithioate, H₂L², were synthesized according to the previously published procedure.¹⁷

H₂L¹: Yield: 83%; m.p.: 152°C. ¹H NMR (δ, ppm, 400 MHz, CDCl₃): 1.39 (3H, d, Me), 1.74 (2H, m, H⁴), 2.56 (3H, s, SCH₃), 2.68–2.72 (4H, m, H^{3;5}), 3.52–3.55 (3H, m, H^{en}), 3.77 (3H, s, OCH₃), 6.73 (1H, s, H⁶), 6.86 (1H, d, H⁴), 7.24 (1H, d, H³), 8.28 (1H, s, CH=N), 12.37 (1H, br, NH) and 12.45 (1H, br, OH). MS Spectra: *m/z* (%) = 365 [M+H]⁺, 364 [M]⁺, 287, 186, 166, 150, 123, 97, 81, 57. Elemental Anal.: Found (Calc): C₁₈H₂₄N₂O₂S₂, C: 59.07 (59.31); H: 6.75 (6.64); N: 7.84 (7.69); S: 17.32 (17.59%).

H₂L²: Yield: 93%; m.p.: 152°C. ¹H NMR (δ, ppm, 400 MHz, CDCl₃): 1.43 (3H, d, Me), 1.79 (2H, m, H⁴), 2.55 (3H, s, SCH₃), 2.64 (2H, t, H³), 2.68 (2H, t, H⁵), 3.61–3.66 (3H, m, H^{en}), 6.99 (1H, d, H³), 8.20–8.23 (2H, m, H^{4,6}), 8.46 (1H, s, CH=N), 12.30 (1H, br, NH) and 14.06 (1H, br,

OH). MS Spectra: *m/z* (%) = 380 [M+H]⁺, 379 [M]⁺, 368, 257, 236, 121, 111, 83, 58. Elemental Anal.: Found (Calc): C₁₇H₂₁N₃O₃S₂, C: 53.98 (53.81); H: 5.41 (5.58); N: 11.03 (11.07); S: 16.71 (16.90%).

2.3. Synthesis of the Copper(II) Complexes

The Cu(II) Schiff base complexes were synthesized by the addition of 10 mL of ethanolic solution of Cu(II) acetate (1 mmol) dropwise to 10 mL methanol/chloroform (1:2 v:v) of Schiff base ligand (1 mmol) in a round bottom flask. The mixture was stirred on ice bath for 2–3h. The complex was filtered and washed several times with distilled water. The obtained brown complexes were dried at room temperature. The purity was checked by thin layer chromatography. In spite of all the efforts, single crystal of these complexes could not be crystallized.

[CuL¹]: Yield: 81%, m.p.: 209 °C. $\Lambda_M = (10^{-3}M, \text{ in DMF, } \text{ohm}^{-1} \text{ cm}^2 \text{ mol}^{-1})$: 8.26; μ_{eff} : 1.76. MS Spectra: *m/z* (%) = 426 [M]⁺, 369, 312, 284, 250, 239, 199, 184, 130, 85, 55. Elemental Anal.: Found (Calc): C₁₈H₂₂N₂O₂S₂Cu, C: 50.82 (50.74); H: 5.06 (5.20); N: 6.33 (6.58); S: 14.82 (15.05%).

[CuL²]: Yield: 96%, m.p.: 239 °C. $\Lambda_M = (10^{-3}M, \text{ in DMF, } \text{ohm}^{-1} \text{ cm}^2 \text{ mol}^{-1})$: 7.94. μ_{eff} : 1.75. MS Spectra: *m/z* (%) = 442 [M+H]⁺, 441 [M]⁺, 395, 380, 373, 290, 267, 159, 111, 69. Elemental Anal.: Found (Calc): C₁₇H₁₉N₃O₃S₂Cu, C: 46.02 (46.30); H: 4.35 (4.34); N: 9.77 (9.53); S: 14.62 (14.54%).

2.4. Catalytic Activity Interpretation

2.4.1. General Procedure for Synthesis of Propargyl aryl (2d, 2e)

For synthesis of propargyl aryl such as **2d**, **2e**^{24,25}, a mixture of phenol or 4-bromophenol (1 mmol), KOH (1.2 mmol) and propargyl bromide (1 mmol) in acetone (10 mL) was heated in a round-bottomed flask for 4 h (TLC control). The solvent was then evaporated and dried to afford (ethynyloxy methyl benzene) and (1-bromo-4-(ethynyloxy methyl benzene)) compounds which was used in the next step without further purification.

2.4.2. General Procedure for Catalytic Test

1 mmol of α -haloketone or alkyl halide, alkyne (1 mmol), sodium azide (1.1 mmol), and water (1 mL)/THF (9 mL) were stirred under reflux for the required time according to Table 3 in the presence of the catalyst (1 mol%). The progress of the reaction was monitored by TLC (*n*-hexane:ethyl acetate = 5:1), and after the completion of the reaction, the remaining suspension was dissolved in CHCl₃ (100 mL) and subsequently washed with water (2 × 100 mL). The organic layer was dried (Na₂SO₄) and evaporated. The crude product was purified by column chromatography on silica gel and eluted with proper solvents.

Characterization data of two new synthesized compounds (**4m**, **4n**) are described below.

(4m): 1-(4-bromophenyl)-2-(4-(phenoxyethyl)-1H-1,2,3-triazol-1-yl)ethanone

Column chromatography on silica gel (EtOAc/*n*-hexane = 2:1) afforded the product as a yellow product; yield: 89%. ¹H NMR (δ, ppm, 400 MHz, CDCl₃): 5.15 (2H, s, CH₂-N), 5.80 (2H, s, CH₂-O), 6.71–8.03 (11H, m, arom, H-triazole). ¹³C NMR (δ, ppm, 100 MHz, CDCl₃): 115.6, 127.1, 127.7, 128.2, 129.8, 131.3, 132.8, 133.7, 156.2, 166.7, 189.0. IR (KBr, cm⁻¹): 3069, 2860, 1725, 1341 (C=N), 1466, 1263. Elemental Anal.: Found (Calc): C₁₇H₁₄N₃O₂Br, C: 54.80 (54.86); H: 3.83 (3.79); N: 11.25 (11.29).

(4n): 2-(4-(phenoxyethyl)-1H-1,2,3-triazol-1-yl)-1-phenylethanone

Column chromatography on silica gel (EtOAc/*n*-hexane = 2:1) afforded the product as a yellow product; yield: 83%. ¹H NMR (δ, ppm, 400 MHz, CDCl₃): 5.15 (2H, s, CH₂-N), 5.80 (2H, s, CH₂-O), 6.80–7.93 (11H, m, arom, H-triazole). ¹³C NMR (δ, ppm, 100 MHz, CDCl₃): 54.4, 61.1, 112.4, 115.6, 124.9, 127.1, 128.2, 131.3, 132.8, 133.7, 156.3, 168.4, 189.0. IR (KBr, cm⁻¹): 3059, 2924, 1695, 1669, 1489, 1220. Elemental Anal.: Found (Calc): C₁₇H₁₅N₃O₂: C: 69.62 (69.61); H: 5.18 (5.16); N: 14.30 (14.33).

2. 5. Details of Calculations

The geometry optimization of the Schiff base ligands and their complexes were performed by using the gradient-corrected density functional theory (DFT) method with B3LYP functional.²⁶ All elements except Cu were assigned 6-311G** basis set.²⁷ LANL2DZ with effective core potential for Cu were used.²⁸ The IR frequencies were calculated at the same level of theory with the key word freq

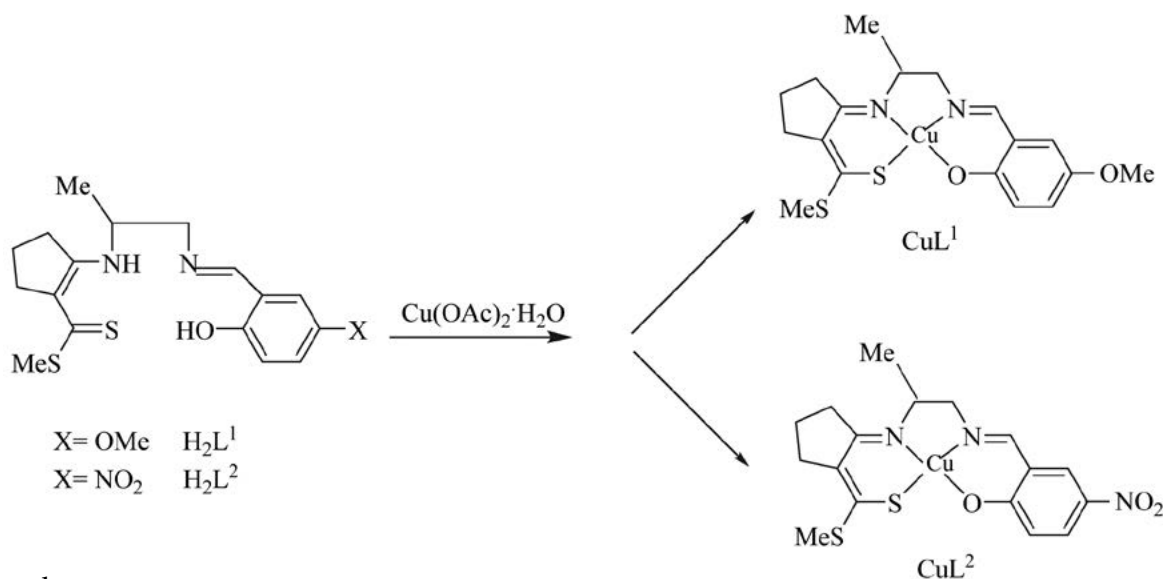
for the optimized structure in order to confirm structure minima without any imaginary. On the basis of calculations the structure properties, the relative stability, HOMO and LUMO energies and the chemical hardness, Mulliken atomic charges and UV data have been discussed in details. In addition, a comparison was made between the theoretical calculated IR and UV data and the experimental measured. The Gaussian 03 package²⁹ with the aid of the Gauss View was employed to obtain the optimized the structures and all the calculations.

2. 6. Antibacterial Assay

The antibacterial activity of the Schiff base ligands and their Cu^{II} complexes against different the bacterial species such as *Staphylococcus aureus* (Gram positive bacteria) and *Escherichia coli* (Gram negative bacteria) were determined by reported disk diffusion method^{30,31} using nutrient agar as the medium. Tetracycline was used as standard reference. The stock solution of test compounds were dissolved in dry dimethylsulfoxide (DMSO exhibited no antibacterial activity against the test bacterial pathogens) to get concentration of 1.00 mg/mL. 100 μL of test bacteria spore suspension was spread on nutrient agar plates. Appropriate well were impregnated be equal volume from the test solution of compounds and carefully placed on agar surface. The plates were incubated for 24 h at 37°C. The antibacterial activity was evaluated by measuring the clear zone surround of growth inhibition.

3. Result and Discussion

The chemical equations concerning the formation of the Schiff base complexes are schematically represented in Scheme 1.



Scheme 1

3. 1. Experimental Results

3. 1. 1. Spectral Properties

The elemental analysis, IR and UV-Vis data and the physical properties such as melting points, yields, magnetic susceptibility of the ligands and their complexes were presented in the experimental section and in Tables 1 and 2. These data showed that the complexes has stoichiometry of the type [ML] where M = Cu and L = Schiff base ligands. All synthesized compounds are stable at room temperature, but decompose on heating. All compounds are insoluble in water but they are readily soluble in DMF, acetonitrile, DMSO and partially soluble in ethanol. The measured molar conductance values in DMF are too low indicating their nonelectrolytic nature of complexes.^{5,32}

3. 1. 1. 1. The Characteristic IR Bands

The IR spectra of Schiff base ligands and their complexes were recorded and their comparative study provides meaningful information regarding the bonding sites of the ligands (see Table 1). The broad band at 3066 and 3413 cm^{-1} was assigned to the free $\nu(\text{OH})$ stretching modes in the spectra of Schiff ligands, but in their Cu(II) complexes this band were not observed, suggesting the chelation of the phenolic oxygen to the copper ion.³³ The band present in the region 2920–2951 cm^{-1} is elated to aliphatic and aromatic C–H stretching vibrations.³⁴ The ligands exhibit imine $\nu(\text{C}=\text{N})$ stretching around 1600 cm^{-1} . Actually, this strong absorption band was shifted to lower wave numbers (bathochromic shift) in the complexes, indicating the participation of azomethine nitrogen in binding with metal ion.^{35,36} The band observed at around 1440 cm^{-1} corresponds to the aromatic C=C stretching vibration.³⁷ Coordination of the Schiff base to the Cu(II) ion through the carbonyl oxygen atom is expected to decrease the electron density in the carbonyl group frequency. The band due to $\nu(\text{C}=\text{O})$ showed a modest decrease in the stretching frequency for the complexes and is shifted to lower frequencies after complexation, indicating the coordination of the carbonyl oxygen atom.³⁸ A medium to strong intensity band located at 1157, 783 and 1099, 752 cm^{-1} in the H_2L^1 and H_2L^2 ligands are attributed to the stretching mode of the $\nu(\text{CS}+\text{CN})$ and (C=S), respectively.

Table 2. Experimental electronic spectral data and their assignment of the compounds in DMF

Compounds	λ (nm)	Assignment
H_2L^1	314, 398	$\pi \rightarrow \pi^*$, $n \rightarrow \pi^*$
H_2L^2	313, 398	$\pi \rightarrow \pi^*$, $n \rightarrow \pi^*$
[CuL ¹]	328, 378	$\pi \rightarrow \pi^*$, LMCT
[CuL ²]	332, 370	$\pi \rightarrow \pi^*$, LMCT

These band was shifted to lower frequency after complexation, due to coordination with the sulfur atom of the C=S group for all the complexes.^{5,17,39} The assignments of bands in the far-IR region are useful as direct information about the metal-ligand coordination bond. The new weak intensity band in the spectra of the Cu^{II} complexes in the region 538–546 cm^{-1} and 443–459 cm^{-1} are attributed to $\nu(\text{Cu}-\text{O})$ and $\nu(\text{Cu}-\text{N})$ bonds, respectively.^{9,40,41} Furthermore, The IR spectra bands at 1332 and 1550 cm^{-1} observed in H_2L^2 compound are assigned to $\nu_s(\text{NO}_2)$, $\nu_{\text{as}}(\text{NO}_2)$ respectively, these absorption bands remained almost at the same position in the [CuL²] complex, indicating that nitro group is not involved in coordination.^{17,18}

3. 1. 1. 2. Electronic Spectra

The electronic spectra of the synthesized compounds were investigated in DMF solvent (1×10^{-4} M) at room temperature. This technique also confirmed the formation of the ligand and its metal complexes. The Schiff base ligands exhibit a relatively intense intraligand absorption bands. The first intense absorption peak is centered at 395 and 398 nm for H_2L^1 and H_2L^2 , respectively, and corresponds to the $n \rightarrow \pi^*$ transition of imine chromofore, while the last peak in high energy (316 for H_2L^1 and 313 nm for H_2L^2) is attributed to the $\pi \rightarrow \pi^*$ transition of the aromatic ring, respectively.^{8,42,43} (See Table 2).

After complexation, a red shift is observed for $\pi \rightarrow \pi^*$ transition. The $n \rightarrow \pi^*$ transition disappears in the spectrum of the complexes due to the coordination of the azomethine nitrogen atom (nitrogen lone pair donation) to the metal ion.^{33,44} The absorption maximum at 378 and 370 nm which could be assigned to ligand to metal charge

Table 1. Some selected experimental and computed IR vibrational modes (cm^{-1}) of the Schiff base ligands and their copper complexes

	compounds	$\nu(\text{Cu}-\text{N})$	(Cu–O)	$\nu(\text{C}=\text{S})$	$\nu(\text{C}-\text{S}+\text{C}-\text{N})$	$\nu(\text{C}-\text{O})$	$\nu(\text{C}=\text{C})$	$\nu(\text{C}=\text{N})$	$\nu(\text{C}-\text{H})$	$\nu(\text{O}-\text{H})$	$\nu(\text{NO}_2)$
Experimental frequencies	H_2L^1	–	–	783	1157	1276	1481	1635	2920	3413	–
	H_2L^2	–	–	752	1099	1266	1477	1649	2938	3066	1332, 1550
	[CuL ¹]	443	546	756	1145	1267	1461	1612	2947	–	–
	[CuL ²]	459	538	740	1090	1220	1453	1610	2951	–	1335,1548
Calculated frequencies	H_2L^1	–	–	730	–	1260	1468	1653	3041	3410	–
	H_2L^2	–	–	775	–	1283	1477	1668	2037	3455	1343, 1519
	[CuL ¹]	470	555	721	–	1277	1434	1636	3080	–	–
	[CuL ²]	472	581	743	–	1266	1460	1646	3102	–	1345,1540

transfer ($S \rightarrow Cu^{II}$ LMCT). The positions of these bands are similar to those observed for square planar copper(II) complexes.^{18,19,45}

3. 1. 1. 3. Mass Spectra Study of the Synthesized Compounds

The mass spectrum of the Schiff base ligands and their copper(II) complexes were recorded. This technique provided strong evidence for the formation of compounds. These spectra show a molecular ion peaks M^+ at m/z 364, 379, 426 and 441 which are in agreement with the empirical molecular formula $C_{18}H_{24}N_2O_2S_2$, $C_{17}H_{21}N_3O_3S_2$, $C_{18}H_{22}N_2O_2S_2Cu$ and $C_{17}H_{19}N_3O_3S_2Cu$, respectively, suggested from elemental analysis.

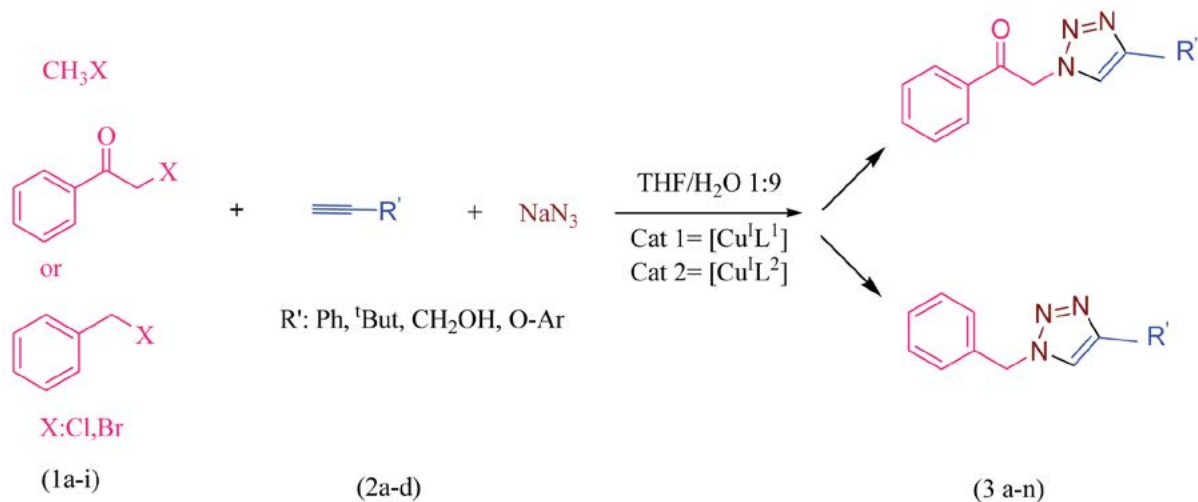
3. 1. 1. 4. Magnetic Susceptibility Measurement

Magnetic moment was measured at room temperature for the Cu^{II} complexes. The complexes show the magnetic moment values at 1.75 and 1.76 B.M. corresponding to one unpaired electron with a very slight orbital contribution are quite close to 1.77 B.M. expected for a $S = 1/2$ as mostly seen for a d^9 system, the magnetic moment values reveals that the titled complexes is monomeric in nature without any of metal-metal interaction.^{5,38} The proposed geometry of the copper(II) complexes is a distorted square planar.⁴⁵

The spectral data are very helpful in supporting the proposed tetradentate Schiff base complex structure and coordination pattern in this study.

3. 1. 2. Catalytic Study

The 'click' 1,3-dipolar Huisgen cycloaddition reaction has been reported in a wide variety of copper(II) complexes. In this work, the click reaction of α -haloketones or alkyl halides (**1a-i**), alkynes (**2a-d**), and sodium azide in water were performed in the presence of two different $[CuL^1]$ and $[CuL^2]$ catalysts (Scheme 2).



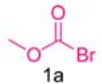
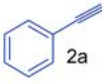
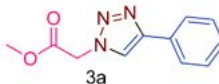
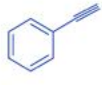
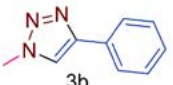
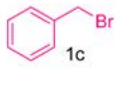
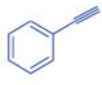
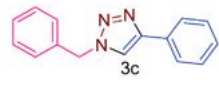
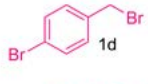

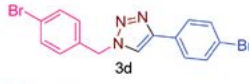
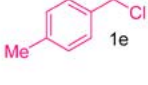
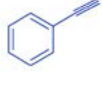
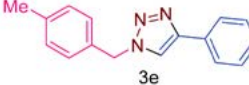
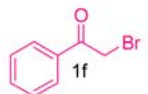
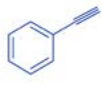
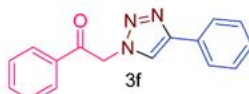
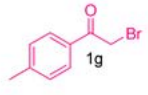
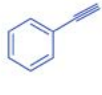
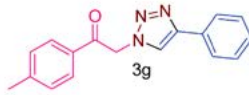
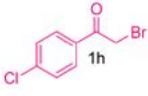
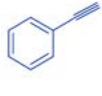
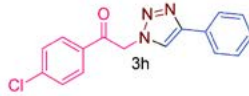
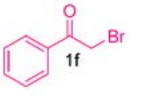
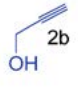
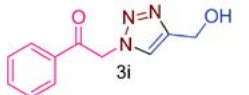
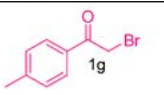

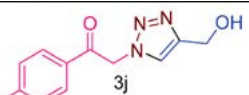
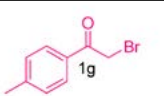
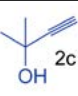
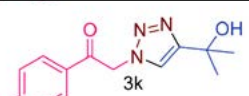
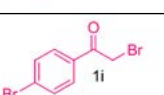
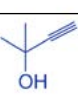
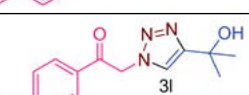
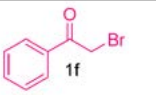
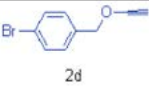
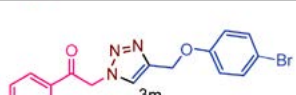
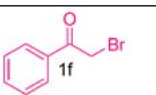
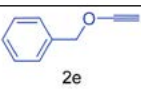
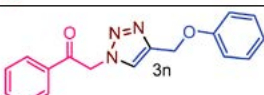
Scheme 2. Synthetic route of Huisgen cycloaddition reaction by the new Cu^{II} complexes catalyst.

Using this methodology only one of possible regioisomers was formed (Table 3). Thirteen of the synthesized products **3a-n** were known compounds and their identity was confirmed by a comparison of their melting point and their spectral properties with literature data (Table 3). Two products **3m** and **3n** are new, and they were characterized by IR, ¹H NMR and ¹³C NMR spectral data and elemental analysis. The yield and reaction time of the synthesized compounds **3m** and **3n** are presented in Table 3. Based on the results, the reaction yields with $[CuL^2]$ catalyst is generally higher than $[CuL^1]$ catalyst. Also, the catalyst $[CuL^2]$ required shorter reaction times than catalyst $[CuL^1]$. Various alkyl, benzyl and benzoyl halides with both electron-donating and -withdrawing substituents were subjected to the same reaction conditions as **3** to furnish the corresponding 1,2,3-triazole derivatives.

3. 1. 3. The Formation Constant Interpretation

Formation constants and thermodynamic parameters are very useful tools for the investigation of interactions between donor and acceptor species and equilibria in solution. In this work, we measured the formation constants of the complexation by UV-Vis spectrophotometric method through titration of a fixed concentration of the ligands (5×10^{-5} M) as a donor with one to ten-fold excess of copper acetate ($10^{-4} - 10^{-5}$ M) as an acceptor at 25 °C in DMF. The absorption measurements were recorded in the range 250–700 nm about 5 min after each addition. The formed complex exhibited different absorption from the free ligand, while the Cu^{II} ion solution showed no absorption at these wavelengths. As an example, the variation of the electronic spectra for H_2L^1 titrated with various concentration of Cu^{II} acetate is shown in Figure 1. By the addition of Cu^{II} solution to a solution of H_2L^1 ligand, the original band of H_2L^1 at $\lambda_{max} = 314$ nm was weakened and a new intense band appeared at $\lambda_{max} = 376$ nm) for the $[CuL^1]$ complex. Isosbestic points suggest that there are only two species in equilibrium.

Table 3. The cycloaddition reaction with copper(II) Schiff base complexes catalyst.

Entry	Bromo keton or Alkyl Halid (1)	Acetylene (2)	Product (3)	Time/ (min)		GC Yelid		m.p. °C (lit) [ref]
				cat1	cat2	cat1	cat2	
1	 1a	 2a	 3a	60	80	81	90	113–115 (116) [25]
2	CH ₃ I 1b	 2a	 3b	128	120	75	92	122–125 (125) [25]
3	 1c	 2a	 3c	40	35	90	95	128–130 (129) [24]
5	 1d	 2a	 3d	60	42	81	92	111–112 (110) [24]
6	 1e	 2a	 3e	50	33	78	82	155–157 (156) [24]
7	 1f	 2a	 3f	20	10	84	92	171–172 (169) [25]
8	 1g	 2a	 3g	30	20	80	89	155–157 (159) [25]
9	 1h	 2a	 3h	55	32	86	92	105–108 (107) [25]
10	 1f	 2b	 3i	60	40	79	83	110–113 (115) [25]
11	 1g	 2b	 3j	70	50	77	85	155–158 (154) [25]
12	 1g	 2c	 3k	85	65	80	95	154–155 (154) [25]
13	 1i	 2c	 3l	75	62	85	92	168–171 (170) [25]
14	 1f	 2d	 3m	80	72	75	90	197 [this work]
15	 1f	 2e	 3n	90	95	80	85	182 [this work]

The complex formation constant were calculated using the SQUAD computer program,⁴⁶ designed to calculate the best value for the formation constant by employing

a non-linear, least square approach. Also, the free energy change, ΔG° , for the formed complexes were determined by $\Delta G^\circ = -RT \ln K_f$ at 25 °C where K_f is the complex forma-

tion constant, R is the gas constant and T is the temperature in the Kelvin scale (Table 4). The electronic effect of the *para* substituted Schiff base ligand plays important role in stability and reactivity of their complexes. The methoxy group is an electron donating group (EDG) or electron releasing group (ERG) that donates some of its electron density into a conjugated π -system *via* resonance or inductive effects, thus making the Schiff base ligand H_2L^1 more nucleophilic, so the interaction of this ligand results in the formation of the charge transfer complex in which a negatively charged acceptor and positively charged donor interact electrostatically and increase the formation constants. On the other hand, NO_2 substituent an electron withdrawing group (EWG) will have the opposite effect on nucleophilicity as an EDG, as it removed electron density from a π -system making the Schiff base ligand H_2L^2 more electrophilic. The acceptor property of the Schiff base ligand is increased by decreasing the electron donating properties of the NO_2 group and therefore leads to decrease the formation constants of the copper(II) complex. Therefore, the formation constant and the free energy data for $[CuL^1]$ are larger than those for $[CuL^2]$ (see Table 4).

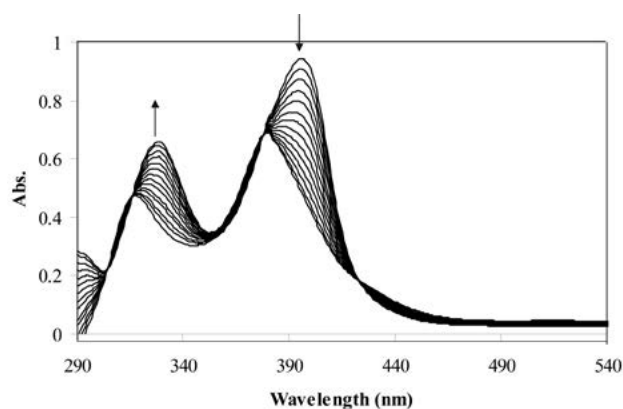


Figure 1. The variation of the electronic spectra of H_2L^1 with Cu(II) acetate in DMF.

Table 4. The result of formation constants and the free energy values for the complexes

Complexes	$\log K_f$	ΔG° (kJ mol ⁻¹)
$[CuL^1]$	5.88(0.10) ^a	-33.55(0.24)
$[CuL^2]$	4.36(0.13)	-24.86(0.32)

^a The numbers in parentheses are the standard deviations.

3. 1. 4. Antibacterial Activity

The results concerning *in vitro* antibacterial investigation of the Schiff base ligands and their copper(II) complexes (Table 5) show a remarkable inhibitor activity against pathogenic bacterial species of Gram positive and Gram negative bacteria. From comparison of observed data (Table 5), it is clear that the inhibition by the com-

plexes is higher than that of corresponding ligands. This may be explained by the chelation theory.^{47,48} On one hand, chelation will reduced the polarity of the metal center because of overlap of the ligand orbital and partial sharing of positive charge of the metal atoms with donor atom present on the ligand. This fact leads to the increase in π -electron delocalization over the whole chelating ring. On the other hand, the chelation will enhanced the lipophilic character of the complexes. This, in turn, increase the diffusion of the complex through the lipid layer of the cell membranes and blocks the metal binding sites in the enzymes of bacteria.^{49,50}

Inhibitory activity of the complexes is a follows $[CuL^2] > [CuL^1]$. The activity depends on the properties of OMe group as electron releasing group and NO_2 as electron withdrawing group on phenyl ring. This can be explained on basis of π -electron delocalization in chelating group as discussed above.

Table 5. Antibacterial screening results

compounds	<i>E. coli</i>	<i>S. aureus</i>
	Diameter of inhibition zone (mm)	
H_2L^1	20	21
H_2L^2	18	20
$[CuL^1]$	29	26
$[CuL^2]$	25	23
tetracycline	32	34

3. 2. Computational Results

3. 2. 1. Description of the Optimized Structures

Molecular structure and atom notation of the compounds with selected bond distances and angles are shown in Figure 2 and Table 6. The Schiff base ligands are coordinated to the metal core through the amine nitrogen (N1), azomethine nitrogen atom (N2), phenolic oxygen atom (O1) and thio sulfur atom (S2). The Cu1–N2, Cu1–N1, Cu1–O1 and Cu1–S2 bond distance in $[CuL^1]$ and $[CuL^2]$ are 1.966, 1.960, 1.908, 2.346 Å and 1.958, 1.968, 1.926, 2.332 Å, respectively. All bond distances are in good agreement with those reported in other similar tetradentate Schiff base complexes.^{18,51} The calculated C10–N1 and C3–N2 bond length in the complexes are close to the value for a double bond, like in similar Schiff base complexes.¹⁶ Compared with the ligand, most of bonds show elongation upon complexation with the metal ion. C10–N1, C3–N2, C15–S2 and C6–O1 bond lengths become longer in both complexes in qualitative agreement with expectation. This finding is due to the formation of Cu1–N1, Cu1–N2, Cu1–O1 and Cu1–S2 bonds which make the C10–N1, C3–N2, C6–O1 and C15–S2 bonds weaker.⁵² The high negative atom charge of imine nitrogen atoms (N1, N2), the phenolic oxygen atoms (O1) and thio sulfur (S2) is: -0.456,

–0.441, –0.688, –0.179 for H_2L^1 and –0.455, –0.436, –0.659, –0.171 for H_2L^2 , respectively. These data suggest that the O1 atom donates more electron density to the copper ion leading to strong Cu1–O1 bonding. This idea corroborated by the short Cu1–O1 bond length in comparison to those of Cu1–N1, Cu1–N2 and Cu1–S2.⁵³

According to calculated results, the angles around the metal center for $[CuL^1]$ and $[CuL^2]$ N1–Cu1–O1 (172.74°, 172.94°), N2–Cu1–S2 (171.85°, 171.68°), N1–Cu1–S2

(90.78°, 91.33°) and N2–Cu1–O1 (90.71°, 91.43°) suggest distorted square planar geometry of the complexes. The dihedral angle between the phenyl and chelated ring is in the range 2.9–4.5° (see Table 6) which indicates the resonance between phenyl groups with the π -electron system of the chelating ring.

There is a good agreement between the bond distance, bond angles and dihedral angles of the solid structure in similar compounds^{19,51} and gas phase calculated values. It

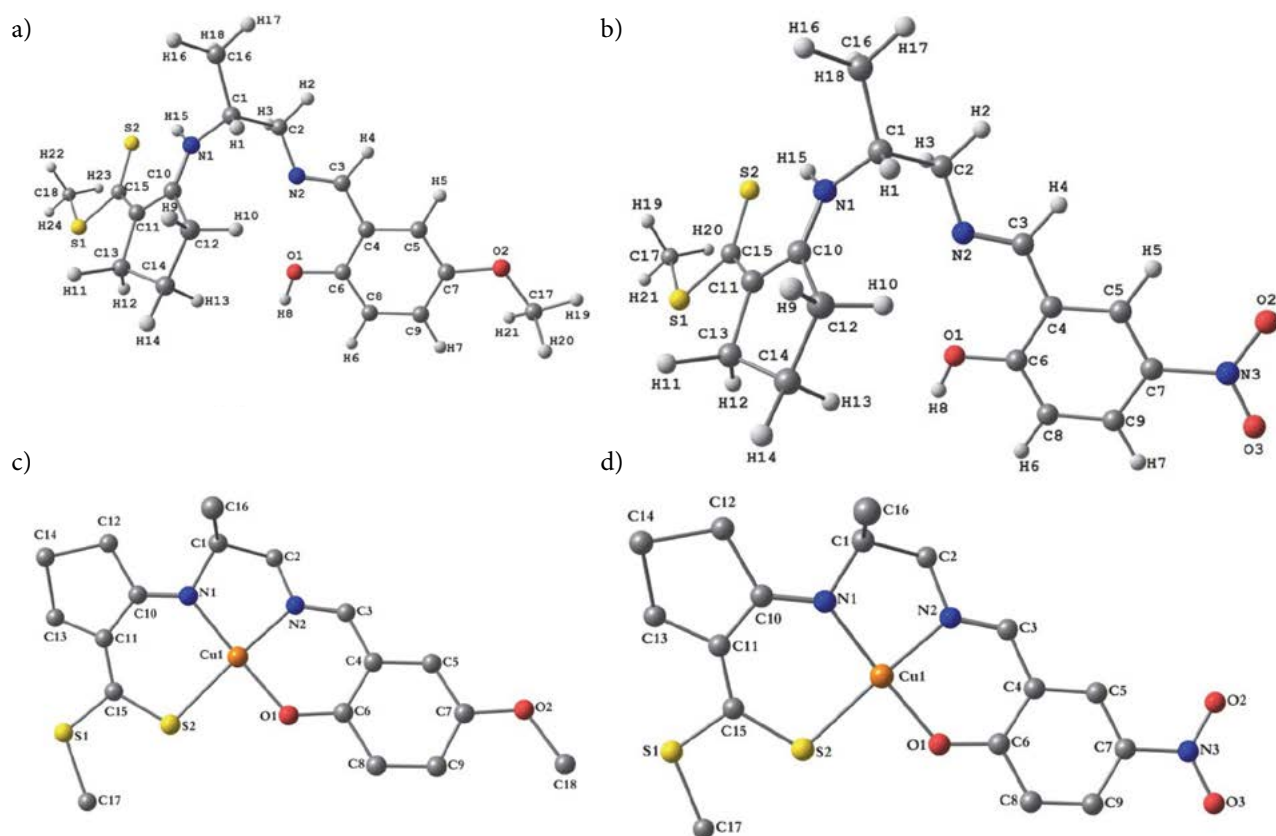


Figure 2. DFT optimized geometry of the (a) H_2L^1 , (b) H_2L^2 , (c) $[CuL^1]$, (d) $[CuL^2]$ with labeling atoms (hydrogen atoms in both complexes have been omitted for clarity).

Table 6. Some selected optimized bond lengths and bond angles of the Schiff base ligands and its complexes

	Band length (Å)				Bond angle (°)			
	Ligands		Complexes		Complexes		Complexes	
	H_2L^1	H_2L^2	CuL^1	CuL^2	CuL^1	CuL^2	CuL^1	CuL^2
N2–C3	1.283	1.281	N2–C3	1.305	1.300	N1–Cu–N2	86.508	86.587
N1–C10	1.325	1.326	N1–C10	1.339	1.340	N1–Cu–O1	172.947	172.744
C6–O1	1.327	1.311	C6–O1	1.392	1.376	N1–Cu–S2	90.781	91.330
C15–S2	1.741	1.740	C15–S2	1.762	1.764	N2–Cu–O1	91.432	90.713
C7–O2	1.396	–	C7–O2	1.404	–	N2–Cu–S2	171.692	171.851
C7–N3	–	1.457	C7–N3	–	1.446	O1–Cu–S2	87.211	87.258
O1–H8	0.973	0.974	Cu1–N1	1.966	1.968	O1–C6–C4–C3	0.24046	0.36152
N1–H15	1.024	1.024	Cu1–N2	1.960	1.958	N2–C3–C4–C6	1.18439	1.25585
			Cu1–O1	1.908	1.916	N1–C10–C11–C15	4.27604	4.35552
			Cu1–S2	2.346	2.332	S2–C15–C11–C10	3.04373	2.91583

should be noted that some differences are due to the X-ray crystal diffraction being applied in the solid phase, while theoretical calculations were carried out in the gas phase.^{10,54}

Careful analysis of the bond lengths and bond angles data leads to the conclusion that Cu complex has a distorted square planar coordination around the Cu^{II} center.

3. 2. 2. Details of Frontier Molecular Orbital Analysis

The HOMO and LUMO molecular orbitals which are called the frontier orbitals and energy level of all mentioned compounds in this study was done using B3LYP/(LANL2DZ/6-311G**) methods. 3D plots of the frontier orbital shapes and their corresponding energy levels are depicted in Figure 3 and Table 7. The E_{HOMO} and E_{LUMO} for all compounds are negative indicating molecules are stable. The plots of HOMO and LUMO orbitals of the ligands show the HOMO surface is mainly located on the cyclo-

pentene ring whereas the LUMO surface is mostly composed on the phenolic aromatic ring.⁵⁵ This LUMO surface is overlapped with C15–S2 and C3–N2 group.

The computed frontier gap ($E_{\text{HOMO}} - E_{\text{LUMO}}$) is very useful indicator in presenting the factors influencing the stability of these compounds. Taking this fact into the consideration, the energy gap levels for the compounds were computed (Table 7). The calculated E_g for the ligands is smaller than their complexes, indicating that the ligands are reactive and kinetically unstable. Since the ligand is more polarized the amount of electron charge transfer from the ligands to the metal increase, i.e. the ligand is soft molecule and easily offer electrons to an acceptor metal centers.^{53,56} For [CuL²] complex, the HOMO orbital includes $\pi(\text{L})$ (87%) character from ligand heteroatom along with minor contribution of $d\pi(\text{Cu})$ orbital (13%). This orbital has π -bonding nature which is concentrated on the chelated ligand. The LUMO orbital has 68% $\pi^*(\text{L})$ character and significant contribution (32%) of $d\pi(\text{Cu})$ orbital. The analysis of molecular orbitals for [CuL²] complex is

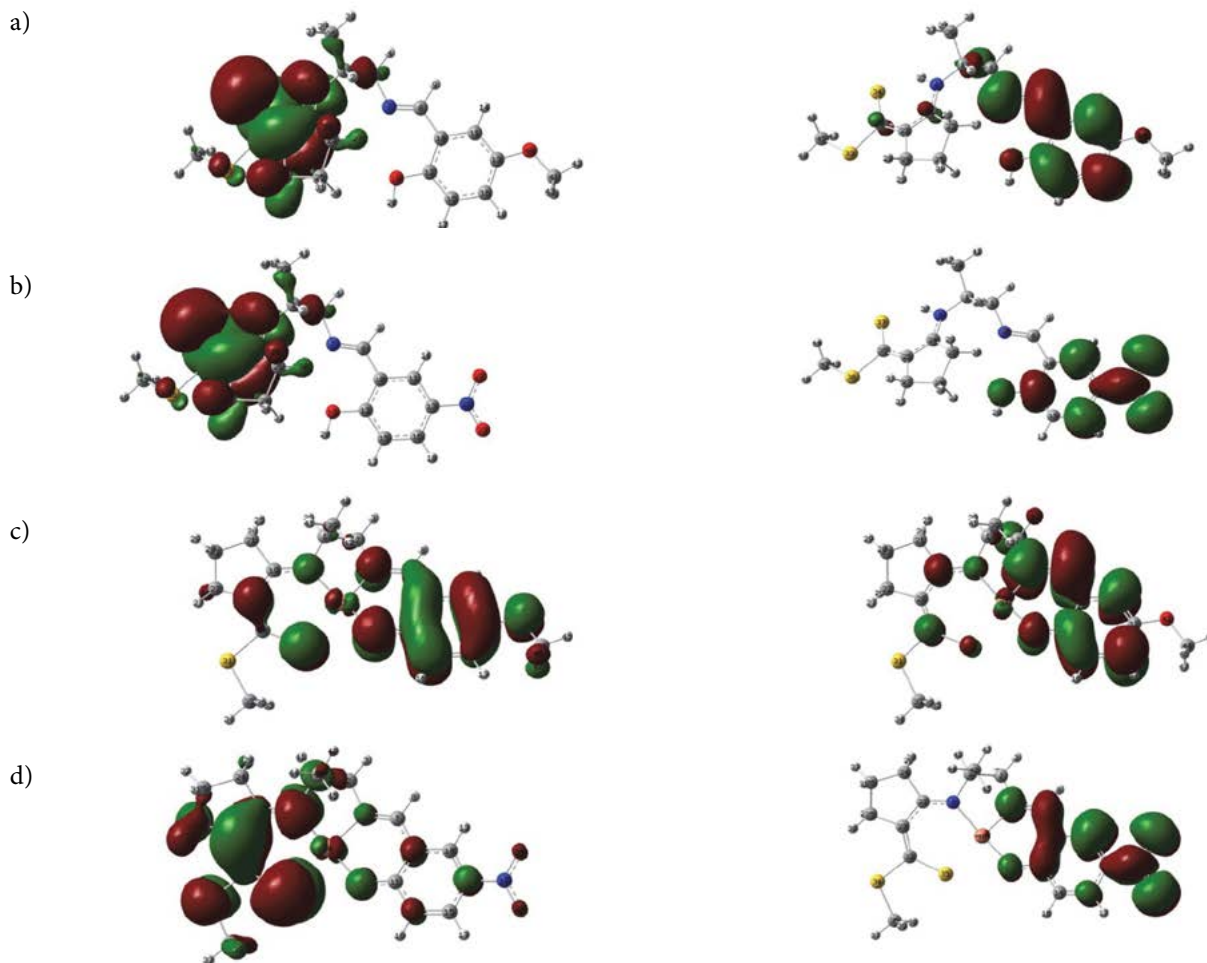


Figure 3. The HOMO (left) and LUMO (right) frontier orbitals views of (a) H₂L¹, (b) H₂L², (c) [CuL¹], (d) [CuL²]

more or less the same as for [CuL¹] complex. The calculated E_g level for the complexes show the E_g [CuL¹] complex is larger than that [CuL²] complex indicating the chemical reactivity of the [CuL¹] decrease and the complex is more stable. This results support the experimental formation constant.

3. 2. 4. Theoretical Study of Hardness, Mulliken Charges and Dipole Moment

To rationalize the relative stability and reactivity of chemical compounds the chemical hardness is useful parameter. The hardness η was calculated from $\frac{1}{2}(IE - EA)$ equation, where IE and EA are the ionization energy and

Table 7. Some of calculated structural parameters for the Schiff base ligand and their Cu(II) complexes

Complexes	HOMO/eV	LUMO/eV	gap/eV	Hardness (η)	Dipole/Debye	HF energy (a.u.)
H ₂ L ¹	-5.417	-3.298	2.119	1.059	3.169	-1756.632
H ₂ L ²	-5.526	-3.264	2.262	1.131	3.182	-1846.602
[CuL ¹]	-5.281	-1.633	3.648	1.824	5.865	-3395.988
[CuL ²]	-5.852	-2.613	3.239	1.615	5.860	-3485.966

3. 2. 3. Theoretical Study of Vibration Mode

Vibrational frequency calculations were performed on the optimized structures of the complexes to search for the imaginary frequency and obtain the vibrational frequencies of compounds in gas phase. Table 1 shows selected experimental and calculated IR band assignments of studied Schiff base ligands and their Cu(II) complexes. The broad band related to O–H stretching vibration of the phenolic group appears at 3410 and 3455 cm⁻¹ in the free ligands spectrum. In the complexes, the O–H peak disappear which indicates coordination of phenolic oxygen atom to central atom.

The multiple bands at around 3000 cm⁻¹ in the ligands and their complexes are assigned to C–H stretching vibration.

The strong bands at 1653 and 1668 cm⁻¹ in the IR spectra of the Schiff base ligands assigned to the $\nu(C=N)$ are changed by 17–22 cm⁻¹ in the spectra of the complexes, indicating coordination of Schiff base through azomethine nitrogen atom.

The intense band in the 1400 cm⁻¹ region is due to the skeleton vibration mode of C=C in the free ligands and their copper(II) complexes.

The $\nu(C-O)$ vibrations were found at 1260 cm⁻¹ and 1283 cm⁻¹ in the spectrum of the free ligands. These bands are shifted to lower or higher frequencies after complexation suggesting that this group takes part in coordination. The Schiff base ligand coordination to the copper ion is substantiated by two medium intensity bands at 470 and 472 cm⁻¹ for [CuL¹] and [CuL²], respectively, attributed to $\nu(M-N)$ and also at 555 and 581 cm⁻¹ for [CuL¹] and [CuL²], respectively, for $\nu(M-O)$ stretching frequencies.^{41,57}

Small differences between the theoretical and experimental vibrational frequencies can be related to (i) the environmental condition (gas phase and solid state) and (ii) from the fact that the experimental values are anharmonic frequencies while the calculated values are harmonic.⁵⁸

electron affinity, respectively. The ionization energy and the electron affinity can be equalized through frontier orbital energies ($EA = -E_{HOMO}$ and $IE = -E_{LUMO}$) according to the Koopman theorem.⁵⁹ Therefore, for the calculation of hardness the following equation $\eta = \frac{1}{2}(E_{HOMO} - E_{LUMO})$ was used for all titled compounds.⁶⁰ As can be seen in Table 7, the H₂L² ligand and [CuL¹] complex have a higher hardness and lower chemical reactivity and higher stability than the other compounds.

Dipole moment is fundamental characteristics to explain the polarization of compounds. The experimental measurements of dipole moment are not always feasible, so we were using the density functional theory to calculate this parameter. On the basis of magnitude of dipole moments (Table 7) all studied compounds are polar. The [CuL²] complex has the smallest dipole moment; that in part explains the instability of the [CuL²] and the decrease the formation constant.

The values of the computed Mulliken net charge on non-hydrogen atoms (active centers) were investigated. Electronegativity plays important role on atomic charge distributions of the non-hydrogen atom. When two atoms are connected together, the atom having higher electronegativity will carry negative charges, while the atom having smaller electronegativity will carry positive charges. As summarized in Table 8, when the carbon is bonded to N1, N2, O1 and S2 atoms, the carbon atomic charges are positive and the most negative atomic charges are attributed to N1, N2, O1 and S2 which have higher electronegativity than the carbon. On the other hand, the results show that the most negative centers in the ligand are bonded to metal ions which carry the positive charge value (Table 8). After complexation, the charge density decrease on the donating atom indicating that the metal ions received the electron density from their surrounding donating sites with high negative charge centers of the ligand. The calculated net charge of the complexes were compared with that free Schiff base ligand in order to show the donating sites in the ligand involved in the chelation and support one of our original ideas of the synthesis.

Table 8. Selected values for the Mulliken charge distributions for non-hydrogen atoms

Compounds	H ₂ L ¹	H ₂ L ²	[CuL ¹]	[CuL ²]
CuI	-	-	1.15996	1.15719
N1	-0.45654	-0.45576	-0.39787	-0.30551
N2	-0.44166	-0.43669	-0.43459	-0.42802
S2	-0.17963	-0.17113	-0.14996	-0.13995
O1	-0.68843	-0.65924	-0.37940	-0.36719
C1	0.19197	0.08296	0.12969	0.13045
C2	0.14316	0.19723	0.17083	0.17661
C3	0.20375	0.03683	0.17469	0.18212
C6	0.27879	0.29780	0.38667	0.41059
C7	0.24649	0.26943	0.21392	0.23924
C10	0.45997	0.46642	0.37940	0.38437
C11	0.22702	0.22699	0.24055	0.24050
C15	0.48696	0.61489	0.49136	0.49244

4. Conclusion

The present study describes the synthesis and characterization of some Schiff base ligands and their Cu^{II} complexes. From the IR and UV-Vis spectra it may be concluded the Schiff base ligand acts as a chelating to the metal ion and bind through nitrogen atoms of the azomethine and amine groups, phenolic oxygen atom and sulfur atom of the C=S group. The stability constant and Gibbs free energy calculations show that the [CuL¹] complex is more stable than [CuL²] complex. The present computational study allows us to obtain optimized structure, molecular parameters, highest occupied molecular orbital energy, lowest unoccupied molecular orbital energy, HOMO-LUMO band gap, IR vibrational frequencies, characteristics of all synthesized compounds. In general a good agreement was found between the theoretical and experimental data. The titled compounds in this study were tested against two pathogenic bacteria in order to assess their antibacterial properties. The results revealed that the complexes possess higher antibacterial activity as free Schiff base ligands. Both complexes are effective catalysts for the cyclization reactions. The percentage product of reactions show [CuL²] complex being more active than [CuL¹] complex.

5. Acknowledgements

We are grateful to Islamic Azad University, Darab branch Council for their financial support.

6. References

1. Y. W. Dong, R. Q. Fan, W. Chen, H. J. Zhang, Y. Song, X. Du, P. Wang, L. G. Wei, Y. L. Yong, *Dalton Trans.* **2017**, 46, 1266–1276. DOI:10.1039/C6DT04159K
2. J. Kumar, A. Rai, V. Raj, *Org. Med. Chem. Int. J.* **2017**, 1, 1–15.
3. M. L. Low, L. Maigre, M. I. M. Tahir, E. R. T. Tiekink, P. Dorlet, R. Guillot, T. B. Ravoo, R. Rosli, J. M. Pages, C. Policar, N. Delsuc, K. A. Crouse, *Eur. J. Med. Chem.* **2016**, 120, 1–12. DOI:10.1016/j.ejmech.2016.04.027
4. A. B. Gündüzalp, İ. Özsen, H. Alyar, S. Alyar, N. Özbek, *J. Mol. Struct.* **2016**, 20, 259–266. DOI:10.1016/j.molstruc.2016.05.002
5. H. G. Sogukömeroğullari, T. Taskin Tok, F. Yilmaz, L. Berber, M. Sonmez, *Turk. J. Chem.* **2015**, 39, 497–509. DOI:10.3906/kim-1412-81
6. Y. Mei Yu, K. Li, Y. Wang, Z. J. Yao, *Polymers* **2017**, 9, 105–115. DOI:10.3390/polym9030105
7. A. Ourari, D. Aggoun, L. Ouahab, *Inorg. Chem. Commun.* **2013**, 33, 118–124. DOI:10.1016/j.inoche.2013.04.002
8. A. Kareem, M. Arshad, Sh. A. A. Nami, N. Nishat, *J. Photochem. Photobiol. Biol.* **2016**, 160, 163–171. DOI:10.1016/j.jphotobiol.2016.03.030
9. I. R. Parrey, A. A. Hashmi, *Canadian. Chem. Trans.* **2015**, 3, 65–71.
10. Z. Asgharpour, F. Farzaneh, A. Abbasi, M. Ghiasi, *Polyhedron* **2015**, 101, 282–289. DOI:10.1016/j.poly.2015.09.030
11. K. H. Yang, *Acta. Chim. Slov.* **2014**, 61, 629–639.
12. M. Mishra, K. Tiwari, P. Mourya, M. M. Singh, V. P. Singh, *Polyhedron* **2015**, 89, 29–38. DOI:10.1016/j.poly.2015.01.003
13. P. Pattanayak, J. L. Pratihari, D. Patra, P. Brandão, V. Felix, *Inorg. Chim. Acta* **2014**, 418, 171–179. DOI:10.1016/j.ica.2014.04.021
14. P. Drabina, J. Svoboda, M. Sedláč, *Molecules* **2017**, 22, 865–883. DOI:10.3390/molecules22060865
15. A. Bhattacharjee, Sh. Halder, K. Ghosh, C. Rizzoli, P. Roy, *New J. Chem.* **2017**, 41, 5696–5706. DOI:10.1039/C7NJ00846E
16. S. Esmailzadeh, L. Azimian, Kh. Shekoochi, H. Esfandiari, M. Asadi, Z. Zare, A. Rahmani nejad, K. Mohammadi, *Inorg. Chim. Acta* **2013**, 405, 155–162. DOI:10.1016/j.ica.2013.05.001
17. M. Asadi, K. Mohammadi, S. Esmailzadeh, B. Etemadi, H. K. Fun, *Polyhedron* **2009**, 28, 1409–1418. DOI:10.1016/j.poly.2009.03.018
18. M. Asadi, K. Mohammadi, S. Esmailzadeh, B. Etemadi, H. K. Fun, *Inorg. Chim. Acta* **2009**, 362, 4913–4920. DOI:10.1016/j.ica.2009.07.025
19. S. Esmailzadeh, L. Azimian, K. Shekoochi, K. Mohammadi, *Spectrochim. Acta Part A: Mol. Biomole. Spect.* **2014**, 133, 579–590. DOI:10.1016/j.saa.2014.05.095
20. S. Behrouz, M. N. Rad, S. Rostami, M. Behrouz, E. Zarehnezhad, A. Zarehnezhad, *Mol. Divers.* **2014**, 18, 797–808. DOI:10.1007/s11030-014-9539-1
21. M. N. Rad, S. Behrouz, M. Behrouz, A. Sami, M. Mardkhoshnood, A. Zarehnezhad, E. Zarehnezhad, *Mol. Divers.* **2016**, 20, 705–718. DOI:10.1007/s11030-016-9678-7
22. E. Zarehnezhad, M. N. Rad, S. Behrouz, S. Esmailzadeh, M. Farjam, *J. Iran. Chem. Soc.* **2017**, 14, 509–519. DOI:10.1007/s13738-016-0999-3

23. S. G. Agalave, S. R. Maujan, V. S. Pore, *Chem. Asian J.* **2011**, *6*, 2696–2718. DOI:10.1002/asia.201100432
24. H. Sharghi, R. Khalifeh, M. M. Doroodmand, *Adv. Synth. Catal.* **2009**, *351*, 207–218. DOI:10.1002/adsc.200800612
25. E. Hashemi, Y. S. Beheshtiha, S. Ahmadi, M. M. Heravi, *Trans. Met. Chem.* **2014**, *5*, 593–601. DOI:10.1007/s11243-014-9838-5
26. A. D. Becke, *J. Chem. Phys.* **1993**, *98*, 5648–5652. DOI:10.1063/1.464913
27. C. Lee, W. Yang, R. G. Parr, *Phys. Rev.* **1988**, *B 37*, 785–789.
28. P. J. Hay, W. R. Wadt, *J. Chem. Phys.* **1985**, *82*, 270–283. DOI:10.1063/1.448799
29. M. J. Frisch, G. W. Trucks, H. B. Schlegel, G. E. Scuseria, M. A. Robb, J. R. Cheeseman, J. A. Montgomery, J. T. Vreven, K. N. Kudin, J. C. Burant, J. M. Millam, S. S. Iyengar, J. Tomasi, V. Barone, B. Mennucci, M. Cossi, G. Scalmani, N. Rega, G. A. Petersson, H. Nakatsuji, M. Hada, M. Ehara, K. Toyota, R. Fukuda, J. Hasegawa, M. Ishida, T. Nakajima, Y. Honda, O. Kitao, H. Nakai, M. Klene, X. Li, J. E. Knox, H. P. Hratchian, J. B. Cross, C. Adamo, J. Jaramillo, R. Gomperts, R. E. Stratmann, O. Yazyev, A. J. Austin, R. Cammi, C. Pomelli, J. W. Ochterski, P. Y. Ayala, K. Morokuma, G. A. Voth, P. Salvador, J. J. Dannenberg, V. G. Zakrzewski, S. Dapprich, A. D. Daniels, M. C. Strain, O. Farkas, D. K. Malick, A. D. Rabuck, K. Raghavachari, J. B. Foresman, J. V. Ortiz, Q. Cui, A. G. Baboul, S. Clifford, J. Cioslowski, B. B. Stefanov, G. Liu, A. Liashenko, P. Piskorz, I. Komaromi, R. L. Martin, D. J. Fox, T. Keith, M. A. Al-Laham, C. Y. Peng, A. Nanayakkara, M. Challacombe, P. M. W. Gill, B. Johnson, W. Chen, M. W. Wong, C. Gonzalez, J. A. Pople, Gaussian 03, Computer program for computational chemistry, Gaussian Inc., Pittsburgh PA, USA; 2004.
30. A. W. Bauer, W. M. Kirby, J. C. Sherris, M. Turck, *Am. J. Clin. Pathol.* **1966**, *45*, 493–496. DOI:10.1093/ajcp/45.4_ts.493
31. R. D. Walker, J. F. Prescott, J. D. Baggot. Antimicrobial susceptibility testing and interpretation of results, Iowa state university press, USA, **2000**, pp. 12–26.
32. D. M. Abd El-Aziz, S. E. H. Etaiw, E. A. Ali, *J. Mol. Struct.* **2013**, *1048*, 487–499. DOI:10.1016/j.molstruc.2013.05.051
33. M. Slehi, F. Rahimifar, M. Kubicki, A. Asadi, *Inorg. Chim. Acta* **2016**, *443*, 28–35. DOI:10.1016/j.ica.2015.12.016
34. K. Ghosh, S. Roy, A. Ghosh, A. Banerjee, A. Bauzá, A. Frontera, S. Chattopadhyay, *Polyhedron* **2016**, *112*, 6–17. DOI:10.1016/j.poly.2016.02.035
35. X. M. Hu, L. W. Xue, G. Q. Zhao, W. C. Yang, *Bull. Chem. Soc. Ethiop.* **2015**, *29*, 407–413. DOI:10.4314/bcse.v29i3.8
36. A. Akbari, Z. Alinia, *Turk. J. Chem.* **2013**, *37*, 867–878. DOI:10.3906/kim-1207-74
37. D. Sakthilatha, R. Rajavel, *J. Chem. Pharm. Res.* **2013**, *5*, 57–63.
38. A. Z. El-Sonbati, M. A. Diab, M. I. Abou-Dobara, H. A. Seyam, *J. Mol. Liq.* **2016**, *218*, 434–456. DOI:10.1016/j.molliq.2016.02.072
39. S. Chandra, A. Rathi, *J. Saudi. Chem. Soc.* **2001**, *5*, 175–182.
40. R. B. Sumathi, M. B. Halli, *Bioinorg. Chem. App.* **2014**, *2014*, 1–11.
41. M. Kudrat, E. Zahan, M. S. Islam, *Russ. J. Gen. Chem.* **2015**, *85*, 979–983. DOI:10.1134/S1070363215040350
42. Z. Asadi, M. Asadi, F. Dehghani Firuzabadi, R. Yousefi, M. Jamshidi, *J. Iran. Chem. Soc.* **2014**, *11*, 423–429. DOI:10.1007/s13738-013-0314-5
43. D. F. Back, G. M. de Oliveira, L. A. Fontana, B. F. Romão, D. Roman, B. A. Iylesias, *J. Mol. Struct.* **2015**, *1100*, 264–271. DOI:10.1016/j.molstruc.2015.07.050
44. M. Asadi, Z. Asadi, N. Savaripoor, M. Dusek, V. Eigner, M. Ranjkesh, M. Sedaghat, *Spectrochim. Acta Part A: Mol. Biomole. Spect.* **2015**, *136*, 625–634. DOI:10.1016/j.saa.2014.09.076
45. S. Basak, S. Sen, S. Mitra, C. Marschner, W. S. Sheldrick, *Struct. Chem.* **2008**, *19*, 115–121. DOI:10.1007/s11224-007-9260-0
46. K. Singh, Y. Kumar, P. Puri, M. Kumar, C. Sharma, *Eur. J. Med. Chem.* **2012**, *52*, 313–321. DOI:10.1016/j.ejmech.2012.02.053
47. D. L. Leggett. Computational Methods for the Determination of Formation Constant, Plenum Press, New York; **1985**. DOI:10.1007/978-1-4684-4934-1
48. L. Dawara, R. V. Singh, *Appl. Organomet. Chem.* **2011**, *25*, 643–652.
49. B. G. Tweedy, *Phytopathology* **1946**, *55*, 910–917.
50. N. Batra, N. Malhotra, S. Assija, *J. Chem. Pharma. Res.* **2014**, *6*, 194–200.
51. N. Kumar Chaudhary, P. Mishra, *Am. J. Appl. Chem.* **2014**, *2*, 19–26. DOI:10.11648/j.ajac.20140201.15
52. G. Grivani, S. Husseinzadeh Baghan, M. Vakili, A. Dehno Khalaji, V. Tahmasebi, V. Eigner, M. Dušek, *J. Mol. Struct.* **2015**, *1082*, 91–96. DOI:10.1016/j.molstruc.2014.10.058
53. O. A. El-Gammal, *Spectrochim. Acta Part A: Mol. Biomole. Spect.* **2010**, *75*, 533–542. DOI:10.1016/j.saa.2009.11.007
54. A. A. Khandar, C. Cardin, S. A. Hosseini-Yazdi, J. McGrady, M. Abedi, S. A. Zarei, Y. Gan, *Inorg. Chim. Acta* **2010**, *363*, 4080–4087. DOI:10.1016/j.ica.2010.08.019
55. Z. G. Niu, L. R. He, L. Li, W. F. Cheng, X. Y. Li, H. H. Chen, G. N. Li, *Acta Chim. Slov.* **2014**, *61*, 786–791.
56. O. A. El-Gammal, *Inorg. Chim. Acta* **2015**, *435*, 73–81. DOI:10.1016/j.ica.2015.06.009
57. A. Akbari, M. Jalili Rasti, *Comput. Res.* **2013**, *1*, 27–33.
58. M. Amirnasr, M. Bagheri, H. Farrokhpour, K. J. Schenk, K. Mereiter, P. C. Ford, *Polyhedron* **2014**, *71*, 1–7. DOI:10.1016/j.poly.2013.12.040
59. T. Koopmans, *Physica* **1934**, *1*, 104–113. DOI:10.1016/S0031-8914(34)90011-2
60. S. Esmailzadeh, L. Azimian, Z. Zare, *Acta Chim. Slov.* **2016**, *63*, 351–362. DOI:10.17344/acsi.2016.2335

Povzetek

Sintetizirali smo dva nova bakrova(II) kompleksa s Schiffovimi bazami in ju okarakterizirali z različnimi fizikalno-kemijskimi in spektroskopskimi metodami, ki razkrivajo popačeno kvadratno planarno geometrijo okoli bakrovega atoma. Analizni podatki potrjujejo stehiometrijo kovina: ligand 1:1. S teorijo gostotnostnega funkcionala (DFT) na B3LYP/(LANL2DZ/6-311G**) nivoju smo proučili strukturne in elektronske lastnosti pripravljenih spojin v vakuumu. Kvantno-mehanski rezultati potrjujejo zaključke dobljene na podlagi eksperimentalnih podatkov. Študij termodinamskih lastnosti tvorbe kompleksov smo izvedli spektrofotometrično pri 25°C. Pri obeh spojinah smo testirali *in vitro* antibakterijsko aktivnost. Proučili smo tudi katalitične lastnosti na primeru klik reakcij. Sintetizirana bakrova kompleksa s Schiffovimi bazami katalizirata 1,3-dipolar Huisgenovo cikloadicijo različno funkcionaliziranih β -azido alkoholov in alkinov v prisotnosti askorbinske kisline v raztopini THF/H₂O (2:1, V/V) pri sobni temperaturi.

Scientific paper

Solvothermal Synthesis and Photocatalytic Activity of BiOBr Microspheres with *Hierarchical* Morphologies

Adriana C. Mera,^{1,2*} Carlos A. Rodríguez,^{1,2} Héctor Valdés,³
Andres F. Jaramillo,⁴ David Rojas⁴ and Manuel F. Meléndrez⁴

¹ Instituto de Investigación Multidisciplinario en Ciencia y Tecnología, Universidad de La Serena, Benavente 980, La Serena, Chile.

² Laboratorio de Química Analítica e Investigación en Fotoquímica y Productos Naturales, Departamento de Química, Facultad de Ciencias, Universidad de La Serena, La Serena, Chile.

³ Universidad Católica de la Santísima Concepción, Facultad de Ingeniería, Laboratorio de Tecnologías Limpias, Concepción, Chile.

⁴ Advanced Nanocomposites Research Group (GINA). Hybrid Materials Laboratory (HML). Department of Materials Engineering (DIMAT), Faculty of Engineering, University of Concepcion, 270 Edmundo Larenas, Box 160-C, Concepcion, Chile 4070409.

* Corresponding author: E-mail: adrymera@hotmail.com, amera@userena.cl
Phone: +56-51-2334881

Received: 10-01-2018

Abstract

BiOBr microspheres with hierarchical morphologies (BiOBr-MicSphe) has potential application in heterogeneous photocatalysis for decontamination of water and air. For this reason, the synthesis, characterization and evaluation of photocatalytic activity of these materials become important. In this article, BiOBr-MicSphe were synthesized using different ranges of reaction temperature (120–200 °C) and reaction time (12 h – 24 h). Samples grown at 145 °C and 18 h showed the higher photocatalytic activity on gallic acid degradation. Morphological properties, chemical composition and structural analysis revealed that sample with higher photocatalytic activity exhibited a microspherical morphology with pure BiOBr tetragonal phase. Besides, adsorption-desorption analysis showed a smaller pore diameter for sample grown at 145 °C and 18 hrs. The results showed that the reaction temperature has a strong influence on the different properties of the material, affecting the photocatalytic activity.

Keywords: BiOBr MicSphe; solvothermal; properties; photocatalytic activity

1. Introduction

Currently, wastewater treatment using new technologies such as advanced oxidation processes (AOP's) for toxic organic removal is under continuous study. The heterogeneous photocatalysis is found among the most promising and efficient AOPs to control environmental pollution, due to its demonstrated efficiency in the degradation and mineralization of a wide range of organic compounds. Heterogeneous photocatalysis is a process based on the utilization of light energy to activate a semiconductor, which modifies the rate of a chemical reaction without being involved itself. The semiconductor can be activated using artificial radiation or solar radiation.^{1,2} The most used semiconductor in the industry today is titanium di-

oxide (TiO₂) Evonik P-25. It offers the benefits of being inert, inexpensive, stable and non-toxic.³ However, due to its wide band gap of 3.2 eV, this material can only absorb light energy in the UV region, which is only around a 5% of the solar spectrum. This makes TiO₂ relatively unattractive for wastewater treatment, since it cannot be activated by natural solar radiation.^{4–6} TiO₂ has been modified to be efficient under visible light using different strategies; however, the increases in photocatalytic efficiency is minimum.^{7–9} Therefore, nowadays most of research that is conducted in the field of photocatalysis, has moved to the development of new materials that are active under visible light.^{10,11}

Recently, the family of bismuth oxyhalides (BiOX, X=Cl, Br, I) has been investigated for their photocatalytic

properties under visible radiation with favorable results.¹² Among them, bismuth oxybromide (BiOBr) has shown promising results.^{13,15} BiOBr has exhibited greater photocatalytic activity than the commercialized *Evonik P25* under UV radiation.¹⁶

BiOBr have been previously synthesized by several methods, such as hydrolysis, hydrothermal, solvothermal, microwave, microemulsion and ionothermal.^{17–23} However, among all available procedures, the solvothermal method appears as one of the most promising, due to the higher photocatalytic activity of the obtained materials.²⁴

In recent years, several authors have reported the synthesis of BiOBr microspheres by solvothermal method. In 2008 J. Zang *et al.*²⁵ grew BiOBr microspheres at 170 °C and 6 h. Samples showed a visible light induced photocatalytic activity for the degradation of methyl orange (MO). In 2011 J. Xu *et al.*,²⁶ using solvothermal method at 180 °C and 12 h, synthesized BiOBr microspheres. The prepared BiOBr catalysts exhibited of pure tetragonal phase, which removed nearly 100 % of RhB from solution after 60 min under simulated solar light irradiation. The high photoactivity was attributed to its relatively large specific surface area and efficient absorption of visible light. Finally, in 2012, Y. Huo *et al.*,²⁵ reported the synthesis of BiOBr microspheres at 160 °C and 12 h. The authors determine that the high photocatalytic activity of BiOBr material for rhodamine B (RhB) degradation under visible-light irradiations could be ascribed to the strong light absorbance with the light multi-reflection, the efficient separation of photo-generated electron–hole pairs, the high crystallization and the large surface area.

All these works reported the obtainment of BiOBr microspheres under single conditions; however, the influence of using different temperatures in the solvothermal synthesis on the properties and photocatalytic activity of these materials has not been reported yet. Besides, considering the high photocatalytic activity of BiOBr, it is necessary to standardize the experimental conditions (reaction temperature and reaction time) of solvothermal synthesis, to obtain a reproducible method which enables to extend the synthesis and application to an industrial scale. The interest in using this material is also because it can be obtained in the form of spheres with *Hierarchical* structures. These structures allow the increase of the surface area of the material, increasing the efficiency of the photocatalytic system. In this work, it is further shown that these can be obtained using temperatures below 150 °C.

The aim of this work is to determine the optimum values of temperature and reaction time for the solvothermal synthesis of BiOBr microspheres with *Hierarchical* structures, to obtain the highest photocatalytic activity. The standardization of conditions (temperature and reaction time) were developed using response surface methodology (RSM).^{27–32} In addition, the obtained materials from standard conditions were characterized to understand the influence of the temperature and time of solvothermal

synthesis, on gallic acid photocatalytic degradation. Gallic acid (model compound) was selected as a representative phenol structure present in agro-industry wastes such as winery wastewaters.^{33,34} This compound is responsible for the inhibitory effects on microbial activity in biological treatment systems, generally used for the treatment of these wastewaters.^{35,36}

2. Experimental

2.1. Preparation of BiOBr Materials

BiOBr Microspheres (BiOBr-MicSphe) were obtained by solvothermal synthesis. The synthesis of materials was performed using a solution of ethylene glycol (Merck 99.5%) with concentration 0.1 M of KBr (99.0% Merck), was added to a solution of ethylene glycol with concentration 0.1 M of bismuth nitrate pentahydrate ($\text{Bi}(\text{NO}_3)_3 \times 5\text{H}_2\text{O}$ (99.0%, Sigma-Aldrich). The mixture was stirred at room temperature and then poured into to an autoclave reactor. The reactor was heated using the experimental design displayed in Table 1. After the reaction times has elapsed, the reactor is cooled down at room temperature, for each experiment. The solids were separated by gravity filtration and washed with distilled absolute ethanol and water. The BiOBr materials obtained were dried at 60 °C for 24 hours.

2.2. Response Surface Modeling

The solvothermal synthesis of BiOBr was carried out with the response surface methodology (RSM) using the software MODDE 7.^{37–40} The multivariate analysis was a composed central circumscribed design (CCC) which is based on a factorial design of two level with 3 central points and 4-star points.^{27–32} The central point was coded as zero and determined in triplicate to statistically validate the terminations assuming homoscedasticity of variance.

The variables evaluated simultaneously were the temperature (ranging from 120 to 200 °C) and reaction time (from 12 to 24 hours). This procedure allows standardization of the experimental conditions (reaction time and reaction temperature) for the synthesis of BiOBr microspheres by solvothermal process. The statistical validation was performed by ANOVA test with a confidence level of 95%.

2.3. Characterization

The materials that exhibited the higher and lower photocatalytic efficiency were selected for characterization further. The morphologies of materials were observed by scanning electron microscopy (SEM, JEOL JSM-6380). Additionally, transmission electron microscopy (TEM) using a JEOL JEM 1200 EX-II. The particles size were determined by using a laser diffraction particle size analyzer

(Microtrac Model S3500). Chemical composition of the samples was measured by means of energy dispersive X-ray spectroscopy (EDS). Micromeritics TriStar II porosity analyzer measured the specific surface area (BET) and the pore size distribution of the materials. The composition of products was examined by means of X-ray diffraction (XRD) in a diffractometer Bruker D4 with X-ray source of Cu K α ($\lambda = 1.5406 \text{ \AA}$). Thermogravimetric meas-

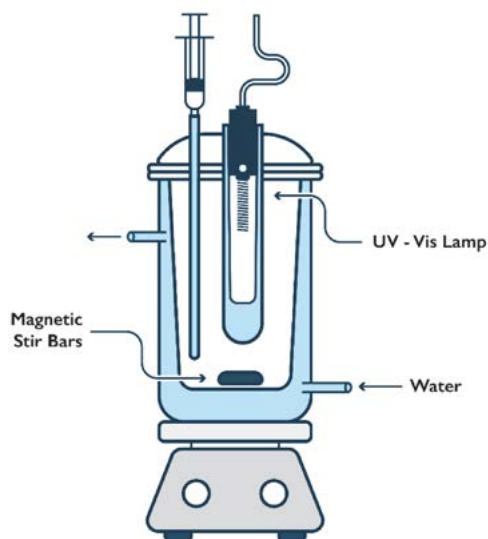


Figure 1. Experimental system used during the photocatalytic assays.

urement (TGA) were determined with a thermobalance model TG209 F1 Iris. Fourier transform infrared (FTIR) spectra were obtained using a Nicolet Nexeus spectrometer. UV-visible diffuse reflectance absorbance (DRS) was determined with a Perkin Elmer Precisely Lambda 35 UV/Vis spectrophotometer.

2. 4. Photocatalytic Efficiency Measurements

The photocatalytic efficiency was evaluated on gallic acid degradation under simulated solar radiation using a xenon lamp (VIPHID 6000 k, 12 W) with spectral range between 380–900 nm.⁴¹ The tests were made in the system of Figure 1, the photocatalytic assays were done in 250 mL of acid gallic aqueous solution (20 mg L^{-1}) adding 0.025 g of the photocatalyst. The reaction mixture was maintained at room temperature and the pH was fixed at 4.5. Before the light was turned on, the solution was kept in dark for 40 min to reach the absorption-desorption equilibrium. Subsequently, solution was irradiated during 60 min and sampling was done every 5 min until 20 min, then every 10 min to complete the 60 min of photocatalytic reaction.³¹ Remaining gallic acid was determined by absorption measurements at 264.5 nm by means of UV-vis spectrophotometry (Shimadzu UV-1601PC). From the photocatalytic activity measurements samples that exhibited the higher and lower activity were selected for further characterization.

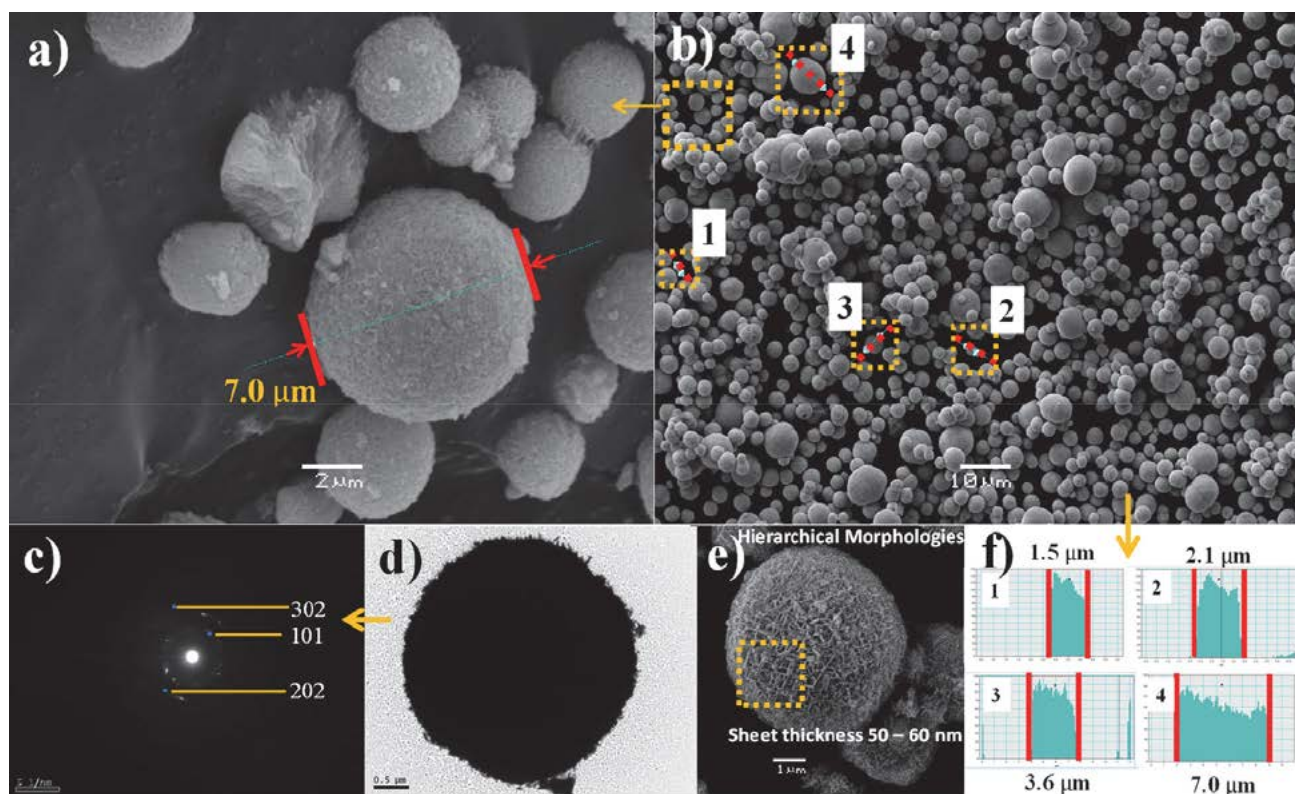


Figure 2. SEM and TEM images of BiOBr obtained for 18 h and 145 °C

3. Results and Discussion

3. 1. Characterization of (BiOBr-MicSphe)

The SEM and TEM analyzes of the BiOBr-MicSphe are shown in Figure 2. The spheres shown correspond to those obtained at a lower temperature (145 °C). The synthesis method used to obtain this type of material is efficient and does not produce another type of morphology different to the spherical one, as shown in the microscopy of Fig. 2a and Fig.2b. BiOBr-MicSphe diameter varied from 7.0 to 1.5 μm (Fig. 2f) and its consistency in the interior is completely porous (Fig. 2a). It is important to mention that, a smaller particle size promotes separation and migration of the photogenerated electron-hole pairs, improving the photocatalytic activity.⁴²

All the synthesized spheres presented hierarchical structures composed of sheets that are interlaced in inside, generating a structure highly porous and with greater surface area in comparison to smooth structures. On the other hand, an analysis of SEAD (selected area electron diffraction) of the sphere shown in Fig. 2d was performed. The diffraction pattern (Fig. 2c) showed the following crystalline planes (101), (202) and (303), characteristic to phases corresponding to BiOBr. Other phases were not found in the analyzes so it is concluded that all the spheres are constituted BiOBr tetragonal type. The above argument is reinforced with the XRD analyzes (Fig. 3) where the phases found for the spheres obtained at 145 °C correspond to tetragonal BiOBr.

The XRD pattern of the BiOBr-MicSphe synthesized at 145 °C and 217 °C, are shown in Fig. 3a and Fig. 3b, respectively. BiOBr synthesized at 145 °C, exhibited tetragonal structure according to the reference JCPDS Card 01-078-0348. No impurity peaks or presences of other phases were observed. In contrast, BiOBr-MicSphe synthesized at 217 °C shows a mixture of two phases. The first one corresponding to the tetragonal BiOBr (JCPDS Card: 01-078-0348), and the second one ascribed to the cubic phase of Bi₂O₃ (JCPDS Card: 01-077-0374). From the XRD pattern, the average size of crystallite (D) can be estimated by using the Scherrer's equation as follows:⁴³

$$D = \frac{K\lambda}{\beta \cos \theta} \quad (1)$$

where λ is the wavelength of X-ray radiation (λ = 0.15406 nm, for copper), K is the Scherrer's constant (K = 0.94), θ is the Bragg angle, β is the half width full maximum of the peak.⁴² The average crystal size for samples grown at 145 °C and 217 °C were 14.2 nm and 40.7 nm, respectively. The observed difference in the crystallite sizes, is a consequence of the different applied temperature during the growth process, since it is well-known that higher temperatures result in bigger crystal size.

The presence of Bi₂O₃ can be a consequence of the increased temperature during the BiOBr fabrication process. The solvent of the reactants is ethylene glycol which is

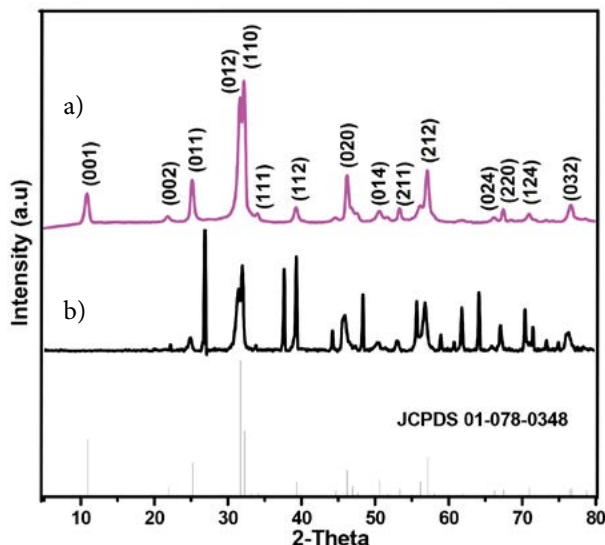
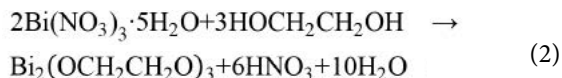
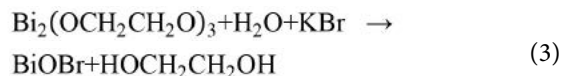


Figure 3. XRD patterns and BiOBr obtained for 18 h at a) 145 °C and b) 217 °C.

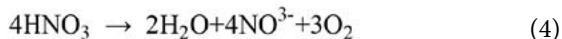
a coordinator agent that prevents premature hydrolysis of bismuth nitrate in nitric acid in the solvothermal synthesis of BiOBr (Eq. 2).³⁰



At low temperature, reacts slowly with water and bromide, forming the BiOBr and releasing the ethylene glycol (Eq. 3).



whenever the temperature increases in autoclave conditions, nitric acid dissociates and acts as a strong oxidizing agent, consuming halides, and transforming the Br⁻ in Br₂ (Eqs. 4 and 5):

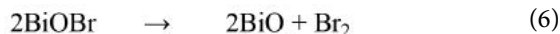


Equation 3, shows that the reaction releases H⁺ ions, whereas that in Eqs. 4 and 5 the reactions consume H⁺. Some works have reported that under acid condition the synthesis of BiOBr is favorable, whereas to basic pH BiOBr materials are poor in halogen.⁴⁴ Thus, as the temperature rises the pH increases favoring the formation of Br₂ and leading to less bromide ions (Br⁻) ions available. In this way, once bromide ions are consumed, Bi³⁺ reacts with O₂ to form Bi₂O₃. This information is supported by the qualitative analysis of chemical composition by EDS (supplementary material (Fig.S1)).

On the other hand, Figure 4 shows the thermograms of BiOBr obtained at 145 °C and 217 °C of the materials that

shown the higher and the lower photocatalytic activity, respectively. It can be clearly seen a loss of weight in a multistage process, where the decomposed products are not stable intermediates for both cases. Both thermograms show that the materials suffer weight loss during the analysis. Between 40 to 300 °C, no significant decrease in weight is observed (about 5%), which is associated with the loss of water of hydration.

It can be seen from the curve corresponding to BiOBr obtained at 145 °C (Fig. 4a), that close to 600 °C the material has a first significant weight loss, which may be generated by the thermal decomposition of the microspheres monoxide bismuth (BIO) and Br₂ (Eq. 6)



The second and last significant weight loss of this material occurs at 900 °C, which may be ascribed to the decomposition of BiO in Bi₂O₃ and metallic bismuth (Eq. 7). A total reduction of 46% of weight is observed from 300 °C to 900 °C.^{46–50}

In the case of sample obtained at 217 °C (Fig. 4b), weight loss starts at 400 °C and only a 35% of weight re-

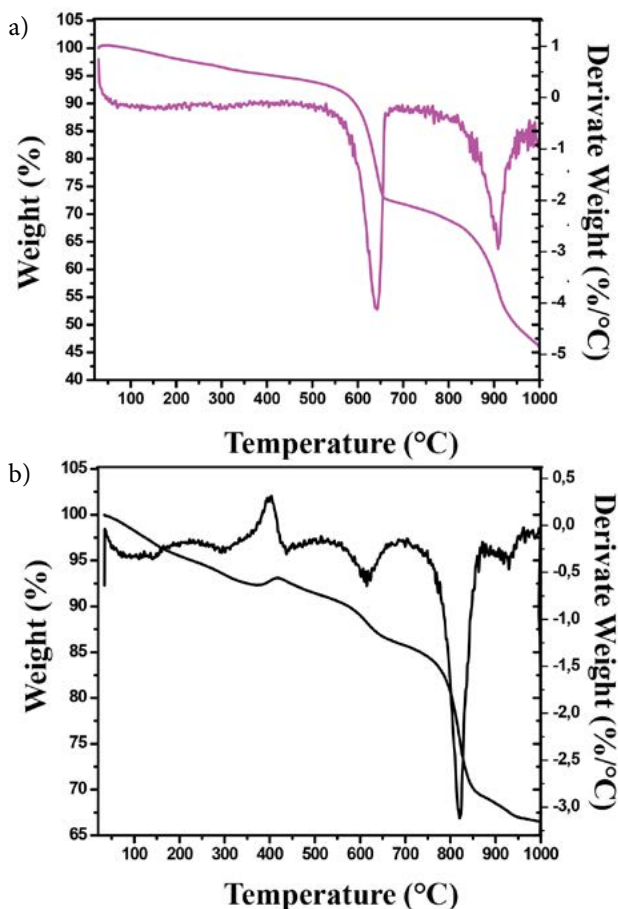


Figure 4. TGA-DTA profile of BiOBr obtained for 18 h at a) 145 °C and b) 217 °C.

duction is observed at 900 °C. These results show that BiOBr synthesized at 217 °C could be more thermally stable than the material synthesized at 145 °C. This higher thermal stability exhibited by BiOBr synthesized at 217 °C is a consequence of the presence of Bi₂O₃, which is known to be more stable for a wide range of temperatures.^{46,47}

The BJH isotherm of the materials synthesized at 145 °C and 217 °C are shown in Fig. 5. The sample obtained at 145 °C exhibit irreversible type IV adsorption isotherms with an H3 hysteresis loop confirming the mesopore structure.⁴⁸ In addition, pore size distribution is around 14 nm, as shown in Fig. 5a (inset). In contrast, the material synthesized at 217 °C exhibits a type II isotherm characteristic of a non-porous material, this material does not exhibit a porous morphology (Fig. 5b).

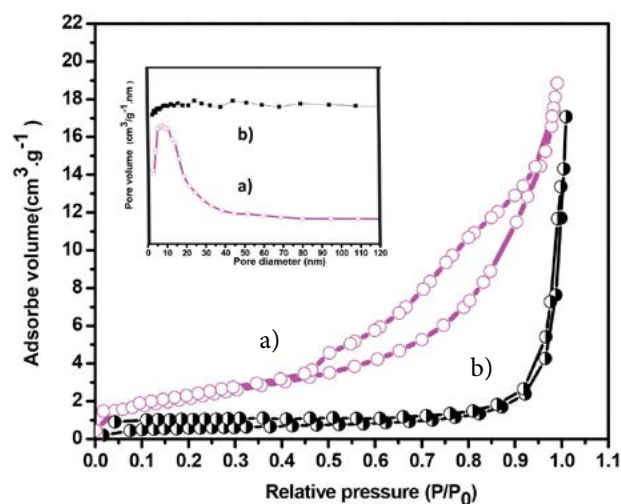


Figure 5. adsorption-desorption isotherms of BiOBr obtained for 18 h at a) 145 °C and b) 217 °C.

Table 1 shows the average values of textural properties of the synthesized materials obtained at different reaction temperatures, determined by nitrogen adsorption at 77 K. The higher value of surface is in relation with the high catalytic activity showed by BiOBr material with microspheres morphology, since it is known that higher surface area favors the catalytic activity.⁴⁹

Table 1: Values of textural properties of BiOBr materials prepared at 18 h reaction using 145 °C and 217 °C, respectively.

Temperature °C	BET m ² /g	Pore diameter (nm)	Pore Volume (cm ³ /g)
145	19	14	0,05
217	3	60	0,05

Figures 6a and 6b show the FTIR spectra of BiOBr-MicSphe synthesized at 145 °C and 217 °C, respectively. Spectrum of pure BiOBr microspheres (material obtained at 145 °C), exhibits two bands around 3500 and 1600 cm⁻¹, which are attributed to OH symmetrical stretching and

scissoring vibrations, due to adsorbed water.^{50,51} The absorption bands located at 512 cm⁻¹ and 770 cm⁻¹ are ascribed to the stretching vibrations of Bi-O (Fig. 5a). Signals registered in the infrared middle and far away from the BiOX, are in accordance with those reported in the literature for this type of materials.⁵² However, from spectrum corresponding of material synthesized at 217 °C, no peaks in the region between 3500 and 1600 cm⁻¹ are observed (Fig. 5b). Is possible that the OH bonds suffer rupture such as consequence of high temperature.

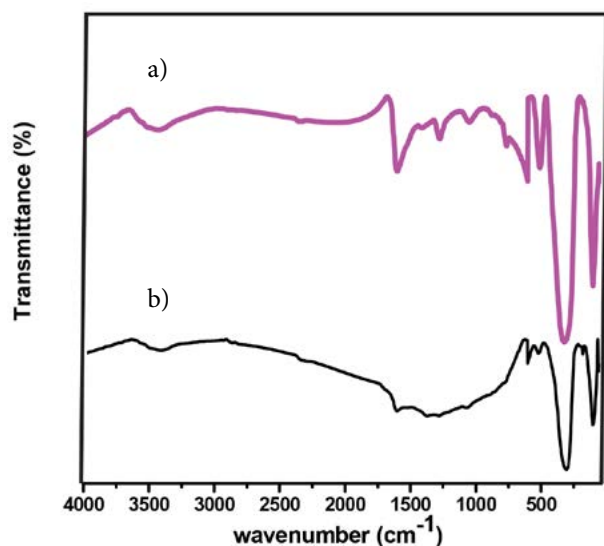


Figure 6. FTIR spectra of BiOBr obtained for 18 h at a) 145 °C and b) 217 °C.

The optical properties of the BiOBr-MicSphe synthesized at 145 °C and 217 °C were studied using diffuse reflectance spectroscopy (DRS) in the UV–vis range. Fig. 7 shows the DRS curves of the BiOBr obtained to different temperatures, from which the band gap were determined.

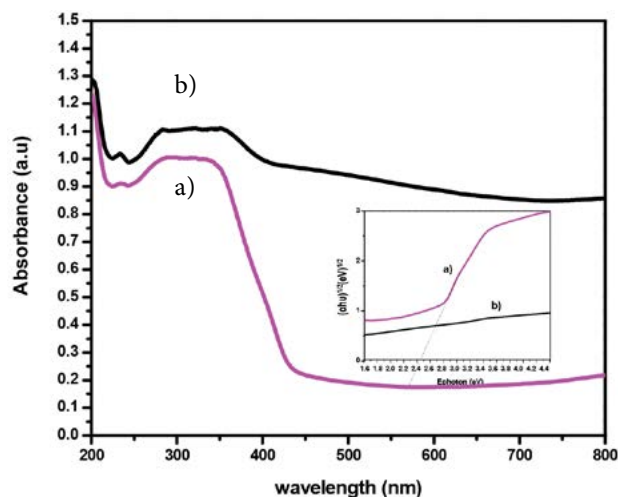


Figure 7. UV-Vis diffuse reflectance spectra (DRS) of BiOBr obtained for 18 h at a) 145 °C and b) 217 °C

The E_g of the materials were calculated by the Tauc representation, using the Eq. 8.

$$\alpha(h\nu) = A \cdot (h\nu - E_g)^{n/2} \quad (8)$$

Where α is the absorption coefficient, h is the Planck constant, ν is the light frequency, E_g is the band gap energy, and n is related to semiconductor transition ($n = 4$ for BiOBr.^{53–54} The inset in Fig. 7 allows the determination of the band gap directly from extrapolation in the Tauc plot. The values found were 2.88 ± 0.01 eV and 2.48 ± 0.01 eV for materials obtained at 145 °C and 217 °C, respectively. These values are in good agreement with those reported previously by several authors for BiOBr microspheres.^{54–55} The lower band gap of the sample grown at 217 °C could be a consequence of the increased crystal size of BiOBr.⁵⁶

In addition, the band-edge position of BiOBr can be estimated by using the following empirical equations.^{43,51}

$$E_{VB} = X - E^e + 0.5 \times E_g \quad (9)$$

$$E_{CB} = E_{VB} - E_g \quad (10)$$

Where E_{VB} is the valence band potential (VB) edge, E_{CB} is the conduction band potential (CB) edge, X is the electronegativity of the semiconductor (6.17 eV for BiOBr,⁵³ E^e is the energy of free electron on the hydrogen scale (about 4.5 eV), and E_g is the band gap energy of the semiconductor. Accordingly, E_{VB} and E_{CB} were calculated to be 3.11 ± 0.01 eV and 0.23 ± 0.02 eV for BiOBr grown at 145 °C, and 2.91 ± 0.01 eV and 0.43 ± 0.02 eV for BiOBr synthesized at 217 °C. These values agree with those reported by other authors.^{57–58} These parameters are very important to identify the reactive species in the photocatalytic reaction.⁵⁹

3. 2. Photocatalytic Efficiency

The 11 experiments performed to obtain the different BiOBr-MicSphe samples by simultaneously varying the temperature and the reaction times in the autoclave reactor are shown in Table 2.

The rate constants were used as response factor (Y); these constants are shown in Table 3 and were calculated considering that reaction kinetics gallic acid degradation follows a pseudo first-order reaction model as expressed in Eq. 11.^{60–61} The reaction order is assumed in catalytic processes when the initial pollutant concentration is low.⁶²

$$\ln \left(\frac{C_0}{C_t} \right) = kt \quad (11)$$

Where C_0 and C_t are the concentration of gallic acid in solution at time 0 and t , respectively, and k is the apparent first-order rate constant.

The polynomial shown in the Eq. 2 obtained by linear regression, represents the weight of the variables, reac-

Table 1: Experimental design and results of the rate constants calculated for each trial.

Experiment	Time hours	Temperature °C	Y exp. k (s ⁻¹)	Y calc. k (s ⁻¹)	% Degradation Experimental
1	12 (-1)	120 (-1)	$4,30 \times 10^{-5}$	$4,53 \times 10^{-5}$	37,7
2	24 (1)	120 (-1)	$4,00 \times 10^{-5}$	$4,33 \times 10^{-5}$	43,2
3	12 (-1)	200 (1)	$3,70 \times 10^{-5}$	$3,34 \times 10^{-5}$	32,5
4	24 (1)	200 (1)	$3,10 \times 10^{-5}$	$3,15 \times 10^{-5}$	37,6
5	9,52 (-√2)	160 (0)	$4,00 \times 10^{-5}$	$4,13 \times 10^{-5}$	39,2
6	24,5 (√2)	160 (0)	$4,10 \times 10^{-5}$	$4,41 \times 10^{-5}$	32,8
7	18 (0)	103,4 (-√2)	$4,90 \times 10^{-5}$	$4,53 \times 10^{-5}$	27,9
8	18 (0)	216,6 (√2)	$2,60 \times 10^{-5}$	$2,84 \times 10^{-5}$	14,7
9	18 (0)	160 (0)	$4,80 \times 10^{-5}$	$5,27 \times 10^{-5}$	43,9
10	18 (0)	160 (0)	$5,10 \times 10^{-5}$	$5,27 \times 10^{-5}$	42,5
11	18 (0)	160 (0)	$5,90 \times 10^{-5}$	$5,27 \times 10^{-5}$	44,6

Table 3: Photocatalytic activity of synthesized BiOBr materials prepared at 18 h reaction using 145 °C and 217 °C, respectively.

Temperature °C	Yield ^a (%)	experimental k [s ⁻¹]	Gallic acid ^b degradation (%)
145	50	$6,00 \times 10^{-5}$	48,2
217	20	$2,84 \times 10^{-5}$	14,7

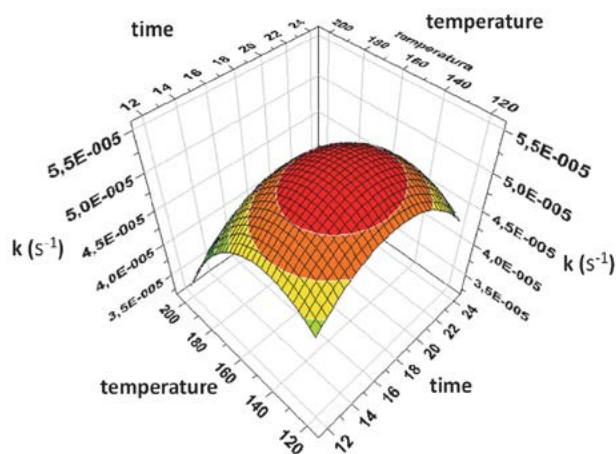
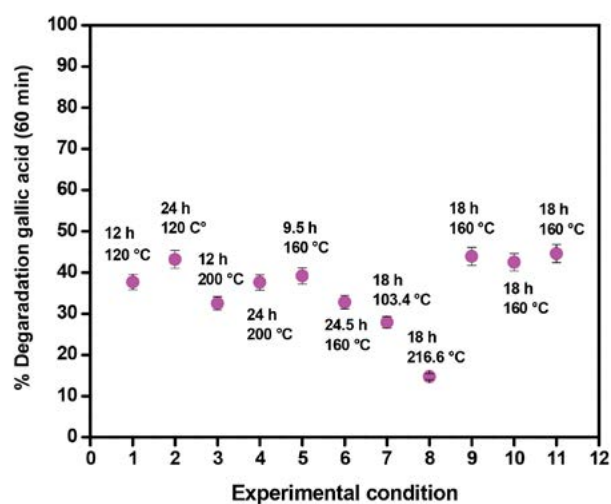
^a Calculated considering the theoretical yield^b After 60 min irradiation

tion time (t) and temperature (T) on the gallic acid degradation pseudo first order constant (Y). The validation of the model was performed using the ANOVA test. The values in parentheses in the response polynomial represent the standard deviation of each encoded coefficient. The model proposed in this study has an adequate correlation coefficient ($R^2 = 0.859$) and cross validation correlation coefficient ($Q^2 = 0.618$), values which validated the proposed model.²⁹

$$Y(k \text{ BiOBr}) = 5.27 \times 10^{-5} (\pm 2.60 \times 10^{-6}) - 9.48 \times 10^{-7}(t) (\pm 1.59 \times 10^{-6}) - 5.94 \times 10^{-6} (T) (\pm 1.59 \times 10^{-6}) - 6.39 \times 10^{-6} (t)^2 (\pm 1.90 \times 10^{-6}) - 7.90 \times 10^{-6} (T)^2 (\pm 1.90 \times 10^{-6}) \quad (12)$$

The Eq. 12 clearly shows that the most important variable in the solvothermal synthesis of BiOBr microspheres is the temperature, which normally exhibits a negative influence on the photocatalytic activity of the materials when it increases. Meanwhile, the reaction time has weak positive influence. A 3-D representation of response surface of the polynomial is shown in Fig. 8, where a noticeable maximum in the temperature axis is observed, indicating the optimum value of this variable to get the more active catalyst. In this case, the best conditions to obtain the most active catalyst are temperature of 145 °C and 18 h of reaction time.

Fig. 9, shows the correlation of photocatalytic degradation percentages on gallic acid with experimental conditions. Table 2 shown the results of the higher and lower

**Figure 8.** 3-D representation of response surface of the polynomial response.**Figure 9.** Correlation of photocatalytic degradation percentages on gallic acid with experimental conditions of table 2.

photocatalytic efficiency, measured as first order rate constant of gallic acid degradation and degradation percentages.

4. Conclusions

In this work, BiOBr microspheres were synthesized by solvothermal process under standardized conditions by controlling the reaction temperature and reaction time. The reaction temperature of 145 °C and time 18 hours, were established as the more appropriate values to obtain BiOBr with microspheres morphology and higher photocatalytic activity on degradation of gallic acid.

In addition, it was determined that the crystalline phase, chemistry composition, morphology, surface area, and size particle of these materials are strongly influenced by the reaction temperature variable, affecting thus directly the photocatalytic activity of these materials. Finally, from the characterization it is possible to conclude that BiOBr samples synthesized using the reported conditions here, are an appropriate material as a photocatalyst for gallic acid degradation under visible light.

5. Acknowledgements

This study was funded by Institutional Improvement Plan in Energy Efficiency and Environmental Sustainability (*Plan de Mejoramiento Institucional en Eficiencia Energética y Sustentabilidad Ambiental*) – Project Grant # PMI ULS 1401 of *Universidad de La Serena*.

6. References

1. F. Arsac, D. Bianchi, J. Chovelon, P. Conchon, C. Ferronato, A. Lair, M. Sleiman, *Mater. Sci. Eng. C*. **2008**, *28*, 722–725. DOI:10.1016/j.msec.2007.10.053
2. J. Herrmann, *Catalysis Today*. **1990**, *53*, 115–129. DOI:10.1016/S0920-5861(99)00107-8
3. U. Gaya, A. Abdullah, *J. Photochem. Photobiol. C*. **2008**, *9*, 1–12. DOI:10.1016/j.jphotochemrev.2007.12.003
4. A. Alinsafia, E. Abdulkarima, M. Ponsa, O. Zahraa, A. Benhammou, A. Yaacoubi, A. Nejmeddine, *Dyes Pigm.* **2017**, *74*, 439–445. DOI:10.1016/j.dyepig.2006.02.024
5. Y. Lan, Y. Lu, Z. Ren, *Nano Energy*. **2013**, *2*, 1031–1045. DOI:10.1016/j.nanoen.2013.04.002
6. M. Henderson, *Surface Science Report*. **2011**, *66*, 185–297. DOI:10.1016/j.surfrep.2011.01.001
7. S. Malato, M. Maldonado, J. Blanco, W. Gernjak, *Catalysis Today*. **2009**, *147*, 1–59. DOI:10.1016/j.cattod.2009.06.018
8. Z. Wang, W. Ma, J. Zao: Sensitization of Titania Semiconductor: A Promising Strategy to Utilize Visible Light, en: *Photocatalysis and Water Purification from Fundamentals to Recent Applications*, Wiley-VCH, Germany, **2018**, pp.199–231.
9. M. Pelaez, N. Nolan, S. Pillai, M. Seery, P. Falaras, A. Kontos, P. Dunlop, J. Hamilton, J. Byrne, K. O'Shea, M. Entezari, D. Dionysiou, *Applied Catalysis B*. **2012**, *125*, 331–349. DOI:10.1016/j.apcatb.2012.05.036
10. A. Di Paola, E. García, G. Marci, L. Palmisano, *J. Hazard. Mater.* **2012**, *211–212*, 3–29. DOI:10.1016/j.jhazmat.2011.11.050
11. C. Li, Z. Qiang, L. Wenhua, Y. Shuangfeng, *Prog Chem*. **2010**, *22*, 2282–2289.
12. S. R. Zhu, M. K. Wu, W. N. Zhao, F.-Y. Yi, K. Tao, L. Han, *J. Solid State Chem*. **2017**, *255*, 17–26. DOI:10.1016/j.jssc.2017.07.038
13. H. An, Y. Du, T. Wang, C. Wang, W. Hao, J. Zhang, *Rare Metals*. **2017**, *27*, 243–251. DOI:10.1016/S1001-0521(08)60123-0
14. X. Zhang, Z. Ai, F. Jia, L. Zhang, *Journal Phys. Chem. C*. **2008**, *112*, 747–753. DOI:10.1021/jp077471t
15. S. R. Zhu, Q. Qi, W. N. Zhao, M. K. Wu, Y. Fang, K. Tao, F. Y. Yi, L. Han, *Dalton Trans*. **2017**, *46*, 11451–11458. DOI:10.1039/C7DT01581J
16. J. Zhang, F. Shi, J. Lin, D. Chen, J. Gao, Z. Huang, X. Ding, C. Tang, *Chem. Mater*. **2008**, *20*, 2937–2941. DOI:10.1021/cm7031898
17. Z. Jiang, F. Yang, G. Yang, L. Kong, M. O. Jones, T. Xiao, P. P. Edwards, *J. Photochem. Photobiol. A*. **2010**, *212*, 8–13. DOI:10.1016/j.jphotochem.2010.03.004
18. H. Deng, J. Wang, Q. Peng, X. Wang, Y. Li, *Chem. Eur. J*. **2005**, *11*, 6519–6524. DOI:10.1002/chem.200500540
19. M. Shang, W. Wang, L. Zhang, *J. Hazard. Mater*. **2009**, *167*, 803–809. DOI:10.1016/j.jhazmat.2009.01.053
20. L. Zhang, X. Cao, X. Chen, Z. Xue, *J. Colloid Interf. Sci*. **2011**, *354*, 630–636. DOI:10.1016/j.jcis.2010.11.042
21. S. R. Zhu, M. K. Wu, W. N. Zhao, P. F. Liu, F. Yi, G. Li, K. Tao, L. Han, *Cryst. Growth Des*. **2017**, *17*, 2309–2313. DOI:10.1021/acs.cgd.6b01811
22. J. Wang, Y. Li, *Chem. Commun*. **2003**, *18*, 2320–2321. DOI:10.1039/b306189b
23. Y. Chen, M. Wen, Q. Wu, *Cryst. Eng. Comm*. **2011**, *13*, 3035–3039. DOI:10.1039/c0ce00955e
24. H. Cheng, B. Huang, Z. Wang, X. Qin, *Chem. Eur. J*. **2011**, *17*, 8039–8043. DOI:10.1002/chem.201100564
25. J. Zhang, F. Shi, J. Lin, D. Chen, J. Gao, Z. Huang, X. Ding, C. Tang, *Chem. Mater*. **2008**, *20*, 2937–2941. DOI:10.1021/cm7031898
26. J. Xu, W. Meng, Y. Zhang, L. Li, C. Guo, *Applied Catalysis B*. **2011**, *107*, 355–362. DOI:10.1016/j.apcatb.2011.07.036
27. Y. Huo, J. Zhang, M. Miao, Y. Jin, *Applied Catalysis B*. **2012**, *111–112*, 334–341.
28. Z. Šumić, A. Vakula, A. Tepić, J. Čakarević, J. Vitas, B. Pavlič, *Food Chemistry*. **2016**, *203*, 465–475. DOI:10.1016/j.foodchem.2016.02.109
29. Contreras D, Freer J, Rodríguez, J, *Inter. Biodeter. Biodegr*. **2006**, *57*, 63–68.
30. D. Contreras, Y. Moreno, Y. Salgado, G. Cardenas, R. Baggio, O. Peña, J. Pivan, *New J. Chem*. **2017**, *31*, 1751–1754. DOI:10.1039/b703592f
31. T. Lundstedt, E. Seifert, L. Abramo, B. Thelin, A. Nyström, J. Pettersen, R. Bergman, *Chemometrics Intell. Lab. Syst*. **1989**, *42*, 3–40. DOI:10.1016/S0169-7439(98)00065-3
32. A. Mera, C. Rodríguez, M.F. Meléndrez, H. Valdés, *J. Mater. Sci*. **2017**, *52*, 944–954. DOI:10.1007/s10853-016-0390-x
33. A. Mera, D. Contreras, N. Escalona, H. Mansilla, *J. Photo-*

- chem. Photobiol. A*. **2016**, *318*, 71–76.
DOI:10.1016/j.jphotochem.2015.12.005
34. F. Beltrán, O. Gimeno, F. Rivas, M. Carbajo, *J. Chem. Tech. Biotechnol.* **2006**, *81*, 1787–1796. DOI:10.1002/jctb.1605
35. M. Arienzo, E. Christen, W. Quayle W, *J. Hazard. Mater.* **2009**, *169*, 94–9. DOI:10.1016/j.jhazmat.2009.03.069
36. M. Petruccioli, J. Duarte, F. Federici, *J. Biosci. Bioengineering.* **2002**, *90*, 381–386. DOI:10.1016/S1389-1723(01)80005-0
37. M. Akassou, A. Kaanane, A. Crolla, C. Kinsley, *Water Sci. Technol.* **2010**, *62*, 475–83. DOI:10.2166/wst.2010.235
38. J. Fernández, J. kiwi, C. Lizama, J. Freer, J. Baeza, H. Mansilla, *J. Photochem. Photobiol. A Chem.* **2012**, *151*, 213–219. DOI:10.1016/S1010-6030(02)00153-3
39. C. Lizama, J. Freer, J. Baeza, H. Mansilla H, *Catalysis Today.* **2002**, *76*, 235–246. DOI:10.1016/S0920-5861(02)00222-5
40. F. Torrades, M. Pérez, H. Mansilla, J. Peral, *Chemosphere.* **2013**, *53*, 1211–1220. DOI:10.1016/S0045-6535(03)00579-4
41. M. Pérez, M. Graells, L. J. Del Valle, E. Centelles, H. Mansilla, *Catalysis Today.* **2017**, *124*, 163–171. DOI:10.1016/j.cattod.2007.03.034
42. B. Leckner, *Sol. Energy.* 1978, *20*, 143–150. DOI:10.1016/0038-092X(78)90187-1
43. A. Mera, Y. Moreno, J. Pivan, O. Peña, H. Mansilla, *J. Photochem. Photobiol. A Chem.* **2014**, *289*, 7–13. DOI:10.1016/j.jphotochem.2014.05.015
44. D. Smilgies, *J. Appl. Crystallogr.* **2009**, *42*, 1030–1034. DOI:10.1107/S0021889809040126
45. Y. Guan, H. Qian, J. Guo J, Yang S, Wang X, Wang S, Fu Y, *Appl. Clay Sci.* **2015**, *114*, 124–132. DOI:10.1016/j.clay.2015.05.017
46. X. Xiao, R. Hu, C. Liu, C. Xing, X. Zuo, J. Nan, L. Wang, *Chem. Eng. J.* **2013**, *225*, 790–797. DOI:10.1016/j.cej.2013.03.103
47. J. Song, C. Mao, H. Niu, Y. Shen, S. Zhang, *Cryst. Eng. Comm.* **2010**, *12*, 3875–3881. DOI:10.1039/c003497p
48. J. Tóth, *Colloids Surf.* **1990**, *49*, 57–69. DOI:10.1016/0166-6622(90)80092-1
49. C. Yu, W. Zhou, H. Liu, Y. Li, D. Dionysiou, *Chem. Eng. J.* **2016**, *287*, 117–129. DOI:10.1016/j.cej.2015.10.112
50. Z. Liu, X. Xu, J. Fang, X. Zhu, J. Chu, B. Li, *Appl. Surf. Sci.* **2012**, *258*, 3771–3778. DOI:10.1016/j.apsusc.2011.12.025
51. Z. Liu, B. Wu, Y. Zhu, D. Yin, L. Wang, *Catal. Lett.* **2012**, *142*, 1489–1497. DOI:10.1007/s10562-012-0899-9
52. J. Cao, X. Li, H. Lin, S. Chen, X. Fu, *J. Hazard. Mater.* **2012**, *239–240*, 316–324. DOI:10.1016/j.jhazmat.2012.08.078
53. Z. Liu, X. Xua, J. Fang, X. Zhua, J. Chua, B. Li, *Appl. Surf. Sci.* **2012**, *258*, 3771–3778. DOI:10.1016/j.apsusc.2011.12.025
54. J. Tauc, R. Grigorovici, A. Vancu, *Phys. Stat. Solid B.* **1966**, *15*, 627. DOI:10.1002/pssb.19660150224
55. D. Wood D, J. Tauc, *Phys. Rev. B.* **1972**, *5*, 3144.
56. X. Xion, L. Ding, Q. Wang, Y. Li, Q. Jiang, J. Hu, *Appl. Catalysis B.* **2016**, *188*, 283–291. DOI:10.1016/j.apcatb.2016.02.018
57. C. Rodriguez, M. Sandoval, G. Cabello, M. Flores, H. Fernández, C. Carrasco C, *Mater. Res. Bul.* **2014**, *60*, 313–321. DOI:10.1016/j.materresbull.2014.08.047
58. P. Wang, P. Yang, Y. Bai, T. Chen, X. Shi, Y. Ye, X. Zhang, *J. Taiwan Ins. Chem. Eng.* **2016**, *68*, 295–300. DOI:10.1016/j.jtice.2016.09.013
59. J. Luo, X. Zhou, L. Ma, X. Xu, *J. Molecular Catalysis A Chem.* **2015**, *410*, 168–176. DOI:10.1016/j.molcata.2015.09.019
60. A. Kontos, I. Arabatzis, D. Tsoukleris, M. Bernard, D. Petrakis, P. Falaras, *Catalysis Today.* **2015**, *101*, 275–281. DOI:10.1016/j.cattod.2005.03.003
61. J. Herrmann, *Catalysis Today.* **1999**, *53*, 115–129. DOI:10.1016/S0920-5861(99)00107-8
62. H. Pardue. *Anal. Chim. Acta.* **1989**, *216*, 69–107. DOI:10.1016/S0003-2670(00)82005-X

Povzetek

Mikrosfere BiOBr s hierarhično morfologijo (BiOBr-MicSphe) imajo potencialno uporabo v heterogeni fotokatalizi v procesih dekontaminacije vode in zraka. Zaradi tega je sinteza, karakterizacija in vrednotenje fotokatalitske aktivnosti teh materialov postala pomembna. V članku poročamo o sintezi mikrosfer BiOBr pri kateri smo uporabljali različne razpone reakcijskih temperatur (120–200 °C) in reakcijskega časa (12 h – 24 h). Vzorci, pripravljani pri 145 °C in 18 h, so pokazali višjo fotokatalitsko aktivnost pri degradaciji galske kisline. Morfološke lastnosti, kemična sestava in strukturna analiza so pokazali, da je imel vzorec z višjo fotokatalitsko aktivnostjo mikrosferično morfologijo s čisto BiOBr tetragonalno fazo. Poleg tega je adsorpcijsko-desorpcijska analiza pokazala manjši premer por v vzorcu, pripravljenem pri 145 °C v 18 urah. Reakcijska temperatura močno vpliva na različne lastnosti materiala, ki posledično vplivajo na fotokatalitsko aktivnost.

Scientific paper

Recovery of Antioxidant Compounds from Aronia Filter Tea Factory by –Product: Novel Versus Conventional Extraction Approaches

Aleksandra Gavarić, Milica Ramić, Jelena Vlačić, Branimir Pavlić,
Robert Radosavljević and Senka Vidović*

Faculty of Technology, University of Novi Sad, 21000, Bulevar cara Lazara 1, Novi Sad, Serbia

* Corresponding author: E-mail: senka.curcin@yahoo.com
+381 21 485 3731

Received: 19-01-2018

Abstract

Black chokeberry (*Aronia melanocarpa* L.) by-product from filter tea factory underwent subcritical water extraction (SWE) in order to recover polyphenolics and determine its antioxidant potential. In the current study Box-Behnken design was applied for optimization. Independent variables used in experimental design were temperature (T, 120–200 °C), extraction time (t, 15–35 min) and hydrochloride concentration (c, 0–1.5%). Experimental results were fitted to a second-order polynomial model where multiple regression analysis and analysis of variance were used to determine fitness of the model and optimal conditions. The optimized SWE conditions for maximum responses of total phenols (TP), total flavonoids (TF) and monomeric anthocyanins (MA) contents, and minimum response of IC₅₀ were temperature of 120.4 °C, extraction time of 15.2 min and absence of acidifier. The predicted values of TP, TF, MA and IC₅₀ at these conditions were: 32.8863 mg GAE/g, 23.5164 mg CE/g, 0.5124 mg C3G/g and 0.0055 mg/mL, respectively.

Keywords: *Aronia melanocarpa* L.; subcritical water extraction; antioxidants; response surface methodology; optimization

1. Introduction

Aronia melanocarpa L. (commonly known as black chokeberry) is a perennial shrub which originates from North America.¹ Aronia berries are one of the richest plant sources of anthocyanins, mainly containing cyanidin glycosides,² which constitutes 25% of the total polyphenols.³ This member of *Rosaceae* family is also recognizable for possessing the highest *in vitro* antioxidant capacity among berries.⁴ Besides anthocyanins, chokeberries are abundant in proanthocyanidins and hydroxycinnamic acid.⁵ Dominant proanthocyanidins are epicatechin oligomers, which have share of 66% in aronia fruit polyphenols.³ There is a growing interest in utilization of anthocyanins and proanthocyanidins, due to their antioxidant potential and positive correlation between their consumption and prevention of colon cancer, cardiovascular disease,¹ diabetes mellitus type II and hepatoprotective effect.⁶ Beside use of aronia berries in medical purposes it is widely exploited in the food industry, either on its own, or mixed with other

fruits (e.g. in juices, syrups, jams, wine production, food colouring, dietary supplements).^{7,8}

Today, biowaste streams e.g. low volume agro-food waste streams like leaves, stems, bulbs, flowers and exhausted cakes pose environmental risks while being an important potential feedstock resource for producing a wide range of novel bioproducts. Their utilization is limited by the lack of technologies able to process heterogeneous mixtures beyond existing technologies, that fully break down the valuable complexity of components, or specific extraction and separation technologies, which are excessively costly. In the production of aronia juice, after extraction step, many phenolic compounds including anthocyanins are still present in the cake and could be valorized by adequate extraction process. Therefore, solids left after production of aronia juice in fruit factory are used as a raw material for the production of fruit filter tea.

Dry aronia cake underwent several processes: cutting, grinding, milling, sifting and fractionating. After these technological processes approximately 20% of input batch is of particle size lower than the particle size of pores

of filter tea bag. Since this fraction cannot be packed into filter bags it represents by-product also known as fruit dust. As this material has particle size lower than 0.315 mm, it could be successfully used for extraction as plant particles with low particle size represent a convenient crude material for extraction. The main reason for that is increased mass transfer of bioactives from powdered plant material to liquid phase.⁹

Solvent extractions are the most common extraction methods for phenolic compounds. Solvents such as ethanol, methanol, acetone, ethyl acetate, as well as their combination and mixture in different proportion with water are the most often used solvents in classical extractions.¹⁰ Classical methods of extraction, apart from using solvents with negative environmental impact, very often exert low selectivity and efficiency of extraction as well as long extraction time. Additionally, further processing of obtained liquid extracts is necessary in order to removal of the solvents. Subcritical water extraction (SWE) is a green solvent extraction technique which uses water at temperatures between 100 and 374 °C and pressure high enough to keep it in the liquid state.¹¹ Water on room temperature is an inadequate extraction solvent for phenolic compounds, due to high dielectric constant. However, variations of temperature allow modification of dielectric constant of water in that way altering its selectivity. At elevated temperature, the initial value of dielectric constant of 80 at 25 °C decreases to 27 at 250 °C which falls between those of ethanol ($\epsilon = 24$) and methanol ($\epsilon = 33$) at 25 °C.¹² Therefore, subcritical water is successfully employed for phenols extraction from different sources.^{13–18} In a great deal of studies its advantage considering extraction efficiency comparing to classical technologies has been confirmed.^{14,16,19} Furthermore, SWE reduces energy consumption by 3–5 folds when compared to traditional solvent extraction.²⁰ However, long exposure of material to high temperatures can cause oxidization of phenolic compounds. Hence, it is necessary to select the most appropriate extraction method and optimize the process in order to achieve maximal extraction efficiency and highest quality of obtained extracts.¹⁰

The main purpose of this study was to investigate the advantages of green extraction technology, subcritical water extraction, over conventional extraction technique in attempt to valorize aronia fruit dust as alternative source of dietary antioxidants. Another reason for choosing aronia filter tea by-product for this investigation is due to its convenient chemical profile regarding polyphenols, mostly anthocyanins and procyanidins responsible for positive effects on human health.

2. Materials and Methods

2.1. Plant Material and Chemicals

The chokeberry fruit dust was purchased from Fructus (Backa Palanka, Serbia), a local filter tea factory, and

stored in paper bags at a room temperature until analysis. Fraction with particle size lower than filter tea bag, i.e. herbal dust, was used as a raw material for the production of chokeberry fruit filter-tea. Moisture content of dried chokeberry powder was 8.66%.

Folin-Ciocalteu reagent, (\pm)-catechin and 1,1-diphenyl-2-picryl-hydrazyl-hydrate (DPPH) were purchased from Sigma (Sigma-Aldrich GmbH, Steinheim, Germany). Gallic acid was purchased from Sigma (St. Louis, MO, USA). All other chemicals used were of analytical reagent grade.

2.2. Maceration

Traditional extraction procedure was performed by maceration of 10.0 g of chokeberry fruit dust with 30, 50 and 70% ethanol (1:10; m/v) at room temperature (25 °C) for 24 h. Extraction was performed in shaker with temperature control (KS 4000i, IKA, Germany), and shaking (150 rpm) was used in order to agitate extraction. After extraction, extracts were immediately filtered through filter paper under vacuum (V-700, Büchi, Switzerland). Extracts were collected into glass flasks and stored at 4 °C until the analysis.

2.3. SWE Procedure

SWE was performed in batch-type high-pressure extractor (Parr Instrument Company, USA) with internal volume 450 mL, and maximum temperature 200 °C, connected with temperature controller (4838, Parr Instrument Company, USA). Extraction procedure was described elsewhere.²¹ Temperature (T, 120–200 °C), extraction time (t, 15–35 min) and HCl concentration (c, 0–1.5%) were independent variables. Operating pressure of 30 bar was kept constant. This pressure was slightly in excess of that required (20 bar) to prevent the formation of steam within the extraction cell. During extraction period, temperature was held constant (stationary phase) for different extraction time depending on experimental run. After the extraction, extractor was cooled in ice-bath during approximately 5 min to reach room temperature. After extraction, extracts were immediately filtered through filter paper under vacuum, collected into glass flasks and stored at 4 °C until the analysis.

2.4. Total Phenols (TP) and Flavonoids Content (TP)

TP content in obtained liquid extracts was determined using Folin-Ciocalteu procedure.²² Content of phenolic compounds was expressed as mg of gallic acid equivalents (GAE) per g dry weight (DW). Total flavonoids content was determined using aluminum chloride colorimetric assay.²³ All experiments were performed in triplicate, and results are expressed as mean values.

2. 5. Determination of Monomeric Anthocyanins Content (MA)

MA content in the samples was estimated using a VIS-spectrophotometer by the pH differential method reported by Abu Bakar et al.²⁴ with slight modifications.²⁵ Two buffer systems, potassium chloride buffer, pH 1.0 (0.0025 M) and sodium acetate buffer, pH 4.5 (0.4 M), were used. Briefly, 400 μ L of sample (diluted liquid extract) was added in 3.6 mL of corresponding buffer solutions and absorbance was measured against a blank probe at 510 and 700 nm. Absorbance (*A*) was calculated as:

$$A = (A_{510} - A_{700})pH_{1.0} - (A_{510} - A_{700})pH_{4.5} \quad (1)$$

Anthocyanin concentration in the extract was calculated and expressed as cyanidin-3-glycoside equivalent (C3G):

$$MA = (A \cdot MW \cdot DF \cdot 1000) / Ma \quad (2)$$

where ΔA is difference in absorbance, MW is a molecular weight for cyanidin-3-glucoside (449.2 g/mol), DF is the dilution factor of the samples and Ma is the molar absorptivity of cyanidin-3-glucoside (26.900 M/cm). Results were expressed as mg of cyanidin-3-glucoside equivalents per g DW.

2. 6. DPPH Assay

Free radical scavenging activity of samples was determined using DPPH assay, previously described by Espin et al.²⁶ A certain volume of diluted sample was mixed with 95% methanol and 90 μ M 1,1-diphenyl-2-picryl-hydrazyl (DPPH) in order to obtain different final concentrations. After incubation on room temperature for 60 min, the absorbance was measured at 515 nm and result was expressed as radical scavenging capacity (RSC, %) which was calculated using following equation:

$$\%RSC = 100 - \frac{(A_{sample} \times 100)}{A_{blank}} \quad (3)$$

where A_{sample} is the absorbance of sample solution and A_{blank} is the absorbance of blank probe. Antioxidant activity was further expressed as inhibition concentration at 50% of RSC value (IC_{50}). IC_{50} represents the concentration of plant extract required to obtain 50% of radical scavenging capacity, expressed as mg per mL. All experiments were performed in triplicate, and results are expressed as mean values.

2. 7. Box-Behnken Design and Statistical Analysis

The extraction efficiency of subcritical chokeberry extract can be influenced by variety of factors such as pressure, temperature, extraction time, pH and volume of the

solvent and time of the static extraction. In the current study RSM coupled with Box-Behnken design (BBD) was applied in order to optimize SWE process. Design consisted of fifteen randomized runs with three replicates at the central point. Independent variables used in experimental design were temperature (*T*, 120–200 °C), extraction time (*t*, 15–35 min) and hydrochloride concentration (*c*, 0–1.5%). In order to normalize parameters, each of the coded variables was forced to range from –1 to 1, so that they all affect the response more evenly, and so the units of the parameters are irrelevant.²⁷ The natural and coded values of independent variables used in BBD are presented in Table 1.

Table 1. Experimental domain with natural and coded values of independent variables used in BBD

Independent variable	Factor levels		
	–1	0	1
Temperature [°C]	120	160	200
Extraction time [min]	15	25	35
c (HCl) [%]	0	0.75	1.5

The response variables were fitted to the following second-order polynomial model (Eq. (4)) which is generally able to describe relationship between the responses and the independent variables:

$$Y = \beta_0 + \sum_{i=1}^3 \beta_i X_i + \sum_{i=1}^3 \beta_{ii} X_i^2 + \sum_{i < j=1}^3 \beta_{ij} X_i X_j \quad (4)$$

where *Y* represents the response variable, X_i and X_j are the independent variables affecting the response, and β_0 , β_i , β_{ii} , and β_{ij} are the regression coefficients for intercept, linear, quadratic and interaction terms, respectively. Optimal extraction conditions were determined considering total phenolic and total flavonoid content, and antioxidant activity simultaneously as responses. Treatment of multiple responses and selection of optimal conditions were based on desirability function *D*.²⁸ The experimental design and multiple linear regression analysis were performed using Design-Expert v.7 Trial (Stat-Ease, Minneapolis, Minnesota, USA). The fitness of the polynomial model equation was expressed by the coefficient of determination (R^2) and its statistical significance was confirmed by *F*-test at a probability (*p*) of 0.05.

3. Results and Discussion

3. 1. Extraction Solvent

Extraction is the first and important step in isolation and purification of bioactive compounds from herbal mate-

rial. Maceration, traditional extraction method, is influenced by several factors such as type and concentration of solvent, solid/liquid ratio, temperature, extraction time, particle size of solute, pH, etc. Ethanol is considered a suitable solvent for extraction of phenols from various sources.^{29,30} This is due to the wide range of phenols that the aqueous ethanol mixtures can dissolve. For dried chokeberry dust, a wide range of ethanol concentration was tested with the result of 50% ethanol being superior regarding yields of TP, TF and MA.³¹ Also in our study, selection of the most appropriate ethanol concentration was based on the yields of TP, TF and MA. Extraction yield for each group of compounds is presented in Fig. 1, from where it could be seen that 50% ethanol provided highest yields of TP and TF and MA. Several authors also reported that the use of medium concentration of ethanol (50%) resulted in higher TP yields compared with other ethanol/water ratios.^{32,33}

Previous studies reported that binary solvent system, containing hydro-organic solvents, was superior comparing to mono-component solvent system in the extraction of phenolic compounds.^{34,35} Water is responsible for swelling of plant material, while ethanol plays a key role in disrupting the bonding between the solutes and plant matrix thus enabling improved mass transfer of the compounds. Čujić et al.³³ investigated effects of extraction time (15, 30, 60 and 90 min) on total phenolic and total anthocyanins contents of aronia dried fruit and concluded that extraction time was not relevant regarding yields of TP and MA. In present study, duration of maceration was fixed (24 h).

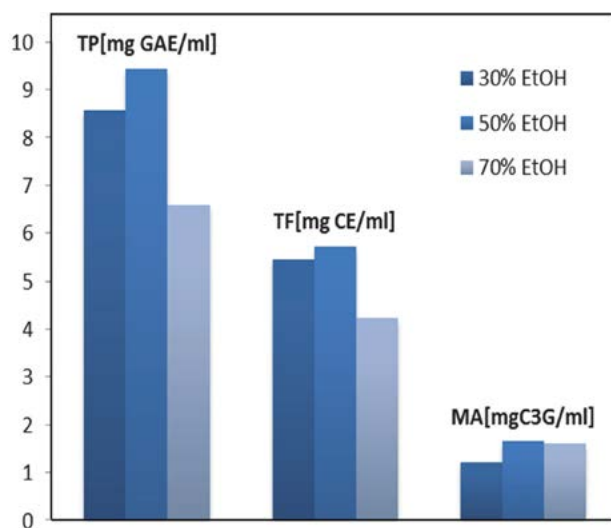


Figure 1. Extraction yields of desirable groups of compounds obtained with different concentration (30, 50 and 70%) of ethanol for 24 h

3.2. Effects of Extraction Parameters on Total Phenolics Content

It is known that processing of aronia berries into juice can significantly affect its polyphenol composition. However, due to their astringent taste and storage issue,

most of the bioavailability tests and clinical trials are conducted with juices instead of berries.³⁶ TP obtained in chokeberry subcritical extracts varied from 13.1579 to

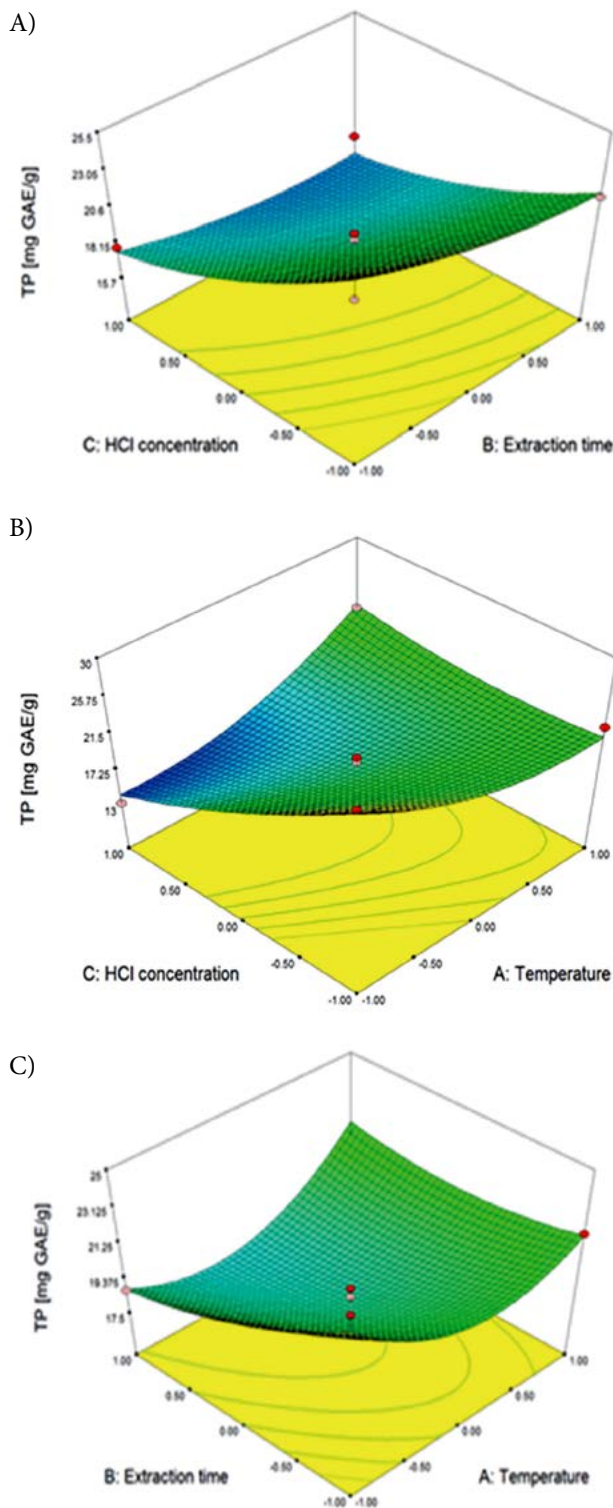


Figure 2. Response surface plots showing combined effects of process variables: (A) HCl concentration and extraction time, (B) HCl concentration and temperature and (C) extraction time and temperature on total phenolics content

Table 2. Box-Behnken design of the three-level and three-variables and observed responses under different experimental conditions

Run	Independent variables			Investigated responses			
	X ₁ Temperature [°C]	X ₂ Time [min]	X ₃ c (HCl) [%]	TP [mg GAE/g]	TF [mg CE/g]	IC ₅₀ [mg/ml]	MA [mg C3G/g]
1	160 (0)	15 (-1)	1.5 (1)	17.8520	4.1595	0.1140	0.0401
2	120 (-1)	25 (0)	0 (-1)	29.5536	22.1000	0.0361	0.3473
3	120 (-1)	15 (-1)	0.75 (0)	24.9044	14.8682	0.0664	0.2672
4	160 (0)	25 (0)	0.75 (0)	17.9643	4.9700	0.0822	0.0508
5	160 (0)	25 (0)	0.75 (0)	18.3911	5.3776	0.1125	0.0574
6	200 (1)	15 (-1)	0.75 (0)	21.8050	11.2604	0.0827	0.0628
7	200 (1)	35 (1)	0.75 (0)	20.6595	6.2840	0.0746	0.0908
8	160 (0)	25 (0)	0.75 (0)	18.8627	5.8600	0.1296	0.0735
9	200 (1)	25 (0)	0 (-1)	22.3665	14.9685	0.0062	0.3300
10	200 (1)	25 (0)	1.5 (1)	22.1419	9.4655	0.0726	0.0521
11	160 (0)	35 (1)	0 (-1)	21.3558	11.2568	0.0214	0.1015
12	160 (0)	15 (-1)	0 (-1)	24.1857	13.1915	0.0291	0.4622
13	120 (-1)	25 (0)	1.5 (1)	13.1579	8.3000	0.1333	0.3348
14	160 (0)	35 (1)	1.5 (1)	17.1333	5.1340	0.1128	0.0414
15	120 (-1)	35 (1)	0.75 (0)	18.7504	10.9809	0.0900	0.3256

Table 3. Estimated coefficients of the fitted second-order polynomial model for TP, TF, IC₅₀ and MA, and analysis of variance (ANOVA) for the investigated systems

Term	Regression coefficient			
	TP [mg GAE/g]	TF [mg CE/g]	IC ₅₀ [mg/ml]	MA [mg C3G/g]
β_0	18.4060	5.4025	0.1081	0.0606
Linear				
β_1	0.0758	-1.7838*	-0.0112	-0.0924*
β_2	-1.3560*	-1.2280**	8.2500E-004	-0.0341
β_3	-3.3971*	-4.3072*	0.0425*	-0.0966*
Cross product				
β_{12}	1.2521	-0.2723	-7.9425E-003	-7.5980E-003
β_{13}	4.0428*	2.0743*	-7.6975E-003	-0.0663
β_{23}	0.5278	0.7273	1.6225E-003	0.0905**
Quadratic				
β_{11}	2.3985*	5.3594*	-0.0185	0.1154*
β_{22}	0.7253	0.0864	-0.0112	0.0107
β_{33}	1.0004	2.9465*	-0.0276**	0.0901**
R ^{2a}	0.9629	0.9682	0.8970	0.8959
CV ^b	6.0900	15.0400	27.6200	45.6000
p _m -Value ^c	<0.0050	<0.0050	<0.0500	<0.0500
p _{lf} -Value ^d	0.0759	0.0535	0.6490	0.01270

* Significant at 5%; **Significant at 10%; a Coefficient of multiple determination; b Coefficient of variance [%]; c Probability of F value for the model; d Probability of F value for the lack of fit

29.5536 mg GAE/g, while TP obtained by maceration with 30, 50 and 70% ethanol provided notably higher values, 306.1392; 351.0761 and 273.3627 mg GAE/g, respectively. The lowest yield for investigated response was obtained at temperature of 120 °C, extraction time of 25 min and added 1.5% HCl, while TP (29.5536 mg GAE/g) was found to be the highest at temperature of 120 °C, extraction time of 25 min and absence of acidifier. This indicates

weak influence of both temperature and extraction time on TP yield. Ju and Howard³⁷ observed 31% decrease of total phenolics in red grape skin subcritical extracts, when temperature increased from 100 to 160 °C.³⁷ Grunovaitė et al.³⁸ reported TP yield (182.89 mg GAE/g extract) of chokeberry pomace subcritical extract obtained at 130 °C. Combined influence of SWE parameters on the TP is presented in Fig. 2.

According to regression coefficients (Table 3), except for linear terms of extraction time and HCl concentration, all other effects of parameters were positive on TP content in SWE extracts. According to *p*-values for the regression coefficients, linear term of time, interaction term between temperature and HCl concentration and quadratic term of temperature exhibited significant influence ($p < 0.05$). The most influential was linear term of HCl concentration ($p < 0.0006$). Coefficient of multiple regression for this model ($p < 0.0045$) indicates excellent correlation between experimental and predicted values which was further supported by CV (6.09%) and R^2 (0.9629).

3. 3. Effects of Extraction Parameters on Total Flavonoids Content

Significant losses of flavonol glycosides occurred during the pressing operation, with 39–49% of the compounds being retained in the cake. The less polar quercetin hexosides (galactoside and glucoside) were retained to a greater extent in the cake than the more polar quercetin diglycosides. According to Wilkes et al.,³⁶ the majority of the non-polar quercetin aglycone was retained in the cake, while only 27% was expressed into the juice.

Experimental values of TF obtained under different SWE conditions are presented in Table 2. TF recovered in chokeberry subcritical extracts varied from 4.1595 to 22.1000 mg CE/g while TF obtained by maceration with 30, 50 and 70% ethanol provided significantly higher values, 194.4607; 213.1274 and 176.1847, respectively. The highest value (22.1000 mg CE/g) of investigated response was obtained under temperature of 120 °C, extraction time of 25 min and absence of acidifier, the same conditions as it was the case with TP content. This is consistent with previous findings, where total flavonol content increased 3.7-fold from 100 to 120 °C in red grape skin subcritical extracts. However, the lowest TF content was observed under temperature of 160 °C, extraction time of 15 min and with added 1.5% HCl. This is in accordance with literature, where total flavonol content of subcritical extracts declined 30% when temperature increased from 120 to 160 °C.³⁷ Combined influence of SWE parameters on the TF is presented in Fig. 3.

Statistical coefficients ($R^2 = 0.9682$, CV = 15.04%) indicated that this model represented satisfying fit to the experimental results. All three linear terms exhibited negative effect on TF content. According to *p*-values for the regression coefficients, linear terms showed significant influence while HCl concentration was the most influential ($p < 0.0004$) parameter, as it was the case with TP content. Interaction term between temperature and HCl concentration showed highly significant ($p < 0.05$) influence on TF content. Also, quadratic terms of temperature and HCl concentration exhibited highly significant ($p < 0.05$) influence.

3. 4. Effects of Extraction Parameters on Monomeric Anthocyanins

Wilkes et al.³⁶ reported that anthocyanins were more susceptible to losses during processing than flavo-

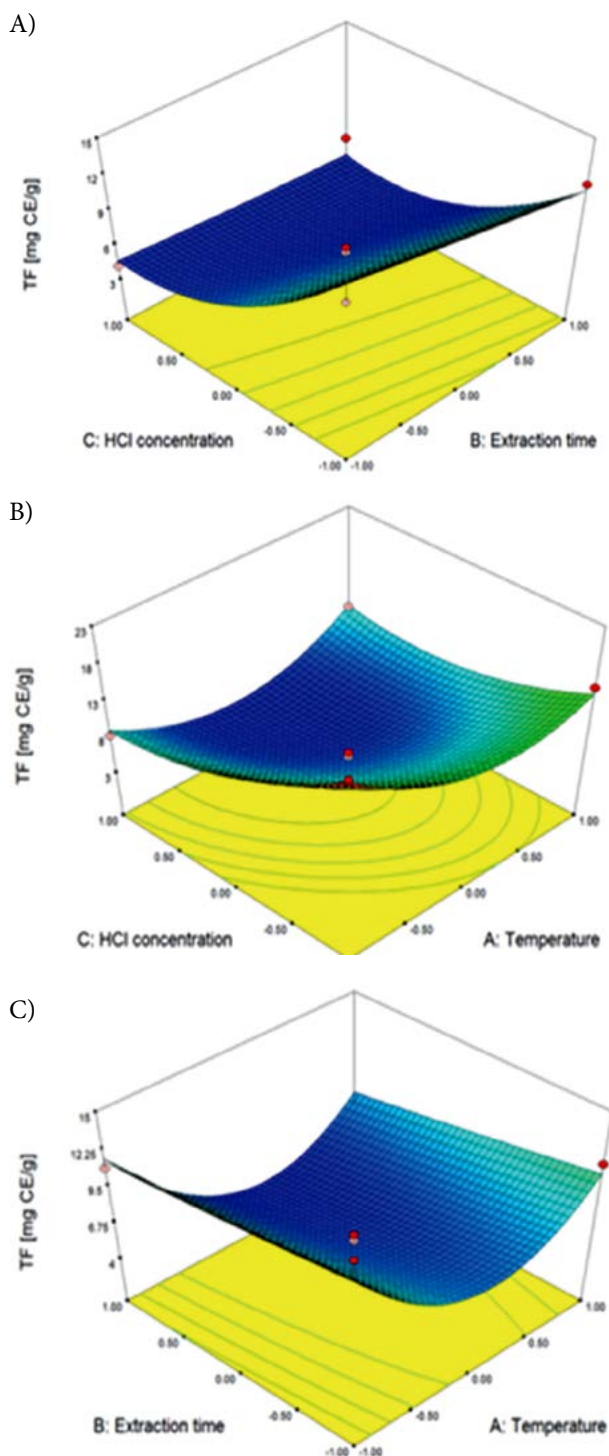


Figure 3 Response surface plots showing combined effects of process variables: (A) HCl concentration and extraction time, (B) HCl concentration and temperature and (C) extraction time and temperature on total flavonoids content

nols, total proanthocyanidins, and hydroxycinnamic acids as a result of thermal degradation, proven by increased levels of protocatechuic acid and phloroglucinaldehyde. The juice pressing step resulted in losses of all polyphenols due to physical removal of skins, while anthocyanins

and total proanthocyanidins were retained in the cake to a greater extent than hydroxycinnamic acids and flavonols. The cake contained 52, 51, 54 and 54% of the levels of cyanidin 3-galactoside, cyanidin 3-glucoside, cyanidin 3-arabinoside and cyanidin 3-xyloside found in the enzyme treated mash, respectively.³⁶ The importance of anthocyanins remaining within the cakes is quite significant, as Kalt et al.³⁹ claimed that antioxidant capacity in blueberries is mainly due to anthocyanins, although other phenolics also contribute to its antioxidant activities.³⁹ As aronia cake is mainly composed of fruit skins, which are high in pigment, rapid mass transport of the anthocyanins from the substrate using subcritical water facilitates fast and effective extraction process.⁴⁰ Experimentally obtained yields for monomeric anthocyanins under different SWE conditions are presented in Table 2, while regression coefficients and statistical analysis of investigated response are presented in Table 3. Extraction parameters demonstrated similar influence to TF and MA ($r = 0.702$), which was rather expected due to anthocyanins being a class of flavonoids. In order to improve understanding of multiple influences of all independent variables, response surface plots were created according to Eq. (2) (Fig.4).

In contrast to the results obtained by Ju and Howard,³⁷ where acidified water used as solvent provided maximum extraction of total anthocyanins (3-glucosides of delphinidin, cyanidin, petunidin, peonidin and malvidin) at 80–100 °C,³⁸ the highest MA yield (0.0462 mg C3G/mL) in our case was observed at temperature of 160 °C, extraction time of 15 min and absence of acidifier. The highest MA yield (1.6590 mg C3G/mL) obtained by maceration with 50% ethanol was above 35-fold higher than the highest MA yield acquired with SWE. The lowest MA yield (0.0040 mg C3G/mL) was obtained at temperature of 160 °C, extraction time of 15 min and addition of 1.5% HCl. Above 414-fold difference between the lowest and the highest MA yields suggests that absence/presence of acidifier has a crucial role in MA yield. Most extraction procedures use acidified solutions of ethanol, methanol, acetone, water, and acetone/methanol/water mixtures, which denature cellular membranes and facilitate solubilization of anthocyanins.³³ Regarding TP, TF and MA yields, the lowest responses were obtained when 1.5% HCl was added, while the highest responses were observed when acidifier was absent. Although hydrochloric acid (<1.0%) is recommended for anthocyanin extraction, addition of excess acid can lead to hydrolysis of labile, acyl and sugar residues.⁴² Ramic et al. reported highest MA yield (2.26 mg C3G/mL) obtained by ultrasound assisted extraction (UAE) of black chokeberry at temperature of 70 °C and extraction time of 60 min.³¹ The highest MA yield obtained by UAE was more than 48-fold higher than the highest MA yield in subcritical chokeberry extract at temperature of 160 °C and extraction time of 15 min. Total anthocyanins were degraded at tempera-

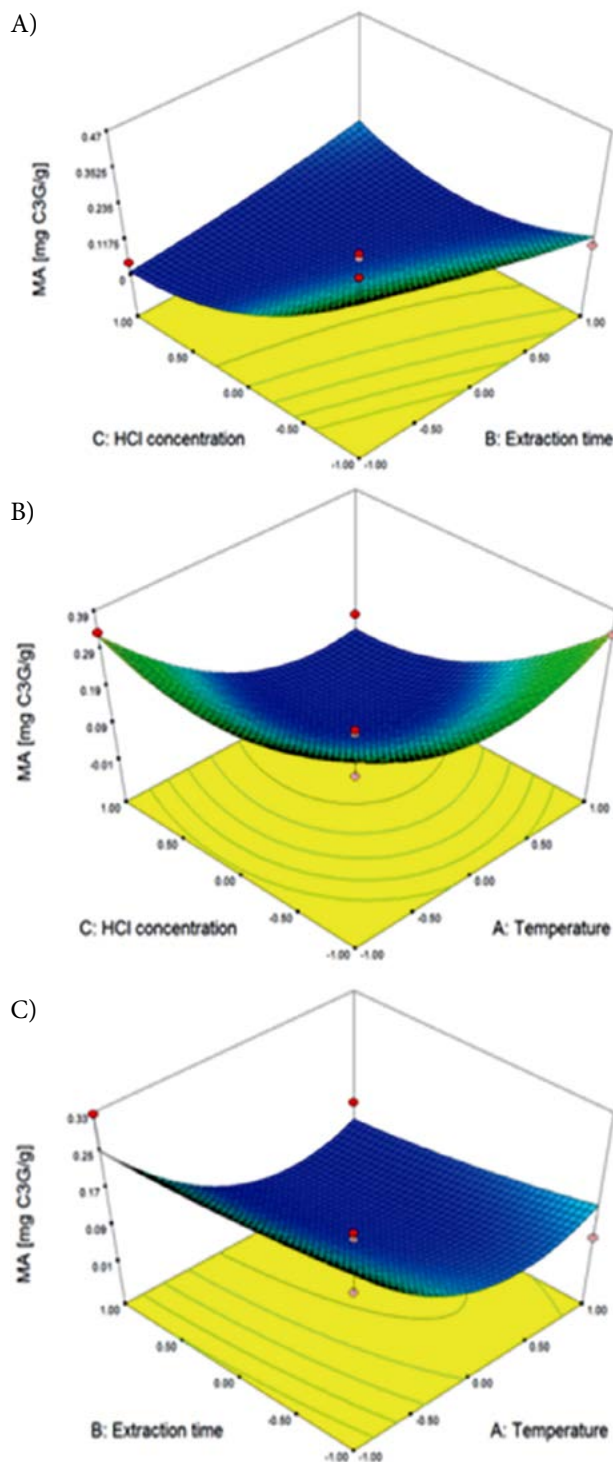


Figure 4 Response surface plots showing combined effects of process variables: (A) HCl concentration and extraction time, (B) HCl concentration and temperature and (C) extraction time and temperature on monomeric anthocyanins yield

tures >100 °C (especially at 140 °C), indicating that 100 °C was the optimum SWE temperature for isolating anthocyanins using acidified water.³⁷ Therefore, elevated temperature (160 °C) could be responsible for notably lower MA yield obtained by SWE in comparison with UAE and maceration.

According to regression coefficients, the effects of linear terms of SWE parameters were all negative on MA content in subcritical extracts. Linear terms of temperature and HCl concentration showed highly significant influence ($p < 0.05$) as well as quadratic term of temperature. The total anthocyanin content of subcritical extracts obtained from red grape skin declined 40% from 110 to 160 °C,³⁷ indicating that elevated extraction temperature could cause rapid degradation and even discoloration of anthocyanins in some cases.⁴² The thermal degradation of anthocyanins follows 1st order reaction kinetics,⁴³ hence high-temperature short-time processing is recommended for maximizing the retention of anthocyanins in foods⁴¹. Therefore, SWE was conducted over the temperature range of 120 to 200 °C in 40 °C increments for a short time (15–35 min) ensuring high superficial fluid velocity through the extraction cell. Interaction term between extraction time and HCl concentration together with quadratic term of HCl concentration exhibited moderately significant influence ($p < 0.1$).

3. 5. Effects of Extraction Parameters on Antioxidant Activity

Increasing temperature from 100 to 160 °C resulted in a linear increase in ORAC values in subcritical extracts derived from red grape skin. The ORAC value of extract obtained by conventional methanol extraction was greater than the ORAC values obtained by SWE from 100 to 140 °C, but less than ORAC values obtained by SWE from 140 to 160 °C. The ORAC values showed negative correlation with total anthocyanins in subcritical extracts, suggesting that anthocyanins are not responsible for antioxidant capacity.³⁷

In this study, antioxidant capacity expressed as IC₅₀ value ranged from 0.0062 to 0.1333 mg/mL. The highest antioxidant activity (0.0062 mg/mL) was observed at temperature of 200 °C, extraction time of 25 min and absence of acidifier, while the lowest activity (0.1333 mg/mL) was obtained at 120 °C, 25 min and with added 1.5% HCl. These results suggest that temperature and absence/presence of acidifier are the most influence parameters affecting antioxidant capacity. Response surface plots which visualize influence of SWE parameters on antioxidant activity are presented in Fig. 5.

In the case of IC₅₀, as it was the case with anthocyanins, linear term of HCl concentration showed highly significant ($p < 0.05$) influence, while quadratic term of HCl concentration showed moderately significant ($p < 0.1$) influence.

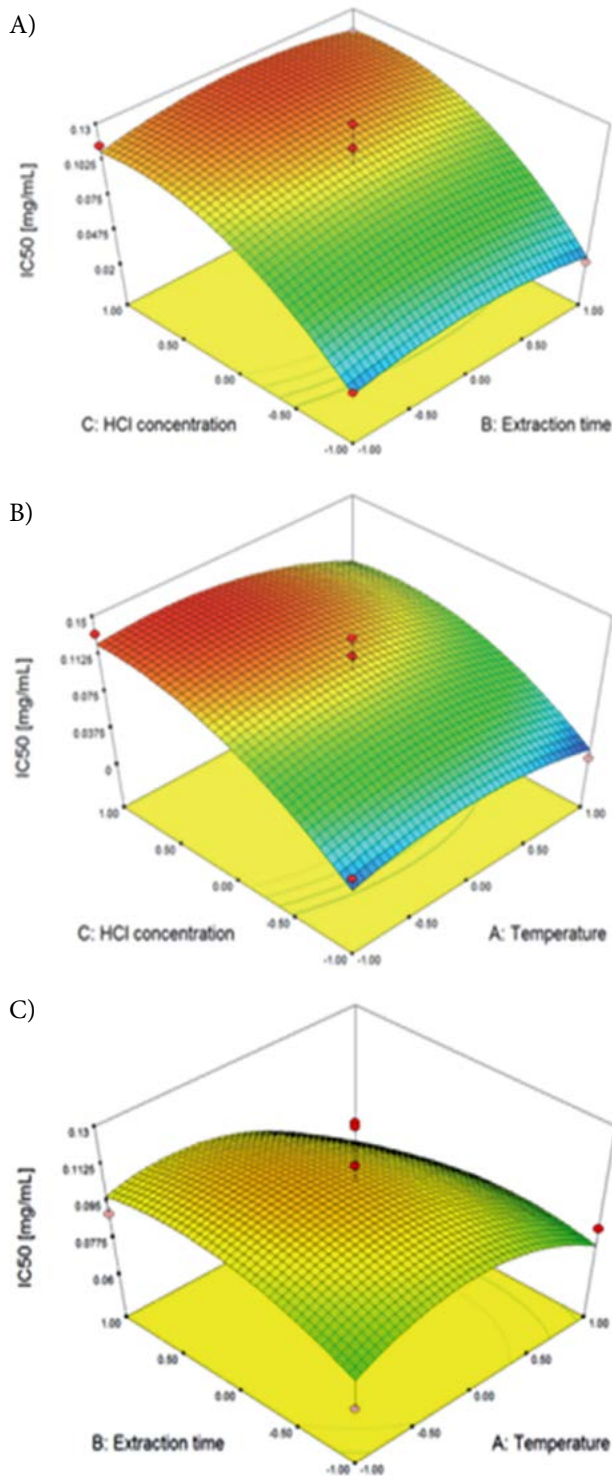


Figure 5 Response surface plots showing combined effects of process variables: (A) HCl concentration and extraction time, (B) HCl concentration and temperature and (C) extraction time and temperature on IC₅₀ value

3. 6. Optimization of SWE Parameters for Maximizing Yields of Polyphenolics

One of the main goals of this investigation was to maximize extraction yields for TP, TF and MA, and to

minimize IC₅₀ value within the range of each extraction parameter. Determination of optimal conditions and predicted values was based on desirability function which was 1, the most desirable response.²⁷ The optimized SWE conditions for maximum response of TP, TF and MA, and minimum response of IC₅₀ were temperature of 120.4 °C, extraction time of 15.2 min and absence of acidifier. Results of this work were in accordance with previous studies where temperature of 120 °C was detected as optimal for SWE of anthocyanins from different berry pomaces and seeds.^{37,40} The predicted values of TP, TF, MA and IC₅₀ value at optimal conditions were 32.8863 mg GAE/g, 23.5164 mg CE/g, 0.5124 mg C3G/g and 0.0055 mg/mL, respectively.

According to particularly high values of coefficients of multiple determination (R^2) for TP and TF (0.9629 and 0.9682), excellent fit between experimental and values predicted by the model is indicated. Although R^2 was relatively high in case of IC₅₀ (0.8970) and MA (0.8959), it was still significantly lower comparing to other responses. However, for all four responses, mathematical models were statistically acceptable due to significant regression ($p_m < 0.05$) and non-significant lack of fit ($p_{lf} > 0.05$), except for MA where lack of fit was significant ($p_{lf} = 0.0127$). Furthermore, coefficient of variance, which represents dispersion degree of the data, is rather low ($CV \leq 15\%$) in all models and supports good fitness of the model providing better reproducibility except in the case of MA and IC₅₀.

4. Conclusions

Previously published data on antioxidant capacity indicators of chokeberry cake are rather scarce. Although aronia pomace is by far the richest source of total phenolics, aronia cake may serve as an alternative low-cost raw material for extraction of dietary antioxidants. The major drawbacks of conventional extraction techniques in general are long time, excessive cost, use of large quantity of organic solvent, poor extraction selectivity and generation of toxic organic waste. These obstacles could be overcome by employing SWE.

The second-order polynomial model has proven to be adequate for mathematical description of SWE of several groups of polyphenolic compounds. Therefore, optimization of extraction conditions in order to simultaneously provide maximum yields for TP, TF and MA and, minimum IC₅₀ value was successfully performed using RSM coupled with BBD. Since statistical and graphical analysis showed that HCl concentration was the most influential factor for all four responses, absence of acidifier was determined as optimal for extraction of polyphenolic compounds. The optimized SWE conditions, for maximum response of TP, TF and MA, and minimum response of IC₅₀, were temperature of 120.4 °C, extraction time of 15.2 min and absence of acidifier. The predicted values of TP,

TF, MA and IC₅₀ at these conditions were: 32.8863 mg GAE/g, 23.5164 mg CE/g, 0.5124 mg C3G/g and 0.0055 mg/mL, respectively.

Recognizing the obtained results it can be concluded that aronia fruit dust, discharged as by-product from filter tea factory, can serve as a valuable source of polyphenols when SWE is applied. Although high-temperature short-time processing is suitable for maximizing the retention of anthocyanins in plant matrices, SWE is not the optimal technology for recovery of monomeric anthocyanins from aronia fruit dust providing notably lower yields in comparison with UAE and maceration.

5. References

1. S. E. Kulling, H. M. Rawel, *Planta Med.* **2008**, *74*, 1625–1634. DOI:10.1055/s-0028-1088306
2. L. Jakobek, M. Seruga, M. Medvidovic-Kosanovic, I. Novak, *Dtsch. Lebensmitt. Rundsch.* **2007**, *103*, 58–64.
3. J. Oszmianański, A. Wojdylo, *Eur. Food Res. Technol.* **2005**, *221*, 809–813. DOI:10.1007/s00217-005-0002-5
4. M. P. Kähkönen, A. I. Hopia, H. J. Vuorela, J. P. Rauha, K. Pihlaja, T. S. Kujala, M. Heinonen, *J. Agric. Food Chem.* **1999**, *47*, 3954–3962. DOI:10.1021/jf990146l
5. P. N. Denev, C. G. Kratchanov, M. Ciz, A. Lojek, M. G. Kratchanova, *Compr. Rev. Food Sci. Food Saf.* **2012**, *11*, 471–489. DOI:10.1111/j.1541-4337.2012.00198.x
6. A. Kokotkiewicz, Z. Jaremicz, M. Luczkiewicz, *J. Med. Food.* **2010**, *13*, 255–269. DOI:10.1089/jmf.2009.0062
7. X. L. Wu, L. W. Gu, R. L. Prior, S. McKay, *J. Agric. Food Chem.* **2004**, *52*, 7846–56. DOI:10.1021/jf0486850
8. A. Nawirska, M. Kwasniewska, *Food Chem.* **2005**, *91*, 221–5. DOI:10.1016/j.foodchem.2003.10.005
9. S. Vidovic, D. Cvetkovic, M. Ramic, M. Dunjic, R. Malbaša, A. Tepic, Z. Šumic, A. Velicanski, S. Jokic, *Ind. Crops Prod.* **2013**, *50*, 338–345. DOI:10.1016/j.indcrop.2013.08.005
10. Dai, J., & Mumper, R. J. *Molecules.* **2010**, *15*(10), 7313–7352. DOI:10.3390/molecules15107313
11. R. S. Ayala, M. L. De Castro, *Food Chem.* **2001**, *75*(1), 109–113. DOI:10.1016/S0308-8146(01)00212-6
12. C. C. Teo, S. N. Tan, J. W. Yong, C. S. Hew, E. S. Ong, *J. Chromatogr. A.* **2010**, *1217*(16), 2484–2494. DOI:10.1016/j.chroma.2009.12.050
13. S. Erşan, O. G. Üstündağ, R. Carle, R. M. Schweiggert, *Food Chem.* **2018**, *253*, 46–54. DOI:10.1016/j.foodchem.2018.01.116
14. J. Vradić, O. Canli, B. Pavlić, Z. Zeković, S. Vidović, M. Kaplan, *J. Supercrit. Fluids.* **2017**, *120*, 86–94. DOI:10.1016/j.supflu.2016.10.016
15. P. P. Singh, M. D. Saldaña, *Food Res. Int.* **2011**, *44*(8), 2452–2458. DOI:10.1016/j.foodres.2011.02.006
16. B. Aliakbarian, A. Fathi, P. Perego, F. Dehghani, *J. Supercrit. Fluids.* **2012**, *65*, 18–24. DOI:10.1016/j.supflu.2012.02.022
17. P. Budrat, A. Shotipruk, *Sep. Purif. Technol.* **2009**, *66*(1), 125–129. DOI:10.1016/j.seppur.2008.11.014

18. P. Rangswi Wong, N. Rangkadilok, J. Satayavivad, M. Goto, A. Shotipruk, *Sep. Purif. Technol.* **2009**, 66(1), 51–56. DOI:10.1016/j.seppur.2008.11.023
19. M. J. Ko, C. I. Cheigh, S. W. Cho, M. S. Chung, *J. Food Eng.* **2011**, 102(4), 327–333. DOI:10.1016/j.jfoodeng.2010.09.008
20. S. Ponnusamy, H. K. Reddy, T. Muppaneni, C. M. Downes, S. Deng, *Bioresour. Technol.* **2014**, 170, 454–461. DOI:10.1016/j.biortech.2014.07.072
21. Z. Zeković, S. Vidović, J. Vladić, R. Radosavljević, A. Cvejin, M. A. Elgndi, B. Pavlič, *J. Supercrit. Fluids.* **2014**, 95, 560–566.
22. V. L. Singleton, J. A. Rossi, *Am. J. Enology Vitic.* **1965**, 16, 144–158.
23. Harborne, J. B. (1989). *Methods in Plant Biochemistry*, Plant Phenolics, vol. 1, Academic Press Ltd., London.
24. M. F. Abu Bakar, M. Mohamed, A. Rahmat, J. Fry, *Food Chem.* **2009**, 113, 479–483. DOI:10.1016/j.foodchem.2008.07.081
25. P. Dzomba, *Afr. J. Agric. Res.* **2013**, 25, 3330–3333.
26. J. C. Espin, C. Soler-Rivas, H. J. Wichers, C. Garcia-Viguera, *J. Agric. Food Chem.* **2000**, 48, 1588–1592. DOI:10.1021/jf9911390
27. D. Baş, I. H. Boyacı, *J. Food Eng.* **2007**, 78(3), 836–845. DOI:10.1016/j.jfoodeng.2005.11.024
28. R. H. Myers, D. C. Montgomery, C. M. Anderson-Cook, *Response Surface Methodology: Process and Product Optimization Using Designed Experiments*, third ed., Wiley, New Jersey, 2009.
29. T. Bahorun, A. Luximon-Ramma, A. Crozier, O. I. Aruoma, *J. Sci. Food Agric.* **2004**, 84(12), 1553–1561. DOI:10.1002/jsfa.1820
30. N. E. Durling, O. J. Catchpole, J. B. Grey, R. F. Webby, K. A. Mitchell, L. Y. Foo, N. B. Perry, *Food Chem.* **2007**, 101(4), 1417–1424. DOI:10.1016/j.foodchem.2006.03.050
31. M. Ramić, S. Vidović, Z. Zeković, J. Vladić, A. Cvejin, B. Pavlič, *Ultrason. Sonochem.* **2015**, 23, 360–368. DOI:10.1016/j.ultsonch.2014.10.002
32. L. G. d'Alessandro, K. Kriaa, I. Nikov, K. Dimitrov, *Sep. Purif. Technol.* **2012**, 93, 42–47. DOI:10.1016/j.seppur.2012.03.024
33. N. Čujić, K. Šavikin, T. Janković, D. Pljevljakušić, G. Zdunić, S. Ibrić, *Food Chem.* **2016**, 194, 135–142. DOI:10.1016/j.foodchem.2015.08.008
34. Z. S. Zhang, D. Li, L. J. Wang, N. Ozkan, X. D. Chen, Z. H. Mao, *Sep. Purif. Technol.* **2007**, 57, 17–24. DOI:10.1016/j.seppur.2007.03.006
35. J. E. Cacace, G. Mazza, *J. Food Sci.* **2003**, 68, 240–248. DOI:10.1111/j.1365-2621.2003.tb14146.x
36. K. Wilkes, L. R. Howard, C. Brownmiller, R. L. Prior, *J. Agric. Food Chem.* **2013**, 62(18), 4018–4025. DOI:10.1021/jf404281n
37. Z. Y. Ju, L. R. Howard, *J. Agric. Food Chem.* **2003**, 51, 5207–13. DOI:10.1021/jf0302106
38. L. Grunovaitė, M. Pukalskienė, A. Pukalskas, P. R. Venskutonis, *J. Funct. Foods.* **2016**, 24, 85–96. DOI:10.1016/j.jff.2016.03.018
39. W. Kalt, J. E. H. McDonald, Donner, *J. Food Sci.* **2000**, 65(3), 390–393. DOI:10.1111/j.1365-2621.2000.tb16013.x
40. J. W. King, R. D. Grabiell, J. D. Wightman, In *Proceedings of the 6th Intl. Symposium on Supercritical Fluids* (Vol. 1, pp. 28–30), **2003**.
41. R. L. Jackman, J. L. Smith, Anthocyanins and betalains. In: Hendry GAF, Houghton JD, editors. *Natural food colorants*. 2nd ed. Glasgow, U.K.: Blacklie Academic & Professional, **1996**, 244–309. DOI:10.1007/978-1-4615-2155-6_8
42. H. Wang, G. Cao, R. L. Prior, *J. Agric. Food Chem.* **1997**, 45, 304–309. DOI:10.1021/jf960421t
43. B. Cemeroglu, S. Velioglu, S. Isik, *J. Food Sci.* **1994**, 59, 1216–7. DOI:10.1111/j.1365-2621.1994.tb14680.x

Povzetek

Odpadne produkte aronije (*Aronia melanocarpa* L.), ki nastajajo pri proizvodnji čaja v filtrnih vrečkah, smo podvrgli subkritični vodni ekstrakciji (SWE) z namenom izolacije polifenolov in določitve njihovih antioksidativnih lastnosti. Za optimizacijo pogojev smo uporabili Box-Behnken-ovo metodo načrtovanja eksperimentov. Neodvisni parametri so bili temperatura (T, 120–200 °C), čas ekstrakcije (t, 15–35 min) in koncentracija hidroklorida (c, 0–1.5 %). Eksperimentalnim podatkom smo prilagodili polinom 2. stopnje ter s pomočjo multiple regresijske in analize variance določili njegovo ustreznost kot tudi optimalne pogoje. Optimizirani SWE pogoji, pri katerih so bile dosežene maksimalne koncentracije skupnih fenolov (TP), skupnih flavonoidov (TF) in monomernih antocianinov (MA) ob minimalni vrednosti IC50, so bili: temperatura 120.4 °C, čas ekstrakcije 15.2 min in odsotnost hidroklorida. Predvidene vrednosti TP, TF, MA in IC50 pri teh pogojih so: 32.8863 mg GAE/g, 23.5164 mg CE/g, 0.5124 mg C3G/g in 0.0055 mg/mL.

Scientific paper

Hydrothermal Synthesis of Novel Magnetic Plate-Like $\text{Bi}_2\text{O}_2\text{CO}_3/\text{CoFe}_2\text{O}_4$ Hybrid Nanostructures and Their Catalytic Performance for the Reduction of Some Aromatic Nitrocompounds

Parisa Zarringhadam and Saeed Farhadi*

Department of Chemistry, Lorestan University, Khoramabad 68151-44316, Iran

* Corresponding author: E-mail: sfarhadi1348@yahoo.com

Tel: +986633120611, fax: +986633120618

Received: 27-01-2018

Abstract

Novel magnetically separable $\text{Bi}_2\text{O}_2\text{CO}_3/\text{CoFe}_2\text{O}_4$ nanocomposites were fabricated by a feasible hydrothermal route. Fourier transform infrared (FT-IR) spectroscopy, X-ray diffraction (XRD), scanning electron microscopy (SEM), energy dispersive X-ray spectroscopy (EDX), transmission electron microscopy (TEM), X-ray photoelectron spectroscopy (XPS), UV-vis diffuse reflectance spectroscopy (DRS), vibrating sample magnetometer (VSM), and N_2 adsorption-desorption analysis were employed to examine the structure, morphology, particle size, phase composition, optical and magnetic properties of the as-synthesized nanocomposites. The results of the findings showed demonstrated the successful coupling of spherical CoFe_2O_4 nanoparticles and plate-like $\text{Bi}_2\text{O}_2\text{CO}_3$ nanostructures. The catalytic performance of magnetic $\text{Bi}_2\text{O}_2\text{CO}_3/\text{CoFe}_2\text{O}_4$ nanocomposites was evaluated in the reduction of some aromatic nitrocompounds such as nitrophenols and nitroanilines by using sodium borohydride (NaBH_4) aqueous solution at room temperature. The $\text{Bi}_2\text{O}_2\text{CO}_3/\text{CoFe}_2\text{O}_4$ nanocomposite with 30 %wt. CoFe_2O_4 exhibited the best performance in the reduction of aromatic nitrocompounds with 100% conversion into the corresponding amino compounds within 15–30 min with rate constant of $0.10\text{--}0.24\text{ min}^{-1}$. The effect of catalyst dosage was also investigated on the efficiency of reduction process. Furthermore, magnetic $\text{Bi}_2\text{O}_2\text{CO}_3/\text{CoFe}_2\text{O}_4$ nanocomposite could be easily removed by an external magnet from the reaction system.

Keywords: Plate-like $\text{Bi}_2\text{O}_2\text{CO}_3$; bismuth-based nanomaterials; cobalt ferrite, magnetic nanocomposite; catalytic reduction; nitrophenols

1. Introduction

Nitrophenols are one of the most organic pollutants in industrial and agricultural waste waters.^{1,2} Nitrophenols and their derivatives are significant by-products produced from pesticides, herbicides and synthetic dyes.^{3–5} Among them, 4-nitrophenol (4-NP) is well known to cause damage to the central nervous system, liver, kidney and both animal and human blood. Hence its removal from the environment is a crucial task.^{6–10} On the other hand, the reduction of 4-NP to 4-aminophenol (4-AP) is essential in pharmaceutical industries for the manufacture of analgesic, antipyretic and other drugs, in photographic developer, corrosion inhibitor, anticorrosion lubricant, etc.^{11,12} Over the past few decades, the catalytic reduction of nitrophenols using NaBH_4 as reducing agent in aqueous medium has received considerable attention as a relatively simple and clean method.¹³ Many reports are available on the ap-

plication of metal and metal oxides nanocatalysts for the reduction of nitrophenols in the presence of NaBH_4 .^{14–22} However, the separation of them from the reaction mixture is an important issue. In order to solve these problems, the magnetic separable nanocomposites such as $\text{Au}/\text{Fe}_3\text{O}_4$,²³ Ag@Pd satellites/ Fe_3O_4 ,²⁴ $\text{Pt}/\text{Fe}_3\text{O}_4/\text{CNTs}$,²⁵ and $\text{Fe}_3\text{O}_4/\text{SiO}_2/\text{Ag}$ ²⁶ have been exploited for the catalytic reduction of nitrophenols in aqueous media. In such approaches, although nanocomposites showed improved recyclability but they suffered from one or more drawbacks such as the usage of expensive noble metals and the multi-step preparation procedures. Hence, the development of an alternative inexpensive, facile and easy-removal magnetic catalyst for the reduction of nitrophenols is highly desirable in the context of environmental and industrial concerns.

During the recent years, bismuth-based nanostructured materials, such as Bi_2O_3 ,²⁷ BiVO_4 ,²⁸ Bi_2WO_6 ,²⁹ Bi_2MoO_6 ,^{30,31}

BiOX (X = Cl, Br, I), and so on,^{32–34} have received a great deal of attention due to their unique catalytic and photocatalytic activities. Among these compounds, some studies have focused on the fabrication of bismuth subcarbonate ($\text{Bi}_2\text{O}_2\text{CO}_3$) and its composites.³⁵ Up to now, many kinds of $\text{Bi}_2\text{O}_2\text{CO}_3$ -based hybrid composites such as $\text{Bi}_2\text{O}_2\text{CO}_3/\beta\text{-Bi}_2\text{O}_3$,³⁶ $\text{Bi}_2\text{O}_2\text{CO}_3/\text{MoS}_2$,³⁷ $\text{Bi}_2\text{O}_2\text{CO}_3/\text{BiOX}$ (X = Cl, Br and I),^{38–40} $\text{Bi}_2\text{O}_2\text{CO}_3/\text{Bi}_2\text{WO}_6$,⁴¹ $\text{Bi}_2\text{O}_2\text{CO}_3/\text{Bi}_2\text{S}_3$,⁴² $\text{Bi}_2\text{O}_2\text{CO}_3/\text{CdS}$,⁴³ $\text{Bi}_2\text{O}_2\text{CO}_3/\text{BiPO}_4$,⁴⁴ g- $\text{C}_3\text{N}_4/\text{Bi}_2\text{O}_2\text{CO}_3$,⁴⁵ $\text{Ag}_2\text{O}/\text{Bi}_2\text{O}_2\text{CO}_3$,⁴⁶ $\text{Ag}/\text{AgBr}/\text{Bi}_2\text{O}_2\text{CO}_3$,⁴⁷ $\text{Ag}_3\text{PO}_4/\text{Bi}_2\text{O}_2\text{CO}_3$,⁴⁸ $\text{Ag}_2\text{CO}_3/\text{Bi}_2\text{O}_2\text{CO}_3$ ⁴⁹ and MWCNTs/ $\text{Bi}_2\text{O}_2\text{CO}_3$ ⁵⁰ have been successfully synthesized, which showed enhanced catalytic or photocatalytic stability and activity than $\text{Bi}_2\text{O}_2\text{CO}_3$ alone. But most of these composites are difficult to separate and recycle, seriously limiting their extensive application. Therefore, fabrication of well-defined and easy separated $\text{Bi}_2\text{O}_2\text{CO}_3$ -based catalysts from the suspended reaction system via a simple process remains to be a great challenge. To overcome this shortfall, coupling $\text{Bi}_2\text{O}_2\text{CO}_3$ with magnetic materials is highly desirable. In this regard, spinel-type metal ferrites (MFe_2O_4) are known to have high magnetic performance as well as excellent chemical stability.⁵¹ Among them, CoFe_2O_4 nanoparticles have a higher strong magnetic property, and therefore, CoFe_2O_4 based composites can be magnetically separable in a suspension by virtue of their own magnetic properties without any introduction of additional magnetic particles. Based on the previous studies, it can be expected that the modification of $\text{Bi}_2\text{O}_2\text{CO}_3$ with CoFe_2O_4 to form $\text{Bi}_2\text{O}_2\text{CO}_3/\text{CoFe}_2\text{O}_4$ nanocomposites may improve the catalytic activity and recyclability. Furthermore, their magnetic nature makes composites magnetically separable from the reaction mixture in a convenient manner. As far as we know, there is no report about CoFe_2O_4 -modified $\text{Bi}_2\text{O}_2\text{CO}_3$ until now.

In this work, novel magnetically separable $\text{Bi}_2\text{O}_2\text{CO}_3/\text{CoFe}_2\text{O}_4$ nanocomposites with high catalytic performance were synthesized via loading various amounts of CoFe_2O_4 nanoparticles on the surface of plate-like $\text{Bi}_2\text{O}_2\text{CO}_3$ nanostructures by a hydrothermal method at 180 °C for 24 h. The structure, morphology, and optical properties of the obtained nanomaterials were characterized in detail. Then, the excellent catalytic activity of the as-prepared $\text{Bi}_2\text{O}_2\text{CO}_3/\text{CoFe}_2\text{O}_4$ composite nanomaterials was evaluated by the reduction of 4-nitrophenol in the presence of aqueous NaBH_4 solution under ambient conditions. In addition, the possible reaction mechanism was proposed based on the experimental results. This study provides a promising candidate for efficient removal of nitrophenols from water by an environment-friendly and economical approach.

2. Experimental

2.1. Materials

Bismuth nitrate pentahydrate ($\text{Bi}(\text{NO}_3)_3 \cdot 5\text{H}_2\text{O}$, 98%), citric acid (98.5%), cobalt(II) nitrate hexahydrate ($\text{Co}(\text{NO}_3)_2 \cdot 6\text{H}_2\text{O}$, 98%), iron(III) nitrate nanohydrate

($\text{Fe}(\text{NO}_3)_3 \cdot 9\text{H}_2\text{O}$, 98%), sodium borohydride (NaBH_4 , 98.5%), 2-nitrophenol (2-NP, 99%), 4-nitrophenol (4-NP, 98%), 2-nitroaniline (2-NA, 99%) and 4-nitroaniline (4-NA, 99%) were obtained from Merck chemical company and used as received without further purification. All other chemicals were of analytical grade, commercially available and used without further purification.

2.2. Methods of Characterization

FT-IR spectra were recorded on a Shimadzu system FT-IR 8400S spectrophotometer in transmission mode from 4000 to 400 cm^{-1} using KBr pellets. The XRD patterns of the samples were obtained on an X-ray diffractometer (Rigaku D-max C III) using Ni-filtered Cu K α radiation ($\lambda = 1.5406 \text{ \AA}$) UV-vis diffuse reflection spectroscopy (DRS) was performed on a Snico S4100 spectrophotometer over the spectral range 200–1000 nm by using BaSO_4 as the reference. The shapes and morphologies of samples were observed by a MIRA3 TESCAN field emission scanning electron microscope (FES-EM) equipped with a link energy-dispersive X-ray (EDX) analyzer. The particle size was determined by a CM120 transmission electron microscope (TEM) at an accelerating voltage of 80 kV. TEM samples were prepared by dropping the ethanol dispersion on a carbon coated copper grid. A PHS-1020 PHSCHINA instrument was used to measure the Brunauer-Emmett-Teller (BET) surface areas of the samples at liquid nitrogen temperature (77 K). Specific surface area calculations were made using Brunauer-Emmett-Teller (BET) method at the relative pressure (p/p_0) between 0.05 and 0.35. Magnetic measurements were carried out at room temperature using a vibrating sample magnetometer (VSM, Magnetic Dadeshpajoh Kashan Co., Iran) with a maximum magnetic field of 10 kOe. X-ray photoelectron spectroscopy (XPS) was conducted using a thermo Scientific, ESCALAB 250Xi, Mg X-ray resource instrument. UV-vis spectra of nitro compounds during the reduction reaction in aqueous solutions were analyzed using a Cary 100 double beam spectrophotometer operated at a resolution of 2 nm with quartz cells with path length of 1 cm in the wavelength range of 200 to 600 nm.

2.3. Preparation of CoFe_2O_4 Nanoparticles

CoFe_2O_4 nanoparticles were prepared by hydrothermal process. $\text{Fe}(\text{NO}_3)_3 \cdot 9\text{H}_2\text{O}$ (1.72 g) and $\text{Co}(\text{NO}_3)_2 \cdot 6\text{H}_2\text{O}$ (0.62 g) were dissolved in 25 mL distilled water (Co/Fe mole ratio of 1:2), and then the solution was adjusted to a pH of 12 with NaOH (6 M). After stirring for 60 min, the mixture was transferred to a 50 mL Teflon-lined stainless steel autoclave and maintained at 180 °C for 12 h before being cooled down in air. The resulting precipitate was filtered, washed with deionized water and ethanol, and dried at 60 °C for 6 h.

2. 4. Preparation of Plate-Like $\text{Bi}_2\text{O}_2\text{CO}_3$ Nanoparticles

To obtain plate-like $\text{Bi}_2\text{O}_2\text{CO}_3$ nanoparticles, 2.0 mmol of bismuth nitrate pentahydrate [$\text{Bi}(\text{NO}_3)_3 \cdot 5\text{H}_2\text{O}$] was dissolved in 20 mL of HNO_3 aqueous solution (1 M), and then 1.5 mmol of citric acid ($\text{C}_6\text{H}_8\text{O}_7$) was added under magnetic stirring. The pH of the solution was adjusted to 6 by adding NaOH aqueous solution (2 M) under magnetic stirring. Finally, the white-colored precursor suspension was transferred into a 50 mL Teflon-lined stainless steel autoclave and heated for 24 h at 180 °C. After hydrothermal treatment, the autoclave was cooled down to room temperature naturally. The resulting precipitate was collected by centrifugation, washed with deionized water several times, and dried at 60 °C for 6 h.

2. 5. Preparation of $\text{Bi}_2\text{O}_2\text{CO}_3/\text{CoFe}_2\text{O}_4$ Nanocomposites

To synthesize $\text{Bi}_2\text{O}_2\text{CO}_3/\text{CoFe}_2\text{O}_4$ nanocomposites, 2.0 mmol of $\text{Bi}(\text{NO}_3)_3 \cdot 5\text{H}_2\text{O}$ was dissolved in 20 mL of HNO_3 (1 M), and then 1.5 mmol of citric acid ($\text{C}_6\text{H}_8\text{O}_7$) was added under magnetic stirring. The pH of the solution was adjusted to 6 by adding NaOH aqueous solution (2 M) under magnetic stirring. Then, the required amount of CoFe_2O_4 nanoparticles (30 and 45 wt%) was added to the $\text{Bi}_2\text{O}_2\text{CO}_3$ precursor suspension. After sonication for 30 min, the homogenized suspension was transferred into a 50 mL Teflon-lined stainless steel autoclave, sealed and maintained at 180 °C for 24 h. Then, the autoclave was naturally cooled down to room temperature and the resulting precipitate was separated by a magnet, washed with deionized water several times, dried at 60 °C and used for further characterization. The obtained samples with 30 and 45 wt% CoFe_2O_4 nanoparticles were denoted as $\text{Bi}_2\text{O}_2\text{CO}_3/\text{CoFe}_2\text{O}_4$ 30% and $\text{Bi}_2\text{O}_2\text{CO}_3/\text{CoFe}_2\text{O}_4$ 45%, respectively.

2. 6. Catalytic Tests

The catalytic performance of the synthesized $\text{Bi}_2\text{O}_2\text{CO}_3/\text{CoFe}_2\text{O}_4$ nanocomposites in the reduction of 4-nitrophenol (4-NP) to 4-aminophenol (4-AP) was evaluated by excess aqueous NaBH_4 solution at room temperature. In a typical catalytic reaction, 2 mL of aqueous solution of 4-NP (0.2 mM) and 0.5 mL of freshly prepared aqueous solution of NaBH_4 (20 mM) were mixed together in a standard quartz cell, having 1 cm path length. The solution color turned to bright yellow rapidly. Then, 5 mg of the $\text{Bi}_2\text{O}_2\text{CO}_3/\text{CoFe}_2\text{O}_4$ nanocomposite was added and stirred at room temperature. The solution was quickly subjected to UV-Vis measurements; afterward, the absorbance of the solution was in situ measured every several minutes (2 min) in the scanning range of 200–500 nm to obtain the successive change about the reaction. In order

to optimized the catalyst amount, similar experiments have been carried out in the presence of various amount of the catalyst (2.5, 5, 10, 15, and 20 mg in 2.5 mL aqueous solutions) on the reduction of 4-NP. The reduction of 2-nitrophenol (2-NP) and 2-nitroaniline (2-NA) and 4-nitroaniline (4-NA) was also carried out under the same conditions. For comparison, similar experiment was performed in the presence of the pure $\text{Bi}_2\text{O}_2\text{CO}_3$ (5 mg) and CoFe_2O_4 (5 mg) catalysts. For recycling experiments, the $\text{Bi}_2\text{O}_2\text{CO}_3/\text{CoFe}_2\text{O}_4$ catalyst was recovered from the solution by an external magnet after completion of the reaction. The magnetically recovered catalyst was washed repeatedly with deionized water, dried at 60 °C and then employed for a new run.

3. Results and Discussion

3. 1. Characterization of $\text{Bi}_2\text{O}_2\text{CO}_3/\text{CoFe}_2\text{O}_4$ Nanocomposites

FT-IR spectra of the as-prepared $\text{Bi}_2\text{O}_2\text{CO}_3$, CoFe_2O_4 and $\text{Bi}_2\text{O}_2\text{CO}_3/\text{CoFe}_2\text{O}_4$ samples are indicated in Figure 1. For pure $\text{Bi}_2\text{O}_2\text{CO}_3$ sample in Figure 1(a), the sharp peaks at ca. 1400 and 845 cm^{-1} are the characteristic stretching

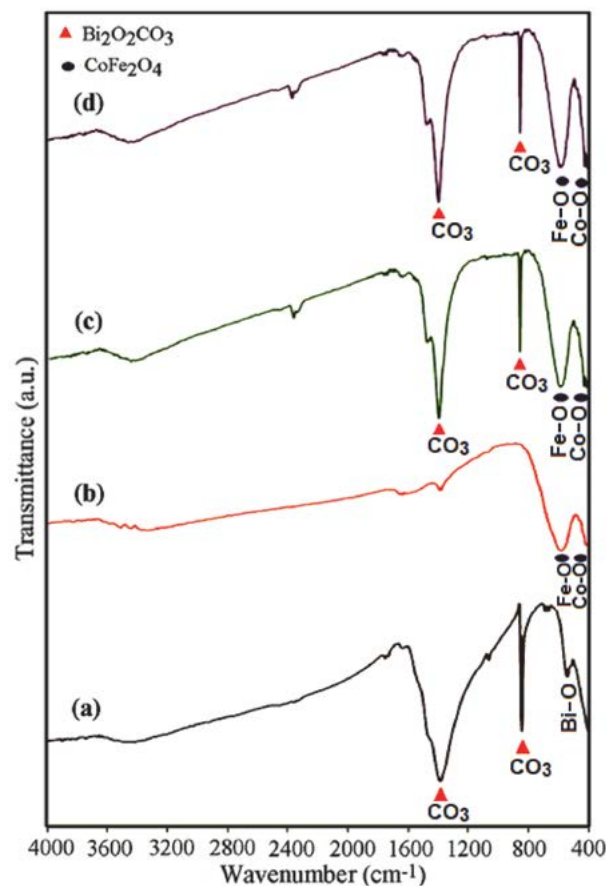


Figure 1. FT-IR spectra of (a) $\text{Bi}_2\text{O}_2\text{CO}_3$, (b) CoFe_2O_4 , (c) $\text{Bi}_2\text{O}_2\text{CO}_3/\text{CoFe}_2\text{O}_4$ 30%, and (d) $\text{Bi}_2\text{O}_2\text{CO}_3/\text{CoFe}_2\text{O}_4$ 45%.

and bending vibrations of CO_3^{2-} groups, respectively.⁵² Meanwhile, the intensive peak at about 550 cm^{-1} was attributed to the stretching vibration of the Bi–O, suggesting the formation of $\text{Bi}_2\text{O}_2\text{CO}_3$.⁵³ In the case of CoFe_2O_4 (Figure 1(b)), the two peaks appeared at 603 and 458 cm^{-1} are related to the stretching vibrations of M–O bonds in the tetrahedral and octahedral sites of spinel-type oxide, respectively.^{54,55} FT-IR spectra of the $\text{Bi}_2\text{O}_2\text{CO}_3/\text{CoFe}_2\text{O}_4$ nanocomposites in Figures 1(c) and (d) show the stretching and bending vibrations correspond to the carbonate group (CO_3^{2-}) in $\text{Bi}_2\text{O}_2\text{CO}_3$ at 1400 and 844 cm^{-1} , besides strong bands of CoFe_2O_4 in the $400\text{--}600\text{ cm}^{-1}$ range. This finding demonstrates the coexistence of $\text{Bi}_2\text{O}_2\text{CO}_3$ and CoFe_2O_4 in the nanocomposites.

The crystal structure of samples was further characterized using XRD. Figure 2 shows the XRD patterns of the $\text{Bi}_2\text{O}_2\text{CO}_3$, CoFe_2O_4 and $\text{Bi}_2\text{O}_2\text{CO}_3/\text{CoFe}_2\text{O}_4$ nanocomposites with different contents of CoFe_2O_4 . The patterns of Figures 2(a) and (b) are well consistent with the tetragonal $\text{Bi}_2\text{O}_2\text{CO}_3$ phase (JCPDS no. 41–1488) and the spinel-type CoFe_2O_4 phase (JCPDS no. 01–1121). As shown in Figures 2(c) and (d), all the $\text{Bi}_2\text{O}_2\text{CO}_3/\text{CoFe}_2\text{O}_4$ samples exhibit a coexistence of both $\text{Bi}_2\text{O}_2\text{CO}_3$ and CoFe_2O_4 phases without any impurity phase, indicating successful synthesis of

composites. In addition, the intensity of characteristic CoFe_2O_4 peaks at $2\theta = 35.76$ and 63.13 in nanocomposite increased with increasing CoFe_2O_4 amount. Besides, the diffraction peaks of $\text{Bi}_2\text{O}_2\text{CO}_3/\text{CoFe}_2\text{O}_4$ nanocomposites exhibited sharp and intense state, indicating a promising crystalline nature which was beneficial for the following catalytic activity.

The shape and morphology of the as-synthesized CoFe_2O_4 , $\text{Bi}_2\text{O}_2\text{CO}_3$ and $\text{Bi}_2\text{O}_2\text{CO}_3/\text{CoFe}_2\text{O}_4$ samples were investigated by FE-SEM. The SEM images of CoFe_2O_4 sample in Figures 3(a) and (b) show a large quantity of nearly uniform monodispersed spheres with an average diameter of about 15 nm . The SEM images in Figures 3(c) and (d) show that the bare $\text{Bi}_2\text{O}_2\text{CO}_3$ sample was formed from plate-like particles which were loosely aggregated. As can be observed, the porous structure was formed by self-assembly of these nanoplates. SEM images of the $\text{Bi}_2\text{O}_2\text{CO}_3/\text{CoFe}_2\text{O}_4$ nanocomposites containing 30% and 45% of CoFe_2O_4 are shown in Figures 3(e) and (f), respectively. It is evident that the shape and morphology of $\text{Bi}_2\text{O}_2\text{CO}_3/\text{CoFe}_2\text{O}_4$ nanocomposites are similar to those of the pure $\text{Bi}_2\text{O}_2\text{CO}_3$, but many spherical CoFe_2O_4 nanoparticles are seen on the surface of plate-like $\text{Bi}_2\text{O}_2\text{CO}_3$ nanostructures. From images, it can be clearly seen that a lot of

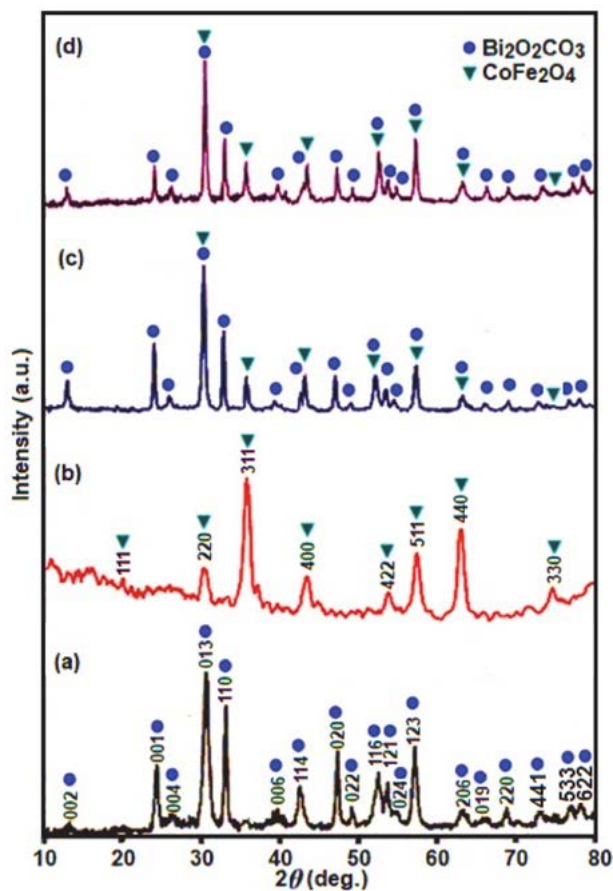


Figure 2. XRD patterns of (a) $\text{Bi}_2\text{O}_2\text{CO}_3$, (b) CoFe_2O_4 , (c) $\text{Bi}_2\text{O}_2\text{CO}_3/\text{CoFe}_2\text{O}_4$ 30%, and (d) $\text{Bi}_2\text{O}_2\text{CO}_3/\text{CoFe}_2\text{O}_4$ 45%.

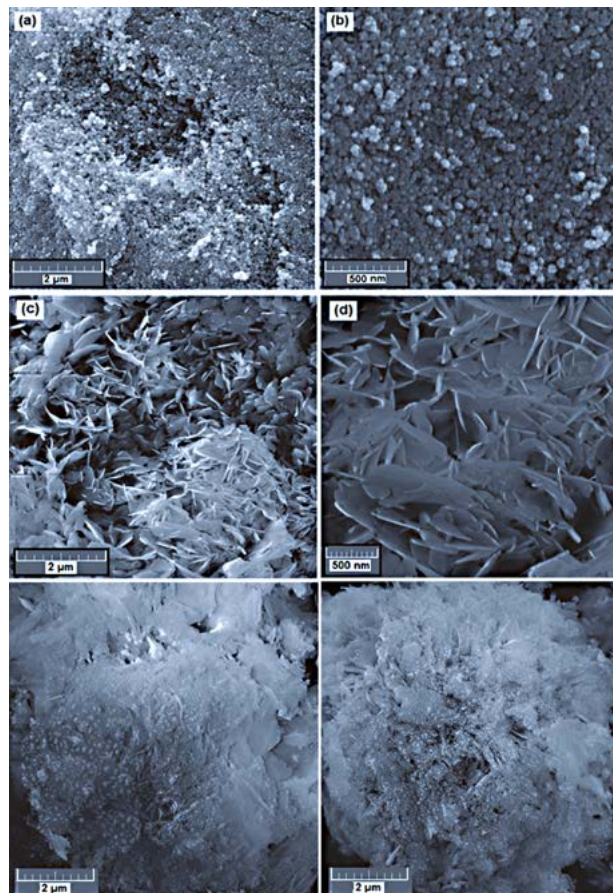


Figure 3. SEM images of (a and b) CoFe_2O_4 , (c and d) $\text{Bi}_2\text{O}_2\text{CO}_3$, (e) $\text{Bi}_2\text{O}_2\text{CO}_3/\text{CoFe}_2\text{O}_4$ 30% (f) $\text{Bi}_2\text{O}_2\text{CO}_3/\text{CoFe}_2\text{O}_4$ 45% samples.

spherical CoFe_2O_4 nanoparticles with a size of about 15–20 nm were well deposited on the $\text{Bi}_2\text{O}_2\text{CO}_3$ nanoplates.

The size and microstructure of the as-prepared $\text{Bi}_2\text{O}_2\text{CO}_3/\text{CoFe}_2\text{O}_4$ samples were further investigated by TEM. The sample powder was sonicated in ethanol for 30 min and a drop of the suspension was dried on a carbon-coated microgrid for TEM measurements. The TEM images in Figure 4(a)–(c) show that the obtained $\text{Bi}_2\text{O}_2\text{CO}_3/\text{CoFe}_2\text{O}_4$ 30% nanocomposite was formed mainly from plate-like particles with a weak agglomeration. Also, from the TEM images in Figure 4(d), it is clear that the $\text{Bi}_2\text{O}_2\text{CO}_3/\text{CoFe}_2\text{O}_4$ 45% consists of plate-like structure with the lengths of 15–40 nm and thicknesses of several nanometers while CoFe_2O_4 nanoparticles show sphere-like shapes. It is obvious from the TEM images that the nanoplates exhibit mostly square-like shapes, although some are rectangular. As can be observed on all images, many spherical CoFe_2O_4 dark-color particles are observed to be deposited on the surface of bright plates of the $\text{Bi}_2\text{O}_2\text{CO}_3$. The average size of CoFe_2O_4 particles was calculated to be 15 nm from the measurements on the TEM micrographs which is in close agreement with the size obtained from XRD analysis. It is clear from the images, the morphology of the $\text{Bi}_2\text{O}_2\text{CO}_3/\text{CoFe}_2\text{O}_4$ composites from TEM images agreed with the SEM results.

The energy dispersive X-ray spectroscopy (EDX) was used to characterize the elemental composition of the as-prepared samples. The EDX spectra of CoFe_2O_4 , $\text{Bi}_2\text{O}_2\text{CO}_3$ and $\text{Bi}_2\text{O}_2\text{CO}_3/\text{CoFe}_2\text{O}_4$ 30% are shown in Figure 5. The EDX spectrum of CoFe_2O_4 in Figure 5(a) shows the existence of Co, Fe and O elements as well as the EDX spectrum of $\text{Bi}_2\text{O}_2\text{CO}_3$ (Figure 5(b)) shows the existence of Bi, C and O elements. In addition, the constituents of $\text{Bi}_2\text{O}_2\text{CO}_3/\text{CoFe}_2\text{O}_4$ 30% were studied by EDX method. As

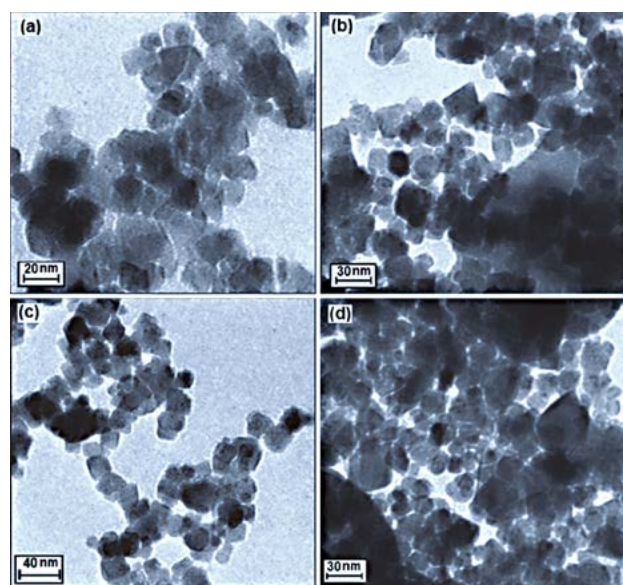


Figure 4. TEM images of (a)–(c) $\text{Bi}_2\text{O}_2\text{CO}_3/\text{CoFe}_2\text{O}_4$ 30%, and (d) $\text{Bi}_2\text{O}_2\text{CO}_3/\text{CoFe}_2\text{O}_4$ 45% samples.

shown in Figure 5(c), the EDX elemental spectrum of the nanocomposite sample exhibits elemental peaks corresponding to both CoFe_2O_4 and $\text{Bi}_2\text{O}_2\text{CO}_3$ and no other impure peaks can be observed, indicating that the composite sample is consisted of CoFe_2O_4 and $\text{Bi}_2\text{O}_2\text{CO}_3$. In all samples, the presence of Au peak at 2.2 KeV is due to SEM-EDX sample holder.

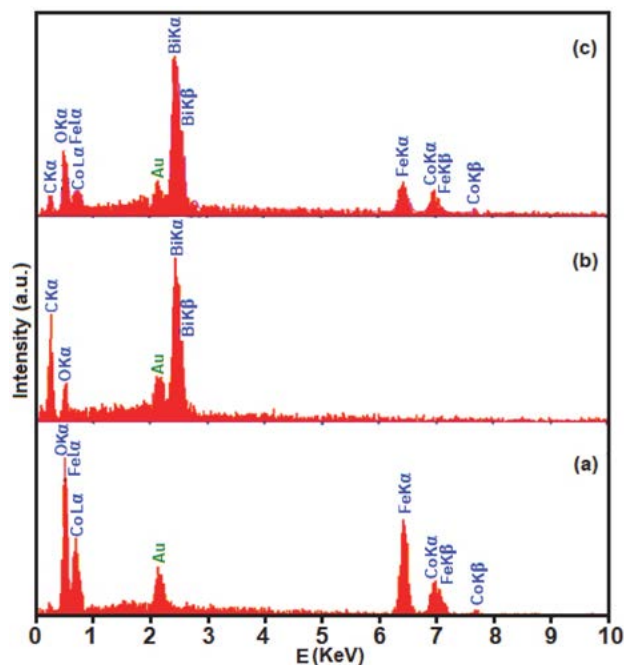


Figure 5. EDX spectra of (a) CoFe_2O_4 , (b) $\text{Bi}_2\text{O}_2\text{CO}_3$ and (c) $\text{Bi}_2\text{O}_2\text{CO}_3/\text{CoFe}_2\text{O}_4$ 30% nanocomposite.

To further determine the composition and element distributions of $\text{Bi}_2\text{O}_2\text{CO}_3/\text{CoFe}_2\text{O}_4$ 30% composite, EDX mapping measurements were also carried out. Figure 6 shows a representative SEM image of the nanocomposite with corresponding EDX elemental mappings. From the maps in Figure 6(b)–(f), can be observed that the Bi, C, O, Co and Fe elements are uniformly distributed over the sample, confirming the homogeneity of the nanocomposite. The EDX elemental mappings of the $\text{Bi}_2\text{O}_2\text{CO}_3/\text{CoFe}_2\text{O}_4$ 30% composite (Figures 6(e) and (f)) display that the elements of Co and Fe from CoFe_2O_4 phase are distributed on the surface of the $\text{Bi}_2\text{O}_2\text{CO}_3$. The EDX mappings results further indicate that the $\text{Bi}_2\text{O}_2\text{CO}_3/\text{CoFe}_2\text{O}_4$ nanocomposites have been successfully synthesized.

The optical properties of the as-prepared $\text{Bi}_2\text{O}_2\text{CO}_3$, CoFe_2O_4 and $\text{Bi}_2\text{O}_2\text{CO}_3/\text{CoFe}_2\text{O}_4$ composites were investigated by the diffuse reflectance UV-vis spectra (DRS) absorption spectroscopy (Figure 7). Figure 7(a) displays the UV-vis diffuse reflectance spectra of the bare $\text{Bi}_2\text{O}_2\text{CO}_3$ (curve i), $\text{Bi}_2\text{O}_2\text{CO}_3/\text{CoFe}_2\text{O}_4$ 30% composite (curve ii) and CoFe_2O_4 (curve iii). Bare $\text{Bi}_2\text{O}_2\text{CO}_3$ shows absorption edge at ~ 400 nm whereas pure CoFe_2O_4 shows good absorbance in the visible light region up to 490 nm. As can be

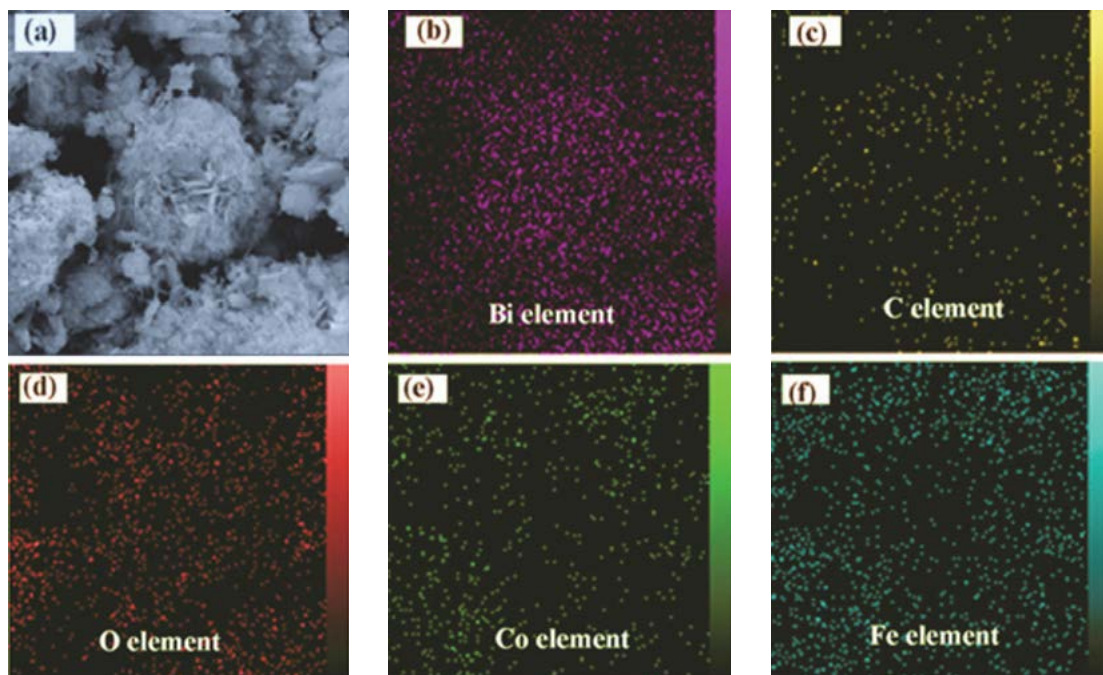


Figure 6. SEM image and the corresponding elemental mapping images of $\text{Bi}_2\text{O}_2\text{CO}_3/\text{CoFe}_2\text{O}_4$ 30%.

seen in curve ii of Figure 7(a), the UV-vis band of $\text{Bi}_2\text{O}_2\text{CO}_3/\text{CoFe}_2\text{O}_4$ nanocomposite indicates an enhancement in absorption intensity in the visible region together with a red shift, compared to that of the pure $\text{Bi}_2\text{O}_2\text{CO}_3$ due to the coupling with CoFe_2O_4 phase. The band gaps (E_g s) of these three samples were calculated by the following formula based on the DRS results:⁵⁷

$$(\alpha h\nu)^{1/2} = B(h\nu - E_g) \quad (1)$$

Where α , h , ν and B are absorption coefficient, plank constant, light frequency, and a constant, respectively. Therefore, E_g value of the samples can be estimated from a

plot $(\alpha h\nu)^{1/2}$ versus photon energy ($h\nu$). The intercept of the tangent to the x axis would give an approximation of the band-gap energy of the samples (Figure 7(b)). As shown in Figure 7(b) (curves i-iii), the E_g values of pure $\text{Bi}_2\text{O}_2\text{CO}_3$, $\text{Bi}_2\text{O}_2\text{CO}_3/\text{CoFe}_2\text{O}_4$ 30% nanocomposite and pure CoFe_2O_4 were found to be 3.49, 2.89 and 2.79 eV, respectively. It is clear that the $\text{Bi}_2\text{O}_2\text{CO}_3/\text{CoFe}_2\text{O}_4$ 30% composite shows a band gaps at 2.89 eV with a red shift compared to that of the pure $\text{Bi}_2\text{O}_2\text{CO}_3$ (3.49 eV), indicating formation of hybrid heterostructures.

The elemental composition and oxidation states of $\text{Bi}_2\text{O}_2\text{CO}_3/\text{CoFe}_2\text{O}_4$ 30% sample were carefully analyzed by XPS. The full XPS spectrum in Figure 8(a) shows that the

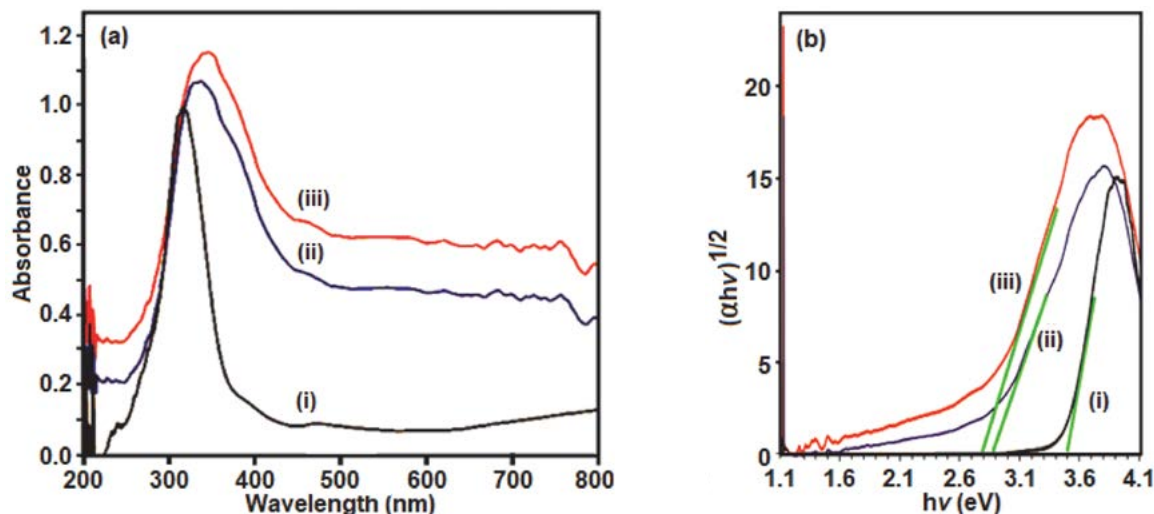


Figure 7. (a) UV-vis diffuse reflectance spectra and (b) $(\alpha h\nu)^{1/2}$ versus $h\nu$ curves of (i) pure $\text{Bi}_2\text{O}_2\text{CO}_3$, (ii) $\text{Bi}_2\text{O}_2\text{CO}_3/\text{CoFe}_2\text{O}_4$ 30% and (iii) CoFe_2O_4 .

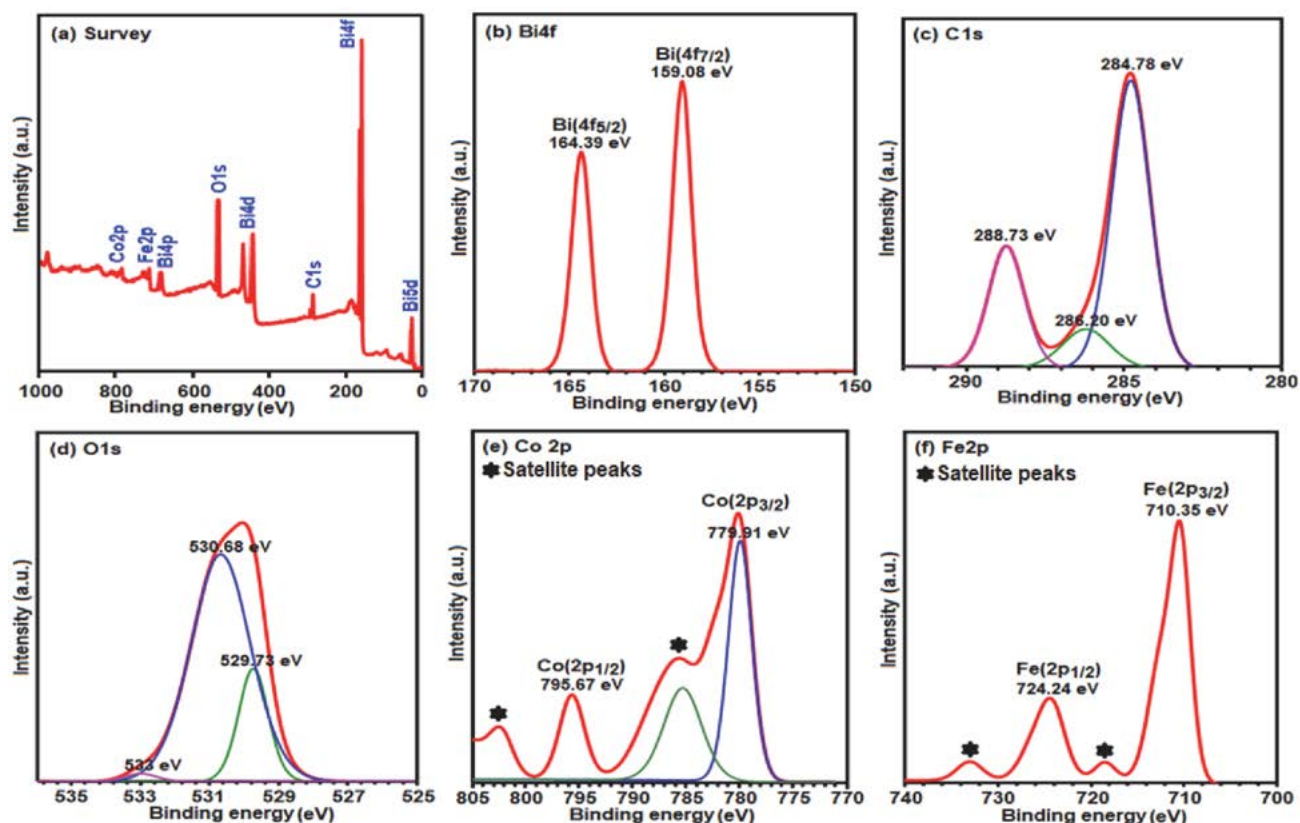


Figure 8. (a) XPS survey spectrum of the $\text{Bi}_2\text{O}_2\text{CO}_3/\text{CoFe}_2\text{O}_4$ 30% nanocomposite. High-resolution XPS spectra of (b) Bi 4f, (c) C 1s, (d) O 1s, (e) Co 2p and (f) Fe 2p.

sample consists of Bi, O, C, Co and Fe elements, in consistent with the EDX results. In order to further investigate the chemical state of each element, the high-resolution XPS spectra of Bi 4f, C 1s, O 1s, Co 2p and Fe 2p for the as-prepared $\text{Bi}_2\text{O}_2\text{CO}_3/\text{CoFe}_2\text{O}_4$ 30% are separately shown in Figure 8(b)–(f). As shown in Figure 8(b), the peaks located at binding energies of 159.08 and 164.39 eV are attributed to Bi 4f_{7/2} and Bi 4f_{5/2}, respectively, indicating the existence of Bi³⁺ ions in the sample.⁵⁸ In Figure 8(c), the peak at 284.78 eV is attributed to carbon reference, while the peak at 288.73 eV corresponds to the carbon of carbonate ion (CO_3^{2-}) in $\text{Bi}_2\text{O}_2\text{CO}_3$.⁵⁸ For the oxygen element (Figure 8(d)), the O 1s peaks are well fitted into three different peaks at 529.73 eV, 530.68 eV and 532 eV. According to the experiment results, the peak located at 529.73 eV is arisen from Bi–O in $\text{Bi}_2\text{O}_2\text{CO}_3$ while that at 530.63 eV is from CO_3^{2-} species and CoFe_2O_4 .⁵⁹ Other small peak at higher binding energy of 532 eV can be attributed to the presence of surface-chemisorbed adsorbed H_2O .⁶⁰ As shown in Figure 8(e), the peaks at 799.91 eV and 795.67 eV could be assigned to Co 2p_{3/2} and Co 2p_{1/2}, respectively, shouldering with satellite peaks at 785.29 eV and 802.27 eV. Figure 8(f) shows Fe 2p peaks at binding energies of 710.35 eV (Fe 2p_{3/2}) and 724.24 eV (Fe 2p_{1/2}) with weak satellite peaks at 718.50 eV and 733.04 eV. The observed Co 2p and Fe 2p photoelectron peaks are consistent with those reported for Co²⁺ and Fe³⁺ in CoFe_2O_4 .⁶¹ The above results

can powerfully support the presence of CoFe_2O_4 in the as-prepared $\text{Bi}_2\text{O}_2\text{CO}_3/\text{CoFe}_2\text{O}_4$ sample, implying the formation of heterojunction between CoFe_2O_4 and $\text{Bi}_2\text{O}_2\text{CO}_3$ in the resulted composite.

The BET surface area and porous structure of the $\text{Bi}_2\text{O}_2\text{CO}_3/\text{CoFe}_2\text{O}_4$ composite were investigated based on nitrogen adsorption–desorption. Figure 9 gives the adsorption–desorption isotherms and the corresponding pore size distribution curve of the $\text{Bi}_2\text{O}_2\text{CO}_3/\text{CoFe}_2\text{O}_4$ 30% sample. As observed in Figure 9, the sample shows a type-III isotherm according to the IUPAC classification.⁶² The isotherm shows a distinct H3 hysteresis loop in the relatively high pressure range ($p/p_0 = 0.8$ –1). Generally, it is believed that the H3 hysteresis loop is related to the mesopores through the aggregates of plate-like particles which were further observed from the corresponding pore size distribution curve in the inset of Figure 9.⁶³ The obtained BET specific surface area of the $\text{Bi}_2\text{O}_2\text{CO}_3/\text{CoFe}_2\text{O}_4$ 30% sample is $88.09 \text{ m}^2 \text{ g}^{-1}$, whereas that of the $\text{Bi}_2\text{O}_2\text{CO}_3$ sample is $8.7 \text{ m}^2 \text{ g}^{-1}$.⁶³ Accordingly, it is clear that the BET surface area of the $\text{Bi}_2\text{O}_2\text{CO}_3/\text{CoFe}_2\text{O}_4$ 30% catalyst is much larger (about 10 times) than that of pure $\text{Bi}_2\text{O}_2\text{CO}_3$. The increased surface area may be also beneficial for the increase of active sites and catalytic activities. The total pore volume is $0.297 \text{ cm}^3/\text{g}$ and the average pore size of this sample is 1.27 nm, which is estimated using the Barrett–Joyner–Halenda (BJH) method from the ad-

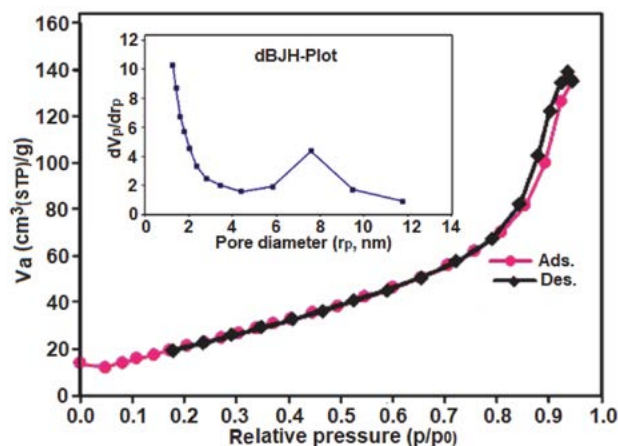


Figure 9. N_2 adsorption–desorption isotherm of the $Bi_2O_2CO_3/CoFe_2O_4$ 30% sample. The inset is the pore size distribution curve.

sorption branch of the N_2 isotherm as shown in the inset of Figure 9.

Figure 10 shows the magnetization measurement for the as-prepared $Bi_2O_2CO_3/CoFe_2O_4$ nanocomposites and pure $CoFe_2O_4$, using a vibrating sample magnetometer (VSM) at room temperature. The magnetization curves of the nanocomposites undoubtedly indicate ferromagnetism orders due to the presence of ferromagnetic $CoFe_2O_4$ nanoparticles. The saturation magnetization values of $Bi_2O_2CO_3/CoFe_2O_4$ 30%, $Bi_2O_2CO_3/CoFe_2O_4$ 45% and pure $CoFe_2O_4$ were found to be 17.15, 28.68 and 63.36 emu/g, respectively. The saturation magnetizations of the magnetic nanocomposites decrease compared with that of pure $CoFe_2O_4$, which can be attributed to the nano-magnetic $Bi_2O_2CO_3$ component. As demonstrated in the inset

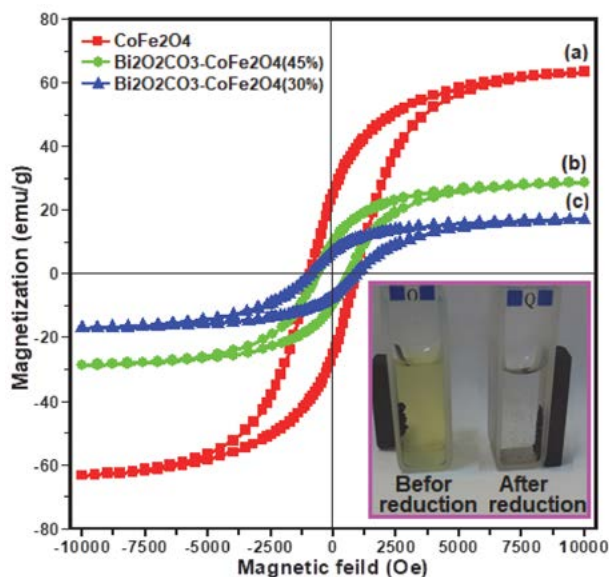


Figure 10. Magnetization curves of (a) pure $CoFe_2O_4$, (b) $Bi_2O_2CO_3/CoFe_2O_4$ 45% and (c) $Bi_2O_2CO_3/CoFe_2O_4$ 30%. The photo inset shows magnetic separation of the nanocomposite catalyst before and after the reduction of 4-NP by $NaBH_4$.

of Figure 10, complete separation of the catalyst colloids from the solution can be achieved under an external magnetic field. The rapid and easy magnetically separation of hybrid from water will assure the effective collection of the used catalysts and avoid the loss of nanoparticles for environmental risks.

3. 2. Catalytic Reduction of 4-Nitrophenol

To investigate the catalytic activity of $Bi_2O_2CO_3/CoFe_2O_4$ nanostructures with different contents of $CoFe_2O_4$, the reduction of 4-nitrophenol (4-NP) to 4-aminophenol (4-AP) by excess $NaBH_4$ in aqueous solution was used as the model reaction (Figure. 11). Usually, 4-NP solution exhibits a strong absorption peak at 317 nm and a weak shoulder peak at 400 nm in the region of 250–550 nm.⁶⁴ After alkali $NaBH_4$ is added into 4-NP solution, the absorption peak at 317 nm disappears; only the one at 400 nm exists and markedly increases, which should be attributed to the production of the intermediate state, 4-nitrophenolate ion.⁶⁵ The intermediate can stably exist for a couple of day still a catalyst is introduced into the above system. Here, the peak at 400 nm gradually decreases, and concomitantly, a new peak at 305 nm appears due to the production of 4-AP.^{66,67} Figure 11(a) exhibits the UV–vis absorption spectra of the 4-NP- $NaBH_4$ - H_2O system after reacting for various durations in the presence of 5 mg pure $Bi_2O_2CO_3$ nanostructures. One can easily find that the peak intensity at 400 nm markedly decreases with the prolonging of the reaction time and disappeared after 32 min. However, $Bi_2O_2CO_3$ nanostructures with different contents of $CoFe_2O_4$ exhibit different catalytic activities for the reduction of 4-NP. As shown in Figure 11(b), it merely took 20 min to completely convert 4-NP to 4-AP in the presence of $Bi_2O_2CO_3/CoFe_2O_4$ 30% nanocomposite. After the same amount of $Bi_2O_2CO_3/CoFe_2O_4$ 45% was used as the catalyst, it took 60 min to complete the reaction (Figure 11(c)). Namely, among various samples, $Bi_2O_2CO_3/CoFe_2O_4$ 30% bears the strongest catalytic activity. Introduction of $CoFe_2O_4$ in the composite significantly improves the catalytic activities of $Bi_2O_2CO_3$. However, an excess addition of $CoFe_2O_4$ showed decrease in catalytic efficiencies. In the present work, the reduction reaction of 4-NP to 4-AP could be reasonably assumed as a pseudo-first-order kinetics with regard to 4-NP owing to the presence of excess $NaBH_4$. This pseudo-first-order kinetics equation can be described as $\ln C_0/C_t = kt$. Here, C_0 and C_t represent the initial and instantaneous concentrations of 4-NP, respectively; and k and t stand for the apparent rate constant and the reaction time in turn. The apparent rate constant values were calculated from the slope of plot of $\ln(C_0/C_t)$ versus reaction time (Figure 11(d)). The apparent rate constant (k) value for the $Bi_2O_2CO_3/CoFe_2O_4$ 30% sample (0.20 min^{-1}) was estimated which is higher than $Bi_2O_2CO_3/CoFe_2O_4$ 45% (0.04 min^{-1}) and pure $Bi_2O_2CO_3$ (0.13 min^{-1}) samples. From the observed results, it was ev-

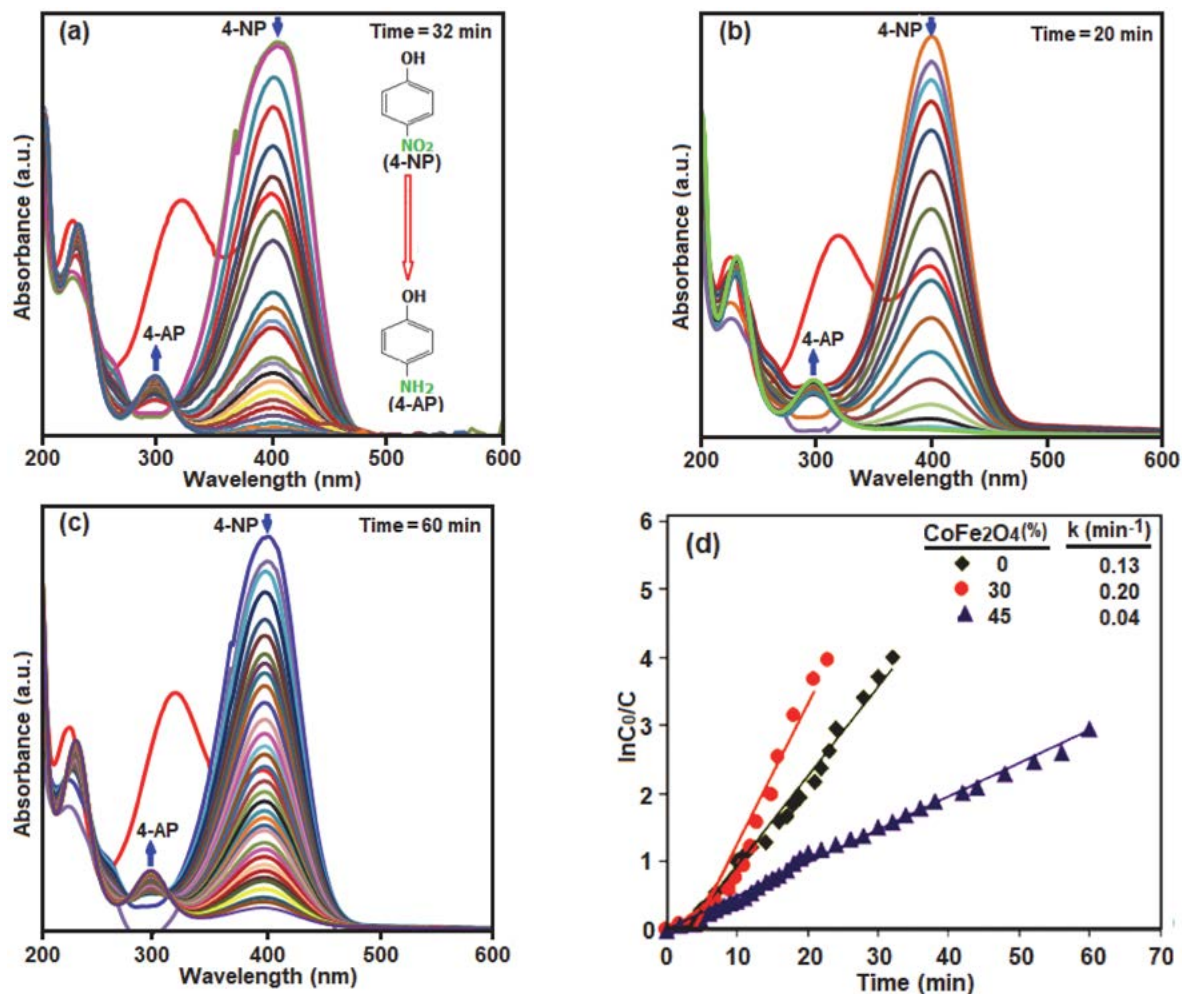


Figure 11. UV-vis spectral changes during the reduction of 4-NP with NaBH₄ over different catalysts: (a) pure Bi₂O₂CO₃, (b) Bi₂O₂CO₃/CoFe₂O₄30%, (c) Bi₂O₂CO₃/CoFe₂O₄45% and (d) Plot of $\ln(C_0/C)$ against the reaction time (the inset is the apparent rate constant values). Conditions: 4-NP (2 mL, 0.2 mM), catalyst (5.0 mg), NaBH₄ (0.5 mL, 20 mM), at 25 °C.

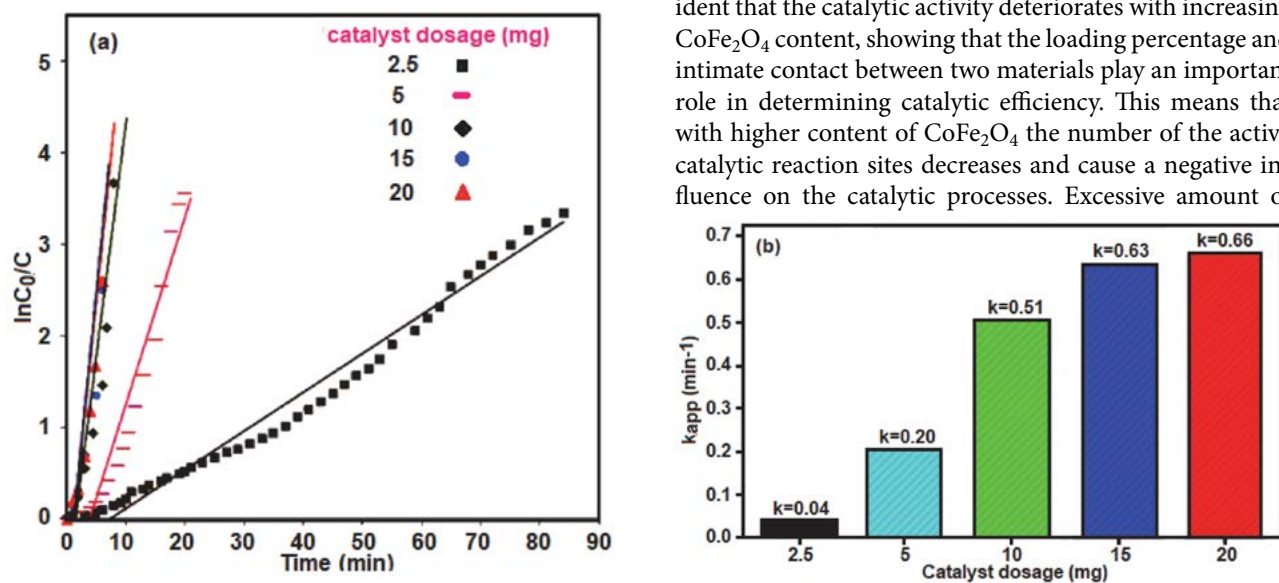


Figure 12 (a) Plot of $\ln(C_0/C)$ against the reaction time in the presence of different amounts of Bi₂O₂CO₃/CoFe₂O₄30% catalyst, and (b) the apparent rate constant values. Conditions: nitro compounds (2 mL, 0.2 mM) and NaBH₄ (0.5 mL, 20 mM), at 25 °C were used in all reactions.

ident that the catalytic activity deteriorates with increasing CoFe₂O₄ content, showing that the loading percentage and intimate contact between two materials play an important role in determining catalytic efficiency. This means that with higher content of CoFe₂O₄ the number of the active catalytic reaction sites decreases and cause a negative influence on the catalytic processes. Excessive amount of

CoFe_2O_4 may cover the active sites at the surface of $\text{Bi}_2\text{O}_2\text{CO}_3$ and also could hinder the contact with 4-NP. The highest catalytic performance of $\text{Bi}_2\text{O}_2\text{CO}_3/\text{CoFe}_2\text{O}_4$ 30% composite can be attributed to intimate contact between $\text{Bi}_2\text{O}_2\text{CO}_3$ and CoFe_2O_4 which facilitates the electron transfer. Moreover, the existence of CoFe_2O_4 in composites makes them magnetically separable during catalytic reactions.

The effect of the catalyst amount on the catalytic efficiency was investigated as well. Figure 12(a) shows linear relationships between $\ln(C_0/C_t)$ and the reaction time in the presence of different amounts of $\text{Bi}_2\text{O}_2\text{CO}_3/\text{CoFe}_2\text{O}_4$ 30% nanostructure. As shown in Figure 12(b), the rate constants (k_{app}) of 4-NP reduction reaction were calculated to be 0.04, 0.20, 0.51, 0.63 and 0.66 min^{-1} from the slope of the straight with various amount of $\text{Bi}_2\text{O}_2\text{CO}_3/\text{CoFe}_2\text{O}_4$ 30% catalyst. The k_{app} increased as the amount of $\text{Bi}_2\text{O}_2\text{CO}_3/\text{CoFe}_2\text{O}_4$ 30% catalyst increasing from 2.5 to 20 mg. A higher dosage of $\text{Bi}_2\text{O}_2\text{CO}_3/\text{CoFe}_2\text{O}_4$ 30% nano-composite in the solution provides more active sites for the

generation of H_2 and e^- (from NaBH_4), led to an increased reaction rate.

Furthermore, it was found that the present catalyst could also catalyze the reduction of other aromatic nitro-compounds including 4-nitroaniline (4-NA), 2-nitroaniline (2-NA) and 2-nitrophenol (2-NP), to corresponding amines. Figure 13(a)-(c) shows the reduction of three nitroarene by NaBH_4 in the presence of $\text{Bi}_2\text{O}_2\text{CO}_3/\text{CoFe}_2\text{O}_4$ 30% nanocomposite. The reductive reactions were completed within 15 min (for 4-NA), 29 min (for 2-NA) and 16 min (for 2-NP), respectively. The calculated reaction rate constants (k_{app}) for these substrates are displayed in Fig. 13(d). The k_{app} values of these substrates are as the following order: 4-NA (0.24 min^{-1}) > 2-NP (0.23 min^{-1}) > 2-NA (0.1 min^{-1}). Since the reactions were carried out under the same experimental conditions, the different rates can be related to the structures of nitrocompounds.

In addition to catalytic activity, the stability and re-usability of catalysts are important issues for their practical applications. The stability of as synthesized $\text{Bi}_2\text{O}_2\text{CO}_3/$

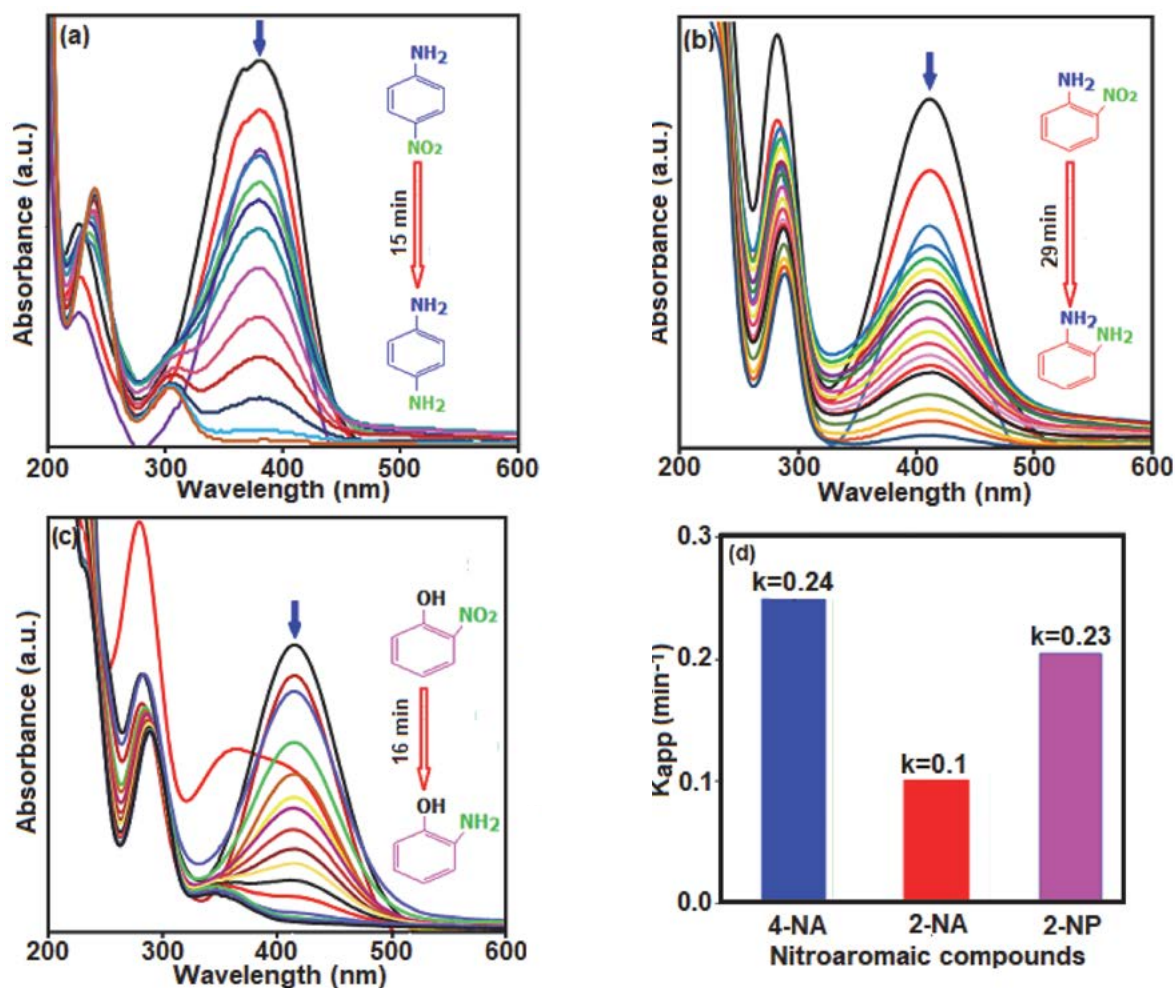


Figure 13. The UV-vis absorption spectra change for the reduction process of (a) 4-nitroaniline (4-NA), (b) 2-nitroaniline (2-NA), and (c) 2-nitrophenol (2-NP) with NaBH_4 in the presence of $\text{Bi}_2\text{O}_2\text{CO}_3/\text{CoFe}_2\text{O}_4$ 30% catalyst. (d) the calculated apparent rate constant values. Conditions: catalyst (5.0 mg), NaBH_4 (0.5 mL, 20 mM), and nitro compound (2 mL, 0.2 mM) at 25 °C.

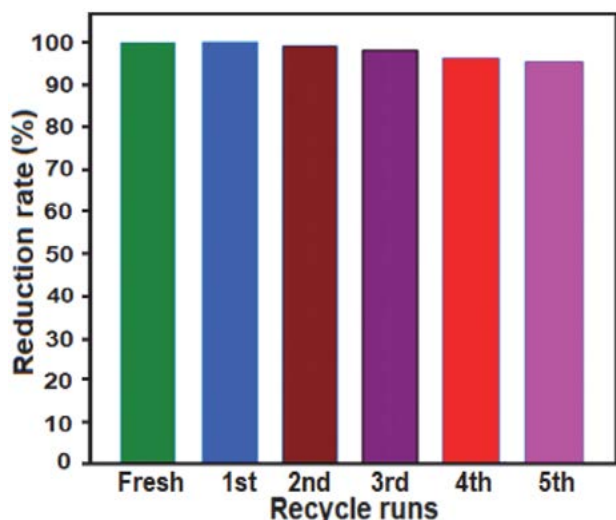


Figure 14. Recyclability of the of $\text{Bi}_2\text{O}_2\text{CO}_3/\text{CoFe}_2\text{O}_4$ 30% nanocomposite in the reduction of 4-NP. Conditions: catalyst (5.0 mg), $[\text{4-NP}] = 0.2 \text{ mM}$ and $[\text{NaBH}_4] = 20 \text{ mM}$, at 25°C .

CoFe_2O_4 30% catalyst was checked by performing four consecutive cycles. The catalyst used in any experiment was collected by external magnetic field, washed with distilled water, dried at 60°C and then employed for a new run without any observable weight loss. As shown in Figure 14, no significant loss of the catalytic activity can be observed after five successive runs of 4-NP reduction, indicating that the present composite catalysts are stable enough during the repeated experiments.

The nature of the recovered catalyst was also tested. As shown in Figure 15 (a) and (b), XRD pattern and FT-IR spectrum of the recycled $\text{Bi}_2\text{O}_2\text{CO}_3/\text{CoFe}_2\text{O}_4$ 30% nanocomposite catalyst did not show significant changes after the fourth run in comparison with the fresh catalyst (see Figures 1(c) and 2(c)). Figures 15(c) and (d) show the SEM and TEM images of the catalyst after five cycles, respectively. It could be observed that the recovered catalyst kept its initial size and morphology (see Figures 3(e)-(f) and 4) and the surface of $\text{Bi}_2\text{O}_2\text{CO}_3$ nanoplates was still decorated with CoFe_2O_4 nanoparticles, revealing the strong binding

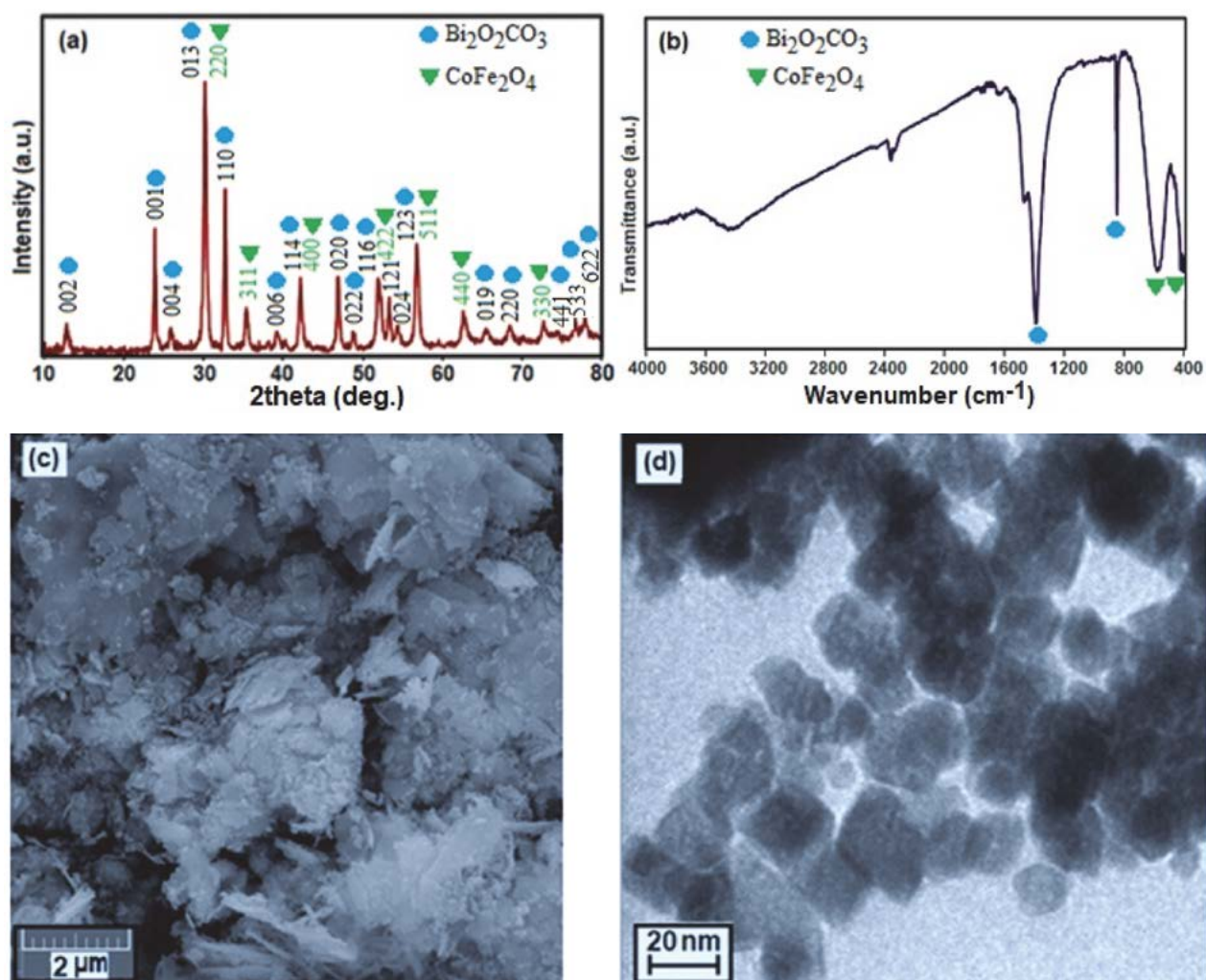


Figure 15. (a) XRD pattern, (b) FT-IR spectrum, (c) SEM image, and (d) TEM image of the recovered $\text{Bi}_2\text{O}_2\text{CO}_3/\text{CoFe}_2\text{O}_4$ 30% nanocomposite after the 5th run.

between the CoFe_2O_4 nanoparticles and $\text{Bi}_2\text{O}_2\text{CO}_3$ nanoplates. Therefore, the as-prepared $\text{Bi}_2\text{O}_2\text{CO}_3/\text{CoFe}_2\text{O}_4$ composites can work as an effective catalyst for the reduction of nitroaromatic compounds with good stability and recyclability.

In order to show the advantage of the present method, we have compared the obtained results in the reduction of 4-NP with NaBH_4 catalyzed by $\text{Bi}_2\text{O}_2\text{CO}_3/\text{CoFe}_2\text{O}_4$ 30% with some reported catalysts in the literature.^{68–80} From Table 1, it is clear that with respect to the reaction conditions and/or reaction times, the present method is more suitable and/or superior. It is clear that reaction in the presence of most reported catalysts required longer reaction times (Table 1, entries 1–10). However, the present catalyst showed close or lower catalytic activity compared with some of the catalysts (Table 1, entries 11 and 12). Also, the results confirm that this magnetic catalyst has higher catalytic activity than that of the previously reported $\text{Bi}_2\text{O}_2\text{CO}_3/\text{NiFe}_2\text{O}_4$ 30% catalyst in the reduction of 4-nitrophenol to 4-aminophenol under same conditions (Table 1, entries 13 and 14). Furthermore, the present nanocomposite can be easily prepared in one-step without the use of harsh, toxic and expensive chemicals which is very important in practical applications.

metals such as Au, Ag, Pt and Pd, $\text{Bi}_2\text{O}_2\text{CO}_3/\text{CoFe}_2\text{O}_4$ composites were easy to available and inexpensive. The preparation procedure of $\text{Bi}_2\text{O}_2\text{CO}_3/\text{CoFe}_2\text{O}_4$ magnetic nanocomposites via hydrothermal method was simple. And the as-prepared $\text{Bi}_2\text{O}_2\text{CO}_3/\text{CoFe}_2\text{O}_4$ magnetic nanocomposites were stable and well-dispersed. Moreover, the prepared $\text{Bi}_2\text{O}_2\text{CO}_3/\text{CoFe}_2\text{O}_4$ nanocomposites were magnetically separable from water with higher long-time use stability. This study provides a new approach for reducing and removing nitroarenes pollutants (e.g. 4-NP) in wastewater without introducing secondary pollutant into the system. Studies on the synthesis of nanocomposites of $\text{Bi}_2\text{O}_2\text{CO}_3$ with other ferrites (MFe_2O_4 ; M = Ni, Zn, Cu, Mn, ...) and their thermal catalytic and photocatalytic applications are currently in progress and underway in our laboratory.

5. Acknowledgements

This work was supported by the Lorestan University Research Council and Iran Nanotechnology Initiative Council (INIC).

Table 1. Comparison of the result obtained for the complete reduction of 4-NP in the present work with those obtained by some reported catalysts.

Entry	Catalyst	Reaction conditions	Reaction time (min)	Ref.
1	Ni-PVA/SBA-15	H_2O , NaBH_4 , r.t.	85	68
2	Hierarchical Au/CuO NPs	H_2O , NaBH_4 , r.t.	80	69
3	Cu NPs	THF/ H_2O , NaBH_4 , 50 °C	120	70
4	PdCu/graphene	EtOH/ H_2O , NaBH_4 , 50 °C	90	71
5	Au-GO	H_2O , NaBH_4 , r.t.	30	72
6	CoFe_2O_4 NPs	H_2O , NaBH_4 , r.t.	50	73
7	FeNi_2 nano-alloy	H_2O , NaBH_4 , r.t.	60	74
8	NiCo_2 nano-alloy	H_2O , NaBH_4 , r.t.	30	75
9	CdS/GO	H_2O , NaBH_4 , r.t.	30	76
10	dumbbell-like CuO NPs	H_2O , NaBH_4 , r.t.	32	77
11	Ni NPs	H_2O , NaBH_4 , r.t.	16	78
12	CuFe_2O_4 NPs	H_2O , NaBH_4 , r.t.	14	79
13	$\text{Bi}_2\text{O}_2\text{CO}_3/\text{NiFe}_2\text{O}_4$ 30%	H_2O , NaBH_4 , r.t.	42	80
14	$\text{Bi}_2\text{O}_2\text{CO}_3/\text{CoFe}_2\text{O}_4$ 30%	H_2O , NaBH_4 , r.t.	20	This work

4. Conclusions

To conclude, a series of novel plate-like $\text{Bi}_2\text{O}_2\text{CO}_3/\text{CoFe}_2\text{O}_4$ magnetic nanocomposites were successfully synthesized via a simple hydrothermal method for the first time and applied to catalyze the reduction of nitroarenes. Compared with the individual $\text{Bi}_2\text{O}_2\text{CO}_3$ and CoFe_2O_4 , the composite catalysts exhibit higher catalytic performance and stability for 4-nitrophenol reduction under ambient conditions. Compared with those noble

6. References

- J. R. Chiou, B. H. Lai, K. C. Hsu and D. H. Chen, *J. Hazard. Mater.* **2013**, 248, 394–400. DOI:10.1016/j.jhazmat.2013.01.030
- Y. Shaoqing, H. Jun and W. Jianlong, *Radiat. Phys. Chem.* **2010**, 79, 1039–1046. DOI:10.1016/j.radphyschem.2010.05.008
- A. C. Apolinario, A. M. Silva, B. F. Machado, H. T. Gomes, P. P. Araujo, and J. L. Figueredo, *Appl. Catal. B: Environ.* **2008**, 84, 75–86. DOI:10.1016/j.apcatb.2007.12.018
- V. Maurino, C. Minero, E. Pelizzetti, P. Piccinini, N. Serpone

- and H. Hidaka, *J. Photochem. Photobiol. A: Chem.* **1997**, *109*, 171–176. DOI:10.1016/S1010-6030(97)00124-X
5. P. Xiong, Y. Fu, L. Wang and X. Wang, *J. Chem. Eng.* **2012**, *195*, 149–157. DOI:10.1016/j.cej.2012.05.007
6. F. R. Zaggout and N. A. Ghalwa, *J. Environ. Manag.* **2008**, *86*, 291–296. DOI:10.1016/j.jenvman.2006.12.033
7. X. Zhu and J. Ni, *Electrochim. Acta*, **2011**, *56*, 10371–10377. DOI:10.1016/j.electacta.2011.05.062
8. Y. Y. Chu, Y. Qian, W. J. Wang and X. Deng, *J. Hazard. Mater.* **2012**, *199*, 179–185. DOI:10.1016/j.jhazmat.2011.10.079
9. C. Rizhi, D. Yan, X. Weihong and X. Nanping, *Chin. J. Chem. Eng.* **2007**, *15*, 884–888. DOI:10.1016/S1004-9541(08)60019-1
10. Z. Wu, J. Chen, Q. Di and M. Zhang, *Catal. Commun.* **2012**, *18*, 55–59. DOI:10.1016/j.catcom.2011.11.015
11. Y. Du, H. Chen, R. Chen and N. Xu, *Appl. Catal. A: Gen.* **2004**, *277*, 259–264. DOI:10.1016/j.apcata.2004.09.018
12. K. I. Min, J. S. Choi, Y. M. Chung, W. S. Ahn, R. Ryoo and P. K. Lim, *Appl. Catal. A: Gen.* **2008**, *337*, 97–104. DOI:10.1016/j.apcata.2007.12.004
13. T. Aditya, A. Pal and T. Pal, *Chem. Commun.* **2015**, *51*, 9410–9431 and reference cited therein.
14. T. R. Mandlimath and B. Gopal, *J. Mol. Catal. A: Chem.* **2011**, *350*, 9–15. DOI:10.1016/j.molcata.2011.08.009
15. Y. C. Chang and D. H. Chen, *J. Hazard. Mater.* **2009**, *165*, 664–669. DOI:10.1016/j.jhazmat.2008.10.034
16. Y. Deng, Y. Cai, Z. Sun, J. Liu, C. Liu, J. Wei, W. Li, C. Liu, Y. Wang and D. Y. Zhao, *J. Am. Chem. Soc.* **2010**, *132*, 8466–8473. DOI:10.1021/ja1025744
17. S. Harish, J. Mathiyarasu, K. Phani and V. Yegnaraman, *Catal. Lett.* **2009**, *128*, 197–202. DOI:10.1007/s10562-008-9732-x
18. J. Huang, S. Vongehr, S. Tang, H. Lu, J. Shen and X. Meng, *Langmuir*, **2009**, *25*, 11890–11896. DOI:10.1021/la9015383
19. H. Koga and T. Kitaoka, *J. Chem. Eng.* **2011**, *168*, 420–425. DOI:10.1016/j.cej.2010.08.073
20. P. Liu and M. Zhao, *Appl. Surf. Sci.* **2009**, *255*, 3989–3993. DOI:10.1016/j.apsusc.2008.10.094
21. J. Wang, X. B. Zhang, Z. L. Wang, L. M. Wang, W. Xing and X. Liu, *Nanoscale*, **2012**, *4*, 1549–1552. DOI:10.1039/c2nr11912a
22. Y. Zhu, J. Shen, K. F. Zhou, C. Chen, X. Yang and C. Li, *J. Phys. Chem. C*, **2010**, *115*, 1614–1619. DOI:10.1021/jp109276q
23. F. H. Lin and R. A. Doong, *J. Phys. Chem. C*, **2011**, *115*, 6591–6598. DOI:10.1021/jp110956k
24. K. Jiang, H. X. Zhang, Y. Y. Yang, R. Mothes, H. Lang and W. B. Cai, *Chem. Commun.* **2011**, *47*, 11924–11926. DOI:10.1039/c1cc14675k
25. H. He and C. Gao, *J. Nanomater.* **2011**, *2011*, 1–10.
26. X. Du, J. He, J. Zhu, L. Sun and S. An, *Appl. Surf. Sci.* **2012**, *258*, 2717–2723. DOI:10.1016/j.apsusc.2011.10.122
27. D. Y. Li, Y. G. Zhang, Y. L. Zhang, X. F. Zhou and S. J. Guo, *J. Hazard. Mater.* **2013**, *258–259*, 42–49. DOI:10.1016/j.jhazmat.2013.02.058
28. R. G. Li, F. X. Zhang, D. G. Wang, J. X. Yang, M. R. Li, J. Zhu, X. Zhou, H. X. Han and C. Li, *Nat. Commun.* **2013**, *4*, 1432. DOI:10.1038/ncomms2401
29. S. M. Sun, W. Z. Wang and L. Zhang, *J. Phys. Chem. C*, **2013**, *117*, 9113–9120. DOI:10.1021/jp4004592
30. G. H. Tian, Y. J. Chen, W. Zhou, K. Pan, Y. Z. Dong, C. G. Tian and H. G. Fu, *J. Mater. Chem.* **2011**, *21*, 887–892. DOI:10.1039/C0JM03040F
31. X. Zhao, J. H. Qu, H. J. Liu and C. Hu, *Environ. Sci. Technol.* **2007**, *41*, 6802–6807. DOI:10.1021/es070598b
32. J. Jiang, K. Zhao, X. Y. Xiao and L. Z. Zhang, *J. Am. Chem. Soc.* **2012**, *134*, 4473–4476. DOI:10.1021/ja210484t
33. Y. N. Wang, K. J. Deng and L. Z. Zhang, *J. Phys. Chem. C*, **2011**, *115*, 14300–14308. DOI:10.1021/jp2042069
34. L. Ye, J. Liu, C. Gong, L. Tian, T. Peng and L. Zan, *ACS Catal.* **2012**, *2*, 1677–1683. DOI:10.1021/cs300213m
35. Z. Ni, Y. Sun, Y. Zhang and F. Dong, *Appl. Surf. Sci.* **2016**, *365*, 314–335. DOI:10.1016/j.apsusc.2015.12.231
36. R. Hu, X. Xiao, S. Tu, X. Zuo and J. Nan, *Appl. Catal. B: Environ.* **2015**, *163*, 510–519. DOI:10.1016/j.apcatb.2014.08.025
37. Q. Wang, G. Yun, Y. Bai, N. An, J. Lian, H. Huang and B. Su, *Appl. Surf. Sci.* **2014**, *313*, 537–544. DOI:10.1016/j.apsusc.2014.06.018
38. H. Lu, L. Xu, B. Wei, M. Zhang, H. Gao and W. Sun, *Appl. Surf. Sci.* **2014**, *303*, 360–366. DOI:10.1016/j.apsusc.2014.03.006
39. N. Guo, Y. Cao, Y. Rong and D. Jia, *RSC Adv.* **2016**, *6*, 106046–106053
40. J. Cao, X. Li, H. Lin, S. Chen and X. Fu, *J. Hazard. Mater.* **2012**, *239*, 316–324. DOI:10.1016/j.jhazmat.2012.08.078
41. X. Huang and H. Chen, *Appl. Surf. Sci.* **2013**, *284*, 843–848. DOI:10.1016/j.apsusc.2013.08.019
42. N. Liang, J. Zai, M. Xu, Q. Zhu, X. Wei and X. Qian, *J. Mater. Chem. A*, **2014**, *2*, 4208–4216. DOI:10.1039/c3ta13931j
43. Y. Ao, L. Xu, P. Wang, C. Wang, J. Hou and J. Qian, *Dalton Trans.*, **2015**, *44*, 11321–11330. DOI:10.1039/C5DT01168J
44. Y. Liu, P. Zhang, H. Lv, J. Guang, S. Li and J. Jiang, *RSC Adv.* **2015**, *5*, 83764–83772.
45. Q. Zhang, H. Y. Wang, S. Z. Hu, G. Lu, J. Bai, X. X. Kang, D. Liu and J. Z. Gui, *RSC Adv.* **2015**, *5*, 42736–42743.
46. N. Liang, M. Wang, L. Jin, S. S. Huang, W. L. Chen, M. Xu, Q. Q. He, J. T. Zai, N. H. Fang and X. F. Qian, *ACS Appl. Mater. Interfaces*, **2014**, *6*, 11698–11705. DOI:10.1021/am502481z
47. L. Jin, G. Q. Zhu, M. Hojamberdiev, X. C. Luo, C. W. Tan, J. H. Peng, X. M. Wei, J. P. Li and P. Liu, *Ind. Eng. Chem. Res.* **2014**, *53*, 13718–13727. DOI:10.1021/ie502133x
48. Y. Hu, C. Dong, K. L. Wu, S. H. Xia, X. Li and X. W. Wei, *Mater. Lett.* **2015**, *147*, 69–71. DOI:10.1016/j.matlet.2014.12.097
49. T. Li, X. Hu, C. Liu, C. Tang, X. Wang and S. Luo, *J. Mol. Catal. A: Chem.* **2016**, *425*, 124–135. DOI:10.1016/j.molcata.2016.10.001
50. X. Zhang, S. Li, S. Hua, J. Chen, W. Jiang, J. Zhang, L. Ji, L. Cai, Y. Wang, W. Song and J. Liu, *Mater. Lett.* **2016**, *185*, 50–53. DOI:10.1016/j.matlet.2016.08.086
51. S. Shylesh, V. Schunemann, and W. R. Thiel, *Angew. Chem., Int. Ed.* **2010**, *49*, 3428–3459. DOI:10.1002/anie.200905684
52. X. F. Shang, W. C. Lu, B. H. Yue, L. M. Zhang, J. P. Ni, Y. Lv and Y. L. Feng, *Cryst. Growth Des.* **2009**, *9*, 1415–1420. DOI:10.1021/cg800730s

53. G. E. Tobon-Zapata, S. B. Etcheverry and E. J. Baran, *J. Mater. Sci. Lett.* **1997**, *16*, 656–657. DOI:10.1023/A:1018527602604
54. Y. S. Fu and X. Wang, *Ind. Eng. Chem. Res.* **2011**, *50*, 7210–7218. DOI:10.1021/ie200162a
55. G. D. Hong, Y. Yamada, T. Nagatomi, Y. Takai and S. Fukuzumi, *J. Am. Chem. Soc.* **2012**, *134*, 19572–19575. DOI:10.1021/ja309771h
56. K. Modi, S. Shah, N. Pujara, T. Pathak, N. Vasoya and I. Jhala, *J. Mol. Struct.*, **2013**, *1049*, 250–262. DOI:10.1016/j.molstruc.2013.06.051
57. J. Gunjagar, A. More, K. Gurav and C. Lokhande, *Appl. Surf. Sci.*, **2008**, *254*, 5844–5848. DOI:10.1016/j.apsusc.2008.03.065
58. Y. C. Huang, W. J. Fan, B. Long, H. B. Li, F. Y. Zhao, Z. L. Liu, Y. X. Tong and H. B. Ji, *Appl. Catal. B: Environ.* **2015**, *185*, 68–76. DOI:10.1016/j.apcatb.2015.11.043
59. D. D. Hu, K. Y. Zhang, Q. Yang, M. J. Wang, Y. Xi and C. G. Hu, *Appl. Surf. Sci.*, **2014**, *316*, 93–101. DOI:10.1016/j.apsusc.2014.07.185
60. H. J. Lu, L. L. Xu, B. Wei, M. Y. Zhang, H. Gao and W. J. Sun, *Appl. Surf. Sci.* **2014**, *303*, 360–366. DOI:10.1016/j.apsusc.2014.03.006
61. S. Singh and N. Khare, *RSC Adv.* **2015**, *5*, 96562–96572.
62. P. Madhusudan, J. Yu, W. Wang, B. Cheng and G. Liu, *Dalton Trans.* **2012**, *41*, 14345–14353. DOI:10.1039/c2dt31528a
63. L. Xu, X. Yang, Z. Zhai and W. Hou, *CrystEngCommun.* **2011**, *13*, 7267–7275. DOI:10.1039/c1ce05671a
64. Z. Jin, M. Xiao, Z. Bao, P. Wang and J. Wang, *Angew. Chem., Int. Ed.* **2012**, *51*, 6406–6410. DOI:10.1002/anie.201106948
65. A. K. Patra, A. Dutta and A. Bhaumik, *Catal. Commun.* **2010**, *11*, 651–655. DOI:10.1016/j.catcom.2010.01.015
66. H. Li, J. K. Jo, L. Zhang, C. S. Ha, H. Suh and I. Kim, *Adv. Funct. Mater.* **2010**, *20*, 3864–3873. DOI:10.1002/adfm.201001067
67. M. Nemanashi and R. Meijboom, *J. Colloid Interface Sci.*, **2013**, *389*, 260–267. DOI:10.1016/j.jcis.2012.09.012
68. R. J. Kalbasi, A. A. Nourbakhsh and F. Babaknezhad, *Catal. Commun.* **2011**, *12*, 955–960. DOI:10.1016/j.catcom.2011.02.019
69. S. Y. Gao, X. X. Jia, Z. D. Li and Y. L. Chen, *J. Nanopart. Res.* **2012**, *14*, 1–11.
70. Z. Duan, G. Ma and W. Zhang, *Bull. Korean Chem. Soc.* **2012**, *33*, 4003–4006. DOI:10.5012/bkcs.2012.33.12.4003
71. A. K. Shil, D. Sharma, N. R. Guha, and P. Das, *Tetrahedron Lett.* **2012**, *53*, 4858–4861. DOI:10.1016/j.tetlet.2012.06.132
72. Y. Choi, H. S. Bae, E. Seo, S. Jang, K. H. Park and B. S. Kim, *J. Mater. Chem.* **2011**, *21*, 15431–15436. DOI:10.1039/c1jm12477c
73. M. Nasrollahzadeh, M. Bagherzadeh and H. Karimi, *J. Colloid Interface Sci.* **2016**, *465*, 271–278. DOI:10.1016/j.jcis.2015.11.074
74. K. L. Wu, R. Yu and X. W. Wei, *Cryst. Eng. Commun.* **2012**, *14*, 7626–7632. DOI:10.1039/c2ce25457c
75. K. L. Wu, X. W. Wei, X. M. Zhou, D. H. Wu, X. W. Liu, Y. Ye and Q. Wang, *J. Phys. Chem. C.* **2011**, *115*, 16268–16274. DOI:10.1021/jp201660w
76. S. Liu, Z. Chen, N. Zhang, Z. R. Tang and Y. J. Xu, *J. Phys. Chem. C.* **2013**, *117*, 8251–8261. DOI:10.1021/jp400550t
77. W. Che, Y. Ni, Y. Zhang and Y. Ma, *J. Phys. Chem. Solid.* **2015**, *77*, 1–7. DOI:10.1016/j.jpccs.2014.09.006
78. D. Z. Jiang, J. Xie, D. Jiang, X. Wei and M. Chen, *Cryst. Eng. Comm.* **2013**, *15*, 560–569. DOI:10.1039/C2CE26398J
79. J. Feng, L. Su, Y. Ma, C. Ren, Q. Guo and X. Chen, *Chem. Eng. J.* **2013**, *221*, 16–24. DOI:10.1016/j.cej.2013.02.009
80. P. Zarringhadam and S. Farhadi, *J. Alloys Compd.* **2017**, *729*, 1046–1057. DOI:10.1016/j.jallcom.2017.09.247

Povzetek

Nove magnetne nanodelce $\text{Bi}_2\text{O}_2\text{CO}_3/\text{CoFe}_2\text{O}_4$ smo pripravili s hidrotermalno sintezo. Infrardečo spektroskopijo (FT-IR), rentgensko difrakcijo (XRD), vrstično elektronsko mikroskopijo (SEM), energijsko disperzivno spektroskopijo rentgenskih žarkov (EDX), presevno elektronsko mikroskopijo (TEM), rentgensko fotoelektronsko spektroskopijo (XPS), UV-Vis difuzno refleksijsko spektroskopijo (DRS), magnetometer z vibrirajočim vzorcem (VSM) in adsorpcijsko desorpcijsko analizo N_2 smo uporabili za preučevanje strukture, morfologije, velikosti delcev, fazne sestave, optičnih in magnetnih lastnosti sintetiziranih nanokompozitov. Rezultati karakterizacije vzorcev so pokazali uspešno vezavo sferičnih nanodelcev CoFe_2O_4 in ploščam podobnih nanostruktur $\text{Bi}_2\text{O}_2\text{CO}_3$. Katalitično aktivnost magnetnih nanokompozitov $\text{Bi}_2\text{O}_2\text{CO}_3/\text{CoFe}_2\text{O}_4$ smo ocenili z redukcijo nekaterih aromatičnih nitro-spojnin, kot so nitrofenoli in nitroanilini, z uporabo vodne raztopine natrijevega borhidrida (NaBH_4) pri sobni temperaturi. Nanokompozit $\text{Bi}_2\text{O}_2\text{CO}_3/\text{CoFe}_2\text{O}_4$ s 30 % CoFe_2O_4 je pokazal najboljše rezultate pri redukciji aromatskih nitro spojin s popolno pretvorbo v ustrezne amino spojine v 15–30 minutah s konstanto hitrostjo $0,10\text{--}0,24 \text{ min}^{-1}$. Poleg tega lahko magnetni nanokompozit $\text{Bi}_2\text{O}_2\text{CO}_3/\text{CoFe}_2\text{O}_4$ zlahka odstranimo iz reakcijskega sistema z uporabo zunanega magneta.

Scientific paper

Complex Formation in a Liquid-Liquid Extraction System Containing Vanadium(IV/V), 2,3-Dihydroxynaphthalene and Thiazolyl Blue

Galya K. Toncheva,¹ Zlatimir T. Zhelev,¹ Vassil B. Delchev¹
and Kiril B. Gavazov^{2,*}

¹ Faculty of Chemistry, University of Plovdiv "Paisii Hilendarski", Plovdiv 4000, Bulgaria

² Faculty of Pharmacy, Medical University of Plovdiv, Plovdiv 4002, Bulgaria

* Corresponding author: E-mail: kgavazov@abv.bg

Received: 28-01-2018

Abstract

Liquid-liquid extraction systems for V^{IV/V} containing 2,3-dihydroxynaphthalene (DN) and 3-(4,5-dimethylthiazol-2-yl)-2,5-diphenyl-2H-tetrazolium bromide (thiazolyl blue, MTT) were studied. The optimum conditions for V^{IV} and V^V extraction were found. V^{IV} is extracted in chloroform as a 1:2:2 complex (V:DN:MTT) with $\lambda_{\max} = 570$ nm and $\varepsilon_{570} = 2.9 \times 10^4$ dm³ mol⁻¹ cm⁻¹. However, this wavelength was found unsuitable for precise spectrophotometric measurements due to time dependent absorbance changes. V^V forms predominantly a 1:1:1 complex with $\lambda_{\max} = 335$ nm. The calibration graph for this oxidation state is linear in the range of 0.06–1.5 $\mu\text{g cm}^{-3}$. The molar absorptivity, Sandell's sensitivity and limit of detection were calculated to be 1.6×10^4 dm³ mol⁻¹ cm⁻¹, 3.2 ng cm⁻² and 0.02 $\mu\text{g cm}^{-3}$, respectively. The ground-state equilibrium geometries of the anionic parts of the extracted ion-associates, [V^{IV}O(DN²⁻)₂]²⁻ and [V^VO₂(DN²⁻)]⁻, were optimized at the BLYP/6-31++G* level of theory.

Keywords: Vanadium(IV/V); 2,3-dihydroxynaphthalene; ternary complex; liquid-liquid extraction; spectrophotometry; DFT calculations

1. Introduction

Vanadium is an essential trace element for living organisms¹ and a pillar of modern technology² with a potentially significant environmental impact due to human activity, such as the burning of fossil fuels, manufacturing of steel alloys, dyes, glass and ceramics, and application as a catalyst in various processes.^{2,3} Vanadium is the fifth most abundant transition element in the Earth's crust with an average content of 0.014%.³ Natural sources of airborne vanadium include continental dust, volcanic activity, marine aerosols and wild forest fires.²

It is known that prolonged exposure to vanadium increases the risk of lung cancer and can damage the integumentary, respiratory, central nervous and digestive systems.⁴ The amount of vanadium resorbed in the gastrointestinal tract is a function of the oxidation state and coordination environment.⁵ The most important oxidation states of vanadium are IV and V. The ability to switch easily between them, along with the stereochemical

flexibility of this element⁶ are key factors that determine its role in biological systems.^{1,7}

Vanadium deficiency in animal species is related to stunted growth, impaired reproduction, altered red blood cell formation, disturbed iron metabolism and abnormalities in blood lipid levels.^{2,8} There is an opinion among health specialists that vanadium deficiency can affect humans in a similar way.² Insufficiently studied issues concerning the balance between its toxicity and essentiality^{8,9} define the necessity for vanadium determination in various samples and call for investigations of coordination compounds, which have the potential to be used for V^{IV}/V^V speciation.

Many methods have been proposed for vanadium determination and speciation.^{10–13} Very sensitive and cost effective are the spectrophotometric methods based on ternary complexes with catechol type ligands.^{14–19} However, the mechanism of colour development in some of these methods^{14,15} is debatable because it is not clear whether

the main spectral bands are due to the formation of coordination compounds or are products of reagent(s) oxidation and polymerization.^{20,21} On the other hand, it is difficult to find conditions for speciation analysis with such reagents as they are capable of reducing V^V to V^{IV} .^{19–26} In fact, little is known about the stabilizing effects of additional reagents on the initial oxidation state of vanadium in ternary complexes of this kind.

Several papers^{27–30} describe liquid-liquid extraction (LLE) of V^V with 2,3-dihydroxynaphthalene (DN), a ligand incorporating a catechol moiety, the interest in which has been revived thanks to Tarafder et al.^{31–33} In a previous paper,²¹ we compared the behaviour of V^{IV} and V^V in a LLE-chromogenic system involving DN and 2,3,5-triphenyl-2*H*-tetrazolium chloride (TTC). We found evidence for aggregation of the ternary complexes in the organic phase and shed light on the differences in the extraction mechanism for V^{IV} and V^V .

Here, we report results for LLE-chromogenic systems containing V^{IV} or V^V , DN and an alternative ion-association reagent: 3-(4,5-dimethylthiazol-2-yl)-2,5-diphenyl-2*H*-tetrazolium bromide (thiazolyl blue, MTT). MTT is a commercially available tetrazolium salt with many applications as a redox³⁴ and ion-association reagent.³⁵ MTT is known to have advantages over similar compounds in terms of stability and molar absorptivity of the obtained complexes^{35–38} and their applicability for V^{IV}/V^V speciation analysis.²⁶

2. Experimental Procedure and Theoretical Details

2. 1. Reagents and Apparatus

Stock V^{IV} aqueous solution (*ca.* 5×10^{-2} mol dm⁻³) was prepared from $VOSO_4 \cdot 5H_2O$ (purum, Fluka AG, Switzerland) and standardized by potassium permanganate titration. Working solutions at a concentration of 2×10^{-4} mol dm⁻³ and pH *ca.* 3.0 were prepared daily by suitable dilution. V^V solution (2×10^{-4} mol dm⁻³) was prepared by dissolving NH_4VO_3 (puriss. p.a., VEB Laborchemie Apolda, Germany) in water. Fresh DN chloroform solutions (2×10^{-3} mol dm⁻³) were prepared daily from the solid reagent (purum, Fluka AG, Switzerland). The concentration of MTT (p.a., LOBA Feinchemie GmbH, Austria) was 3×10^{-3} mol dm⁻³ (aqueous solution). The chloroform (p.a., Valerus, Bulgaria) was additionally distilled. The acidity of the aqueous medium was set by the addition of buffer solution, prepared by mixing 2.0 mol dm⁻³ aqueous solutions of CH_3COOH and ammonia. pH was measured by a Hanna HI-83141 pH meter (Romania). Absorbance measurements were performed by using a Camspec M508 spectrophotometer (United Kingdom), equipped with 1 cm path-length glass cells. Distilled water was used throughout the work.

2. 2. Procedure

Aliquots of V^{IV} or V^V solution, buffer solution (1 cm³) and MTT solution were placed into 125 cm³ separatory funnels. The volume was made to 10 cm³ with water. An aliquot of DN chloroform solution was added and the organic phase was made up to 10 cm³ with chloroform. The funnel was shaken for a fixed time period (10–240 s). After the separation of the phases, a portion of the organic extract was transferred through filter paper into the spectrophotometer cell. The absorbance was measured against chloroform or simultaneously prepared blank solution (containing all of the reagents with the exception of vanadium).

2. 3. Theoretical Details

The structures of the anionic coordination compounds were optimized at the BLYP/6-31++G* level of theory as described in the literature.²¹ The charge and multiplicity for $[V^{IV}O(DN^{2-})_2]^{2-}$ were set to -2 and doublet, respectively. The theoretical calculations were performed with the GAUSSIAN 03 program package. The results were visualized with the ChemCraft program.

3. Results and Discussion

The following variables were considered for the performed LLE-spectrophotometric optimisation experiments: organic solvent, wavelength for spectrophotometric measurements, pH, extraction time and concentration of the reagents.

3. 1. Choice of Organic Solvent and Spectral Characteristics

Chloroform,²¹ dichloroethane,³⁹ ethyl acetate²⁹ and methyl isobutyl ketone³⁰ were used in previous studies as extraction solvents for DN-containing complexes. Preliminary investigations showed that chloroform is the best solvent for the V^{IV}/V^V -DN-MTT species. Absorption spectra of these species are shown in Fig 1. Fig. 1a includes spectra obtained with a low DN concentration (8.0×10^{-5} mol dm⁻³). Significant differences can be observed for the two oxidation states. The V^{IV} complex (spectrum 1) has two intensive maxima (at 330 and 560 nm), while the V^V complex (spectrum 2) is characterized by an intense maximum (at 335 nm). Another maximum for this oxidation state is at 680 nm; the corresponding band is broad and low intensive.

Spectra with a high DN concentration (1.6×10^{-3} mol dm⁻³) are depicted in Fig. 1b. The spectral changes accompanying the increase of the DN concentration can be attributed to reduction of V^V to V^{IV} . However, this reduction is only partial: there is no complete matching of the two spectra as observed under similar conditions in

our previous studies²¹ for the couple V^{IV}-DN-TTC and V^{IV}-DN-TTC.

It should be mentioned that the absorbance of the blank is not stable in time (Fig. 1c). The increase of the ab-

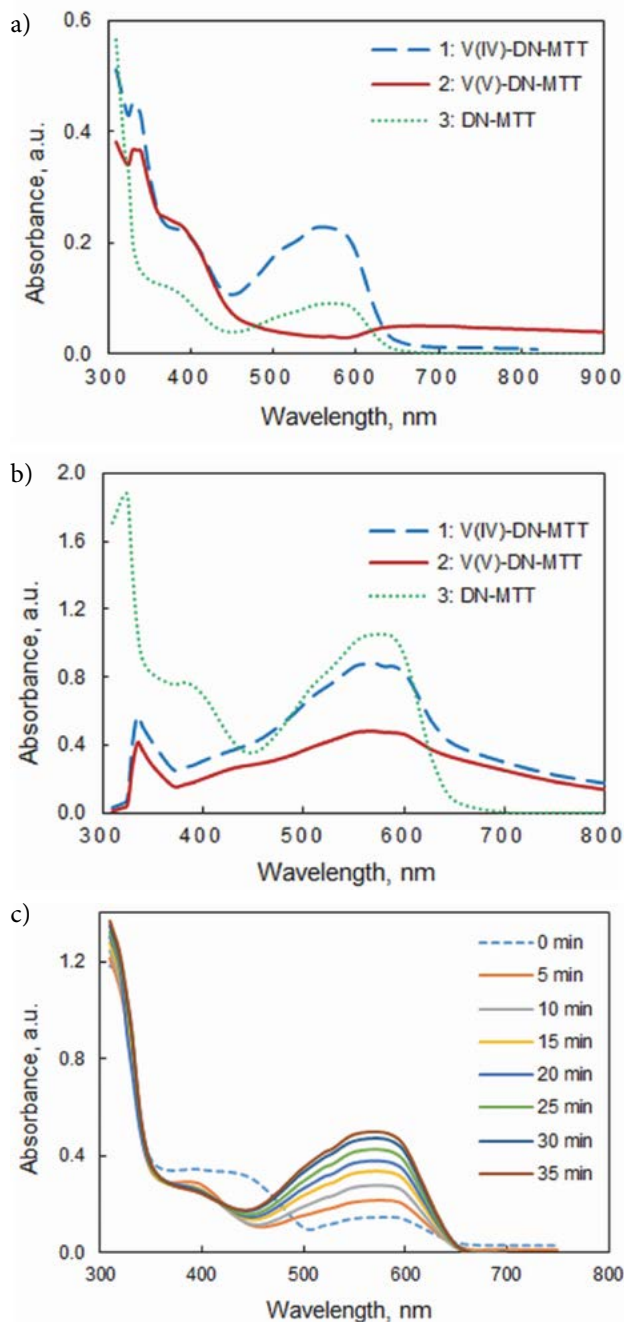


Figure 1. Absorption spectra in chloroform. **a)** At a low DN concentration, $8 \times 10^{-5} \text{ mol dm}^{-3}$: 1 – V^{IV}-DN-MTT against blank; 2 – V^V-DN-MTT against blank; 3 – blank (DN-MTT) against chloroform. $c_{V(IV)} = c_{V(V)} = 3 \times 10^{-5} \text{ mol dm}^{-3}$, $c_{MTT} = 1.5 \times 10^{-4} \text{ mol dm}^{-3}$, pH 5, extraction time 2 min. **b)** At a high DN concentration, $1.6 \times 10^{-3} \text{ mol dm}^{-3}$: 1 – V^{IV}-DN-MTT against blank; 2 – V^V-DN-MTT against blank; 3 – blank (DN-MTT) against chloroform. $c_{V(IV)} = c_{V(V)} = 3 \times 10^{-5} \text{ mol dm}^{-3}$, $c_{MTT} = 2.4 \times 10^{-4} \text{ mol dm}^{-3}$, pH 5, extraction time 2 min. **c)** Influence of time on the spectrum of the blank: $c_{DN} = 4 \times 10^{-4} \text{ mol dm}^{-3}$, $c_{MTT} = 1.0 \times 10^{-4} \text{ mol dm}^{-3}$, pH 5, extraction time 2 min.

sorbance at 580 nm fits well to a second order polynomial equation: $y = -0.0001x^2 + 0.0138x + 0.1477$, $R^2 = 0.9996$. The observed instability can be attributed to aggregation of the DN-MTT species in the organic phase. To eliminate this factor, in our further studies, we measured the absorbance at wavelengths outside the range of instability.

3. 2. Effect of pH

The effect of pH on the extraction is shown in Fig. 2. The absorbance of the V^{IV} complex was measured at 335 nm (series 1) and 700 nm (series 1'). There are no significant differences in the pH profile for these wavelengths. This indicates that only one complex is extracted under the mentioned conditions (high DN concentration). Our further experiments were carried out at pH 5.0.

Series 2 represents the results for the complex obtained with V^V. The course of the obtained curve is different, especially for the pH region above 5.5. This is in agreement with the concept that different complexes are formed with V^{IV} and V^V under the experimental conditions.

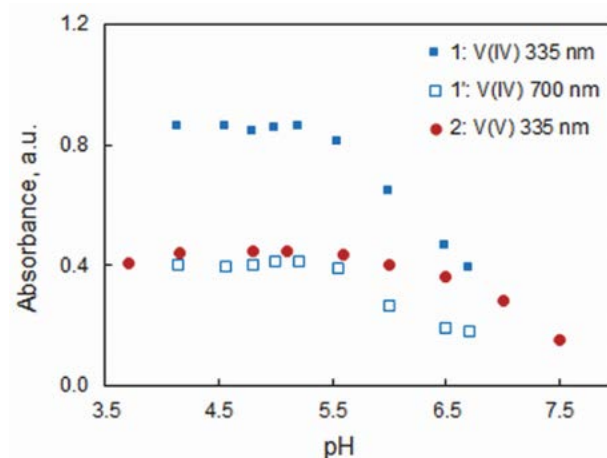


Figure 2. Absorbance of the V^{IV} complex (1 and 1') and V^V complex (2) vs pH of aqueous phase. 1, 1' – $c_{V(IV)} = 4 \times 10^{-5} \text{ mol dm}^{-3}$, $c_{DN} = 1.6 \times 10^{-3} \text{ mol dm}^{-3}$, $c_{MTT} = 1.0 \times 10^{-4} \text{ mol dm}^{-3}$, $\lambda = 335 \text{ nm}$ (1) or 700 nm (1'); 2 – $c_{V(V)} = 3 \times 10^{-5} \text{ mol dm}^{-3}$, $c_{DN} = 6.0 \times 10^{-4} \text{ mol dm}^{-3}$, $c_{MTT} = 1.0 \times 10^{-4} \text{ mol dm}^{-3}$, $\lambda = 335 \text{ nm}$, extraction time 2 min.

3. 3. Effect of Extraction Time

The influence of extraction time on the absorbance was followed in the interval from 10 seconds to 4 minutes. The results show that the time of 1.5 min is sufficient for quantitative extraction. Extraction times longer than 2.5 min can lead to a slight decrease of the absorbance. Hence, we extracted for 2 min in the further experiments.

3. 4. Effect of DN Concentration

The effect of DN concentration is shown in Fig. 3. Fig. 3a represents the results for V^V. The absorbance at 335 nm is maximal when $c_{DN} \geq 6 \times 10^{-4} \text{ mol dm}^{-3}$. Fur-

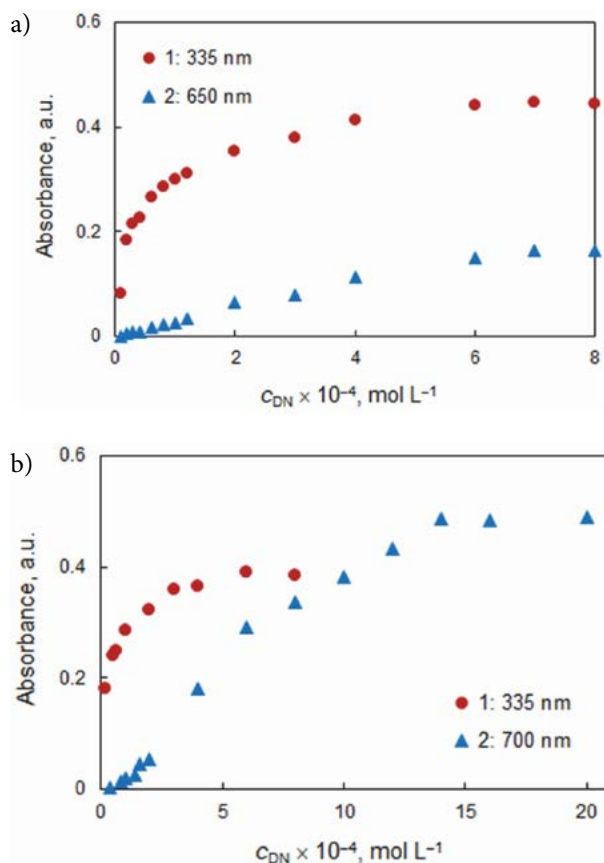


Figure 3. Absorbance of extracted complexes of V^V (a) and V^{IV} (b) vs DN concentration. a) $c_{V(V)} = 2 \times 10^{-5} \text{ mol dm}^{-3}$, $c_{MTT} = 1.5 \times 10^{-4} \text{ mol dm}^{-3}$, pH 5.5, $\lambda = 335 \text{ nm}$ (1) and 650 nm (2). b) $c_{V(IV)} = 2 \times 10^{-5} \text{ mol dm}^{-3}$ (1) or $4 \times 10^{-5} \text{ mol dm}^{-3}$ (2); $c_{MTT} = 3.5 \times 10^{-4} \text{ mol dm}^{-3}$ (1) or $1.0 \times 10^{-4} \text{ mol dm}^{-3}$ (2); pH 5.5 (1) or 5.0 (2); $\lambda = 335 \text{ nm}$ (1) and 700 nm (2).

ther studies were performed at this DN concentration. Fig. 3b shows the results for V^{IV} . It is noteworthy that the saturation at the two wavelengths (335 and 700 nm) is achieved at different DN concentrations: $6 \times 10^{-4} \text{ mol dm}^{-3}$ (for 335 nm) and $1.4 \times 10^{-3} \text{ mol dm}^{-3}$ (for 700 nm). This can be explained with the formation of different ternary complexes (see below): a 1:1 (V^{IV} :DN) complex with λ_{max} close to 335 nm and a 1:2 (V^{IV} :DN) complex with absorbance bands at higher wavelengths ($\lambda_{\text{max}} = 570 \text{ nm}$). Similar behaviour has been noticed in the V^{IV} -DN-TTC system.²¹

3.5. Effect of MTT Concentration

The effect of MTT concentration is shown in Fig. 4. Fig. 4a gives the results for V^V at the optimum DN concentration ($6 \times 10^{-4} \text{ mol dm}^{-3}$). The absorbance at 335 nm reach its maximal value for $c_{MTT} \geq 8 \times 10^{-5} \text{ mol dm}^{-3}$. Our further studies were performed at $c_{MTT} = 1 \times 10^{-4} \text{ mol dm}^{-3}$. The saturation curves for V^{IV} are more complex (Fig. 4b). The absorbance steeply increases to about $c_{MTT} = 6 \times 10^{-5} \text{ mol dm}^{-3}$ and then decreases. A narrow plateau is

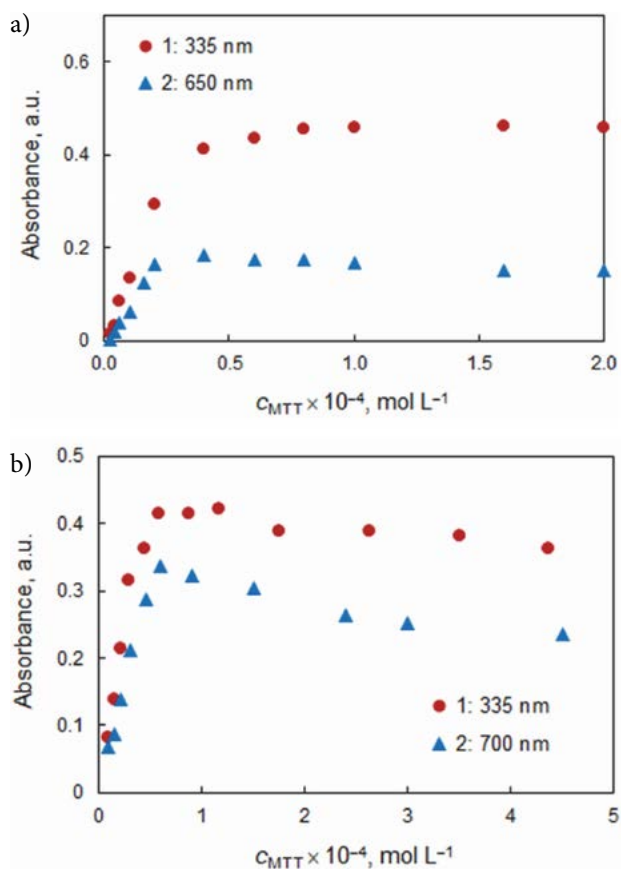


Figure 4. Absorbance of extracted complexes of V^V (a) and V^{IV} (b) vs MTT concentration. a) $c_{V(V)} = 3 \times 10^{-5} \text{ mol dm}^{-3}$, $c_{DN} = 6.0 \times 10^{-4} \text{ mol dm}^{-3}$, pH 5.5, $\lambda = 335 \text{ nm}$ (1) and 650 nm (2). b) $c_{V(IV)} = 2 \times 10^{-5} \text{ mol dm}^{-3}$ (1) or $3 \times 10^{-5} \text{ mol dm}^{-3}$ (2); $c_{DN} = 4.0 \times 10^{-4} \text{ mol dm}^{-3}$ (1) or $1.6 \times 10^{-3} \text{ mol dm}^{-3}$ (2); pH 5.0; $\lambda = 335 \text{ nm}$ (1) and 700 nm (2).

observed in the concentration range from 6×10^{-5} to $1.2 \times 10^{-4} \text{ mol dm}^{-3}$ for $\lambda = 335 \text{ nm}$.

3.6. Molar Ratios, Formulae and Equations

To determine the DN : V molar ratios in the ternary complexes, we used two methods: the straight line method of Asmus⁴⁰ and the mobile equilibrium method⁴¹ (Fig. 5). These methods give reliable results for relatively weak chemical bonds.^{42,43} The MTT : V molar ratios were determined by the Yoe & Jones method⁴⁴ (Fig. 6). The method is applicable for strong bonds,^{42,43} for which the two above-mentioned methods are usually inappropriate.

The results given in Fig. 5 (full markers; lines 1 and 1') show that there is a difference in the molar ratio for 335 nm (DN: $V^{IV} = 1:1$) and 700 nm (DN: $V^{IV} = 2:1$). Fig. 6a, in its turn, shows that the molar MTT: V^{IV} ratio is 2:1 independently of the wavelength. Therefore, the composition of the two ternary complexes is 1:1:2 (V^{IV} :DN:MTT; low DN concentration) and 1:2:2 (optimum conditions).

The following equation can be proposed for V^{IV} extraction under the optimum conditions (Table 1):

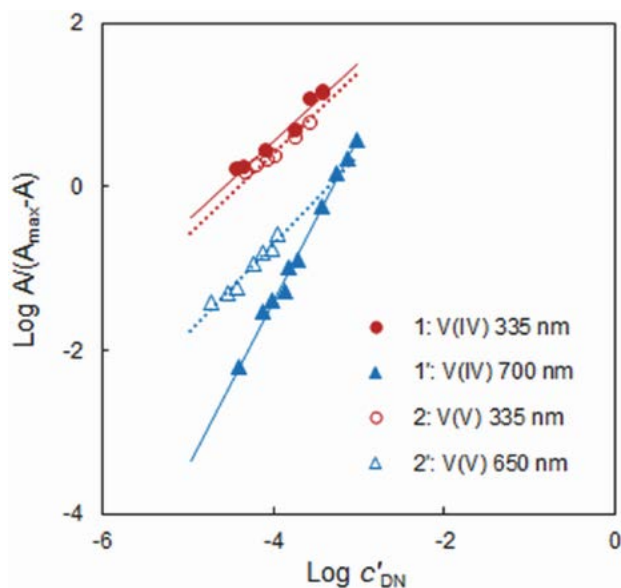
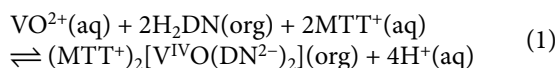


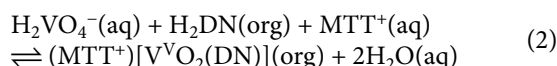
Figure 5. Determination of the DN:V^{IV} (1,1') and DN:V^V (2,2') molar ratios by the mobile equilibrium method at different wavelengths. Straight line equations: 1) $y = 0.97x + 4.45$; 1') $y = 2.01x + 6.66$; 2) $y = 1.00x + 4.41$; and 2') $y = 1.09x + 3.64$.



The optimised ground-state geometry of the anionic chelate, $[\text{V}^{\text{IV}}\text{O}(\text{DN}^{2-})_2]^{2-}$, is shown in Fig. 7, structure I. In contrast to the V^{IV} complex with DN and TTC²¹ for which a 1:2:1 composition has been determined (the anionic chelate in it contains one doubly deprotonated and one singly deprotonated ligand, structure II), the two DN ligands in the present research are doubly deprotonated. As a result, the four V–O bonds (with the oxygen atoms of DN) have

equal length (2.020 Å) and the structure is more stable. The dihedral angle between the two planar DN ligands is higher than that described in the literature.²¹ (Fig. 7, structure II) and the structure is not twisted: $\text{C}_{19}\text{O}_{24}\text{V}_{25}\text{O}_{22} = \text{C}_5\text{O}_{21}\text{V}_{25}\text{O}_{23} = 152.7^\circ$ and $\text{C}_4\text{O}_{22}\text{V}_{25}\text{O}_{24} = \text{C}_{18}\text{O}_{23}\text{V}_{25}\text{O}_{21} = -152.7^\circ$. The corresponding angles for structure II are 144.0° , 158.7° , -134.3° and -129.5° .

The composition of the ternary complex of V^V is 1:1:1 (see Fig. 5, lines 2 and 2', and Fig. 6b). Its extraction can be expressed by equation 2.



Similar equation was proposed for the V^V–DN–TTC system.²¹ However, it was considered only as a first stage of a series of processes leading ultimately to the formation of a V^{IV} complex. In contrast to $(\text{TT}^+)[\text{V}^{\text{V}}\text{O}_2(\text{DN})]$,²¹ $(\text{MTT}^+)[\text{V}^{\text{V}}\text{O}_2(\text{DN})]$ is a stable ion-pair, less susceptible to oxidation-reduction events. Hence, MTT plays a stabilizing role on V^V in a higher degree than TTC.

The optimised ground-state geometry of $[\text{VO}_2(\text{DN})]^{2-}$ is shown in Fig. 7, structure III. The complex is tetrahedral with distances $\text{V}_{14}-\text{O}_{11} = \text{V}_{14}-\text{O}_{12} = 1.927$, $\text{V}_{14}-\text{O}_{13} = 1.636$ and $\text{V}_{14}-\text{O}_{15} = 1.641$.

Table 1. Optimum conditions for extraction of the ternary complexes

Parameter	Optimal value/range		Figure
	V ^{IV}	V ^V	
pH	5.0–5.2	4.8–5.5	Fig. 2
Concentration of DN, mol L ⁻¹	1.6×10^{-3}	6×10^{-4}	Fig. 3
Concentration of MTT, mol L ⁻¹	1.2×10^{-4}	1×10^{-4}	Fig. 4
Extraction time, s	120	120	–

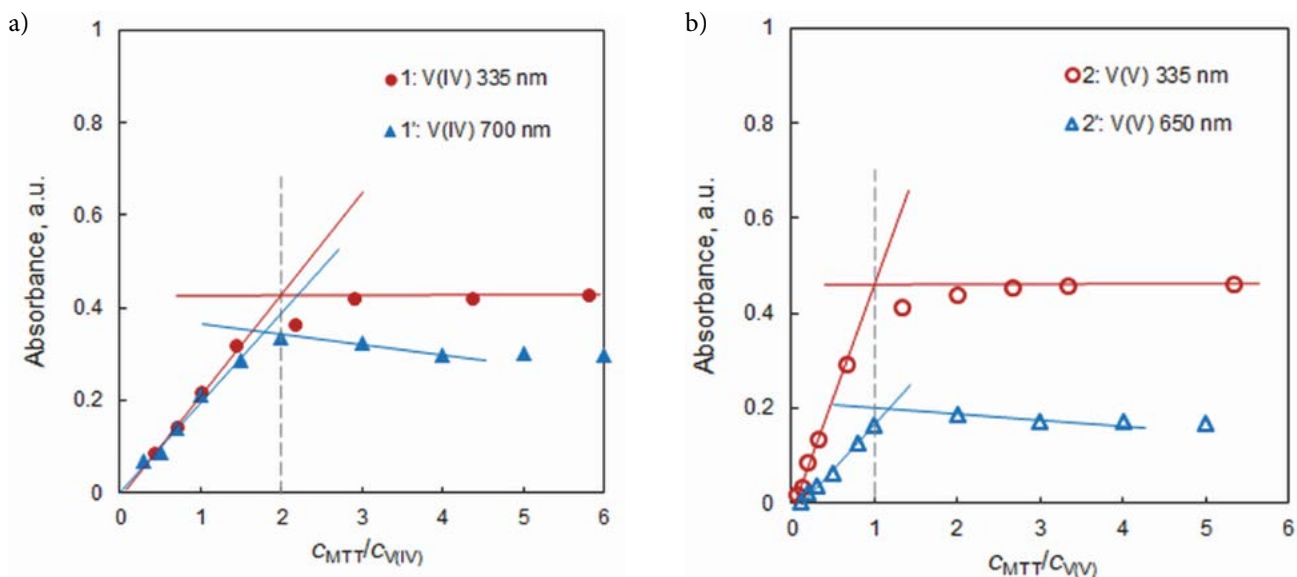


Figure 6. Determination of the MTT:V^{IV} (a) and MTT:V^V (b) molar ratios by the Yoe & Jones method.

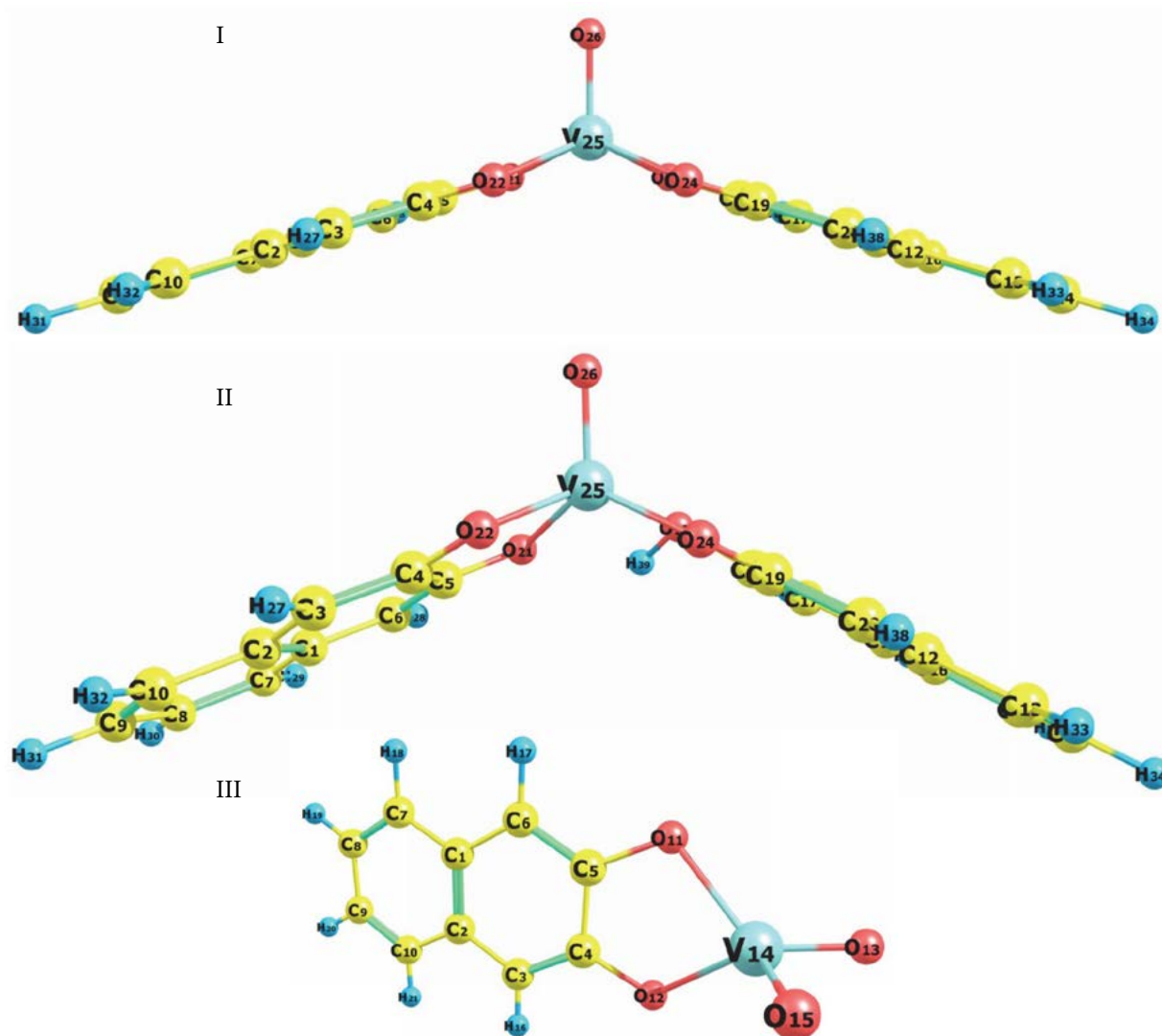


Figure 7. The optimized ground-state geometry of $[V^{IV}O(DN^{2-})_2]^{2-}$ (I), $[V^{IV}O(DN^{2-})(DNH)]^{-}$ (II)²¹ and $[V^VO_2(DN^{2-})]^{-}$ (III).²¹

3. 7. Analytical Characteristics

Under the optimum conditions (Table 1), V^{IV} is extracted as an ion-association complex, $(MTT^+)_2 [VO(DN^{2-})_2]$. Its molar absorptivity at λ_{max} ($\epsilon_{570} = 2.9 \times 10^4 \text{ dm}^3 \text{ mol}^{-1} \text{ cm}^{-1}$; Fig. 1b), calculated from the absorbance measured immediately after the extraction, is higher than the molar absorptivities of similar complexes (Table 2). However, this wavelength was found unsuitable for precise spectrophotometric measurements due to the above-mentioned instability of the absorbance (Fig. 1c). Because of the relatively high DN concentration, the results for the second maximum ($\lambda = 335 \text{ nm}$; $\epsilon_{335} = 1.9 \times 10^4 \text{ dm}^3 \text{ mol}^{-1} \text{ cm}^{-1}$) were also not satisfactory (high absorbance of the blank; insufficient repeatability).

By comparing the conditions for V^{IV} and V^V (Table 1), it is noticeable that lower reagents concentrations are needed for quantitative extraction of V^V . It was found that the results are repeatable and the dependence between the

absorbance at $\lambda_{max} = 335 \text{ nm}$ and concentration of V^V is linear ($R^2 = 0.9994$, $N = 10$) in a wide range ($0.06\text{--}1.5 \mu\text{g cm}^{-3}$). The regression equation was $A = 0.316\gamma - 0.0002$. The standard deviations of the slope and intercept were 0.003 and 0.002, respectively. The limits of detection (LOD) and quantitation (LOQ) calculated as 3 and 10 times SD of the intercept divided by the slope were $0.02 \mu\text{g cm}^{-3}$ and $0.06 \mu\text{g cm}^{-3}$. The molar absorptivity and Sandell's sensitivity were $1.6 \times 10^4 \text{ dm}^3 \text{ mol}^{-1} \text{ cm}^{-1}$ and 3.2 ng cm^{-2} .

4. Conclusions

Vanadium(IV) and vanadium(V) form different chloroform-extractable ternary complexes with DN and MTT. Under the optimum conditions, V^{IV} is extracted as a 1:2:2 complex (V:DN:MTT) with $\lambda_{max} = 570 \text{ nm}$. V^V , in its turn, forms a 1:1:1 complex with $\lambda_{max} = 335 \text{ nm}$. This com-

Table 2. Influence of the cationic ion-association reagent on the complex's characteristics

Complex*	Composition	Organic solvent	λ_{\max} , nm	ϵ_{\max} , dm ³ mol ⁻¹ cm ⁻¹	Ref.
V ^V -DN	1:2	MIBK	530	1.5×10^4	30
V ^V -DN-CTAB	Not studied	ethylacetate	530	1.5×10^4	29
V ^V -DN-TV	1:2:1	chloroform	342	1.5×10^4	28
V ^V -DN-INT	1:2:1	chloroform	340	2.5×10^4	27
V ^{IV} -DN-TTC	1:2:1	chloroform	333	2.1×10^4	21
V ^V -DN-MTT	1:1:1	chloroform	335	1.6×10^4	This work
V ^{IV} -DN-MTT	1:2:2	chloroform	570	2.9×10^4	This work

* – The initial oxidation state of vanadium is given

Abbreviations: CTAB, cetyltrimethylammonium bromide; TV, tetrazolium violet; INT, idonitrotetrazolium chloride; TTC, triphenyltetrazolium chloride

plex is obtained under mild conditions (low concentration of the reagents and wide pH range) and can be used for spectrophotometric determination of vanadium. When the DN concentration is not very high, the well-documented in the literature $V^V \rightarrow V^{IV}$ reduction by DN (a catecholic type ligand) is not observed. This fact can be a starting point for future research on the development of a method for spectrophotometric determination of V^V and V^{IV} in their co-presence.

5. References

- H. E. Michibata, Vanadium: biochemical and molecular biological approaches. Springer, Dordrecht-Heidelberg-London-New York, **2012**. DOI:10.1007/978-94-007-0913-3
- B. Gummow, in: J. O. Nriagu, (Ed.): Encyclopedia of Environmental Health, Elsevier, Burlington, **2011**; pp. 628–636. DOI:10.1016/B978-0-444-52272-6.00661-
- K. K. Chatterjee, Uses of Metals and Metallic Minerals, New Age International (P) Ltd. Publishers, New Delhi, India, **2007**, pp. 272–275.
- A. Padilla-Rodríguez, J. A. Hernández-Viezas, J. R. Peralta-Videa, J. L. Gardea-Torresdey, O. Perales-Pérez, F. R. Román-Velázquez, *Microchem. J.* **2015**, *118*, 1–11. DOI: 10.1016/j.microc.2014.07.011
- Rehder, D., in: A. Sigel, H. Sigel, R. K.O. Sigel (Eds.): Interrelations between Essential Metal Ions and Human Diseases, Springer, **2013**, pp. 139–169. DOI: 10.1007/978-94-007-7500-8
- V. Ugone, E. Garribba, G. Micera, D. Sanna, *J. Chem. Educ.* **2015**, *92*, 1098–1102. DOI: 10.1021/ed500794m
- D. Rehder, *Metallomics* **2015**, *7*, 730–742. DOI: 10.1039/C4MT00304G
- K. Gruzewska, A. Michno, T. Pawelczyk, H. Bielarczyk, *J. Physiol. Pharmacol.* **2014**, *65*, 603–611.
- Ghosh, R.; Banik, S., in: D. Bagchi, A. Swaroop (Eds.): Food Toxicology, CRC Press, Boca Raton, 2017, pp. 337–354.
- M. J. C. Taylor, J. F. Staden, *Analyst* **1994**, *119*, 1263–1276. DOI: 10.1039/AN9941901263
- Z. L. Chen, G. Owens, *Anal. Chim. Acta* **2008**, *607*, 1–14. DOI: 10.1016/j.aca.2007.11.013
- K. Pyrzyńska, *Microchim. Acta* **2005**, *149*, 159–164. DOI: 10.1007/s00604-004-0304-5
- W.-Y. He, K.-P. Wang, J.-Y. Yang, *Toxicol. Environ. Chem.* **2018**, DOI: 10.1080/02772248.2018.1428325
- C. Agarwal, M. Deb, R. Mishra, *Anal. Lett.* **1990**, *23*, 2063–2075. DOI: 10.1080/00032719008052550
- C. Agrawal, K. S. Patel, R. K. Mishra, *Bull. Chem. Soc. Jpn.* **1991**, *64*, 2616–2618. DOI: 10.1246/bcsj.64.2616
- T. Prasada Rao, M. L. P. Reddy, A. R. Pillai, *Talanta* **1998**, *46*, 765–813. DOI: 10.1016/S0039-9140(97)00262-2
- Z. Marczenko, M. Balcerzak, Metod'y spektrofotometrii v UF i vidimoy oblastiakh v neorganicheskom analize (in Russian), Binom. Laboratoriya znaniy, Moscow, **2007**.
- Gavazov, K. B., *Acta Chim. Slov.* **2012**, *59*, 1–17.
- N. K. Temel, R. Gürkan, *Acta Chim. Slov.* **2018**, *65*, 138–149. DOI:10.17344/acsi.2017.3724
- A. M. Nardillo, J. A. Catoggio, *Anal. Chim. Acta* **1975**, *74*, 85–99. DOI: 10.1016/S0003-2670(01)82782-3
- K. B. Gavazov, G. K. Toncheva, V. B. Delchev, *Open Chem.* **2016**, *14*, 197–205. DOI: 10.1515/chem-2016-0022
- K. Kustin, S.-T. Liu, C. Nicolini, D. Toppen, *J. Am. Chem. Soc.* **1974**, *96*, 7410–7415. DOI: 10.1021/ja00831a600
- J. H. Ferguson, K. Kustin, *Inorg. Chem.* **1979**, *18*, 3349–3357. DOI: 10.1021/ic50202a015
- K. Gavazov, Z. Simeonova, A. Alexandrov, *Russ. J. Inorg. Chem.* **2001**, *46*, 427–431.
- S. Adediran, R. Pratt, *Biochemistry* **2008**, *47*, 9467–9474. DOI: 10.1021/bi801153j
- P. Racheva, K. Gavazov, V. Lekova, A. Dimitrov, *J. Iran. Chem. Res.* **2008**, *1*, 113–121.
- Z. Simeonova, K. Gavazov, A. Alexandrov, *Cent. Eur. J. Chem.* **2006**, *4*, 258–266. DOI: 10.2478/s11532-006-0011-7
- V. Lekova, K. Gavazov, A. Dimitrov, P. Racheva, *Sci. Res. Union Sci. Plovdiv, Ser. C* **2007**, *6*, 171–174.
- R. K. Mondal, D. P. S. Rathore, P. K. Tarafder, in: National Seminar on Significant Advancements in Plasma/Flame/Associated Techniques and their Applications in Chemical Characterization of Atomic Minerals (SAP-2013), AMD Hyderabad, India, January 23–24 **2013**: AMD Hyderabad, India, pp. 83–84.
- R. K. Mondal, D. P. S. Rathore, P. K. Tarafder, *Explor. Res. Atomic Miner.* **2013**, *23*, 113–116.

31. P. K. Tarafder, R. K. Mondal, *Rev. Anal. Chem.* **2011**, *30*, 73–81. DOI: 10.1515/REVAC.2011.016
32. P. K. Tarafder, S. K. Pradhan, R. K. Mondal, *J. Radioanal. Nucl. Chem.* **2016**, *309*, 1021–1028. DOI: 10.1007/s10967-016-4738-0
33. P. K. Tarafder, P. K. Ghosh, S. K. Pradhan, *J. Radioanal. Nucl. Chem.* **2017**, *313*, 353–360. DOI: 10.1007/s10967-017-5334-7
34. R. W. Sabnis, Handbook of biological dyes and stains: synthesis and industrial applications, Wiley, Hoboken, US, **2010**, pp. 485–487. DOI: 10.1002/9780470586242
35. K. B. Gavazov, A. N. Dimitrov, V. D. Lekova, *Russ. Chem. Rev.* **2007**, *76*, 169–179. DOI: 10.1070/RC2007v076n02ABEH003655
36. K. B. Gavazov, V. D. Lekova, G. I. Patronov, *Acta Chim. Slov.* **2006**, *53*, 506–511.
37. P. V. Racheva, K. B. Gavazov, V. D. Lekova, A. N. Dimitrov, *J. Anal. Chem.* **2010**, *65*, 21–25. DOI: 10.1134/S1061934810010053
38. G. K. Toncheva, T. S. Stefanova, K. B. Gavazov, *Oriental J. Chem.* **2015**, *31*, 327–332. DOI: 10.13005/ojc/310137
39. S. Kostova, V. Stajkovska, A. Aleksandrov, *Sci. Works Plovdiv Univ. Chem.* **2000**, *29*, 9–14.
40. E. Asmus, *Fresenius' J. Anal. Chem.* **1960**, *178*, 104–116. DOI: 10.1007/bf00467200
41. Z. Zhiming, M. Dongsten, Y. Cunxiao, *J. Rare Earths* **1997**, *15*, 216–219.
42. M. I. Bulatov, I. P. Kalinkin, Prakticheskoe rukovodstvo po fotokolorimetriceskim i spektrofotometriceskim metodam analiza (in Russian), Khimiya, Leningrad, **1986**.
43. K. B. Gavazov, *Chemistry* **2013**, *22*, 222–253.
44. J. H. Yoe, A. L. Jones, *Ind. Eng. Chem. Anal. Ed.* **1944**, *16*, 111–115. DOI: 10.1021/i560126a015

Povzetek

Proučili smo ekstrakcijski sistem tekočina–tekočina za $V^{IV/V}$, ki vsebuje 2,3-dihidroksinaftalen (DN) in 3-(4,5-dimetiltiazol-2-il)-2,5-difenil-2*H*-tetrazolijev bromid (tiazolil modro, MTT). Določili smo optimalne pogoje za ekstrakcijo V^{IV} in V^V . V^{IV} smo ekstrahirali v kloroformu kot 1:2:2 kompleks (V:DN:MTT) z $\lambda_{max} = 570$ nm in $\epsilon_{570} = 2.9 \times 10^4$ dm³ mol⁻¹ cm⁻¹, vendar ta valovna dolžina ni primerna za natančne spektrofotometrične meritve zaradi časovno odvisne spremembe absorbance. V^V tvori predvsem 1:1:1 kompleks z $\lambda_{max} = 335$ nm. Za to oksidacijsko stanje je umeritvena krivulja linearna v območju 0.06–1.5 µg cm⁻³. Vrednosti za molsko absorptivnost, Sandellovo občutljivost in mejo detekcije so 1.6×10^4 dm³ mol⁻¹ cm⁻¹, 3.2 ng cm⁻² in 0.02 µg cm⁻³. Osnovno stanje struktur anionov prisotnih v ravnotežju, $[V^{IV}O(DN^{2-})_2]^{2-}$ in $[V^VO_2(DN^{2-})]^-$, smo optimizirali na BLYP/6-31++G* nivoju teorije.

Scientific paper

Factors Influencing Imazapyr Herbicide Removal from Wastewater Using Photocatalytic Ozonation

Salma Bougarrani,^{1,*} Laila El Azzouzi,¹ Soukaina Akel,¹ Lahbib Latrach,²
Asmae Bouziani¹ and Mohammed El Azzouzi¹

¹ Laboratory of Spectroscopy, Molecular Modeling, Materials, Nanomaterials, Water and Environment, (LS3MN2E) Faculty of Sciences, University Mohammed V. BP 1014, Rabat, Morocco.

² Faculty of Sciences Semlalia, Cadi Ayyad University, PO Box: 2390, Marrakech, Morocco.

* Corresponding author: E-mail: salma.bougarrani@gmail.com
Tel: + 212 660425050, Fax: + 3535698213

Received: 28-02-2018

Abstract

This study investigates the degradation of imazapyr herbicide from wastewater by photocatalytic ozonation using TiO₂ as a semiconductor. Effects of operational parameters on imazapyr removal efficiency including TiO₂ dosing, initial herbicide concentration and pH were also studied. Obtained results showed that more than 90% of removal efficiency representing the disappearance of imazapyr was maintained until 7 μM in the presence of 200 mgL⁻¹ of UV100-TiO₂. Otherwise, the degradation of imazapyr followed the first-order kinetics with a photocatalytic rate constant of 0.247 min⁻¹, and complete degradation was achieved within 20 min using photocatalytic ozonation for 5 μM of Imazapyr at pH 7.

Keywords: Degradation; Imazapyr herbicide; Ozonation; Photocatalytic Ozonation; Wastewater treatment

1. Introduction

Persistent organic pollutants such as pesticides have attracted global environmental concerns in recent decades due to its adverse impacts on the environment and public health. Among the various pesticides, imazapyr is one of the most widespread types of contaminants of waters and soils, often found in the municipal sewage effluents and soil with varying trace concentrations in different parts of the world.¹⁻²

Imazapyr, 2-(4-methyl-5-oxo-4-propan-2-yl-1H-imidazol-2-yl) pyridine-3-carboxylic acid, being a hetero aromatic molecule,³ is a non-selective herbicide which belongs to the imadazolinone family. Imazapyr is a persistent herbicide, with a half-life varying from 21 days to 49 months, and a high mobility in soils.³⁻⁴ Therefore, it is likely suspected to contaminate groundwater.⁵ Elimination of imazapyr present in drinking water by treatment with ozone has been demonstrated to be unsuccessful since half of the initial compound remains in water after the process. The photocatalytic oxidation of imazapyr has been studied previously using commercial TiO₂ as well as newly synthesized mesoporous TiO₂ materials.⁶ However, more studies are still needed to better understand the effect of the oxidative approaches on the control of this herbicide.

In recent years, various technologies have been developed and tested in laboratory scales or pilot plants to remove various recalcitrant organic pollutants from wastewater in order to minimize the potential health risks associated with exposure to these chemical pollutants.⁴ One of the alternatives to gain greater mineralization efficiency is the use of ozone in the presence of catalyst in order to enhance the free hydroxyl radicals production.⁴⁻⁵ The photocatalytic ozonation have been studied by many studies worldwide and the high efficiency of this treatment has been explained by a synergistic effect between ozonation and photocatalysis. The photogenerated electrons can react with ozone molecules generating ozonide radicals while decreasing the possible recombination of electronehole pairs. Pizarro *et al.*,⁵ and Ibrahim *et al.*,⁶ reported that among six different advanced oxidation processes, photocatalytic ozonation was the most efficient for completing mineralisation of 4-chloronitrobenzene. These promising techniques are used for the treatment of contaminated water and wastewater to evaluate their capability in the decomposition of pollutants such as pesticides and to assess the treatment efficiencies of these combinations.⁷

The advanced oxidation processes (AOPs) have been developed as one of the most promising options in the removal of various persistent organic pollutants by the generation of hydroxyl radicals (OH).^{8–9} Due to its low-cost and chemical stability, semi-conductor material like TiO₂ has been successfully used in recent years.^{10–12} However, The degradation of Imazapyr has also been investigated by other authors using photocatalysis and ozone and results showed lower concentration compared to photocatalytic ozonation.^{13–30} The photocatalytic ozonation degradation of pesticides is largely dependent on operating parameters such as TiO₂ dosage, initial herbicide concentration and solution pH.^{31–32} Understanding the effects of these factors on the photocatalytic degradation efficiency have an importance when designing a sustainable and efficient technique for wastewater treatment.

Based on this background informations, the present study aimed at performing a comprehensive evaluation of the capacity of photocatalytic ozonation to remove imazapyr from wastewater.

The laboratory studies reported in this paper investigates the capacity and the applicability of TiO₂-photocatalytic ozonation in removing imazapyr herbicide from wastewater. Operational parameters such as TiO₂ initial concentration, initial herbicide concentration and pH were also investigated.

2. Material and Methods

Imazapyr herbicide, (95%) was purchased from American Cyanamid Company. TiO₂ Hombikat UV100 (99%) was purchased from Sachtleben Chemie in powdered form. The chemical structure of imazapyr herbicide is shown in figure 1. Potassium indigo trisulfonate was purchased from Riedel-de Hahn AG. The other chemicals used in the experiments were purchased from Riedel-de Hahn AG. They were all of analytical grade and used without further purification. All solutions were prepared using Milli-Q water at room temperature collected from Milli-Q apparatus (Millipore, Bedford).

Sample analysis from the study of the photocatalytic degradation of imazapyr was carried out using a mass spec-

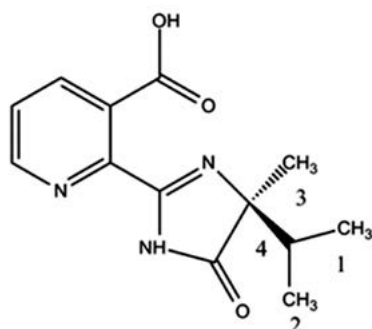


Figure 1: Chemical structure of imazapyr herbicide.

trometry coupled to electrospray ionization system (ESI) for a qualitative and quantitative analysis. MS analysis was performed on Bruker Esquire 3000 plus mass spectrometer equipped with an ESI interface and an ion trap (Bruker-Daltonics Analytik GmbH Bremen, Germany). The ESI probe tip and capillary potentials were set at 2.5 kV and 25 V, respectively. The concentration of aqueous ozone was determined by Spectrometric method indigo trisulfonate according to Sanchez *et al.*,¹³ and mouradi *et al.*¹⁷ The absorption analysis of the indigo was monitored by Shimadzu UV-160A UV-Vis Spectrophotometer at 600 nm.

Titanium dioxide (100 % anatase, average particle size of 10 nm and BET Method–Brunauer, Emmett and Teller [BET] surface of > 250 m² g⁻¹) was used without any pre-treatment.

In a typical reaction, 200 mg/L of TiO₂ were added to 500 mL of 5 μM of imazapyr solution in a double walled cylindrical photoreactor (figure 2). Then, the solution was exposed to ultrasonic treatment for 2 minute in order to suspend the catalyst. Immediately afterwards, the stirring was started and maintained over 1h in the dark to ensure the adsorption equilibrium between the solution and the catalyst particles. The imazapyr degradation experiments were carried out in a simple photocatalyzed ozonation reactor, as presented in figure 2, with combining photocatalysis and ozonation.

The irradiation experiments were carried out under light generated by a medium pressure mercury lamp at 150W in a Duran cell (λ > 300 nm), placed inside the reactor. A cooling water system was set up to prevent overheating of the lamp and of the solution. Samples were taken every 10 min and filtered two times in order to remove all the catalyst. The photocatalytic ozonation degradation of Imazapyr herbicide was investigated in an aqueous suspension 1: 3 acetone/water mixture in the presence of pure titanium used as a catalyst. Imazapyr showed important

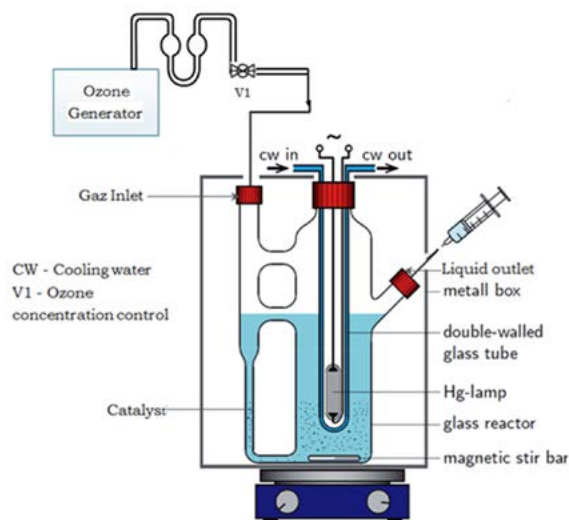


Figure 2: Scheme of photocatalytic ozonation reactor used for imazapyr degradation.

fragments molecular ion peak at $m/z = 262$ and $m/z = 284$. The MS-ESI detects the Imazapyr under two forms (combined to H^+ which gives $m/z = 262$ and combined to Na^+ with $m/z = 284$) and their degradation was followed as a function of time.

3. Results and Discussion

3.1. Effect of TiO_2 Dose on Imazapyr Degradation

Variations of Imazapyr removal rate under different TiO_2 dose are presented in figure 3. Imazapyr degradation increased slowly and reached the maximum removal rate of 93.0% in the concentration of 200 mg/L. Thus, this TiO_2 dose (200 mg/L) could be considered as the optimal concentration of Hombikat UV 100. The optimal amount of Hombikat UV 100 agrees well with reported results by other authors.^{14–26} This improvement can be attributed to the increasing of active sites by providing more TiO_2 particles, which plays the semiconductor role in the photocatalysis process. Consequently, the formation of electron-hole pairs and reactive hydroxyl radicals on the surface of semiconductor increased, which improved the oxidation of imazapyr into other intermediates.^{15–27}

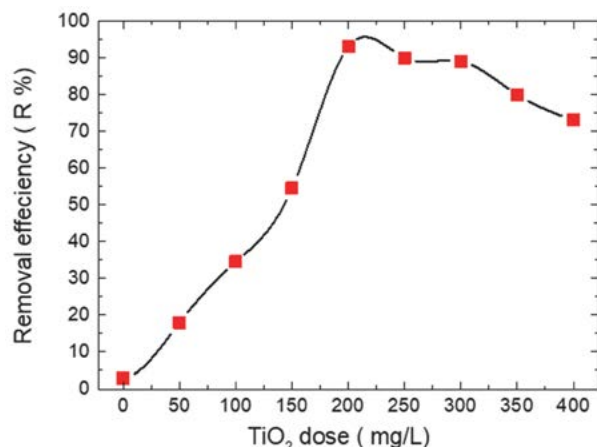


Figure 3: Removal rate of imazapyr under variation of TiO_2 concentration. $C(\text{Imazapyr}) = 5 \mu\text{M}$; stirring speed = 1000 min^{-1} , aqueous suspension 1 : 3 acetone/ Milli-Q water.

3.2. Effect of Initial Herbicide Concentration

The pollutant concentration in water is an important factor to determine the oxidation efficiency and the synergistic effects of photocatalytic ozonation processes.^{12–15} The effect of the initial herbicide concentration was studied for six concentrations of imazapyr by photocatalytic ozonation. The initial herbicide concentrations were $1 \mu\text{M}$, $3 \mu\text{M}$, $5 \mu\text{M}$, $7 \mu\text{M}$, $9 \mu\text{M}$ and $15 \mu\text{M}$ (0.26 mg/L , 0.79 mg/L , 1.31 mg/L , 1.83 mg/L , 2.36 mg/L , 3.9 mg/L respectively).

For this series of experiments the catalyst and the ozone doses were kept constant at 200 mg/L and 10 mg/L respectively. The irradiation time was fixed at 10 min for all samples after the adsorption step under dark conditions.

Obtained results showed that more than 90% of removal efficiency representing the disappearance of imazapyr was maintained until $7 \mu\text{M}$, further increase of imazapyr concentration leads to decrease in removal efficiency (figure 4). A possible explanation resides in the fact that as imazapyr concentration rises, it is possible that more organic substances are deposited on the surface of TiO_2 , whereas less number of photons are available to reach the catalyst surface and the probability of reaction between imazapyr molecules and oxidizing species also decreases, thus resulting in less degradation percentage.^{18–32}

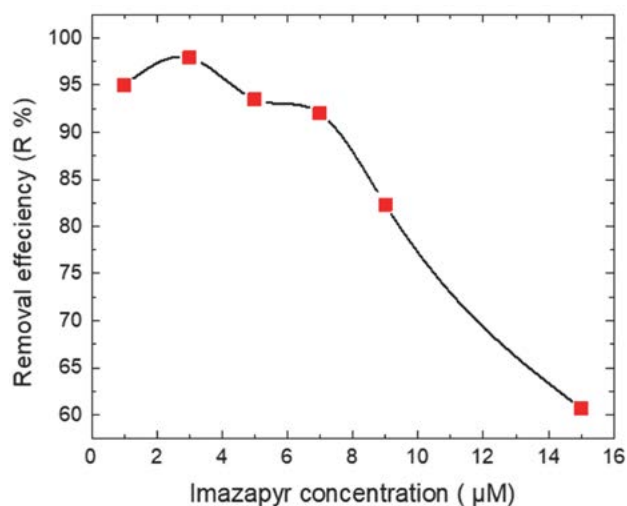


Figure 4: Removal efficiency of imazapyr as a function of imazapyr concentration, $m_{\text{catalyst}} = 100 \text{ mg}$; stirring speed = 1000 min^{-1} , aqueous suspension 1 : 3 acetone/ Milli-Q water.

3.3. Effect of pH Influence on Imazapyr Degradation

Knowledge of the kinetics required to assess the efficiency of systems engineered for the oxidation of a variety of pollutants. Reliable kinetic studies require obvious substrate decay measurements. Thus, for comparison of the efficiency of these treatment processes, kinetic studies of imazapyr decomposition were carried out.

In all experimental runs, imazapyr concentration was found to decrease with irradiation time. A first order kinetics fitting of the thus obtained concentration vs. time plots allows to calculate the respective first order rate constants. Based on the exponential decay of concentration of imazapyr, the photoactivity profile was fitted assuming a first order reaction.

$$C = C_0 \exp(-k \cdot t) \quad (1)$$

In which C is the concentration of imazapyr at time t , C_0 is the initial concentration, and k is the observed rate constant.

Many authors have reported that the kinetic behavior of photocatalytic reaction can be described by a modified Langmuir–Hinshelwood model, Atitar *et al.*,¹⁸ and Djerdj *et al.*¹⁹

The influence of pH on the effectiveness of imazapyr degradation by photocatalytic ozonation is shown in figure 5. The degradation experiments were carried out at pH values of 3, 7, and 10. Imazapyr removal rate reached a maximum at pH 7 with a first order rate constant of 0.247 min^{-1} . However, for pH 3 and 10, the photocatalytic activity decreased appreciably. The rates constant at pH 3 and pH 10 are 0.107 min^{-1} , 0.134 min^{-1} respectively (Table 1). The study of pH influence on the photocatalytic ozonation process would be helpful to understand its underlying mechanism and would help obtaining a higher degree of removal. Based on the exponential decay of imazapyr concentration, the degradation by photocatalytic ozonation profile was fitted assuming a first order reaction model. Similar finding have been reported by Usharani *et al.*,¹⁴ and by Gar Alalma *et al.*¹⁵ These authors have reported first order reaction kinetics for the degradation and mineralization of chlorinated pesticides and insecticides and other various water pollutants by photocatalytic ozonation.^{14–33}

The results, shown in figure 5, demonstrates that the optimal conditions for imazapyr degradation with photocatalytic ozonation is neutral pH. On the other hand, the combination of two oxidation systems, ozonation and photocatalysis, for water treatment under optimal conditions are reported to have increased oxidation efficiencies (synergy) compared to the sum oxidation efficiencies of these two oxidation systems separately.^{32–36} Several studies have discussed the synergistic effects of photocatalytic ozonation on degradation and removal of different substances from aqueous solutions and the effects are reported in terms of the degradation and/or mineralization effi-

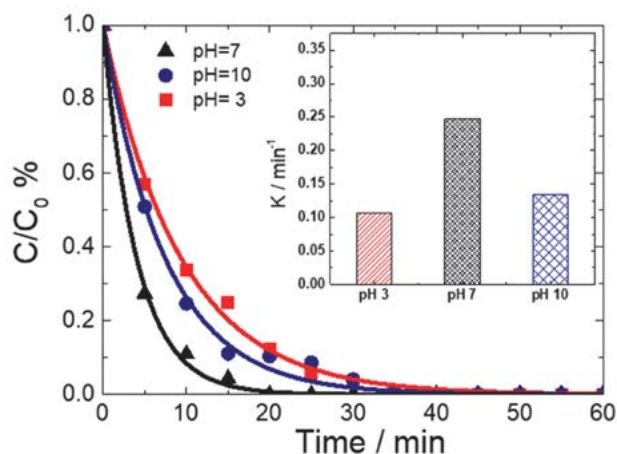


Figure 5: Concentration of imazapyr as a function of time for different pH. $C(\text{Imazapyr}) = 5 \mu\text{M}$; stirring speed = 1000 min^{-1} , $m \text{ TiO}_2 = 100 \text{ mg}$, aqueous suspension 1 : 3 acetone/ Milli-Q water.

ciencies or oxidation rate constants of model water pollutants.^{17–27} The efficiency of photocatalytic ozonation is mainly attributed to the formation of more reactive and non-selective hydroxyl radicals in the oxidation medium, which react with almost all organic molecules at a rate of $10^6 - 10^9 \text{ M}^{-1}\text{s}^{-1}$.^{18–25–37} The photogenerated electrons can react with ozone molecules generating ozonize radicals while decreasing the possible recombination of electron hole pair, so better electron- whole separation. In addition to the synergistic effects which occur during photocatalytic ozonation compared to simple photocatalysis in presence of oxygen. Bougarrani *et al.*,³⁶ and Wang *et al.*,²⁴ also reported similar results for the mineralization of aniline, dibutyl phthalate, respectively.

Table 1: Rate constant of imazapyr degradation with photocatalytic ozonation for different pH.

pH	Photocatalytic ozonation		
	Rate constant K	R ²	Standard Deviation
3	0.107 (min^{-1})	0.997	0.0012
7	0.247 (min^{-1})	0.997	0.0009
10	0.134 (min^{-1})	0.995	0.0015

4. Conclusions

This study demonstrated the ability of photocatalytic ozonation using TiO_2 as semiconductors for the degradation of imazapyr herbicide as organic pollutants. Imazapyr degradation is strongly influenced by the operating parameters such as TiO_2 concentration, initial imazapyr concentration and pH. Under optimized conditions (TiO_2 dose of 200 mg/L , $5 \mu\text{M}$ of initial imazapyr concentration and pH 7), up to 95% of imazapyr removal was achieved within 20 min with removal rate constant of 0.247 min^{-1} . Results of the present investigation suggest that photocatalytic ozonation using TiO_2 is efficient for the removal of imazapyr form wastewater. The high efficiency of photocatalytic ozonation could be explained by a synergistic effect between ozonation and photocatalysis. The photogenerated electrons can react with ozone molecules generating ozonize radicals while decreasing the possible recombination of electron hole pair, so better electron- whole separation.

Therefore, the application of photocatalytic ozonation under the optimal conditions is recommended for organic pollutants treatment such as imazapyr herbicides in order to promote environmental and human health protection.

5. References

- Assalin M. R., De Moraes S. G., Queiroz C. N., Ferracini V. L. & Duran N., *J Environ Sci Health B*, **2009**, *45*, 1, 89–94.
DOI:10.1080/03601230903404598

2. Antoniou M. G., Zhao C., O'Shea K. E., Zhang G., Dionysiou D., Han C., Nadagouda M. N., Choi H., Fotiou T., Triantis T. M. & Hiskia. *RSC adv.* **2016**, 1–34.
3. Atitar M. F., Dillert R. & Bahnemann D. W. *J. Phys. Chem. C.* **2017**, 121 (8), 1–36. DOI:10.1021/acs.jpcc.6b11673
4. Oller I., Gernjak W., Maldonado M. I., Perez-Estrada L. A., Sanchez-Perez J. A., Malato S., *J Hazard Mater B*, **2006**, 138, 507–517. DOI:10.1016/j.jhazmat.2006.05.075
5. Pizarro P., Guillard C., Perol N., Herrmann J.-M., *Catal. Today*, **2005**, 101, 211–218. DOI:10.1016/j.cattod.2005.03.008
6. Ebrahimi H., Ghorbani Shahna F., *Arch Environ Prot*, **2017**, 43, 65–72. DOI:10.1515/aep-2017-0006
7. Bamba D., Atheba P., Robert D., Trokourey A., Dongui B., *Environ. Chem. Lett.* **2008**, 6, 163–167. DOI:10.1007/s10311-007-0118-x
8. Boggard O. K., Gimsing A. L., *Pest Manag Sci.* **2008**, 64, 441–456. DOI:10.1002/ps.1512
9. Shifu C., Yunzhang L., *Chemosphere*, **2007**, 67, 1010–1017. DOI:10.1016/j.chemosphere.2006.10.054
10. Okehata K., El-Din M. G., *Ozone Sci. Eng.*, **2005**, 27, 83.
11. Maddila S., Rana S., Pagadala R. & Jonnalagadda S. B., *Desalination Water Treat*, **2015**, 1–15.
12. Maddila S., Ndabankulu V. O., Jonnalagadda S. B., *Global Nest J.* **2016**, 18(2), 269–278.
13. Sanchez L., Peral J., & Domenech X., *Appl Catal B*, **1998**, 19, 1, pp. 59–65. DOI:10.1016/S0926-3373(98)00058-7
14. Usharani, Muthukumar M., and Kadirvelu K., *Int. J. Environ. Res.* **2012**, 6(2), 557–564.
15. Gar Alalma M., Tawfika A., Ookawara S., *J. wat Proc Eng.* **2015**, 8, 55–63.
16. Hameed B. H., Akpan U. G., *J Hazard Mater.* **2009**, 170, 520–529. DOI:10.1016/j.jhazmat.2009.05.039
17. Mouradi, M., Bouizgaren, A., Farissi, M. and Ghoulam, C., *Irrigation and Drainage* **2017**,
18. Atitar M. F. and Bahnemann D. W., *J. Phys. Chem. C*, **2017**, 1–36.
19. Djerdj I., Arcon D., Jagliid Z., Niederberger M. *J. Solid State Chem.* **2008**, 181, 1571–1581. DOI:10.1016/j.jssc.2008.04.016
20. Lissemore L., Hao C.Y., Yang P., Sibley P. K., Mabury S., and Solomon K. R. *J. Chemosphere*, **2006**, 64, 717–729. DOI:10.1016/j.chemosphere.2005.11.015
21. Sato, K., Iwashima, N., Wakatsuki, T. and Masunaga, T., *J. Soil Sci. Plant Nutr.*, **2011**, 57(4), pp.607–618. DOI:10.1080/00380768.2011.594966
22. Bargaz, A., Isaac, M. E., Jensen, E. S. and Carlsson, G., *J. Soil Sci. Plant Nutr.*, **2016**, 179 (4), 537–546.
23. Armaković S. J., Armaković S., Finčur N. L., Šibul F., Vione D., Šetrajčić J. P. & Abramović B. F. *RSC Advances*, **2015**, 5 (67), 54589–54604. DOI:10.1039/C5RA10523D
24. Wang R. M., Liu C. M., Zhang H. Z., Chen C. P., Guo L., Xu H. B., Yang S. H. *Appl. Phys. Lett.* **2004**, 85, 2080–2082. DOI:10.1063/1.1789577
25. Putra E. K., Pranowo R., Sunarso J., Indraswati N., Ismadji S. *Water Res.* **2009**, 43, 2419–2430. DOI:10.1016/j.watres.2009.02.039
26. Klavarioti, M., Mantzavinos, D., Kassinos, D. *Environ. Int.* **2009**, 35, 402–417. DOI:10.1016/j.envint.2008.07.009
27. Kümmerer, K. *J. Environ. Manage.* **2009**, 90, 2354–23. DOI:10.1016/j.jenvman.2009.01.023
28. Zhang G., Wang Q., Zhang W., Yuan T. and Wang P. *Photochem Photobiol Sci*, **2017**, 98–103.
29. Safari G. H., Hoseini M., Seyedsalehi M., Kamani H., Jaafari J., Mahv A. H. *Int. J. Environ. Sci. Technol.* **2015**, 12 603–616. DOI:10.1007/s13762-014-0706-9
30. Bourgin M., Borowska E., Helbing J., Hollender J., Kaiser H. P., Kienle C., McArdell C. S., Simon E. & Gunten U. *Water Res.* **2017**, 122, 234–245. DOI:10.1016/j.watres.2017.05.018
31. Ebrahimi H., Shahna F. G., Bahrami A., Jaleh B. & Abed K. A. *Arch Environ prot.* **2017**, 43 (1), 65–72. DOI:10.1515/aep-2017-0006
32. Bougarrani S., El azzouzi L., Bouziani A., Akel S., Latrach L., Baicha Z., El azzouzi M. *Mor. J. Chem.* **2017**, 5 (3), 446–452.
33. Hermosilla D., Merayo N., Gascó A. & Blanco Á. *Environ Sci Pollut Res*, **2015**, 22 (1), 168–191. DOI:10.1007/s11356-014-3516-1
34. Iglesias O., Fernández deDios M.A., Tavares T., Sanromán M. A. & Pazos M. J. *Ind. Eng. Chem* **2015**, 27 (1), 276–282. DOI:10.1016/j.jiec.2014.12.044
35. Ismail A., Abdelfattah I., Faisal M. & Hela A. *J Hazard Mater.* **2018**, 342 (15), 519–526. DOI:10.1016/j.jhazmat.2017.08.046
36. Bougarrani S., Skadell K., Arndt R., El Azzouzi M., and Gläser R., *J. Environ. Chem. Eng.*, **2018**, 6 (2), 1934–1942. DOI:10.1016/j.jece.2018.02.026
37. Zhang G., Wang Q., Zhang W., Yuan T. & Wang P. *Photochem Photobiol Sci.* **2017**, 15 (8), 98–103.

Povzetek

Študija preučuje razgradnjo herbicida Imazapyr iz odpadnih vod s fotokatalitično ozonacijo katalizirano s TiO₂. Preučevali smo vpliv količine dodanega TiO₂, koncentracije herbicida in pH vrednosti. Rezultati so pokazali, da lahko dosežemo 90 % razgradnjo pri koncentracijah herbicida Imazapyr v koncentracijah do 7 µM ob prisotnosti UV100–TiO₂ v koncentraciji 200 mgL⁻¹. Razpad herbicida Imazapyr lahko opišemo s kinetiko prvega reda s konstanto fotolize 0.247 min⁻¹. S fotokatalitično ozonacijo smo dosegli popolno razgradnjo 5 µM herbicida Imazapyr pri pH vrednosti 7 v 20 min.

Short communication

Interaction Between the Rubidium Cation and [2.2.2]Paracyclophane: Experimental and Theoretical Study

Emanuel Makrlík,^{1,*} Stanislav Böhm,² David Sýkora,²
Magdalena Kvičalová¹ and Petr Vaňura²

¹ Faculty of Environmental Sciences, Czech University of Life Sciences, Kamýcká 129, 165 21 Prague 6 - Suchbát, Czech Republic

² University of Chemistry and Technology, Prague, Technická 5, 166 28 Prague 6, Czech Republic

* Corresponding author: E-mail: makrlik@centrum.cz

Phone: +420 376 594 672

Received: 21-06-2017

Abstract

By means of electrospray ionization mass spectrometry (ESI-MS), it was evidenced experimentally that the rubidium cation (Rb^+) reacts with the electroneutral [2.2.2]paracyclophane ligand ($\text{C}_{24}\text{H}_{24}$) to form the cationic complex $[\text{Rb}(\text{C}_{24}\text{H}_{24})]^+$. Moreover, applying quantum chemical calculations, the most probable conformation of the proven $[\text{Rb}(\text{C}_{24}\text{H}_{24})]^+$ complex was solved. In the complex $[\text{Rb}(\text{C}_{24}\text{H}_{24})]^+$ having a symmetry very close to C_3 , the “central” cation Rb^+ , fully located in the cavity of the parent [2.2.2]paracyclophane ligand, is coordinated to all three benzene rings of [2.2.2]paracyclophane via cation- π interaction. Finally, the binding energy, $E(\text{int})$, of the considered cation- π complex $[\text{Rb}(\text{C}_{24}\text{H}_{24})]^+$ was evaluated as -99.3 kJ/mol, confirming the formation of this fascinating complex species as well. This means that the [2.2.2]paracyclophane ligand can be considered as a receptor for the rubidium cation in the gas phase.

Keywords: [2.2.2]Paracyclophane; Rubidium cation; Cation- π interaction; DFT calculations; Structures.

1. Introduction

It is well-known that π -prismoids and certain hydrocarbon cyclophanes are capable of forming π -complexes with some small metal cations, where benzene rings act as π -donors for the respective complexes.¹ This fascinating complexation behavior is especially effective for [2.2.2]paracyclophane and related structures.^{2,3} Pierre et al.³ have reported the preparation of the silver triflate complex of [2.2.2]paracyclophane and claimed that it was the first member of a new class of compounds; owing to the complexation properties, they proposed the name π -prismoid for such hydrocarbon cyclophanes. Furthermore, Vögtle et al.⁴ have shown that concave hydrocarbon cyclophanes can extract certain metal ions from an aqueous phase into a nonpolar phase. They have tested these hydrocarbons as ionophores and have shown that PVC-[2.2.2]paracyclophane membranes demonstrated remarkable sensitivity toward the univalent silver cation.⁴ Recently, the first-principles model of Fermi resonance in the alkyl CH stretch

region has been applied to 1,2-diphenylethane and [2.2.2]paracyclophane.⁵ Finally, the role of the metal formal charge in the cation- π interactions has been evaluated with relativistic DFT methods involving a versatile π -cryptating structure, namely [2.2.2]paracyclophane.⁶

Cation- π interaction refers to the noncovalent attraction between a cation and a π -system.^{7,8} Its strength is often comparable with the interaction between a cation and traditional ligands, including water, alcohols, and amines. As a result of this cation- π interaction, there are extraordinarily important driving forces in molecular recognition processes in many biological and artificial systems.^{9–12} The considered cation- π interaction is a well-established phenomenon in the gas phase, as well as in the solid state,^{13–19} and is known to play very important role in the stabilization of tertiary structures of various proteins.²⁰

We must emphasize that the cation- π interactions of [2.2.2]paracyclophane ($\text{C}_{24}\text{H}_{24}$; see Figure 1) with the



Figure 1. Structural formula of [2.2.2]paracyclophane ($C_{24}H_{24}$).

“soft” cations Ag^+ ,^{3,21,22} and Tl^+ ²³ have been investigated and proven quite unambiguously.

However, up to now, interaction of the mentioned electroneutral [2.2.2]paracyclophane ligand with a very bulky cation has not been studied and [2.2.2]paracyclophane was considered to be a receptor for the transition metal cations.⁶ On the other hand, in our previous work we show, that paracyclophane [2.2.2] could also encapsulate light alkali metal cation Na^+ .²⁴

Therefore, in the present work, electrospray ionization mass spectrometry (ESI-MS) was applied as an experimental technique for characterization of the cation- π interaction between the very voluminous heavy univalent rubidium cation (Rb^+) and this [2.2.2]paracyclophane ligand in the gas phase. In this context we must state that the cation Rb^+ was chosen for the present study especially for the sake of an expected fascinating structure of the resulting cationic complex involving the [2.2.2]paracyclophane ligand. Furthermore, by means of quantum chemical DFT calculations, the most probable conformation of the experimentally evidenced cationic complex $[Rb(C_{24}H_{24})]^+$ in the gas phase was suggested.

2. Experimental

[2.2.2]Paracyclophane (puriss., $\geq 99\%$) was purchased from Aldrich, while rubidium chloride (puriss., $\geq 99\%$), $RbCl$, was supplied by Fluka. Other chemicals used (Lachema, Brno, Czech Republic) were of reagent grade purity. In this context it should be stated that rubidium has two stable isotopes, i.e., ^{85}Rb (natural abundance: 72.168%) and ^{87}Rb (natural abundance: 27.832%).

The mass spectra were measured on the 3200 Q TRAP (AB Sciex, Canada) mass spectrometer. This instrument was equipped with an electrospray ion source. The experiments were carried out in a positive-ion mode. Nitrogen was used as a nebulizer gas. The operating conditions for the mass spectrometer were set as follows: ion-spray voltage 5.5 kV; curtain gas 10 arbitrary units, ion source gas(1) 18 arbitrary units and ion source gas(2) 0 arbitrary units; ion source temperature ambient; declustering potential 35 V and entrance potential 10 V. Mass spectra were recorded from m/z 100 to 800. A mixture of

[2.2.2]paracyclophane (8×10^5 mol/L) and $RbCl$ (2×10^{-3} mol/L) dissolved in methanol/chloroform (1:1) was introduced into the ESI source via a PEEK capillary at a flow rate of 10 $\mu L/min$.

3. Results and Discussion

3.1. Electrospray Ionization Mass Spectrometry

Figure 2 depicts an ESI mass spectrum measured in a positive-ion mode for a mixture of [2.2.2]paracyclophane ($C_{24}H_{24}$) with $RbCl$ in a methanol/chloroform (1:1) solution. The intense peaks in the mass spectrum at m/z 397 and 399 evidently belong to the cationic complex $[Rb(C_{24}H_{24})]^+$. Besides, two insets in Figure 2 represent the real and calculated isotope patterns of the cationic cluster $[Rb(C_{24}H_{24})]^+$ related to the presence of two stable isotopes of rubidium, i.e., ^{85}Rb and ^{87}Rb , in natural abundances 72.168 and 27.832%, respectively. It is necessary to emphasize that under the present experimental conditions, the cationic complex species $[Rb(C_{24}H_{24})]^+$ was proven in the gas phase. No other [2.2.2]paracyclophane complexes with Rb^+ were found by using this experimental method.

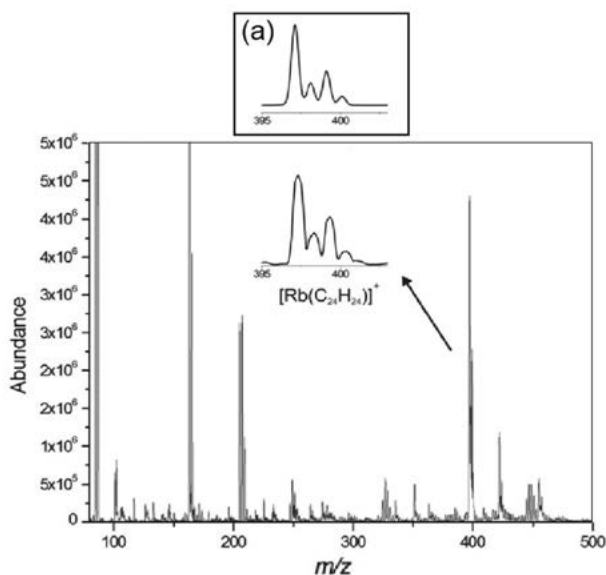


Figure 2. Positive-ion mode ESI mass spectrum of a mixture of [2.2.2]paracyclophane (8×10^5 mol/L) with $RbCl$ (2×10^{-3} mol/L) in methanol/chloroform (1:1). The inset shows the real isotope pattern of the $[Rb(C_{24}H_{24})]^+$ complex on an expanded mass scale. The inset (a) provides the calculated isotope pattern of the considered $[Rb(C_{24}H_{24})]^+$ complex.

Furthermore, Figure 3a shows a collision induced dissociation (CID) mass spectrum of the ions $[^{85}Rb(C_{24}H_{24})]^+$ (m/z 397), where the only one significant fragment ion signal was found at m/z 85. Analogously, in a

CID mass spectrum of $[^{87}\text{Rb}(\text{C}_{24}\text{H}_{24})]^+$ given in Figure 3b, the sole fragment ions at m/z 87 were observed. These facts clearly indicate that the only significant fragmentation channel in the investigated complex $[\text{Rb}(\text{C}_{24}\text{H}_{24})]^+$ is the loss of one electroneutral [2.2.2]paracyclophane ligand, similarly as in our recent paper.²³

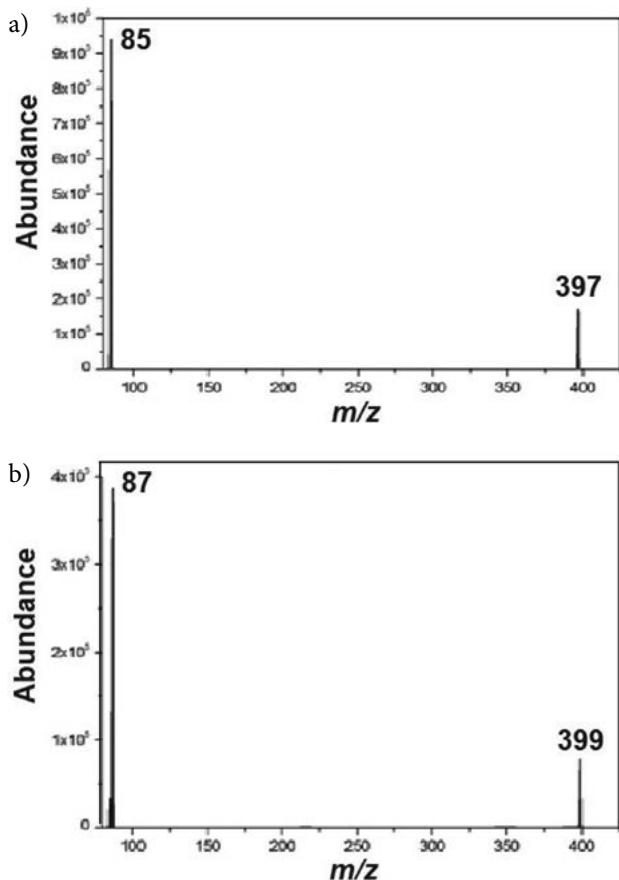


Figure 3. CID mass spectra of (a) $[^{85}\text{Rb}(\text{C}_{24}\text{H}_{24})]^+$ and (b) $[^{87}\text{Rb}(\text{C}_{24}\text{H}_{24})]^+$ ions obtained with nitrogen (1×10^{-2} mbar) at collision energy of 15 eV (laboratory frame).

In summary, we have evidenced experimentally that the cationic complex $[\text{Rb}(\text{C}_{24}\text{H}_{24})]^+$ must be present in the gas phase, and when the mentioned complex is collisionally activated, it decomposes almost exclusively via elimination of the electroneutral [2.2.2]paracyclophane molecule (i.e., $\text{C}_{24}\text{H}_{24}$), while the charge is retained on the rubidium atom in the form of Rb^+ .

3. 2. Quantum Chemical DFT Calculations

The theoretical calculations were performed at the density functional level of theory by using modern hybrid ω -B97XD functional including long range and dispersion corrections,²⁵ employing the Gaussian 09 suite of programs.²⁶ Modern balanced def2-TZVP basis set²⁷ was used, and the optimizations were unconstrained. In order

to increase the numerical accuracy and to reduce oscillations during the molecular geometry optimization, two-electron integrals and their derivatives were calculated by using the pruned (99,590) integration grid, having 99 radial shells and 590 angular points per shell. This was ensured by means of the Gaussian 09 keyword “integral(ultrafinegrid)”.

The most probable conformation of the $[\text{Rb}(\text{C}_{24}\text{H}_{24})]^+$ cationic complex was predicted on the basis of the thorough conformational analyses (i. e., eight very different initial mutual positions of the [2.2.2]paracyclophane ligand and the Rb^+ cation were considered during the geometry optimization) and the respective vibrational frequency analyses, analogously as in our articles.^{28–32}

During the model calculations, the molecular geometries of the free [2.2.2]paracyclophane ligand and its cation- π complex with Rb^+ were optimized, similarly as in our previous papers.^{28–32} The optimized conformation of this free [2.2.2]paracyclophane, having a symmetry very close to C_3 , is given in Figure 4.

Furthermore, we must emphasize that the only conformation was obtained by the full DFT optimization of the [2.2.2]paracyclophane - Rb^+ complex (i.e., $[\text{Rb}(\text{C}_{24}\text{H}_{24})]^+$), which is shown in Figure 5. It should be

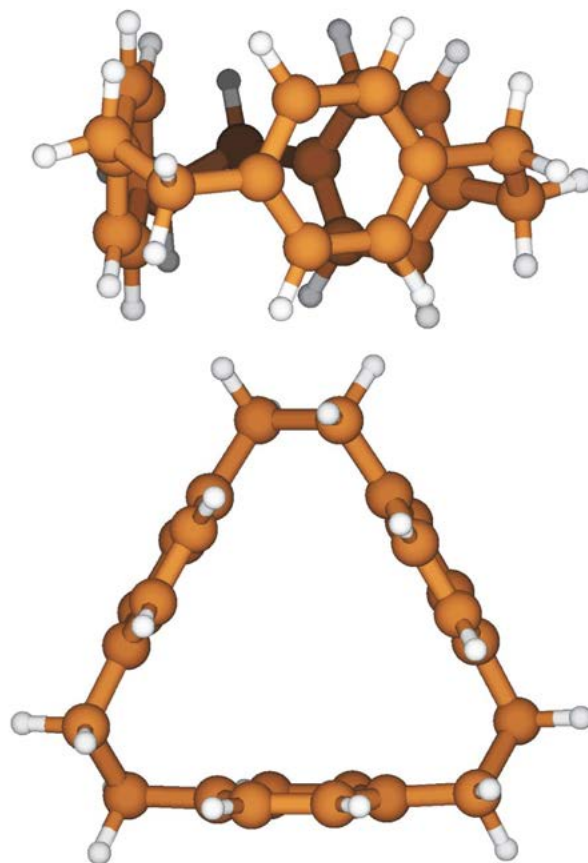


Figure 4. Two projections of the DFT optimized structure of free [2.2.2]paracyclophane (ω -B97XD / def2-TZVP).

stated that the respective vibrational calculations found no imaginary frequencies. In the cationic complex $[\text{Rb}(\text{C}_{24}\text{H}_{24})]^+$ with a symmetry very close to C_3 as well, the “central” cation Rb^+ , fully located in the cavity of the parent [2.2.2]paracyclophane ligand, is coordinated to all three benzene rings of [2.2.2]paracyclophane via cation- π interaction (the distances between the “central” cation Rb^+ and the centroids of the three benzene rings are 2.88, 2.88, and 2.88 Å), as also presented in detail in Figure 5. Further conformation of the $[\text{Rb}(\text{C}_{24}\text{H}_{24})]^+$ complex was not found by using the above-mentioned theoretical procedure. Besides, from comparison of Figure 4 with Figure 5, it is obvious that the inclusion of the rubidium cation causes a slight deformation of the ligand molecule in the considered $[\text{Rb}(\text{C}_{24}\text{H}_{24})]^+$ complex. It must be pointed out that encapsulation of light alkali metal cation Na^+ do not cause any deformation of the mentioned [2.2.2]paracyclophane ligand (see Figure 6).²⁴

Finally, the binding energy, $E(\text{int})$, of the $[\text{Rb}(\text{C}_{24}\text{H}_{24})]^+$ complex, involving the 7point correction for the basis set superposition error (BSSE),^{33,34} was calculated as -99.3 kJ/mol. Recently, the binding energy of the

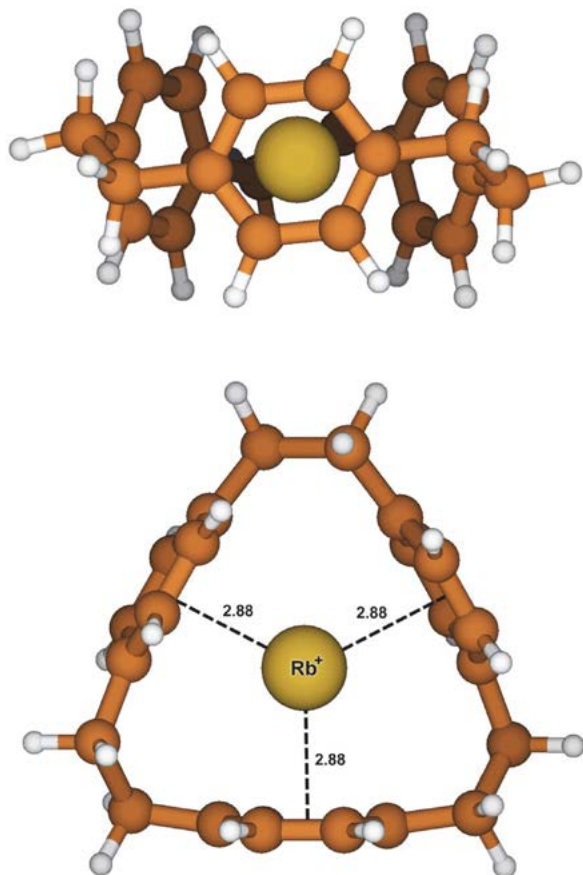


Figure 5. Two projections of the DFT optimized structure of the $[\text{Rb}(\text{C}_{24}\text{H}_{24})]^+$ complex (ω -B97XD / def2-TZVP); the distances between the “central” cation Rb^+ and the centroids of the three benzene rings are 2.88, 2.88, and 2.88 Å.

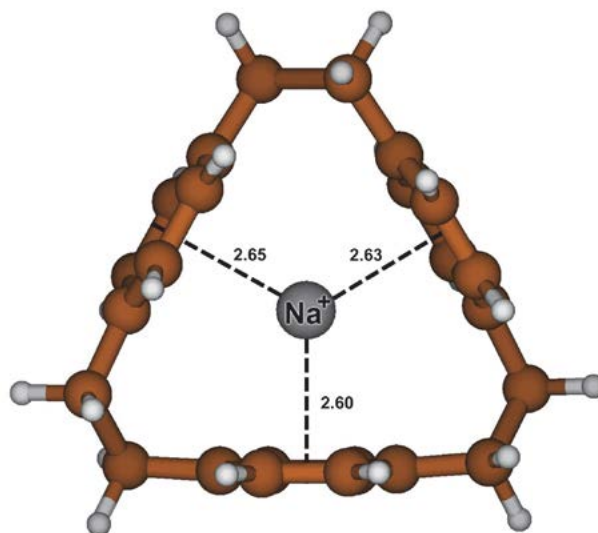


Figure 6. DFT optimized structure of the $[\text{Na}(\text{C}_{24}\text{H}_{24})]^+$ complex (ω -B97XD / def2-TZVP); the distances between the “central” cation Na^+ and the centroids of the three benzene rings are 2.65, 2.63, and 2.60 Å (Ref. ²⁴).

complex [2.2.2]paracyclophane – Tl^+ (i.e., $[\text{Tl}(\text{C}_{24}\text{H}_{24})]^+$) in the gas phase has been determined as -198.1 kJ/mol.²³ It means that the stability of the investigated complex $[\text{Rb}(\text{C}_{24}\text{H}_{24})]^+$ in the gas phase is substantially lower than that of the mentioned $[\text{Tl}(\text{C}_{24}\text{H}_{24})]^+$ complex species, although the deformation of the ligand, caused by an inclusion of the Tl^+ cation is even higher, than in the case of the Rb^+ cation.²³ This is evidently caused by the higher “softness” of Tl^+ in comparison with Rb^+ .

4. Conclusions

In this work, we have shown that an experimental (ESI-MS) and theoretical (DFT calculations) approach can provide important information concerning the noncovalent binding interaction between the electroneutral [2.2.2]paracyclophane ligand and the univalent rubidium cation (Rb^+) in the gas phase. On the basis of the mentioned experimental method, the cationic complex $[\text{Rb}(\text{C}_{24}\text{H}_{24})]^+$ was evidenced quite unambiguously. In addition, employing DFT calculations, the most probable conformation of this fascinating rubidium(I) complex was suggested. In the resulting complex $[\text{Rb}(\text{C}_{24}\text{H}_{24})]^+$ with a symmetry very close to C_3 , the “central” cation Rb^+ , fully located in the cavity of the parent [2.2.2]paracyclophane ligand, is coordinated to all three benzene rings of [2.2.2]paracyclophane via cation- π interaction. It means that [2.2.2]paracyclophane can be considered as a receptor for the rubidium cation in the gas phase. As follows from the previous facts, the present work may be a significant contribution especially to both experimental and theoretical study of [2.2.2]paracyclophane, as well as to structural chemistry in general.

5. Acknowledgements

This work was supported by the Grant Agency of Faculty of Environmental Sciences, Czech University of Life Sciences, Prague, Project No.: 42900/1312/3114 entitled “Environmental Aspects of Sustainable Development of Society”, as well as by the Czech Ministry of Education, Youth, and Sports (Project MSM No.: 20/2015).

6. References

- Comprehensive Supramolecular Chemistry, vol. 1, edited by J. L. Atwood, J. E. D. Davis, D. D. MacNicol, F. Vögtle, Pergamon, Oxford, UK, 1996.
- F. Vögtle, S. Ibach, M. Nieger, C. Chartroux, T. Krüger, H. Stephan, K. Gloe, *Chem. Commun.* **1997**, 1809–1810. DOI:10.1039/A703715E
- J. L. Pierre, P. Baret, P. Chautemps, M. Armand, *J. Am. Chem. Soc.* **1981**, *103*, 2986–2988. DOI:10.1021/ja00401a013
- J. Gross, G. Harder, A. Siepen, J. Harren, F. Vögtle, H. Stephan, K. Gloe, B. Ahlers, K. Cammann, K. Rissanen, *Chem. Eur. J.* **1996**, *2*, 1585–1595. DOI:10.1002/chem.19960021218
- E. G. Buchanan, J. C. Dean, T. S. Zwier, E. L. Sibert III, *J. Chem. Phys.* **2013**, *138*, 064308/1–064308/11. DOI:10.1063/1.4790163
- A. O. Ortolan, G. F. Caramori, G. Frenking, A. Muñoz-Castro, *New J. Chem.* **2015**, *39*, 9963–9968. DOI:10.1039/C5NJ02384J
- D. A. Dougherty, *Science* **1996**, *271*, 163–168. <https://www.ncbi.nlm.nih.gov/pubmed/8539615>
- A. S. Mahadevi, G. N. Sastry, *Chem. Rev.* **2013**, *113*, 2100–2138. DOI:10.1021/cr300222d
- J. C. Ma, D. A. Dougherty, *Chem. Rev.* **1997**, *97*, 1303–1324. DOI:10.1021/cr9603744
- K. S. Kim, P. Tarakeswar, J. Y. Lee, *Chem. Rev.* **2000**, *100*, 4145–4185. DOI:10.1021/cr990051i
- N. Zacharias, D. A. Dougherty, *Trends Pharm. Sci.* **2002**, *23*, 281–287. <https://www.ncbi.nlm.nih.gov/pubmed/12084634>
- G. W. Gokel, *Chem. Commun.* **2003**, 2847–2852. DOI:10.1039/b305483g
- D. Schröder, H. Schwarz, J. Hrušák, P. Pyykkö, *Inorg. Chem.* **1998**, *37*, 624–632. DOI:10.1021/IC970986M
- A. Gapeev, C. N. Yang, S. J. Klippenstein, R. C. Dunbar, *J. Phys. Chem. A* **2000**, *104*, 3246–3256. DOI:10.1021/jp992627d
- S. Tsuzuki, M. Yoshida, T. Uchamaru, M. Mikami, *J. Phys. Chem. A* **2001**, *105*, 769–773. DOI:10.1021/jp003287v
- H. Huang, M. T. Rodgers, *J. Phys. Chem. A* **2002**, *106*, 4277–4289. DOI:10.1021/jp013630b
- Y. Mo, G. Subramanian, J. Gao, D. M. Ferguson, *J. Am. Chem. Soc.* **2002**, *124*, 4832–4837. DOI:10.1021/ja0174433
- A. S. Reddy, G. N. Sastry, *J. Phys. Chem. A* **2005**, *109*, 8893–8903. DOI:10.1021/jp0525179
- D. Vijay, G. N. Sastry, *Phys. Chem. Chem. Phys.* **2008**, *10*, 582–590. DOI:10.1039/B713703F
- K. Sakurai, T. Mizuno, H. Hiroaki, K. Gohda, J. Oku, T. Tanaka, *Angew. Chem., Int. Ed. Engl.* **2005**, *44*, 6180–6183. DOI:10.1002/anie.200500806
- C. Cohen-Addad, P. Baret, P. Chautemps, J. L. Pierre, *Acta Crystallogr., Sect. C: Cryst. Struct. Commun.* **1983**, *C39*, 1346–1349. DOI:10.1107/S0108270183008483
- P. G. Jones, P. Bubenitschek, F. Heirtzler, H. Hopf, *Acta Crystallogr., Sect. C: Cryst. Struct. Commun.* **1996**, *C52*, 1380–1384. DOI:10.1107/S0108270195017008
- E. Makrlík, S. Böhm, D. Sýkora, B. Klepetářová, P. Vaňura, M. Polášek, *Chem. Phys. Lett.* **2015**, *642*, 39–42. DOI:10.1016/j.cplett.2015.10.074
- E. Makrlík, D. Sýkora, S. Böhm, P. Vaňura, *J. Mol. Struct.* **2018**, *1154*, 79–82. DOI:10.1016/j.molstruc.2017.10.027
- J.-D. Chai, M. Head-Gordon, *Phys. Chem. Chem. Phys.* **2008**, *10*, 6615–6620. DOI:10.1039/b810189b
- M. J. Frisch, G. W. Trucks, H. B. Schlegel, G. E. Scuseria, M. A. Robb, J. R. Cheeseman, G. Scalmani, V. Barone, B. Menucci, G. A. Petersson, H. Nakatsuji, M. Caricato, X. Li, H. P. Hratchian, A. F. Izmaylov, J. Bloino, G. Zheng, J. L. Sonnenberg, M. Hada, M. Ehara, K. Toyota, R. Fukuda, J. Hasegawa, M. Ishida, T. Nakajima, Y. Honda, O. Kitao, H. Nakai, T. Vreven, J. A. Montgomery, Jr., J. E. Peralta, F. Ogliaro, M. Bearpark, J. J. Heyd, E. Brothers, K. N. Kudin, V. N. Staroverov, R. Kobayashi, J. Normand, K. Raghavachari, A. Rendell, J. C. Burant, S. S. Iyengar, J. Tomasi, M. Cossi, N. Rega, J. M. Millam, M. Klene, J. E. Knox, J. B. Cross, V. Bakken, C. Adamo, J. Jaramillo, R. Gomperts, R. E. Stratmann, O. Yazyev, A. J. Austin, R. Cammi, C. Pomelli, J. W. Ochterski, R. L. Martin, K. Morokuma, V. G. Zakrzewski, G. A. Voth, P. Salvador, J. J. Dannenberg, S. Dapprich, A. D. Daniels, Ö. Farkas, J. B. Foresman, J. V. Ortiz, J. Cioslowski, D. J. Fox, Gaussian 09, Revision C.01. Gaussian Inc., Wallingford, CT (2009).
- F. Weigend, R. Ahlrichs, *Phys. Chem. Chem. Phys.* **2005**, *7*, 3297–3305. DOI:10.1039/b508541a
- J. Kříž, J. Dybal, E. Makrlík, P. Vaňura, B. A. Moyer, *J. Phys. Chem. B* **2011**, *115*, 7578–7587. DOI:10.1021/jp203221k
- E. Makrlík, P. Vaňura, R. Rathore, *Monatsh. Chem.* **2015**, *146*, 521–525. DOI:10.1007/s00706-014-1370-y
- E. Makrlík, P. Vaňura, *Mol. Phys.* **2015**, *113*, 3712–3716. DOI:10.1080/00268976.2015.1054326
- E. Makrlík, S. Böhm, P. Vaňura, P. Ruzza, *Mol. Phys.* **2015**, *113*, 1472–1477. DOI:10.1080/00268976.2015.1006276
- E. Makrlík, J. Kvičala, P. Vaňura, *Mol. Phys.* **2016**, *114*, 2046–2051. DOI:10.1080/00268976.2016.1177221
- L. Turi, J. J. Dannenberg, *J. Phys. Chem.* **1993**, *97*, 2488–2490. DOI:10.1021/j100113a002
- J. E. Rode, J. C. Dobrowolski, *Chem. Phys. Lett.* **2002**, *360*, 123–132. DOI:10.1016/S0009-2614(02)00779-0

Povzetek

Z uporabo elektrosprej ionizacijske masne spektrometrije (ESI-MS) smo dokazali, da rubidijev kation (Rb^+) z elektronevtralnimi [2.2.2] paraciklofanskimi ligandi ($\text{C}_{24}\text{H}_{24}$) tvori kationski kompleks $[\text{Rb}(\text{C}_{24}\text{H}_{24})]^+$. S pomočjo kvantno-kemijskih izračunov smo določili tudi najbolj verjetno konformacijo tega kompleksa. Ugotovili smo, da ima simetrijo zelo blizu C_3 , da je „osrednji“ kation Rb^+ v celoti umeščen v prostor matičnega [2.2.2]paraciklofanskega liganda, in koordiniran z vsemi tremi benzenskimi obroči [2.2.2]paraciklofana preko kation- π interakcije. Ocenili smo energijo vezave, $E(\text{int})$, obravnavanega kation- π kompleksa $[\text{Rb}(\text{C}_{24}\text{H}_{24})]^+$. Vrednost $-99,3$ kJ/mol potrjuje verjetnost nastanka tega zanimivega kompleksa, kar pomeni, da [2.2.2]paraciklofanski ligand lahko obravnavamo kot receptor Rb^+ v plinski fazi.

Erratum for

“Trans-Activation Response Element RNA is Detectable in the Plasma of a Subset of Aviremic HIV-1–Infected Patients”

Anžej Hladnik,¹ Jana Ferdin,¹ Katja Goričar,¹ Steven G. Deeks,²
Boris M. Peterlin,² Ana Plemenitaš,¹ Vita Dolžan¹ and Metka Lenassi^{1,*}

* Corresponding author: E-mail: metka.lenassi@mf.uni-lj.si,
Tel: +386-1-5437658; Fax: +386-1-5437641

Acta Chim Slov. 2017 Sep; 64(3): 530-536. ID 2863.
DOI: 10.17344/acsi.2016.2863

With this Erratum, we would like to acknowledge that
Anžej Hladnik and Jana Ferdin contributed equally to the published work.
Therefore, the authorship of the manuscript should have been written as follows:

Trans-Activation Response Element RNA is Detectable in the Plasma of a Subset of Aviremic HIV-1–Infected Patients

Anžej Hladnik,^{1,3} Jana Ferdin,^{1,3} Katja Goričar,¹ Steven G. Deeks,²
Boris M. Peterlin,² Ana Plemenitaš,¹ Vita Dolžan¹ and Metka Lenassi^{1,*}

* Corresponding author: E-mail: metka.lenassi@mf.uni-lj.si,
Tel: +386-1-5437658; Fax: +386-1-5437641

³ These authors contributed equally to this work.

DRUŠTVENE VESTI IN DRUGE AKTIVNOSTI SOCIETY NEWS, ANNOUNCEMENTS, ACTIVITIES

Vsebina

Poročilo o delu v letu 2017	S51
Koledar važnejših znanstvenih srečanj s področja kemije, kemijske tehnologije in kemijskega inženirstva	S55
Navodila za avtorje	S62

Contents

Report for 2017	S51
Scientific meetings – chemistry, chemical technology and chemical engineering	S55
Instructions for authors	S62

POROČILO PREDSEDNIKA SLOVENSKEGA KEMIJSKEGA DRUŠTVA O DELU DRUŠTVA V LETU 2017

V letu 2017 je bilo društvo aktivno na številnih področjih. Izvajali smo redne letne aktivnosti, pri katerih je bil glavni poudarek na rednem izdajanju društvene revije Acta Chimica Slovenica ter organizaciji največjega letnega dogodka društva, konference »Slovenski kemijski dnevi 2017«.

Slovenski kemijski dnevi 2017 so bili organizirani v Portorožu, v Kongresnem centru Grand hotela Bernardin, od 20–22. septembra 2017.

Programskemu in organizacijskemu odboru je predsedoval takratni predsednik društva, prof. dr. Venčeslav Kaučič, skupaj s člani odbora v zasedbi prof. dr. Marija Bešter Rogač, prof. dr. Zorka Novak Pintarič, prof. dr. Darja Lisjak, prof. dr. Marjan Veber in prof. dr. Janez Plavec. Na posvetovanju je bilo predstavljenih več kot 100 prispevkov v obliki predavanj in posterjev. Delo je potekalo plenarno in v dveh vzporednih sekcijah. Udeleženci konference so bili zelo zadovoljni s kakovostjo znanstvenih in strokovnih prispevkov ter spremljevalnim programom srečanja. Na konferenci je sodelovalo 16 sponzorjev. Objavili smo Zbornik povzetkov in referatov konference, ki je dostopen na USB ključku ter na voljo v številnih strokovnih knjižnicah po Sloveniji.

Plenarni predavatelji so bili: **prof. dr. Barbara Malič** (Institut »Jožef Stefan«), **prof. dr. Jurij Lah** (Fakulteta za kemijo in kemijsko tehnologijo, Univerza v Ljubljani), **prof. dr. András Perczel** (Eötvös Loránd University, Institute of Chemistry, Madžarska) in **prof. dr. Ferenc Friedler** (Pázmány Péter Catholic University Budapest, Madžarska). Poleg štirih plenarnih predavanj so udeleženci poslušali sedem "keynote" vabljenih predavanj, ki so jih izvedli **prof. dr. Iztok Turel** (Fakulteta za kemijo in kemijsko tehnologijo, Univerza v Ljubljani), **prof. dr. Darja Lisjak** (Institut »Jožef Stefan«), **doc. dr. Boštjan Genorio** (Fakulteta za kemijo in kemijsko tehnologijo, Univerza v Ljubljani), **prof. dr. Zdenko Časar** (Lek d.d.), **prof. dr. Gregor Mali** (Kemijski inštitut), **prof. dr. Slobodan Gadžurić** (Faculty of Science, University of Novi Sad, Srbija) in **doc. dr. Matjaž Finšgar** (Fakulteta za kemijo in kemijsko tehnologijo, Univerza v Mariboru).

V sklopu konference smo 21. septembra 2017 izvedli redni občni zbor društva, na katerem smo izvolili novo vodstvo za mandatno obdobje september 2017 – september 2021. Predsedevanje društva je prevzel dr. Albin Pintar, podpredsedstvo prof. dr. Marjan Veber, prof. dr. Zdravko Kravanja in prof. dr. Matjaž Valant. Vlogo tajnikov so člani društva zaupali prof. dr. Mariji Bešter Rogač in dr. Maticu Lozinšku, vlogo blagajnika pa dr. Samu Andrenšku. Izvolili smo tudi nove člane glavnega odbora, nadzornega odbora in častnega razsodišča.

V letniku Acta Chimica Slovenica 2017 (vol. 64) so izšle štiri številke s skupno 105 originalnimi znanstvenimi

članki, 2 preglednima člankoma in 9 kratkimi prispevki na skupno 1055 straneh z dvokolonskim tiskom. V slovenskem delu revije so bila na 129 straneh kot društvene vesti objavljena sekcijška poročila, sezname diplomskih, magistrskih in doktorskih del s področja kemije v letu 2017 in en slovenski strokovni članek o kemijskem laboratoriju celjske kraljice. Tretja številka je bila posvečena konferenci mladih znanstvenikov z naslovom »Cutting Edge«, četrta pa **akademiku profesor Mihi Tišlerju** ob njegovi 90. letnici. V uredništvo je prispelo preko 1200 prispevkov, vendar jih zaradi neustrezne tehnične priprave in dokumentacije zavrnilo več kot 80 % brez recenzije. Slaba polovica recenziranih člankov je pozitivno ocenjenih. Objavljeni članki pokrivajo aktualna področja organske, anorganske, fizikalne in analizne kemije, kemije materialov, kemijskega, biokemijskega in okoljskega inženirstva ter splošne, uporabne in biomedicinske kemije. Pisani so v angleškem jeziku s slovenskim povzetkom. Faktor vpliva (Impact Factor) ACSi za leto 2016 znaša IF = 0,984 in se je kljub prizadevnemu delu urednikov nekoliko znižal (IF = 1,167 za 2015). Na internetni strani <http://acta.chem-soc.si> objavljamo elektronsko verzijo revije Acta Chimica Slovenica, kar povečuje branost ter mednarodno odmevnost revije. Članki, objavljeni v ACSi, so povzeti tudi v Chemical Abstracts Plus, Current Contents (Physical, Chemical and Earth Sciences), Science Citation Index Expanded in Scopus. V pričetku leta 2017 smo uvedli uporabo licence Creative Commons, ki ureja avtorske pravice objavljenih člankov.

Januarja 2018 je nova odgovorna urednica ACSi poslala prof. dr. Ksenija Kogej, z odhodom prejšnjega odgovornega urednika prof. dr. Aleksandra Pavka pa sta se v uredniškem odboru zamenjala tudi dva področna urednika (namesto M. Bešter-Rogač in A. Pavko sedaj K. Kogej in A. Podgornik). S prvo številko v letu 2018 bo ACSi izhajala le še v elektronski obliki, zato uredniški odbor pripravlja spremembe v elektronskem obveščanju bralcev o izhajanju revije. Tako načrtujemo nadgradnjo spletne strani in tudi novo vrsto člankov – vabljenih tematske članke, ki bodo pisani na vabilo UO. Pričakujemo, da bo ta kategorija člankov prispevala k večji branosti in odmevnosti revije. Tako kot v prejšnjih letih bodo tudi v 2018 izšle 4 številke ACSi. Četrta številka bo posvečena **prof. dr. Ivanu Kregarju**.

Društvo je bilo tudi v letu 2017 uspešno pri prijavi na Javni razpis za sofinanciranje izdajanja domačih znanstvenih periodičnih publikacij v letu 2017 in 2018. Dobili smo odobrena sredstva v višini 36.284,08 EUR za obe leti, kar je letno 18.142,04 EUR. V primerjavi s preteklim razpisom (2015 in 2016) je to 21.565,04 EUR manj. V letu 2017 smo prejeli sredstva v treh obrokih.

Zahvaljujem se tudi vsem institucijam, ki so v letu 2017 finančno podprle izdajanje revije. Te so Fakulteta za

kemijo in kemijsko tehnologijo Univerze v Ljubljani, Fakulteta za Kemijsko in kemijsko tehnologijo Univerze v Mariboru, Kemijski inštitut, Inštitut »Jožef Stefan« in Fakulteta za farmacijo Univerze v Ljubljani. Sponzorji revije so bili z objavo oglasa Krka d.d., Novo mesto, Donau Lab d.o.o. Ljubljana in Helios Domžale, d.o.o.

V letu 2017 smo nadaljevali z aktivnostmi za pridobivanje novih članov. Medse smo jih privabili 26, od tega 6 študentov. Za ta namen smo konec leta 2017 pričeli s prenovno grafične podobe društva ter s pomočjo grafične oblikovalke izdelali plakate, ki nagovarjajo nove člane k vpisu. Plakate smo že razobesili po številnih inštitucijah, s to aktivnostjo bomo nadaljevali tudi v letu 2018. Za nove člane smo uvedli simbolno darilo (reprezentančne kemične svinčnike) ob njihovem vpisu v društvo. Člane smo o aktivnostih v letu 2017 še pogosteje obveščali preko elektronske pošte in preko spletne strani društva, proti koncu leta 2017 pa smo za namene promocije in obveščanja vzpostavili tudi Facebook in Twitter profil društva, ki sta hitro in dobro zaživela.

Člani Slovenskega kemijskega društva so bili dejavni tudi **na področju mednarodnega sodelovanja**. Predvsem je potrebno omeniti članstvo društva v mednarodnih združenjih IUPAC, ECTN, IUCr, EURACHEM, EuCheMS, EFCE, EPF in ECA.

Poleg članstva v teh organizacijah, so se izvajale tudi nekatere druge pomembne mednarodne aktivnosti:

Predsednik društva Venčeslav Kaučič in tajnik društva Marjan Veber sta se udeležila generalne skupščine ECTN na Malti od 1–4 aprila 2017. Na tem srečanju je bil Marjan Veber izvoljen za glavnega zakladnika tega evropskega združenja.

Prof. dr. Zdravko Kravanja se je udeležil generalne skupščine EFCE v Barceloni, 1. oktobra 2017. Generalna skupščina poteka v sklopu »10th World Congress of Chemical Engineering, WCCE10«, ki se ga udeležujejo tudi člani društva.

Predsednik Slovenskega kemijskega društva, prof. dr. Venčeslav Kaučič se je udeležil generalne skupščine EuCheMS v Rimu, Italija, od 26–27. septembra 2017. Na generalni skupščini so podpisali dokument »Research and Education Without Borders After Brexit: A Position Paper« in obravnavali druge pomembne teme na evropski ravni. Potekale so tudi priprave na 7. kongres EuCheMS, ki bo leta 2018 v Liverpoolu, UK, od 26–30. avgusta. Slovensko kemijsko društvo skrbi za promocijo konference preko spletne strani, družabnih omrežij in z deljenjem letakov.

Predsednica sekcije EURACHEM Slovenija, Dr. Nireta Hrastelj in drugi člani društva, so aktivno sodelovali pri organizaciji delavnice »9th Proficiency testing in analytical chemistry, microbiology and laboratory medicine 0 Current Practice and Future Directions«, ki je bila od 9–12. oktobra 2017 v Portorožu.

Kristalografska sekcija je pod vodstvom prof. dr. Antona Medena in drugih aktivnih članov organizirala

25. Slovensko-hrvaško kristalografsko srečanje, ki je potekalo od 14–18. junija 2017 na FKKT, UL.

Prof. dr. Venčeslav Kaučič se je v Rimu udeležil Generalne skupščine EuCheMS, ki je potekala 26. in 27. septembra 2017.

Od 7–14. julija 2017 se je prof. dr. Venčeslav Kaučič, takrat še v vlogi predsednika Slovenskega kemijskega društva in titularnega člana ChemRAWN odbora IUPAC, udeležil sestanka Generalne skupščine in Izvršilnega odbora IUPAC, ki sta potekala v Sao Paulo, Brazilija. Poleg naštetih dveh dogodkov je v času IUPAC GA potekal še sestanek predsednikov kemijskih društev – World Chemistry Leadership Meeting in dvodnevni sestanek ChemRAWN odbora.

Predsednik Sekcije za polimere dr. David Pahovnik, se je od 2–7. julija 2017 udeležil generalne skupščine Evropske polimerne federacije, ki je potekala v Lyonu, Francija. Sekcija za polimere je septembra 2017 za člane sekcije organizirala tudi predavanje prof. Devona A. Shipa iz Clarkson univerze, Potsdam, NY, ZDA.

Člani IUPAC Affiliate Membership Program so v letu 2017 prejeli šest številčk revije Chemistry International, imeli možnost ugodnejših kotizacij pri udeležbi na konferencah IUPAC ter pri nakupu literature (nomenklature itd.).

Člani društva so bili aktivni pri pripravi na organizacijo dveh mednarodnih konferenc, ki bosta potekali leta 2018 in 2019 in kjer pričakujemo številčno mednarodno udeležbo. To sta konferenci ECIS 2018 (32nd Conference of The European Colloid and Interface Society: 2–7. september 2018, Ljubljana) in konferenca EAAOP-6 (6th European Conference on Environmental Applications of Advances Oxidation Processes: 26–30. junij 2019, Portorož).

Društvo se je v letu 2017 uspešno prijavilo na Javni razpis ARRS za sofinanciranje delovanja v mednarodnih znanstvenih združenjih v letu 2017, kjer smo bili uspešni pri vseh oddanih vlogah.

15. junija 2017 je društvo v sodelovanju s Kemijskim inštitutom slavnostno odkrilo doprsni kip prof. Maksa Samca. Dogodek je potekal v okviru tedna Kemijskega inštituta. Častni gost in slavnostni govorec prireditve je bil predsednik Državnega zbora Republike Slovenije dr. Milan Brglez. Nekaj besed o delu in življenju akademika Maksa Samca je, kot predstavnik Slovenske akademije znanosti in umetnosti ter Slovenskega kemijskega društva, povedal tudi akad. prof. dr. Branko Stanovnik. Doprsni kip je delo akademskega kiparja Marjana Keršiča Belača, za idejno zasnovo podstavka in njegovo izvedbo pa je poskrbel akademski kipar Jiri Kočica.

Ljubljana, 15. marec 2018

dr. Albin Pintar
predsednik društva

Mariborska podružnica

Mariborska podružnica se je v letu 2017 usmerila v izpolnitev ciljev, ki si jih je zastavila v preteklem letu.

Člani mariborske podružnice smo se udeležili že tradicionalne konference „Slovenski Kemijski Dnevi, ki so potekali na v Portorožu. Predsedovali smo posameznim sekcijam in sodelovali kot predavatelji.

Skrb Mariborske podružnice je tudi stalno izobraževanje članov. V ta namen smo organizirali strokovna predavanja in razne seminarje, na katerih so predavali priznani tuji in domači strokovnjaki. Predavanja so pokrivala pomembna področja teoretične in uporabne kemije, kemijske in procesne tehnike ter kemijskega izobraževanja. V mesecu Maju smo gostili tujega predavatelja dr. Lam Hon Loong iz Univerze Nottingham, Tehnična fakulteta Malezija. Njegovo področje je v okviru procesne tehnike.

Prav tako smo v mesecu Maju gostili direktorja podjetja Sanofarm d.o.o. Simona Štalo, ki se je predstavil s predavanjem iz področja Fitoterapija in njen pomen. V nadaljevanju je predstavil način dela v majhnem in interdisciplinarnem kolektivu. Predavanje je bilo še posebej dobrodošlo za absolvente druge stopnje, ki na nek način zaključujejo ali pa vsaj delno zaključujejo izobraževanje in se začno postavljati na lastne noge.

Aktivno smo sodelovali tudi pri mednarodnih poletnih šolah. V mesecu juliju na naši fakulteti potekala 22. mednarodna poletna šola na temo visokotlačnih tehnologij: »ESS-HPT« The European Summer school in High Pressure Technology, ki jo je organiziral naš Laboratorij za Separacijske procese in produktno tehniko v sodelovanju s Tehnološko fakulteto v Grazu.

dr. Regina Fuchs-Godec

Poročilo Sekcije za kristalografijo za leto 2017

Sekcija za kristalografijo pri Slovenskem kemijskem društvu je v letu 2017 skupaj s hrvaškim kristalografskim društvom iz Zagreba organizirala 25. (jubilejno) zaporedno srečanje slovenskih in hrvaških kristalografov. Srečanje je potekalo v Sloveniji v Ljubljani v prostorih nove stavbe Fakultete za kemijo in kemijsko tehnologijo. Kot vsako leto je bila tudi tokrat udeležba mednarodna, zato je bil uradni jezik srečanja angleščina. S sredstvi donatorjev in sponzorjev ter veliko prostovoljnega dela članov sekcije smo uspeli organizirati srečanje tako, da smo obdržali tradicijo, da za udeležence ni bilo kotizacije.

Podobno kot na prejšnjih konferencah, so se tudi tokrat povabilu za sodelovanje odzvali ugledni, mednarodno uveljavljeni plenarni predavatelji. To so bili Elena Boldyreva (Novosibirsk, Rusija), »High-pressure studies of organic and coordination compounds«; Jeremy Karl Cockroft (London, Združeno kraljestvo), »Powder Diffraction: an Essential Complementary Tool for those Skilled in the Art but one with Pitfalls for the Unwary«; **Marjan Marinšek** (Ljubljana, Slovenija), »Microstructure evolution in cermet anodes for solid oxide fuel cells«; Krešimir Molčanov (Zagreb, Hrvaška), »Stacking of planar conjugated rings – beyond aromatics«; **Dietmar Stalke**, (Göttingen,

Germany) »More than 100 years of Lewis' diagrams – still valid in the light of charge density?«. Novost na srečanjih je bila dobro obiskana delavnica za uporabo programa Olex² (prav tako brezplačna za udeležence), ki jo je vodil Horst Puschmann (Durham, Združeno kraljestvo),

Konferenca je bila po obisku in po kakovosti prispevkov uspešna. Udeleženci so v 66 prispevkih v obliki predavanj osvetlili številna področja kristalografije. Srečanje je bil tako v strokovnem delu kot na družabnih dogodkih (vodena ekskurzija po Ljubljani z vožnjo po Ljubljani in večerjo na Ljubljanskem gradu) spet priložnost za izmenjavo spoznanj, navezavo stikov in intenzivno učenje mlajših kolegov.

Zaradi omejenih sredstev v raziskovalnih programih ni projektih, smo se slovenski kristalografi v letu 2017 lahko le v omejenem številu (en udeleženec) udeležili svetovnega kongresa IUCr v Hyderabadu v Indiji.

Aktivno poteka delo za pripravo 26. Slovensko-hrvaškega kristalografskega srečanja, ki bo junija 2018 v Poreču. S hrvaškimi kolegi pa bomo sodelovali tudi pri kandidaturi za organizacijo Evropske konference o praškovni difrakciji.

prof. dr. Anton Meden

KOLENDAR VAŽNEJŠIH ZNANSTVENIH SREČANJ S PODROČJA KEMIJE IN KEMIJSKE TEHNOLOGIJE

SCIENTIFIC MEETINGS – CHEMISTRY AND CHEMICAL ENGINEERING

2018

July 2018

- 1 – 5 WORLD POLYMER CONGRESS MACRO18
Cairns Queensland, Australia
Information: <http://www.macro18.org>
- 1 – 6 24TH IUPAC INTERNATIONAL CONFERENCE ON PHYSICAL ORGANIC CHEMISTRY
(ICPOC 24)
Faro, Portugal
Information: <http://icpoc24.ualg.pt/>
- 2 – 6 XVI INTERNATIONAL IUPAC CONFERENCE ON HIGH TEMPERATURE MATERIALS
CHEMISTRY (HTMC-XVI)
Ekaterinburg, Russian Federation
Information: <http://htmc16.ru/>
- 3 – 8 5TH INTERNATIONAL CONGRESS ON CHEMISTRY FOR CULTURAL HERITAGE
(CHEMCH 2018)
Bucharest, Romania
Information: <http://www.chemch2018.ro>
- 8 – 11 8TH INTERNATIONAL CONFERENCE ON ENGINEERING FAILURE ANALYSIS
Budapest, Hungary
Information: <https://www.elsevier.com/icefa-conference>
- 8 – 12 PREPA 12 – SYMPOSIUM »SCIENTIFIC BASES FOR THE PREPARATION OF
HETEROGENEOUS CATALYSTS«
Louvain-la-Neuve, Belgium
Information: https://www.ldorganisation.com/v2/produits.php?langue=english&cle_menus=1238916539
- 8 – 13 27TH IUPAC INTERNATIONAL SYMPOSIUM ON PHOTOCHEMISTRY
Dublin, Ireland
Information: <https://iupac.org/event/27th-iupac-international-symposium-photochemistry/>
- 8 – 13 22ND INTERNATIONAL CONFERENCE ON PHOSPHORUS CHEMISTRY
Budapest, Hungary
Information: <http://www.icpc22.mke.org.hu/>
- 9 – 13 EUROMEMBRANE 2018
Valencia, Spain
Information: <http://euromembrane2018.org/>
- 10 – 14 25TH INTERNATIONAL CONFERENCE ON CHEMISTRY EDUCATION ICCE 2018)
Sydney, Australia
Information: <http://www.icce2018.org/>
- 12 – 15 7TH INTERNATIONAL CONGRESS ON SUSTAINABILITY SCIENCE & ENGINEERING
Ohio, USA
Information: <http://icosse.org/2018>

- 15 – 20 THE 18TH INTERNATIONAL SYMPOSIUM ON SOLUBILITY PHENOMENA AND RELATED EQUILIBRIUM PROCESSES (ISSP)
Tours, France
Information: <http://issp18.org/>
- 15 – 20 28TH INTERNATIONAL CONFERENCE ON ORGANOMETALLIC CHEMISTRY
Florence, Italy
Information: <http://www.icomc2018.com/>
- 16 – 17 SUPPORTING FAIR EXCHANGE OF CHEMICAL DATA THROUGH STANDARDS DEVELOPMENT
Amsterdam, Netherlands
Information: www.go-fair.org
- 23 – 25 WORLD CONGRESS & EXPO ON CHEMICAL ENGINEERING & CATALYSIS
Osaka, Japan
Information: <https://scientificfederation.com/catalysis-2018/>
- 30 – Aug 4 43RD INTERNATIONAL CONFERENCE ON COORDINATION CHEMISTRY
Sendai, Japan
Information: <http://iccc2018.jp>
-
- August 2018**
- 12 – 17 18TH INTERNATIONAL BIOTECHNOLOGY SYMPOSIUM
Montréal, Canada
Information: <http://ibs2018montreal.org/>
- 25 – 29 23RD INTERNATIONAL CONGRESS OF CHEMICAL AND PROCESS ENGINEERING
CHISA 2018
Prague, Czech Republic
Information: <http://2018.chisa.cz/>
- 25 – 29 21ST CONFERENCE ON PROCESS INTEGRATION, MODELLING AND OPTIMISATION FOR ENERGY SAVING AND POLLUTION REDUCTION PRES 2018
Prague, Czech Republic
Information: <http://2018.chisa.cz/>
- 26 – 30 ECC7 – 7TH EuCheMS CHEMISTRY CONGRESS
Liverpool, UK
Information: <https://www.euchems2018.org/>
- 26 – 30 35TH INTERNATIONAL CONFERENCE ON SOLUTION CHEMISTRY (ICSC)
Szeged, Hungary
Information: <http://www.mke.org.hu/ICSC2018>
- 26 – 31 22ND INTERNATIONAL MASS SPECTROMETRY CONFERENCE (IMSC) 2018
Florence, Italy
Information: <http://www.imsc2018.it/>
- 30 – 31 ICOSSE 2018 : 20TH INTERNATIONAL CONFERENCE ON OPERATING SYSTEMS AND SOFTWARE ENGINEERING
Bangkok, Thailand
Information: <https://www.waset.org/conference/2018/08/bangkok/ICOSSE>
- 30 – Sep 3 INTERNATIONAL SUMMER SCHOOL “SUPRAMOLECULAR CHEMISTRY IN MEDICINE AND IN TECHNOLOGY: ADVANCES AND CHALLENGES”
Varna, Bulgaria
Information: <http://supramedchem.orgchm.bas.bg>

September 2018

- 2 – 6 SMARTER 6 meeting
Ljubljana, Slovenia
Information: <https://smarter6.ki.si/>

- 2 – 6 EUROPEAN CONFERENCE ON RESEARCH IN CHEMICAL EDUCATION (ECRICE)
Warsaw, Poland
Information: <http://www.ecrice2018.pl/>
- 2 – 6 EFMC-ISMIC 2018 – XXV EFMC INTERNATIONAL SYMPOSIUM ON MEDICINAL CHEMISTRY
Ljubljana, Slovenia
Information: www.efmc-ismc.org
- 2 – 7 69TH ANNUAL MEETING OF THE INTERNATIONAL SOCIETY OF ELECTROCHEMISTRY
Bologna, Italy
Information: <http://annual69.ise-online.org/>
- 2 – 7 32ND CONFERENCE OF EUROPEAN COLLOID AND INTERFACE SOCIETY (ECIS)
Ljubljana, Slovenia
Information: <http://ecis2018.fkkt.uni-lj.si/index.html>
- 3 – 7 25TH INTERNATIONAL CONFERENCE ON HIGH RESOLUTION MOLECULAR SPECTROSCOPY – BILBAO 2018
Bilbao, Spain
Information: <http://www.chem.uni-wuppertal.de/conference/>
- 4 – 7 12TH CONFERENCE ON POLYMER-SOLVENT COMPLEXES AND INTERCALATES (POLYSOLVAT-12)
Grenoble, France
Information: <https://iupac.org/event/12th-conference-polymer-solvent-complexes-intercalates-polysolvat-12/>
- 4 – 7 N-LIGANDS2018 – 7TH EuCheMS CONFERENCE ON NITROGEN-LIGANDS
Lisbon, Portugal
Information: <http://www.n-ligands2018.com/>
- 5 – 7 ADVANCED INORGANIC MATERIALS GREEN AND UNCONVENTIONAL SYNTHESIS APPROACHES AND FUNCTIONAL ASSESSMENT (AIM 2018)
Padova, Italy
Information: <http://www.chimica.unipd.it/silvia.gross/workshop/home.html>
- 5 – 7 TBMCE 2018 – THE FIRST INTERNATIONAL CONFERENCE ON TECHNOLOGIES AND BUSINESS MODELS FOR CIRCULAR ECONOMY
Portorož, Slovenia
Information: <https://tbmce.um.si>
- 5 – 8 15TH EURASIA CONFERENCE ON CHEMICAL SCIENCES
Rome, Italy
Information: <http://www.eurasia2018.org>
- 9 – 12 24TH CONFERENCE ON ISOPRENOIDS
Białystok, Poland
Information: <https://isoprenoids-24.uwb.edu.pl/>
- 9 – 12 12TH EUROPEAN SYMPOSIUM ON BIOCHEMICAL ENGINEERING SCIENCES
Lisbon, Portugal
Information: <http://esbes2018.org/>
- 9 – 12 16TH EUROPEAN CONFERENCE ON MIXING
Toulouse, France
Information: <http://inpact.inp-toulouse.fr/MIXING16/>
- 9 – 13 EUROPEAN CORROSION CONGRESS
Prague, Czech Republic
Information: <http://www.eurocorr2018.org/>
- 9 – 14 8TH IUPAC INTERNATIONAL CONFERENCE ON GREEN CHEMISTRY
Bangkok, Thailand
Information: <http://www.greeniupac2018.com>

- 10 – 14 9TH INTERNATIONAL CONFERENCE FOR CONVEYING AND HANDLING OF PARTICULATE SOLIDS
London, UK
Information: <http://www.constableandsmith.com/events/chops-2018/>
- 13 – 15 2ND EDITION OF GLOBAL CONFERENCE ON CATALYSIS, CHEMICAL ENGINEERING & TECHNOLOGY (CAT-2018)
Rome, Italy
Information: <https://catalysis-conferences.magnusgroup.org/>
- 16 – 19 DISTILLATION & ABSORPTION CONFERENCE 2018
Florence, Italy
Information: <http://www.aidic.it/da2018/>
- 16 – 21 22ND INTERNATIONAL CONFERENCE ON ORGANIC SYNTHESIS (22-ICOS)
Florence, Italy
Information: <http://www.22-icos-florence.it>
- 16 – 21 13TH INTERNATIONAL CONFERENCE ON SOLID STATE CHEMISTRY
Pardubice, Czech Republic
Information: <http://www.ssc-conference.com/2018/>
- 17 – 18 4TH INTERNATIONAL CONFERENCE ON CHEMICAL ENGINEERING
Vancouver, Canada
Information: <https://chemicalengineering.conferenceseries.com/>
- 18 – 21 11TH INTERNATIONAL DRYING SYMPOSIUM
Valencia, Spain
Information: <http://www.ids2018.webs.upv.es/>
- 19 – 21 SLOVENIAN CHEMICAL SOCIETY ANNUAL MEETING 2018
Portorož, Slovenia
Information: <http://chem-soc.si/scs-annual-meeting-2018>
- 19 – 21 17TH RUŽIČKA DAYS »TODAY SCIENCE - TOMORROW INDUSTRY«
Vukovar, Croatia
Information: <http://www.ptfos.unios.hr/ruzicka/2014/>
- 19 – 22 25TH CONGRESS OF THE SOCIETY OF CHEMISTS AND TECHNOLOGISTS OF MACEDONIA
Ohrid, Macedonia
Information: <http://www.sctm.mk/congress/index.php/SCTM/25Congress>
- 24 – 27 XII ITALIAN FOOD CHEMISTRY CONGRESS (CHIMALI 2018)
Camerino, Italy
Information: <http://chimali2018.unicam.it/>
- 30 – Okt. 3 5TH INTERNATIONAL SYMPOSIUM ON GREEN CHEMISTRY, SUSTAINABLE DEVELOPMENT AND CIRCULAR ECONOMY
Skiathos island, Greece
Information: <http://greenchem5.civil.auth.gr/>
- 30 – Okt. 4 13TH CONFERENCE ON SUSTAINABLE DEVELOPMENT OF ENERGY, WATER AND ENVIRONMENT SYSTEMS - SDEWES CONFERENCE
Palermo, Italy
Information: <http://www.palermo2018.sdewes.org>

October 2018

- 4 – 5 2ND SYMPOSIUM ON ORGANIC AND INORGANIC CHEMISTRY, SOUTHERN AFRICA
Gaborone, Botswana
Information: https://www.chalmers.se/en/conference/Organic_Inorganic_Chemistry
- 4 – 5 INTERNATIONAL SUSTAINABLE PRODUCTION AND CONSUMPTION CONFERENCE
Manchester, UK
Information: <http://www.icheme.org/ispc>

- 7 – 12 27TH EUCHEMS CONFERENCE ON MOLTEN SALTS AND IONIC LIQUIDS (EUCHEMSIL2018)
Lisboa, Portugal
Information: <http://www.euchemsil2018.org/>
- 10 – 12 EAST-WEST CHEMISTRY CONFERENCE 2018 (EWCC2018)
Lviv, Ukraine
Information: <http://ewcc2018.org/>
- 14 – 17 4TH INTERNATIONAL CONFERENCE ON BIOINSPIRED AND BIOBASED CHEMISTRY & MATERIALS
Nice, France
Information: <http://www.unice.fr/nice-conference/>
- 14 – 18 14TH IUPAC INTERNATIONAL CONGRESS OF PESTICIDE CHEMISTRY
Rio de Janeiro, Brazil
Information: <https://iupac.org/event/14th-iupac-international-congress-of-pesticide-chemistry/>
- 16 – 19 IBERO AMERICAN CHEMISTRY CONGRESS
Lima, Peru
Information: <http://sqperu.org.pe/congreso-2018/>
- 18 – 19 INTERNATIONAL WORKSHOP ON ENERGETIC MATERIALS
Istanbul, Turkey
Information: <http://iwem2018.istanbul.edu.tr>
- 19 – 21 3RD INTERNATIONAL CONGRESS OF CHEMISTS AND CHEMICAL ENGINEERS OF BOSNIA AND HERZEGOVINA
Sarajevo, Bosnia and Herzegovina
Information: <http://www.pmf.unsa.ba/hemija/kongres/index.php/en>
- 21 – 24 15TH INTERNATIONAL CONFERENCE ON MICROREACTION TECHNOLOGY
Karlsruhe, Germany
Information: <http://dechema.de/en/IMRET2018.html>
- 24 – 25 IES2018 – 25TH SEMINAR AND SYMPOSIUM ON INFORMATION AND EXPERT SYSTEMS IN THE PROCESS INDUSTRIES
Belgrade, Serbia
Information: <http://bg.ac.rs/en/members/faculties/FTM.php>
- 28 – 31 XXIX INTERAMERICAN CONGRESS OF CHEMICAL ENGINEERING INCORPORATING THE 68TH CANADIAN CHEMICAL ENGINEERING CONFERENCE
Toronto, Canada
Information: <http://www.csche2018.ca/>

November 2018

- 4 – 7 2018 – SUSTAINABLE INDUSTRIAL PROCESSING SUMMIT
Rio de Janeiro, Brazil
Information: <https://www.flogen.org/sips2018/>
- 4 – 8 EMERGING POLYMER TECHNOLOGIES SUMMIT
Hanoi, Vietnam
Information: <http://emts18.org/index.html>
- 5 – 7 MicrobiotaMi 2018
Milano, Italy
Information: <https://microbiotami.com/>
- 5 – 9 XXIII INTERNATIONAL CONFERENCE ON CHEMICAL REACTORS
Ghent, Belgium
Information: http://conf.nsc.ru/CR_23/en/

- 7 – 9 14TH INTERNATIONAL CONFERENCE ON POLYSACCHARIDES-GLYCOSCIENCE
(14TH ICPG)
Praha, Czech Republic
Information: <http://www.polysaccharides.csch.cz/index.html>
- 25 – 29 30TH INTERNATIONAL SYMPOSIUM ON THE CHEMISTRY OF NATURAL PRODUCTS
AND THE 10TH INTERNATIONAL CONGRESS ON BIODIVERSITY
Athens, Greece
Information: <http://www.iscnp30-icob10.org/>

2019

January 2019

- 29 IYPT2019 OPENING CEREMONY
Paris, France
Information: <http://www.iypt2019.org/>

February 2019

- 12 EMPOWERING WOMEN IN CHEMISTRY: A GLOBAL NETWORKING EVENT
Online
Information: <https://iupac.org/100/global-breakfast/>

March 2019

- 31 – Apr. 4 AIChE SPRING MEETING 2019 AND 15TH GLOBAL CONGRESS ON PROCESS SAFETY
New Orleans, USA
Information: <https://www.aiche.org/conferences/aiche-spring-meeting-and-global-congress-on-process-safety/2019>

May 2019

- 19 – 24 14TH IUPAC INTERNATIONAL CONGRESS OF CROP PROTECTION CHEMISTRY
Ghent, Belgium
Information: <https://www.iupac2019.be>

June 2019

- 2 – 6 14TH INTERNATIONAL SYMPOSIUM ON MACROCYCLIC AND SUPRAMOLECULAR
CHEMISTRY
Lecce, Italy
Information: <https://ismsc2019.eu/>
- 16 – 19 LOSS PREVENTION 2019
Delft, The Netherlands
Information: <http://lossprevention2019.org/>
- 16 – 20 17TH INTERNATIONAL CONFERENCE ON CHEMISTRY AND THE ENVIRONMENT
– ICCE2019
Thessaloniki, Greece
Information: <http://www.euchems.eu/events/17th-international-conference-chemistry-environment-icce2019/>

- 16 – 20 12TH IWA INTERNATIONAL CONFERENCE ON WATER RECLAMATION AND REUSE
Berlin, Germany
Information: <http://efce.info/IWA+Conference+2019.html>
- 26 – 28 THERMODYNAMICS 2019
Huelva, Spain
Information: <http://efce.info/Thermodynamics+2019.html>
- 26 – 30 6TH EUROPEAN CONFERENCE ON ENVIRONMENTAL APPLICATIONS OF
ADVANCED OXIDATION PROCESSES (EAAOP-6)
Portorož, Slovenia
Information: <http://eaaop6.ki.si/>

July 2019

- 1 – 3 CONGRESS ON NUMERICAL METHODS IN ENGINEERING
Guimarães, Portugal
Information: www.cmn2019.pt
- 5 – 12 IUPAC 2019 PARIS FRANCE
Paris, France
Information: <https://www.iupac2019.org/>
- 21 – 26 THE 18TH INTERNATIONAL SYMPOSIUM ON NOVEL AROMATIC COMPOUNDS
(ISNA-18)
Sapporo City, Japan
Information: <https://iupac.org/event/18th-international-symposium-novel-aromatic-compounds-isna-18/>
- 30 – Aug. 1 8TH INTERNATIONAL CONFERENCE FOR NETWORK FOR INTER-ASIAN CHEMISTRY
EDUCATORS (NICE)
Taipei, Taiwan
Information: <https://iupac.org/event/8th-international-conference-network-inter-asian-chemistry-educators/>

September 2019

- 15 – 19 11TH EUROPEAN CONGRESS OF CHEMICAL ENGINEERING – ECCE11 &
4TH EUROPEAN CONGRESS OF APPLIED BIOTECHNOLOGY – ECAB5
Florence, Italy
Information: http://efce.info/ECCE12_ECAB5-p-112545.html
- 25 – 27 SLOVENIAN CHEMICAL SOCIETY ANNUAL MEETING 2019
Maribor, Slovenia
Information: <http://chem-soc.si/slovenski-kemijski-dnevi-2019>

Acta Chimica Slovenica

Author Guidelines

Submissions

Submission to ACSi is made with the implicit understanding that neither the manuscript nor the essence of its content has been published in whole or in part and that it is not being considered for publication elsewhere. All the listed authors should have agreed on the content and the corresponding (submitting) author is responsible for having ensured that this agreement has been reached. The acceptance of an article is based entirely on its scientific merit, as judged by peer review. There are no page charges for publishing articles in ACSi. The authors are asked to read the Author Guidelines carefully to gain an overview and assess if their manuscript is suitable for ACSi.

Additional information

- Citing spectral and analytical data
- Depositing X-ray data

Submission material

Typical submission consists of:

- full manuscript (PDF file, with title, authors, abstract, keywords, figures and tables embedded, and references)
- supplementary files
 - **Full manuscript** (original Word file)
 - **Statement of novelty** (Word file)
 - **List of suggested reviewers** (Word file)
 - **ZIP file containing graphics** (figures, illustrations, images, photographs)
 - **Graphical abstract** (single graphics file)
 - **Proposed cover picture** (optional, single graphics file)
 - **Appendices** (optional, Word files, graphics files)

Incomplete or not properly prepared submissions will be rejected.

Submission process

Before submission, authors should go through the checklist at the bottom of the page and prepare for submission.

Submission process consists of 5 steps.

Step 1: Starting the submission

- Choose one of the journal sections.
- Confirm all the requirements of the **checklist**.
- Additional plain text comments for the editor can be provided in the relevant text field.

Step 2: Upload submission

- Upload full manuscript in the form of a Word file (with title, authors, abstract, keywords, figures and tables embedded, and references).

Step 3: Enter metadata

- First name, last name, contact email and affiliation for all authors, in relevant order, must be provided. Corresponding author has to be selected. Full postal address and phone number of the corresponding author has to be provided.

- **Title and abstract** must be provided in plain text.
- Keywords must be provided (max. 6, separated by semicolons).
- Data about contributors and supporting agencies may be entered.
- **References** in plain text must be provided in the relevant text field.

Step 4: Upload supplementary files

- Original Word file (original of the PDF uploaded in the step 2)
- **Statement of novelty** in a Word file must be uploaded
- All **graphics** have to be uploaded in a single ZIP file. Graphics should be named Figure 1.jpg, Figure 2.eps, etc.
- **Graphical abstract image** must be uploaded separately
- **Proposed cover picture** (optional) should be uploaded separately.
- Any additional **appendices** (optional) to the paper may be uploaded. Appendices may be published as a supplementary material to the paper, if accepted.
- For each uploaded file the author is asked for additional metadata which may be provided. Depending of the type of the file please provide the relevant title (Statement of novelty, List of suggested reviewers, Figures, Graphical abstract, Proposed cover picture, Appendix).

Step 5: Confirmation

- Final confirmation is required.

Article Types

Feature Articles are contributions that are written on editor's invitation. They should be clear and concise summaries of the most recent activity of the author and his/her research group written with the broad scope of ACSi in mind. They are intended to be general overviews of the authors' subfield of research but should be written in a way that engages and informs scientists in other areas. They should contain the following (see also general directions for article structure in ACSi below): (1) an introduction that acquaints readers with the authors' research field and outlines the important questions to which answers are being sought; (2) interesting, new, and recent contributions of the author(s) to the field; and (3) a summary that presents possible future directions. Manuscripts normally should not exceed 40 pages of one column format (letter size 12, 33 lines per page). Generally, experts in a field who have made important contribution to a specific topic in recent years will be invited by an editor to contribute such an **Invited Feature Article**. Individuals may, however, send a proposal (one-page maximum) for an Invited Feature Article to the Editor-in-Chief for consideration.

Scientific articles should report significant and innovative achievements in chemistry and related sciences and should exhibit a high level of originality. They

should have the following structure:

1. Title (max. 150 characters),
2. Authors and affiliations,
3. Abstract (max. 1000 characters),
4. Keywords (max. 6),
5. Introduction,
6. Experimental,
7. Results and Discussion,
8. Conclusions,
9. Acknowledgements,
10. References.

The sections should be arranged in the sequence generally accepted for publications in the respective fields and should be successively numbered.

Short communications generally follow the same order of sections as Scientific articles, but should be short (max. 2500 words) and report a significant aspect of research work meriting separate publication. Editors may decide that a Scientific paper is categorized as a Short Communication if its length is short.

Technical articles report applications of an already described innovation. Typically, technical articles are not based on new experiments.

Preparation of Submissions

Text of the submitted articles must be prepared with Microsoft Word. Normal style set to single column, 1.5 line spacing, and 12 pt Times New Roman font is recommended. Line numbering (continuous, for the whole document) must be enabled to simplify the reviewing process. For any other format, please consult the editor. Articles should be written in English. Correct spelling and grammar are the sole responsibility of the author(s). Papers should be written in a concise and succinct manner. The authors shall respect the ISO 80000 standard [1], and IUPAC Green Book [2] rules on the names and symbols of quantities and units. The Système International d'Unités (SI) must be used for all dimensional quantities.

Graphics (figures, graphs, illustrations, digital images, photographs) should be inserted in the text where appropriate. The captions should be self-explanatory. Lettering should be readable (suggested 8 point Arial font) with equal size in all figures. Use common programs such as MS Excel or similar to prepare figures (graphs) and ChemDraw to prepare structures in their final size. Width of graphs in the manuscript should be 8 cm. Only in special cases (in case of numerous data, visibility issues) graphs can be 17 cm wide. All graphs in the manuscript should be inserted in relevant places and **aligned left**. The same graphs should be provided separately as images of appropriate resolution (see below) and submitted together in a ZIP file (Graphics ZIP). Please do not submit figures as a Word file. In **graphs**, only the graph area determined by both axes should be in the frame, while a frame around the whole graph should be omitted. The graph area should be white. The legend should be inside the graph area. The style of all graphs should be the same. **Figures and illustrations** should be of sufficient quality for the printed version, i.e. 300 dpi minimum. **Digital images and photographs** should be of high quality (minimum 250 dpi resolution). On submission, figures should be of good enough resolution to be assessed by the referees, ideally as JPEGs. High-resolution figures (in JPEG,

TIFF, or EPS format) might be required if the paper is accepted for publication.

Tables should be prepared in the Word file of the paper as usual Word tables. The captions should appear above the table and should be self-explanatory.

References should be numbered and ordered sequentially as they appear in the text, likewise methods, tables, figure captions. When cited in the text, reference numbers should be superscripted, following punctuation marks. It is the sole responsibility of authors to cite articles that have been submitted to a journal or were in print at the time of submission to ACSi. Formatting of references to published work should follow the journal style; please also consult a recent issue:

1. J. W. Smith, A. G. White, *Acta Chim. Slov.* **2008**, *55*, 1055–1059.
2. M. F. Kemmere, T. F. Keurentjes, in: S. P. Nunes, K. V. Peinemann (Ed.): *Membrane Technology in the Chemical Industry*, Wiley-VCH, Weinheim, Germany, **2008**, pp. 229–255.
3. J. Levec, Arrangement and process for oxidizing an aqueous medium, US Patent Number 5,928,521, date of patent July 27, **1999**.
4. L. A. Bursill, J. M. Thomas, in: R. Sersale, C. Collela, R. Aiello (Eds.), *Recent Progress Report and Discussions: 5th International Zeolite Conference*, Naples, Italy, 1980, Gianini, Naples, **1981**, pp. 25–30.
5. J. Szegezdi, F. Cszimadia, Prediction of dissociation using microconstants, http://www.chemaxon.com/conf/Prediction_of_dissociation_constant_using_microconstants.pdf, (assessed: March 31, 2008)

Titles of journals should be abbreviated according to Chemical Abstracts Service Source Index (CASSI).

Special Notes

- Complete characterization, **including crystal structure**, should be given when the synthesis of new compounds in crystal form is reported.
- Numerical **data should be reported with the number of significant digits corresponding to the magnitude** of experimental uncertainty.
- **The SI system of units and IUPAC recommendations** for nomenclature, symbols and abbreviations should be followed closely. Additionally, the authors should follow the general guidelines when citing spectral and analytical data, and depositing crystallographic data.
- **Characters** should be correctly represented throughout the manuscript: for example, 1 (one) and l (ell), 0 (zero) and O (oh), x (ex), D7 (times sign), B0 (degree sign). Use Symbol font for all Greek letters and mathematical symbols.
- The rules and recommendations of the **IUBMB** and the **International Union of Pure and Applied Chemistry (IUPAC)** should be used for abbreviation of chemical names, nomenclature of chemical compounds, enzyme nomenclature, isotopic compounds, optically active isomers, and spectroscopic data.
- **A conflict of interest** occurs when an individual (author, reviewer, editor) or its organization is involved in multiple interests, one of which could possibly corrupt the motivation for an act in the

other. Financial relationships are the most easily identifiable conflicts of interest, while conflicts can occur also as personal relationships, academic competition, etc. **The Editors** will make effort to ensure that conflicts of interest will not compromise the evaluation process; potential editors and reviewers will be asked to exempt themselves from review process when such conflict of interest exists. When the manuscript is submitted for publication, **the authors** are expected to disclose any relationships that might pose potential conflict of interest with respect to results reported in that manuscript. In the Acknowledgement section the source of funding support should be mentioned. The statement of disclosure must be provided as Comments to Editor during the submission process.

- **Published statement of Informed Consent.** Research described in papers submitted to ACSi must adhere to the principles of the Declaration of Helsinki (<http://www.wma.net/e/policy/b3.htm>). These studies must be approved by an appropriate institutional review board or committee, and informed consent must be obtained from subjects. The Methods section of the paper must include: 1) a statement of protocol approval from an institutional review board or committee and 2), a statement that informed consent was obtained from the human subjects or their representatives.
- **Published Statement of Human and Animal Rights.** When reporting experiments on human subjects, authors should indicate whether the procedures followed were in accordance with the ethical standards of the responsible committee on human experimentation (institutional and national) and with the Helsinki Declaration of 1975, as revised in 2008. If doubt exists whether the research was conducted in accordance with the Helsinki Declaration, the authors must explain the rationale for their approach and demonstrate that the institutional review body explicitly approved the doubtful aspects of the study. When reporting experiments on animals, authors should indicate whether the institutional and national guide for the care and use of laboratory animals was followed.
- To avoid conflict of interest between authors and referees we expect that not more than one referee is from the same country as the corresponding author(s), however, not from the same institution.
- Contributions authored by **Slovenian scientists** are evaluated by non-Slovenian referees.
- Papers describing **microwave-assisted reactions** performed in domestic microwave ovens are not considered for publication in *Acta Chimica Slovenica*.
- *Manuscripts that are **not prepared and submitted** in accord with the instructions for authors are not considered for publication.*

Appendices

Authors are encouraged to make use of supporting information for publication, which is supplementary material (appendices) that is submitted at the same time as the manuscript. It is made available on the Journal's web site and is linked to the article in the

Journal's Web edition. The use of supporting information is particularly appropriate for presenting additional graphs, spectra, tables and discussion and is more likely to be of interest to specialists than to general readers. When preparing supporting information, authors should keep in mind that the supporting information files will not be edited by the editorial staff. In addition, the files should be not too large (upper limit 10 MB) and should be provided in common widely known file formats to be accessible to readers without difficulty. All files of supplementary materials are loaded separately during the submission process as supplementary files.

Proposed Cover Picture and Graphical Abstract Image

Graphical content: an ideally full-colour illustration of resolution 300 dpi from the manuscript must be proposed with the submission. Graphical abstract pictures are printed in size 6.5 x 4 cm (hence minimal resolution of 770 x 470 pixels). Cover picture is printed in size 11 x 9.5 cm (hence minimal resolution of 1300 x 1130 pixels)

Authors are encouraged to submit illustrations as candidates for the journal Cover Picture*. The illustration must be related to the subject matter of the paper. Usually both proposed cover picture and graphical abstract are the same, but authors may provide different pictures as well.

* The authors will be asked to contribute to the costs of the cover picture production.

Statement of novelty

Statement of novelty is provided in a Word file and submitted as a supplementary file in step 4 of submission process. Authors should in no more than 100 words emphasize the scientific novelty of the presented research. Do not repeat for this purpose the content of your abstract.

List of suggested reviewers

List of suggested reviewers is a Word file submitted as a supplementary file in step 4 of submission process. Authors should propose the names, full affiliation (department, institution, city and country) and e-mail addresses of three potential referees. Field of expertise and at least two references relevant to the scientific field of the submitted manuscript must be provided for each of the suggested reviewers. The referees should be knowledgeable about the subject but have no close connection with any of the authors. In addition, referees should be from institutions other than (and preferably countries other than) those of any of the authors.

How to Submit

Users registered in the role of author can start submission by choosing USER HOME link on the top of the page, then choosing the role of the Author and follow the relevant link for starting the submission process. Prior to submission we strongly recommend that you familiarize yourself with the ACSi style by browsing the journal, particularly if you have not submitted to the ACSi before or recently.

Correspondence

All correspondence with the ACSi editor regarding the paper goes through this web site and emails. Emails are sent and recorded in the web site database. In the correspondence with the editorial office please provide ID number of your manuscript. All emails you receive from the system contain relevant links. **Please do not answer the emails directly but use the embedded links in the emails for carrying out relevant actions.** Alternatively, you can carry out all the actions and correspondence through the online system by logging in and selecting relevant options.

Proofs

Proofs will be dispatched via e-mail and corrections should be returned to the editor by e-mail as quickly as possible, normally within 48 hours of receipt. Typing errors should be corrected; other changes of contents will be treated as new submissions.

Submission Preparation Checklist

As part of the submission process, authors are required to check off their submission's compliance with all of the following items, and submissions may be returned to authors that do not adhere to these guidelines.

1. The submission has not been previously published, nor is it under consideration for publication in any other journal (or an explanation has been provided in Comments to the Editor).
2. All the listed authors have agreed on the content and the corresponding (submitting) author is responsible for having ensured that this agreement has been reached.
3. The submission files are in the correct format: manuscript is created in MS Word but will be **submitted in PDF** (for reviewers) as well as in original MS Word format (as a supplementary file for technical editing); diagrams and graphs are created in Excel and saved in one of the file formats: TIFF, EPS or JPG; illustrations are also saved in one of these formats. The preferred position of graphic files in a document is to embed them close to the place where they are mentioned in the text (See **Author guidelines** for details).
4. The manuscript has been examined for spelling and grammar (spell checked).
5. The **title** (maximum 150 characters) briefly explains the contents of the manuscript.
6. Full names (first and last) of all authors together with the affiliation address are provided. Name of author(s) denoted as the corresponding author(s), together with their e-mail address, full postal address and telephone/fax numbers are given.
7. The **abstract** states the objective and conclusions of the research concisely in no more than 150 words.
8. Keywords (minimum three, maximum six) are provided.
9. **Statement of novelty** (maximum 100 words) clearly explaining new findings reported in the manuscript should be prepared as a separate Word file.
10. The text adheres to the stylistic and bibliographic requirements outlined in the **Author guidelines**.
11. Text in normal style is set to single column, 1.5 line spacing, and 12 pt. Times New Roman font is

recommended. All tables, figures and illustrations have appropriate captions and are placed within the text at the appropriate points.

12. Mathematical and chemical equations are provided in separate lines and numbered (Arabic numbers) consecutively in parenthesis at the end of the line. All equation numbers are (if necessary) appropriately included in the text. Corresponding numbers are checked.
13. Tables, Figures, illustrations, are prepared in correct format and resolution (see **Author guidelines**).
14. The lettering used in the figures and graphs do not vary greatly in size. The recommended lettering size is 8 point Arial.
15. Separate files for each figure and illustration are prepared. The names (numbers) of the separate files are the same as they appear in the text. All the figure files are packed for uploading in a single ZIP file.
16. Authors have read **special notes** and have accordingly prepared their manuscript (if necessary).
17. References in the text and in the References are correctly cited. (see **Author guidelines**). All references mentioned in the Reference list are cited in the text, and vice versa.
18. Permission has been obtained for use of copyrighted material from other sources (including the Web).
19. The names, full affiliation (department, institution, city and country), e-mail addresses and references of three potential referees from institutions other than (and preferably countries other than) those of any of the authors are prepared in the word file. At least two relevant references (important papers with high impact factor, head positions of departments, labs, research groups, etc.) for each suggested reviewer must be provided.
20. Full-colour illustration or graph from the manuscript is proposed for graphical abstract.
21. **Appendices** (if appropriate) as supplementary material are prepared and will be submitted at the same time as the manuscript.

Privacy Statement

The names and email addresses entered in this journal site will be used exclusively for the stated purposes of this journal and will not be made available for any other purpose or to any other party.

ISSN: 1580-3155

Koristni naslovi

Slovensko kemijsko društvo
Slovenian Chemical Society



Slovensko kemijsko društvo

www.chem-soc.si

e-mail: chem.soc@ki.si



Wessex Institute of Technology

www.wessex.ac.uk



SETAC

www.setac.org



European Water Association

<http://www.ewa-online.eu/>



European Science Foundation

www.esf.org



European Federation of Chemical Engineering

<https://efce.info/>



IUPAC

INTERNATIONAL UNION OF
PURE AND APPLIED CHEMISTRY

International Union of Pure and Applied Chemistry

<https://iupac.org/>

Novice evropske zveze kemijskih društev (EuCheMS) najdete na:



EuCheMS: Brussels News Updates

<http://www.euchems.eu/newsletters/>



DONAU LAB Ljubljana
Member of LPPgroup

Donau Lab d.o.o., Ljubljana
Tbilisjska 85
SI-1000 Ljubljana
www.donaulab.si
office-si@donaulab.com

Planetarni centrifugalni mikser **ARM-310CE**

Brezkontaktno mešanje in disperzija

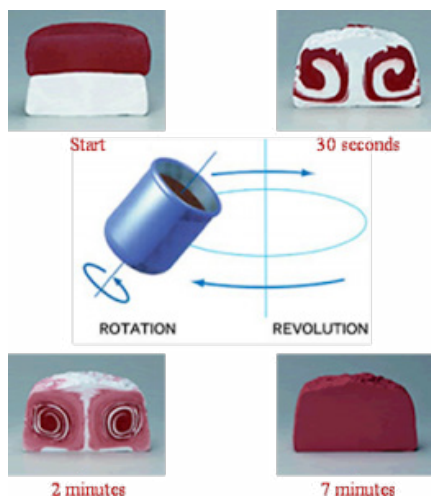
Tudi za zelo viskozne materiale

Širok spekter uporabe

Atraktivna cena



THINKY





SLOVENSKI KEMIJSKI DNEVI 2018

PLENARNI PREDAVATELJI



prof. dr. Markus Antonietti

Max-Planck inštitut, Potsdam,
Nemčija



prof. dr. Paolo Fornasiero

Univerza v Trstu, Italija



prof. dr. Zdravko Kravanja

Fakulteta za kemijo in kemijsko
tehnologijo, Univerza v Mariboru



prof. dr. Janez Plavec

Kemijski inštitut, Ljubljana



Slovensko kemijsko društvo
Slovenian Chemical Society

REGISTRACIJE: <http://www.chem-soc.si/slovenski-kemijski-dnevi-2018>

BODITE NEUSTAVLJIVI

MAGNEZIJ Krka 300



Granulat za pripravo napitka vsebuje magnezijev citrat in vitamin B₂.



Magnezij in vitamin B₂ prispevata k zmanjšanju utrujenosti in izčrpanosti ter normalnemu delovanju živčnega sistema.



Magnezij prispeva tudi k delovanju mišic.



www.magnezijkrka.si

- ✔ Okus po pomaranči in limeti. ✔ Brez konzervansov.
- ✔ Brez umetnih barvil, arom in sladil. ✔ Ena vrečka na dan.

Prehransko dopolnilo ni nadomestilo za uravnoteženo in raznovrstno prehrano. Skrbite tudi za zdrav življenjski slog.

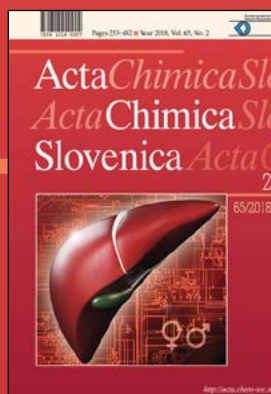
NOVO

 KRKA

ActaChimicaSlovenica

ActaChimicaSlovenica

LiverSex presents the first multi-tissue and multi-level computational metabolic model, which is able to describe the sexual aspects in hepatic metabolism. *LiverSex* is able to provide detailed insights into gender dependent complex liver pathologies in liver-related disease development and progression. (see page 253)



Year 2018, Vol. 65, No. 2

